Control Aspects of a Full–body Enhancive Robotic Exoskeleton

Maciej Grzegorz Napora

Submitted in accordance with the requirements for the degree of

Doctor of Philosophy

The University of Leeds

School of Mechanical Engineering

Institute of Design, Robotics and Optimisation

April 2019

Acknowledgements

"Standing on the shoulders of giants."

First and foremost, I would like to thank my parents Dorota and Grzegorz for their support during writing this thesis. I am grateful to Prof. Abbas Dehghani for managing the project with kindness and Mr Robert Bloomfield of Mechatech for supporting it. I also wish to thank Thomas Magill for his indispensable help with technical aspects. I owe special recognition for him, Dr Pourshid Jan Fani and Mr Konstantinos Drosos, my colleagues, for splendid atmosphere of cooperation. I would like to thank as well Dr Jongrae Kim for his supervision.

Maciej Napora

The candidate confirms that the work submitted is his own and that appropriate credit has been given where reference has been made to the work of others.

Abstract

A robotic exoskeleton is a solution that would help maintain the level of daily life and professional activities of a user when she/he gets older. Moreover, in industries such as heavy construction, assembling or warehouses, the use of enhancive exoskeletons by able-bodied will add efficiency premium due to partial automation of processes and decrease likelihood and cost of work related injuries. Another expected area of application of exoskeletons are search and rescue situations in confined spaces, where the heavy equipment cannot access. Based on the literature review, currently, a gap in the knowledge of controlling of such devices for civilian applications exists.

Control requirements for the robotic exoskeletons are specified and different control laws (Master–Slave Position Control, Direct and Indirect Force Control laws) are evaluated against them. Force Control laws are shown to be superior.

A motion capture study was conducted and requirements for bandwidth of upper and lower extremities, from which limits on electronics bandwidth and control algorithm sample rate are derived, was determined to be less than 10 Hz. Control electronics and torque control algorithm (required by Force Control laws) for a novel design of an enhancive exoskeleton joint are proposed and developed. The design comprises two identical hydraulic cylinders opposing each other and connected by a link. Such arrangement allows for greater range of motion of the joint, e.g. when used as a knee joint.

The simulation with gait as an input trajectory shows that the developed coupled control of actuators allows for minimisation of directly measured human–machine interaction force, while maintaining synchronous extension of the piston rods of the two actuators. A model–based selection was performed to find acceptable controller settings. The control strategy requires only one load cell and one linear variable differential transducer, hence decreasing the cost of hardware.

The simulated control algorithm was validated experimentally on a prototype of a single joint and robotic knee connected in parallel for emulation of gait. A full body enhancive robotic exoskeleton model, with contact to the ground, was investigated for stability during gait. Shape and design of contact surface were evaluated.

Contents

List of Figures

List of Tables

Nomenclature

$\alpha, \beta, \mu, \eta, \varepsilon, \gamma, \delta, \iota$ angle

$\ddot{x}$	second time derivative of x
ΔE^{met}	change of metabolic energy of the operator
Δx	change of x variable
$\dot{x}$	first time derivative of x
$\mathbb{R}$	set of real numbers
$\mathcal{A}$	area
$\mathcal{L}$	Lagrangian of manipulator
$\mathcal{V}$	volume
ν	torque at a human–machine interaction point
Ω_X^Y	rotation matrix, transforms vector representation from frame of reference X to representation in frame of reference Y
τ	torque at rotary joint of a machine
τ_{act}	torque due to actuator
τ_{des}	desired value of torque
τ_{dist}	torque due to disturbance
τ_{HM}	torque due to human
$\tilde{x}$	filtered value of x
ϱ	pressure

$\|x\|$	denotes absolute value of x
a, b, c, d, e, l	length
$a \cdot b$	dot product between a and b
$a \times b$	if a and b are vectors, $\times$ denotes a cross product; if a and b are scalar, it denotes simply multiplication of scalars
$A^\top$	if A is matrix, the symbol denotes its transpose
A^{-1}	if A is a square matrix, the symbol denotes its inverse
$C(\theta, \dot{\theta})$	centrifugal and Coriolis acceleration terms vector
DoF	degree of freedom
EGU	engineering unit
F	force
F/T	force/torque
F^{dem}	demanded value of force
f_{act}	cutoff frequency of middle–level force controller with knee cap stabilisation pertaining to force control
f_{kc}	cutoff frequency of middle–level force controller with knee cap stabilisation pertaining to positioning
g	gravity acceleration, about 9.81m/s^2
$G(s), H(s)$	transfer function
J_P	Jacobian of manipulator
K	feedback gain matrix of the middle–level controller
k	gain of middle–level controller
k_p, k_d, k_i	proportional, derivative, integral gain of PID controller for knee cap stabilisation
k_{kc}	gain of the coupled low–level controller pertaining to knee cap positioning

k_{pp}, k_{ii}, k_{dd}	proportional, derivative, integral gain of PID controller for low–level force control
m	mass
$M(\theta)$	kinetic energy matrix (inertia matrix)
N_{filt}	inverse of time constant for low–pass first order filter of PID controller for knee cap stabilisation
N_{nfilt}	inverse of time constant for low–pass first order filter of PID controller for low–level force control
q	flow
r	extension of rod of hydraulic actuator
$R(\theta)$	torque induced at joints of the machine due to gravitation
r_{err}	error of extension of hydraulic pistons, misalignment from synchronous extension
s	complex number frequency parameter in Laplace transform
T	time constant
t	time variable
t_s	settling time
u	control signal
$up,\ low$	upper, lower respectively
x_{sp}	spool displacement in servo–valve
θ	vector of manipulator configuration space angles, rotation at manipulator joints)
Ξ	vector denoting force acting at a human–machine interaction point and torque acting on exoskeleton segment
p	vector denoting position coordinates of interaction points and orientation of exoskeleton segment

$\hat{R}(\theta)$	torque calculated by the controller to cancel dynamic effects of the gravity
$R(\theta)$	torque induced at joints of the manipulator due to gravitation
ADC	Analogue Digital Converter
DAC	Digital Analogue Converter
FC	Force Control
FoR	Frame of Reference
GRF	Ground Reaction Force
LVDT	Linear Variable Differential Transducer
MSPC	Master–Slave Position Control

Chapter 1

Introduction

1.1 Background

The first reported attempts to build a device actively amplifying human strength and endurance which couples with portions of human body date back to the 1960s. *Mizen* of Cornell Aeronautical Laboratory designed a non–powered, full–body structure which kinematics were compliant with human body ranges of motion [5, 6]. General Electric, in cooperation with US governmental institutions, followed similar direction of building "man amplifiers" resulting in a prototype called Hardiman I [7–9]. The device consisted of two overlapping suits, an inner structure used for capturing rotational position of human joints (master) and an outer powered load bearing exoskeletal structure (slave). The device did not meet the project objectives, and was not reported to walk. There are no reported attempts to built similar device from 1970s until the year 2000, in which *Kazerooni*'s research group focused their research on lower body load carrying wearable robots. As a result a prototype named Berkeley Lower Extremity Exoskeleton (BLEEX) was conceived [10–15]. The device employed a novel control scheme called *Virtual Torque Control* [16–19], which allowed it to follow a user while he[1] walked with minimal extra effort whilst carrying approx. 50 kg of payload mounted as a backpack. Supported by the US Departament of Defence, Berkeley Bionics (UC Berkely's spin off company) designed military field–deployable lower body exoskeletons: ExoHiker and ExoClimber (2005) [20]; and Human Universal Load Carrier (2008), which was demonstrated to carry up to 90 kg of payload without impeding wearer's moves as well as to decrease metabolic cost of the user [21, 22]. HULC technology was licensed to the Lockheed Martin with an intention of further field–ready military development.

[1] *he* = *she* and *his* = *her* are used throughout this report irrespective of the subject's gender

In 2005 *Jacobsen* et al. of Sarcos presented a full–body load–bearing enhancive exoskeleton named XOS created with financial support from Defense Advanced Research Projects Agency programme *Exoskeletons for Human Performance Augmentation* [23]. The device has been intended to be used in logistics to reduce both strain and exertion of the military personnel for tasks involving repetitive heavy lifting. It is capable of carrying up to 90 kg of load attached to a robot's manipulator guided by body of the operator. In 2010 Sarcos, after becoming a part of the Raytheon corporation, revealed next generation of the exoskeleton named XOS 2 with a plan of the tethered device entering the military service in 2015 [24–26]. Also in 2010, PERCRO's Body Extender designed with support from the Italian Ministry of Defense was unveiled. It is a full–body, load–bearing, all joints actuated, enhancive exoskeleton for material handling capable of lifting up to 100 kg held in robot upper extremities manipulators [27–29]. The control system was designed to allow for natural moves of the user whilst maintaining the balance of the robot by means of controlling the Zero–Moment Point (ZMP). A user enclosed in the exoskeleton was able to perform restricted moves, natural walking pattern was not achieved.

A separate class of exoskeletons comprises devices that assist human muscular system by providing assisting torque to the joints. *Yamamoto* et al. of Kanagawa Institute of Technology developed a full–body, muscle hardness sensing exoskeleton for assisting nurses in lifting patients from a bed [30–33]. *Pratt* developed an active knee brace named RoboKnee [34]. The device produced torque for assistance (empowering wearer) during walking, climbing and descending stairs and squatting. *Kong* of Sogang University developed (2005) lightweight (3 kg) exoskeleton connected to a caster walker for assistance during walking and standing up for elderly and patients named EXPOS [35, 36]. The device was governed by a fuzzy controller taking as inputs muscle hardness measured by inflatable sensors. The second generation of the exoskeleton was named SOBAR (2008) and was actuated by DC motors with high gear reduction ratio for higher torque production [37–39]. *Sankai*, *Kawamoto* et al. of Sankai Laboratory at University of Tsukuba developed a lower extremities assistive exoskeleton named Hybrid Assistive Limb (HAL). The HAL's controller governs the device using myoelectrical signals obtained from the wearer's body, ground reaction force (GRF) as well as kinematic parameters obtained from the device [40–49]. It was demonstrated to lower electrical activity of the muscles (fatigue) for tasks involving walking, climbing stairs and standing up. Several other versions of HAL were also developed. A device with controller able to reproduce walking patterns triggered by user intention for walking

support of paraplegics was built [50]. Single legged version of the device was created for restoration of motor functions for hemiplegic and monoplegic patients immobilised by stroke [51, 52] and poliomyelitis [53]. The developers also presented upper extremities exoskeleton for assistance of reaching movement during meal consumption [54, 55]. A full–body version for heavy work (e.g. lifting patients nursing personnel during hygiene activities) was constructed [56, 57]. In the early 2010's HAL was successfully applied to rehabilitation of patients after stroke, which was attributed largely to the EMG feedback in the control mechanism [58, 59]. A stepwise process for robot development and confirmatory trials in clinical environment was proposed as a reconciliation of differences between robot development process and methods used in medicine [60, 61]. As a result of these efforts, HAL for Medical Use - Lower Limb Model by *Sankai's* and *Kawamoto's* spin–off company Cyberdyne Inc. was certified for conformance with the requirements of Medical Device Directives in the European Union [62].

Exoskeletons have also been present in the medical field as rehabilitation and orthotic devices for patients with musculoskeletal disorders since early 1970's: *Grundmann* of Winsconsin University under supervision of *Seireg* [63]; *Vukobratović* et al. of "Milhailo Pupin" Institute in Belgrade [64]. *Vukobratović*'s lower body active orthoses were tethered and allowed an operator supported by crutches to move by means of following predefined gait patterns. The control algorithm of the device employed a novel concept for device stabilisation named the *zero–moment point* (ZMP) [65]. The devices, although being a limited success, spurred development of control algorithms of bipedal walking robots, which later became fundamental to the field [66]. Also NASA has been working on assistive/rehabilitation lower–body exoskeleton that can be used for exercising the astronauts in the state of zero gravity [67].

At the time when this document is written, the exoskeleton technology has matured and devices are available for customers to be rented. It has been manifested in February 2014 in publication of safety standard for personal care robots in which exoskeletons for welfare are also included [68]. The very first wearable robot to obtain the certification was two legged version of HAL for assistance in daily life activities with intention to be manufactured by the *Cyberdyne* [62], which was made possible based on research into safety of non–medical personal care robots [69].

1.2 Motivation for Research

The population projection for the Organisation for Economic Co–operation and Development countries shows that the number of people aged between 20–49 will decrease by 2% by the year 2025 (from 518 mln in year 2014), whilst the number of those aged 50 and above will grow by 19% (from 401 mln) [70]. The ageing of workforce and society in general will have unprecedented impact on economy of developed countries. Exoskeleton is a solution that would help maintain the level of daily life and professional activities of a user while he gets older. Moreover, in industries such as heavy construction, assembling or logistics use of enhancive exoskeletons by able bodied will add efficiency premium due to partial automation of processes and decrease likelihood and cost of work related injuries. Another expected area of application of exoskeletons are search and rescue situations in cases were the heavy equipment cannot access the confined or remote spaces as well as when the response time is essential.

Enhancive exoskeletons like BLEEX or Sarcos XOS after initial phase of development were licensed to military companies and their details became confidential. Nonetheless, the same technology might be applied to aforementioned civilian applications, yet currently a gap in understanding and in the art of controlling of such devices exists. Sarcos XOS was reported mainly in the media, and no information on control of Sarcos, apart from the patents [24, 71], is published. It is however certain that the device employs plurality of multi–axis force sensors providing information about human–operator interaction force for governing the robot based on the *Direct Force Control* law [71] (see section 2.5.1). Selection of such sensors and the control law imposes restrictions on the human–machine interface. Moreover, commercially available F/T sensors are expensive (over £6,000 per sensor [72]) and most likely overengineered for the application. On the other end of the spectrum is well–documented BLEEX, which governed by the *Virtual Torque Control* (see section 2.5.3) and does not require measurement of the interaction force, thus allows for more flexible frame design. However robustness and stability of this model–based control law is an issue [14, 17–19]. Moreover the *Virtual Torque Control* has not yet been applied for activities other than walking, specifically no attempt to building a device which is a full–body exoskeleton with upper extremities involved in variety of tasks has been reported. Understanding of allowable and required properties of the interaction between a full–body exoskeleton and the user upper extremities is therefore limited. In contrast to the assistive exoskeletons, which naturally can be divided into segments acting on single joint (for example different embodiments of HAL from full–body [56, 57] to single legged [51] –

see sections 1.1, 2.9), to the best of author's knowledge the modularity of control law of enhancive, load–bearing exoskeletons has not yet been investigated, however full–body extender by PERCRO is made of modular frame segments with the actuators built–in [27–29]. Also, since an exoskeleton encloses a human, safety of operation is a paramount. The standard [68] (see Appendix C) gives general notions about safety of wearable robots for welfare, but information on solutions providing safe operation of enhancive exoskeletons is limited. For example impedance of BLEEX lower–body exoskeleton increases when robot approaches configuration in which it is not possible to maintain balance [15, claim 15], [16], whereas NTU exoskeleton [73–75] and PERCRO Body Extender [28, 29] rely on control of ZMP to prevent robot from tripping.

Taking into consideration the urgency and expected benefits of exoskeletal devices to the society, the author research interest is motivated by the importance of problems in the domain of control that need to be tackled before the technology could be made widespread.

1.3 Aims and Objectives

1.3.1 Aims

- To identify challenges in control of an enhancive full–body exoskeleton for human power amplification and design a dynamic model addressing these.

- To provide control strategy for a novel design of a joint for an enhancive exoskeleton coupling with the operator's body segments.

1.3.2 Objectives

To meet the aims mentioned above, the following objectives are defined for this research:

- Establish requirements for an enhancive full–body exoskeleton, with focus on control aspects.
- Survey potential control strategies for the entire robot, establish the most appropriate candidate for the considered device.
- Conduct motion capture study to gather biometric kinematic and dynamic data.
- Choose sensors and control electronics for a novel single joint prototype with hydraulic actuation. Develop electronics and software for the platform.
- Construct control–oriented model of the single joint prototype and simulate the

proposed controller with input data from motion capture study. Evaluate performance of the controller, select its parameters and assess its stability.

- Validate the joint design and control strategy on a prototype.
- Construct a model of a full–body load–bearing exoskeleton with the aim of allowing it to walk, based on biometric data from motion capture.

1.4 Scope of the Research

This research presents a design process of an enhancive full–body exoskeleton. The scope of the project is limited to:

- establishment of requirements for an enhancive full–body exoskeleton
- evaluation of control strategies against requirements
- development of a control strategy for a novel exoskeleton joint design actuated with hydraulic cylinders
- development of electronics interfacing with sensors and executing proposed control algorithm
- validation and verification of the joint design with the controller on a prototype
- development of a full–body exoskeleton model and evaluation of its simulation walking

1.5 Contribution of the Research

The proposed novel control algorithm, although developed for an enhancive full–body exoskeleton, can be potentially used in any machine requiring control of torque produced at a rotary joint, such as a robot manipulator with force controlled interaction with environment.

The simulation of the entire model showed feasibly of such structure to perform gait, although mass of entire structure can be a limiting factor for sagittal stability. Detailed contributions of this research work are as follows:

1. Following system engineering approach, requirements for a full–body enhancive exoskeleton were gathered and derived. Contending control strategies were evaluated against these. Control strategies based on control of machine–interaction

force were assessed to be superior to *Master Slave Position Control*, which matches angles at the joint of exoskeleton to angles of joints of operator.

2. Data from motion capture study was analysed. The bandwidth of motion of a human for all performed tasks, including walking, but excluding running, was assessed to be less than 10 Hz. This was established as well for upper extremities, which was not found in literature before. If running is considered, the bandwidth of motion was assessed to be 40 Hz.

3. An algorithm for governance of a single exoskeleton joint with two hydraulic actuators was simulated and shown to minimise human–machine interaction force during gait. The maximum interaction forces are not excessive. It was demonstrated that the controller allows for synchronous extension of rods of the actuators. The proposed coupled control uses only one linear variable differential transducer and one load cell for measurement of force exerted by actuators. Therefore, it reduces cost of equipment. The force control of hydraulic cylinders is considered to be difficult, so the results of controlling coupled actuators contributes to the body of knowledge.

4. The coupled control algorithm parameters were selected to minimise cost functions: (1) total energy transferred between the robot and operator; (2) integral of human–machine interaction force

5. It was shown experimentally on the prototype that the control electronics with the coupled controller algorithm implemented allows for minimisation of human–machine interaction within movement range of the joint. Synchronous extension of hydraulic rods was maintained. Displacement was emulated using a robotic knee to examine performance of the controller for slow displacement first. Secondly, load of 60 kg was attached to a link of the prototype (close to its free moving end). Prototype was displaced by hand with bandwidth of 0.6 Hz, touching a handle connected to a F/T sensor. It was shown that force exerted by an operator does not exceed 30 N. That translates to force amplification of about 20:1, which is similar to reported performance of existing exoskeletons.

6. A model of an enhancive exoskeleton was simulated for gait. A platform coupling with a foot with a heel and curved front allowing for roll over was demonstrated to allow for most natural gait pattern. It was established that a force has to be exerted by an operator to allow for sagittal stability of the device. Force of 600

N is required to maintain sagittal stability for a model of weight of 175 kg. Total mass of the device is therefore a limiting factor for mobility of the device.

1.6 Outline of the Thesis

The thesis is organized and divided into eight chapters. The chapter number and title are depicted in the flowchart as shown in Fig. 1.1 and the outline of each chapter is summarised below:

In **chapter 1** introduction to the background, motivation, aims and objectives for the development of a full–body enhancive exoskeleton are provided. Furthermore, the chapter describes the scope and the contributions of this research.

In **chapter 2** literature on control of exoskeletons is covered. Control goals of exoskeletons are outlined. Force control laws are explained in detail. Emphasis is put on enhancive devices and design consideration behind the described control laws. Details on control algorithms for existing devices (BLEEX, Sarcos XOS, HAL) are given.

In **chapter 3**, following the system engineering approach, requirements elicited in course of the project meetings are listed and control laws are evaluated against them.

In **chapter 4** a novel mechanical design of a joint for an enhancive exoskeleton is described. Hydraulic system overview is given. Requirements for control of electronics are derived for sensors from the joint design and for bandwidth from motion capture study. Sensors are chosen for the design. Electronics and software design meeting the requirements is proposed.

In **chapter 5** control goals for governing the novel joint prototype are outlined. Middle level controller for two opposing linear actuators connected using knee cap is described and simulated with input data from the motion capture study. It allows for minimisation of human–machine interaction force measured using force/torque sensor. In principle, *Direct Force Control* law with modification for synchronisation of linear displacement of actuators is used. A low level control, named coupled control is proposed. It allows for actuators to produce required torque at a joint, whilst maintaining synchronisation of extension of actuators, when model of hydraulic circuit is included. It has an advantage of using reduced number of instrumentation. Performance of the machine is shown, and parameters of controller are selected to minimise control goals.

In **chapter 6** the proposed middle level controller with coupled control at lowest level is validated and verified. Experiments are conducted with a robotic knee emulating operators knee. Load up to 60 kg is attached and it is shown that the force felt by

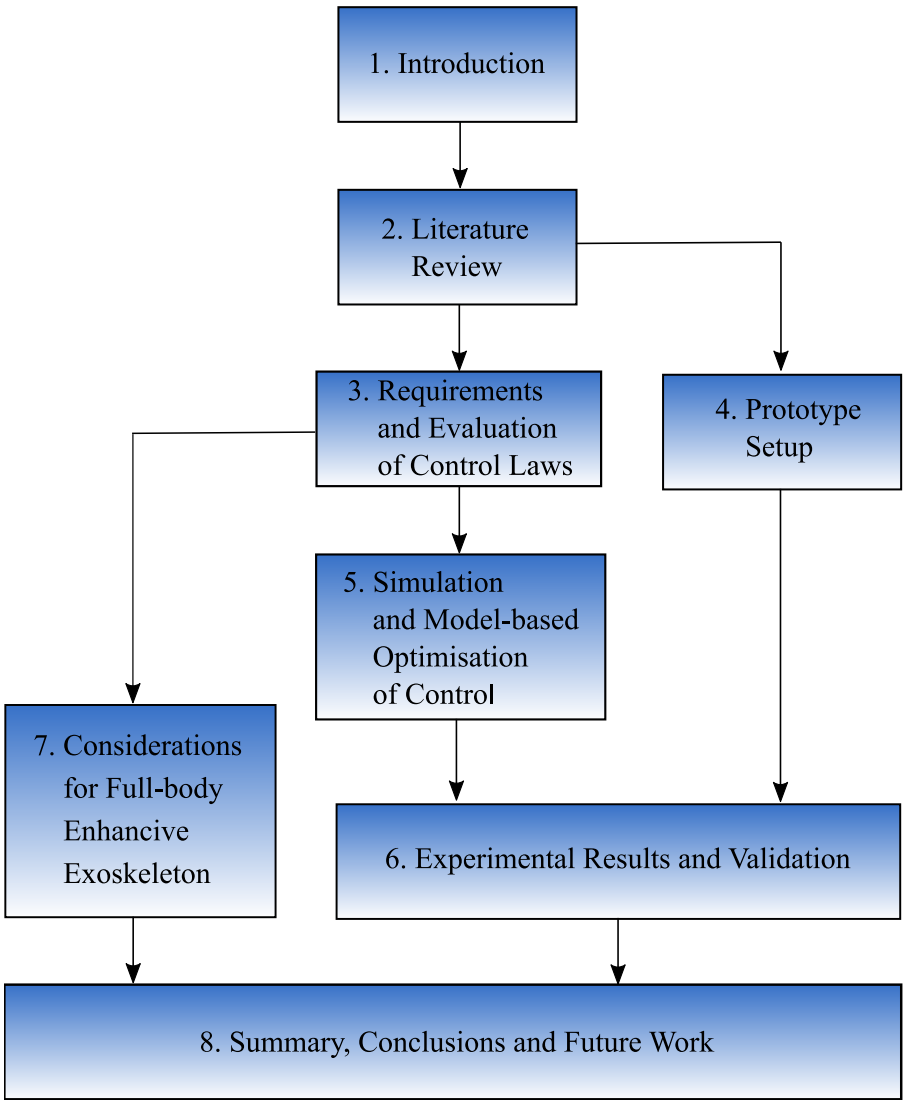

Figure 1.1: Flowchart of the thesis organization.

operator is scaled down 20 times.

In **chapter 7** a model of a full–body exoskeleton is proposed and simulated using kinetic and dynamic data from the motion capture study. 3 designs of platform are proposed and evaluated. Sagittal stability of the entire model is evaluated.

In **chapter 8** a summary of the research work reported in this thesis is provided, highlighted are the main contributions and it presents the recommendations for future work.

The report is supplemented by Appendices, most importantly **Appendix A** in which control goals for exoskeletons are explained, and **Appendix C** in which safety of the devices is considered.

Chapter 2

Literature Review

2.1 Introduction

This chapter is intended to provide literature review on exoskeletons. The emphasis is put on control laws of enhancive devices. Firstly, human body treated as a physical object is described from a point of view of the properties recognised in the design process of exoskeletons (section 2.2). Secondly, control laws and their design considerations are discussed in general (sections 2.3, 2.4, 2.5 and 2.8). Lastly, state–of–the–art enhancive (BLEEX in section 2.6 and XOS in section 2.7) and assistive exoskeletons (HAL–3 in section 2.9) are described in detail. In section 2.10 criterion for maintaining dynamic balance (postural stability) employing notion of Zero–Moment Point is outlined.

2.2 Human Body

For the purpose of governance of an exoskelton, the human body–exoskeleton system is treated as a cybernetic system. Two objects are coupled and mutually affect each other through power and information exchange. The exoskeleton is a machine that can be described in engineering terms but the other object, that is human body, is far more complex than any human creation. In order to describe and quantify human locomotion for the engineering purpose, a new domain applying mechanistic paradigm called biomechanics emerged on brink of medical discipline of physiology [76]. Drawing from the domain, input–output pairs in the human body–exoskeleton system can be identified and a proper human–machine interface in the form of a measurement system and robot's structure can be designed.

Human body is capable of numerous manoeuvres in the environment using both

lower and upper extremities as well as the core. Among all of those, the task of walking is the most basic [77], [76]. To realise this aspect of human locomotion the lower–body part of the exoskeleton is coupled with the user for the purpose of gait augmentation or restoration. Thus understanding of the gait process is paramount for designing an exoskeleton. During walking, the majority of human segments displacement occurs in the sagittal plane. The main joints involved in walking are the hip, knee and the ankle, which is built of the talocrural (flexion–extension) and the subtalar joint (inversion–eversion). In Fig. 2.1 a cycle of normal gait is depicted. Most generally operation of a leg in normal gait in a healthy person can be divided into two phases with different functions: the stance phase (approx. 62% of the gait cycle duration) and the swing phase (approx. 38%). An exoskeleton system, in order to realise control, has to follow or aid the legs for each of the functions. Moreover, it can be observed that equivalent kinematic chain to human legs changes its configuration [76, 77]. During the swing phase of any of the legs an open kinematic chain is formed, whereas during so called double support phase a closed kinematic chain is formed (total approx. 24 %). The situation directly affects dynamics of the system. It is then beneficial to recognise which leg is in contact with the ground. A biological parameter suitable for that is the Ground Reaction Force (GRF, also called Floor Reaction Force – FRF). During the stance phase the centre of GRF shifts from a heel to toes [77], [78] (see Fig. 2.2), so not only binary information about contact with the ground can be retrieved but also periods of the gait cycle can be recognised. Several sensors for GRF measurement have developed. For example, in Fig. 2.3 a GRF sensor used in HAL–3 is depicted. In Figs. 2.4a and 2.4b similar sensors used in BLEEX are shown. The highest levels of GRF occur at the heel and the ball of the foot, that is where measuring elements are placed.

In contrast to the lower extremities, usually the upper extremities are involved in a much more diverse range of tasks requiring interaction with numerous objects, tools and living organisms [76]. There are also given greater manoeuvrability. For that reason it is more advisable to analyse their biomechanics in context of the task they are intended to perform. Nonetheless, movement in each joint in the body is caused by forces acting on nearby bones [76]. In Fig. 2.5 forces actuating a joint are depicted. Straightening movement (extension) is caused by a muscle named an extensor acting with force F_{ext}. Bending movement (flexion) is caused by an antagonistic muscle called extensor acting with force F_{flex}. The net torque at the joint τ is also affected by gravitation (G), environment interaction (F_{hum}) and joint reaction (R) forces against which muscles counteract to displace portion of the body to a desired position. However not

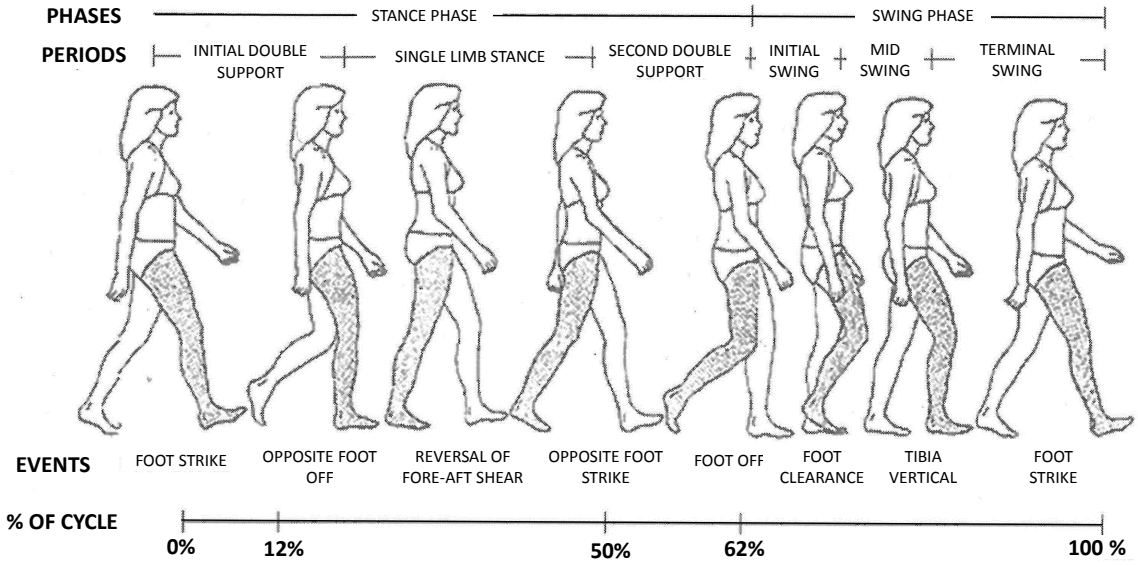

Figure 2.1: Normal gait cycle [77].

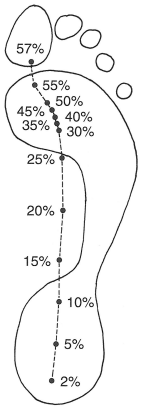

Figure 2.2: Ground Reaction Force centre during walking [76].

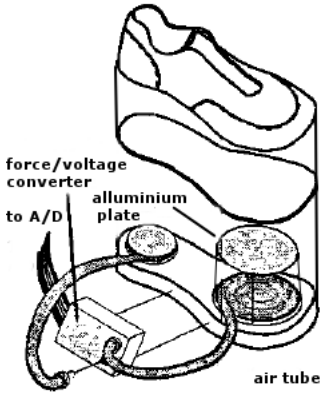

Figure 2.3: GRF sensor of HAL–3 [45].

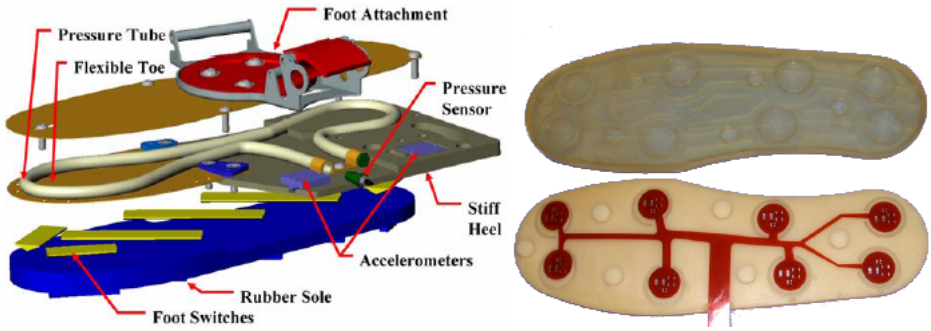

(a) (b)

Figure 2.4: Two version of GRF sensor of BLEEX: a) with switches and tube [12], b) with MEMS sensors [79].

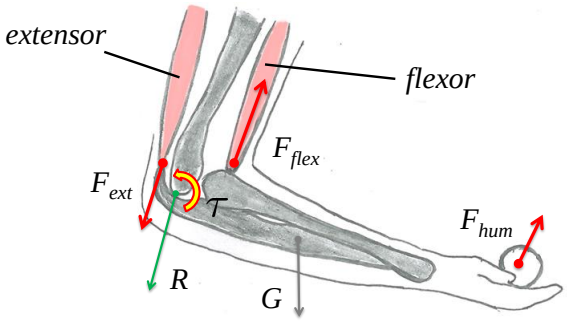

Figure 2.5: Forces acting at a human joint.

only always true [41], in the most common mode of operation, when flexor exerts a force the extensor relaxes and vice versa. This involuntary reflex is called *the reciprocal inhibition* or *the stretch reflex* and is governed by the nervous system [78].

Muscle system is governed by a nervous system that excites muscle to perform a desired task. During the force exertion a phenomenon of bioelectricity[1] generation occurs. The electromyographic (EMG) signals have properties naturally predisposing them for estimation of muscle activity, that is "...during isometric contractions, a linear proportionality exists among a corresponding quantified EMG measure and the registered force" [78]. Bioelectric signal frequency spectrum is in a range from 10 to 500 Hz, with the dominant components in the 50 to 150 Hz range [78]. The amplitude ranges from 0 to 6 mV peak–to–peak (0 to 1.5 mV RMS). Muscles activity estimation during locomotion using bioelectricity has had however several drawbacks:

- existance of electrodes placed directly on the human skin
- "no universally accepted method of measurement, processing, and quantification of EMG signals[...]
- during movement, the relationship of EMG/force cannot be described by linear algebraic equations.
- the choice and location of electrodes and the applied processing methods have a significant role in the evaluation of the EMG/force relationship." [78]

Despite the disadvantages, EMG signals have been used in HAL for governance of the exoskeleton (see section 2.9). Recently electrodes capable of sensing the bioelectric signals through clothing were developed for that purpose [80,81].

[1]The analysis of bioelectric activity of muscles in the time domain is called electromyography (EMG), hence bioelectric signals are more commonly referred to as EMG signals

2.3 Overview of Control Systems of Exoskeletons

2.3.1 Control Goals

The general concept of an active exoskeleton as a device working in parallel with a human body is understood intuitively. The main distinctions between an enhancive and an assistive exoskeleton are the control goals the device is intended to meet. For the purpose of this report following definitions are taken into consideration:

assistive exoskeleton – a device that produces torque assisting human *muscular system* confinable to each joint in performing certain activities[2].

enhancive exoskeleton – a device that transfers majority of the force resulting from its own mass or inertia as well as from the interaction with an external load or inertia to the base (ground), rather than to the user body, thus supports *musculoskeletal system* of human in performing certain tasks[3].

In Fig. 2.6 general schemes for power and information exchange in assistive and enhancive exoskeletons are depicted. Enhancive exoskeleton forms a barrier between the user and the environment changing properties of the interaction, whilst the assistive one aids the user during the interaction with the environment through power production. With respect to that, assistive exoskeletons act like extra muscles.

The question arises how the general ideas of e.g. *shadowing* human movements translate into engineering terms. Moreover, what is *natural*, *comfortable* or *indifferent* for an able–bodied person in their late teens or early 20's, whose body and motor control are characterised by the plasticity of the early maturity phase of ontogenesis, might be perceived as a hassle for an elderly person. The allowable value of measure of comfort (control goal) is then a subjective measure influenced by both the physical and psychological factors.

It is accepted that for a lower extremity orthosis the difference between measured metabolic cost (oxygen consumption/carbon dioxide production) with and without orthosis performing a certain task is a "good determinant of an energetic advantage" provided by the device [82]. *Popović* considers also the heart rate [83]. On the other

[2] This definition is taken after *Kong* [38], see Fig. 2.24. Note that such device can exert extra stress on the skeletal system or soft tissues of the user.

[3] This definition is similar to *Kazerooni's* understanding of exoskeletons for human performance augmentation [22]. Since the control system of the device diminishes the interaction of the musculoskeletal system of an operator with the environment, it allows for much greater human body augmentation as observed from the outside of the human–robot system.

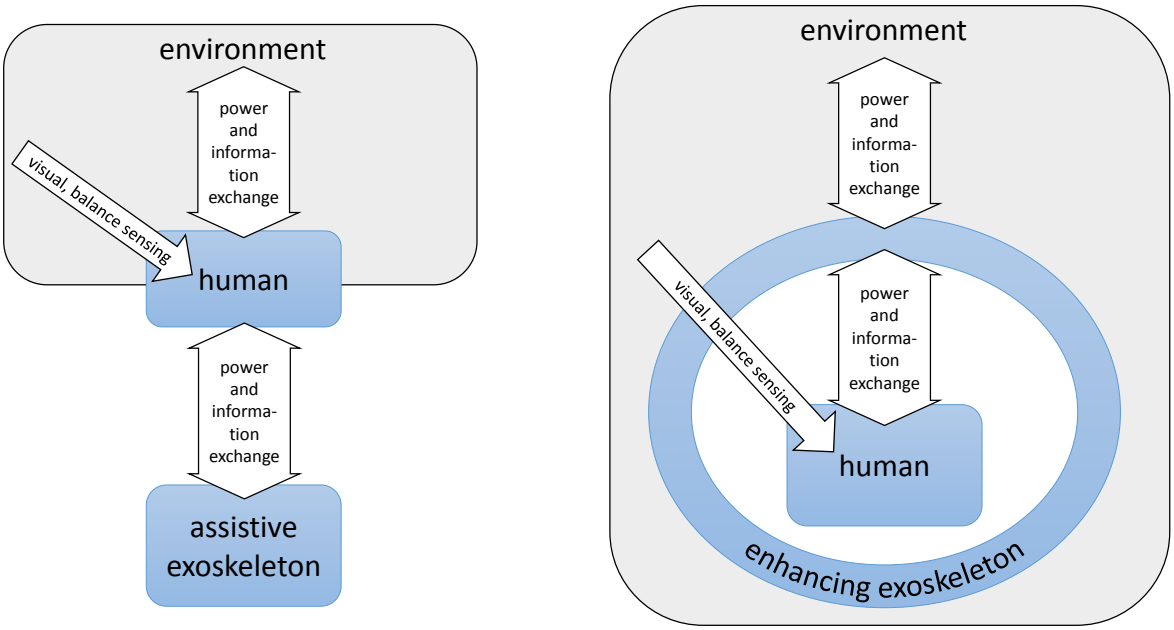

Figure 2.6: Power and information exchange in assistive and enhancive exoskeletons. (a) assistive exoskeleton, (b) enhancive exoskeleton

hand, developers of HAL system use parameters based on electromyography (EMG) to assess the level of effort (added or diminished), which the device exerts on the user [45]. Two elementary questions are immediately identified:

- Can the measures for performance of the lower body exoskeletal devices be applied to the upper body as well?
- What are the other objective measures for the performance of the full–body exoskeletons?

In the engineering approach, the initial step in the control system design process of any machine is usually the establishment of the control goals [84] (see Fig. A.1). In Appendix A possible control goals for full–body exoskeletons that correspond to the general ideas describing behaviour of exoskeletons are explained. Those are:

- to increase [85], decrease (see section 2.9), maintain metabolic cost of mechanical work of musculoskeletal system (see section 2.6 and 2.7)
- to decrease of metabolic cost of isometric force production of musculoskeletal system
- reproduction of movement trajectory of user (see section 2.4)
- lowering of human body internal forces
- lowering of stress within exoskeleton structure [57]

– lowering of power consumption of the exoskeleton

It is a trivial statement that human body is a mechanical system and the same laws of physics apply to it on the macro–level as to the other physical bodies. The listed control goals are based on these basic laws as well as on knowledge from more specialised medical domains, i.e. human physiology, metabolism and biomechanics.

2.3.2 Control System Structures

Based on distinction of the aspect of human locomotion being measured, the types of control systems of existing exoskeletons can be generalised into two main groups:

– control system based on kinematic (position) and kinetic (force) data,
– control system based on electric activity of muscles (EMG).

In Fig. 2.7a the control system utilising kinetic and kinematic data as a feedback signal is depicted. Based on concious user intention or involuntary reflexes, the nervous system generates a signal to activate a particular groups of muscles. The signal propagates along path of a nerve. After some delay resulting from biochemical properties of the nervous tissue and length of the nerve, the muscle is activated, which results in force exerted by the muscle. The force puts portion of a body in motion or causes a force to be exerted on the environment or encompassing exoskeleton. This (kinetic and kinematic) effects can be measured and based upon them, controller can calculate commands to guide actuators to achieve a desirable control objective of the machine (e.g. minimisation of human–machine interaction force). In the middle of the control system diagram is a an added. It represents interaction of two properties of the same type, being subject to physical principle of superposition of force or addition of displacement. Two feedback loops exist. One consists of the exoskeleton, mentioned adder, exoskeleton sensory system, and controller. These are closed into of feedback loop The second loop is human nervous system, body, human sensory system and the mentioned adder. Feedback is realise by means of measurement of external forces, position of body or some object by human sensory system (e.g. by sense of sight. In other words: data, which encompass “movement geometry, forces and moments that are exerted when the body and its surroundings interact”, can be used to determine the state of the human body (for example by solving the inverse kinematics problem) [78]. Basing on the computed information a control unit can produce control signal to actuators of an exoskeletal device. That way, for example, the follow–up control strategy or *shadowing* of user's

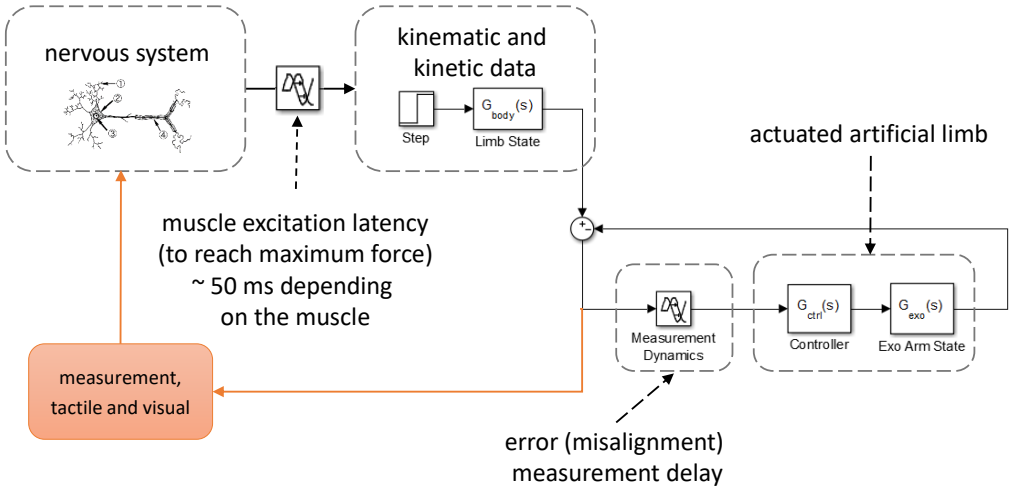

(a)

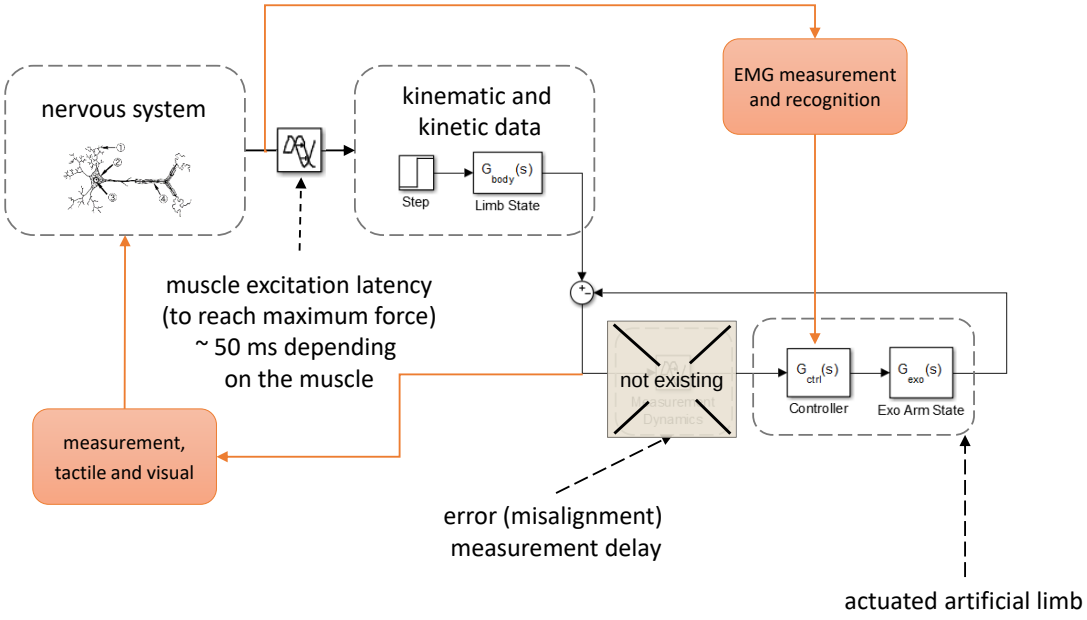

(b)

Figure 2.7: Generalised structure of control systems used in exoskeletal devices. (a) Control system based on kinetic and kinematic data. (b) Control system based on electromyography (EMG).

actions can be accomplished. The implementation of this approach introduces challenges which stem from the fact that human body is a convoluted structure consisting of a tangled network of bones, muscles and tendons with a layer of soft tissues on top of it, which can be approximated as a rigid kinematic chain only to a certain degree. Moreover, in order to tackle the complexity of the considered structure, whilst being as non–invasive as possible, the measurement system itself introduces both mechanical as well as electrical complications. That way, the sensory system is expected to be a source of measurement errors in forms of unintended displacement of the sensors caused by the fact that attachment of the objects to the human skin might be unreliable.

The problems with capturing human locomotion are considered in the section 2.4, where master–slave position control is described. *Racine* believes [16] that these problems were critical for failure of the pioneering approach to construction of an exoskeleton called the Hardiman [7].

In the desirable case, the measurement system would introduce only linear dynamics. In the even more desired case, its dynamics would be neglected. Methods of analysis of such systems and controller synthesis for them are well established in the domain of control engineering, so the problem becomes simplified. This statement sets a strong direction for the design of the measurement system and the frame.

Developers of the BLEEX, being aware of these difficulties, propose a control system which does not include "...direct measurements from the operator or from where the operator contacts the exoskeleton" [13]. This control law is called *Vitrual Joint Torque Control*. It is considered in depth in sections 2.5.3 and 2.6. Instead, the controller estimates properties of human–machine interaction based on sensors mounted on the frame. The control scheme employed allows the device to "shadow the wearer's voluntary and involuntary movements". Authors point out that in order to allow such configuration to be used its "sensitivity to operator's forces and torques" must be high. In general, such property is undesirable due to the fact that "a high gain could cause instability or poor responsiveness" [84].

The difficulties discussed in the previous paragraphs can be circumvented by implementation of an alternative control scheme based on the measurement of electromyographic potentials. The block diagram representing the control scheme employing EMG is depicted in Fig. 2.7b. In this scheme, there is no signal in the exoskeleton system from the adder realising superposition. Measurement system of kinetic or kinematic data does not exist. The exoskeleton controller guides the actuators based on activity of the muscles. The feedback loop is closed through measurement of nervous system

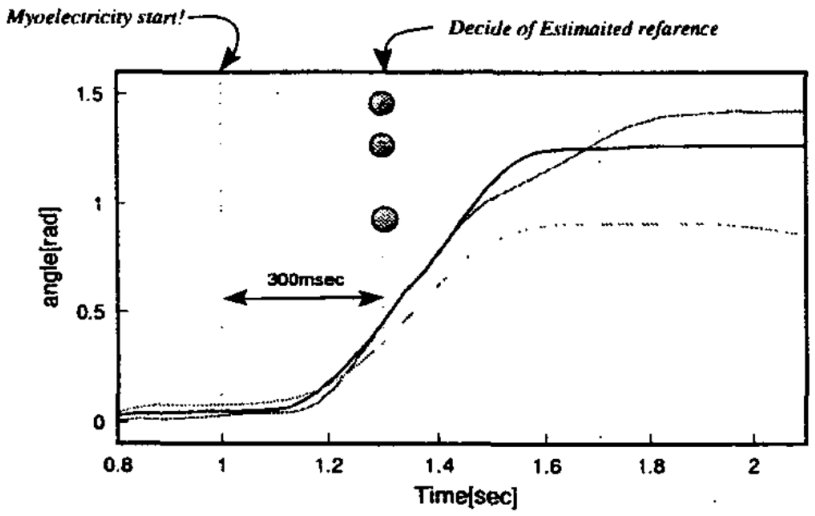

Figure 2.8: EMG signal and angle of joint [40].

activity, rather the results of this activity on the adder as in Fig. 2.8. In this scheme, the feedback loop is closed primarily through the neuromuscular system of the user. For example, developers of HAL introduced a method of controlling assistive exoskeleton using the EMG (so called Cybernics Voluntary Control, see section 2.9). They confirmed that the bioelectric signal precedes the force generation by a muscle prducing flexion of muscle [40] (see Fig. 2.8).

The generalised structure of an controller for exoskeletal devices is depicted in Fig. 2.9 (compare it for example to Fig. 2.31). At the lowest level, the control is realised by sub–controller of an actuator. The set–point for that sub–controller is given by an intermediate level, in which entire machine is governed using a task–appropriate control *regime*. For a different task, a different *regime* or different set of settings within the same control structure is applied. That switching is realised based on a decision of the top–layer controller. On that level, comparing certain signals to thresholds [12,16–19,41,42,45,46,48,86], or employing a classifier based on methods of artificial intelligence [87] the user intention is recognised.

2.4 Master–Slave Position Control

The most straightforward approach to controlling an exoskeleton is using kinematic data measured from human and feeding it to the control system of the robot, which reproduces it in the machine's joints. This is referred to as *Master–Slave Position Control*.

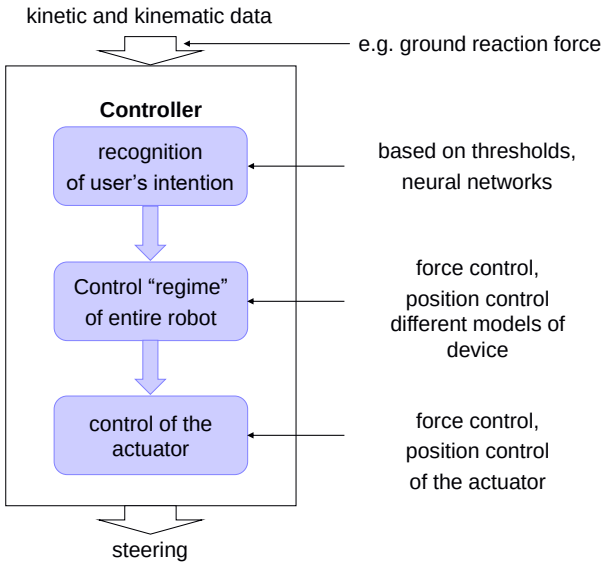

Figure 2.9: Hierarchical structure of exoskeleton control systems.

Principle of the Master–Slave Position Control

For the *Master–Slave Position Control* law two robot manipulators are used. They are connected in a way that the human operator controlling one of the manipulators, which is called the master arm, generates commands that are mapped "on the fly" to the remote manipulator, which is called the slave. *Master–Slave Position Control* law is used in settings where environmental factors might present significant hazard to the user: space, nuclear plants, battlefield, surveillance, and underwater [88].

One of the first reported attempts to control an exoskeleton through spatial correspondence of user's and machine's joints whilst providing kinaesthetic force–feedback was Hardiman [7]. In such configuration, the user was enclosed by two overlapping suits. The master suit was the inner suit manipulated by the user. It provided commands to the outer exoskeleton, which served as a slave. Block diagram of system realising master–slave position control in joint space is depicted in Fig. 2.10. The device following this pioneering approach was never reported to achieve unsupported walking. The challenge that might have been impossible to overcome at that time was the delay in communication of both suits. It is a known problem present in all teleoperated devices. Control system based on spatial correspondence in the joint space, that is when the aim is "to match the machine joint angles one–to–one with the corresponding human joint angles through feedback control" was also considered by developers of BLEEX [16] (see section 2.6). For the lower body, load–bearing, NTU exoskeleton, employing the concept

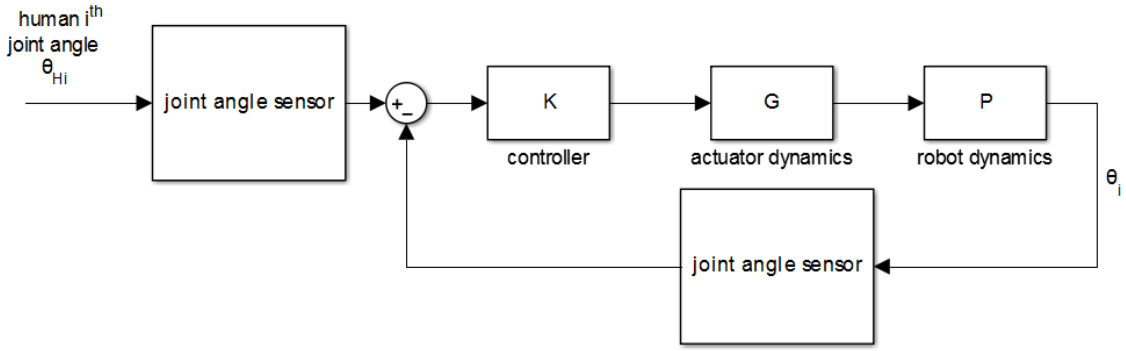

Figure 2.10: Block diagram of *Master–Slave Position Control* in joint space (adapted from [16]). θ_{Hi} – human i^{th} joint angle, θ_i – robots i^{th} joint angle

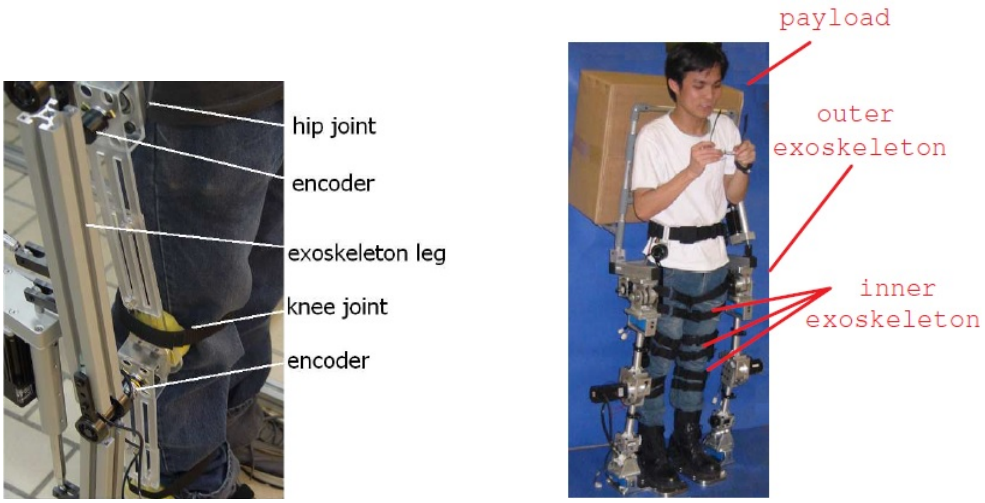

(a) (b)

Figure 2.11: NTU exoskeleton, note the space allocated for the measurement system. (a) Close up of the knee portion [74]. (b) Overview [75].

of the inner and the outer layer (depicted in Fig. 2.11), data captured from the measurement system is used directly for *Master–Slave Position Control* of the swing leg, as well as indirectly for balancing the gait by control of the Zero Moment Point [65,73–75]. The DOFs of the exoskeleton are only restricted to the sagittal plane, and all of them are actively actuated. The control problem of the load–bearing portion of the system is basically a control of a multi–link inverted pendulum (with a load located at a trunk), with a goal of keeping it in equilibrium, whilst matching spatially human joints during walking.

The *Master–Slave Position Control* law can be implemented also in the operational space. The control goal is to match the position and orientation of any of the chosen user's body segments and corresponding segments of the machine. The drawback of

this solution is that accurate data must be available on joint centres of rotation and on the dimensions of human body segments [16]. These are especially difficult to locate for the hip and the shoulder joints.

Design Consideration of Master–Slave Position Control

When the machine is governed by the *Master–Slave Position Control*, in principle, the user "must be able to move to desired position to initiate a resulting machine movement" [16]. It implies that the user joints must be instrumented and he must be able to move without being obstructed by the machine whilst wearing this movement capturing device. In Fig. 2.11b, it can be observed that user legs have room for manoeuvring in the sagittal plane, but in order to capture motion in the coronal and transverse planes, additional space would have to be allocated too.

It should also be noted, that the centre of the user joints must be tracked during move, so that the exact angles can be reproduced in the outer exoskeleton. This implies considerations for the design of the outer exoskeleton. Its kinematics must match closely those of the user (centres of joints and length of links), so that interference between the two is avoided. For the NTU exoskeleton, the instantaneous center of rotation of the human knee joint was not taken into consideration whilst designing the knee joint of the exoskeleton. Simple rotational joint was used instead, which resulted in additional prismatic joint being required along the robot spine (backpack), between it and user's waist, to accommodate for the variable displacement during walking [75]. If movement in the other planes was also allowed, similar solution would have to be added for them, which would most likely cause interference with the upper body structure of the exoskeleton. Designers of BLEEX, when they experimented with *Master–Slave Position Control* also encountered the issue and had to modify the vest to allow for a vertical displacement of the harness by 3 – 6 cm.

Selection of the encoders for measuring the position at the angles requires also attention. In Appendix B assessment of precision of the encoders is conducted. The results show that for a kinematic chain representing a full–body exoskeleton a resolution higher than 12–bit is required to obtain positioning uncertainty lower than 1 cm at end effector coupling with hands of the user.

As explained, the principle by which the device is governed and the size of the movement capturing system requires a significant space between the machine and the user to be allocated. That in turn would make the outer structure bulky. This needs to be

given a special consideration since the control scheme implies that almost all degrees of freedom must be *actively* actuated (user is dynamically detached from the exoskeleton so he/she cannot support it at all). This is a case for the NTU exoskeleton. It would also result in the weight of the actuation system being significant. The actuation system moving almost each joint of the heavy outer exoskeleton would require then great amount of power, most likely contradicting the need of being untethered. The NTU exoskeleton has never been reported to be untethered, and *Low* et al. admit that it was a challenge for them [75]. Fault in the operation of a massive exoskleton actuated using highly rated forces would pose also a significant risk to the user and the environment. In such situation, the standard for personal care robots (which include exoskeletons) [68] requires safeguarding or complementary protective measures to be implemented (see Appendix C), among which most suitable are force restriction or safety–related force control of the interaction between exoskeleton and the user.

If control goal is obtained and the links of human body and the machine are aligned, the interaction force between the exoskeleton and the user is kept $Xi = 0$. The goal of reproducing movement trajectory is met inherently. In that situation however, as explained inAppendix A, it is also implied that the metabolic cost of mechanical work of the user performing a certain task being enclosed in an exoskeleton and not wearing it remains unchanged ($\Delta E_{met} = 0$). Also the metabolic cost of isometric force production is not changed. This might be favourable when user guides a device carrying entire load, but the control scheme does not allow in principle for an exoskeleton to support user's muscles in performing a certain task, for example climbing up a slope ($\Delta E_{met} < 0$) or even standing ($\Delta E_{iso}^{mus} < 0$). The opposite situation, when the user supports an exoskeleton in performing a certain activity ($\Delta E_{met} > 0$) is also considered to be an erroneous condition of the controller.

The principle of operation of the *Master–Slave Position Control* law, if the design physically decouples the user from the robot, deprives the device of the main"... capability of the ... exoskeleton stems from the combined benefit of the human intellect provided by the pilot and the strength advantage offered by the exoskeleton" [14]. One can argue that providing haptic feedback would maintain information flow from the environment to the user, but most likely the information would be depleted of many core values, e.g. information regarding balance of the robot. In addition, such sensory and haptic systems would add extra complexity, hence size, to the system. The same goal might be achieved by a much simplre method, that is by allowing controlled physical contact. *Racine* claims about Hardiman that "the most ambitious attempt at a

lower extremity exoskeleton failed because the nature of the control system made its implementation into compact wearable design unfeasible. In effect, one of the major challenges in controlling an exoskeleton is that the human is actually coupled with the machine and is an integral part of the dynamics of the system" [16].

2.5 Force Control

In robotic systems the goal of maintaining set point of force between the robot manipulator and its environment is recognised. For exoskeletal systems the problem can be reformulated with goal of maintaining set value of interaction force between the robot and the user. As considered in Appendix A, the metabolic cost can then be controlled. Further, if the interaction force $\Xi \equiv 0$ then:

- $\Delta E_{met} = 0$, the metabolic cost of mechanical work performed by the user is unchanged;
- metabolic cost of static force production E_{iso}^{mus} is unchanged;
- the exoskeleton moves in concert with the user, gets away from the contact points, so the distance between the user and the robot is kept minimal;
- no dangerous forces are exerted at the interaction points, likelihood of user injury is decreased.

The variables controlled in BLEEX and Sarcos XOS 1 robots, are the interaction forces between the user and the exoskeleton, so that they are kept zero or relatively small [16–18,71]. The control objective in both devices is the same, regardless of the fact that BLEEX is a lower extremity exoskeleton, whilst XOS 1 is a full–body exoskeleton.

2.5.1 Direct Force Control

Principle of Direct Force Control

The interaction force between an exoskeleton (robot) and a user can be measured directly at all contact points. This control law is referred to as *Direct Force Control* [16]. Let a user enclosed in an exoskeleton be considered as depicted in Fig. 2.12. The user and robot are in contact in N points $p^i \in \mathbb{R}^3$, where $i \in \{1, \ldots, N\}$. Let $p \in \mathbb{R}^{6N}$ denote a position coordinates of interaction points and orientation of exoskeleton segment in

contact in inertial frame of reference with origin at O_0 :

$$p = \left[(p^i)^\top, (\alpha^i)^\top\right]^\top = \left[p_x^i, \quad p_y^i, \quad p_z^i, \quad \alpha_x^i, \quad \alpha_y^i, \quad \alpha_z^i\right]^\top, \text{where } i \in \{1, \dots, N\} \tag{2.1}$$

where $p^i \in \mathbb{R}^3$ – vector of Cartesian coordinates of i$^{\text{th}}$ contact point in reference frame with origin at O_0:

$$p^i = [p_x^i, p_y^i, p_z^i]^\top \tag{2.2}$$

$\alpha^i \in \mathbb{R}^3$ – orientation angles of exoskeleton segment in i$^{\text{th}}$ contact with operator in the reference frame with origin at O_0, defining rotation completely, for example yaw–pitch–roll angles:

$$\alpha^i = [\alpha_x^i, \alpha_y^i, \alpha_z^i]^\top \tag{2.3}$$

Accordingly, the human–machine interaction force/torque column vector $\Xi \in \mathbb{R}^{6N}$ is

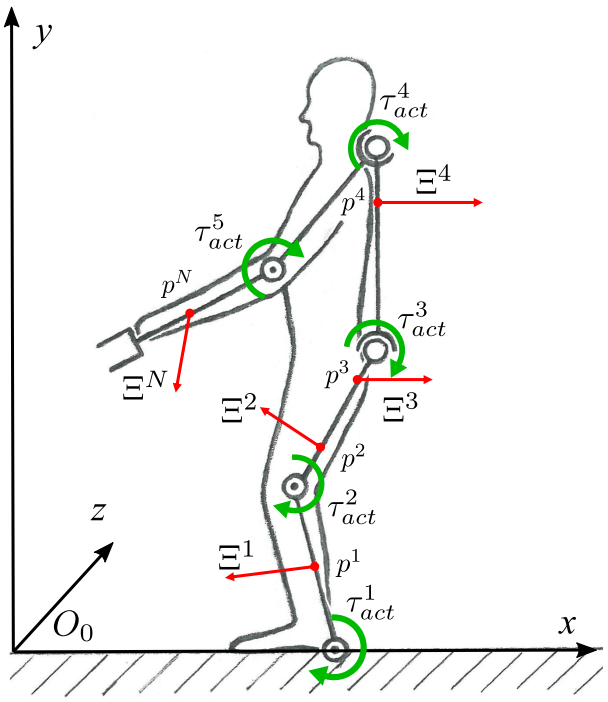

Figure 2.12: A human wearing an exoskeleton.

denoted :

$$\Xi = \left[(\Xi^i)^\top, (\nu^i)^\top\right]^\top = \left[\Xi_x^i, \quad \Xi_y^i, \quad \Xi_z^i, \quad \nu_x^i, \quad \nu_y^i, \quad \nu_z^i\right]^\top, \text{where } i \in \{1, \dots, N\} \tag{2.4}$$

where $\Xi^i \in \mathbb{R}^3$ is force corresponding to p^i,

$$\Xi^i = [\Xi^i_x, \Xi^i_y, \Xi^i_z]^\top \tag{2.5}$$

$\nu^i \in \mathbb{R}^3$ is torque corresponding to rotation α^i:

$$[\nu^i = \nu^i_x, \nu^i_y, \nu^i_z]^\top \tag{2.6}$$

The torque due to the human imposed at joints of the robot is modelled as [16]:

$$\tau_{HM} = K_H(\theta_H - \theta), \tag{2.7}$$

where $\tau_{HM} \in \mathbb{R}^L$, L – number of degrees of freedom. For the robot depicted in Fig. 2.12 L = 5 only if the sagittal plane is considered. K_H is the human–machine impedance; $\theta \in \mathbb{R}^L$ – robot configuration (angles) in joint reference frames; $\theta_H \in \mathbb{R}^L$ – corresponding angles at user joints in the equivalent model.

Let $P : \theta \in \mathbb{R}^L \longrightarrow p \in \mathbb{R}^{6N}$ describe relation of coordinate parameters θ to contact points p. The Jacobian $J_P \in \mathbb{R}^{6N \times L}$ of P at θ is of the form:

$$J_P(\vec{\theta}) = \left[\frac{\partial p^i_x}{\partial \theta_j}, \frac{\partial p^i_y}{\partial \theta_j}, \frac{\partial p^i_z}{\partial \theta_j}, \frac{\partial \alpha^i_x}{\partial \theta_j}, \frac{\partial \alpha^i_y}{\partial \theta_j}, \frac{\partial \alpha^i_z}{\partial \theta_j}\right]^\top_{\vec{\theta}}, \text{ where } j \in \{1, \dots, L\}, i \in \{1, \dots, N\} \tag{2.8}$$

Relation between angular velocity $\dot{\theta}$ and velocity $\dot{p}$ of contact points is given by:

$$\dot{p} = J_P(\,\theta\,) \cdot \dot{\theta} \tag{2.9}$$

Denoting Lagrangian of the exoskeleton as:

$$\mathcal{L}(\,\theta, \dot{\theta}\,) = E_{kin}(\,\theta, \dot{\theta}\,) - E_{pot}(\,\theta\,) \tag{2.10}$$

where E_{kin} – kinetic energy, E_{pot} – potential energy of a manipulator. Generalised equations of motions take form:

$$\tau^j_{act} + \sum_{i=1}^{N} \frac{\partial \dot{\alpha}^{\,i}}{\partial \dot{\theta}_j} \nu^{\,i} + \sum_{i=1}^{N} \frac{\partial p^{\,i}}{\partial \theta_j} \Xi^i = \frac{\mathrm{d}}{\mathrm{d}t} \frac{\partial \mathcal{L}}{\partial \dot{\theta}_j} - \frac{\partial \mathcal{L}}{\partial \theta_{\,j}}, \quad \forall j \in [1, ..., L] \tag{2.11}$$

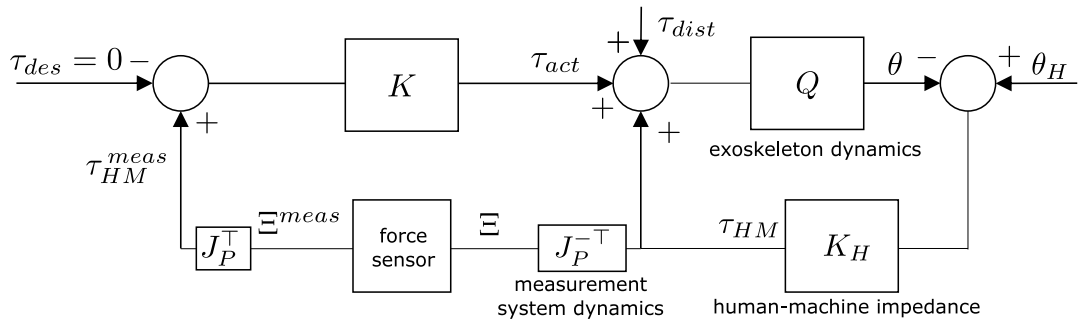

Figure 2.13: A block diagram for *Direct Force Control* law (adapted from [16]).

where $\tau_{act} \in \mathbb{R}^L$ is a vector of torques generated by actuators. *Racine* [16] writes:

$$\tau_{HM}^{j} = \sum_{i=1}^{N} \frac{\partial \dot{\alpha}^{\,i}}{\partial \dot{\theta}_j} \nu^{\,i} + \sum_{i=1}^{N} \frac{\partial p^{\,i}}{\partial \theta_j} \Xi^i \tag{2.12}$$

which after application of the chain rule can be expressed using Jacobian (see Eq. (2.9))[4]:

$$\tau_{HM} = \left[\sum_{i=1}^{N} \frac{\partial \alpha^{\,i}}{\partial \theta_j} \nu^{\,i} + \sum_{i=1}^{N} \frac{\partial p^{\,i}}{\partial \theta_j} \Xi^i \right]_{L \times 1} = J_P(\,\theta\,)^\top \cdot \Xi, \text{ where } j \in \{1, \ldots, L\} \tag{2.13}$$

Eq. (2.13) can be used to construct a control law with a block diagram depicted in Fig. 2.13:

τ_{HM}^{meas} – torque due to human calculated from measured force
τ_{dist} – joint torque vector due to gravity or external forces acting on the robot
K – controller gain matrix

At the centre of the diagram is an adder representing physical superposition of torques (forces are reduces to torques through exoskeleton geometry). Torques acting on the machine dynamics Q are: torque due to actuators, due to external disturbance (external force or load attached) and torque due to interaction with an operator. The torque induced due to interaction with the human cannot be measured directly, but the force and torques at the interaction points can be measured by an F/T sensors. Based upon the measurement Ξ_{HM}^{meas}, and knowing the Jacobian derived from the system geometry, τ_{HM}^{meas} can be calculated, which is τ_{HM} burdened by error of the measurement system. In the controller (electronics) the value is compared to $\tau_{des} = 0$ value by the adder located on the left of the block diagram. The output from the adder, error, is

[4]The Eq. (2.13) is commonly used in robotics to describe static relationship between force applied to an end–effector to torque at the joints [89]. Other derivation employs the *principle of virtual work*.

amplified by some chosen gain and based upon the value actuators apply torque, which is super-positioned with torque to to human and disturbance torque.

Assuming validity of Eq. (2.13), for the value of τ_{HM}^{meas} compared to set point $\tau_{des} = 0$, in the steady state it can be written:

$$0 = J_P^{meas}(\,\theta\,)^{\top} \cdot \Xi^{meas} \tag{2.14}$$

where $J_P^{meas}(\,\theta\,)$ relates measurement points p_{meas}^{i} to θ.

If p_{meas}^{i} were chosen uniquely, that is $\forall\, m \neq n \in \{1, \ldots, N\}$, then immediately from Rouché–Kronecker–Capelli theorem it is concluded that the system of linear Eqs. (2.14) has one and only solution $\Xi^{meas} = 0$.

Design Considerations of Direct Force Control

The control law has implications in the design of the exoskeleton. If the user and the robot are in contact points other then p_{meas}^{i} the equation $\tau_{HM}^{meas} = \tau_{HM}$ no longer holds true and $\tau_{HM}^{meas} = J_P^{meas}(\,\theta\,)^{\top} \cdot \Xi^{meas}$, the interaction force in unmeasured points is not controlled and thus it is most likely that the user will be burdened by that contact.

An approach to solving the problem might be to isolate the number of contact points between the user and the robot by adequate design of the robot frame and the human machine–interface. Each part of such ergonomic interface then should be equipped with a force sensor. However it is discussed in [16] that creating a comfortable sensing interface for lower body exoskeleton, which would contact the shank or thigh of the user is very difficult since those areas have very low tolerance for long lasting or repetitive rubbing or pressing forces. In addition, many body segments lack flat surfaces and vary in shape and dimensions across the user population. Restricting the interaction areas, whilst providing comfort to the user, would then require the interface to be custom–fitted to a particular user.

Another implication of the control law is that not only normal component of the interaction force has to be measured, but all the force components in the controlled plane (e.g. sagittal plane) must be registered [16]. Otherwise, if certain force components are not registered, the error of the calculated torque due to the user will be given

by expression (from Eq. (2.13)):

$$error(\tau_{HM}) = J_P^{meas}(\theta)^\top \cdot \Xi^{meas} - J_P^{meas}(\theta)^\top \cdot \Xi = J_P^{meas}(\theta)^\top \cdot \Delta\Xi^{meas} \qquad (2.15)$$

where $\Delta\Xi^{meas}$ denotes unmeasured components of the interaction force. Which of the components of the interaction force can be neglected might be a research question.

Racine [16] remarks that it is possible to construct *Direct Force Control* law for a lower extremity exoskeleton only limiting measured interaction forces to feet and back of the user. However he argues that, given the state of the technology, it has been difficult to embed multiple–axis force/torque sensors into a sole of an exoskeleton. Such sensors should measure and withstand highly rated forces due to the weight of the user. As a consequence, *Kazerooni* sums up efforts to construct robust GRF sensor for BLEEX as failures due to the material fatigue in long–run field tests under this repetitive stresses [22]. Moreover, the measurement of the GRF most likely would be corrupted by the shear force component due to the bending of the exoskeleton sole. The robot sole must be given certain level of flexibility between the toe joint and the ball of the foot to keep the natural gait pattern of a user.

Designing an interface equipped with a sensor measuring force exerted at the back of the user is more practical. This area is a relatively flat surface accustomed to withstanding high pressures. Although, *Virtual Torque Control* (see section 2.5.3) is used as a control law for BLEEX, for the robot segment in contact with the back of the user the interaction force is measured directly using a multi–axis force sensor. By introduction of this sensor *Virtual Torque Control* law order is reduced and controller performance refined. The sensor used in BLEEX is force/torque multiaxis sensor depicted in Fig. 2.14.

If considering also upper extremities, *Kazerooni* remarks that the human hands are more suitable for precise force and torque manipulation of any type of robotic manipulators or haptic systems [22]. This is in opposition to the lower limbs for which load supporting task takes priority over precision of locomotion. He states that this is a property of the human locomotion system and is controlled on the level of involuntary reflexes.

Direct Force Control with Non–Zero Interaction Force

In the case $\Xi \neq 0$ (see Eq. (2.4)), the *Master–Slave Force Control* can be constructed for an exoskeleton [90, 91]. In Fig. 2.15 a control scheme for *Master–Slave*

Figure 2.14: ATI Detla SI–165–15 F/T multiaxis sensor used in BLEEX to connect exoskeleton spine to the vest enclosing the user [16, 72]. Diameter: 94.5 mm; Height: 33.3 mm; Weight: 0.913 kg; Sensing ranges: $\Xi_x, \Xi_y \pm 165$ N, $\Xi_z \pm 495$ N, $\nu_x, \nu_y, \nu_z \pm 15$ N·m.

Force Control law is depicted. The control goal is to minimise *error*. That way the force exerted on human from the environment is reduced by $(1+K_h)$, where K_h is force amplification factor.

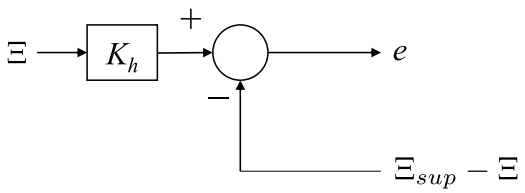

Figure 2.15: Block diagram of master–slave force controller. Ξ – interaction force between exoskeleton and the user, Ξ_{sup} – force by which exoskeleton acts on the enviroment, e – error.

2.5.2 Virtual Force Control

Principle of Virtual Force Control

In section 2.5.1 *Direct Force Control* law for exoskeletons was described. The main drawback associated with this control scheme is the difficulty of measuring the interaction forces between the robot and the user due to properties of human body as well as technological limitations of the available force sensors. As a solution to the problem, the *Virtual Force Control* law may be proposed [16, p. 94]. The block diagram of this control scheme is depicted in Fig. 2.16. $\Xi^{dest}(t) = 0$ is the desired interaction force, Ξ^{est} is the estimated (calculated) interaction force. τ_{HM} is not measured in this control

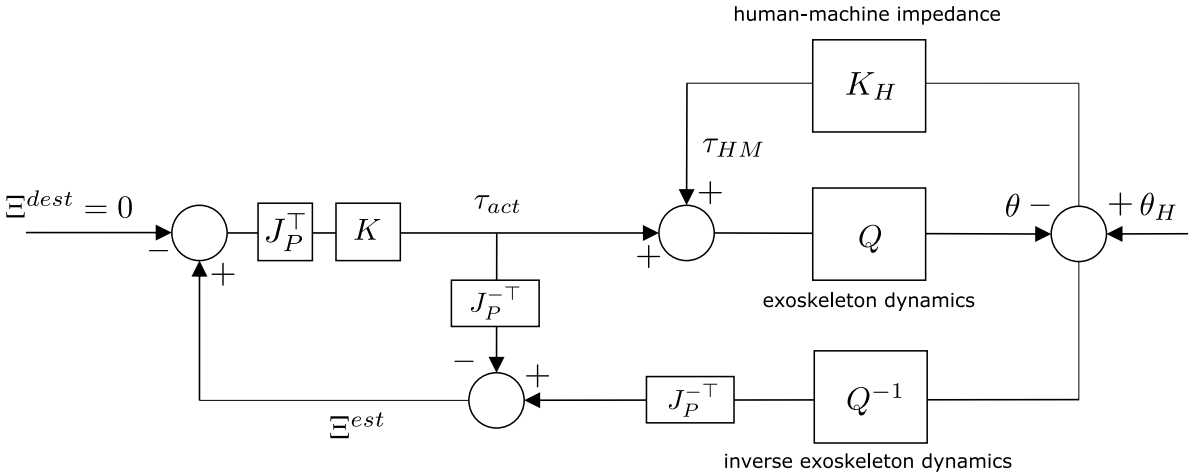

Figure 2.16: A block diagram for *Virtual Force Control* law (adapted from [16]).

scheme. It is in contrast to *Direct Force Control* (see Fig. 2.13), where it is measured indirectly. Generalised forces (torques) are estimated from measurement of machine joints displacement and their derivatives with full knowledge of Q^{-1} – machine inverse dynamics. Measured actuator torques are then subtracted from the estimated generalised forces. The result is τ_{HM}, torque due to the operator. It is compared to 0 on the right of the block diagram, and the error is multiplied by a chosen gain. The signal becomes desired torque at the joints of exoskeleton and control signal of the actuators can be computed. Note that for the proper functioning of the control scheme, τ_{dist} has to be 0. In this method interaction forces are estimated through an inverse of mathematical model of the system Q^{-1}, thus the system might be considered to be employing an observer. The recreated information is used as a feedback to the controller.

Design Considerations of Virtual Force Control

However improved comparing to the *Direct Force Control*, the virtual force control is not free from one very serious drawback. The Jacobian $J_P(\,\theta\,)$ must be known. This implies that interaction points must be known a priori. Problems experienced for the design of ergonomic human–machine interface remain the same as for *Direct Force Control*.

2.5.3 Virtual Generalised Force Control

Principle of Virtual Generalised Force Control *Racine* [16] proposes an extension of *Virtual Force Control* law to generalised forces. This is done by noting

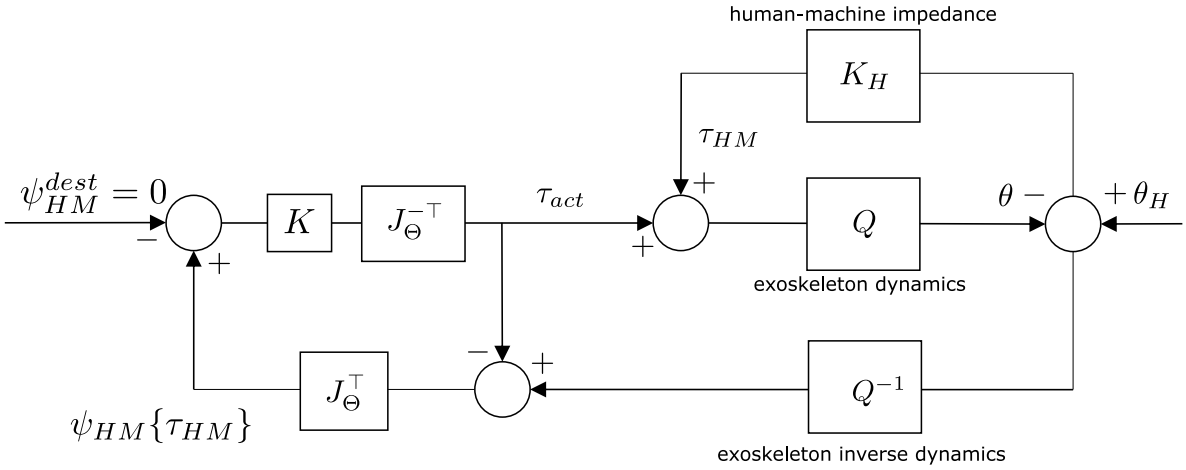

Figure 2.17: A block diagram for *Virtual Generalised Force Control* law (adapted from [16]).

the fact that the selection of *the generalised coordinates* is not tied to the configuration space (angles at the joints), but the coordinates can be chosen freely, as far as they describe the robot configuration unambiguously.

Let $J_\Theta(\vartheta)$ denote Jacobian of $\Theta : \vartheta \in \mathbb{R}^L \longrightarrow \theta \in \mathbb{R}^L$, where ϑ are *generalised coordinates* in a different base. Multiplying Eq. (2.13) on the left side by $J_\Theta(\vartheta)^\top$ yields:

$$J_\Theta(\vartheta)^\top \cdot \tau_{HM} = J_\Theta(\vartheta)^\top \cdot J_P(\theta)^\top \cdot \Xi \tag{2.16}$$

$$\psi_{HM} = J_\Theta(\vartheta)^\top \cdot J_P(\theta)^\top \cdot \Xi \tag{2.17}$$

where ψ_{HM} denotes component of the *generalised force due to the human* acting on ϑ. From Rouché–Kronecker–Capelli theorem it is concluded that if $\psi_{HM} = 0$, and $\det\left[J_\Theta(\vartheta)^\top\right] \neq 0$ the system of linear Eqs. (2.17) has one and only solution $\Xi^{meas} = 0$. Thus, it can be stated that in order to maintain interaction forces $\Xi \equiv 0$, it is sufficient to stabilise components of *generalised forces due to the human* $\psi_{HM} = 0$ associated with any *generalised coordinates* that describe the robot's configuration unambiguously.

If Θ is chosen to be the identity function, then its Jacobian is of form of the identity matrix $J_\Theta = I \in \mathbb{R}^L$ and $\psi_{HM} = \tau_{HM}$, the feedback to the controller is directly the torque due to the user. This law is referred to as *Virtual Joint Torque Control* by Racine [16].

Design Considerations of Virtual Generalised Force Control The control laws based on stabilisation of *generalised force* do not require any knowledge about

real interaction points between the user and the machine. Instead, any contact is controlled indirectly by governing the behaviour of *generalised forces* acting on conveniently selected *generalised variables*. Moreover, if the *configuration space* (angles at joints) are chosen as *generalised variables*, any interaction forces, through projection to torques at the joints, are fed as feedback to the controller.

The *generalised force control laws* do not require any information about the properties of the user's body and any characteristics of the human–machine interface, thus allow for a flexible design of the robot, which in turn can be easily adjusted to various users. The main disadvantage, comparing to the *Master–Slave Position Control* and *Direct Force Control*, is the necessity of knowing the model of the machine Q (and its inverse Q^{-1}) with the mass properties identified.

2.6 Control of BLEEX

At the University of California, Berkeley *Kazerooni* and his students developed a prototype of a lower body exoskeleton for human strength and endurance augmentation named BLEEX (depicted in Fig. 2.18a). Areas of application of the device are search and rescue as well as military logistics. The aim of the project was to develop a platform "providing soldiers, disaster relief workers, wildfire fighters, and other emergency personnel the ability to carry major loads such as food, rescue equipment, first–aid supplies, communications gear and weaponry with minimal effort over any type of terrain for extended periods of time" [21]. Berkeley Bionics (a spin off company) developed three other variants of lower body exoskeletons based on BLEEX: ExoHiker, ExoClimber, HULC. The ExoHiker is a lower extremities exoskeleton designed as a device for load carrying over a terrain with small changes in altitude. It is capable of transporting of up to 90 kg while the operator is burdened with a negligible load. Performance evaluation showed that 0.5 kg of lithium polymer batteries is sufficient for a 68 km travel whilst carrying 68 kg backpack. The weight of the device itself is 14.5 kg. The ExoClimber weights 23 kg and is capable of carrying up to 90 kg of payload using 0.5 kg of batteries. On flat terrain its battery requirements are the same as for ExoHiker. With 0.5 kg of extra batteries it is capable of ascending 300 m of steep incline. In Fig. 2.18b Human Load Carrier (HULC) is depicted. The HULC incorporated features of ExoHiker and ExoClimber , plus reducing the effort of the user. It is reported to decrease metabolic cost of walking with 3.2 km/h speed by 5% – 12% whilst not carrying any payload , and up to 15% when loaded with 37 kg [21, 22].

(a) (b)

Figure 2.18: a) BLEEX, b) HULC [21].

Overview of BLEEX

The paradigm behind designing BLEEX was to approximate a 75 kg man walking with 1.3 m/s speed. Hence, the device is quasi–anthropomorphic [10, 12, 13, 92, 93]. It is capable of carrying 34 kg of payload mounted at the backpack (75 kg minus weight of the exoskeleton) [11]. Examining Fig. 2.19 it can be seen that the device has 7 DoFs per leg. The hip joint is given 3 DoFs: adduction/abduction, inversion/eversion, flexion/extension. The knee joint has 1 DoF: flexion/extension. The ankle comprises 2 DoFs: flexion/extension, abduction/addution. Sole of the exoskeleton's foot is flexible to allow flexion/extension so the 8^{th} DoF can be recognised also. The ranges of motion of each joint correspond to ranges of motion of male military personnel and are greater to those required for the gait in an ordinary human. Hip flexion/extension is designed to accommodate for the bending of the torso also. Out of all DoFs, those at the hip, knee, ankle are actively actuated in the sagittal plane by hydraulic bidirectional actuators. In later prototypes, an additional hydraulic actuator was added to assist abduction/adduction of the hip joint in the coronal plane (see Fig. 2.19c). DC brushless electric motors with a harmonic drive for that purpose were also proposed and examined [94], [95]. The abduction/adduction movement in the ankle joint is passively actuated by a spring mechanism. The actuators torque and speed were selected to allow the robot to follow human gait patterns. The total power consumption for the

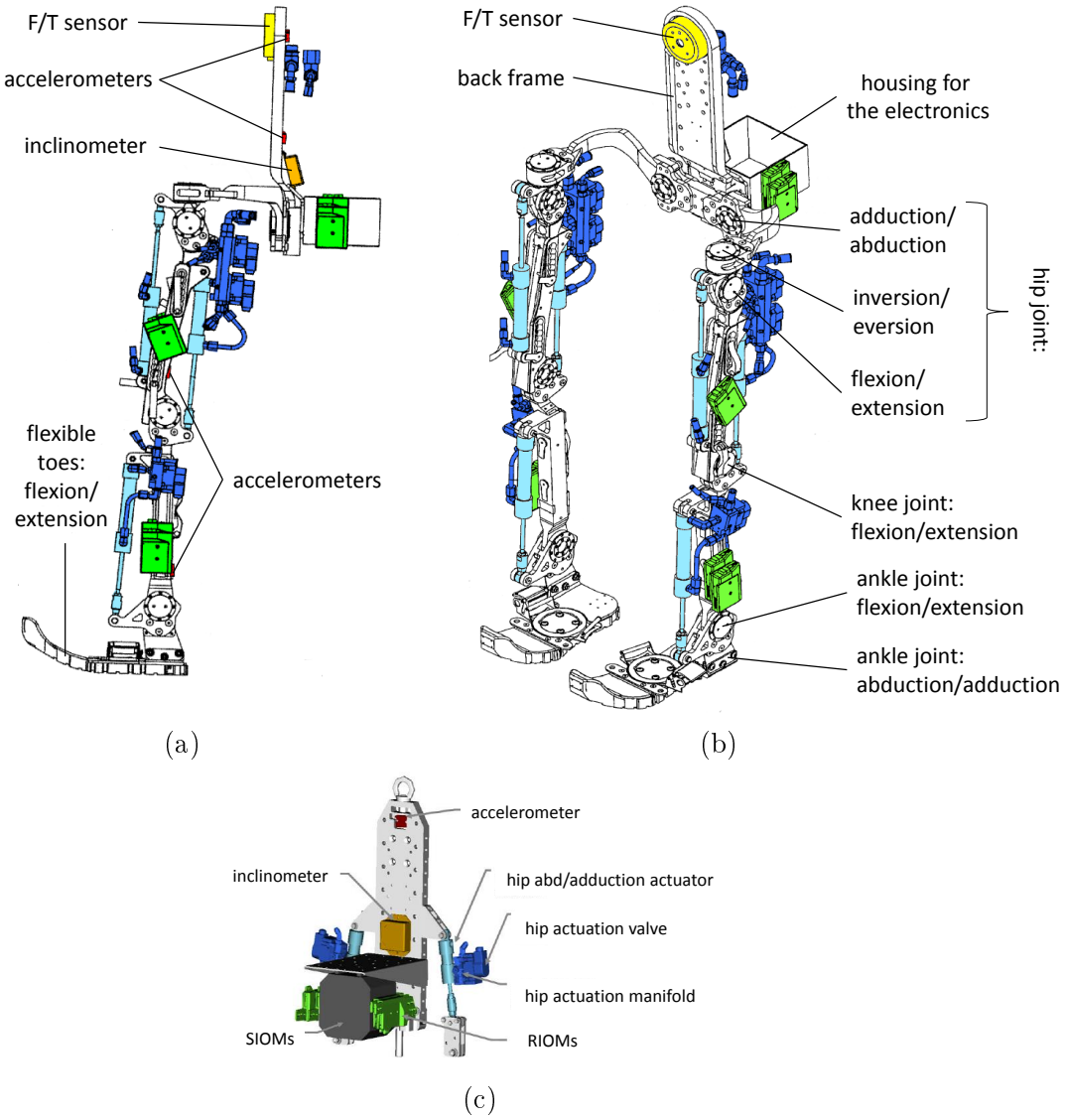

Figure 2.19: Schematic drawings of BLEEX: a) side view, b) perspective view (adapted from: [15]), c) torso back view (version with abduction/adduction hip actuator).(adopted from: [13]). Exoskeleton parts: hydraulic actuators (light blue), manifolds, valves and hosing (dark blue), remote input/output modules (green), force/troque sensor (yellow), accelerometers (red), inclinometer (orange).

hydraulic system was determined to be approx. 2.27 kW (including 10 % safety factor) and 220 W for the electronics. This was translated to the requirement of 20 litres per minute of hydraulic flow at 6.9 MPa. To satisfy the power requirements a 27 kg hybrid hydraulic–electric power unit (HEPU) using two–stroke internal combustion engine was developed [96–98].

In order to allow shadowing of the user moves, the robot utilises a novel control approach called *Virtual Torque Control* [14, 16–19, 86, 99]. To feed the data from the

sensors to the supervisory input/output unit a real–time high speed communication network has been developed [18, 100, 101].

Sensitivity Amplification Controller of BLEEX

The BLEEX exoskeleton is governed by *Virtual Torque Control* described in section 2.5.3, also referred to as *Sensitivity Amplification Control*. As it is explained further, "it requires large sensitivity to pilot forces, which invalidates certain assumptions of the standard control design methodologies" [96]. Noting that the human–machine interaction points p and their number in the Jacobian (see Eq. (2.8)) are chosen freely, the robot moves to minimise the interaction force at all contact points and in consequence shapes to couple to the user body segments. The high sensitivity is required for robot to perform the coupling motion quickly. In consequence, exoskeleton is perceived from outside as performing the task of following the user (moving in concert, shadowing). *Kazerooni* remarks that the system is also sensitive to external forces but does not regard it as a significant drawback: "The key to stabilizing the exoskeleton and preventing it from failing in response to external forces depends on the pilot's ability to move quickly (e.g., step back or sideways) to create a stable situation for himself and the exoskeleton" [14].

The control scheme of BLEEX is strongly model–based. The exact control–oriented dynamic model of the exoskeleton changes during walking depending on status of feet contact with the ground (see section 2.2). The control regime applied in each of the phases changes in accordance. Decision about switching between the phases is taken based on the information from the GRF sensors embedded in the soles of the exoskeleton (see prototypes of proposed sensors in Figs. 2.4a, 2.4b). The recognised configurations of the exoskeleton are: single support (one leg off the ground, see Fig. 2.1), double support with single redundancy (one of the heels off the ground), double support with double redundancy (both heels off the ground). Moreover, jump (no contact with the ground) and double support (both heels touch the ground) are recognised. For brevity of this document, only model and control in the sagittal plane in the single stance phase is described, but complete elaboration can be found in [16], [17–19,86]. For the purpose of governing the exoskeleton, the dynamics of the robot are derived using Lagrangian formulation of the mechanics. Using the kinematics model (depicted in Fig. 2.20), and knowing m_j masses and inertias I_j of the links j, either by computer–aided design or by means of object identification [86, 99], the Lagrangian of the system (2.10) can be

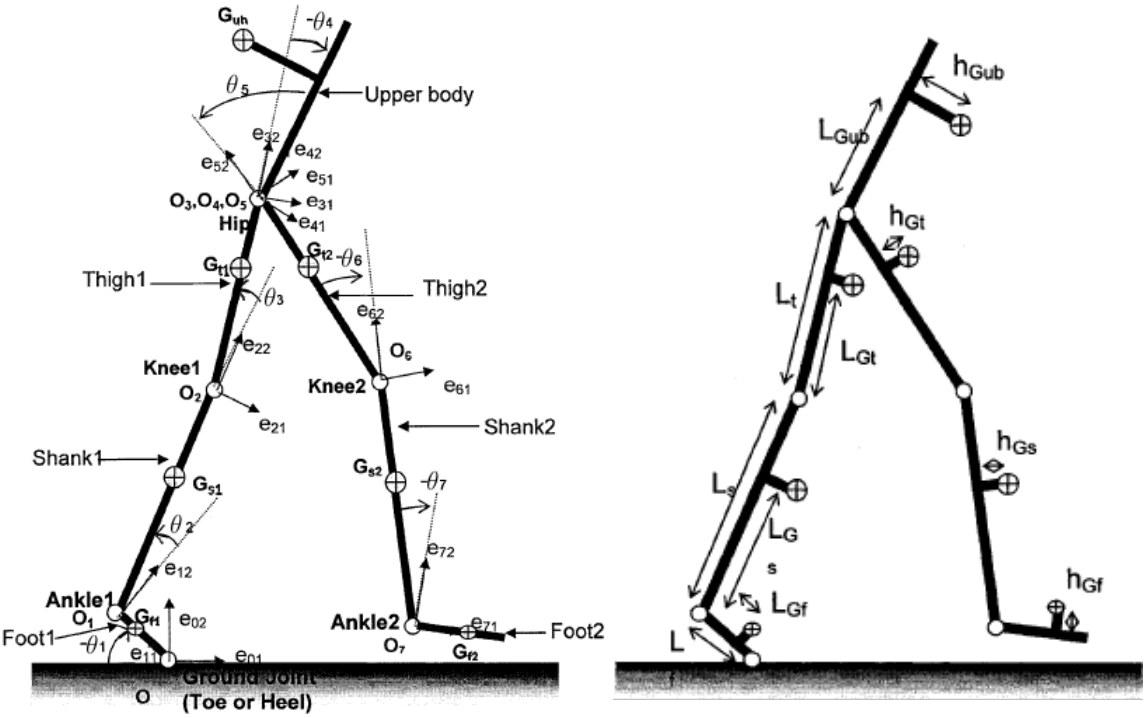

Figure 2.20: Control oriented model of BLEEX in the saggital plane: a) O_j – origin of local frames of reference (FoR), e_{j1}, e_{j2} – local FoRs basis vectors, q_j – configuration variable with respect to the local FoR; b) L_x – lengths of robot segments (distance between neighbouring origins), L_{Gx} – distance between local origin and translation of the centre of the gravity along L_x, h_{Gx} – distance of CoG to the line connecting neighbouring frame origins [16].

derived, and the right side of the Eq. (2.11) rewritten:

$$\left[\frac{\mathrm{d}}{\mathrm{d}t}\frac{\partial \mathcal{L}}{\partial \dot{\theta}_j} - \frac{\partial \mathcal{L}}{\partial \theta}_j\right]_{L\times 1} = M(\theta)\,\ddot{\theta} + C(\theta,\dot{\theta})\,\dot{\theta} + R(\theta), \quad \forall j \in [1,...,L] \tag{2.18}$$

where $M(\theta)$ is kinetic energy matrix (inertia matrix), $C(\theta,\dot{\theta})$ – centrifugal and Coriolis acceleration terms vector, $R(\theta)$ – joint vector induced by gravity. Joint angles θ are measured using encoders embedded in the joints, except for the flexible joint at the foot (θ_1), where the angle is calculated by subtracting θ_j ($j = 2,...,N$) from the absolute angle of the torso (measured using inclinometer, see Fig. 2.19). Angular speed $\dot{\theta}$ is measured using a setup of two linear accelerometers per robot's segment and angular acceleration $\ddot{\theta}$ is calculated as its derivative. Full set of sensors and control electronics is listed in Table 2.1. Inertia and mass of the torso link vary as payload is added and deduced, but using in–line force sensors and F/T sensor mounted at the torso segment

Table 2.1: Sensors of BLEEX [13], [95], ⋆ – version with abduction/adduction.

electronics	**per actuator**	**per exoskeleton**
encoder (Gurley Precision Instruments Model R119)	1	6 [8]⋆
linear accelerometer (Silicon Design 2210)	2	14 [16]⋆
single axis force sensor	1	6 [8]⋆
servo valve	1	6 [8]⋆
ROIMs	1	10
foot switches	N/A	2
load distribution sensor	N/A	2
inclinometers	N/A	1
(Microstrain FAS-G gyro enhanced inclinometer)		
F/T sensor	N/A	1
(ATI Detla SI–165–15)		
control computer	N/A	1

of the exoskeleton (see Figs. 2.19, 2.14) they can be identified by a straightforward procedure (see [92]). Using Eq. (2.13) and Eq. (2.18) the generalised equations of motion for the system (Eq. (2.11)) take the form:

$$\tau_{act} + \tau_{HM} = M(\theta)\,\ddot{\theta} + C(\theta, \dot{\theta})\,\dot{\theta} + R(\theta) \tag{2.19}$$

where $\tau_{act}^{1} = 0$ due to the fact that flexion/extenstion of the joint at the sole is not actuated.

Using the corollary from the section 2.5.3 in order to minimise the interaction force between the exoskeleton and the user it is sufficient to stabilise the joint due to the human τ_{HM} around 0, which is derived from the Eq. (2.19) as:

$$\hat{\tau}_{HM} = \hat{M}(\theta)\,\ddot{\theta} + \hat{C}(\theta, \dot{\theta})\,\dot{\theta} + \hat{R}(\theta) - \tau_{act}^{meas} \tag{2.20}$$

where hat ($\hat{}$) denotes estimated value based on the model, and τ_{act}^{meas} is torque exerted by the actuators measured by the single axis force sensors mounted on the actuator (rod of cylinder or shaft of the electric motor). The stabilising reference signal for the

actuators can be computed employing PD controller with gravity cancellation (see [89]) applied to the state space with the error expressed as $\hat{\tau}_{HM}$:

$$\tau_{act} = K_p\,\hat{\tau}_{HM} + K_d\,\frac{\mathrm{d}\hat{\tau}_{HM}}{\mathrm{d}t} + \hat{R}(\,\theta\,) \tag{2.21}$$

where K_p and K_d are proportional and derivative gains of the controller. On the lowest level of the control hierarchy, for tracking of the reference signal by the hydraulic actuators, *Racine* proposes *Multiple Sliding Surface Adaptive Control* [16].

Kazerooni remarks that the problem of selection of K_p, K_d is non–trivial [17–19,86]. In the Eq. (2.21) $K_p, K_d \in \mathbb{R}^{L\times L}$ can be chosen to be diagonal. Large gains lead to faster convergence to the set point $\tau_{HM} = 0$ and as a consequence the robot is more sensitive to user movements and the user is not burdened with the exoskeleton. This can be shown by setting $K_d = 0$, and substituting Eq. (2.21) into Eq. (2.20), then the torque due to the human is:

$$\hat{\tau}_{HM} = (I + K_p)^{-1}\left[\hat{M}(\,\theta\,)\,\ddot{\theta} + \hat{C}(\,\theta,\dot{\theta}\,)\,\dot{\theta}\,\right] \tag{2.22}$$

Next substituting Eq. (2.22) into Eq. (2.21) and Eq. (2.21) into Eq. (2.19) the relation can be written:

$$(K_p)(I + K_p)^{-1}\left[\hat{M}(\,\theta\,)\,\ddot{\theta} + \hat{C}(\,\theta,\dot{\theta}\,)\,\dot{\theta}\,\right] + \hat{R}(\,\theta\,) = M(\,\theta\,)\,\ddot{\theta} + C(\,\theta,\dot{\theta}\,)\,\dot{\theta} + R(\,\theta\,) + \tau_{HM} \tag{2.23}$$

where $I \in \mathbb{R}^{L\times L}$ stands for the identity matrix. Then using properties of square matrices:

$$\left[I - (K_p + 1)^{-1}\right]\left[\hat{M}(\,\theta\,)\,\ddot{\theta} + \hat{C}(\,\theta,\dot{\theta}\,)\,\dot{\theta}\,\right] + \hat{R}(\,\theta\,) = M(\,\theta\,)\,\ddot{\theta} + C(\,\theta,\dot{\theta}\,)\,\dot{\theta} + R(\,\theta\,) + \tau_{HM} \tag{2.24}$$

If the exoskeleton properties are estimated correctly $\hat{M}(\,\theta\,) = M(\,\theta\,)$, $\hat{C}(\,\theta,\dot{\theta}\,) = C(\,\theta,\dot{\theta}\,)$, $\hat{R}(\,\theta\,) = R(\,\theta\,)$ and K_p is sufficiently large, $[I - (K_p + 1)^{-1}]$ approaches I identity, and expressions on both sides of Eq. (2.24) cancel each other, thus $\tau_{HM} = 0$. Ideally, the user walks not feeling the exoskeleton at all, but in practice, "the forces applied by the actuators effectively reduce the impedance felt by the user wearing the enhancer" [15]. Adjusting K_p the magnitude of the force felt by the user in the transient state of system can be adjusted. On the other hand, from the same relation it can be seen that the error in the machine dynamics estimation causes the user to be burdened with the exoskeleton, and the larger the K_p is, the larger the part of error of

$\Delta\hat{M}(\theta)\ddot{\theta}, \Delta\hat{C}(\theta,\dot{\theta})$ is added to the τ_{HM}[5]. Analyses of model parameters variation by system sensitivity function show that in the worst case the system might even become unstable [14, 17–19].

Robustness of the *Virtual Torque Control* law can be improved by introduction of force measurement using a sensor mounted between the vest and the torso link [16]. Let the single support phase be considered in Fig. 2.20a. If $p_{sens} = [p^x_{sens}, p^y_{sens},\ \alpha^z_{sens},]^\top$ stands for p^x_{sens}, p^y_{sens} – position of sensor, α^z_{sens} – orientation around Z axis in the inertial FoR and $\theta_{stance} = [\theta_1, \theta_2, \theta_3, \theta_4]^\top$ is reduced joint angle vector, the Jacobian of $R_{sens} : \theta\ \in \mathbb{R}^4 \longrightarrow\ p_{sens} \in \mathbb{R}^3$ can be used to estimate torques due to the user induced in joints of the stance leg:

$$\tau^{meas}_{HM\_stance} = \left[\hat{\tau}^1_{HM}, \hat{\tau}^2_{HM}, \hat{\tau}^3_{HM}, \hat{\tau}^4_{HM}\right]^\top = J^\top_{R_{sens}} [\Xi_x, \Xi_y, \nu_z]^\top \tag{2.25}$$

The measured $\tau^{meas}_{HM\_stance}$ torque vector for the stance leg and estimated $\tau^{meas}_{HM\_swing}$ torque for the swing leg can be concatenated and substituted into Eq. (2.21) serving as an error in the controller. As a consequence, the control of the stance leg becomes *Direct Force Control* and does not depend on the model of the stance leg (including the load at the backpack). The highest rated forces that occur between the load and human torso are measured directly and controlled by actuators of the stance leg. The swing leg is still controlled using the estimated torque. Introduction of force sensor reduces also order of the control law, thus it becomes less computationally demanding. In addition to the single support stance, *Racine* applies the reduced control law to the double stance and the double stance with single support [16].

In order to tackle the problem of sensitivity to the model parameters variation and uncertainty due to the changing load mounted at the backpack, a hybrid control scheme has been also proposed [96]. *Master–Slave Position Control* for the stance leg was combined with *Virtual Torque Control* for the swing leg. Angles at the human joints were captured using 7 inclinometers: 2 on the feet, 2 on the shanks, 2 on the thights and 1 on the torso. The preliminary examination ruled out using the *Master–Slave Position Control* for swing leg because the user was not able to freely initiate the movement due to the rigid connection to the exoskeleton at the foot. In order to allow

[5] *Virtual Generalised Force Control* law has been recently applied to control of continuum robots to allow a compliant motion during endoscopy [102]. The problem of identification of properties is approached by application of tools from the domain of machine learning (namely by Support Vector Machines). The difference between actual and estimated generalised force is corrected by offline training and then online estimation of the model error via SVR. Due to the similarity of the control laws applied to the considered robot and the BLEEX exoskeleton it might be possible to tackle the problem in a similar manner.

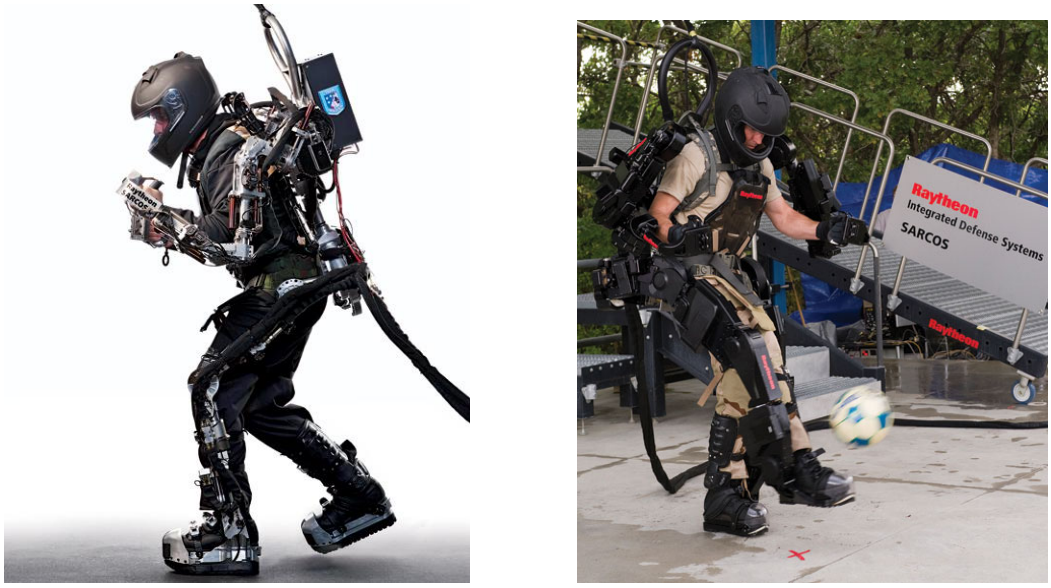

(a) (b)

Figure 2.21: XOS exoskeletons family. (a) Sarcos XOS 1 [23]. (b) Raytheon XOS 2 [26].

movement of the torso in the stance phase, a custom vest was designed that allows for the harness to be lifted vertically off the human shoulders by approximately 3 – 6 cm (compare with design considerations for the law in section 2.4). The evaluation of the hybrid control law showed inferior performance to the sensitivity amplification control with the user being able to walk at 0.5 m/s with a payload of 18 kg on a treadmill using handrails for maintaining stability in coronal plane, which became an issue after loosening the harness.

2.7 Control of XOS Exoskeletons Family

Members of the XOS exoskeletons family are prime examples of robotic devices governed by the *Direct Force Control* law. In Fig. 2.21a, the first generation of XOS by Sarcos company is depicted. In Fig. 2.21b, the second generation by Raytheon (XOS 2) is presented. The device is intended to aid military personnel in their duty. The company representative stated that "...the robotic suit [is developed] to help with the many logistics challenges faced by the military both in and out of theater. Repetitive heavy lifting can lead to injuries, orthopedic injuries in particular. The XOS 2 does the lifting for its operator, reducing both strain and exertion. It also does the work faster. One operator in an exoskeleton suit can do the work of two to three soldiers." [25]

The patent held by Jacobsen of Sarcos (2008)(World Intellectual Property Insti-

tution [71], EU [103], US [104]) describes (claim 1) a device closely reassembling in structure and operation XOS1:
"A robot displacement device for use with a robotic frame shaped to approximate and be coupleable to at least a portion of a human body and configured to *mimic movement of the human body*, the robot displacement device *comprising*[6]:

(a) *a plurality of force sensors* attached to the robotic frame along the extremities of the robotic frame configured to sense an adjustable *controlling interface force status relationship* between the sensors and the extremities of the human body, and output a force signal;
(b) a force computational system attached to the robotic frame configured to receive the force signal from the sensors, compute a force of gravity and a direction of gravity relative to the robotic frame, calculate a movement force required *to maintain the controlling force status relationship*, and generate and transmit an actuation signal corresponding to the movement force; and
(c) a drive system attached to the robotic frame configured to receive the transmitted actuation signal on an ongoing basis from the force computational system and displace a portion of the robotic frame in order to maintain the controlling force status relationship."

The frame of the patented device is depicted in Fig. 2.22. For the particular configuration, the human–robot interaction areas for which "interface force status relationship (IFSR)" is maintained are coloured, but in general, sensors measuring force and torque can be placed at points [71]:

– "between the feet of the operator and exoskeleton, ...
– between the pelvis of the exoskeleton and the pelvic harness attached to the operator
– between the exoskeleton spine structure and the shoulder harness attached to the operator
– between the hands and/or wrists of the operator and the exoskeleton arms ...
– other locations are also possible"

In the described device, the human–machine interaction force is measured upon multiple axes by a sensing system functionally similar to previously mentioned F/T

[6]According to the US patent law [105], the word "comprising" is used to denote inclusiveness (synonymous with *including*, *characterised by*), as used in the text, means that any (a) exoskeletal device using force sensors AND (2) to compute desired displacement force AND (c) for governing its frame falls into the claim of the patent.

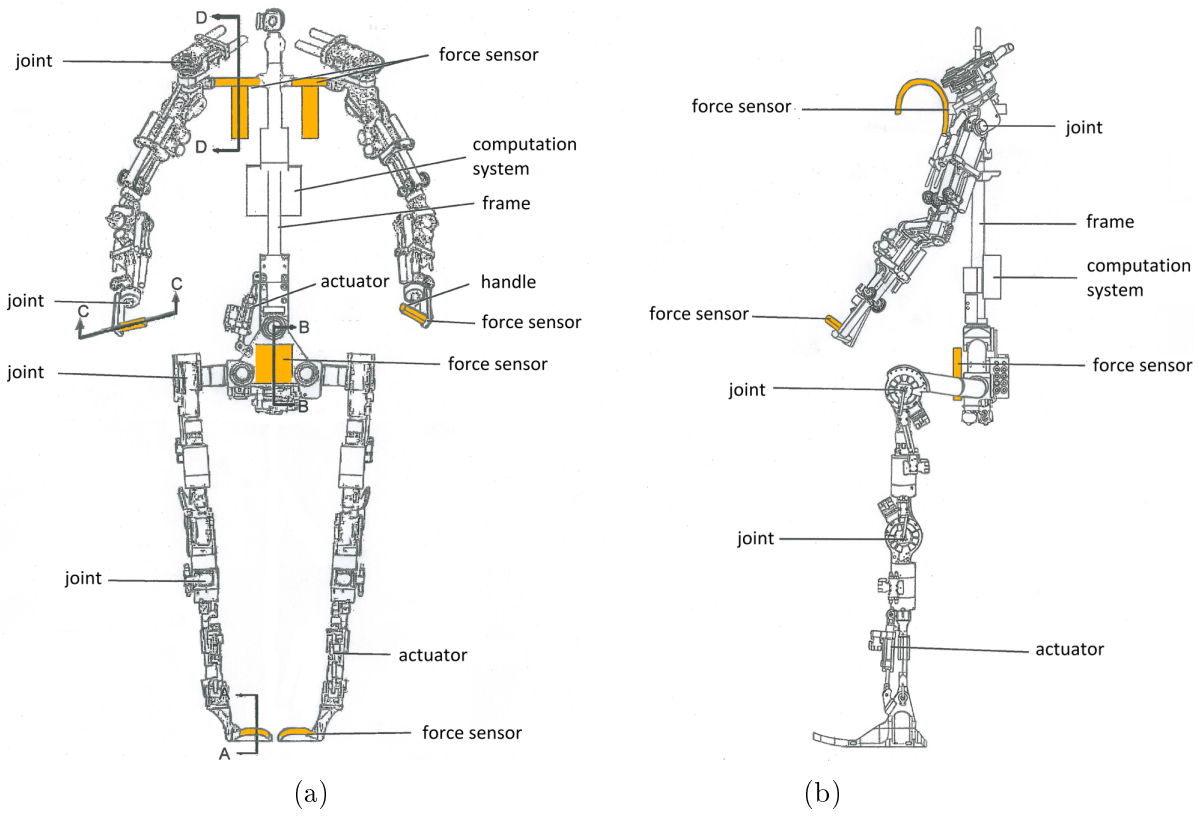

(a) (b)

Figure 2.22: Drawing of Sarcos XOS1 (adapted from [71]). Areas contacting the user coloured in yellow. (a) Frontal view. (b) Lateral view.

sensors (see for example Fig. 2.14). The principle of operation of the device is to maintain some set value of the IFSR by appropriate displacement of the frame. Any forceful contact exceeding IFSR results in the exoskeleton moving its portion to "get out of the way". The device can be configured to "minimise interaction force applied by the operator of the robotic frame to the robotic frame itself". That way it is made possible "to achieve natural, intuitive control while keeping the interaction force between the operator and the exoskeleton many times less than the weight of the payload being transported by the system."

In Fig. 2.23, the block diagram of control law of XOS1 is depicted. In essence, the *Direct Force Control* scheme is employed (compare with Fig. 2.13). The torque due to actuators is computed from the equation:

$$\tau_d = \hat{R}(\theta) + K_s(s_L, s_R)J^{\top}(\theta)K_f(s_L, s_R)(\Xi_{filt} - s_{\{L \text{ or } R\}} \cdot m_P g) \tag{2.26}$$

where [71]:

θ – robot joints angle vector

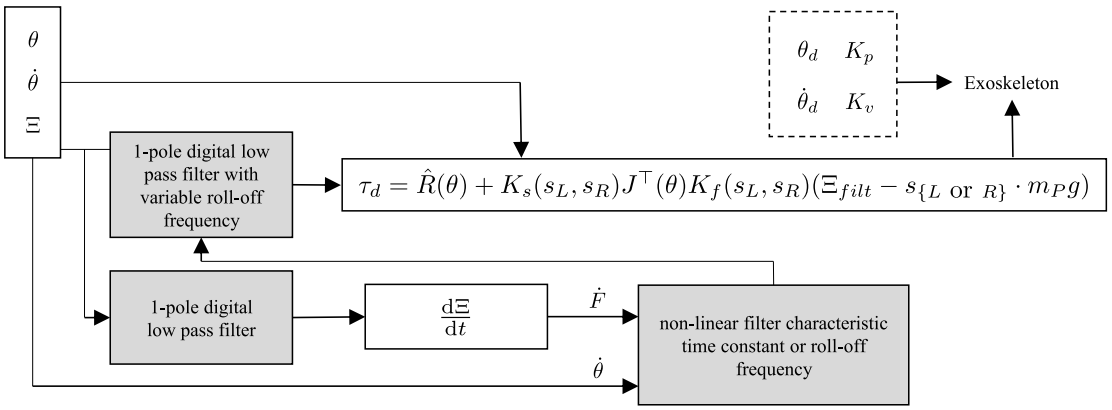

Figure 2.23: Control law of XOS1 (adapted from [71]).

$\dot{\theta}$ – robot joints velocity vector

$\hat{R}(\theta)$ – gravity/load compensation vector ("depends on the overall exoskeleton and payload configuration in the presence of of gravity, the mass properties of the links and payload, interaction forces and moments between the exoskeleton and the ground, as well as the force–moment interactions between the operator and the robot", compare with $\hat{R}(\vec{\theta})$ in Eq. (2.21))

τ_d – computed torque commands producing desired displacement

Ξ – force and moments resulting from interaction between the operator and the exoskeleton

Ξ_{filt} – low-pass filtered interaction force and moment vector

$J^\top(\theta)$ – Jacobian matrix relating the translational and angular velocity of the system to robot joints velocity vector (see Eq. (2.9)).

$m_P \cdot g$ – quantity close to the weight of the user, typically set to 0 for contact points other than feet or to any other desired force–moment value (resisting or assisting)

g – gravity vector (measured in a frame of reference attached to the exoskeleton, using an IMU attached to the pelvis)

s_L, s_R – scaling factors for control of lower body legs (L–left, R–right)

K_f – force–moment feedback gain matrix

K_s – sense feedback gain matrix

Comparing Eq. (2.25) and Eq. (2.21) to Eq. (2.26), it can be seen that Ξ_{filt} corresponds to $[\Xi_x, \Xi_y, \nu_z]^\top$, τ_d is τ_{act}, $\hat{R}(\theta)$ is the same, and the XOS1 controller is a proportional (P) controller with gravity compensation.

In [71] Jacobsen proposes ways for the behaviour of the device to be modified by manipulation of values of K_s and K_f matrices. In certain approach the matrices can be

diagonal. Manipulation of diagonal values of K_s allows then switching on or deactivation (when element is 0) of corresponding frame portion of the exoskeleton. Further, in order to optimise stability and power, a sliding gains scheme may be implemented by manipulation of K_s and K_f during gait phases: single–leg, two–leg support and swing phase. High gains are desired for effortless mobility and object manipulation, and are preferably used for non–load bearing portions of the system. However, they also lead to higher power consumption. Low gains are more suitable for load bearing portions of the system as they prevent system from instability under heavy payloads. At the lowest level of control, the computed τ_d can be utilized to calculate parameters: θ_d – desired joint position, $\dot{\theta}_d$ – desired joint velocity, K_v – calculated velocity, K_p – calculated position gain which are used to maintain desired IFSR.

2.8 Control of Assistive Exoskeletons

Assistive exoskeletons comprise a separate class of exoskeletons. The principle of their operation is to produce torque assisting joints rather than to transfer a load mounted on an exoskeletal manipulator to the ground. Their goal is to decrease user's metabolic cost of mechanical work ($\Delta E_{met} < 0$, see Appendix A) so that the performance (strength and endurance) of user's muscles is increased. In Fig. 2.24 a generalised scheme for control of assistive exoskeleton is depicted. The object to be controlled (plant) is the *human body*. It is actuated both by *muscles* controlled by *brain* and *robot actuators* controlled by *robot controller*. This way two feedback loops are formed in the system. The main goal of the controller is to determine the direction and magnitude of the torque for interaction with the human so that the intention or the reflex from *brain* is realised also by *the robot actuator*. The intention of the user cannot be fed into the controller directly so it has to be estimated by parameters measured from the human body, either biological or dynamic [38].

Yamamoto developed such full–body exoskeleton for assisting nurses in lifting patients from a bed [30–33]. The device used muscle hardness sensors placed on *biceps brachii*, *rectus femoris* and *erector spinae* muscles to detect torque generated by muscles. The sensors were made of silicon rubber with load cells embedded in it. For ensuring safety of the device in hospital environment, novel fan–like pneumatic actuators were developed. The control system of the device was limited only to the lifting load placed on the forearms of a nurse.

Kong developed EXPOS [35, 36]. The device had one DoF per each hip and knee

joint, which were actuated through linkages connected to caster walker moving in front of the patient. The control algorithm was based on fuzzy–logic and recognised user intention during gait based on novel muscle hardness sensor made of inflatable cuffs and angular parameters of joint measured by potentiometers. The important objective *Kong* addressed in the design of his assistive exoskeletons is that the mechanical impedance for human–robot interaction (defined by the relation 2.27) should be low, preferably zero [34, 37–39], so that force high–fidelity is achieved and the actuator is back–driveable. Mechanical impedance:

$$Z(\omega) = \frac{f(\omega)}{v(\omega)}, \text{ where } \omega \in (0, +\infty) \tag{2.27}$$

where: ω – pulsatance, $f(\omega)$ – force, $v(\omega)$ – velocity. On the other hand, elements such as gear trains or hydraulic cylinders have high–impedance and without energy buffering element (e.g. serially connected spring) might cause discomfort or harm to the user. In order to solve the issues with imperfect impedance of actuators *impedance compensator* can be introduced to the control system (see Fig. 2.24). For example, for a DC motor with a spring connected serially as an elastic element *Kong* proposes a PD controller optimally tuned by solution of LQ problem with a disturbance observer employed to account for variations in the mechanism's model. Fig. 2.25 presents frequency characteristics of actuator impedance for human–robot interaction. Note the relative flatness of magnitude and phase within frequency range 4–8 Hz, which is considered to be frequency of motion for lower extremities during gait. This solution was used in *Kong's* second generation exoskeleton named SOBAR (2008) [37–39].

Pratt when designing the RoboKnee used linear series elastic actuators under governance of force feedback to allow lowering metabolic effort of the user whose intention was recognised using two load cells embedded in the shoe. Due to low mechanical impedance the user experienced comfortable and natural operation.

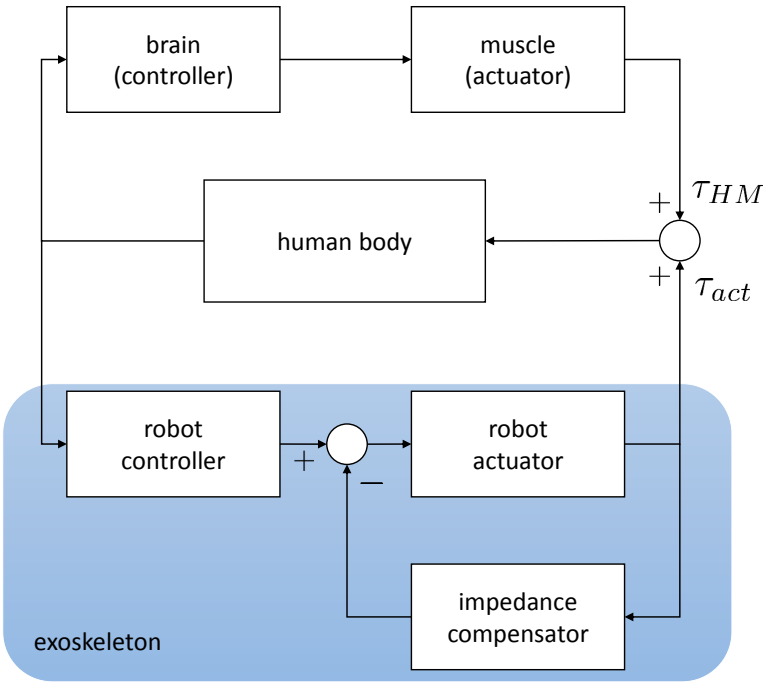

Figure 2.24: Control scheme of an assistive exoskeleton (adapted from [38]).

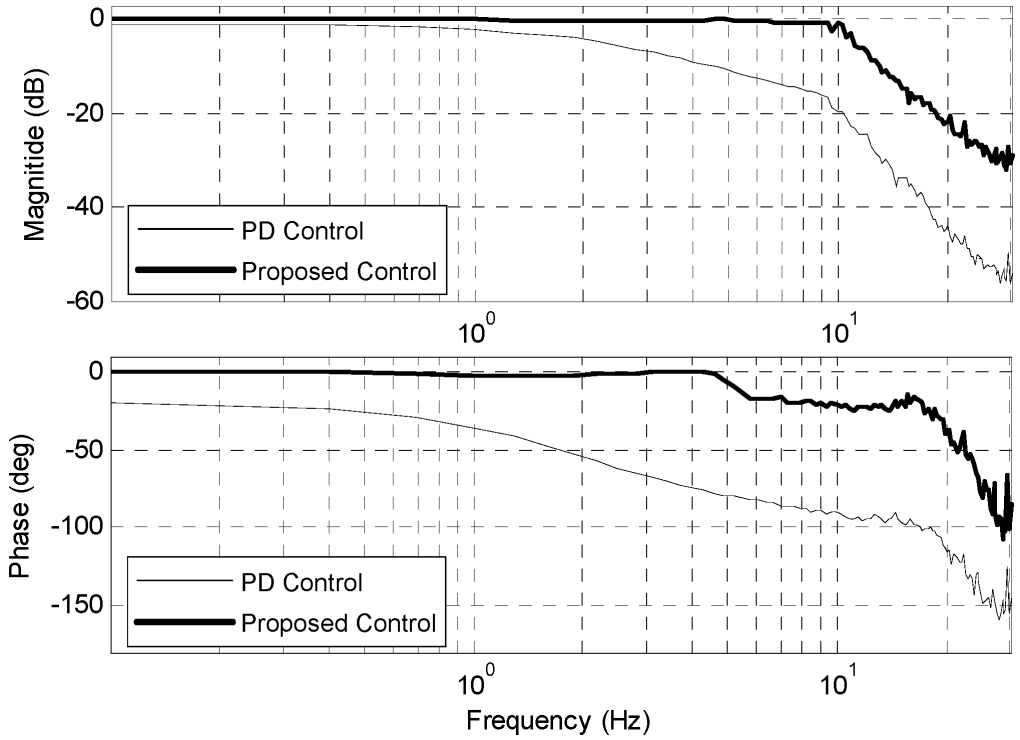

Figure 2.25: Frequency characteristics of mechanical impedance of actuator for human–machine interaction [38].

2.9 Control of HAL Exoskeletons Family

Hybrid Assistive Limb (HAL) by Sankai Laboratories is a name of family of assistive exoskeletons. Several variants targeting different needs have been developed. In Fig. 6.12 some of them are depicted. In Figs. 2.26a and 2.26b the HAL for Welfare Use – Lower Limb Model is depicted. It is adapted for assistance for people with weakened lower limb functions such as elderly in tasks involving walking, standing up and sitting down, climbing stairs. The exoskeleton has one actuator per joint placed at the knee and hip joint in a manner that the lower limbs are actively actuated in the sagittal plane. In Fig. 2.26c HAL for Medical Use – Lower Limb Model (HAL–ML–05 EU model) is depicted. This version is intended to be used for rehabilitation in cases when the user might not have voluntary control of the lower limbs [59]. For that reason, an additional actuator has been placed at the ankle joint [51,106]. In Fig. 2.26d full–body HAL–5 model for assistance in task involving heavy work is depicted. It has 8 actively actuated DoFs, one per each knee, hip, shoulder and elbow joint.

Exact control algorithm of HAL exoskeletons family varies from version to version and depends on the user's physical capabilities (degree of motor functions impairment) and the tasks in which the robot is intended to assist. Generally, HAL is governed by a hybrid controller. Two control modes can be distinguished: so called Cybernics[7] Voluntary Control (CVC) and Cybernics Autonomous Control (CAC), which together allow the exoskeleton to perform tasks according to user's intention [51, 53, 56–59, 108]. The HAL's controller employing CVC governs assistive toruque of the actuators according to the user's voluntary intention sensed as the bioelectrical signals (BES) from the surface of the body, most importantly the muscle activity (EMG). Ground Reaction Force (also called Floor Reaction Force) and angular position of the HAL's joints measured by potentiometers is also used to determine the state of the user's body and consequently his intent (compare with section 2.3.2, see Fig. 2.7). This is in contrast with CAC, in which these signals are used as main estimators of user's intentions. Observing certain parameters, user position proceeding action, GRF or position of centre of the gravity (CoG) his actions can be deducted and appropriate control can be applied to support consecutive movement. Those remain only sources of information when BES are too weak to be detected or properly recognised, which occurs in cases of paralysis [46, 50, 51, 58, 59, 106].

[7] *cybernics* is a term proposed by *Sankai* to describe "a new domain of interdisciplinary research centred on cybernetics, mechatronics, and informatics, [that] integrates neuroscience, robotics, systems engineering, information technology, kansei engineering, ergonomics, physiology, social science, law, ethics, management, economics etc." [107]

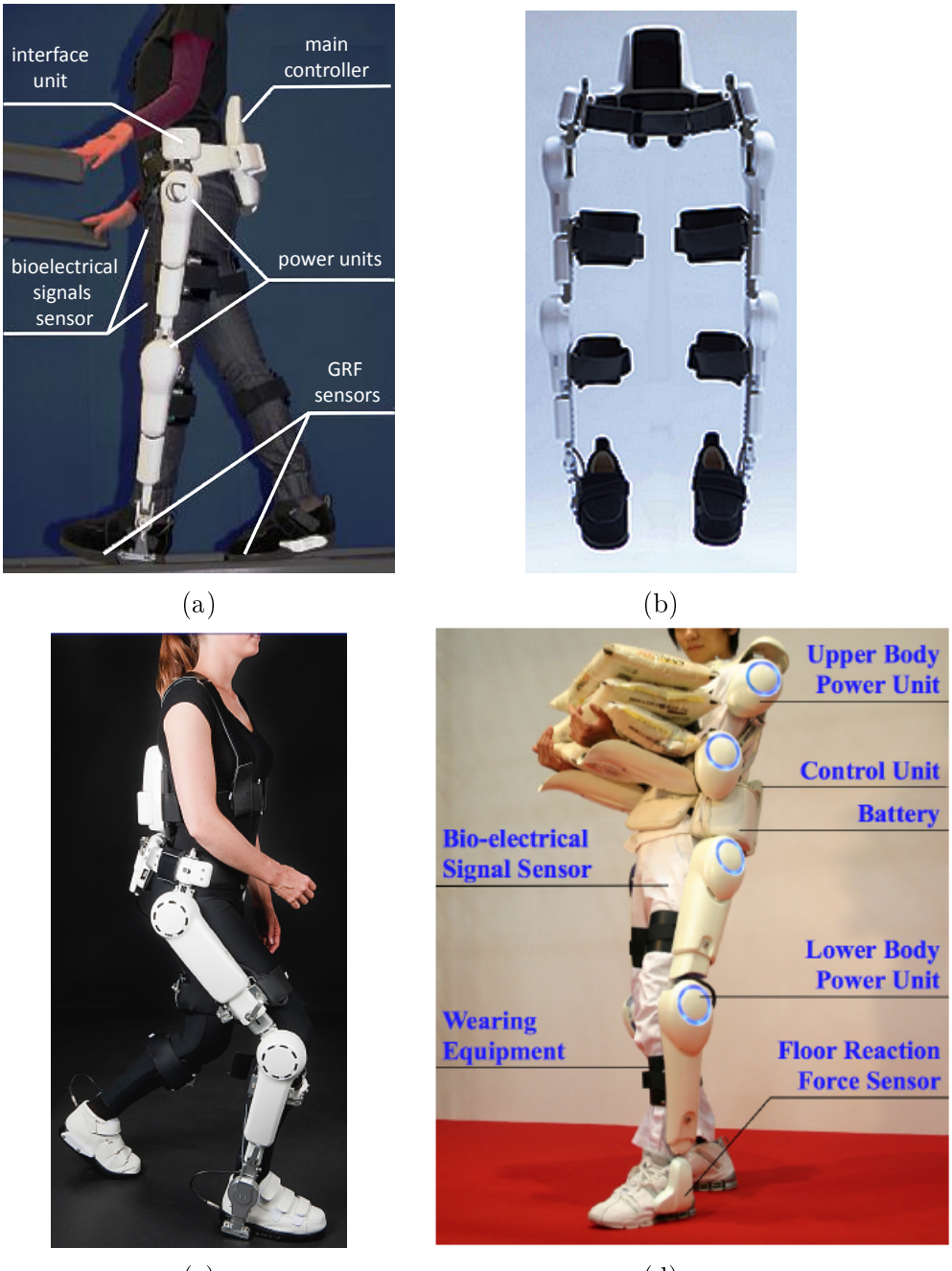

Figure 2.26: Hybrid Assistive Limb variants: a) HAL for Welfare Use – Lower Limb Model, side view [52], b) HAL for Welfare Use, front view [62], c) HAL for Medical Use – Lower Limb Model [HAL–ML-05 EU model] [59], d) HAL–5 full body [57].

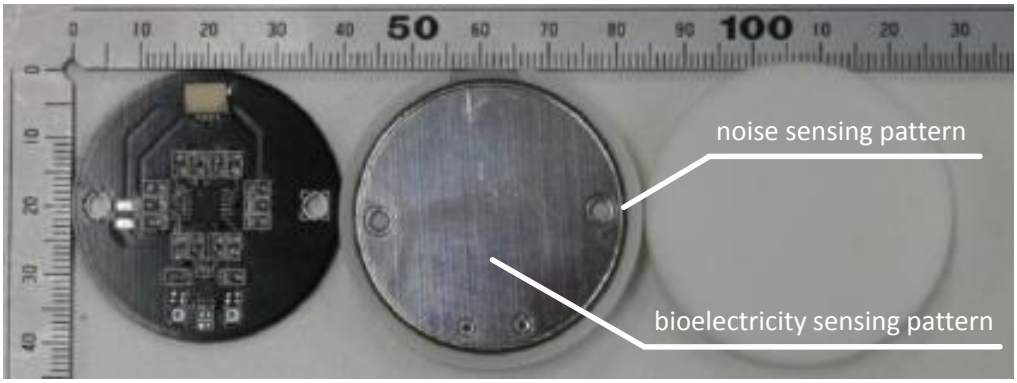

Figure 2.27: Hybrid capacitive–resistive electrodes: circuit board, sensing lead and case (adapted from [81]). Approx. 40 mm in diameter and 4 mm thick.

Cybernics Voluntary Control

When working in the CVC mode, HAL administers the required torque to the joints based on levels of bioelectric signals (BES, also called EMG signals) sensed (see section 2.2). It has been reported that the relationship between the joint torque (muscle force) and myoelectrical signals levels of muscle under isometric contraction is linear [109]. Experiments by developers of HAL confirmed the relationship and its applicability to control of wearable robots [40–42, 49]. They also confirmed that the bioelectric signal precedes the torque generation at the joint [40]. Moreover, HAL's developers established that in order to employ the EMG signals in the control system, the signals have to be preconditioned to filter out the noise due to movement artefacts of the electrodes and connection cables (range 0 – 20 Hz [78]). This was done in HAL–3's measurement system, in which the signal from the electrodes, after being amplified, was filtered by a high–pass filter with 33 Hz cut off frequency. Simultaneously, it was also low–pass filtered with a cut off frequency of 500 Hz. However successful in the clinical setting, the main drawback of using the EMG signals in control of wearable robots appeared to be the need of skin surface preparation by shaving it and covering with conductive gel. Hence, the so called wet electrodes, used commonly in clinical setting, has not been eventually favoured due to the user's discomfort and robustness issues over a long time of operation. In order to tackle the problem hybrid capacitive–resistive electrodes (depicted in Fig. 2.27) have been developed [80,81]. The electrodes have two inputs with optimised electrical impedance, one for electrostatic noise and one for BES. High reliance has been achieved by noise cancellation using differential amplifier. As a result, problems with delays and distortion of filters have been circum-

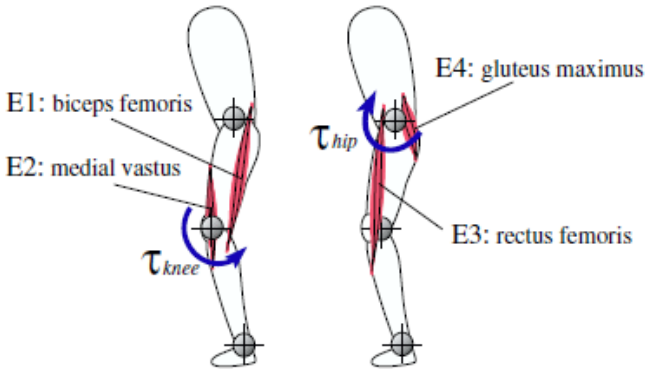

Figure 2.28: Main muscles actuating the knee joint (left) and the hip joint (right), where the BES is sensed for HAL's control [42].

vented. The electrodes are capable of sensing BES with almost the same robustness as wet electrodes. Working in the capacitive mode they can operate through a 2.2 mm thick jeans cloth. They are also capable to work as dry resistive electrodes when placed directly on the skin with even better performance.

In order to estimate torque at a human joint, two electrodes are placed at antagonistic muscles actuating it. For lower–body's HAL–3's measurement setup, electrodes are placed at *medial vastus* (extensor), *biceps femoris* (flexor) for the knee joint and *rectus femoris* (flexor), *gluteus maximus* (extensor) for the hip joint (see Fig. 2.28). The assistive torque of the actuators is determined from formula [41–43, 49, 53, 57]:

$$\tau^j_{act}(t) = \alpha^j(K^j_{flex}e^j_{flex}(t) - K^j_{ext}e^j_{ext}(t)) \tag{2.28}$$

where:

$\tau_{act}(t)$ – actuator torque
j – joint (left, right knee, hip etc.)
α – adjustable assistance coefficient ($\alpha \in [0, 1]$)
K_{flex}, K_{ext} – experimental proportionality coefficients between BES levels and torque of flexor (extensor)
$e_{ext}(t)$, $e_{flex}(t)$ – BES levels measured at joint extensor (flexor) after preprocessing

Since raw output from the electrodes is not suitable as input to the controller, BES levels e_{ext}, e_{flex} are preprocessed (integrated over a certain interval, smoothed) before

being used [48,49]. Root Mean Square transform has been also proposed [44]:

$$RMS(r(t)) = \sqrt{\frac{1}{T}\int_0^T r^2(t)\mathrm{d}t} \tag{2.29}$$

where T – inegration interval, $r(t)$ – raw signal from the electrodes.

Proportionality coefficients K_{flex}, K_{ext} vary from user to user and are different for different joints. Thus, before applying the control method, these parameters have to be identified. For that purpose several calibration methods involving experiments examining muscle activity under changing load have been proposed [41,42,44,49,53,56,80,81]. α is chosen arbitrarily to provide comfortable assistance.

The robot is governed using the Eq. (2.28) when a limb acts moving through an environment. However legs during gait function as a support for the rest of the body (stance phase) as well as propel through space to advance forward (swing phase). The objectives during these phases vary and more specific control can be applied. Because of that in the HAL controller the task of walking is divided into phases in which different control regimes are applied [41,42,45,46,48]. At the highest level (see section 2.3.2, Fig. 2.9) the decision regarding the active control regime is taken through a state machine with levels of GRF as transition conditions. GRF is measured using sensor depicted in Fig. 2.3. The sensor operates measuring the the pressure in two tubes (located in the heel and the ball) embedded in a sole of an exoskeleton. One of the applications of GRF force to control of the lower body exoskeleton is described in [41]. The leg is in the swing phase when the GRF measured at the ball and at the heel is equal to 0. Otherwise, it is in the stance phase. In both of the phases, torque at the hip and at the knee is governed by Eq. (2.28). However it has been observed in this setup that hip does not extend in the terminal period of the stance phase due to torque generated based on activity of hip flexor. As a solution, K_{flex} in the Eq. (2.28) is set to 0 when GRF measured at the heel is smaller then half of the maximum value:

$$\begin{aligned} \tau_{hip}(t) = &\quad K_{flex}^{hip} e_{flex}^{hip}(t) - K_{ext}^{hip} e_{ext}^{hip}(t) && \text{if } GRF_{heel}(t) \geq \tfrac{GRF_{max}}{2} \\ \tau_{hip}(t) = &\quad -K_{ext}^{hip} e_{ext}^{hip}(t) && \text{if } GRF_{heel}(t) < \tfrac{GRF_{max}}{2} \end{aligned} \tag{2.30}$$

An alternative control scheme for walking for HAL was proposed in [48]. The control given by Eq. (2.28) is not used. Instead, the assistive torque in certain phases is adjusted comparing BES levels without assistance and with certain degree of assistive

torque. The gait is divided into three phases: Phase 1 (swing), Phase 3 (stance) and Phase 2, which is a phase in between when muscles do not work and extend freely in terminal phase of the swing. During each phase extensors and flexors of the joints work in one of the modes: active (exert force in direction of muscle contraction), passive (exert force and elongate), free (does not work). The state (phase) of the leg is detected using the GRF sensor. In Fig. 2.29 the state machine with transition conditions is shown. Exemplary parameters for an operator are given. In Table 2.2 modes of muscles in each phase are given. In Table 2.3 control for the hip joint and the knee joint in each of the phases is given. θ_{hip}, θ_{knee} are the angles at the joint, 0 when standing up straight, positive in the direction of flexion and negative in direction of extension. The parameters selected were: $\tau^{hip}_{phase1} = 12$ N (const.), $\tau^{hip}_{phase3} = 4$ N (const.), $K_p = 7$, $K_d = 0$, $\beta = 0.8$. The standing up task can be similarily divided into phases based on GRF and angles at the joint measured using potentiometers [41,42,46,106]. CVC control was also adapted for single legged version of HAL for patients with hemiplegia [52, 53].

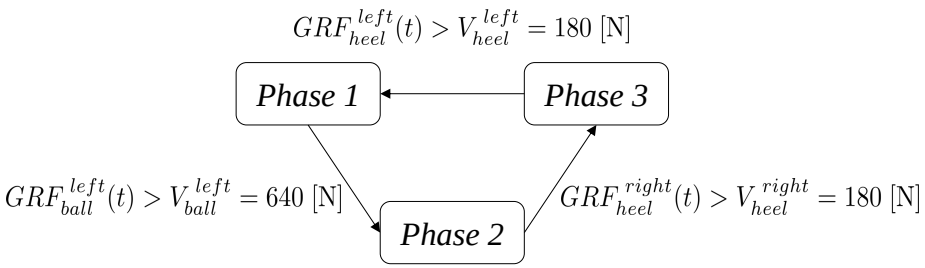

Figure 2.29: State machine of HAL for detecting phase of the gait of right leg (adapted from [48]).

Table 2.2: HAL's muscles modes [48].

	Phase1		Phase2		Phase3	
					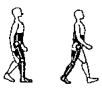	
Joint	Direction	Mode	Direction	Mode	Direction	Mode
Hip	Flexion	Active	Extension	Free	Extension	Active
Knee	Flexion ↓ Extension	Free	Flexion	Free	Flexion ↓ Extension	Passive

Table 2.3: Control regimes of HAL in different phases of gait [48].

	Phase 1	Phase 2	Phase 3
hip	τ^{hip}_{phase1}	0	τ^{hip}_{phase3}
knee	$-\beta\theta_{hip}$	0	$K_p\theta_{knee} + K_d\theta_{knee}$

Cybernics Autonomous Control

In the Cybernics Autonomous Control the BES are not used. Instead the decision about intention is recognised using position of the user and GRF. The controller follows prerecorded trajectories of the legs of a healthy subject [50, 59, 81, 108]. This type of control is suitable for patients with paralysis of the lower limbs. At the highest level, the decision which leg has to be moved is taken based on the tilt of torso in the lateral plane (see Fig. 2.30). For that purpose a gyroscope can be employed. If the inclination in any direction exceeds a threshold (0.05 rad) a movement of an opposite leg is initiated to follow reference angular position $q_{ref\_\{r,l\}}$ and speed $\dot{q}_{ref\_\{r,l\}}$ trajectories (see Fig. 2.31). Alternatively, a GRF can be used to detect shifting CoG. The administered torque is calculated using PD controller:

$$\tau_{\{r,l\}} = k_{\{r,l\}}(q_{ref\_\{r,l\}} - q_{\{r,l\}}) + k'_{\{r,l\}}(\dot{q}_{ref\_\{r,l\}} - \dot{q}_{\{r,l\}}) \tag{2.31}$$

where:

$k_{\{r,l\}}$, $k'_{\{r,l\}}$ – PD controller settings
$q_{ref\_\{r,l\}}$, $\dot{q}_{ref\_\{r,l\}}$ – measured angles at the joints (hip, knee, ankle)

The CAC was adapted also for a single legged version of HAL for patient with impairment of knee flexor (hemiplegia) [51]. The gait was divided into phases using GRF sensor, and assistive torque was mainly applied in the swing phase to clear the impaired leg from the ground.

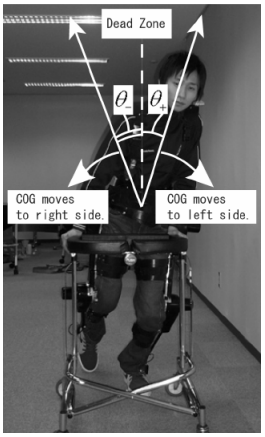

Figure 2.30: Torso angle estimation for HAL in CAC mode [50].

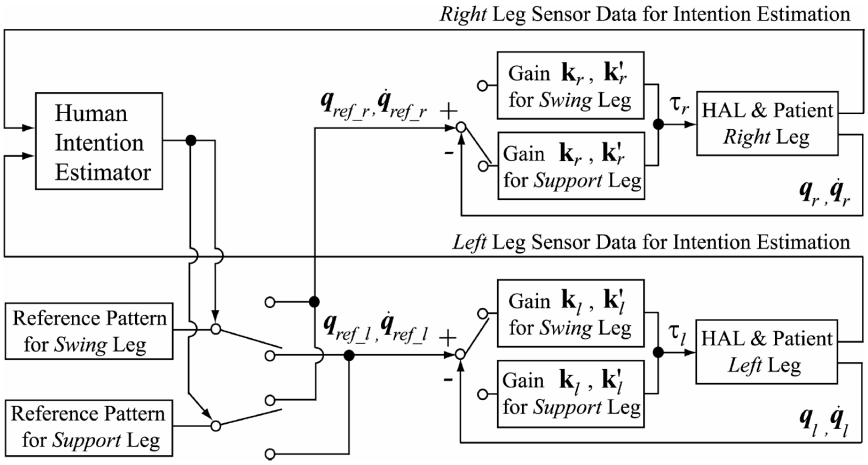

Figure 2.31: Cybernics Autonomous Control of HAL [50].

2.10 Dynamic Balance and Zero–Moment Point

This separate section is devoted to an important aspect of bipedal locomotion, which is maintaining dynamic balance (stability of posture). If and only if dynamic balance is maintained, a mechanism performing gait, or as a fact any activity, will not overturn (fall down). Because enhancive exoskeletons transfer the forces due to load, its own mass and the user to the ground through a sole, they are subject to this requirement. To examine and satisfy the dynamic balance, a notion of Zero–Moment Point was introduced by *Vukobratović* [1].

Let us introduce notion of Zero–Moment Point in context of an enhancive exoskeleton. Consider a rigid exoskeleton foot with a flat contact surface in single–stance phase with contact with a flat surface, as in Fig. 2.32a. For the purpose of the argument lets omit segments of kinematic chain above the ankle joint located at point A and consider that forces/torques due to machine dynamics above ankle, forces/torques due to the load and the user (including force between operator's foot and exoskeleton sole) are reduced to force $\mathbf{F}_{\mathrm{A}} = [F_{\mathrm{AX}}, F_{\mathrm{AY}}, F_{\mathrm{AZ}}]$ and torque $\mathbf{M}_{\mathrm{A}} = [M_{\mathrm{AX}}, M_{\mathrm{AY}}, M_{\mathrm{AZ}}]$ acting at the point A and expressed in FoR with an origin at 0 (axis Z along gravity field, which is normal to the ground surface, see Figure 2.32b). Other forces (torques) acting on the sole are: force due to gravity $\mathbf{G} = \mathrm{m_S} \cdot \mathbf{g}$ at point G, where $\mathrm{m_S}$ – mass of the sole, $\mathbf{g}$ – gravity vector; and reaction force $\mathbf{R} = [R_{\mathrm{X}}, R_{\mathrm{Y}}, R_{\mathrm{Z}}]$ and reaction torque $\mathbf{M} = [M_{\mathrm{X}}, M_{\mathrm{Y}}, M_{\mathrm{Z}}]$, both attached at some point P. R_{Z} – is normal force due to contact with the ground, R_{X} and R_{Y} are frictious and act in horizontal plane by nature of properties

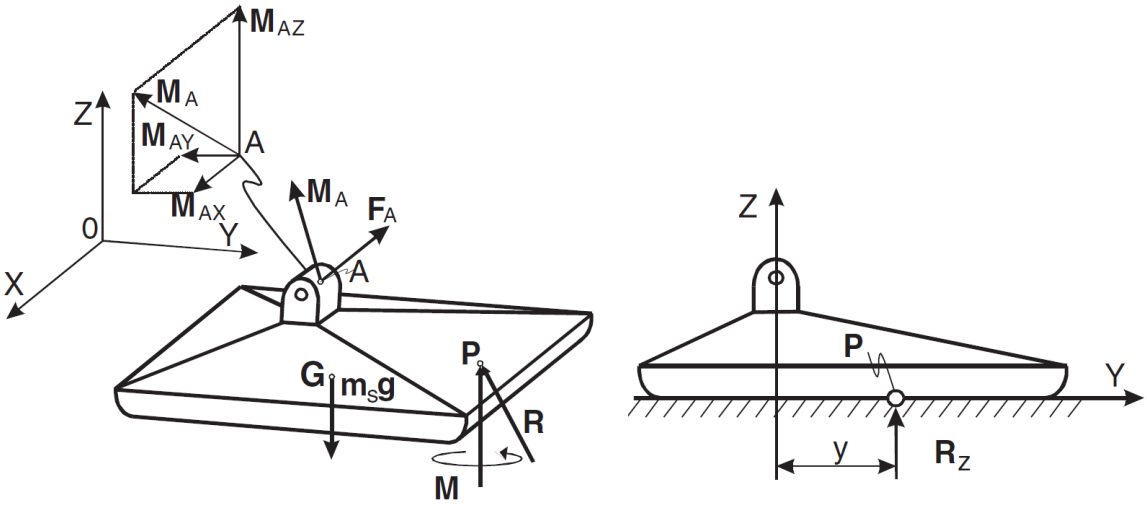

(a) (b)

Figure 2.32: Sole of a humanoid robot for defining of notion of Zero–Moment Point [1].

of friction. M_{Z} is due to the same properties. We are looking for some point P, which has properties of the ground reaction contact $M_{\mathrm{X}} = M_{\mathrm{Y}} = 0$. At this point there are no friction forces acting in planes perpendicular to the horizontal (ground) plane, normal vector is along the line of intersection of planes perpendicular to the horizontal plane and P lies on the intersection of all 3 planes. We demand that the sole is in static equilibrium, with 0 linear and angular velocity with respect to FoR with origin at O. In such case, static equilibrium equations take form:

$$\mathbf{R} + \mathbf{F}_{\mathrm{A}} + m_{\mathrm{S}}\mathbf{g} = 0 \tag{2.32}$$

$$\overrightarrow{\mathrm{OP}} \times \overrightarrow{\mathbf{R}} + \overrightarrow{\mathrm{OG}} \times (m_{\mathrm{s}}\mathbf{g}) + \mathbf{M}_{\mathrm{A}} + \mathbf{M} + \overrightarrow{\mathrm{OA}} \times \overrightarrow{\mathbf{F}_{\mathrm{A}}} = 0 \tag{2.33}$$

where $\vec{\mathrm{OP}}$, $\vec{\mathrm{OG}}$, $\vec{\mathrm{OA}}$ are vectors from origin O to points P, G and A respectively. From Eq. (2.32) $\mathbf{R}$ can be calculated. Since vertical component of P is known and equals 0, let us project Eq. (2.33) on the horizontal plane:

$$(\overrightarrow{\mathrm{OP}} \times \overrightarrow{\mathbf{R}})^H + (\overrightarrow{\mathrm{OG}} \times (m_{\mathrm{s}}\mathbf{g}))^H + \mathbf{M}_{\mathrm{A}} + (\overrightarrow{\mathrm{OA}} \times \overrightarrow{\mathbf{F}_{\mathrm{A}}})^H = 0 \tag{2.34}$$

Unconstrained system of linear equations (2.34) always has a solution. But a physical constraint exists. That is, horizontal components of P must be within the polygon of the shape of the exoskeleton sole. If this constrain is satisfied, point P is called Zero–Moment Point and it is necessary and sufficient condition for the machine to be in dynamic balance, because condition $M_{\mathrm{X}} = M_{\mathrm{Y}} = 0$ (hence the ZMP name) is satisfied.

If the calculated point P is not within the polygon of the sole, there is unbalanced torque causing the machine to overturn (angular acceleration of the machine is non–zero in FoR with origin at O). For the exoskeleton to be in dynamic balance (postural stability), there are constraints on $\mathbf{F}_{\mathrm{A}}$ and $\mathbf{M}_{\mathrm{A}}$, hence requirements on the control strategy.

2.11 Summary

From section 2.2, where properties of human body are considered, it is concluded that Ground Reaction Force sensors have to be incorporated into the exoskeleton system to recognise configuration in which the user's body is during various tasks. The problem can be stated in other words as finding Jacobian of the robot (Eq. 2.8). This is a role of high level control algorithm. Such algorithm has been only reported to exist for BLEEX. It requires special design of flexible sole with switches embedded. For full–body enhancive exoskeletons such high level control has not been proposed. The problem of determining the Jacobian is connected with placement of sensors sensing human–machine interaction force on the exoskeleton frame. The placement was done for Sarcos XOS, but the justification is not available. Selection process and exemplary settings of parameters of middle level controller gains or investigation into stability range has not been reported. Also, where filters are used, there is no information on chosen time constants.

According to the literature, *Master–Slave Position Control* law is not suitable for control of enhancive exoskeletons (see section 2.4). Working exoskeletons were demonstrated to be governed by *Direct Force Control* law (full–body exoskeletons Sarcos XOS 1 and Ratheon XOS 2, see sections 2.5.1, 2.7) or *Virtual Torque Control* law (lower–body BLEEX, see sections 2.5.3, 2.6). However, performance of the machines neither in simulation nor experimental, given for example as recordings of human–machine interaction force between robot and operator, is missing.

Information on force control of low level actuators, especially hydraulic cylinders, in context of exoskeletons is also scarce. *Racine* developed multiple sliding surface adaptive control law for BLEEX [16] but evaluation of the controller working as part of the robot, for example during gait, is not available. There is no information on performance of low level controller of actuators of full–body exoskeletons.

Racine is also only author to consider sagittal stability of enhancive exoskeletons. He developed a guard preventing the machine from entering instability region. Such control mechanism would have to be developed for an enhancive full–body exoskeleton,

extending the model with upper extremities in which load can be carried.

However control based on bioelectric signals (EMG) was demonstrated to successfully govern assistive exoskeletons (see section 2.8, and HAL in section 2.9), it is not suitable for enhancive exoskeletons as they are defined in section 2.3.1.

Chapter 3

Requirements and Evaluation of Control Laws for Full–body Exoskeletons

3.1 Introduction

The main conclusion from the literature review (see chapter 2) is that the exoskeleton is a biomechatronic device. Design of such machine involves experts and knowledge from domains of mechanical engineering, electrical engineering, telecommunications engineering, control engineering, computer engineering as well as biology, particularly human physiology. To describe and specify a machine under consideration, a number of meetings compromising of specialists from those disciplines was conducted. The result is a list of provisions, which is included in this section (End Users' Needs, see Table 3.2). On the basis of the End Users' Needs list, Project Requirements were derived. Suitability of the control laws for governing of full–body exoskeletons with respect to the project requirements is evaluated. Criteria by which the laws are judged are dual: for the controller itself [110] and for the measurement system [111] employed by the controller.

3.2 Requirements in the Exoskeleton Project

In order to encompass the large complexity of the task of designing of an exoskeleton, the system engineering approach was applied. In course of the meetings with the supervisors and the industrial partner initial understanding of the problem was captured

Table 3.1: Expressions used for specifying provisions levels according to [112].

	Provision	**Positive**	**Negative**
Importance ↑	requirement	shall	shall not
	recommendation	should	should not
	permission	may	need not
	possibility and capability	can	cannot

in form of provisions[1] about desired characteristics and functionality of an operational machine [2]. Provisions are expressed using verbs denoting levels of importance (see Table 3.1). The End Users' Needs[3] are given in Table 3.2.

Table 3.2: End Users' Needs in the Exoskeleton Project [114]

Unique Identifier	Need
N-1	The device shall be a full body exoskeleton.
N-2	The kinematic design of the frame shall allow the device to perform activities specified in Appendix D.
N-3	The frame shall be adjustable for different user size.
N-4	The frame shall be modular.
N-5	The joint and the actuator for each DOF shall be a separable module.
N-6	The primary product shall be untethered, i.e. energetically independent.
N-7	The load carrying capacity shall be the maximum achievable amount, considering the safety.[4]

[1] *Provisions* are more often referred to as requirements, although this is not strictly valid because the set of provisions encompasses requirements, recommendations, permissions, possibilities and capabilities.

[2] Very similar approach was used by designers of Mindwalker rehabilitation exoskeleton [113]

[3] *End Users' Needs* within the system engineering approach by convention are the provisions describing the device from the holistic (top–level) view.

[4] The safest recommendation is to assume that the robot *shall* exert minimal forces on the user due to the load carried. Allowable levels for human–robot physical interactions are currently subject of research in the domain of biomechanics, and those must be strictly controlled to be kept within allowable limits. [68].

Table 3.2 (Cont.)

N-8	The system shall be able to sense human motion (kinematics and dynamics).
N-9	The device shall be easy to use.
N-10	The device shall be easily adaptable to a new user.
N-11	The device shall be safe.
N-12	The device shall be reliable.
N-13	The device shall be weight efficient.
N-14	The power consumption of the device shall be efficient.
N-15	The operation (as explained in Appendix D) duration time shall be long.
N-16	The system shall be cost-effective.
N-17	The appearance of the device shall be acceptable.
N-18	The user shall not be burdened with any extra effort to carry the exoskeleton (while not carrying any payload).
N-19	The device shall comply with University of Leeds standards.
N-20	The device shall comply with BS EN ISO 13482:2014.[5]
N-21	There shall be a feasible maintenance scheme in place.
N-22	The device shall have an acceptable life-cycle.
N-23	The device may increase the metabolic cost during load carrying task.[6]
N-24	The actuators of the device should be dynamically strong enough to perform activities specified in Appendix D except for running.
N-25	The device should not impede movements.[4]
N-26	The device may be clean.

[5] Deviation allowed in the prototype for N–20: The device *may comply with BS EN ISO 13482:2014*. Taking into consideration requirements imposed by the norm, achieving full compliance with it is beyond timeframe for building a prototype. Safety-related sensory system and algorithms seem still to be viable fields of innovation.

[6] Definition of metabolic cost of using exoskeleton is given in Appendix A. Considering Footnote 4, the safest recommendation is to keep the forces minimal, hence $\Delta E_{met} = 0$.

Table 3.2 (Cont.)

N-27	The device may be easily put on and off by the user without any assistance.
N-28	The noise produced by the primary product may be socially acceptable.
N-29	The Type 1 variation of the device may be possible to achieve via modular changes (low cost, assistive, with the minimum possible actuators). [7]
N-30	The Type 3 variation of the device may be possible to achieve via modular changes (lower limb with a backpack frame, enhancive).
N-31	The Type 5 variation of the device may be possible to achieve via modular changes (lower limb exoskeleton, hung from a frame or the ceiling, used for rehabilitation).[7]
N-32	The design should allow for subsystems of the product to be used as orthotic devices.[7]

The End Users' Needs were used to derive the following sets of requirements for device under consideration:

- Control System General Requirements [110]
- Measurement System General Requirements [111]

They have their source in safety standards and in the literature on exoskeletons and human biomechanics. Derived requirements are listed in Table 3.3.

Table 3.3: Project requirements for enhancive exoskeleton controller (CS) and measurement system (MS).

Unique Identifier[8]	Requirement
CS-1	The controller shall be adaptable to different users.
CS-2	The controller shall allow performing activities listed in the Appendix D.[9]

[7] Measurement system and control law of full–body exoskeleton are not reusable for this type of robot.

[8] Unique Identifiers are not sequential and are taken from another document

[9] This provision covers also "CS-13: The controller may allow performing activities not listed in the Appendix [Appendix D]"

Table 3.3 (Cont.)

CS-3	The controller shall be robust.
CS-5	The control method, as implemented in the controller, shall be safe.
CS-6	The device shall be stable when governed by the controller during putting on and off.
CS-7	The device governed by the controller shall be stable while carrying the load.
CS-8	The device governed by the controller shall be stable in case of collision.
CS-9	The controller shall prevent hazardous physical contact during human–robot interaction.
CS-10	The controller should be reusable in orthotic devices.
CS-11	The control method, as implemented in the controller, shall not induce vibrations on the device.
CS-12	The activity of musculoskeletal system shall be controllable by the controller.
CS-14	The controller shall allow for the modularity of the frame.
MS-1	The measurement system shall be adaptable to different users.
MS-2	The measurement system shall allow performing activities listed in the Appendix D.
MS-3	The measurement system shall be ergonomic.
MS-4	The measurement system shall be non-obtrusive.
MS-5	The mechanical complexity of measurement system shall be low.
MS-6	The power consumption using the measurement system shall be low.
MS-7	The measurement system shall be safe.
MS-8	The measurement system shall sense human motion kinematics.
MS-9	The measurement system should be reusable in orthotic devices.
MS-10	The activity of musculoskeletal system shall be observable by the measurement system.
MS-11	The measurement system shall sense human motion dynamics.

Table 3.3 (Cont.)

MS-12	The measurement system shall allow for the modularity of the frame.

3.3 Evaluation of Control Laws for Exoskeletons with Respect to Project Requirements

In [16] *Racine* evaluates usefulness of several control laws for governance of lower body exoskeletons. The results of the analysis are presented in Table 3.4. In *Racine's* comparison the EMG control law is given the worst score. It must be however noted that criteria for which this control law was given the lowest marks have been intensive fields of research since early 2000's when the analysis was performed. Due to the proliferation of cheap and fast microcontrollers and advancements in artificial intelligence methods, particularly in the domain of the pattern recognition, this method nowadays would score higher on computational requirements, adaptability to different users, speed of development. The most convincing example that this control law can be successfully used for exoskeletons is the HAL family of exoskeletons. It must be also noted that using the measurement of muscles activity, the control might be designed so that the metabolic cost of performing of a certain task by the user is lowered, heightened, or kept on the same level. Myosignal (EMG) control is however rejected as a candidate for an enhancive full–body exoskeleton because by principle the measurement system is capable only of observing activity of the muscles disregarding the interaction force between machine and user (state of musculoskeletal system). Hence, while being suitable for assistive devices, it is not feasible to use it for control of enhancive devices (compare with definitions of enhancive and assistive exoskeletons in section 2.3.1).

User–command and programmed–gait control are not considered as candidates for the control of a full–body exoskeleton given the limited number of activities they can cover, and due to the fact that the upper limbs should move freely and not be involved in interaction with the interface for the lower body. Since the objective is to control the upper limbs of an exoskeleton, using solely the ground–reaction force control law is also not feasible. This control law requires very precise model of the user too.

The considered control laws for enhancive full–body exoskeletons might be categorised into two groups:

– *Master–Slave Position Control* (abbreviated MSPC), where controlled variables are angles at joints of the exoskeleton, with an objective to match them to oper-

Table 3.4: Benchmarking of lower–body exoskeleton control laws by *Racine* [16].

Selection index / **Control method**	User-command	Myosignal	Programmed gait	Master-slave	Force feedback	Ground reaction force	Virtual force	Virtual torque
1. Adaptability to different operators	5	1	2	1	3	2	5	5
2. Ability to conduct different activities	1	2	1	5	5	5	5	5
3. Controller robustness	1	1	2	5	5	2	3	4
4. Ergonomics	5	5	5	2	2	4	4	5
5. Non-obtrusive	1	2	5	1	2	3	5	5
6. Speed of development	4	1	4	2	2	3	5	5
7. Low # human sensors	3	1	5	2	2	3	5	5
8. Low # machine sensors	3	3	4	4	3	1	1	3
9. Low mechanical hardware complexity	5	5	5	1	2	2	4	5
10. Low computational requirements	5	2	3	4	3	1	2	2
Total Score	**33**	**23**	**36**	**27**	**29**	**26**	**39**	**44**

ator's joint angles;

– *Force Control* (abbreviated FC, including *Direct Force Feedback*, and *Virtual Force* techniques), where the controlled variable is human–machine interaction force.

The evaluation of these control methods with regard to the project requirements is given in Table 3.5. For each requirement, a numeric value is assigned. Below is given evaluation. MSPC refers to considerations of *Master–Slave Position Control* and FC refers to considerations of *Fore Control*.

Table 3.5: Evaluation of the control laws for enhancive exoskeleton.

Unique Identifier[10]	Master-slave position methods	Direct Force methods	Indirect Force methods
CS-1	5	5	5
CS-2	5	5	5
CS-3	4	5	3
CS-5	1	5	4
CS-6	3	4	3
CS-7	3	4	4
CS-8	1	4	3
CS-9	1	5	5
CS-10	1	4	3
CS-11	2	5	5
CS-12	1	4	5
CS-14	3	3	2
MS-1	1	3	5
MS-2	2	5	5
MS-3	2	3	5

[10]Unique Identifiers are not sequential and are taken from another document

Table 3.5 (Cont.)

MS-4	1	3	5
MS-5	1	3	4
MS-6	1	5	5
MS-7	1	4	4
MS-8	5	2	2
MS-9	1	5	3
MS-10	1	4	3
MS-11	1	5	5
MS-12	5	2	5
Total:	52	97	98

CS–1: The controller shall be adaptable to different users.

MSPC: The controller scores high for that requirement. Registered joint angles are simply fed to the control system of the outer exoskeleton with the aim of matching them together.

FC: The controller does not depend on a model of user body, so it is instantaneously adaptable to a new operator.

CS–2: The controller shall allow performing activities listed in the Appendix D.

MSPC: If the measurnoement system captures human motion *perfectly*, and the kinematics of the outer exoskeleton match *perfectly* those of the user, then controller allows for wide range of manoeuvres, including those listed. The controller itself scores high, but not the measurement system (see MS–2).

FC: The force control methods do not limit the activities performed by the operator in any way. They can move their extremities freely within the robot, and the robot moves in concert.

CS–3: The controller shall be robust.

MSPC: The controller does not rely neither on a model of human body nor the device, thus it is not subject to identification uncertainties. However, this is under assumption that the lower–level control is robust enough to allow actuators to perform under changing, uncertain load.

FC: The *Indirect Force* methods depend heavily on the machine dynamics model so the controller robustness becomes a concern. Thus they are given intermediate score. On the other hand, *Direct Force* methods require identification of machine parameters to be performed.

CS–5: The control method, as implemented in the controller, shall be safe.

MSPC: The control law would not prevent highly rated forces to be exerted on the user in case of interference with the outer exoskeleton. The law is considered to be very unsafe. Moreover, any measurement error or imperfections in fitting of the outer exoskeleton to a certain user would cause uncontrolled forces to be exerted on the user at unintended locations.

FC: The *Direct Force Control* law is inherently safe as it aims at minimising the interaction force between the machine and the user. The *Virtual Force Control* law possesses this property to some extend, but since the interaction force is estimated, it should be given a lower mark.

CS–6: The device shall be stable when governed by the controller during putting on and off.

MSPC: If the inner exoskeleton is being put on and off, or when part of the inner suit unintentionally detaches, the outer exoskeleton would perform unpredictable moves. This however might be solved by implementation of additional rules in the controller. Intermediate score is thus given for that requirement.

FC: Since the force methods are designed to operate with a goal of minimising the interaction force, they are generally stable. Temporary loss of contact with operator's

limb of the robot frame would not cause uncontrolled behaviour. However virtual control methods are less resilient to loosing stability if permanently unloaded with the human–robot interaction force as described by *Kazerooni* [18].

CS–7: The device governed by the controller shall be stable while carrying the load.

MSPC: In principle, the user is detached from the outer exoskeleton, so his/her balance perception is not used for load stabilisation. Supporting the outer exoskeleton in such situation would be considered erroneous condition of the controller. The law is given the lowest score. However, it could be improved to a certain degree by addition of haptic feedback.

FC: Since in the normal operation mode the user is in non–forceful physical contact with the robot, he can sense dynamical behaviour of the load. The kinematic chain between the load and the user body allows for information to flow from the load–bearing end effector to the operator's sensory system. Moreover, if necessary, he can support the device in maintaining the balance.

CS–8: The device governed by the controller shall be stable in case of collision.

MSPC: As for CS–7, since the user is detached from the outer load–bearing exoskeleton, the sensing of collision situation is limited. Supporting the outer structure is considered to be an erroneous condition of the controller. Again, the law could be slightly improved by incorporation of the haptic feedback, but in general, it scores low. In addition to the problems mentioned, the high gain controllers might induce vibrations or cause the loss of stability if the input to the controller is a high frequency signal, as for example when bumping into an obstacle (see CS–11).

FC: Similarly to the point C–7, user intellect can be utilised to govern the device in case of hazardous situation. According to [18] *Indirect Force* methods are not stable without the presence of an operator, but by the controller design this vulnerability enables the user to steer the device into a safe behaviour in case of collision.

CS–9: The controller shall prevent hazardous physical contact during human–robot interaction.

MSPC: The control law does not take into account interaction force between a user and the robot. Lowest score is given for that requirement. Due to the high gain in the contoller feedback loop, the device might induce vibrations or even loose stability. Such situation might lead to uncontrolled, unintended force being exerted on a user body. Successful implementation of the *Master–Slave Position Control* would then require safety–related force control as described in the standard [68].

FC: The goal of the force control laws is to apply controlled force (with values depending on the chosen goal of the metabolic cost of the user ΔE_{met}) at the points of human–machine interaction. In general, the force methods are the safest class of the laws for governing the exoskeletons.

CS–10: The controller should be reusable in orthotic devices.

MSPC: The purpose of the orthotic devices is to add torque (inject energy: $\Delta E_{met} < 0$) to the joint. For the considered device, if all the conditions for successful implementation are met, $\Delta E_{met} = 0$. The control law is thus unsuitable for usage in the orthotic devices.

FC: The orthotic devices require torque to be applied to power a human joint. Force methods can achieve lowering of the metabolic cost of performing of an activity ($\Delta E_{met} < 0$) or can allow an energetically costly activity to be performed by a disabled user. *Indirect Force* methods utilise estimation of force, so they would be less useful in the orthotic devices.

CS–11: The control method, as implemented in the controller, shall not induce vibrations on the device.

MSPC: The realisation of a servomechanism quickly following user moves would require a high gain to be used in the feedback loop. Such control schemes are naturally predisposed to induce vibrations or even loose stability (in the sense of the Lyapunov stability). The issue might be solved by implementation of additional rules in the controller, but the law generally scores low for this requirement.

FC: The force methods, in general, prevent forceful contact between the robot and the user. The likelihood of induction of harmful vibrations is highly reduced, with human–machine interface acting naturally as a damper.

CS–12: The activity of musculoskeletal system shall be controllable by the controller.

MSPC: Successful implementation of the control law results at best in $\Delta E_{met} = 0$ (see CS–10). Any other value is not possible to achieve. Moreover, in the presence of inaccuracy of the measutement system or imperfect fitting of the outer exoskeleton, the metabolic cost is not controllable (because there is no control of the human–machine interaction force). The law is given the lowest score.

FC: If the interaction force is controlled, the metabolic cost is controlled too. See *Appendix A – Control Goals* for elaboration.

CS–14: The controller shall allow for the modularity of the frame.

MSPC: The controller objective of matching joints of inner and outer exoskeleton allows for separation of the controller into subroutines confinable to each joint. However, that way, the effects of cross–coupling between joints are not taken into account. To prevent the worst case of loosing stability in presence of uncertain or changing machine parameters, demands on robustness on the actuators under governance of the controller are very high. Moreover, this would lead to suboptimal performance of the controller.

FC: For *Direct Force Control* Jacobian has to be updated to reflect geometry of the manipulator each time new module is introduced into the system. For *Indirect Force Control*, in such situation, general equations of motion have to be adjusted.

MS–1: The measurement system shall be adaptable to different users.

MSPC: The inner exoskeleton would have to be custom fitted to each user. Centres of joint rotation need to be tracked during movement. This is considered to be a difficult task especially for knee and shoulder joints. The accuracy of measurement instrumentation, which is embedded into the inner exoskeleton would rely on the qual-

ity of attachments to the human skin. Perspiration or user clothing would introduce measurement error as braces would slip causing unintended displacement of locomotion capturing system. These problems can be addressed by precise tailoring of the inner suit, but dimensions of the user's body segments as well as properties of his/her musculoskeletal system would have to be known for that. To follow user movements without interference, the outer exoskeleton would have to be also tailored to match dimensions and properties (length of body segments, centres of joint rotation) of a particular user. The control law scores low for this requirement.

FC: The measurement system for *Indirected Force* methods is easily adaptable to different users. Any contact with the machine is taken into account in the controller. *Direct Force* methods require careful consideration for the design of the human–machine interface so that the repetitive contact with the brace does not cause abrasions.

MS–2: The measurement system shall allow performing activities listed in the Appendix D.

MSPC: As a result of the inner layer of an exoskeleton being instrumented, the ranges of motion are restricted. The user will not be able to perform some of the task listed or the measurement system will not be able to capture them whilst simultaneously remaining compact.

FC: The measurement system allows for versatile manoeuvres to be performed by the user, most likely covering all of those listed.

MS–3: The measurement system shall be ergonomic.

MSPC: The fact that the measurement system has to be mounted on the user and connected to the outer exoskeleton at some point makes the design not ergonomic, potentially causing bruises and chafes at the point of repetitive contact over a period of time (for example 8 hour work shift or 10 km march). The same conditions can even lead to muscle/tendon strains.

FC: Considerations for the design of the human–machine interface are described in sections 2.5.1, 2.5.2 and 2.5.3. Generally, indirect force methods allow for more compact and slimmer interfaces than direct force methods for which a sensor has to be

placed at the point of the interaction.

MS–4: The measurement system shall be non-obtrusive.

MSPC: Non–actuated hardware is mounted on the inner layer potentially impeding the user moves, decreasing ranges of joints or flexion/extension of the extremities.

FC: The goal of the controller is to minimise the interaction force, so as far as the frame is designed not to interfere with the user body, the measurement system is non–obtrusive.

MS–5: The mechanical complexity of measurement system shall be low.

MSPC: The inner exoskeleton introduces extra mechanical complexity to the system.

FC: Mechanical complexity of the measurement system is reduced by the absence of instrumentation mounted on the operator. *Direct Force* methods require more complex instrumentation mounted on the frame of the robot, whilst *Indirect Force* methods further reduce the complexity by substitution of the physical force sensors by their virtual analogues.

MS–6: The power consumption using the measurement system shall be low.

MSPC: The principle of the master–slave position control dictates that all of the outer exoskeleton DoFs are actively powered. Given the fact that the structure becomes bulky to allow the user to move within it (so that the controller will follow), the power consumption is increased tremendously. It is worth noting that the extra mass of the upper body actuators increases power consumption of the lower body actuators.

FC: Only actively actuated DoFs consume power. Some of the DoFs can be passively actuated only. For non–actuated DJs the user has to provide energy. Overall power consumption depends on number of actively actuated joints, so it can be custom–fitted to the exoskeleton application.

MS–7: The measurement system shall be safe.

MSPC: The exoskeleton using the master–slave position control would be bulky, with many heavy actuators mounted on the full–body frame (1 per each DoF), consuming high power, using heavy energy sources attached to the structure. Adding to this the fact that the exoskeleton governing law does not explicitly control the human–robot interaction force, the device would be extremely unsafe. This point of paramount importance, which cannot be stressed enough.

FC: Measurement system is mounted on a frame of the exoskeleton. It does not introduce additional hazards.

MS–8: The measurement system shall sense human motion kinematics.

MSPC: The system, after custom–fitting to a particular user, would measure human motion kinematics.

FC: Although the measurement system does not measure human motion kinematics explicitly, the information on kinematics of the interaction points are implicitly included into the controller through the employment of Jacobian.

MS–9: The measurement system should be reusable in orthotic devices.

MSPC: The measurement system is not reusable in the orthotic devices (see CS–10).

FC: Orthotic devices are instruments for application of assistive or resistive torque (forces) to the user joint. The force methods are thus suitable for orthotic devices.

MS–10: The activity of musculoskeletal system shall be observable by the measurement system.

MSPC: Since the human–robot interaction force is not measured (see CS–12), the activity of the musculoskeletal system is not observable by the measurement system.

FC: Since the interaction force is measured, the activity of the musculoskeletal system is observable.

MS–11: The measurement system shall sense human motion dynamics.

MSPC: The system does not measure human motion dynamics. It measures only configuration of the user's body segments.

FC: The measurement system senses human motion dynamics.

MS–12: The measurement system shall allow for the modularity of the frame.

MSPC: Measurement of angles at human and machine joints by principle is confined to individual joints, so the law scores perfectly for this requirement.

FC: The *Direct Force Control* law relies on measurement of interaction force by a F/T sensor attached to one of the modules, so this portion has to be present in the system always. For the *Indirect Force Control* law there is no such requirement.

3.4 Summary

The listed requirements bring thinking about an exoskeleton as a biomechatronic device into focus. Achieving a prototype fulfilling all the listed provisions might be outside the scope of the research project, but the exercise gives a direction for the development cycle, starting with mechanical design, through actuator design, electronics design, ending in the controller design. Testability (verifiability) of all the requirements might be also not achievable in the research setting. Special emphasis is placed on safety of the prototype. At each stage of testing or evaluation the machine and its environment should not endanger an operator or a researcher.

According to Table 3.5, force methods score much ahead of *Master–Slave Position Control* law. The *Master–Slave Control* scores exceptionally low on safety criteria, which are intentionally emphasized in the project requirements. Number of design constraints concerning fitting the exoskeleton to a particular user, which have to be met to make the control law successful, in combination with predicted poor performance of the device, do not make the option a best choice for governing exoskeletons. This is mainly due to fundamental flaw in the design behind this control law, that is explicitly matching portions of the robot frame to segments of human body. The paramount aspect

in controlling a machine working in parallel with a user should be the human–machine interaction force, so that the human power, which is function of muscle force, can be magnified. The secondary goal of moving an exoskeleton in concert with the human moves is then met inherently.

Indirect and Direct Force methods are given almost the same score. *Direct Force* methods score better for safety and robustness, whilst indirect methods are given higher marks for the design of the measurement system.

It is then concluded that force control laws are much better candidates for full–body enhancive exoskeletons than *Master–Slave Position Control* law, yet their performance comparing to each other has to be investigated further, most desirably through development experiments with a user inside the exoskeleton.

Chapter 4

Prototype Setup

4.1 Introduction

A novel solution for constructing an exoskeleton joint unit, allowing for increased range of motion required e.g. for a joint connecting segments coupling with a knee, is described in this section. The joint is intended to be a part of a full–body enhancive exoskeleton, thus allows for sufficiently large torque and is capable of tranmitting forces occuring in such structure. Its mechanical and actuation design is a result of joint of team effort of engineers acknowledged in the designated section of this document. It compromises of two opposing hydraulic cylinders, with two load cells mounted at ends of the rods, connected by a link. The design is different from a joint actuated by one hydraulic actuator with a load cell mounted on a rod used in BLEEX [10, 12, 13, 92, 93, 95], actuated by an electric motor with a harmonic drive for BLEEX [94] and cables and pulleys with electric motor and reduction unit used for PERCRO [27]. It is different as well from a cable and pulley actuator for XOS [24]. In section 4.4, a method for assessing bandwidth of motion of exoskeleton segments, including upper extremities is described. The method is based on data acquired from a motion capture study. The result is fundamental for selection of sensors and actuation system, as well as, assessing minimum sample rate of control electronics. Selected sensors meeting measurement range and bandwidth are described in section 4.5. In section 4.6 a control electronics architecture and software architecture is proposed for controlling considered design of the exoskeleton joint.

4.2 Mechanical Overview

In course of the project a prototype of an exoskeleton single joint was built. It was constructed to fulfil the requirements outlined in section 3.2 of this thesis. The main focus is to enable joint to follow an operator during gait (as well as other tasks outlined in Appendix D) with human–machine force minimised. The prototype is depicted in Fig. 4.1. It is a quasi–anthropomorphic structure designed to couple with a human leg. Links are made of alluminium extrusions with cross section of 45×45 mm manufactured by MiniTec company[1]. Knee cap and brackets holding hydraulic pistons are made of stainless steel (316 grade, EN: 1.4401). The rest of custom made parts is manufactured out of aluminium alloy 6061.Total mass of the joint parts is 32.86 kg. Mass of specific parts from SolidWorks[2] (Computer Aided Design software) is given in Table 4.1.

Table 4.1: Mass of parts of single joint prototype.

element	**mass [kg]**
single link	3.66 kg
bracket	1.96 kg
knee cap	10.46 kg
load cell and adaptors	0.72 kg
hydraulic actuator	3.15 kg
centre of the joint with bearings	3.16 kg
Total	**32.865 kg**

Actuators are affixed using rotary joints with pins in the centre. Links, as well as centre of the joint and the kneecap are also connected using rotary joints, but include bearings. The role of the bearings is to transfer loads occurring in the structure, as well as to minimise friction. The joint is actuated using two opposing hydraulic pistons connected through a knee cap. This configuration is novel and has not been examined in existing literature. It allows for increased range of motion of the joint. The top of the joint is fixed permanently to a support frame. Also few sensors are incorporated into the prototype. There is an encoder in the centre of the joint for measuring angular displacement (flexion/extension) of the joint. Two load cells for measuring forces exerted by the actuator are connected to actuator rods. The upper actuator extension is measured using an LVDT (linear variable differential transducer). A 6 degree F/T

[1] `https://www.minitec.co.uk/`
[2] `http://www.solidworks.com/`

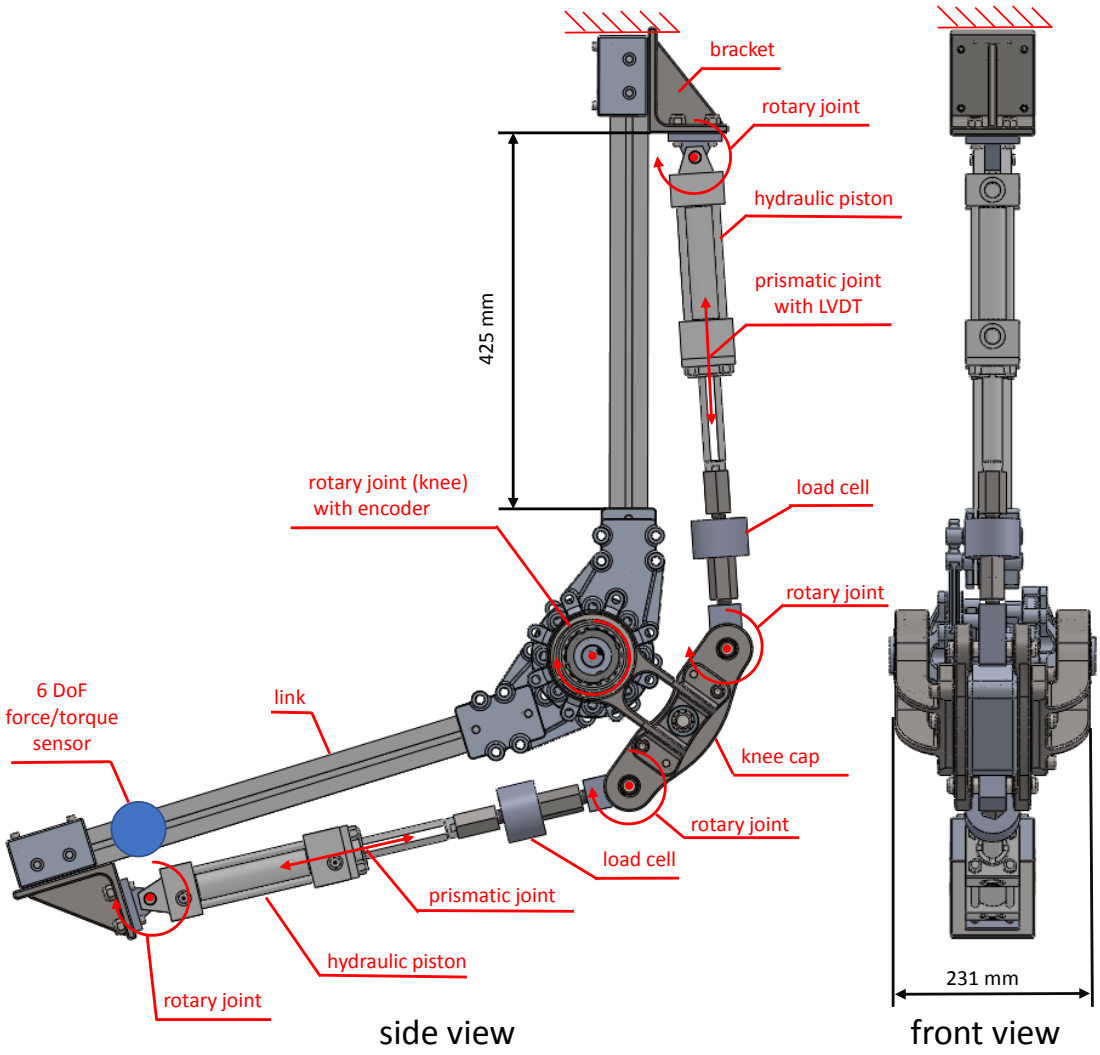

Figure 4.1: Single joint prototype – side and front view.

sensor is mounted at the end of the lower link for measuring forces and torques exerted on the joint prototype. This allows for employment of *Direct Force Control* (see section 2.5.1) for human–machine interaction force minimisation. The novel configuration of two opposing actuators indroduces a problem of knee cap positioning within allowable range of rod extension, whilst the interaction force is minimised. The problem is addressed in this thesis in subsequent sections.

4.3 Hydraulic System

For the protype described in section 4.2, a hydraulic system was designed. Its specification should allow the joint prototype to follow a user during the task of walking on a flat surface (as well as other tasks outlined in Appendix D).

Hydraulic actuators, comparing to other types of actuators, have higher output to torque ratio, and power to mass ratio. A comparison between realised hydraulic actuators, pneumatic actuators, electric motor and human muscle (for reference) is given in Table 4.2 after [4]. The values are given for actuator itself, without axillary equipment: without valve, pump and tank for hydraulic actuator; without compressor, tank, valve for pneumatic actuator; electric motor is a direct–drive motor. It is seen that hydraulics outperform pneumatics in the comparison. From Fig. 4.2 it is seen the bandwidth (maximum frequency of motion) is comparable. Moreover, due to the compressibility of air (energy storage), pneumatics are considered to be unsafe at higher pressures of the circuit [115]. Comparison between hydraulics and electric motors is more complex. Different types of electric motors exist and they can be paired with different types of gears. On the one hand, hydraulic actuators require valves and pump, which add to the mass of the application, but on the other hand electric motors have to be paired with a proper type of gear to increase torque output (direct–drive motor in Table 4.2 has smaller torque output per unit of mass). They also require proper housing to dissipate heat from the current flow through the winding and power electronics. They also require bearings. Where the entire hydraulic circuit can be powered by a single, large enough pump, each motor, in many DoFs system like exoskeleton, needs to have a gear and separate housing. Moreover, gears decrease the angular speed (and hence the bandwidth). They as well decrease efficiency of the unit. They increase apparent inertia of the motor with square of the gear ratio. A comparison would have to be done on case to case basis, taking into account system engineering of the entire application, most importantly number of actively powered DoFs. Although the paper is nearly 30 years old, it is worth to quote [4]: "...hydraulic actuators continue to have the overall best characteristics; with design advances for bandwidth, intrinsic compliance, and better packaging championed by such groups as Jacobsen and colleagues, hydraulic actuators appear to be the actuation to beat for general macrorobotics". However, the most recent (2019) exoskeleton reported in professional press under development by Sarcos (a company founded by Jacobsen), named Sarcos XO Max, which is intended to be a commercialised for use in the manufacturing work environment, is "all–electric" [116]. "Get–out–of–the–way" (*Direct Force Control*) is used and the load and mass of the

Table 4.2: Comparison of actuator characteristics based on specification of existing machines [4]. Values given for actuator itself, without taking into account auxiliary equipment, e.g. pump for hydraulic actuator.

actuator	**torque/mass** [Nm/kg]	**power/mass** [W/kg]
McGill/MIT **electric motor**	15	200
Sarcos Dexterous Arm **electro–hydraulic rotary actuator**	120	600
Utah/MIT Dexterous Hand **electro–pneumatic servo–valve**	20	200
human biceps muscle	20	50

exoskeleton are transferred to the ground. The exoskeleton is intended to manipulate up to 90 kg. The force reduction ratio is 20.

Advantages of hydraulic systems that make them a viable solution for powering enhancive exoskeletons are [117]:

- For comparatively small devices, large torques can be developed by hydraulic actuators. This is due to the fact that their torque is proportional to pressure difference, which is only limited by safe stress levels. This is in contrast to electric motors for which torque is proportional to current limited by magnetic saturation and losses in the magnetic material. Smaller sizes of hydraulic motors are advantageous for a highly constrained mechanical design of exoskeleton, which is coupling with human body.
- Basically, in terms of the transfer function from flow to speed, hydraulic actuators are a quadratic resonance with a high natural frequency. Hence they allow for higher speed responses compared to electric motors, which are basically lag devices

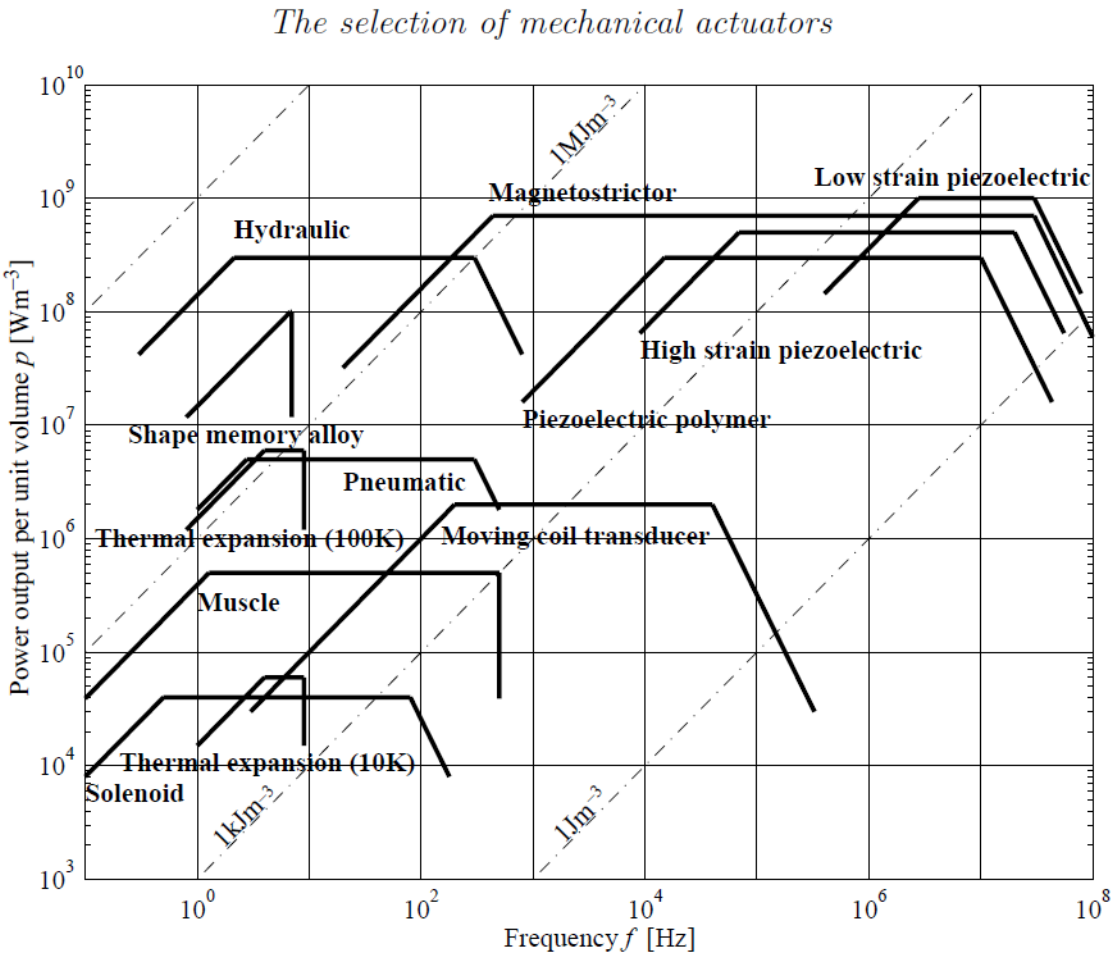

Figure 4.2: Power output per unit volume as function of frequency (maximum frequency is bandwidth) [2].

considering transfer function from voltage to speed. The ratio of torque to inertia is large, therefore allows for fast start, stops and movement reversal. On the whole, higher bandwidths and gains are possible with hydraulic devices in closed (servo) loops.

- The stiffness (inverse of slope of speed–torque curve) of hydraulic devices is higher compared to other drive devices. This is due to low leakages in components, which results in smaller drop of speed as loads increase. Therefore positional stiffness is increased and positional error is decreased.
- Hydraulic actuators are capable of maintaining their load capacity indefinitely because of cooling effects of fluid flow through the system. On the other hand, electrical components would usually cause excessive heat generation limiting their performance.

Despite the advantages, hydraulic systems have disadvantages from the point of view of control engineering:

- The control signal (voltage applied to the solenoid) fundamentally controls the derivative of force/torque rather then force/torque itself. The control signal acts to control a spool valve, which in turn governs the flow into and out of the actuators. The flow subsequently causes a pressure differential, which is proportional to force/torque of the actuators [118].
- The hydraulic system, treated as a controlled object, is non–linear and its parameters estimation is burdened by uncertainty. For example, supply pressure to an actuator may vary in system if other actuators operate in the same circuit. Characteristics of the fluid flow (the flow and pressure coefficients) are functions of load and supply pressure and may vary for different operating conditions. Moreover, the effective bulk modulus can change under various load conditions, oil temperature, and air content in the oil [119]. Other sources of non–linearities include:"servo–valve hysteresis resulting from the electromagnetic characteristics of the torque motor, asymmetric actuation (unequal piston cross sectional areas acting in the two directions of motion), transmission non–linearities ..., variations in the trapped fluid volume (such as between the servovalve and the actuator) that are introduced by the actuator movement ... and the presence of flow forces and their effect on the spool position" [120]. Other sources of non–linearities and uncertainties are external and internal leakage, Coulomb friction in the actuator, variable gradient of orifices and fluid flow dead band [121].

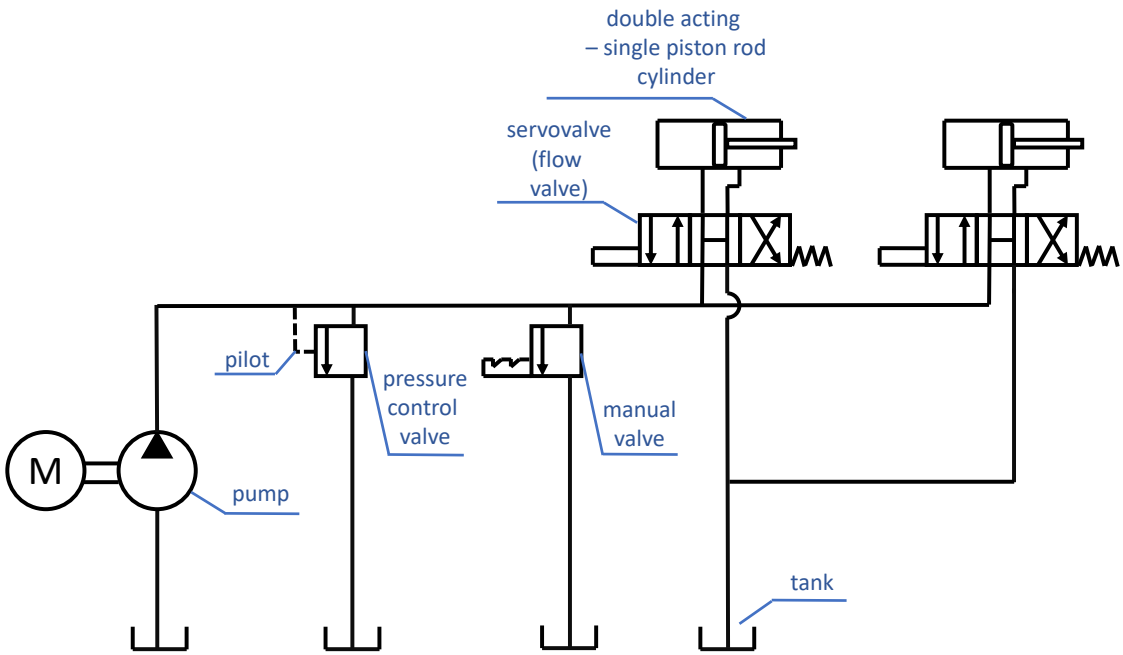

Figure 4.3: Hydraulic circuit for the single joint prototype.

– Hydraulics are highly sensitive to characteristics of the load applied. If the characteristics of load are non–linear this further complicates analysis. Also effects of inertial coupling, centrifugal and Coriolis forces (in a multi–degree–of–freedom mechanism, such as an exoskeleton) affect the performance [120].

In Fig. 4.3 a hydraulic circuit for the single joint prototype is depicted. The circuit is supplied by an external pump operating at 150 bar driven by an electric motor powered by mains electricity. The flow of the pump is 6 l/min. It has an automatic pressure control valve and a manual valve. Two double acting, single piston rod hydraulic cylinders are connected to the circuit through directional control valves. The length of the supply and return hose for each of the cylinders is 7 m. This is because the hydraulic pump and tank are placed in a designated area for safety reasons. The contol valves were manufactured by Bosch–Rexroth and have a part number [122]:

4WR PEH 6 C3 B12L - 2x/G24KO/A1M

This type is a 4–position 4–way valve (4th is a fail–safe position, where both hydraulic chambers of actuators are connected to a tank). It is a high–response directional control valve, pilot–operated with electrical position feedback and integrated electronics. The integrated electronics compare specific command value (–10 V to +10 V signal) with actual position of the spool. If deviation occurs the stroke solenoid is activated, which

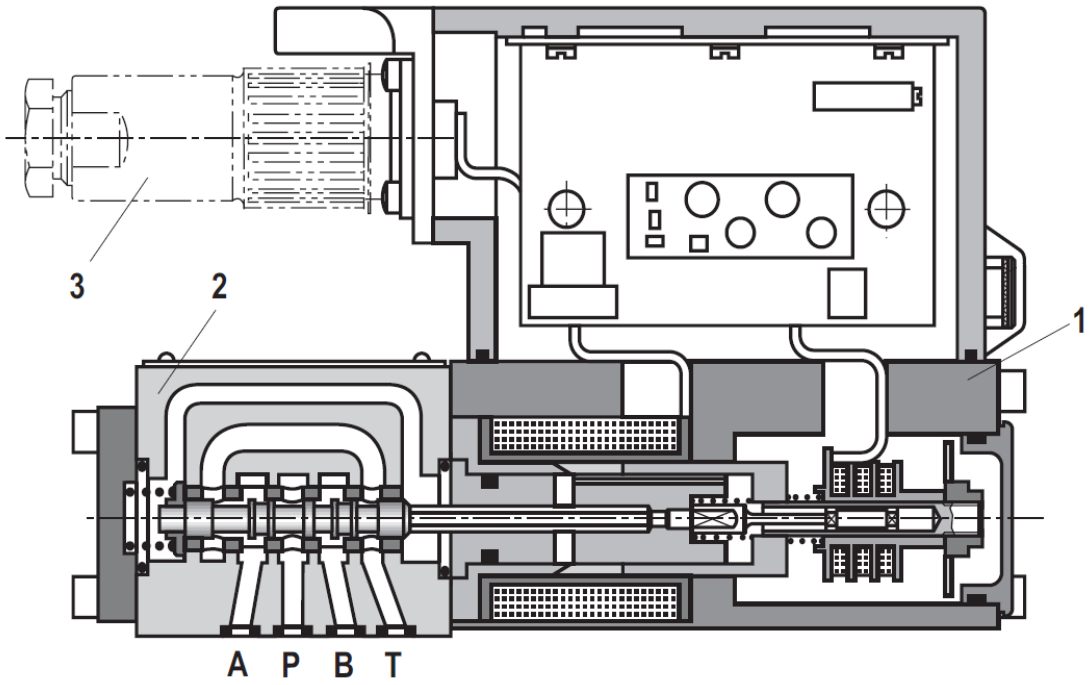

Figure 4.4: Bosch Rexroth 4WRPEH valve cross–section. 1 – control solenoid with position transducer, 2 – valve body, 3 – mating connector [122].

adjusts the spool via magnetic field against the spring. The integrated electronics realise a PID controller for spool positioning. In Fig. 4.4 a cross section through the valve and its ancillaries is depicted. Solenoid, valve body and electronics are visible. P is a port connected to a fluid supply, T – port connected to a tank , A,B – ports connected to the hydraulic actuator. In Fig. 4.5 the characteristic from the command signal (U) to flow ($q_{\{i,o\}}$ – in and out) for the valve is depicted. It is linear (its hysteresis is minimal and less than 0.2 % according to manufacturer) and realises equation:

$$q_{\{i,o\}} = q_{Vnom} \frac{U}{|U_{max}|} \sqrt{\frac{\Delta\varrho}{35}} \tag{4.1}$$

where $q_{Vnom} = 6$ l/min for the particular valve, and $\Delta\varrho$ – pressure difference across the valve (on either side of the orifice) in $[bar]$, $U_{max} = 10$ V. Eq. (4.1) is equivalent to a set of equations describing the fluid flow (q_o – fluid flow out of the valve, q_i – fluid flow into the valve) distribution in the valve [117, 119]:
$x_{sp} \geq 0$ (extension):

$$q_i = c_d w x_{sp} \sqrt{\frac{2}{\rho}(\varrho_s - \varrho_i)} \qquad q_o = c_d w x_{sp} \sqrt{\frac{2}{\rho}(\varrho_o - \varrho_e)} \tag{4.2}$$

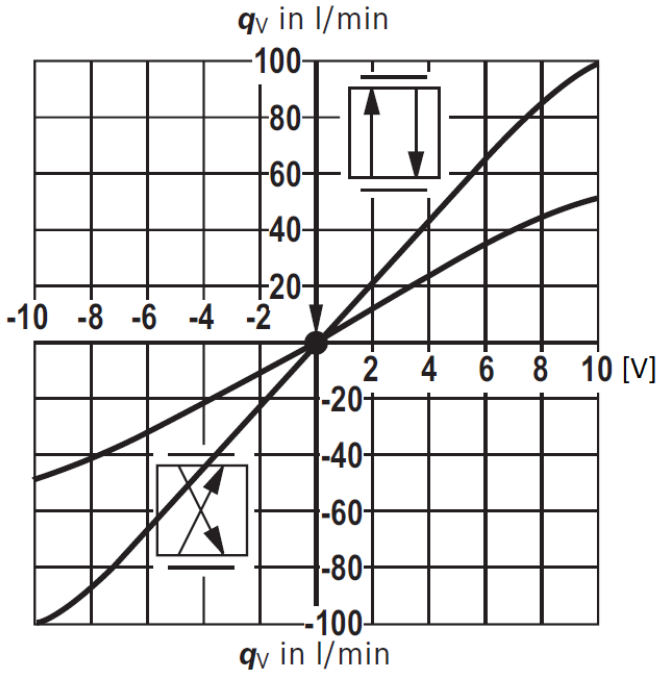

Figure 4.5: A valve characteristic from command signal (-10 V to + 10 V) to flow through the valve [122].

$x_{sp} < 0$ (retraction):

$$q_i = c_d w x_{sp} \sqrt{\frac{2}{\rho}(\varrho_i - \varrho_e)} \qquad q_o = c_d w x_{sp} \sqrt{\frac{2}{\rho}(\varrho_s - \varrho_o)} \tag{4.3}$$

where q_i and q_o are respectively fluid flows into and out of the valve. c_d is the orifice coefficient of discharge, ρ is the mass density of the fluid, ϱ_s is pump supply pressure, ϱ_e is the return pressure. ϱ_i and ϱ_o are the input and output line pressures, respectively. w is the area gradient that relates the spool displacement (x_{sp}) to orifice area. The relationship of the spool displacement x_{sp}, and the input voltage (u) for a proportional valve can be expressed as a first–order system [117, 119]:

$$u = \frac{\tau}{k_{sp}} \frac{\mathrm{d}x_{sp}}{\mathrm{d}t} + \frac{1}{k_{sp}} x_{sp} \tag{4.4}$$

where τ and k_{sp} are gains describing the valve dynamics. u – input voltage.

Hydraulic cylinders by Miller Fluid Power are used in the prototype. Their order code is [123]:

HV284RXB–0150–4”–0100 R11T-O

It is a type of heavy–duty hydraulic cylinders with cap fixed clevis mount, retainer

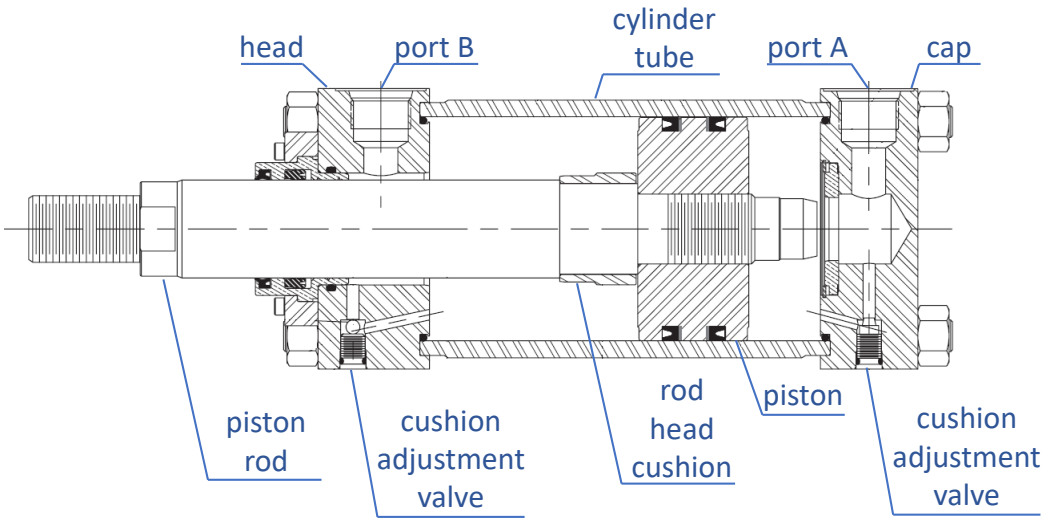

Figure 4.6: Cross section of HV284 hydraulic cylinder, bore diameter 1.5" (adapted from: [122]).

held bronze bushing and both rod and cap cushioned. Its bore diameter is 1.5", stroke is 4", rod diameter is 1". The hydraulic cylinder is depicted in Fig. 4.6. The stroke of rod of the hydraulic cylinder allow two opposing actuators to cover wider range of motion, including that required for gait.

4.4 Bandwidth of Motion and Sample Rate

Closed–loop bandwidth and sample rate of the control system are fundamental to system engineering of a full–body exoskeleton. Actuators must operate within bandwidth for considered tasks. Sensors must allow for sampling as quickly as, or faster than the minimal sampling rate. Electronics and real–time communication system must process data as quickly as the sample rate. In order to determine the requirement for minimal sample rate of exoskeleton control algorithm, the bandwidth of motion of exoskeleton segments has to be determined first.

4.4.1 Motion Capture Study

A pilot motion study was conducted in the School of Biomedical Sciences of the University of Leeds for the purpose of deriving requirements for the full–body exoskeleton. Ethical Approval was granted for the study. It is attached as Appendix G. For the study, reflective markers (17.5 mm in diameter) were placed at easily palpable body

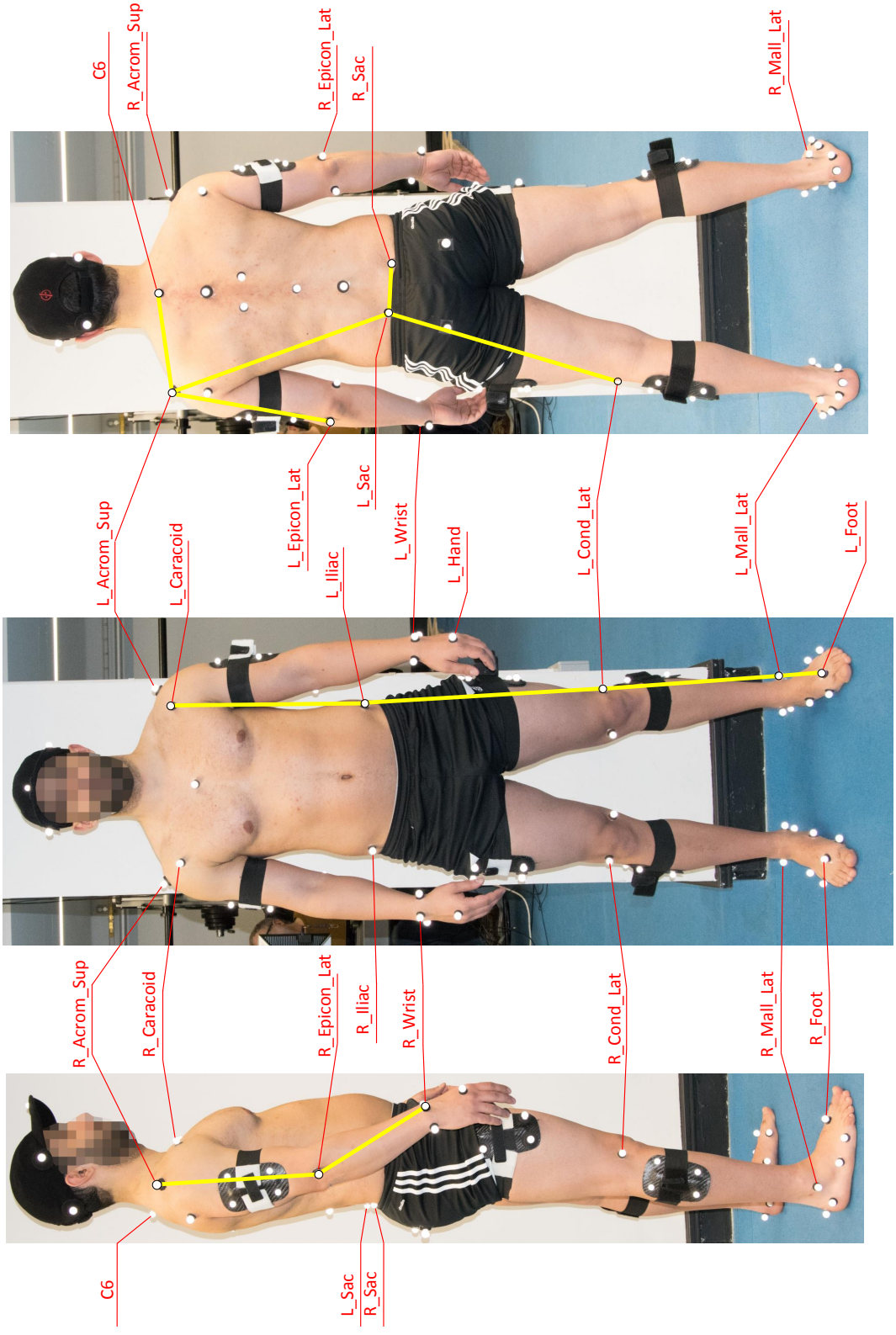

Figure 4.7: Markers placement for the motion capture study. Yellow lines connect markers between which angle is measured.

landmarks of the lower and upper extremities as well as the core of a healthy subject's body (Fig. 4.7). The subject was 29 year old male weighting 92.3 kg and 182 cm tall. His right hand is the dominant one. He performed activities he would do wearing a full–body exoskeleton: *ground level walking (gait), running, walking backwards, side step, lifting a box from the ground, jump, lifting hands above head.* The manoeuvres were recorded with 13 Qualisys Oqus cameras at 400 FPS [124]. Angular displacement between joints was calculated using the formula:

$$q_{a,b,c} = \cos^{-1}\left(\frac{\vec{v}_{b,a} \cdot \vec{v}_{b,c}}{\|\vec{v}_{b,a}\| \, \|\vec{v}_{b,c}\|}\right) \tag{4.5}$$

where: $\vec{v}_{b,a} = a - b$, $\vec{v}_{b,c} = c - b$, $a, b, c \in \mathbb{R}^3$ ($\mathbb{R}$ – set of real numbers) are coordinates of markers in Cartesian space. The selected markers are joined by yellow lines in Fig. 4.7. If amplitude of discrete spectral analysis at point k (frequency) is denoted as $\|X_k\|$, then power of the signal is calculated as:

$$P = \sum_{k=1}^{N/2} \|X_k\|^2 \tag{4.6}$$

where N - number of samples. The bandwidth was considered to be 99% of signal power of angular displacement of the joints ($\omega_{BW} = 99\% \cdot P$). A subset of markers was considered:

Acrom_Sup – superior acromion

Caracoid – coracoid process

Cond_Lat – lateral femoral epicondyle

C6 – spinous process of cervical vertebra C6

Epicon_Lat – lateral humeral epicondyle

Foot – 2nd metatarsophalangeal joint capsule (index toe)

Iliac – anterior superior iliac spine (iliac crest)

Mall_Lat – lateral malleolus

Sac – lateral lumbar indentations (sacroiliac joints)

Wrist – top of the wrist (dorsal radio–carpal ligament)

To illustrate, in Fig. 4.8 an amplitude spectrum of angular displacement between markers L_Acrom–L_Epicon_Lat–L_Wrist is depicted. In Fig. 4.9 percentage of power contained between 0 Hz and a frequency is depicted for the same markers. In Fig. 4.10 and Fig. 4.11, the same characteristics are shown for L_Iliac–L_Cond_Lat–L_Mall_Lat markers (a knee) respectively.

Table 4.3: Bandwidth of human motion for different activities. Values of 99% of entire signal power are given in [Hz]. Bold – mean from a sample, normal text – standard deviation of sample.

activity name	number of samples	x_Cond_Lat – x_Mall_Lat – x_Foot		x_Iliac – x_Cond_Lat – x_Mall_Lat		x_Caracoid – x_Iliac – x_Cond_Lat		x_Sac – y_Sac – y_Cond_Lat		x_Sac – x_Acrom_Sup – x_Epicon_Lat		C6 – x_Acrom_Sup – x_Epicon_Lat		x_Acrom_Sup – x_Epicon_Lat – x_Wrist	
x{, y}		L	R	L	R	L	R	L, R	R, L	L	R	L	R	L	R
ground level walking	5	**10.0**	**8.8**	**4.0**	**2.4**	**5.9**	**7.1**	**5.6**	**5.7**	**8.1**	**9.1**	**4.9**	**5.7**	**6.8**	**8.8**
		2.4	1.9	1.6	0.1	0.1	0.6	0.6	1.7	3.8	5.1	1.3	2.0	3.4	1.9
running	3	**37.2**	**20.0**	**11.6**	**33.5**	**41.5**	**35.2**	**17.6**	**36.0**	**23.1**	**37.5**	**33.5**	**18.8**	**20.0**	**20.0**
		48.8	10.9	7.6	46.7	17.6	33.0	8.4	29.2	20.6	46.4	39.5	17.8	21.6	10.9
walking backwards	4	**6.6**	**5.4**	**2.7**	**4.2**	**6.3**	**8.0**	**9.6**	**6.7**	**6.8**	**3.9**	**9.4**	**7.1**	**3.8**	**5.4**
		1.2	0.6	0.6	0.2	1.7	2.2	1.2	1.9	1.6	1.1	5.2	4.6	0.8	0.6
side step	4	**5.3**	**5.5**	**3.4**	**3.7**	**3.5**	**2.9**	**2.8**	**3.3**	**4.5**	**7.1**	**4.3**	**5.6**	**2.4**	**5.5**
		0.5	0.4	0.3	0.3	0.5	0.5	0.2	0.5	0.9	6.7	0.6	2.9	1.3	0.4
lifting a box from the ground	4	**1.9**	**1.8**	**1.2**	**1.6**	**0.7**	**0.9**	**2.9**	**2.3**	**0.8**	**0.7**	**1.0**	**1.0**	**2.5**	**1.8**
		0.2	0.3	1.2	0.7	0.5	0.1	1.2	0.7	0.3	0.3	0.2	0.1	0.2	0.3
jump	5	**5.3**	**5.4**	**2.7**	**2.6**	**1.9**	**1.5**	**5.2**	**4.2**	**1.9**	**1.8**	**3.1**	**3.3**	**3.1**	**5.4**
		0.2	0.2	0.5	0.5	0.3	0.8	0.8	0.6	0.2	0.2	0.8	0.8	0.4	0.2
lifting hands above head	3	**5.7**	**5.0**	**3.1**	**2.2**	**2.7**	**2.2**	**3.4**	**3.6**	**1.5**	**1.7**	**1.8**	**1.8**	**1.4**	**5.0**
		1.9	2.3	0.4	1.9	1.7	2.0	1.2	1.2	2.0	1.5	1.5	1.2	0.4	2.3

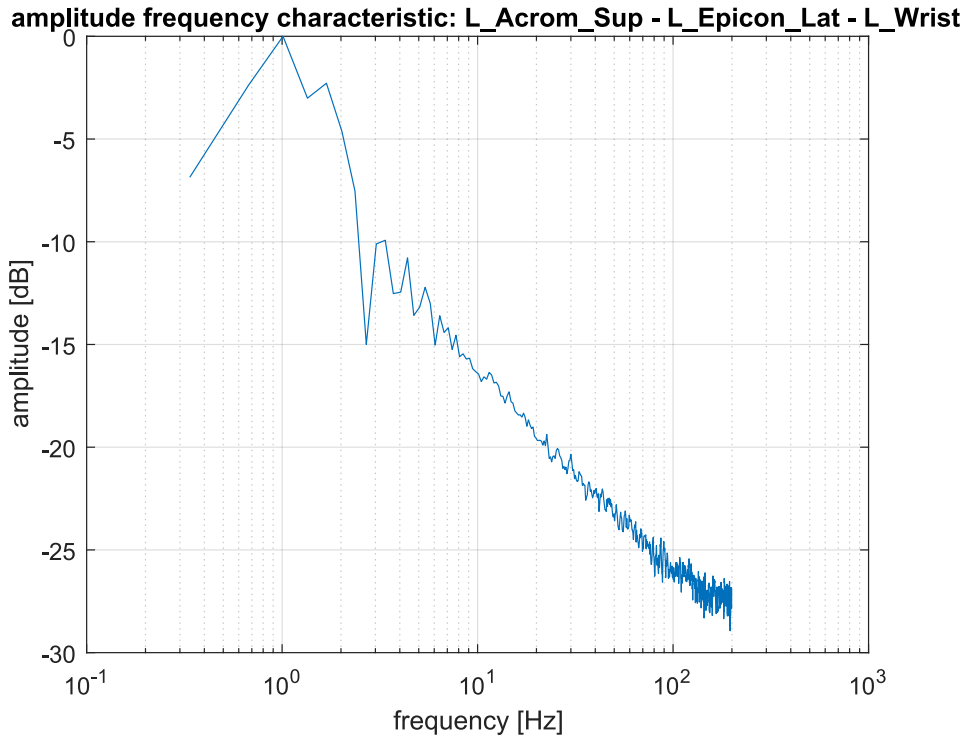

Figure 4.8: Amplitude of frequency analysis of human joint angular displacement for elbow during walking.

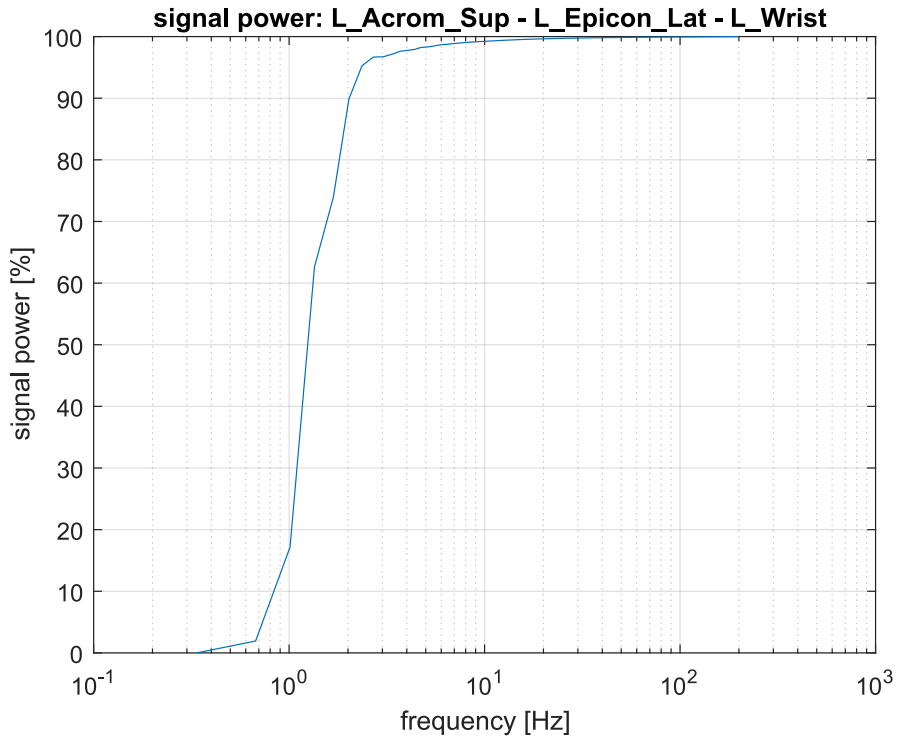

Figure 4.9: Relationship between signal power of human joint angular displacement and frequency for elbow during walking.

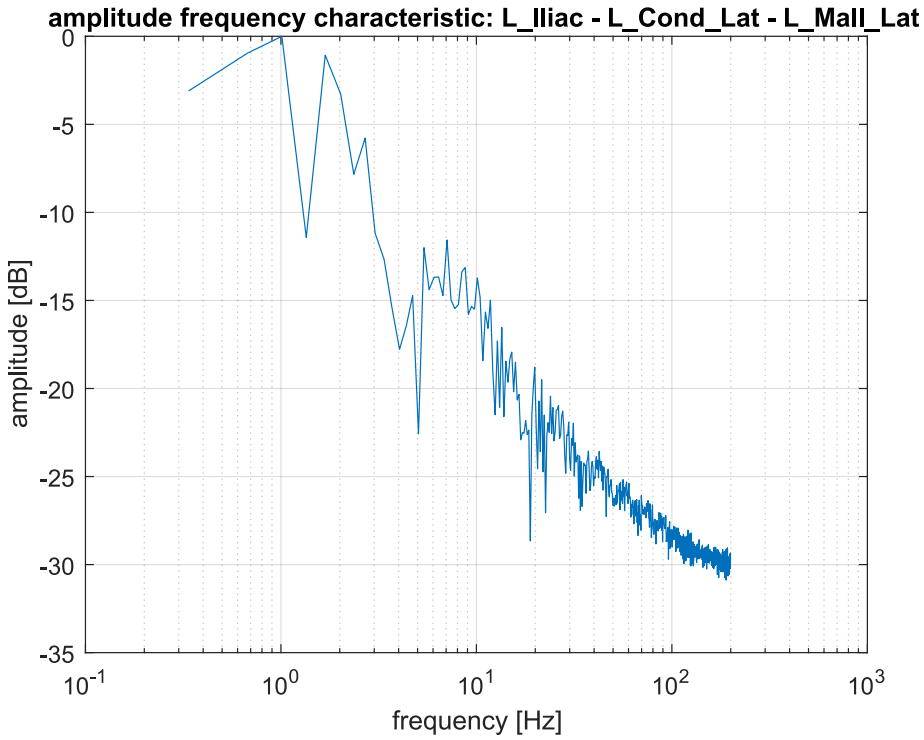

Figure 4.10: Amplitude of frequency analysis of human joint angular displacement for knee during walking.

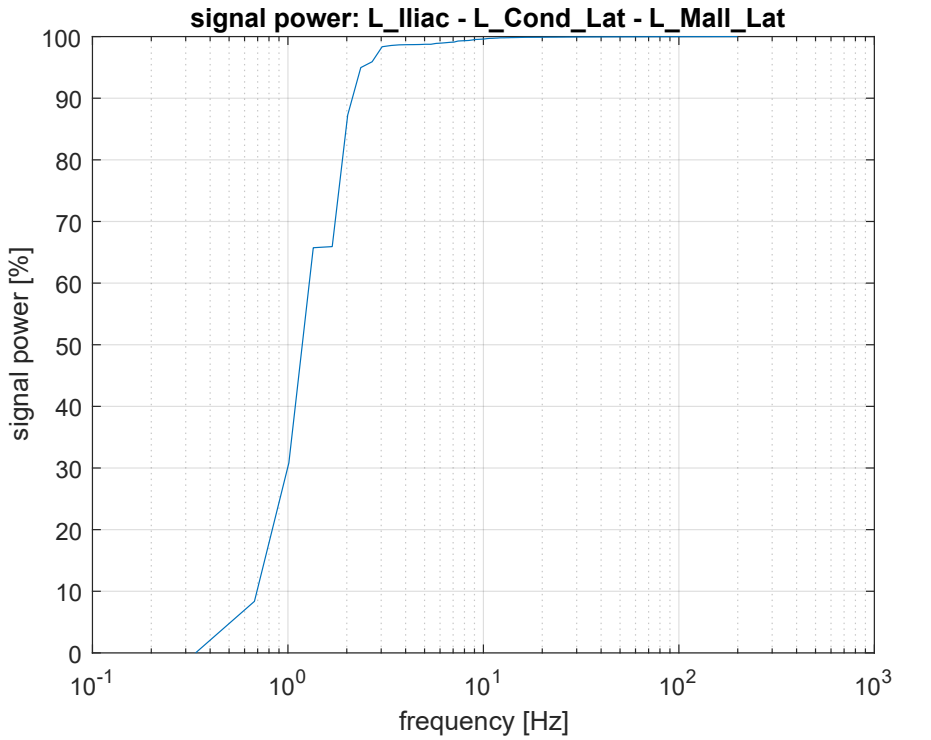

Figure 4.11: Relationship between signal power of human joint angular displacement and frequency for knee during walking.

Few trends emerge examining results shown in Table 4.3. The upper limbs have similar bandwidth to lower limbs for the examined tasks. Running has on average higher bandwidth than other activities, but the study has to be more carefully designed to decrease standard deviation of the results. The mean for running is high possibly because the noise of movement of the tissue beneath the marker being superimposed on the signal describing angular displacement of a joint (the 99% of power freq. can be crossing into power of the noise).

4.4.2 Sample Rate of the Control System

Devlopers of BLEEX based the lower–body exoskeleton mechanical and actuator design on motion data from an average human during gait [10], [13], [12]. The structure is described to be "*almost anthropomorphic*", which states that exoskeleton joint coordinates are assumed to be equal to human joint coordinates. In [16] Racine, considers bulk of human gait bandwidth (ω_{BW}) to be contained below 30 Hz (60 Hz taking into account random disturbances and faster pace) for purpose of the control system sampling rate (ω_S) selection. Although Whittaker–Nyquist–Kotelnikov–Shannon theorem [125], [126] states that in order to reconstruct unknown, band–limited continuous signal it is sufficient to sample it at least twice as fast as the highest frequency component contained in the signal ($\omega_S \geq 2 \cdot \omega_{BW}$), for BLEEX control loop rate (ω_S) was chosen to be 2 kHz. This is supported by *a heuristic rule stating that a sample rate should be chosen 40 times higher than a bandwidth of a closed–loop system* ($\omega_S \geq 40 \cdot \omega_{BW}$) [125]. Implementing the rule should allow for satisfactory tracking effectiveness, disturbance rejection and mitigating measurement noise in systems with analogue sensors with anti–aliasing filter. The latter is considered to be the stringiest requirement, demanding *the sample rate (ω_S) to be 30 to 100 times faster than the bandwidth (ω_{BW}).*

If an exoskeleton is designed to perform tasks listed in Table 4.3, with exception of running, the considered bandwidth of motion should be at least 10 Hz. The heuristic rule dictates then that the sufficient sample rate is 400 Hz. However, if running is considered, the same principle suggests sampling rate to be set higher, at least approx. 1.6 kHz.

4.5 Sensors

A number of sensors are employed for the prototype depicted in Fig. 4.1: an encoder, linear variable differential transducer (LVDT), two load cells, 6 degree–of–freedom force/torque sensor. These are required for the Direct Force Control (see section 2.5.1) as the mid–level control law and for Force Control of hydraulic actuators at the low level.

4.5.1 Encoder

The encoder used in the prototype of the single joint depicted in Fig. 4.1 is Hengstler AC36 absolute encoder, order code (see [127]):

AC36 0014 A R.41 SD B

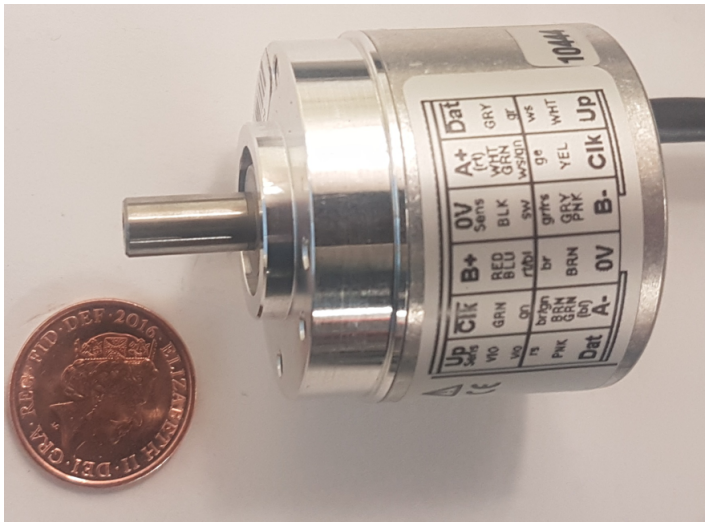

Figure 4.12: Hengstler AC36 encoder.

It is an optical absolute encoder in small casing with overall length of 36 mm and diameter of 38.1 mm. It is depicted in Fig. 4.12. The encoder has a resolution of 14 bits for an angular position measurement (with velocity up to 10 000 rpm), transmitted over Synchronous Serial Interface (SSI) using binary code [128]. It is equipped with SinCos interface (2048 periods per rotation, 1 V peak to peak). The bandwidth of the sensor is 500 kHz, with baud rate of 1 MHz (allowing for measurement with frequency 71 kHz with 14 bit interface). This is well above required 400 Hz (1.6 kHz for running) considered as bandwidth of motion of exoskeleton segments (see section 4.4). According to Appendix B 14 bit encoder introduces approx. 2 mm positioning error due to

Figure 4.13: Solartron S–series AS10 linear variable differential transducer.

quantisation. Moreover, the encoder has absolute accuracy of ±35". The error affects calculation of Jacobian required for Direct Force Control (see section 2.5.1).

4.5.2 Linear Variable Differential Transducer

In the prototype of the single joint a linear variable differential transducer (LVDT) is used for measurement of extension of rod of the upper hydraulic cylinder (see Fig. 4.1). The sensor used is [129]:

Solartron S-series AS10

It is depicted in Fig. 4.13. The sensor operates on the principle of movement of a core with respect to secondary coils, while the primary coil is excited by alternating current. The output from the sensor is analog voltage ±10 V, proportional to the displacement. The measured displacement is ±50 mm (range of 100 mm). Its bandwidth is 460 Hz, which is sufficient for tasks considered in section 4.4 (except for running). Non–linearity of the sensor is smaller than 0.2 % of full scale output.

The extension of second cylinder r_{low} can be calculated from measurement of joint angular displacement θ' by an encoder placed inside the joint (see section 4.5.1), extension of the upper rod of hydraulic cylinder r_{up} and geometric properties of the joint prototype (see Fig. 4.14). The values for constant properties were acquired from a model designed in Solidworks. The extension of the rod of the lower hydraulic cylinder is then calculated as:

$$\hat{r}_{low} = e - c_{retracted} \tag{4.7}$$

From law of cosines:

$$e = \sqrt{b^2 + a^2 - 2ab \cdot \cos\delta} \tag{4.8}$$

$$\delta = \mu - \gamma - \alpha \tag{4.9}$$

where μ is an undricted angle and can be approximated using measured value of $\theta\,'$ as:

$$\mu \approx |\theta\,' + \Delta\theta\,'| \tag{4.10}$$

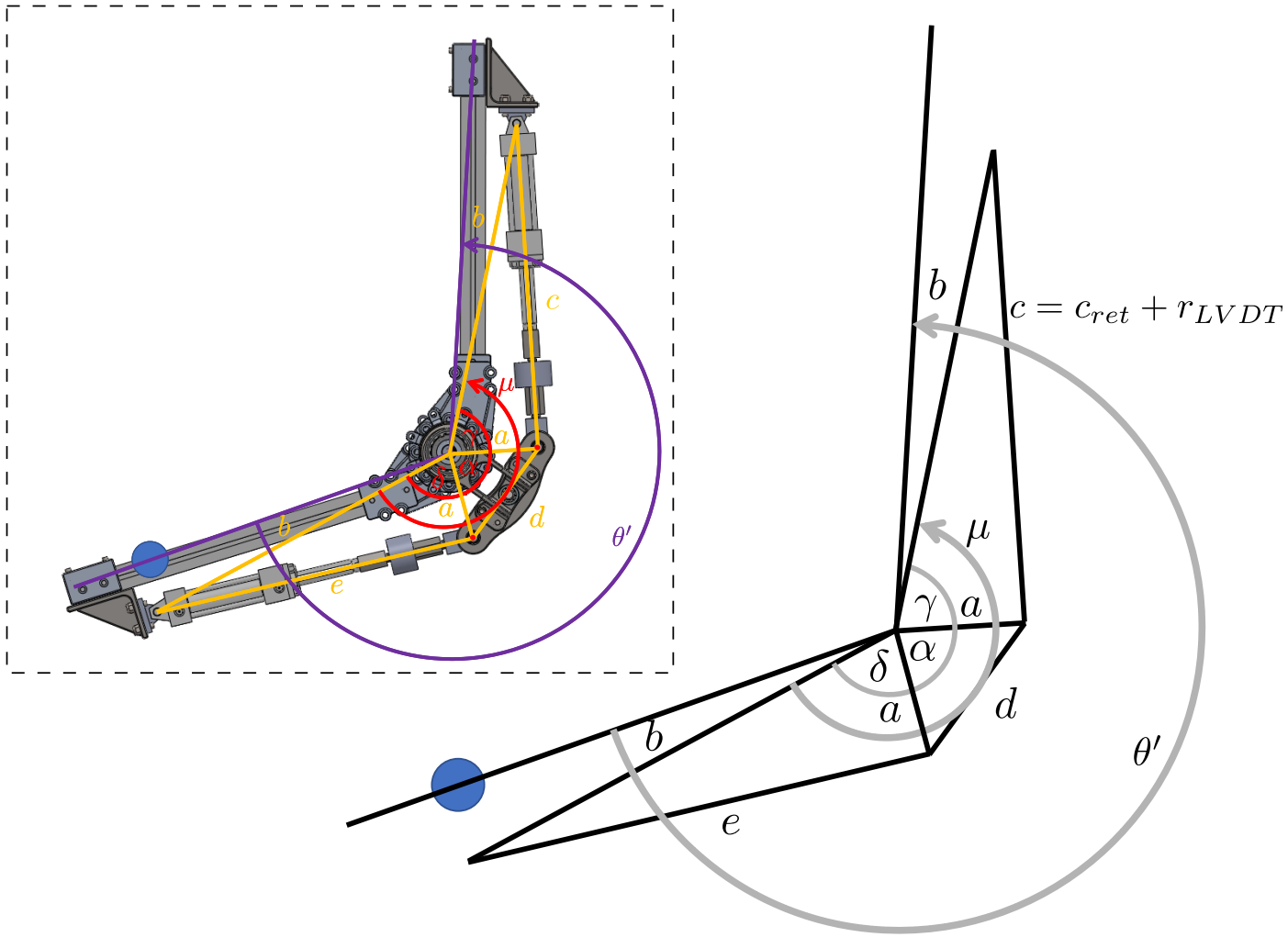

Figure 4.14: Single joint prototype from Fig. 4.1 with geometric properties outlined. $a = 160.08$ mm, $d = 200$ mm $b = 574.62$ mm, $\alpha = 77.32°$, $c_{retracted} = 482$ mm (length from the joint with pin to another joint with pin while the rod entirely retracted)

where $\Delta\theta'$ is a correction term for error in estimating of μ, which can be found empirically or equated to 0. $|\cdot|$ stands for absolute value. From law of cosines again:

$$\gamma = \cos^{-1}\left(\frac{c^2 - b^2 - a^2}{-2ab}\right) \tag{4.11}$$

where:

$$c = r_{up} + c_{retracted} \tag{4.12}$$

4.5.3 Load Cells

In the prototype, on the ends of the rods of the hydraulic cylinders, load cells are mounted (see Fig. 4.1). The used sensors are Novatech F256–Z4616 (for a datasheet see [130]).They are depicted in Fig. 4.15. These are tension–compression load cells with measurement range of ±20 kN. Each of them is connected to SGA Analogue Strain Gauge Load Cell Amplifier (for a datasheet see [131, 132]). The output from the amplifier can be set to be ±10 V for range of ±20 kN. The amplifier has built in second order (-12dB/oct) low pass filter. Its cutoff frequency can be set from 1 Hz to 5 kHz. The chosen setting for the filter is 50 Hz, which is larger then the 10 Hz limit for bandwidth for exoskeleton motion (see section 4.4). The bandwidth of the sensor itself is mechanically limited by natural frequency of mass spring (sensor) system given by [133]:

$$F_n = \frac{1}{2\pi}\sqrt{\frac{K}{m}} \tag{4.13}$$

where F_n – natural frequency [Hz], $K = 2.0 \times 10^8$ [N/m] – stiffness of the sensor, m – the mass attached to the sensor. It is difficult to derive interactive mass m in the case of the sensor employed in the configuration of the prototype. However, in [133] it is stated that "*force input frequencies up to one tenth of the mass systems natural frequency yield measurement errors of less than 1%*". Taking mass m to be equal to 1000 kg, which is more than the weight of the exoskeleton with load, Eq. (4.13) yields the natural frequency to be 225 Hz. Using the cited rule, measurement for frequencies less than 22.5 Hz, which is above the considered bandwidth of 10 Hz, should yield measurement errors of less than 1%. Moreover, the measurement is burdened by non–linearity (0.05% of rated load of 20kN), hysteresis (0.05% of rated load), creep (0.05% of applied load), repeatability (0.02% of rated load) errors.

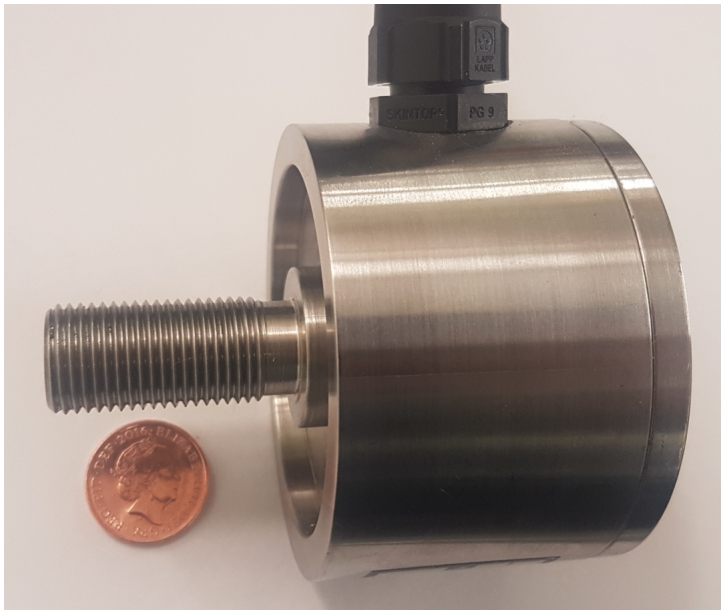

Figure 4.15: Novatech F256 load cell.

4.5.4 6 Degree–of–Freedom Force/Torque Sensor

In the prototype depicted in Fig. 4.1, a 6 degree–of–freedom force/torque sensor is employed. It is a JR3 sensor (depicted in Fig. 4.16), order code (for a datasheet see [134]):

67M25A3–I40S–A 200N12

The output from the sensor is normalised by integrated electronics to be ±10 V for each degree of freedom. The value of force exerted in a certain axis is computed by multiplying a vector of voltages by a calibration matrix provided by manufacturer. The range for measurement of forces Ξ_x and Ξ_y (in plane parallel to the flat face of the sensor) is ±200 N. Ξ_z (axis perpendicular to the plane of Ξ_x and Ξ_y) is in the range of ±400 N. The range for ν_x, ν_y, ν_z is ±12 Nm. According to the manufacturer, signal for each axis is filtered using a built–in low pass filter with a cutoff frequency of 1 kHz. The same principle of limiting bandwidth by the natural frequency of the mass–spring system applies as for a load cell (described in section 4.5.3). The stiffness for Ξ_x and Ξ_y is 1.3×10^7 N/m, for 1.3×10^8 N/m. Similar to Eq. (4.13), stiffness for torque measurement can be defined as:

$$F_n = \frac{1}{2\pi}\sqrt{\frac{\kappa}{I}} \tag{4.14}$$

where F_n – natural frequency, κ – stiffness of the sensor (torsional spring), I – moment of inertia of a body attached to the sensor. Value for ν_x and ν_y is $\kappa_{x,y} =$

53000 N/rad, for ν_z $\kappa_z = 15000$ N/rad.

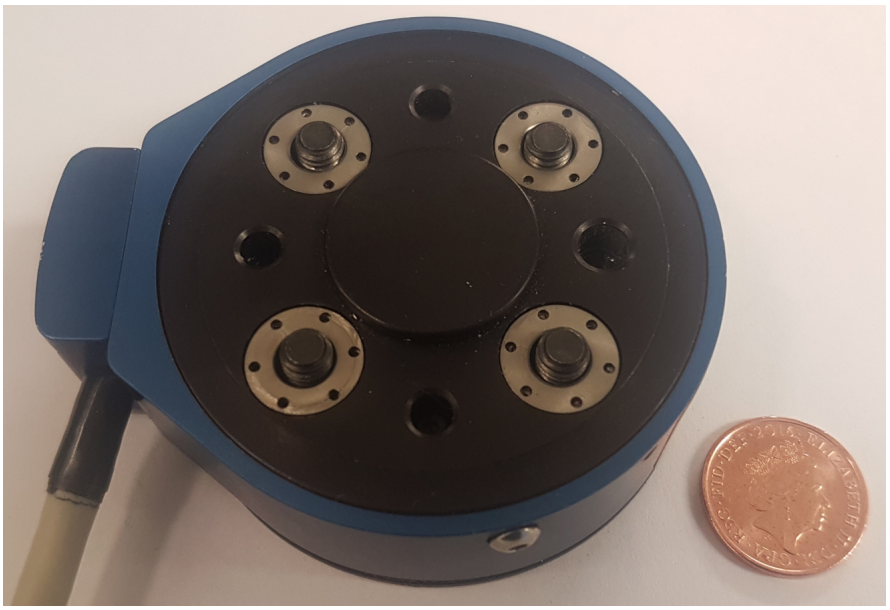

Figure 4.16: 6 degree–of–freedom force/torque sensor by JR3, model 67M25A3

4.6 Control Electronics and Software

Control electronics and real–time software were developed for the single joint prototype described in section 4.2. It allows for interfacing with the sensors (see section 4.5) and servo–valves of hydraulic actuators (see section 4.3). It is capable of calculating steps of the control algorithm for mid–level control and low–level control. The execution of the control loop can be set to be 2 kHz, which is higher than the required minimum sample rate (see section 4.4).

4.6.1 Control Electronics

At the centre of the electronics is National Instruments MyRIO [135]. The controller is built around Xilinx Zynq–7010 System–on–a–Chip (SoC). The chip features Dual–core ARM Cortex–A9 (clocked at 667 MHz) and Artix–7 Field–Programmable Gate Array (FPGA) with 28K Programmable Logic Cells [136]. The controller is equipped with 256 MB of DDR3 memory. Both the processor and FPGA are programmed using LabView.

A hardware block diagram of control electronics is depicted in Fig. 4.17. The FPGA communicates with peripherals, acquires measurement from the sensors and

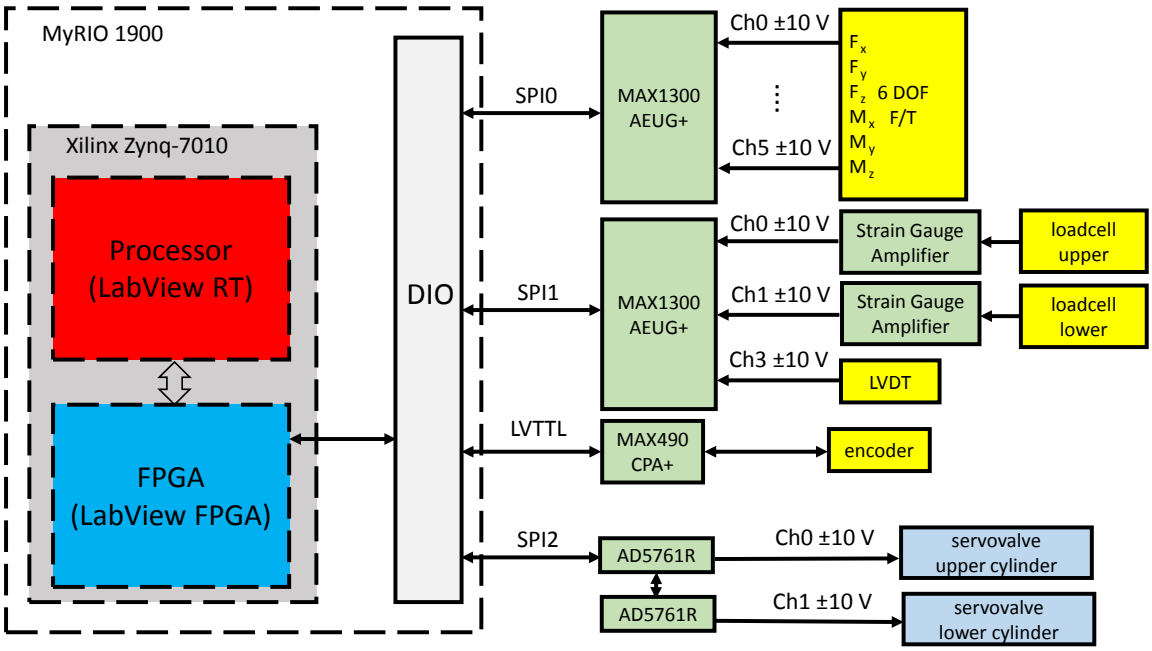

Figure 4.17: A hardware block diagram for control electronics. AO – analogue output, DIO – digital input/output.

applies control signal to the servovalves.

MAX490CPA+ Slew–Rate–Limited RS-485/RS-422 Transceiver [137] is used for translation of DIO voltages in range of LVTTL (Low–Voltage Transistor–Transistor Logic) from MyRIO FPGA to voltages required by SSI communication employed by the encoder (see section 4.5.1). Maximum data rate is 2.5 Mbps (178 kS/s over 14–bit interface), which is more than minimum sample rate.

MAX1300AEUG+ 8- Channel, ±3 x V_{REF} Multirange Inputs, Serial 16–Bit ADCs [138] is used as an Analogue–to–Digital Converter (ADC) for sampling analogue signal from the 6 degree-of–freedom force/torque sensor (1st chip), strain gauge amplifiers and LVDT (2nd chip). It has a programmable range, which can be set to ±3 x V_{REF}, that is ± 12.288 V using internal reference voltage of 4.096 V. It has ± 2 LSB (least significant bit) integral non–linearity error, –1 to +2 differential non–linearity error and maximum offset error of ±20 mV. The Successive Approximation Register (SAR) allows for 115 kS/s maximum sample rate, which is far more than the required sample rate (see section 4.4). The chip communicates with the FPGA over SPI (serial peripheral interface).

SGA Analogue Strain Gauge Load Cell Amplifier [131,132] is used for amplification of the signal from the load cell. It has programmable bridge sensitivity. It can be set to 1.99 mV/V for the Novatech F265 load cell (see section 4.5.3, which has 2 mV/V output

characteristic, adjustment is applied in software of real–time target). It is equipped with offset cancelling circuit, selectable filter (which can be set to among other options to 10 Hz or 50 Hz, which covers the required bandwidth). The non–linearity error is 0.03% of the full–range.

Two Multiple Range, 16-Bit, Bipolar/Unipolar Voltage Output DACs (Digital–to–Analogue Converters) are used to drive servovalve input (actuator control signal) [139]. They share a single SPI bus. The analogue output range of the DAC can be set to ± 10 V. Typical settling time is 7.5 μs..

Electronics hardware for the prototype is depicted in Fig. 4.18.

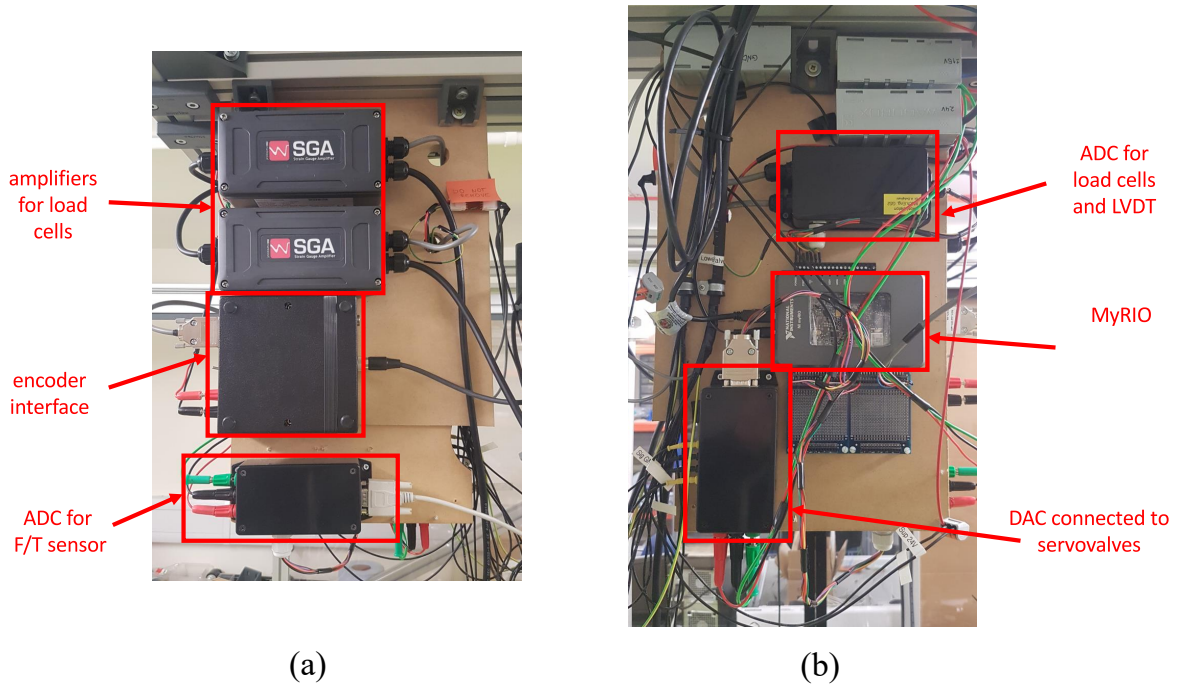

Figure 4.18: Electronics hardware for the joint prototype. (a) right side (b) left side.

4.6.2 Software

Application of control algorithms described in chapter 5 requires software to meet specific timings, otherwise the operation of the system fails. Hence the software is hard real–time [140]. A counter is implemented in the FPGA using LabView that triggers execution of the software. It initiates FPGA communication cycle with the peripherials: over SSI with the encoder, over SPI with ADCs and with DACs. A state–machine is implemented for that purpose with the following states:

'Idle' – waiting for a command from the Graphical User Interface (GUI);

'Initialise' – sending initialisation commands to peripherals, e.g. seting up the ADCs;

'Run' – periodically acquiring raw readings from the sensors and updating DAC, triggered by a timer;

The FPGA timer generates an interrupt that triggers execution of software on real–time target (processor) [141]. The timer cycle can be adjusted in the program. As discussed in section 4.4, 500 μs (2 kHz) is more than sufficient for the tasks performable by the exoskeleton. The real–time target converts raw values to engineering units, calculates values for a control algorithm step, is capable of writing values to a file, and provides display of measured and state variables. The flowchart of the implemented software on both real–time target and FPGA is shown in Fig. 4.19. The timing of the control loop, when FPGA state machine is in 'Run' mode, is depicted in Fig. 4.20. Explanations are given in the caption. In Fig. 4.4 time duration of the communication intervals and real–time software execution duration are shown with explanation.

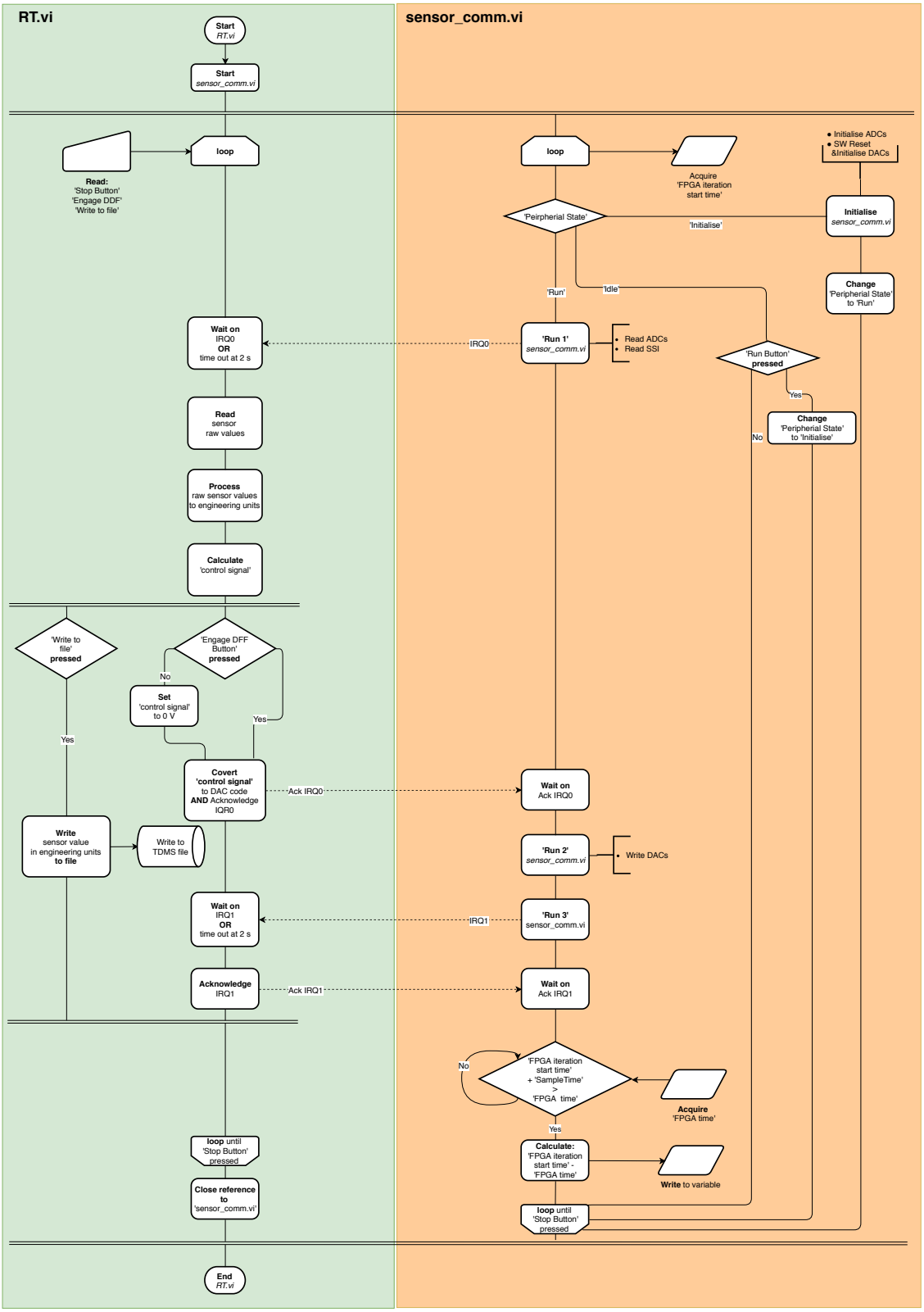

Figure 4.19: Software flowchart according to norm [3]. *RT.vi* – software running on real–time target, performing double precision calculations, interfacing with developer (operator), writing to file. It is shaded green. *sensor_ comm.vi* – software running on FPGA, performing communication with peripherals: ADCs, DACs and encoder over SSI. IRQ0, IRQ1 – interrupts. It is shaded orange.

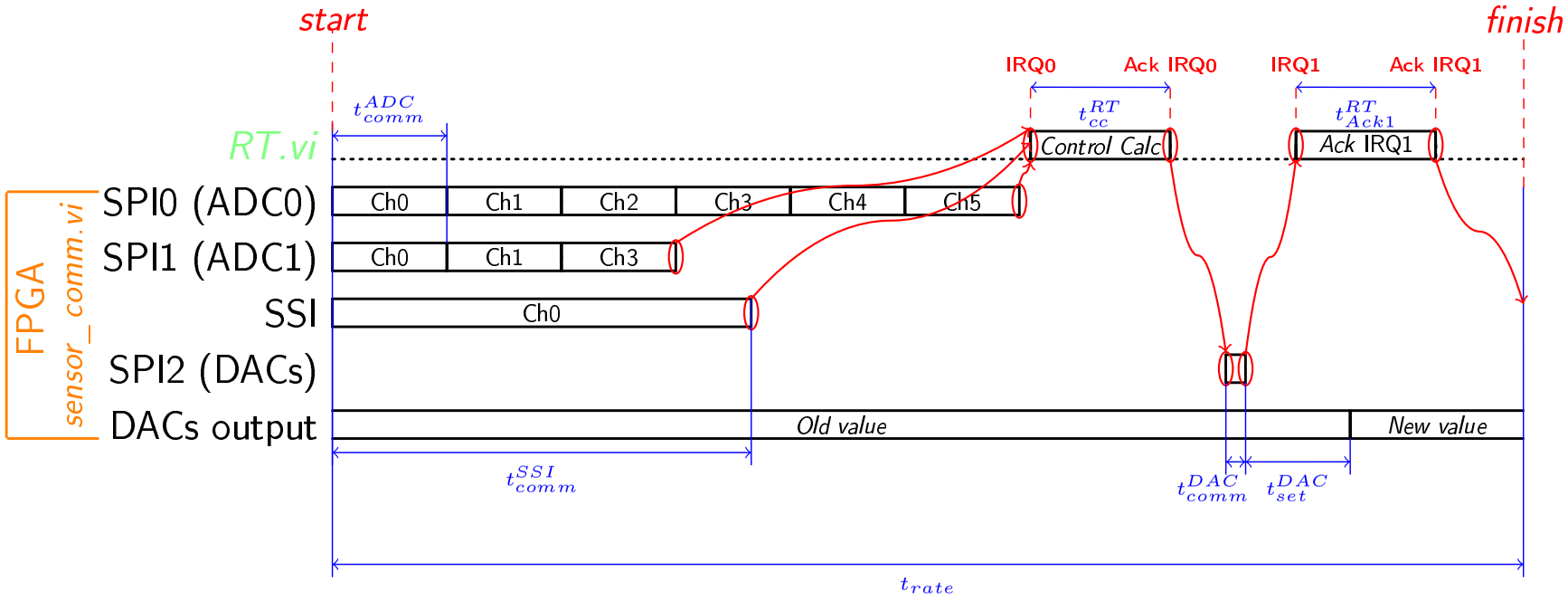

Figure 4.20: Timing diagram of the software during single control loop execution in state 'Run'. *sensor_comm.vi* – software running on FPGA, *RT.vi* – software running on the real–time target (processor). Buses: SPI0 communication bus connected to ADC0, measuring output from F/T sensor (Ch0 – Ch5); SPI1 – connected to ADC1 measuring output from load cells (Ch0, Ch1) and LVDT (Ch3); SSI – bus connected to the encoder; SPI2 – connected to daisy–chained DACs. DACs output – analogue output of the DACs. IRQ0 – interrupt issued by FPGA after communication on SPI0, SPI1, SSI ended. Ack IRQ0 – acknowledgement of IRQ0 issued by the real–time target after data has been read converted to engineering units and the control algorithm computed servo–valve voltages (converted to DAC's code). IRQ1 – interrupt issued by FPGA after communication on SPI2 has finished. Ack IRQ1 – acknowledgement of IRQ0 issued by the real–time target. *Old value* – value from previous control loop execution present of output of DACs. *New value* – value from the current loop execution present on the output of DACs. *start* – beginning of the control loop execution in 'Run' state. *finish* – end of the control loop execution in 'Run' state. Duration required for execution of portions of the software is given in Table 4.4. Arrows between the intervals denote sequentiality.

Table 4.4: Duration of time intervals in Fig. 4.20.

symbol	duration [ms]	explanation
t_{comm}^{ADC}	8.2	Time duration for transfer of analogue measurement over SPI bus from a single channel of ADC, for each channel data has to be transferred sequentially.
t_{comm}^{SSI}	30	Time duration for transfer of encoder measurement over SSI bus.
t_{comm}^{DAC}	1.4	Time duration for transfer of control command over SPI bus to two daisy–chained DACs.
t_{set}^{DAC}	7.5	Settling time of DAC output according to IC's specification.
t_{CC}^{RT}	*unspecified*	Duration of the interval depends on computational load of the processor (e.g. whether writing to file is performed in parallel with the main software sequence), scheduling priorities set in the operating system, memory access latency etc. Such timing analysis is a problem on its own.
t_{Ack1}^{RT}	*unspecified*	as explained above
t_{rate}	minimum of 'SampleTime'	Single control loop execution time is at least 'SampleTime' (adjustable through GUI, the user interface). If software sequence of dependent FPGA communication and RT calculations lasts less, duration of the software sequence, the value is measured by a timer implemented in FPGA and can be found experimentally and recorded.

4.7 Prototype Specification

The specification of the prototype is shown in Table 4.5. It is based on computer model of the device, experimental data and manufacturers' specification, as specified in the comments column of the table. In Fig. 4.21 maximum torque produced at the joint as a function of the joint angle is shown. In Fig. 4.22, phase characteristic of the spool response $\phi_{sp}(x_{sp}(s)/u(s))$ of the servo–valve is shown.

Table 4.5: Specification of the prototype joint.

parameter	symbol	unit	value	comment
prototype mass	m	kg	32.9	For details see Table 4.1. Mass excludes hydraulic power unit.
piston stroke	r_{max}	m	0.1 (0.2)	In constructed prototype hydraulic cylinders of 0.1 m stroke are used. 2 adaptors of 5 cm per cylinder are used to connect to load cell. A version can be constructed without the adaptors, and hydraulic cylinders with pistons of 0.2 m.
piston area on side of port A (without rod)	$\mathcal{A}^{\mathrm{A}}$	m^2	1.14×10^{-3}	
piston area on side of port B (with rod)	$\mathcal{A}^{\mathrm{A}}$	m^2	6.33×10^{-4}	

Table 4.5 (Cont.)

joint angle at extreme extension	θ_2^{ext}	deg	-13	
joint angle at extreme flexion	θ_2^{flex}	deg	-87 (-168)	In brackets for stroke of 0.2 m.
joint range	$\lvert\theta_2^{flex} - \theta_2^{ext}\rvert$	deg	74 (155)	In brackets for stroke of 0.2 m. An encoder providing absolute angle measurement with 14–bit precision is used in prototype. However larger in diameter than 12–bit incremental encoder used in BLEEX [16], it has the advantage of not requiring the procedure of setting of the reference each time the electronics are switched on. Absolute measurement is required to make the device operable, especially when it constitutes of many joints.
joint angular velocity during flexion at 3 V (30% input)	$\dot{\theta}_{30\%}^{flex}$	deg/s	-50.8	Value measured experimentally.

Table 4.5 (Cont.)

joint angular velocity during extension at -3 V (30% input)	$\dot{\theta}_{30\%}^{ext}$	deg/s	35	Value measured experimentally.
minimum joint angular velocity during flexion	$\dot{\theta}_{min}^{flex}$	deg/s	-170	Value calculated from $\dot{\theta}_{30\%}^{flex}$.
maximum joint angular velocity during extension	$\dot{\theta}_{max}^{ext}$	deg/s	117	Value calculated from $\dot{\theta}_{30\%}^{ext}$.
supply pressure of hydraulic circuit	ρ_s	bar	150	
hydraulic pump nominal flow	q_{Vnom}	l/min	6	Hydraulic circuit is powered from a stationary unit consisting of mains powered pump, tank, accumulator, relieve valve, two servo–valves. Unit is of considerable dimensions, mounting it on the exoskeleton frame would be troublesome. Valves are connected with ports of hydraulic cylinders with about 7 meters long pipes.

Table 4.5 (Cont.)

maximum flexion torque	τ_{max}^{flex}	Nm	2740 [at -45 deg]	Characteristic is shown in Fig. 4.21. Knee joint range for BLEEX is 120 deg [10]. But comparing the maximum absolute torque of BLEEX with Fig. 4.21 it is seen that for position far into flexion, the maximum absolute torque degrades to 0 sharply. The considered joint prototype maintains flat characteristic further into flexed position, never reaching 0.
minimum extension torque	τ_{min}^{ext}	Nm	-1520 [at -45 deg]	Characteristic is shown in Fig. 4.21.
minimum flexion torque	τ_{min}^{flex}	Nm	1580 [at -168 deg]	Characteristic is shown in Fig. 4.21.
torque to actuator mass (incl. knee cap)	—	Nm/kg	250 (95)	Compare with Table 4.2.
maximum extension torque	τ_{max}^{ext}	Nm	-880 [at -168 deg]	Characteristic is shown in Fig. 4.21.

Table 4.5 (Cont.)

control loop sample rate (duration of execution)	$\bar{t}_{rate}$	ms	3.4	Measured, average value.
phase shift of $x_{sp}(s)$ at $u(s)$ of 10 Hz	$\phi_{sp}^{10\text{Hz}}$	deg	5	According to the manufacturer's specification [122]. Charateristic shown in Fig. 4.22.

4.8 Summary

In this section a novel design of an enhancive exoskeleton joint was presented. An actuation system for the design employs a hydraulic circuit powering two double acting hydraulic cylinders. Required bandwidth of motion was assessed to be 10 Hz for considered tasks, except for running. If running is considered, the bandwidth must be higher, at least 40 Hz. Based on the result, the sample rate of control electronics was chosen to be 2 kHz. Sensors were selected to meet requirements for the range and bandwidth. The selection of the sensors allows for observability of the robotic manipulator state. The extension of the lower actuator can be calculated from available measurements and geometric properties of the joint. An electronics architecture was proposed. At the centre of it is National Instruments MyRIO. Also, a software architecture was proposed allowing for implementation of a controller presented in subsequent chapter 5.

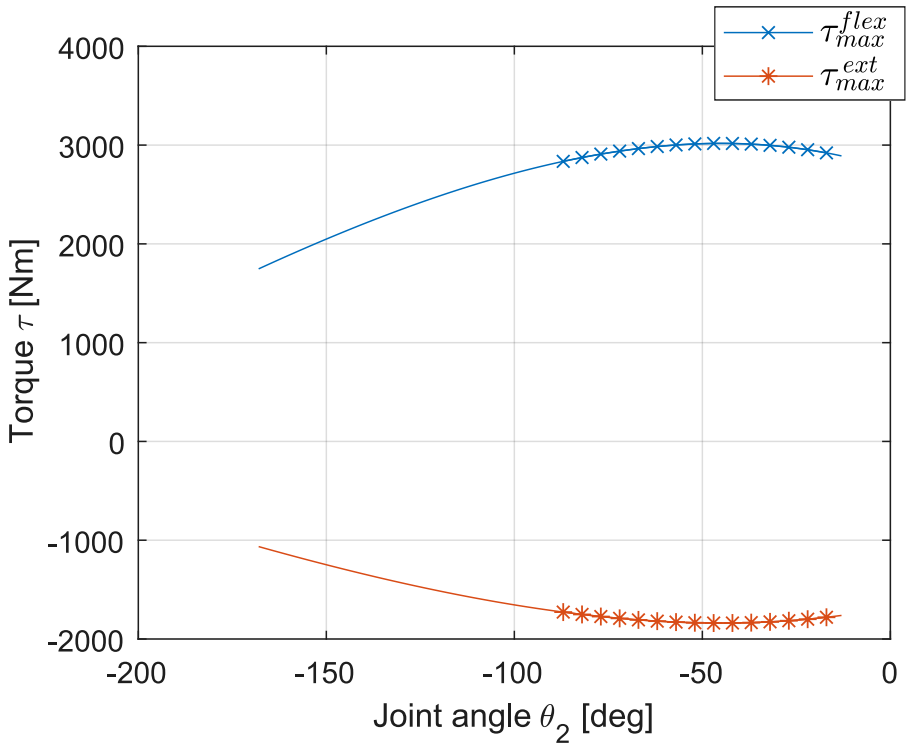

Figure 4.21: Maximum torque produced at the joint as a function of the joint angle. Maximum flexion torque $\tau_{max\ flex}$: blue marker x – short piston version (stroke of 0.1 m), blue line – – long piston version (stroke of 0.2 m). Maximum extension torque $\tau_{max\ ext}$: red marker x short piston version (stroke of 0.1 m), red line – long piston version (stroke of 0.2 m).

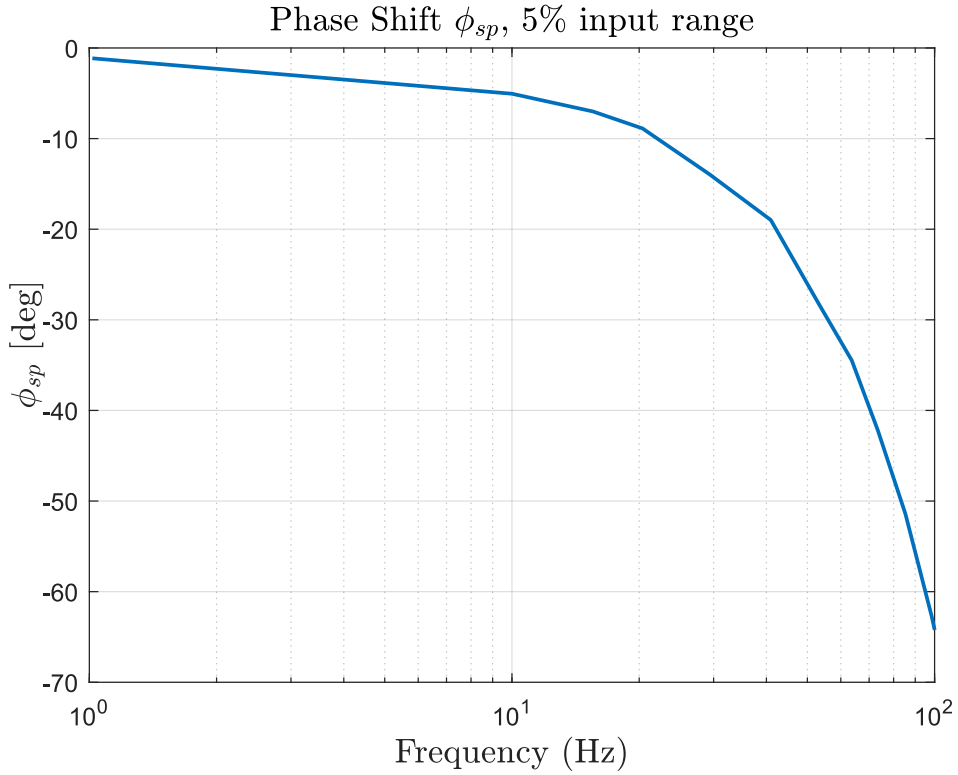

Figure 4.22: Phase characteristic of spool response $\phi_{sp}(x_{sp}(s)/u(s))$ of the servo–valve displacement according to the manufacturer's specification [122]. $x_{sp}(s)$ – Laplace transform of displacement, $u(s)$ – Laplace transform of control signal, s – Laplace operator.

Chapter 5

Simulation of Control and Model–based Parameters Selection for the Prototype Joint

5.1 Introduction

The main objective of a controller for a full–body enhancive exoskeleton is to allow its segments to move in concert with segments of operator's body. The controller is divided into 3 tiers (see section 2.3.2): high level control, middle level control, and low level control. The purpose of the highest tier is to recognise a state of the robot, e.g. which leg of the robot (or both) is in contact with the ground. An appropriate model of the robot can then be used by the middle level. The objective of the middle level controller is to perform calculations on the model with a goal of minimising the controlled variable. The output commands of the middle level control are the set values for the actuators. The low level control ensures following of these commands. As discussed in section 3, for the middle level controller, Force Control laws are superior to Master–Slave Position Control. In this section the human–machine interaction force is the controlled variable. The novel design of a joint with two opposing hydraulic actuators introduces a problem of positioning of the knee cap, while simultaneously controlling the interaction force. A control scheme is proposed to satisfy the control objectives. The control is simulated on a two degree of freedom model (one coupling with a hip, and one coupling with a knee) following ankle trajectory. Performance of the control strategies is evaluated using cost functions related to human–machine interaction force and knee cap positioning. The problem of controlling force exerted by

linear hydraulic actuators is considered to be difficult [142], due to non–linear nature of equations describing its dynamics and parameters uncertainty. A low level control strategy utilising the fact of coupling of force of the actuators is proposed to improve the performance. It is compared to independent proportional control of hydraulic actuators. Lastly, parameters selection using proposed cost functions is performed to find settings of the proposed coupled control of low level actuators yielding acceptable performance from point of view of the operator.

5.2 Middle–Level Controller

In this section relationship between a cost function of form of integral of squared human–machine interaction force and absolute power exchanged between the robot in operator is demonstrated. At each step of introducing controller elements, the changes are evaluated using those functions. A gravity cancellation scheme is proposed to minimise the human–machine interaction force in the first approach. Model–based approach to prototyping of the controller is used. It is simulated with Simulink, with a model created using Simscape Multibody library[1], imported from SolidWorks. Details of implementation of the model and controller are included in Appendix E. The subsystems hierarchy is depicted in Fig. E.1. The input to the simulation is obtained from motion capture study described in section 4.4.

Direct Force Control (see section 2.5.1) law is employed for minimisation of the residual interaction force. The reasons are:

1. It is more suitable for a full-body exoskeletons as the upper extremities are intended to be in contact with loads possessing masses and inertias of unknown, changing values, as wells as unknown forces and torques, inducing torque due to disturbance τ_{dist} at exoskeleton joints (see Figure 2.13), which effects are burden on a user. In Fig. 2.17, for Virtual Generalised Force Control, τ_{dist} is not shown as for laws proper operation it is assumed to be 0. The measurement of human–machine interaction forces allows for direct identification of these effects. In case of Indirect Force Control laws, this could be realised by inclusion of them in the model. But without a priori knowledge, as is the case with the nature of unknown disturbance, it is not feasible, rendering the system not to be output controllable. Validity of estimation of the output of the plant (human–machine interaction force) is burdened by this unknown. Placing a sensor between a user

[1] `https://uk.mathworks.com/products/simmechanics.html`

and an exoskeleton increases mechanical complexity of the machine, as explained in section 3.4. This could be circumvented by placing of a sensor between the exoskeleton and the environment (load masses and inertias) in order to measure forces and torques inducing τ_{dist}. However such sensor would need to have a larger range, hence mass and dimensions, than one placed between exoskeleton and operator, which measures values of interaction forces decreased by forces applied by actuators. Possibility of applying disturbance present in models composed of many segments.

2. Direct Force Control allows for simulation of a portion of an exoskeleton kinematic chain, treating subsequent segments as a mass attached to its end. This enables for modularity and makes it possible for practical evaluation of the controller on a single joint prototype. Moreover, placement of the sensor between exoskeleton frame and an operator provides means of measurement of interface forces for purpose of mid–level and low–level controller performance evaluation.
3. Although Direct Force Control is used in simulation and during evaluation on the prototype, the mid–level control has clearly defined interface to low–level controller. Thus the prototype with proposed low–level actuator control can also to be governed by Indirect Force Control law on the middle level.

A method of determining demanded force of linear actuators from a torque signal is described. Lastly, knee cap positioning scheme with minimisation the interaction force is proposed.

5.2.1 Control Goals

The primary control goal of the controller for an exoskeleton under consideration is to minimise absolute value of force/torque components of Ξ human–machine interaction force/torque (wrench) over time (see section 2.5). The exoskeleton then inherently follows an operator at considered contact points. This can be expressed as a problem of multi–objective optimisation with a weighted cost function of form:

$$E_{\Xi}(\tau_{act}) = \sum_{i=1}^{N} \left(\lambda_i \int_{t_{start}}^{t_{end}} \left\| \Xi^i \right\|^2 \mathrm{d}t + \kappa_i \int_{t_{start}}^{t_{end}} \left\| \nu^i \right\|^2 \mathrm{d}t \right), \qquad \forall t_{start}, t_{end} \in \mathbb{R} : t_{start} < t_{end} \tag{5.1}$$

where Ξ^i is vector of forces acting at i$^{\text{th}}$ contact point given by Eq. (2.5), ν^i is torque acting on exoskeleton segment at i$^{\text{th}}$ interaction point given by Eq. (2.6). t_{start}, t_{end}

are time of start and end of manoeuvre. N is a number of interaction points. $\lambda_i \geq 0$, $\kappa_i \geq 0$ are constant weights, chosen by design to conveniently assign importance to components of human–machine interaction force. $\|\cdot\|$ is norm in Euclidean space. The optimisation problem is then:

$$\underset{\forall \tau_{act} \in S}{\text{minimise}} \;\; E_{\Xi}(\tau_{act}) \tag{5.2}$$

where $S \subset \mathbb{R}^L$ is a subset of permitted values of joints torque (control signal). L is number of manipulator joints. The cost function given by Eq. (5.1) in context of deriving of control law for an exoskeleton is used by authors in [143]. The rationale behind performing minimisation of human–machine interaction force as stated by Eq. (5.2) is that instantaneous value of flow of energy (power) between robot and user is minimised as explained in Appendix A, if Ξ is maintained close to 0. Metabolic expenditure is then close to $\Delta E_{met} = 0$. We are interested in minimising magnitude of instantaneous energy transfer between robot and human operator. We can write total energy transferred during manoeuvre (regardless whether positive or negative) as:

$$W^{\dagger} = \sum_{i=1}^{N} \left(\int_{t_{start}}^{t_{end}} \left| \Xi^i \cdot \dot{p}^i \right| \, \mathrm{d}t + \int_{t_{start}}^{t_{end}} \left| \nu^i \cdot \dot{\alpha}^i \right| \, \mathrm{d}t \right) \tag{5.3}$$

where p^i is position of contact point given by Eq. (2.2), corresponding to Ξ^i. α^i is rotation of exoskeleton segment with contact at i$^{\text{th}}$ point given by Eq. (2.3), corresponding to ν^i. Eq. (5.3) can be expressed as:

$$W^{\dagger} = \sum_{i=1}^{N} \left(\int_{t_{start}}^{t_{end}} \left\| \Xi^i \right\| \left\| \dot{p}^i \right\| \left| \cos(\varphi_p^i) \right| \, \mathrm{d}t + \int_{t_{start}}^{t_{end}} \left\| \nu^i \right\| \left\| \dot{\alpha}^i \right\| \left| \cos(\varphi_\alpha^i) \right| \, \mathrm{d}t \right) \tag{5.4}$$

where φ_p^i is angle between Ξ^i and $\dot{p}^i$, φ_α^i is angle between ν^i and $\dot{\alpha}^i$. Since $\cos(\varphi_p^i) \in [-1, 1]$ and $\cos(\varphi_\alpha^i) \in [-1, 1]$, $W^{\dagger}$ is bounded by:

$$W^{\dagger} \leq \sum_{i=1}^{N} \left(\int_{t_{start}}^{t_{end}} \left\| \Xi^i(t) \right\| \left\| \dot{p}^i(t) \right\| \, \mathrm{d}t + \int_{t_{start}}^{t_{end}} \left\| \nu^i(t) \right\| \left\| \dot{\alpha}^i(t) \right\| \, \mathrm{d}t \right) \tag{5.5}$$

$\|\Xi^i(t)\|$, $\|\dot{p}^i(t)\|$, $\|\nu^i(t)\|$, $\|\dot{\alpha}^i(t)\|$ are positive, real–valued functions. Since they represent physical variables their values never approaches infinity on interval $[t_{start}, t_{end}]$. Hence, the functions are square–integrable on this interval. Therefore Cauchy–Schwarz

inequality can be applied:

$$\int_{t_{start}}^{t_{end}} \left\|\Xi^i(t)\right\| \left\|\dot{p}^i(t)\right\| \, \mathrm{d}t \leq \Phi_p^i \Psi_p^i \tag{5.6}$$

$$\int_{t_{start}}^{t_{end}} \left\|\nu^i(t)\right\| \left\|\dot{\alpha}^i(t)\right\| \, \mathrm{d}t \leq \Phi_\alpha^i \Psi_\alpha^i \tag{5.7}$$

where:

$$\Phi_p^i = \sqrt{\int_{t_{start}}^{t_{end}} \left\|\Xi^i(t)\right\|^2 \mathrm{d}t}, \quad \Phi_\alpha^i = \sqrt{\int_{t_{start}}^{t_{end}} \left\|\nu^i(t)\right\|^2 \mathrm{d}t} \tag{5.8}$$

$$\Psi_p^i = \sqrt{\int_{t_{start}}^{t_{end}} \left\|\dot{p}^i(t)\right\|^2 \mathrm{d}t}, \quad \Psi_\alpha^i = \sqrt{\int_{t_{start}}^{t_{end}} \left\|\dot{\alpha}^i(t)\right\|^2 \mathrm{d}t} \tag{5.9}$$

We have therefore:

$$W^\dagger \leq \sum_{i=1}^{N} \left(\Phi_p^i \Psi_p^i + \Phi_\alpha^i \Psi_\alpha^i\right) \tag{5.10}$$

Ψ_p^i and Ψ_α^i are dependent only on a chosen trajectory, and for considered task are constant. Inequality (5.10) states that there is an upper bound on $W^\dagger$. If Φ_p^i and Φ_α^i are minimised, the upper bound is made smaller. One way of minimising the upper bound is then to perform minimisation of expression given by Eq. (5.2). Using Eq. (5.8) the cost function in Eq. (5.1) can be expressed as:

$$E_\Xi(\tau_{act}) = \sum_{i=1}^{N} \left(\lambda_i {\Phi_p^i}^2 + \kappa_i {\Phi_\alpha^i}^2\right) \tag{5.11}$$

The values of absolute instantaneous force/torque at contact points are limited by properties of human body. The exact maximal values are domain of study of biomechanics, but at this stage can be assumed by sensible consideration. They can be expressed as constraints:

$$\left\|\Xi^i(t)\right\| \leq \Xi_{max}^i, \ \forall i \in [1, ..., N] \tag{5.12}$$

$$\left\|\nu^i(t)\right\| \leq \nu_{max}^i, \ \forall i \in [1, ..., N] \tag{5.13}$$

The cost function of form as in Eq. (5.1) has an advantage of penalising high values of force/torque with power of 2. That way it is possible to find a solution that does not violate Ineqs. (5.12) and (5.13).

Simulink implementation of $W^{\dagger}$ is shown in Fig. E.32. Implementation of E_{Ξ} is shown in Fig. E.33.

5.2.2 Gravity Cancellation

The model of the single joint prototype (see section 4.2) is provided with a virtual joint (a hip joint), close to the fixing point with the base. Simulink implementation using Multibody library is shown in Fig. E.23. The centre of the 6 DoF force/torque sensor is able then to follow a trajectory in 2 dimensional space (sagittal plane). Frames of reference can be assigned following Denavit–Hartenberg convention [89] as in Fig. 5.1. Gravity acts along $-y$ direction of FoR0. An approximation is made, the prototype joint is modelled as a two degree of freedom manipulator. The mass distribution is changing with displacement of the pistons, but this effect is neglected. The knee cap, which is relatively heavy (see Table 4.1), contributes mass to both the first and the second link. Geometric properties are acquired from Solidworks model. l_{cy1}, l_{cy2} are equated to 0 ($l_{cy1} = 0.077$ m, $l_{cy2} = 0.078$ m in the model). Other parameters are: $l_1 = 0.679$ m, $l_2 = 0.573$, $l_{cx1} = 0.484$ m, $l_{cx2} = 0.192$ m. For the depicted device a potential energy is expressed as [89]:

$$E^{pot} = E_1^{pot} + E_2^{pot} = (m_1 l_{cx1} + m_2 l_1) g \sin(\theta_1) + m_2 l_{cx2} g \sin(\theta_1 + \theta_2) \tag{5.14}$$

where: E_1^{pot}, E_2^{pot} – potential energies of the links, $g = 9.81$ m/s^2 – gravitational acceleration, m_1, m_2 – masses of the links. Estimated torques required at joints (produced by actuators) to cancel human–machine interaction force due to gravity are:

$$\hat{R} = [\hat{R}_1 \hat{R}_2]^{\top} \tag{5.15}$$

$$\hat{R}_1 = \frac{\partial E^{pot}}{\partial \theta_1} = (m_1 l_{cx1} + m_2 l_1) g \cos\theta_1 + m_2 l_{cx2} g \cos(\theta_1 + \theta_2) \tag{5.16}$$

$$\hat{R}_2 = \frac{\partial E^{pot}}{\partial \theta_2} = m_2 l_{cx2} g \cos(\theta_1 + \theta_2) \tag{5.17}$$

Combining the equations of motion in the general form (see Eq. (2.19)) and Eq. (5.15):

$$\tau_{HM} = M(\theta)\ddot{\theta} + C(\theta, \dot{\theta})\dot{\theta} + R(\theta) - \hat{R}(\theta) \tag{5.18}$$

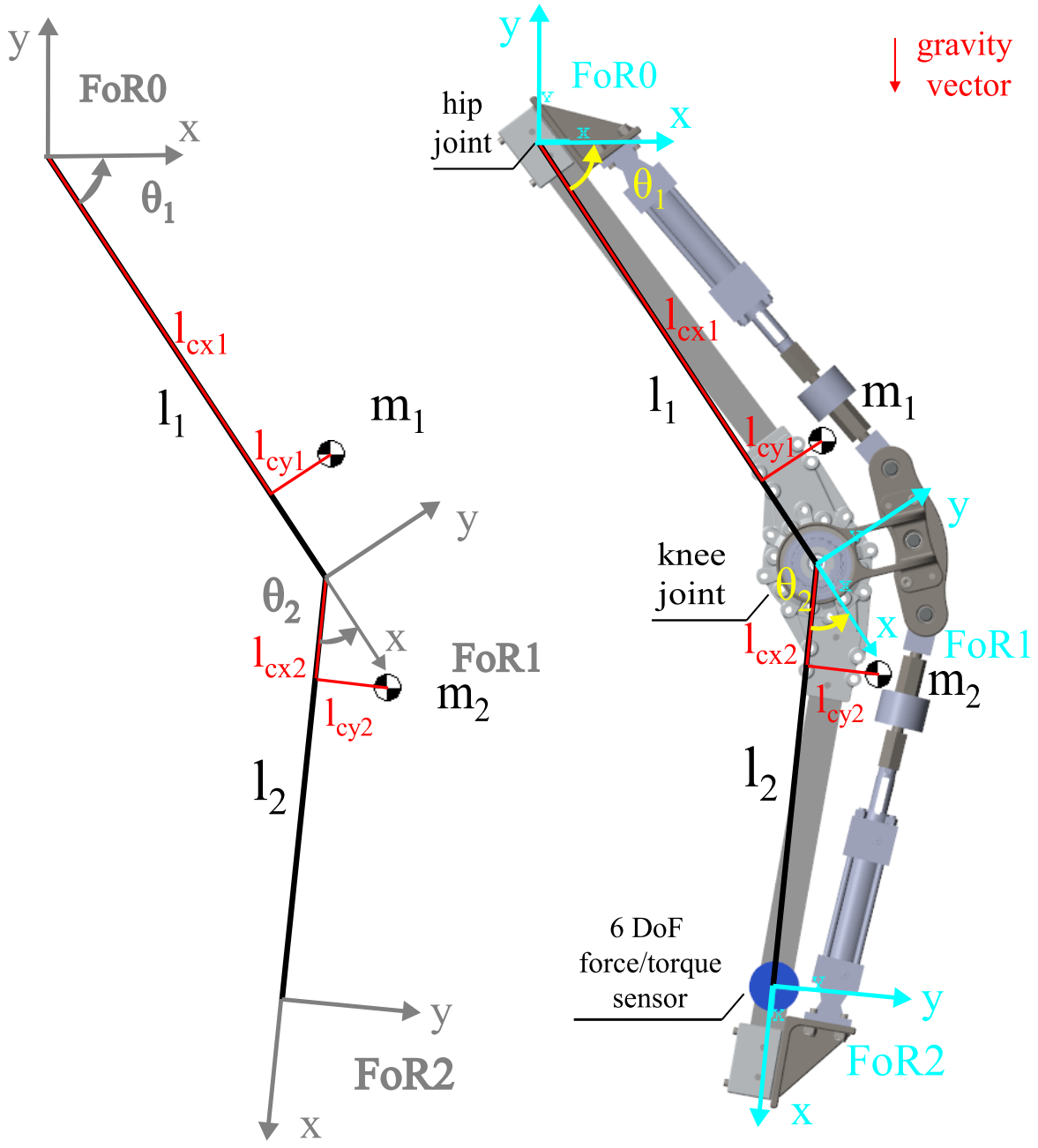

Figure 5.1: Ptototype joint with a virtual hip joint and assigned frames of reference. θ_1 – angular displacement of the first joint (virtual hip joint) relative to FoR0; θ_2 – angular displacement of the second joint (knee joint) relative to FoR1; l_1 – vector from origin of FoR0 to origin of FoR1; l_2 – vector from origin of FoR1 to origin of FoR2; l_{cx1}, l_{cy1} – x and y coordinates from origin of FoR0 to centre of mass of the first link in reference frame FoR1; l_{cx2}, l_{cy2} – x and y coordinates from origin of FoR1 to centre of mass of the second link in reference frame FoR2; m_1, m_2 – mass of links.

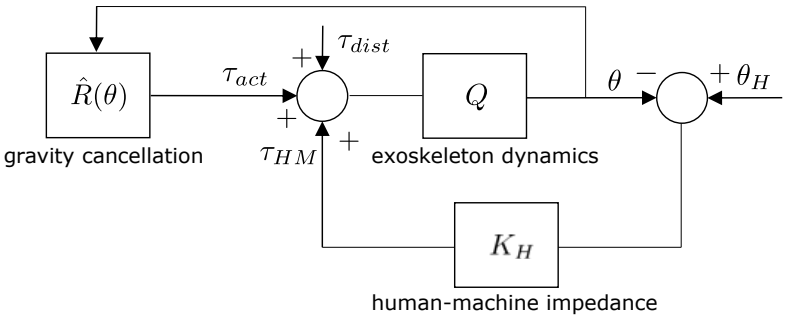

Figure 5.2: Block diagram of the gravity cancellation scheme. τ_{HM} – torque due to operator, τ_{dist} – torque due to disturbance, K_H is the human–machine impedance; $\theta \in \mathbb{R}^2$ – robot configuration (angles) in reference frames; $\theta_H \in \mathbb{R}^2$ – corresponding angles at user joints in the equivalent model

where $M(\theta) \in \mathbb{R}^{2\times2}$ is kinetic energy matrix (inertia matrix), $C(\theta, \dot{\theta}) \in \mathbb{R}^{2\times2}$ – centrifugal and Coriolis acceleration terms vector, $R(\theta)$ – torque induced at joints of the machine due to gravitation (complex, the prototype employs 5 rotational DoF and 2 prismatic DoF, heavy knee cap changes its position), $R(\theta) - \hat{R}(\theta)$ – error of modelling of torque due to gravity, $\tau_{HM} \in \mathbb{R}^2$ – torque due to operator. In effect, the user will be burdened with components due to respective forces. If gravity cancellation is modelled accurately, that is $R(\theta) - \hat{R}(\theta) = 0$, and in static case, that is $\theta = 0$ and $\dot{\theta} = 0$, the torque $\tau_{HM} = 0$. Through Eq. (2.14) it is concluded that the interaction force Ξ is 0.

The block diagram of the gravity cancellation scheme is depicted in Fig. 5.2. It uses an open–loop controller. The controlled variables, which are two components of human–machine interaction force Ξ in x and y axis and an interaction torque n^z around z axis, expressed in reference frame FoR0 (see Fig. 5.1), are not measured. The control scheme however makes use of manipulator configuration θ. For purpose of simulating the controller, the centre of 6 DoF force/torque sensor, which is interaction point between a user and an exoskeleton, is displaced to follow an arbitrary trajectory. In simulation, the connection to an operator is modelled as a subsystem of a Cartesian Joint[2] (for forcing translation in a plane, along x and y components) and Revolute Joint[3] (for allowing free, dependent rotation around z axis of segments of manipulator link). It is connected to a solid representing 6DoF force/torque sensor. In Fig. 5.3 the trajectory is depicted. The interaction point is following a user during gait in the sagittal plane. The forced displacement at the Cartesian Joint p is derived from motion capture data described in section 4.4. It is a vector of displacement of a marker placed on lateral malleolus (Lat_Mall) in reference frame of marker placed on anterior superior

[2] `https://uk.mathworks.com/help/physmod/sm/ref/cartesianjoint.html`
[3] `https://uk.mathworks.com/help/physmod/sm/ref/revolutejoint.html`

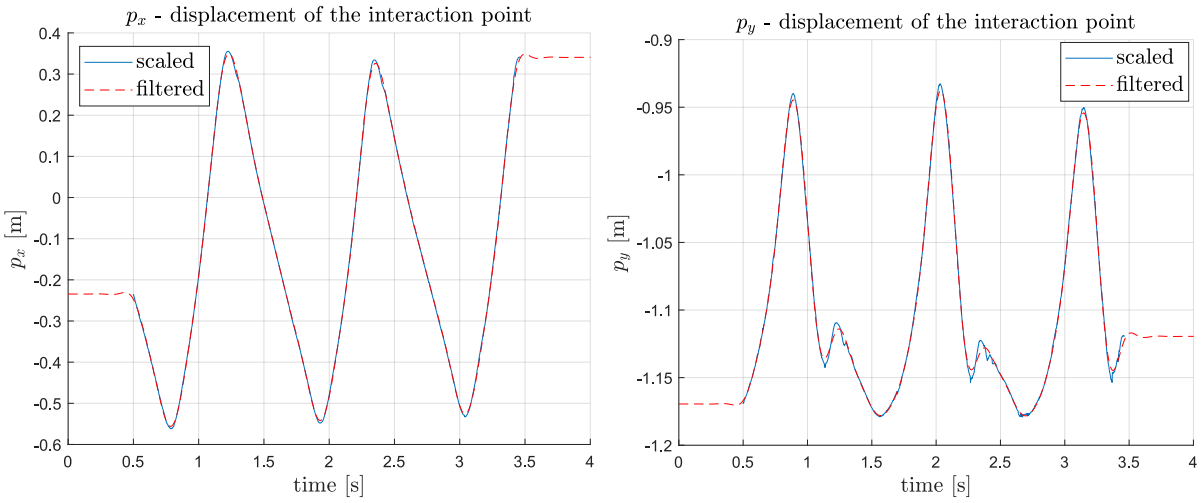

(a) (b)

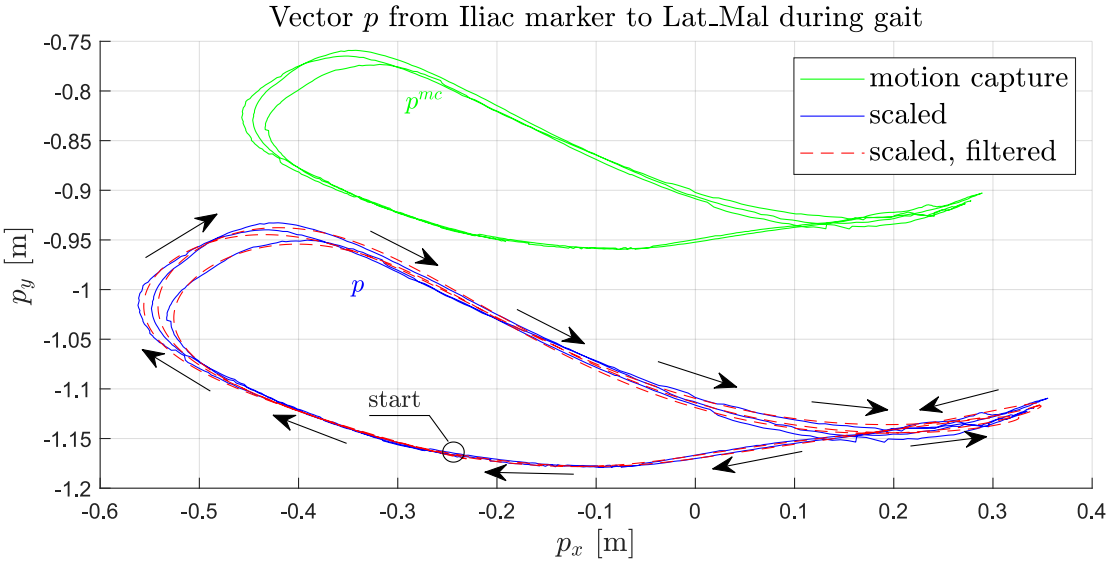

(c)

Figure 5.3: Displacement of a marker placed on lateral malleolus (Lat_Mall) in the reference frame of marker placed on anterior superior iliac spine (Iliac). Green – original data from motion capture, blue – data scaled by a coefficient (scaling coefficient $s_{coef} = 1.2288$), red – data filtered using first–order filter. (a) – p_x displacement, (b) – p_y displacement, (c) – displacement $p = [p_x\ p_y]^\top$ in the sagittal plane. Arrows point direction of movement.

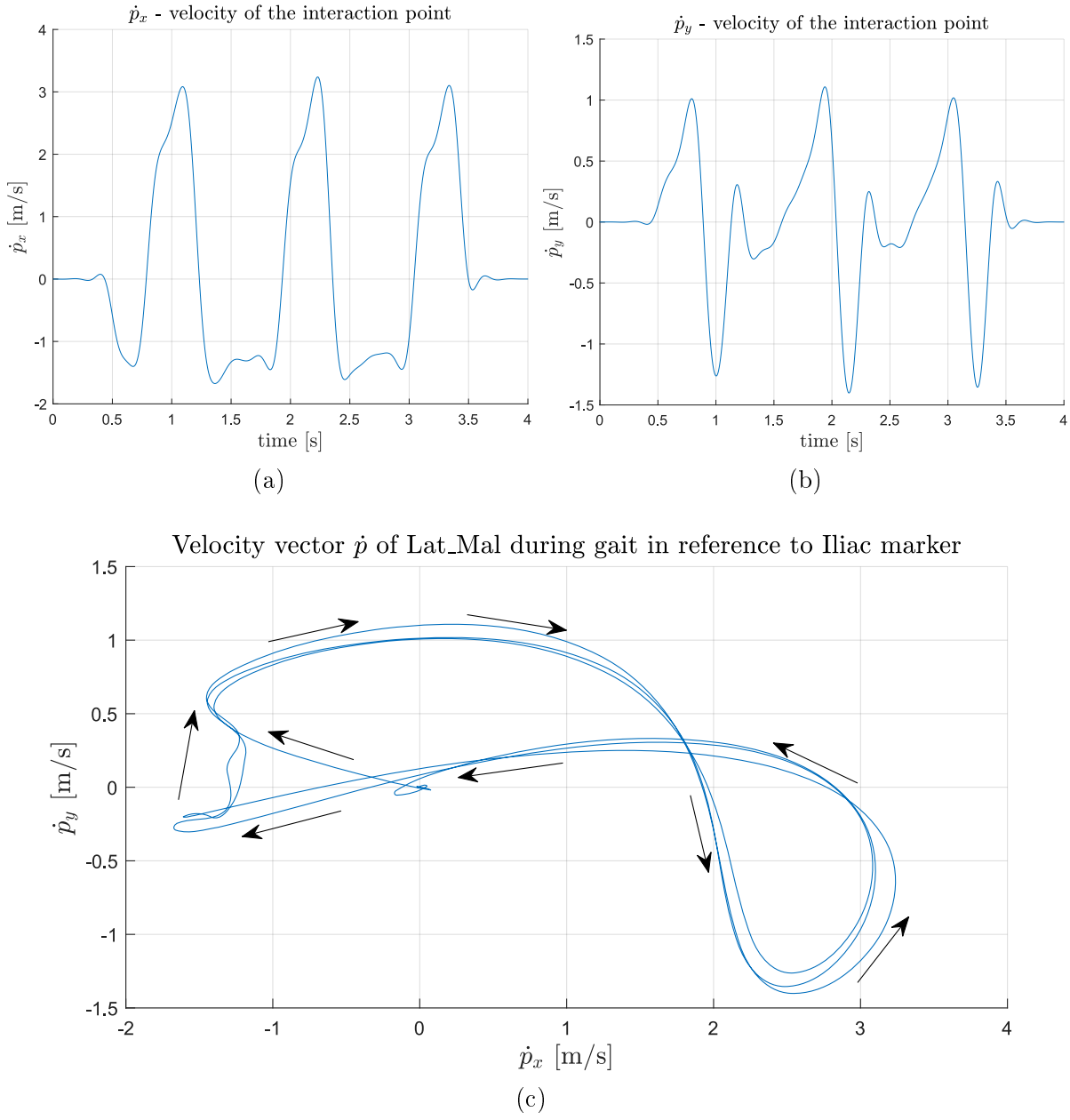

Figure 5.4: Velocity of a marker placed on lateral malleolus (Lat_Mall) in the reference frame of marker placed on anterior superior iliac spine (Iliac). (a) – $\dot{p}_x$ velocity, (b) – $\dot{p}_y$ velocity, (c) – velocity vector $\dot{p} = [\dot{p}_x\ \dot{p}_y]^\top$ in the sagittal plane. Arrows represent evolution in time.

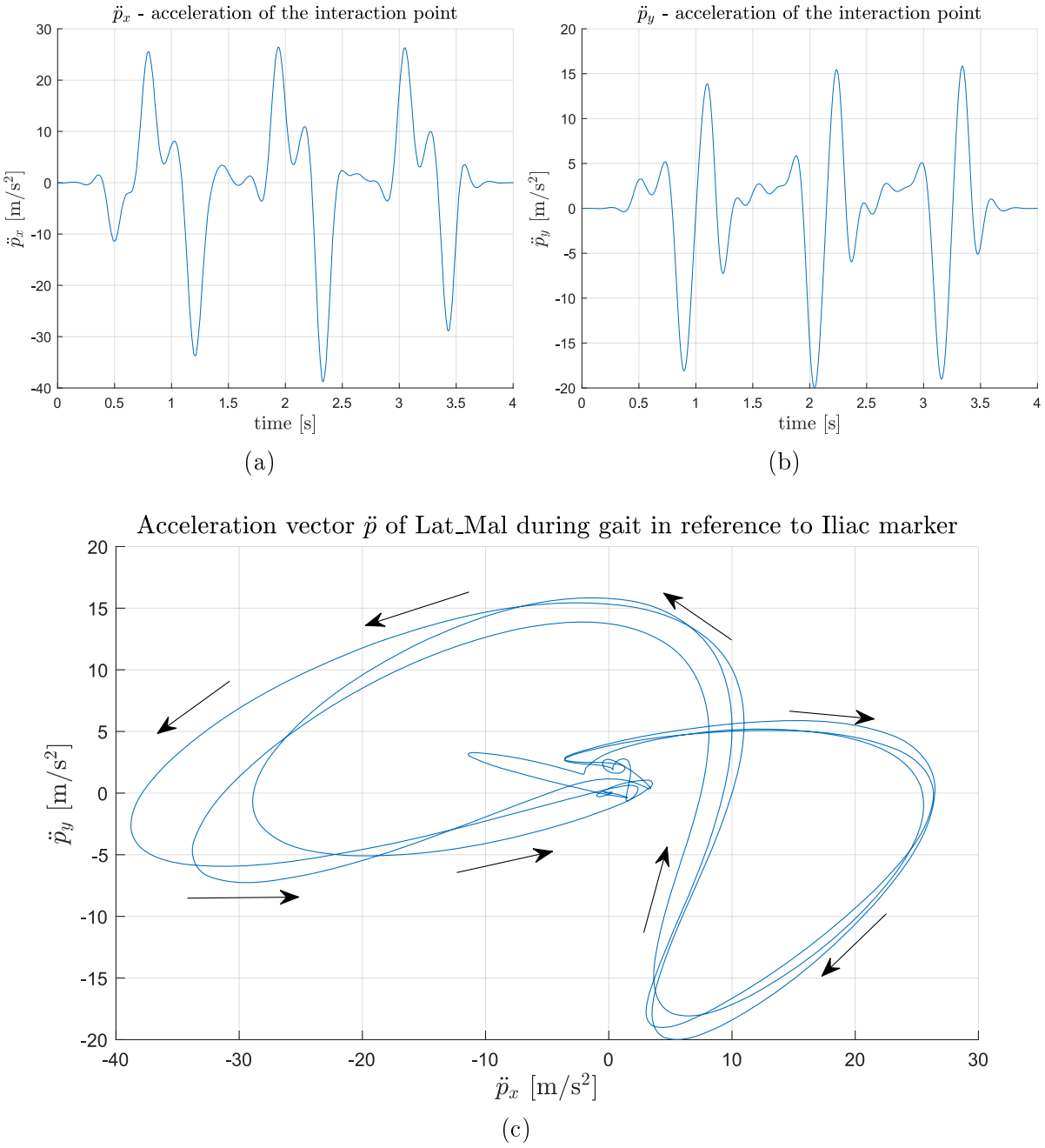

Figure 5.5: Acceleration of a marker placed on lateral malleolus (Lat_Mall) in the reference frame of marker placed on anterior superior iliac spine (Iliac). (a) – $\ddot{p}_x$ acceleration, (b) – $\ddot{p}_y$ acceleration, (c) – acceleration vector $\ddot{p} = [\ddot{p}_x\ \ddot{p}_y]^\top$ in the sagittal plane. Arrows represent evolution in time.

iliac spine (Iliac) padded with constant displacement data lasting about 0.5 s at the recorded beginning of gait data and at its end (so that the entire manoeuvre lasts 4 s). and multiplied by a scaling coefficient s_{coef}:

$$p = \begin{bmatrix} p_x \\ p_y \end{bmatrix} = s_{coef} \cdot p^{\,mc} = s_{coef} \begin{bmatrix} p_x^{mc} \\ p_y^{mc} \end{bmatrix} \tag{5.19}$$

where p_x, p_x^{cm} is displacement in anteroposterior axis of scaled, and original marker respectively, p_y, p_y^{cm} is displacement in craniocaudal axis of scaled, and original marker respectively. The scaling coefficient s_{coef} had to be introduced because of use of adaptors mounted on both sides of the load cells due to mismatching threads with ends of the rods in the considered prototype. This causes extension of the links of the joint. However, this extra length does not incur loss of generality of considerations for control in this section. If length between brackets depicted in Fig. 4.1 is 425 mm, then the shortest person fitting the joint for task of walking is 2.12 m tall ($s_{coef} = 1.18$, motion capture data for a 1.8 m tall person). Maximum knee angle is –45°. The measured range of motion of the prototype joint is –74.39° to –6.09°. If a smaller person would use it for walking, the extension of pistons would be too large. The tallest person able to use the exoskeleton would be 2.29 m tall, and the maximum knee angle –12°. If a taller person was to use it, he/she would not be able to extend his/her leg fully during gait. Again, without losing the generality, the scaling coefficient s_{coef} is chosen to be 1.2288, which corresponds to 2.21 m tall person. In Fig. 5.3 blue line represents raw data from motion capture multiplied by aforementioned scaling coefficient, and red represents padded and filtered using zero–phase filtering Matlab function `filtfilt`[4] with coefficients of 4$^{\text{th}}$ order Butterworth filter with cutoff frequency of 5 Hz designed using `butter` [5] (compare with bandwidth in section 4.4). `filtfilt` function runs on data twice – in positive and negative direction of time, resulting in zero–phase shift 8$^{\text{th}}$ order filtered data.

(5.20)

The filtering was applied to alleviate measurement error of the motion capture system. For simplicity, interaction with the ground is omitted, the stance phase and the swing phase of the leg are lumped together into one motion. Simulink solver `ode15`, with which the model was simulated, requires providing first two derivatives of displacement

[4] `https://uk.mathworks.com/help/signal/ref/filtfilt.html`
[5] `https://uk.mathworks.com/help/signal/ref/butter.html`

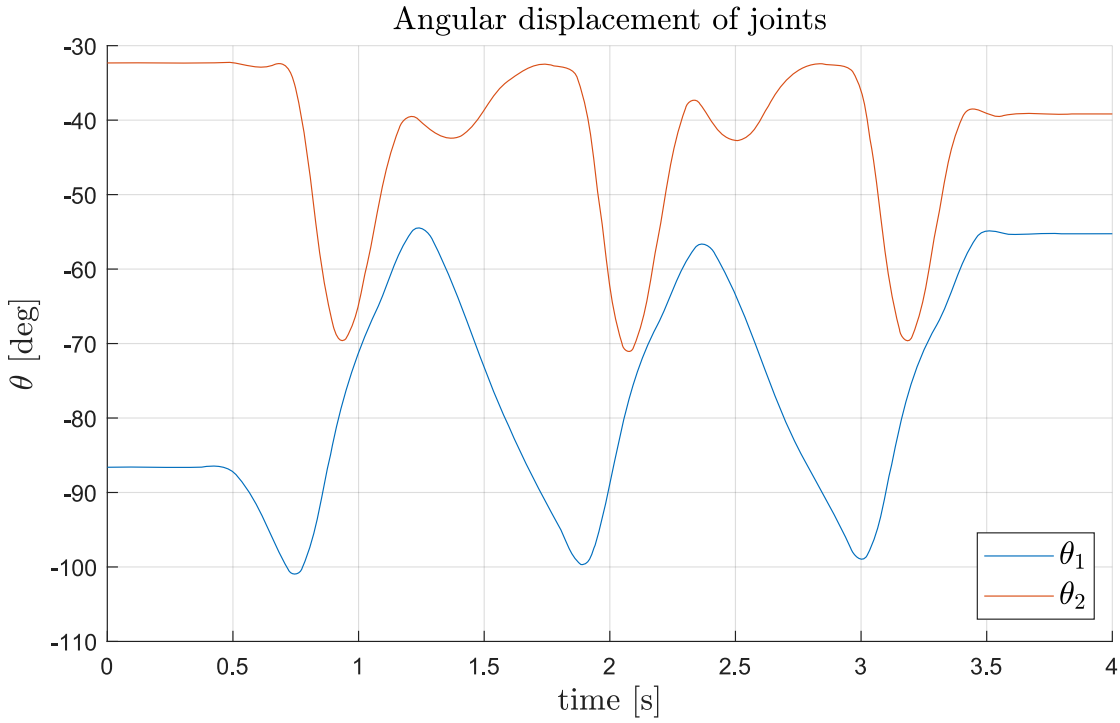

Figure 5.6: Angular displacement θ at the manipulator joints for input depicted in Fig. 5.3 (gait).

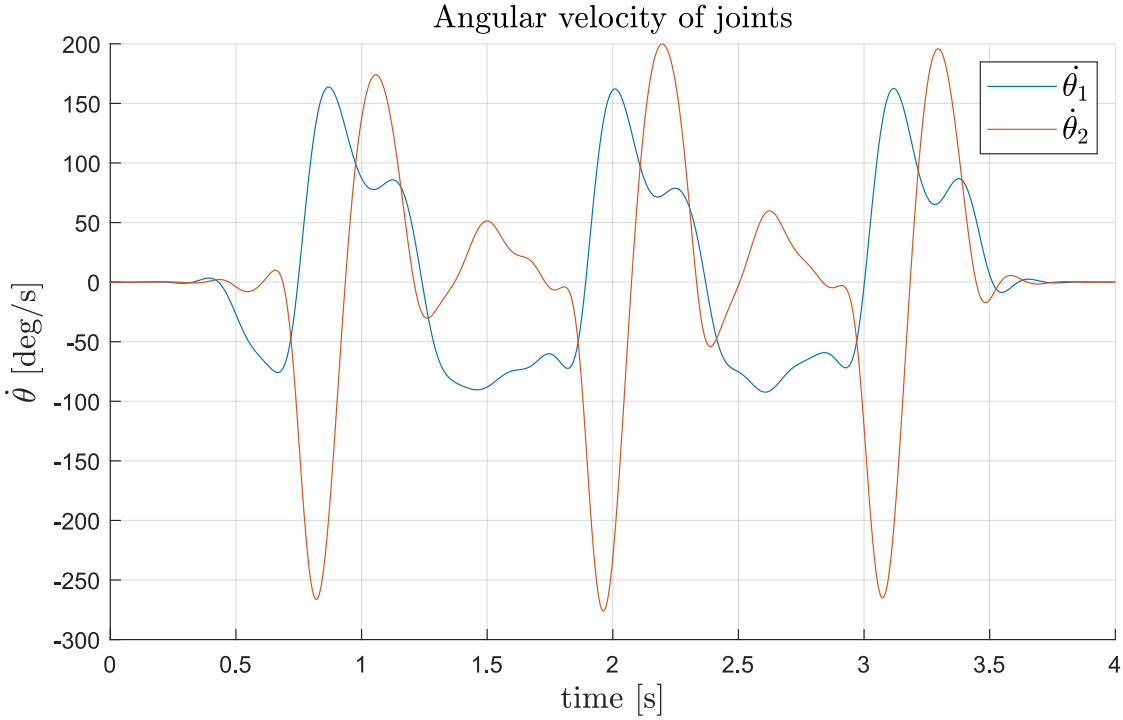

Figure 5.7: Angular velocity $\dot{\theta}$ at the manipulator joints for input depicted in Fig. 5.3 (gait).

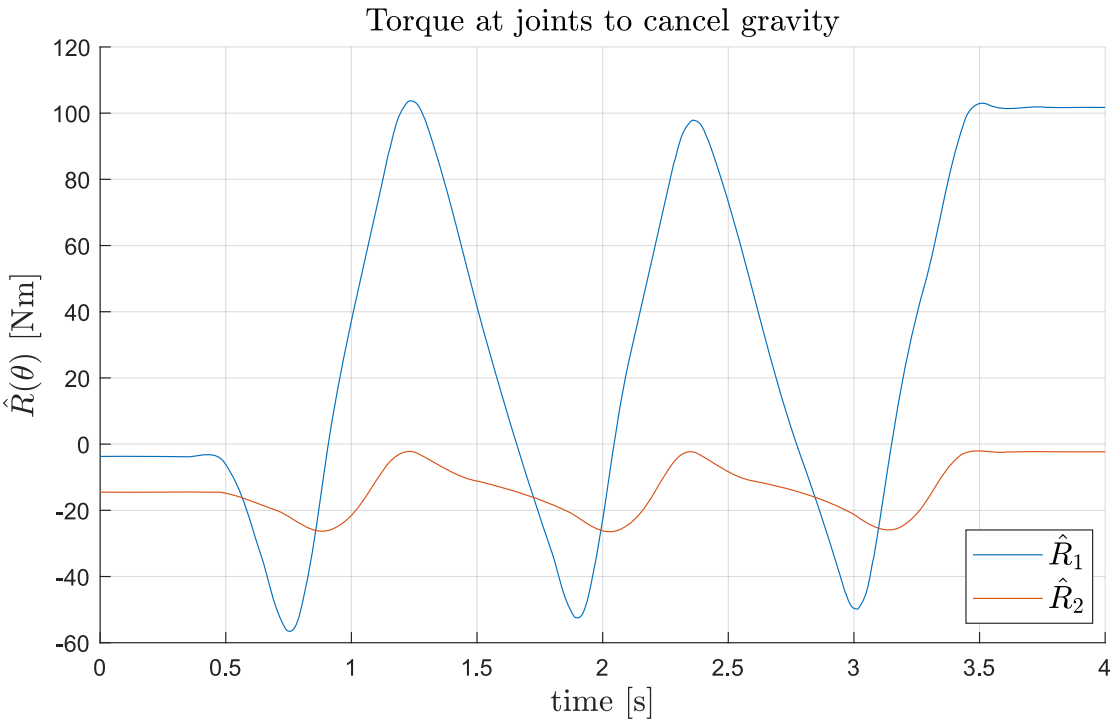

Figure 5.8: Torque $\hat{R}(\theta)$ at the joints required to cancel gravity during gait. $m_1 = 16$ kg, $m_2 = 16$ kg.

signal (velocity and acceleration) to Simulink–PS Converter [6]. Simulink block diagrams pertaining to the trajectory generation are shown in Figs. E.21 and E.20. The derivatives where calculated from padded and filtered data using `diff` function[7]. Matlab scripts performing these operations are Scripts E.1 and E.2. First derivative $\dot{p}$ is shown in Fig. 5.4. Second derivative $\ddot{p}$ is shown in Fig. 5.5.

In Fig. 5.6 resulting angular displacement θ is depicted. θ_2 is the angle of the prototype joint. It is in range of –70.7° to –32.3°, that is in range of the measured joint displacement. Angular velocity at joints is depicted in Figure 5.7.Minimum angular speed at the prototype joint (second joint) $\dot{\theta}_2$ is -276 deg/s. Comparing to value for the actual prototype: $\dot{\theta}_{min}^{flex} = -170$ deg (minimum angular velocity during flexion), it is seen that pump with a flow of 6 l/min is not sufficient to enable following of the gait. Maximum angular speed at the prototype joint required is 200 deg/s ($\dot{\theta}_{max}^{ext}$ – actual prototype value of 117 deg/s). The conclusion is that a pump with higher a flow has to be chosen. Since the angular speed is proportional to flow in/out of the cylinder, simulations in this chapter are performed with a pump that is rated at flow of 12 l/min. This is twice the flow of the pump of the actual prototype. The torque required to can-

[6] `https://uk.mathworks.com/help/physmod/simscape/ref/simulinkpsconverter.html`
[7] `https://uk.mathworks.com/help/matlab/ref/diff.html`

cel gravity, calculated using Eq.(5.16) and Eq. (5.17), is depicted in Fig. 5.8. Using the CAD software and looking at performance of the gravity cancellation controller, m_1 was chosen to be 16 kg, and m_2 to be 16 kg. $\hat{R}_1$ maximum absolute torque required at the first joint (hip joint) is 105 Nm. $\hat{R}_2$ maximum absolute torque required at the second joint (knee joint) is 26 Nm. The mass of the kneecap and the knee joint require a larger actuator torque at the first joint in this setup to actuate. In Figs. 5.9 and 5.10 the components of the human–machine interaction force in anterioposterior (x) and craniocaudal (y) axis respectively, that is in reference frame FoR0, are depicted. It can be seen that the interaction force is smaller in each direction. The cost functions $W^{\dagger}$ given by Eq. (5.3) and E_{Ξ} given by Eq. (5.1) (with $\lambda = 1$) were calculated. Without gravity cancellation: $W^{\dagger} = 444$ J, $E_{\Xi} = 3.55 \times 10^5$. With gravity cancellation: $W^{\dagger} = 441$ J, $E_{\Xi} = 3.34 \times 10^5$. Recorded torque around z direction in the Revolute Joint, part of connection to the operator, is as expected 0. This because of the fact that displacement α_z is dependent on two forced displacements p_x and p_y. In Fig. 5.11 absolute value of the interaction force $\Xi_{x,y}$ in the sagittal plane without control applied, and $\Xi^{grav}_{x,y}$ with gravity cancellation are depicted. Maximum force $\Xi_{x,y}$ felt by an operator is 952 N. If the control is applied, the maximum absolute force $\Xi^{grav}_{x,y}$ is 926 N.Applying gravity cancellation does not decrease absolute interaction force significantly. It also does not decrease value of cost functions E_{Ξ} and $W^{\dagger}$. Examining Fig. 5.10 it is seen that before the manoeuvre and after it, that is when the manipulator is static, absolute value of the force component in direction of gravitational field (Ξ_y) is decreased, which is the goal of gravity cancellation controller. The drawback is that during intervals in which the gravitational force would assist the movement, this assistance is cancelled, resulting in greater absolute human–machine interaction force required in downward direction (Ξ_y). Ξ_x is not significantly affected. It is a separate problem what magnitude of the interaction force is acceptable as explained in section 5.2.1.

5.2.3 Human–Machine Force Minimisation Using Force Feedback

In previous section (5.2.2) a gravity cancellation control scheme was proposed (open–loop control) for the joint prototype. The human–interaction force, while greatly reduced, still might prove to be burdensome for a user and cause discomfort or injury. Also, the control law relies on identification of mass properties and geometries of the manipulator. To reduce the force further and to account for errors in parameter identification a closed–loop control is proposed. In this setup the interaction force is measured

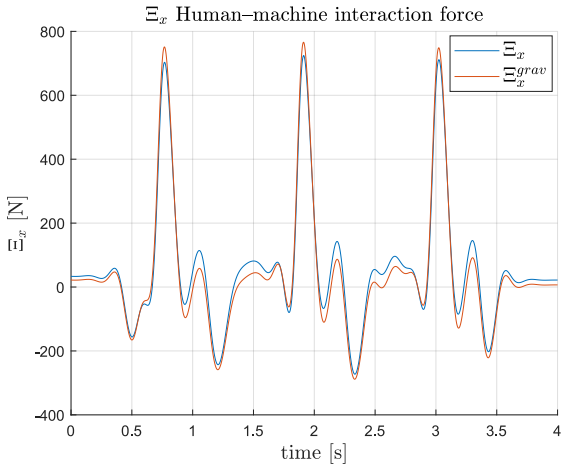

Figure 5.9: Human–machine interaction force in anteriorposterior axis with gravity cancellation. Ξ_x – with no control (blue), Ξ_x^{grav} – with gravity cancellation (red).

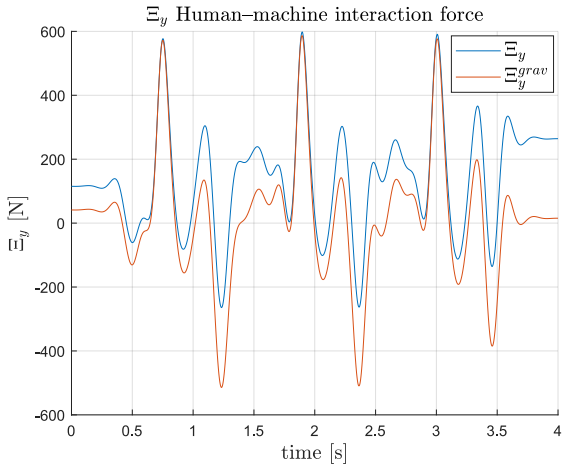

Figure 5.10: Human–machine interaction force in craniocaudal axis with gravity cancellation. Ξ_y – with no control (blue), Ξ_y^{grav} – with gravity cancellation (red).

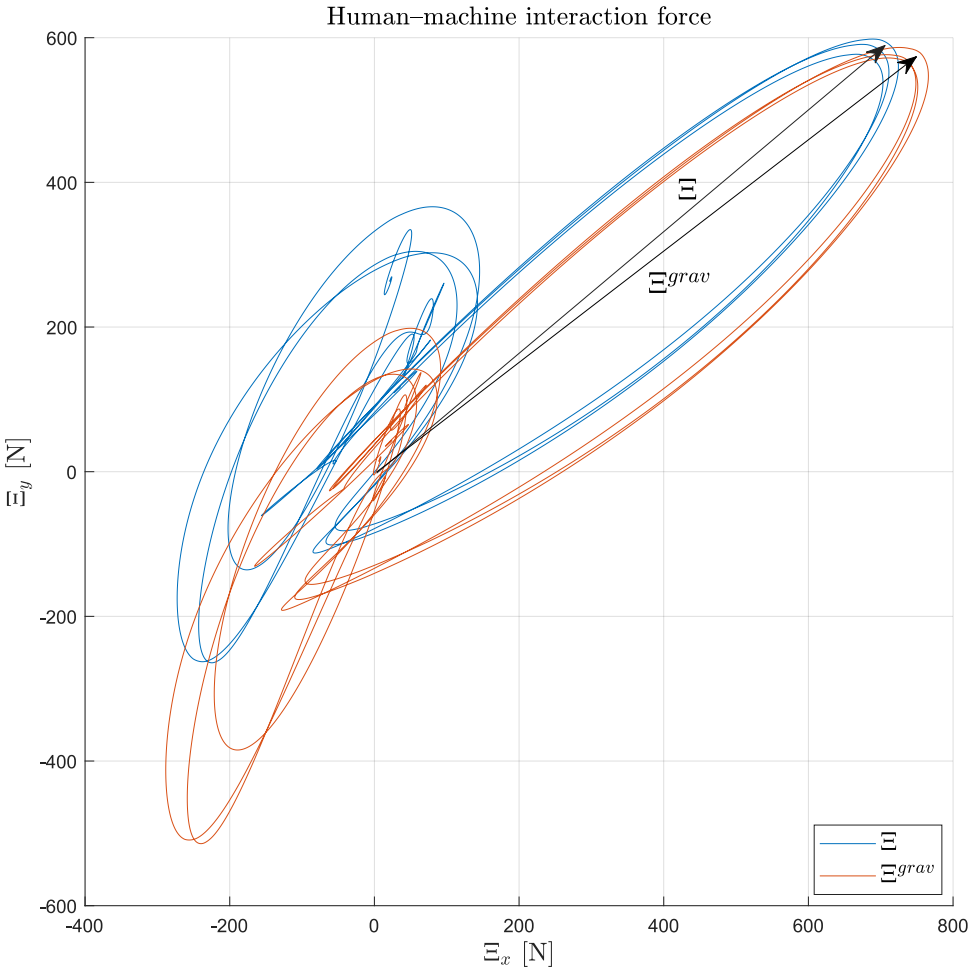

Figure 5.11: Human–machine interaction force in sagittal plane with gravity cancellation. $\Xi_{x,y}$ – with no control (blue), $\Xi_{x,y}^{grav}$ – with gravity cancellation (red).

directly (see the Direct Force Control law, section 2.5.1). The full manipulator Jacobian given for the mechanism depicted in Fig. 5.1 is given by [89]:

$$J(\theta) = \begin{bmatrix} -l_1 \sin\theta_1 - l_2 \sin(\theta_1 + \theta_2) & -l_2 \sin(\theta_1 + \theta_2) \\ l_1 \cos(\theta_1) + l_2 \cos(\theta_1 + \theta_2) & l_2 \cos(\theta_1 + \theta_2) \\ 0 & 0 \\ 0 & 0 \\ 0 & 0 \\ 1 & 1 \end{bmatrix} \tag{5.21}$$

The relationship given by Eq. (2.13) uses the Jacobian relating the human–machine interaction force $\Xi \in \mathbb{R}^6$ expressed in reference frame of FoR0, given by Eq. (2.4), to torque due to the operator τ_{HM}. Ξ can be directly measured using 6 DoF froce/torque sensor described in section 4.5. A control scheme can be proposed as in Fig. 2.13, combined with gravity cancellation scheme. A feedback controller can then be proposed:

$$\tau_{act} = KJ^{\top}(\theta)\Xi + \hat{R}(\theta) \tag{5.22}$$

where $\hat{R}(\theta)$ – estimated torque to cancel gravity given by Eq. (5.15), $K \in \mathbb{R}^2$, is of diagonal form:

$$K = \begin{bmatrix} k_1 & 0 \\ 0 & k_2 \end{bmatrix} \tag{5.23}$$

Combining general equations of motion of the system (see Eq. (2.19)) and Eq. (5.22) with Eq. (2.4):

$$[I + K]\tau_{HM} = M(\theta)\ddot{\theta} + C(\theta, \dot{\theta})\dot{\theta} + P(\theta) - \hat{P}(\theta) + \tau_{dist} \tag{5.24}$$

It follows:

$$\tau_{HM} = [I + K]^{-1}\left[M(\theta)\ddot{\theta} + C(\theta, \dot{\theta})\dot{\theta} + R(\theta) - \hat{R}(\theta) + \tau_{dist}\right] \tag{5.25}$$

where:

$$[I + K]^{-1} = \begin{bmatrix} \frac{1}{1+k_1} & 0 \\ 0 & \frac{1}{1+k_2} \end{bmatrix} \tag{5.26}$$

It is tempting to use Eq. (2.13) to find an expression for Ξ as function of K in

Eq. (5.25). However, in the considered case of Eq. (5.21), the Jacobian transpose $J^{\top}(\theta)$ is not of full column rank, and therefore the left inverse does not exist. Recalling from section 5.2.2, where it is stated that that forced displacements are in p_x and p_y directions, and rotation α_z is dependent. Thus relevant Ξ_x, Ξ_y are non–zero ($\Xi^* = [\Xi_x \;\; \Xi_y]^{\top}$), and torque ν_z is zero. Reduced dimension Jacobian can then be expressed:

$$J^*(\theta) = \begin{bmatrix} -l_1 \sin\theta_1 - l_2 \sin(\theta_1 + \theta_2) & -l_2 \sin(\theta_1 + \theta_2) \\ l_1 \cos(\theta_1) + l_2 \cos(\theta_1 + \theta_2) & l_2 \cos(\theta_1 + \theta_2) \end{bmatrix} \tag{5.27}$$

If the manipulator is not in a singular configuration, that is $\det\left(J^{*\top}(\theta)\right) \neq 0$, then $J^{*\top}(\theta)$ is invertible, and:

$$\Xi^* = J^{*-\top}(\theta) \cdot \tau_{HM} \tag{5.28}$$

$$\Xi^* = J^{*-\top}[I + K]^{-1}\left[M(\theta)\ddot{\theta} + C(\theta,\dot{\theta})\dot{\theta} + P(\theta) - \hat{P}(\theta) + \tau_{dist}\right] \tag{5.29}$$

Taking $k = k_1 = k_2$, from Eqs. (5.29) and (5.26) it can be seen that if design parameters $k_1 = k_2 = k \in (-\infty, -2) \cup (0, +\infty)$, effects of terms of inertial, centrifugal, Coriolis and of gravity cancellation modelling error on the values of components of human–machine interaction force vector Ξ^* are reduced by a factor of $k + 1$. Also, the operator feels the value of components of interaction force resulting from torque due to the disturbance reduced by the same factor. The disturbance torque is due to a load mass and inertia, external forces. Simulink subsystem implementing middle–level controller is shown in Fig. E.3. Values of human–machine interaction force for Direct Force Control law with gravity cancellation from the gait simulation are depicted in Figs. 5.12 and 5.12, in anteriorposterior and craniocaudal axis respectively. In Figs. 5.14 and 5.15 close–ups on $t \in [0.65, 1.1]$ s interval of corresponding plots are shown. It can be observed that there exist pairs of plots of Ξ^* components symmetric around t axis. Such pairing exists between one positive and one, and only one (and vice versa), negative value of gain k. The pairing relation is $k_{negative} = -(k_{positive} + 2)$. The most outlying pair is for $k = 0$ (no force–feedback) and $k = -2$. Instantaneous values of components of Ξ^* have the same magnitude, but opposing signs. This signifies that the transfer of energy between manipulator and operator is of negative quantity with respect to the other gain k of the duplet. Since by definition the cost function $W^{\dagger}$ (see Eq. (5.3)) is concerned with absolute instantaneous power and E_{Ξ} (see Eq. (5.1)) with components of Ξ^* to the power of 2, within each pair, the values of cost functions are nearly identical. This is reflected in Table 5.1. Moreover, the larger the absolute value of k, the smaller are values of cost functions, approaching 0. In Figs. 5.12, 5.13, 5.14,

Table 5.1: Cost functions $W^{\dagger}$ and E_{Ξ} (with $\lambda = 1$) values for different gains k. (a) – positive values of k, (b) – negative values of k.

(a)

k	$W^{\dagger}$ [J]	E_{Ξ}
0	441	3.241×10^5
1	221	8.422×10^4
10	40.3	2.803×10^3
65	6.7	7.796×10^1
130	3.4	1.979×10^1

(b)

k	$W^{\dagger}$ [J]	E_{Ξ}
–2	445.4	3.453×10^5
–3	222.1	8.562×10^4
–12	40.3	2.811×10^3
–67	6.7	7.8×10^1
–132	3.4	1.980

5.15 it seen that at a given time point, values of Ξ^* components for k in either positive or negative range lie on the same side of t axis and approach it with the increase of absolute value of k. The conclusion is that changing k, the instantaneous magnitude and direction of force burdening the operator can be adjusted.

In Figs. 5.16 and 5.17 boundaries of Ξ^* for varying k, plotted on the sagittal plane, calculated using Matlab `boundary` function [8] are depicted. For a certain k entire Ξ^* force trajectory is contained within its boundary. It is seen that within positive or negative range (considered separately), with each increase of the absolute value of k, the new boundary has smaller circumference, but retains shape and is contained within a boundary of previous, smaller absolute k value. Each boundary encircles point $\Xi^* = [0\ 0]^{\top}$. If previously mentioned pairs, given by relation $k_{negative} = -(k_{positive} + 2)$, are considered, it is seen that their respective boundaries are point reflections.

In Figs. 5.18 and 5.19 torques required at the first joint and the second joint respectively, for varying gain k, are depicted. Close-ups on the interval $t \in [0.65, 1.1]$ s are shown in Figs. 5.20 and 5.21. While increasing absolute value of k to $+\infty$, instantaneous values of required actuator torque approach some optimal theoretical value, for which, as discussed in above paragraph, boundaries approach to $\Xi^* = [0\ 0]^{\top}$, and cost functions $W^{\dagger}$ and E_{Ξ} approach 0. The manipulator moves on its own, without interference with the operator. It is important to notice that this theoretical, optimal value of instantaneous actuator torque is approached on a line perpendicular to t axis from 0 if k is increased in positive range $k \in [0, +\infty]$, and approached from outside (from top, $+\infty$, or from bottom, $-\infty$, of the graph) if in negative range $k \in [+\infty, -2]$. This implies that absolute value of components of τ_{act} for any k from positive range is always smaller than for any k from negative range. The advantage is that the exoskele-

[8] https://uk.mathworks.com/help/matlab/ref/boundary.html

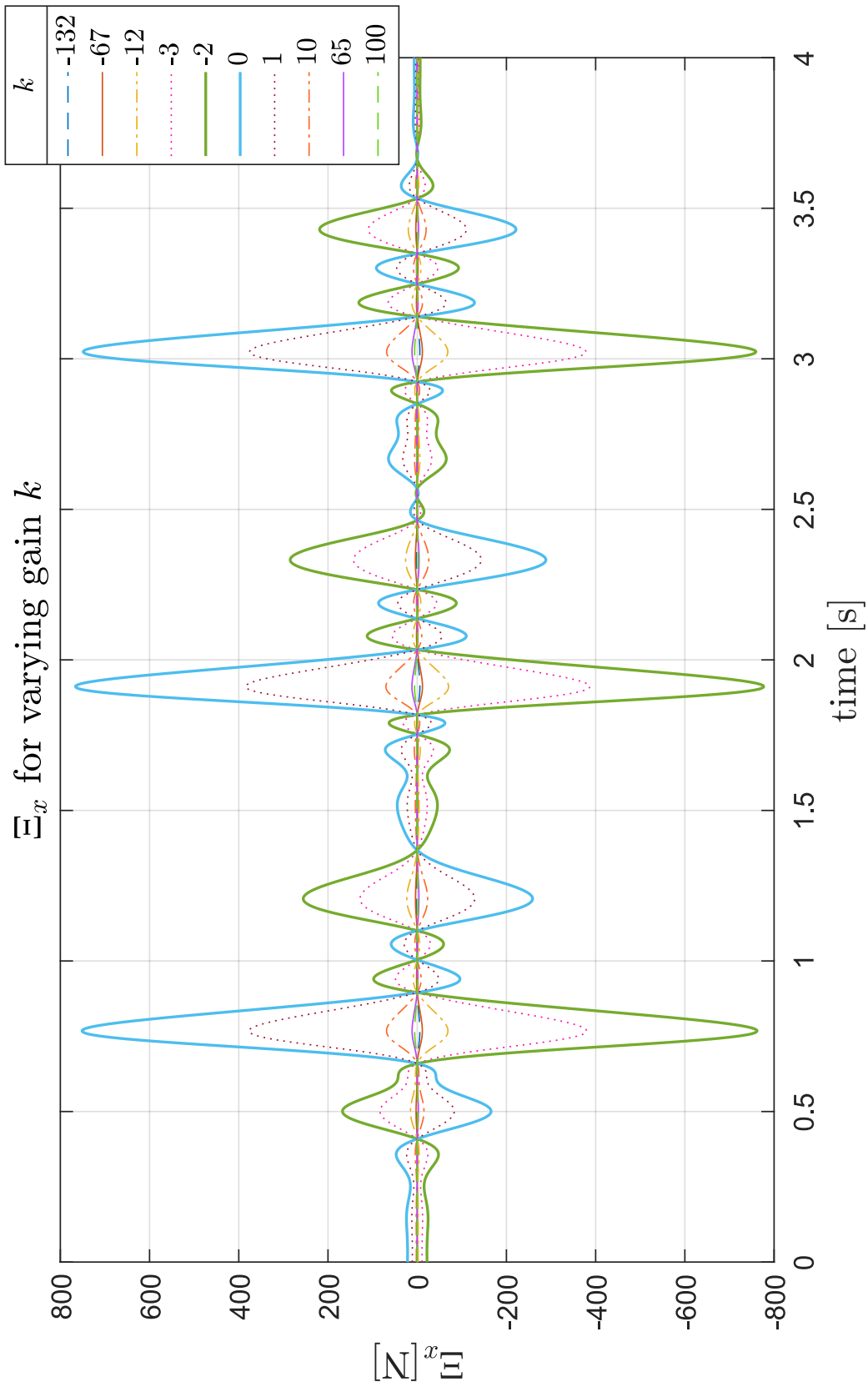

Figure 5.12: Human–machine interaction force in anteriorposterior axis for varying gain k. Direct Force Control law with gravity cancellation.

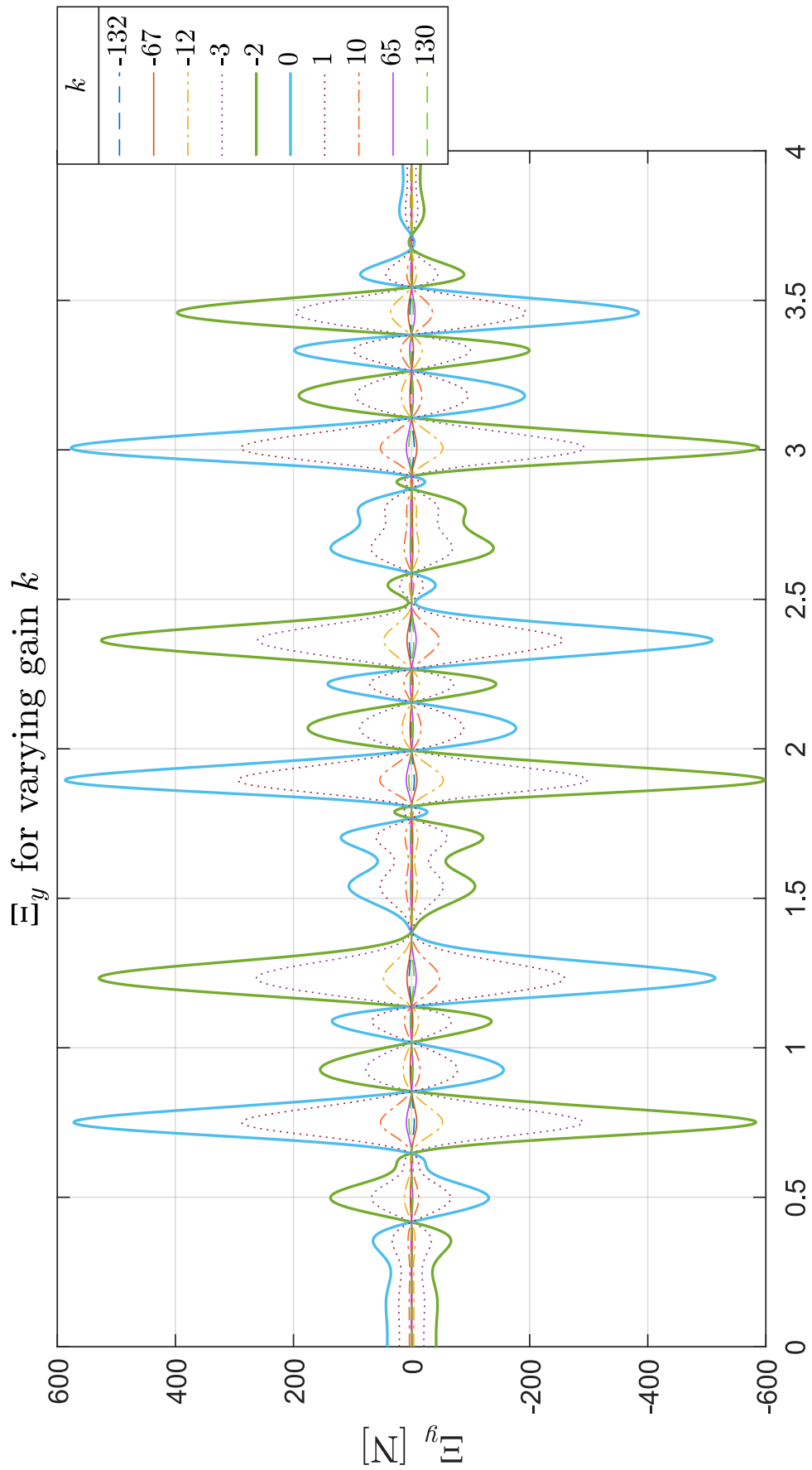

Figure 5.13: Human–machine interaction force in craniocaudal axis for varying gain k. Direct Force Control law with gravity cancellation.

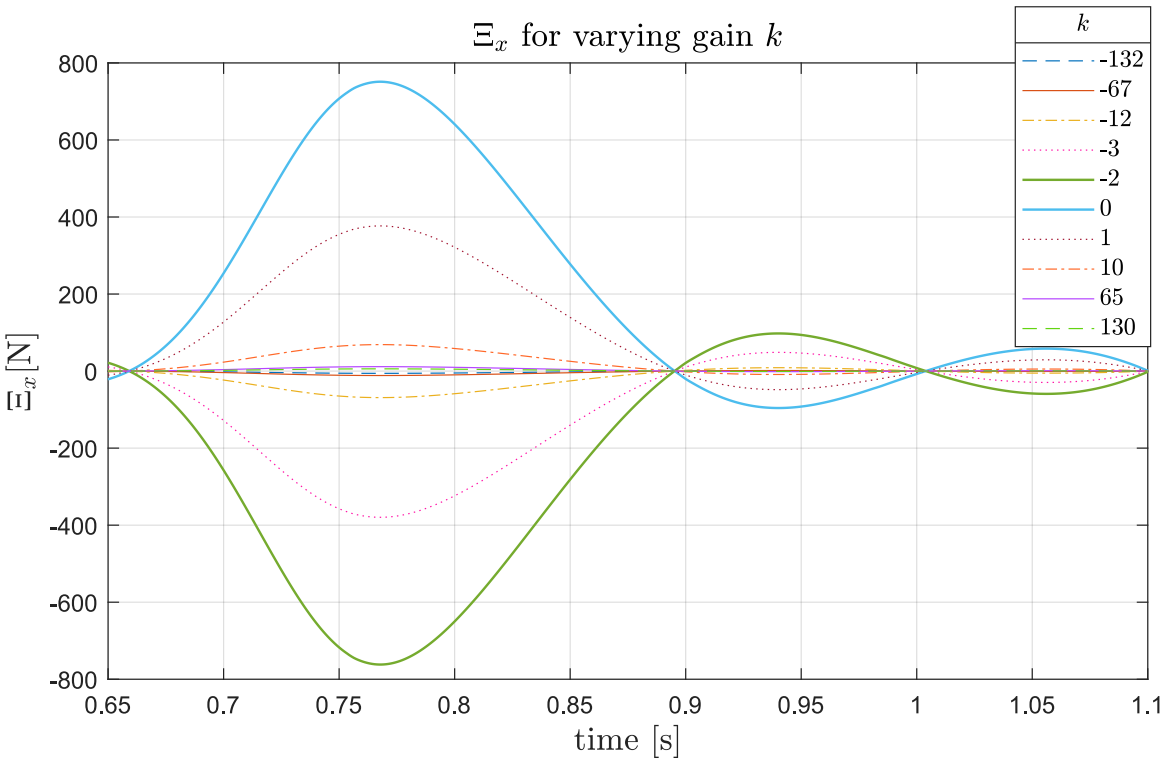

Figure 5.14: Human–machine interaction force in anterior-posterior axis for varying gain k. Direct Force Control law with gravity cancellation. Close–up on Fig. 5.12.

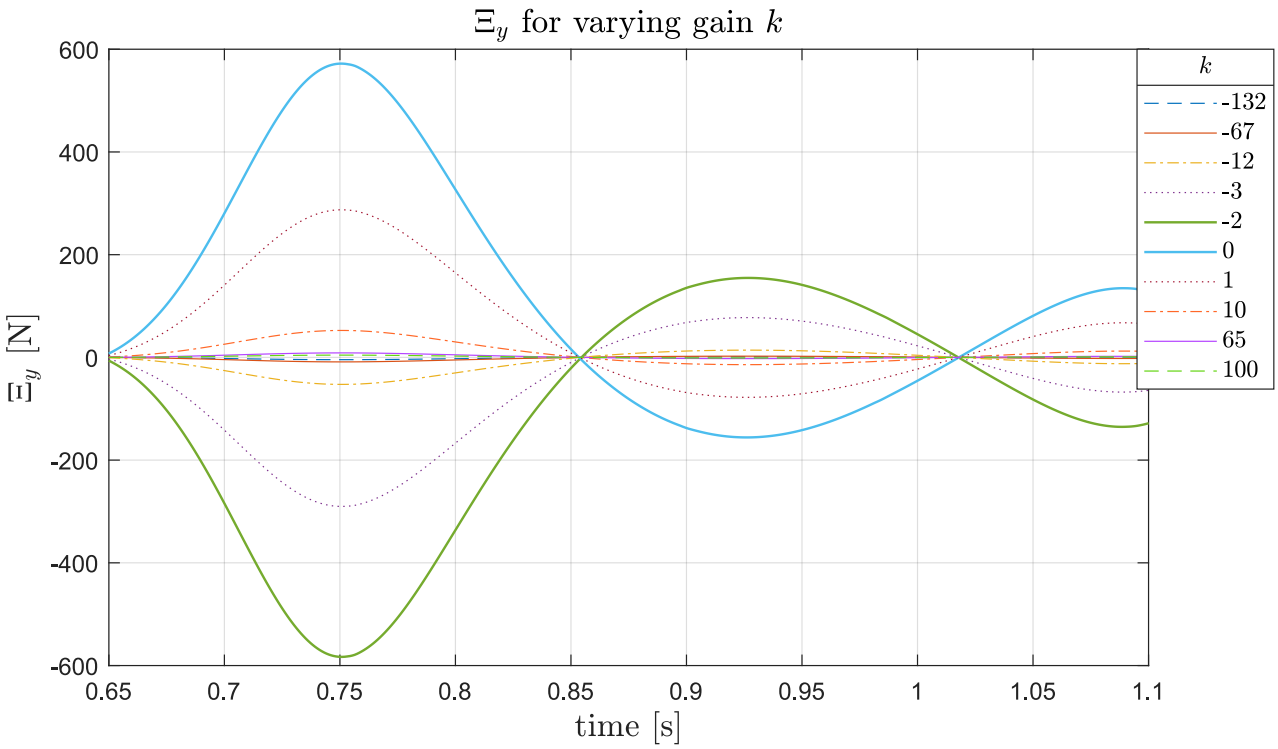

Figure 5.15: Boundaries for human–machine interaction force in sagittal plane for varying gain k. Direct Force Control law with gravity cancellation. Close–up on Fig. 5.13.

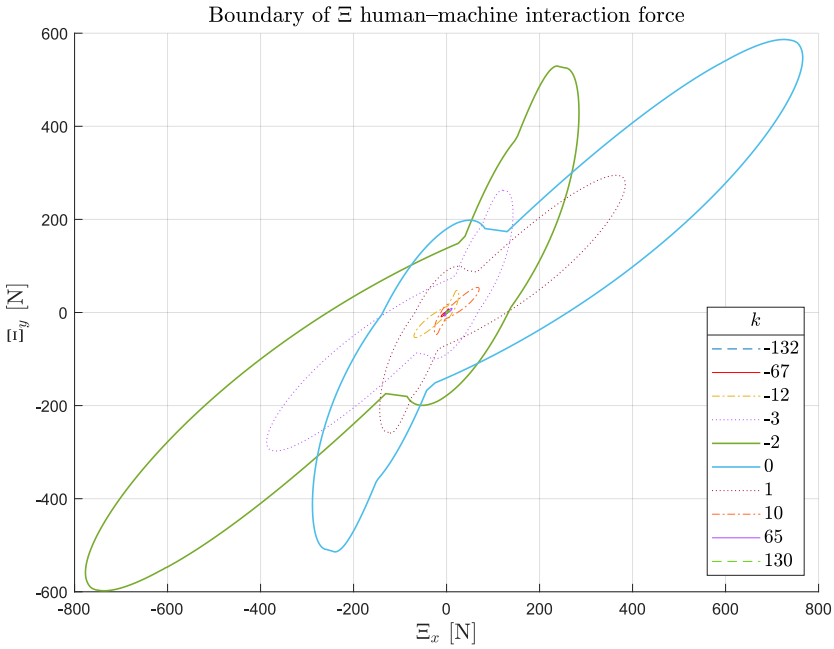

Figure 5.16: Boundaries of human–machine interaction force plots in sagittal plane for varying gain k. Direct Force Control law with gravity cancellation.

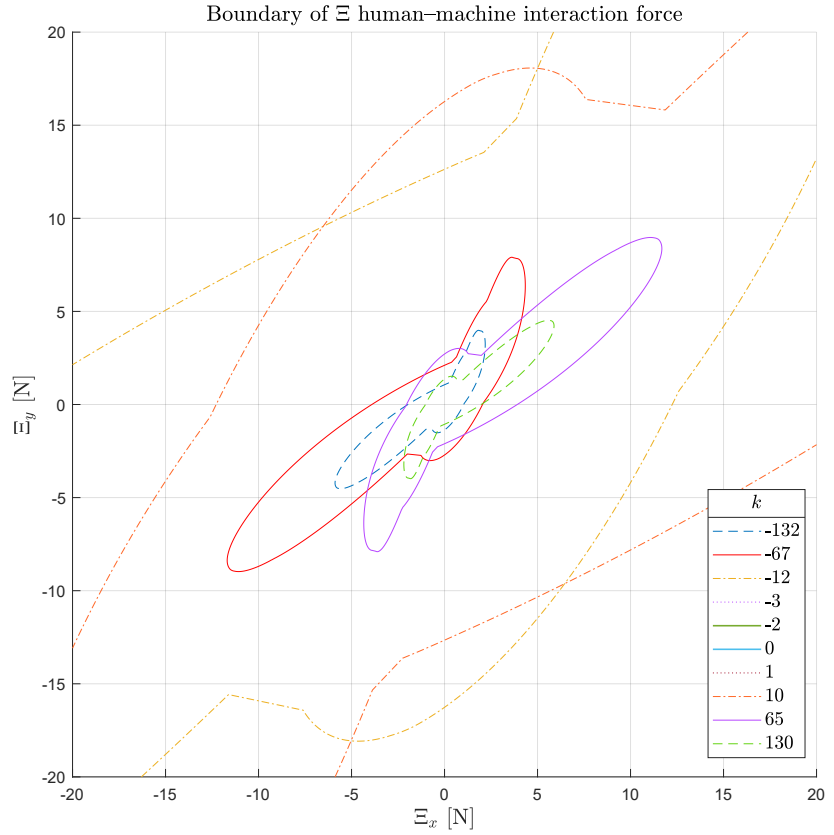

Figure 5.17: Boundaries of human–machine interaction force plots in sagittal plane for varying gain k. Direct Force Control law with gravity cancellation. Close–up on Fig. 5.16.

ton provides certain level of assistance to the user during motion. If the requirement is that the user must exert energy to move the exoskeleton, k has to be chosen from positive range.

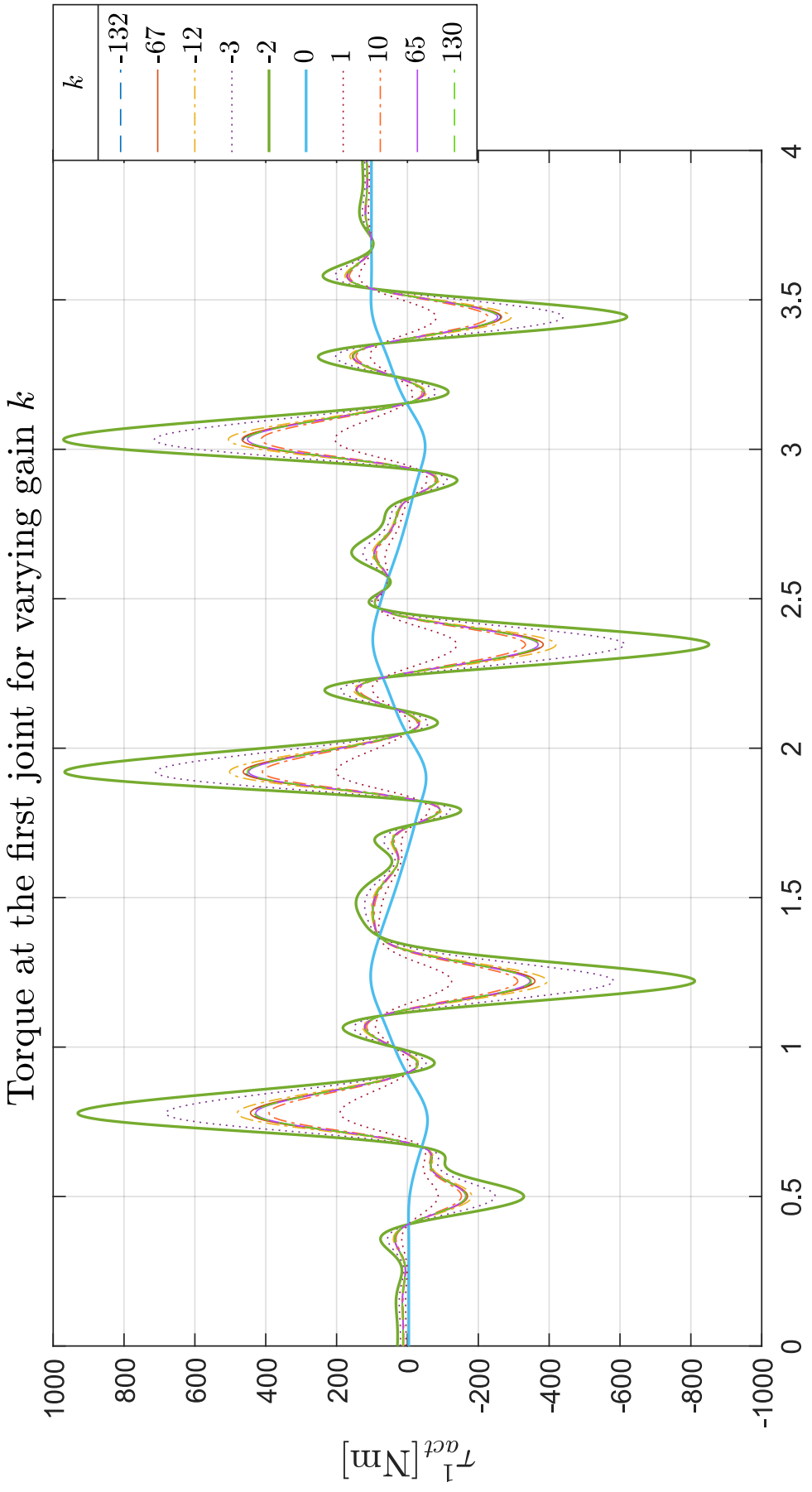

Figure 5.18: Actuator torque at the first joint (hip joint) for different gains k. Direct Force Control law with gravity cancellation.

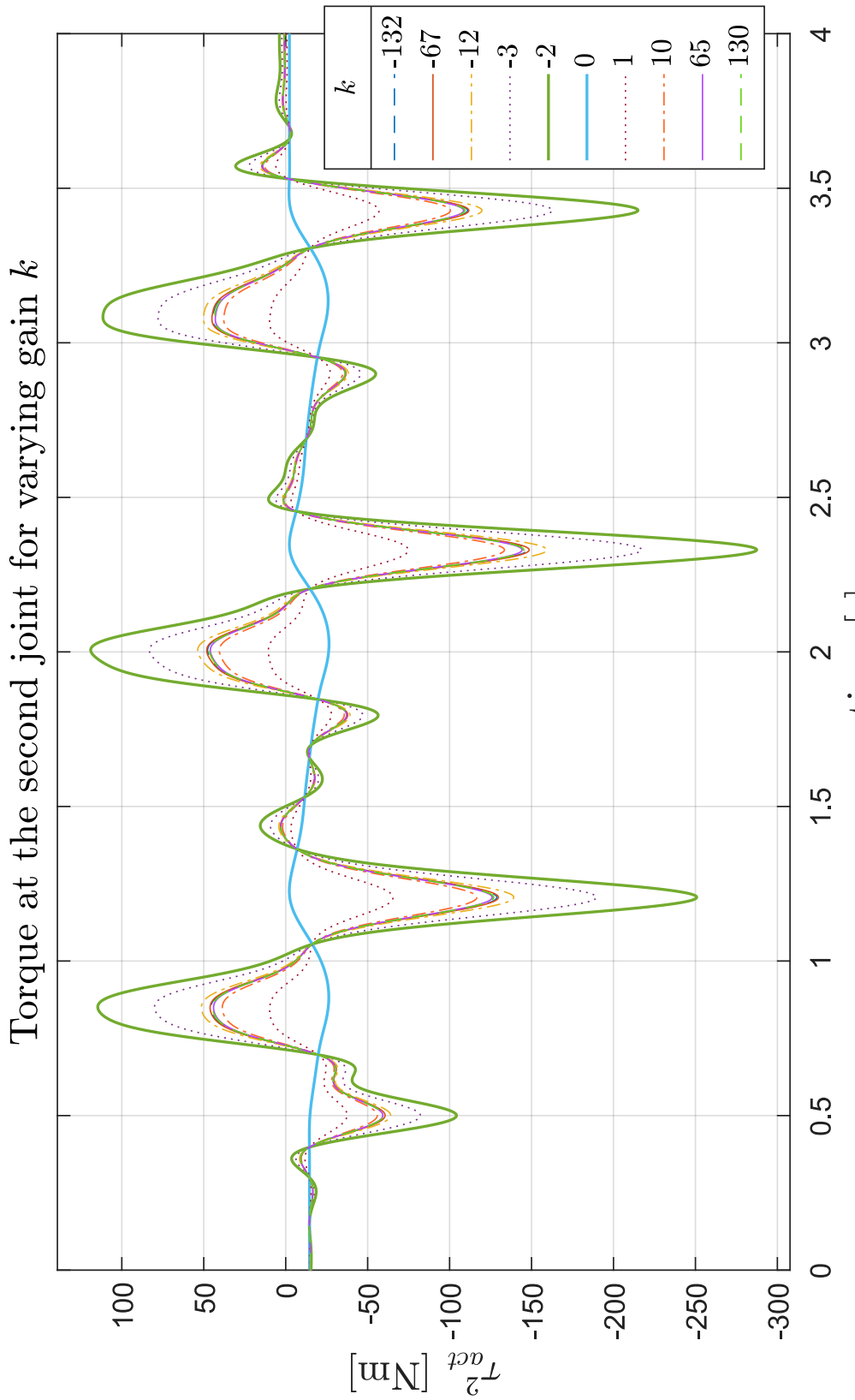

Figure 5.19: Actuator torque at the first joint (knee joint) for different gains k. Direct Force Control law with gravity cancellation.

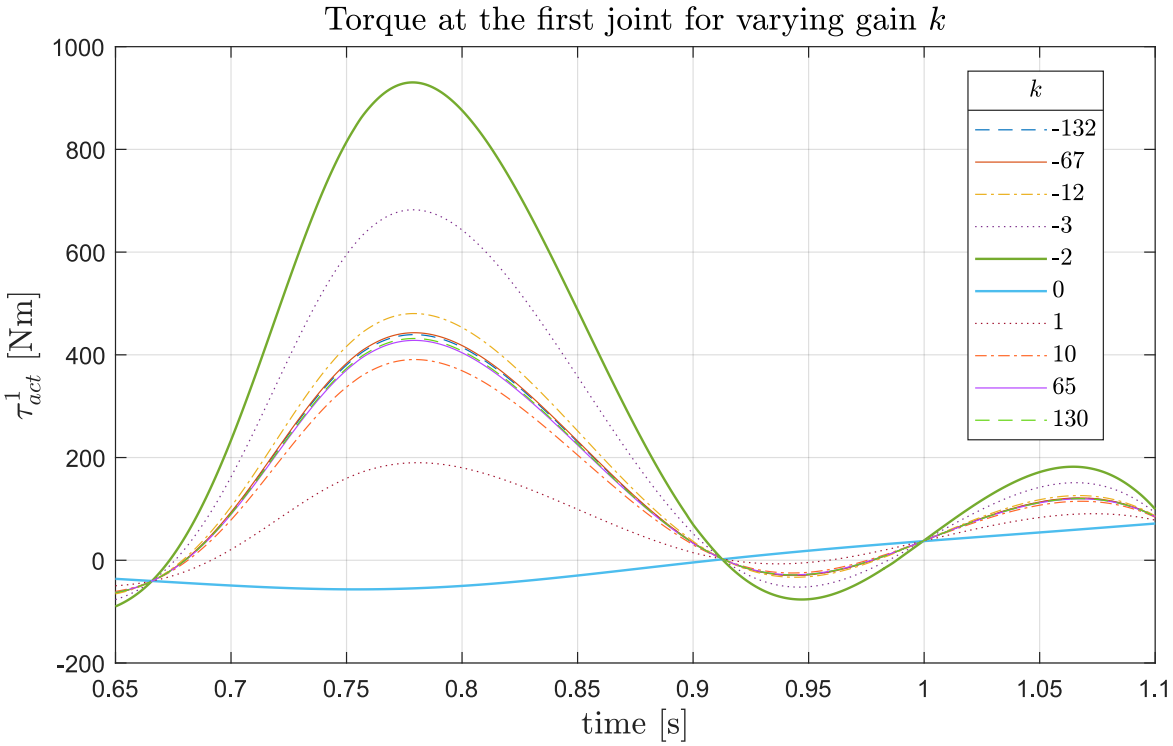

Figure 5.20: Actuator torque at the first joint (hip joint) for different gains k. Direct Force Control law with gravity cancellation. Close–up on Fig. 5.16.

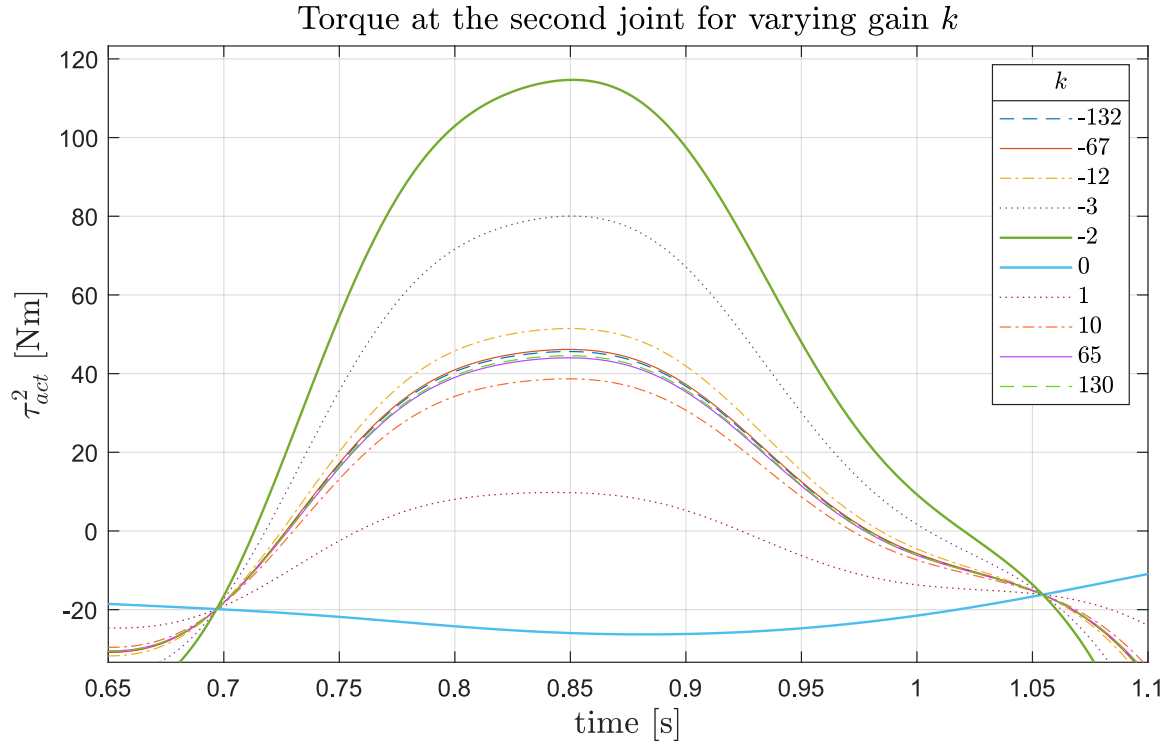

Figure 5.21: Actuator torque at the second joint (knee joint) for different gains k. Direct Force Control law with gravity cancellation. Close–up on Fig. 5.19.

5.2.4 Joint Torque to Linear Actuator Force

In the considered system, a problem of calculating required actuator force from prescribed torque $\tau_{act} = [\tau_1 \ \tau_2]^\top$ given by Eq. (5.22) arises. From principle of virtual work, assuming that two actuators are extend by the same displacement, equating work done by torque τ_2 around angular displacement $\Delta\varepsilon$ and actuator force F_{act}^{dem} along Δl actuator extension:

$$2\Delta\varepsilon \cdot \tau_2 = 2\Delta l \cdot F_{act}^{dem} \tag{5.30}$$

where $\varepsilon = \mu/2$, if actuators are extended the same length, is an undirected angle depicted in Fig. 5.22 (showing characteristic geometric properties of the joint), μ is given by Eq. (4.10):

$$\mu \approx |\theta\,' + \Delta\theta\,'| = |\theta_2 - \pi + \Delta\theta\,'| \tag{5.31}$$

where θ_2 is Denavit–Hartenberg configuration variable of second (knee) joint. Rearranging Eq. (5.30) to obtain expression for actuator force, and from the fact that operation in Eq. (5.31) inverts a directed negative angle (which is the case), hence the scalar product is negative:

$$F_{act}^{dem} = -\frac{\Delta\varepsilon}{\Delta l}\tau_2 = -\frac{\partial\varepsilon}{\partial l}\tau_2 \tag{5.32}$$

The problem of calculating $\partial l/\partial\varepsilon$ arises. Using law of cosines:

$$l = \sqrt{a^2 + b^2 - 2ab\cos\left(\frac{\alpha}{2} - \varepsilon\right)} \tag{5.33}$$

Therefore:

$$\frac{\partial l}{\partial\varepsilon} = -\frac{ab\sin\left(\frac{\alpha}{2} - \varepsilon\right)}{\sqrt{a^2 + b^2 - 2ab\cos\left(\frac{\alpha}{2} - \varepsilon\right)}} \tag{5.34}$$

In Fig. 5.23 exemplary values of Eq. (5.34) during gait for angular displacement of θ_2 shown in Fig. 5.6 are depicted. μ is calculated using Eq. (5.31) with $\Delta\theta' = 0$. Value of $\partial l/\partial\varepsilon$ is positive. In Fig. 5.24 extension of the rods of hydraulic actuators are depicted. They are forced to extend the same distance. It is seen that for the considered input being displacement of θ_2 (see Fig. 5.6), the extension of each rod does not violate constrains and is within margins of 0 and 0.1 m. In Fig. 5.25 results for the lower rod extension is depicted. With correction term $\Delta\theta'$ equated to 0 the estimation error is constant, about 25 mm. If $\Delta\theta' = \frac{9}{360}\pi$ rad, the estimation error is reduced to less than 1 mm.

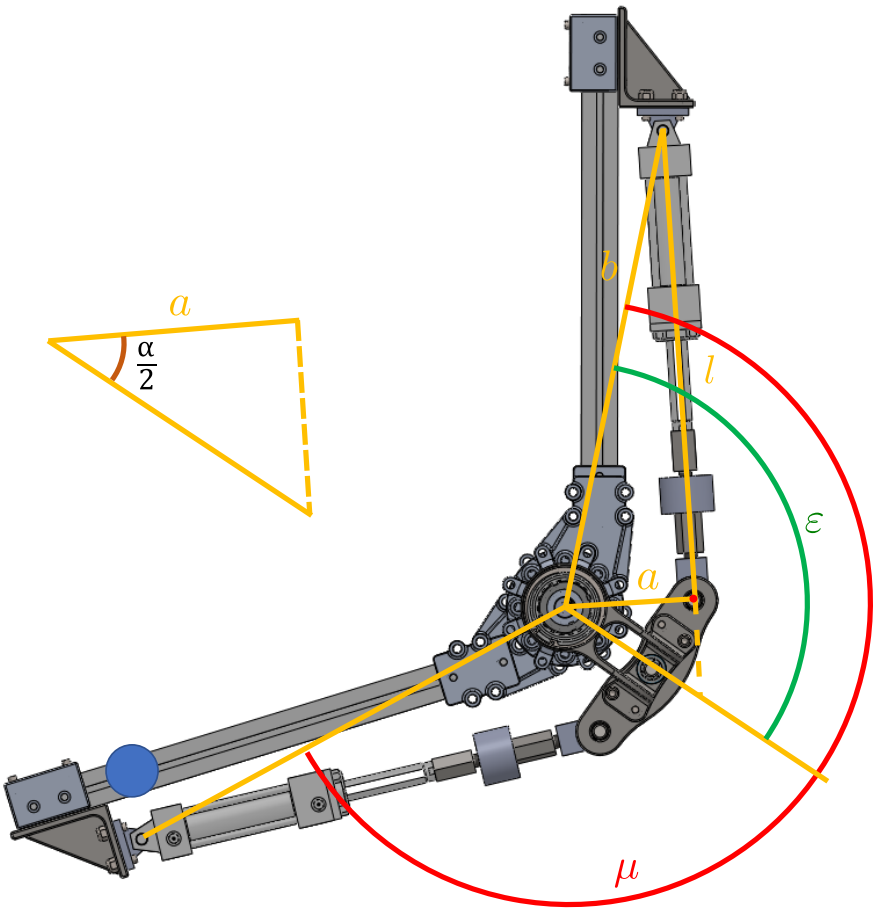

Figure 5.22: Single joint – torque to force calculation. $\alpha = 77.32°$, ε, μ – angles, geometric properties describing state of the machine; a, l – lengths describing the machine.

5.2.5 Knee Cap Positioning

While sections 5.2.2 and 5.2.3 concern with primary objective of the controller, that is minimisation of instantaneous absolute human–machine interaction force, there is a secondary objective of maintaining rods extension within physical limits:

$$0 \leq r_{up} \leq r_{max} \tag{5.35}$$

$$0 \leq r_{low} \leq r_{max} \tag{5.36}$$

where r_{up}, r_{low} are extension of the upper and lower rod respectively (see 4.5.2). $r_{max} = 0.1$ m is maximum extension of the rod. Constraints given by Eqs. (5.35) and (5.36) are of non–linear nature. The constraints can be met by imposing an equivalent control goal,

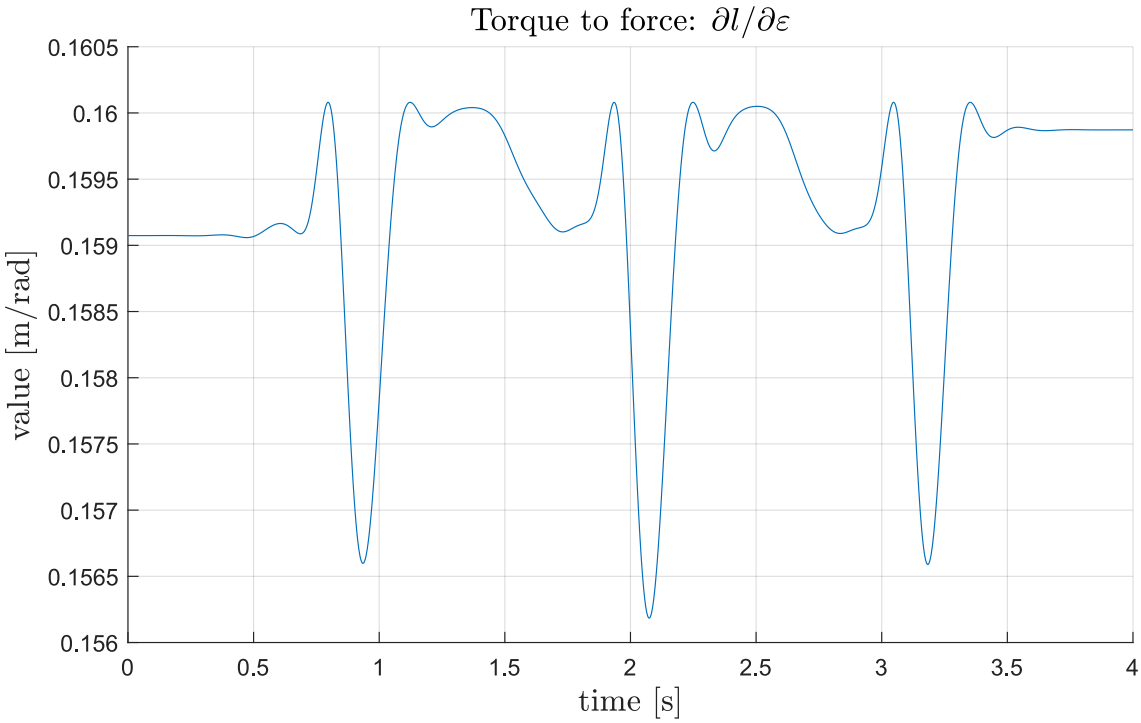

Figure 5.23: Value of $\partial l/\partial \varepsilon$ (Eq. (5.34)) for θ_2 joint displacement depicted in Fig. 5.6

which is synchronisation of extension of rods. The proposed cost function is of form:

$$E_r(\tilde{F}^{dem}_{act\ up}, \tilde{F}^{dem}_{act\ low}) = \int_{t_{start}}^{t_{end}} [r_{up}(t) - r_{low}(t)]^2 \, \mathrm{d}t, \quad \forall t_{start}, t_{end} \in \mathbb{R} : t_{start} < t_{end} \tag{5.37}$$

where $F^{dem}_{act\ up}$ and $\tilde{F}^{dem}_{act\ low}$ are force exerted by the upper and lower cylinder respectively. Simulink implementation of E_r is shown in Fig. E.31. The minimisation procedure can be expressed as:

$$\underset{[\tilde{F}^{dem}_{act\ up}, \tilde{F}^{dem}_{act\ low}] \in S_r}{\text{minimise}} \quad E_r(\tilde{F}^{dem}_{act\ up}, \tilde{F}^{dem}_{act\ low}) \tag{5.38}$$

where S_r is a set of allowed values of the control signal. In case of ideal actuators $S_r = \mathbb{R}^2$. The problem can than be treated as a problem of r_{low} tracking the signal r_{up}. In time domain properties such as response time, overshoot, settling time become important.

In the first approach the actuators are assumed to be ideal, capable of exerting prescribed magnitude of force instantaneously. Their dynamics are neglected. For such system a control scheme depicted in Fig. 5.26 is proposed. It is meant to fulfil the primary control goal of human–machine force minimisation given by Eq. (5.2) and the

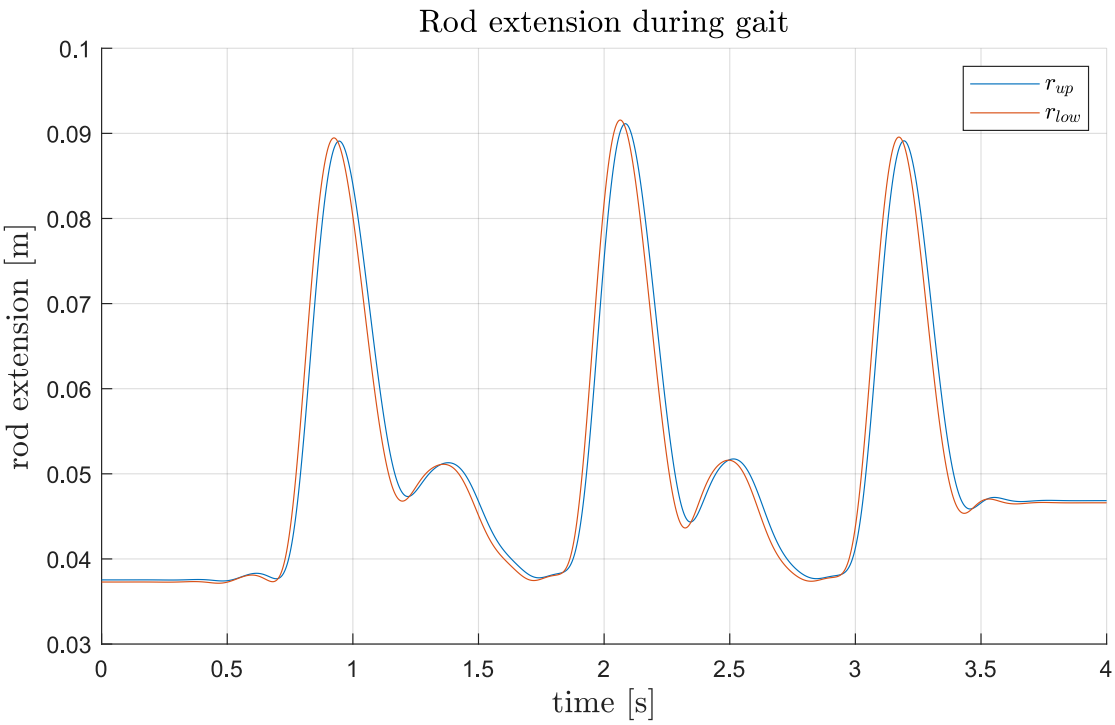

Figure 5.24: Equidistant rods extension for θ_2 joint displacement depicted in Fig. 5.6, blue – upper. Red – lower.

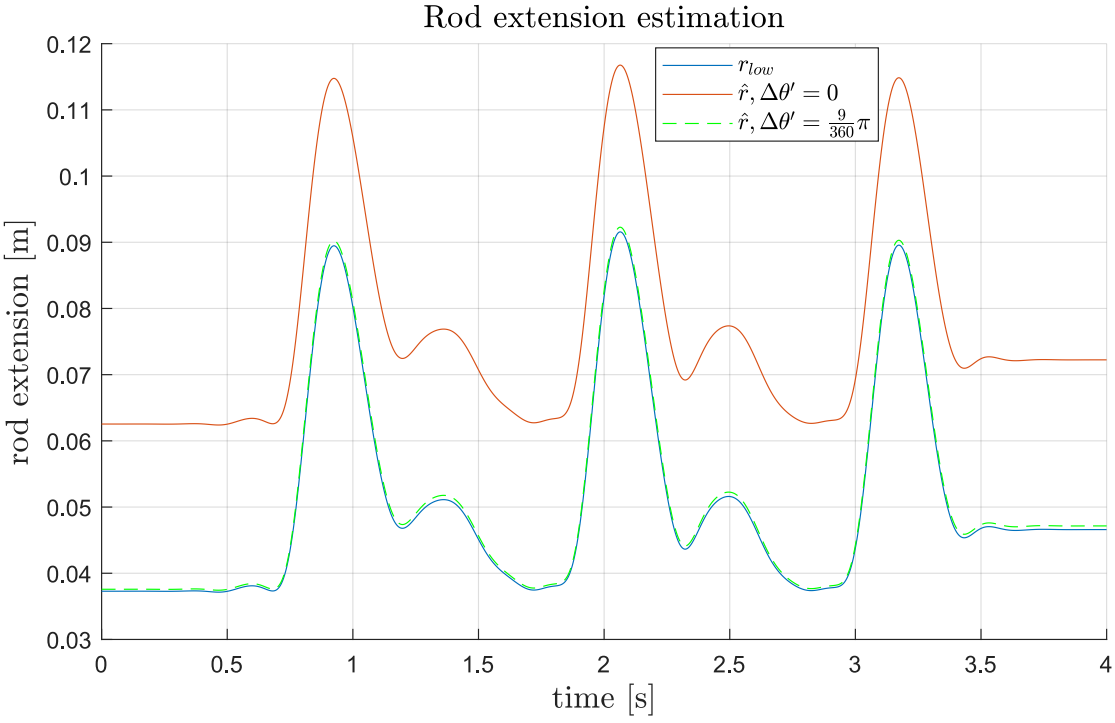

Figure 5.25: Lower rod extension estimation using Eq. (5.31). Blue – actual value, red – estimated value with $\Delta\theta' = 0$, yellow – estimated value with $\Delta\theta' = \frac{9}{360}\pi$ rad.

secondary control goal of knee cap positioning given by Eq. (5.38). Gravity cancellation, as described in section 5.2.2, and Direct Force Feedback, as described in Subection 5.2.3, are used. In the control scheme, the force exerted by the upper actuator is prescribed as:

$$\tilde{F}^{dem}_{act\ up}(s) = H_{act}(s) \cdot F^{dem}_{act}(s) \tag{5.39}$$

where F^{dem}_{act} is given by Eq. (5.32). $\tilde{F}^{dem}_{act\ up}$ is filtered with a first–order (single–pole) low–pass filter of transfer function:

$$H_{act}(s) = \frac{1}{T_{act}s + 1} \tag{5.40}$$

where $T_{act} \in \mathbb{R}_{>0}$ is filter time constant, design parameter, which corresponds to a cutoff frequency of f_{act}. The filtering is introduced because F^{dem}_{act} depends on force measurement of Ξ, which is burdened by noise. Filtering is also intended to improve stability in presence of high gains of K. The force exerted by the lower actuator is composed of two terms, one intended to minimise the interaction force and one dependent on positioning of the actuators, to give the knee cap extra push if misaligned. It is of form:

$$\tilde{F}^{dem}_{act\ low}(s) = \tilde{F}^{dem}_{act}(s) + \tilde{F}_{kc}(s) \tag{5.41}$$

$$\tilde{F}_{kc}(s) = H_{kc}(s) \cdot \mathrm{SR}\left[G_{kp}(s) \cdot r_{err}(s)\right] \tag{5.42}$$

where r_{err} is knee cap positioning error:

$$r_{err} = r_{up} - r_{low} \tag{5.43}$$

Filter transfer function is of form:

$$H_{kc}(s) = \frac{1}{T_{kc}s + 1} \tag{5.44}$$

where $T_{kn} \in \mathbb{R}_{>0}$ is a filter time constant, design parameter, which corresponds to a cutoff frequency of f_{kc}. The filtering is again introduced to alleviate measurement noise of rods extension by LVDT. $\mathrm{SR}(\cdot)$ is a slew rate limiter[9], a non–linear operator which imposes constraint on output signal in time domain:

$$\left|\frac{\mathrm{d}\tilde{F}_{kc}}{\mathrm{d}t}\right| \leq c_{sr} \tag{5.45}$$

[9] `https://uk.mathworks.com/help/simulink/slref/ratelimiter.html`

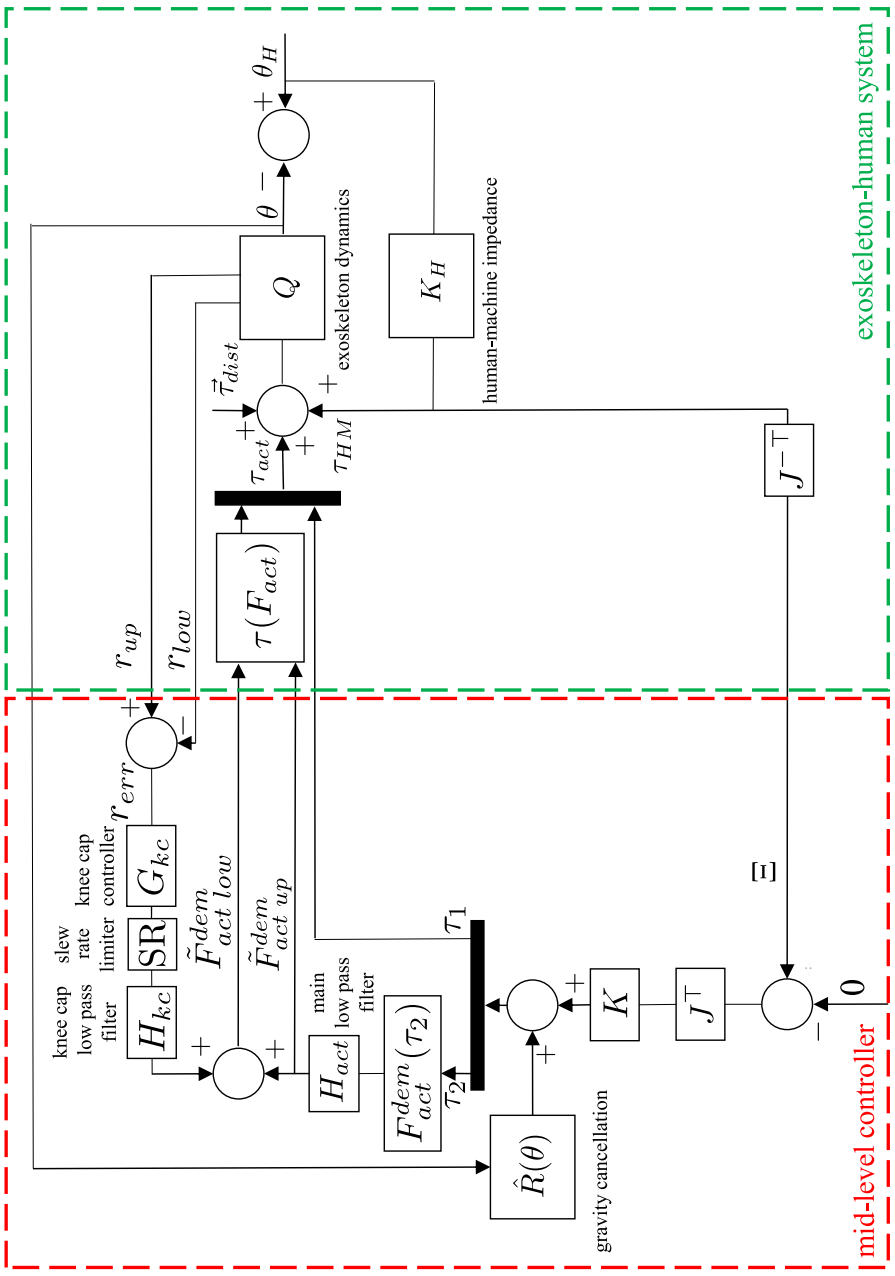

Figure 5.26: A block diagram of proposed Direct Control Law for the joint prototype with knee cap positioning.

where $c_{sr} \in \mathbb{R}_{>0}$ is a design parameter. It is intended to limit the rate of change of aligning force $\tilde{F}_{kc}$, with a goal of reducing Ξ when rods are misaligned, and the synchronising controller takes action. Details of Simulink subsystem implementation are shown in Fig. E.29. Transfer function of a PID controller block in Simulink[10] is of form:

$$G_{kc}(s) = k_p + k_i \frac{1}{s} + k_d \frac{N_{filt}}{1 + N_{filt}\frac{1}{s}} \tag{5.46}$$

where k_p – proportional gain, k_i – integral gain. Transfer function of derivative term requires clarification. It can be represented as:

$$k_d \frac{N_{filt}}{1 + N_{filt}\frac{1}{s}} = (k_d s) \cdot \left(\frac{1}{\frac{1}{N_{filt}} s + 1} \right) \tag{5.47}$$

which is analogous to derivation with derivative gain k_d of first–order filtered signal with time constant of $\frac{1}{N_{filt}}$. This is done to prevent unwanted high frequency noise from exciting the controller. Matlab proprietary algorithm was used to find gains of the controller[11]. The PID tuner operates on the model of the system. The algorithm linearises the plant at operating point given by initial settings. It allows for choosing control focus: reference tracking (performance), disturbance rejection (robustness), and a balance between both. It has an option of adjusting response time, transient response in the time domain and bandwidth and phase margin in the frequency domain. In Fig. 5.27 value of $r_{err}(t) = r_{up}(t) - r_{low}(t)$ are shown for gains given in Table 5.2, with controller linearised for initial conditions $r_{up} = 0.0726$ m, $r_{low} = 0.0045$ m, and balanced control goal. The end effector is held still at $p = [-0.2344, -1.1694]^\top$ m for the duration of the simulation. Parameters are: $c_{sr} = +\infty$, $k = 65$, $H_{kc}(s) = 1$, $f_{act} = 1.5$ Hz. For the controller in forms of P controller and PI controller the tuning algorithm was unable to find initial stabilising controller. In fact, for set 1 (P controller) and set 2 (PI controller) it can be observed that the system is not stable and oscillates in time with increasing amplitude. For set 3 and set 4 (PD controller), the system is stable, but steady–state error is observed. The steady–state error is decreased with increased gains of the controller. It is expected that adding integrating term to the controller causes steady–state error to reduce to 0. From Fig. 5.28 it is seen that this

[10] https://uk.mathworks.com/help/simulink/slref/pidcontroller.html

[11] https://uk.mathworks.com/help/slcontrol/ug/introduction-to-automatic-pid-tuning.html

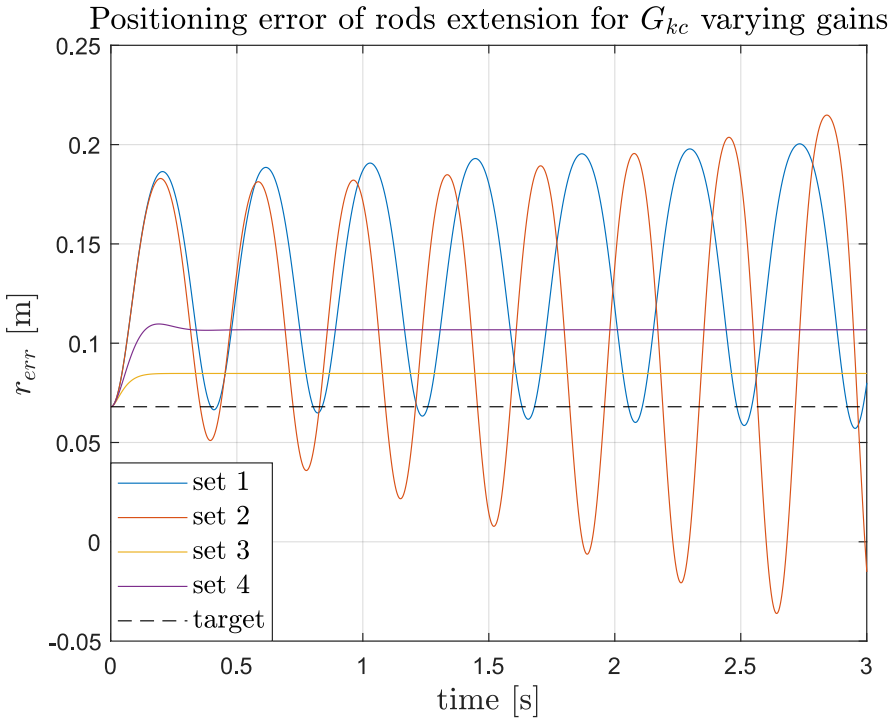

Figure 5.27: Positioning error of rods extension for different gains of controller given by Eq. (5.46). Settings are given in Table 5.2. Initial conditions $r_{up} = 0.0726$ m, $r_{low} = 0.0045$ m. Parameters: $c_{sr} = +\infty$, $k = 65$, $H_{kc}(s) = 1$, $f_{act} = 1.5$ Hz

happens indeed. Settings for the controller are given in Table 5.3. Parameters c_{sr}, k, $H_{kc}(s)$, f_{act} are set as before. Solution for $t_{res} = 0.6$ s violates constraints given by Inequalities (5.35) and (5.36). With decrease t_{res}, the value of t_s settling time is decreased, that is time to $|r_{err}| < 0.001$ m. $t_{res} = 0.04$ s, $t_{res} = 0.02$ s (slower) and $t_{res} = 0.01$ s (faster) yield allowable solutions.

To show performance of the proposed controller, it was simulated with two chosen PID settings, for $t_{res} = 0.02$ s and $t_{res} = 0.01$ s. Simulation was divided into stages:

stage 1 – $t \in [0, 5)$ s, the objective of the controller is to maintain initial conditions: $r_{up} = 0.0726$ m, $r_{low} = 0.0045$ m. The end effector is held still at $p =$

Table 5.2: Different PID controller gains in Fig. 5.27.

	k_p	k_i	k_d	N_{filt}
set 1	3977	0	0	–
set 2	3979	1393	0	–
set 3	1.183×10^4	0	645	1467
set 4	5411	0	291	3809

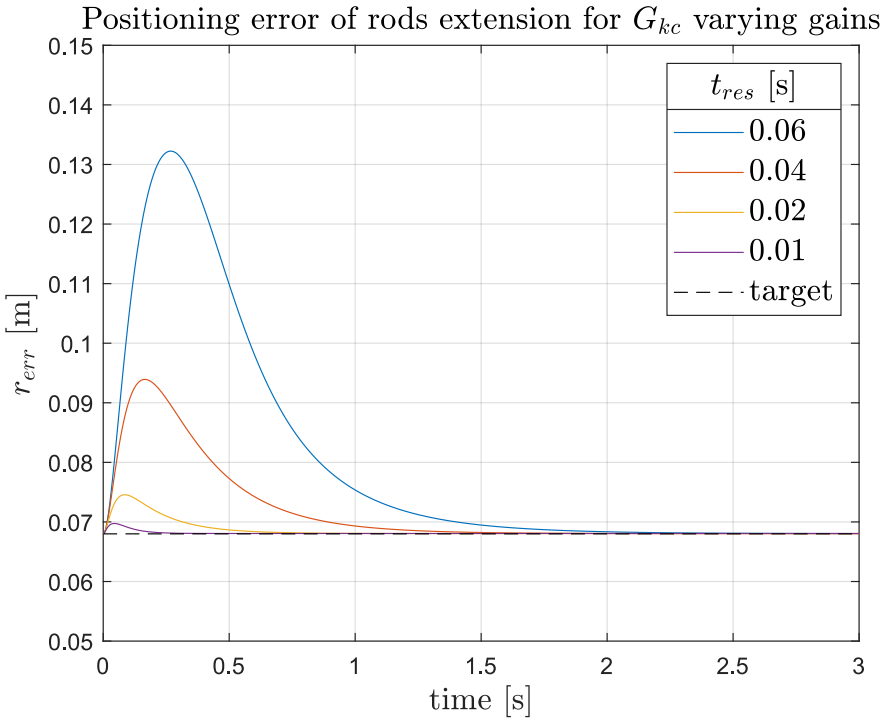

Figure 5.28: Positioning error of rods extension for different gains of controller given by Eq. (5.46). Settings are given in Table 5.3. Initial conditions $r_{up} = 0.0726$ m, $r_{low} = 0.0045$ m. Parameters: $c_{sr} = +\infty$, $k = 65$, $H_{kc}(s) = 1$, $f_{act} = 1.5$ Hz

$[-0.2344, -1.1694]^\top$ m for the duration of this stage.

stage 2 – $t \in [5, 10)$ s, the objective of the controller is to synchronise extension of the rods, $r_{up} = r_{low}$: minimise cost function given by Eq. (5.38), while looking at the cost function given by Eq. (5.2). The end effector is held still at $p = [-0.2344, -1.1694]^\top$ m for the duration of this stage.

stage 3 – $t \in [10, 14)$ s, the objective is to synchronise rods extension (Eq. (5.38)), while minimising the interaction force (Eq. (5.2)) during gait.

In Fig. 5.30 r_{err} error of rod extension positioning during stage 1 for $t_{res} = 0.2$ s is depicted. During this phase, the controller integrator and filter for differentiating have to move from initial 0 condition to steady state condition. The same applies to the filters. Settings of k, f_{act} do not affect the trajectory. Decreasing f_{kc} may lead to slow action due to the phase shift, resulting in instability. So might decrease of c_{sr}. The fact that system with ideal actuators not being stable in initial condition, without control applied is a major discrepancy between the idealised system and system with hydraulic actuators. In case of hydraulic actuators, if 0 control signal is applied, the actuator spool moves to the middle position (see Fig. 4.3), blocking flow through port A and

Table 5.3: Different PID controller gains in Fig. 5.28 in stage 1. t_{res} – response time. t_s – settling time, time to $|r_{err} - r_{target}| < 0.001$ m.

t_{res} [s]	k_p	k_i	k_d	N_{filt}	t_s [s]
0.06	2895	5484	321	350	1.63
0.04	6461	1.767×10^4	486	524.5	1.07
0.02	24820	1.194×10^5	981.2	1049	0.43
0.01	91880	1.017×10^6	2003	2098	0.1

port B (see Fig. 4.6). The system is therefore stable, allowing only for small movement due to compressability of fluid in chambers and in the dead volume (including piping). In Fig. 5.31 computed forces at the actuators yielding the solutions shown in Fig. 5.30 are depicted. It is observed that force for the lower actuator is higher than for the lower.

In Fig. 5.29 the performance of the controller in all 3 stages is shown. The values of cost functions E_Ξ, E_r, t_s (settling time) were calculated for stage 2. They are shown in Table 5.4. Due to no displacement, $W^\dagger$ is 0 in all cases. It is seen that for $c_{sr} = +\infty$ the values of E_Ξ are very high. This is due to the fact that at time $t = 5$ a change of the desired value of r_{err} occurs, the plant is subject to step input. At that even, the magnitude of force Ξ is very large, producing two picks – in positive and negative direction. To prevent this undesirable performance, a rate limiter given by Eq. (5.45) was added to the system. A trade off exists, if $c_{sr} = 4 \times 10^4$, E_Ξ is reduced, but E_r increases slightly, so does t_s settling time for $t_{res} = 0.02$ s. However, the change of E_r and settling time is in feasible range. Setting c_{sr} too low might lead to instability and increasing oscillations of the knee cap. That is the case for $c_{sr} = 4\times10^4$ and $t_{res} = 0.1$ s.. For $c_{sr} = 4\times10^4$, the value of E_Ξ decreases with increased k. $t_{res} = 0.2s$, t_s is 0.43 s. In Fig. 5.32, for $c_{sr} = 4\times10^4$ and $t_{res} = 0.2$ s, r_{err} error of rod extension positioning during stage 2 is depicted. In Fig. 5.33 actuator forces producing the solution are depicted ($k = 65$). Values of human–machine interaction force for $c_{sr} = 4 \times 10^4$, $k = 65$ are depicted in Figs. 5.34 and 5.35, in anteriorposterior and craniocaudal axes respectively. In Fig. 5.36 the human–machine interaction force in sagittal plane for $t_{res} = 0.02$ s, $c_{sr} = 4 \times 10^4$, $k = 65$, is depicted. Maximum absolute force is 68 N.

In Table 5.5 values of cost functions for stage 3 are shown. It is seen that E_Ξ does not change for decreased c_{sr}. $W^\dagger$ does not change significantly. Faster controller (t_{res}

Table 5.4: Cost functions E_Ξ (with $\lambda = 1$), E_r values for different gains k and controller settings in Eq. (5.46) for stage 2. $W^\dagger = 0$. US – unstable, increasing oscillations of the knee cap.

c_{sr} (see Eq. (5.45))	k (see Eq. (5.26))	t_{res} [s]	E_Ξ	E_r	t_s [s]
$+\infty$	10	0.02	4.8×10^5	2.5×10^{-5}	0.36
		0.01	6.38×10^5	2.64×10^{-5}	0.22
	65	0.02	3.46×10^5	2.3×10^{-5}	0.34
		0.01	4.66×10^5	2.49×10^{-5}	0.21
	130	0.02	1.91×10^5	2.29×10^{-5}	0.33
		0.01	2.57×10^5	2.36×10^{-5}	0.21
4×10^4	10	0.02	5.77×10^3	1.27×10^{-4}	0.54
		0.01	–	–	US
	65	0.02	4.11×10^2	1.25×10^{-4}	0.54
		0.01	–	—	US
	130	0.02	1.13×10^2	1.24×10^{-4}	0.54
		0.01	–	–	US

= 0.01 s) compared to the slower (t_{res} = 0.02 s) does not change E_Ξ, but decreases E_r. Increase in k decreases E_Ξ, does not affect E_r. The values in Table 5.5 can be compared to Table 5.1 were values of the same cost functions were calculated for a controller following gait without knee cap positioning. It is seen that for the same value of k knee cap positioning scheme increases slightly E_Ξ. This can be compensated by increase of k itself. In Fig. 5.37 r_{err} is depicted for $t_{res} = 0.2$ s, $c_{sr} = 4 \times 10^4$, $k = 65$.. It is seen that $|r_{err}|$ does not exceed 4 mm. In Fig. 5.38 actuator forces yielding the solution are shown. Values of human–machine interaction force for $c_{sr} = 4 \times 10^4$, $k = 65$ are depicted in Figs. 5.39 and 5.40, in anteriorposterior and craniocaudal axes respectively. In Fig. 5.41 the human–machine interaction force in sagittal plane , for $c_{sr} = 4 \times 10^4$, $k = 65$, is depicted. Maximum absolute force does not exceed 22 N.

Table 5.5: Cost functions E_Ξ (with $\lambda = 1$), $W^\dagger$, E_r values for different gains k and controller settings in Eq. (5.46) for stage 3. US – unstable, increasing oscillations of the knee cap.

c_{sr} (see Eq. (5.45))	k (see Eq. (5.26))	t_{res} [s]	E_Ξ	$W^\dagger$ [J]	E_r
$+\infty$	10	0.02	3.91×10^3	4.18×10^1	7.85×10^{-6}
		0.01	3.93×10^3	4.17×10^1	4.31×10^{-7}
	65	0.02	1.3×10^2	7.28	7.84×10^{-6}
		0.01	1.32×10^2	7.25	4.31×10^{-7}
	130	0.02	3.37×10^1	3.69	7.84×10^{-6}
		0.01	3.38×10^1	3.66	4.32×10^{-7}
4×10^4	10	0.02	3.92×10^3	4.18×10^1	7.85×10^{-6}
		0.01	–	–	US
	65	0.02	1.3×10^2	7.3	7.84×10^{-6}
		0.01	–	–	US
	130	0.02	3.36×10^1	3.69	7.84×10^{-6}
		0.01	–	–	US

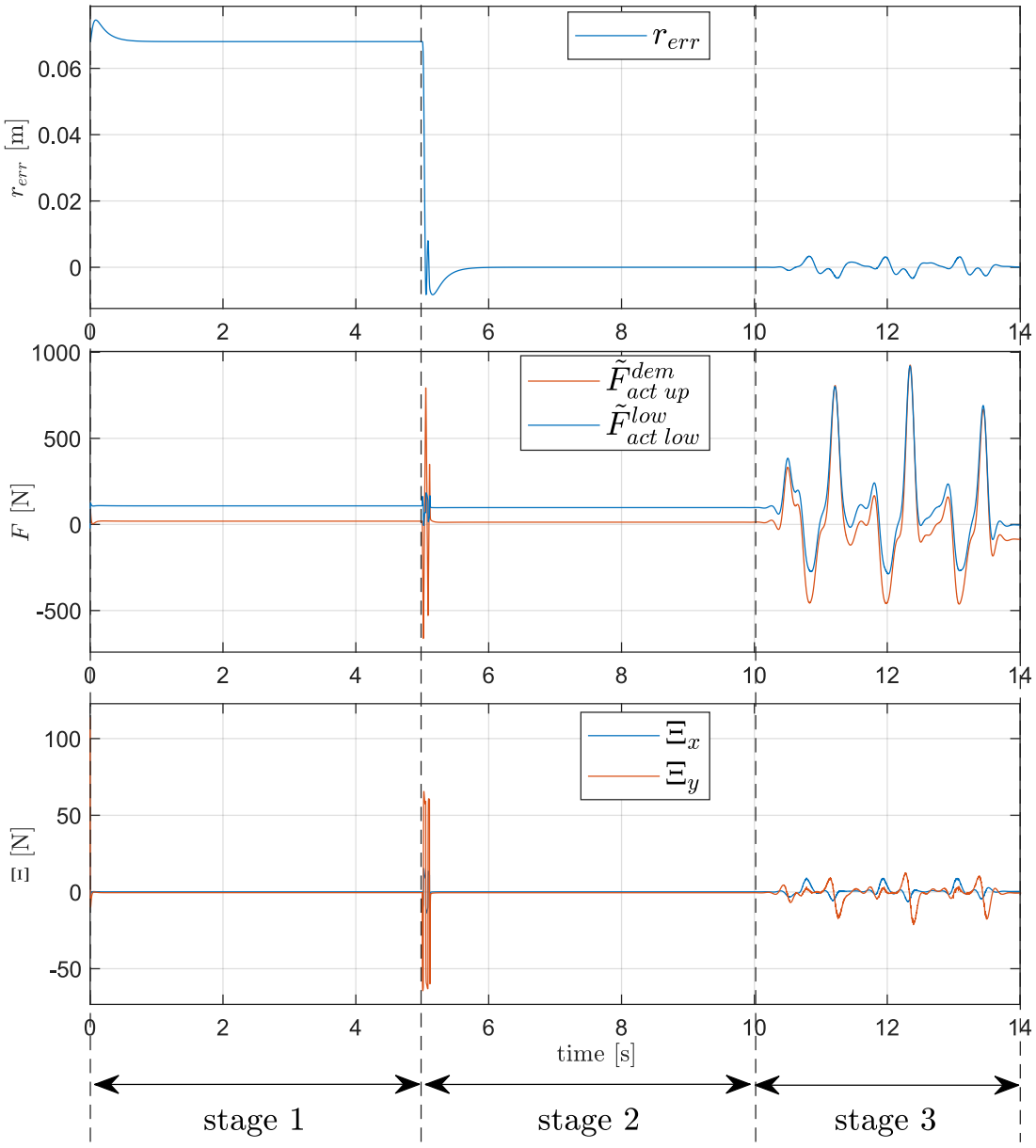

Figure 5.29: Performance of middle–level controller with ideal actuators. (top) – positioning error of rods extension, (middle) – force at the actuators, (bottom) – human–machine interaction force in sagittal plane for controller with knee cap positioning. $k = 65$, $f_{act} = 1.5$ Hz, $H_{kc}(s) = 1$, $c_{sr} = 4 \times 10^4$, $t_{res} = 0.02$ s (see knee cap controller settings in Table 5.3).

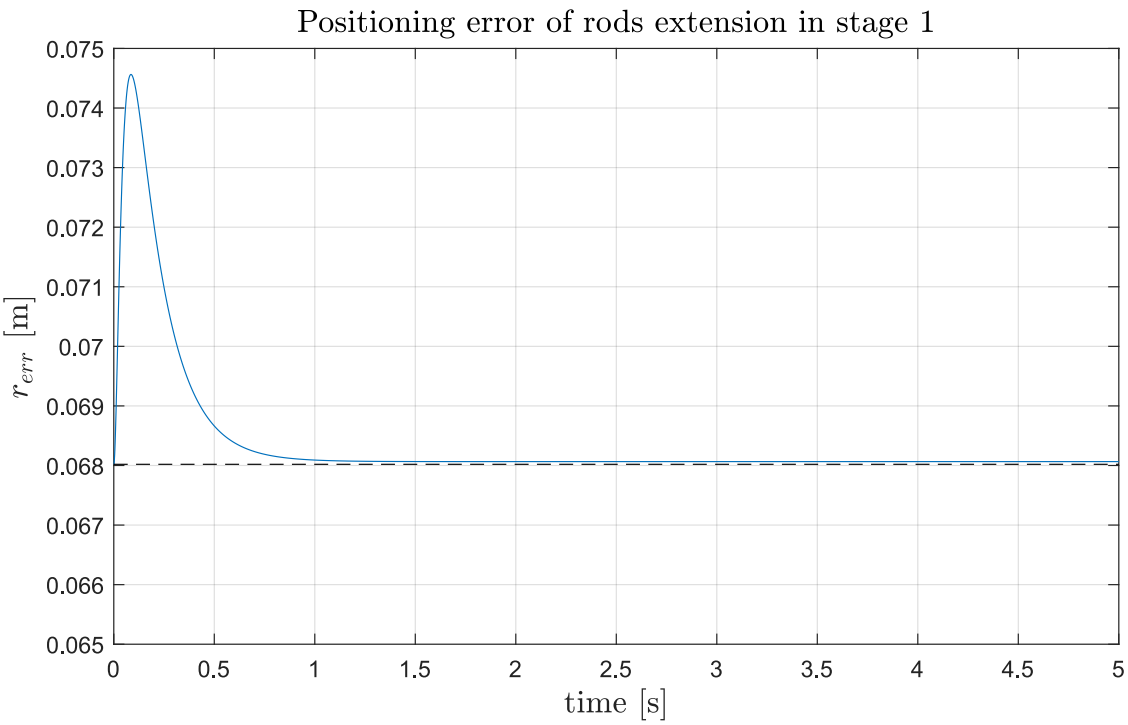

Figure 5.30: Positioning error of rods extension for controller given by Eq. (5.46) during stage 1 (close–up on Fig. 5.29). Settings: $k = 65$, $f_{act} = 1.5$ Hz, $H_{kc}(s) = 1$, $c_{sr} = 4 \times 10^4$, $t_{res} = 0.02$ s. Holding value at initial conditions $r_{up} = 0.0726$ m, $r_{low} = 0.0045$ m.

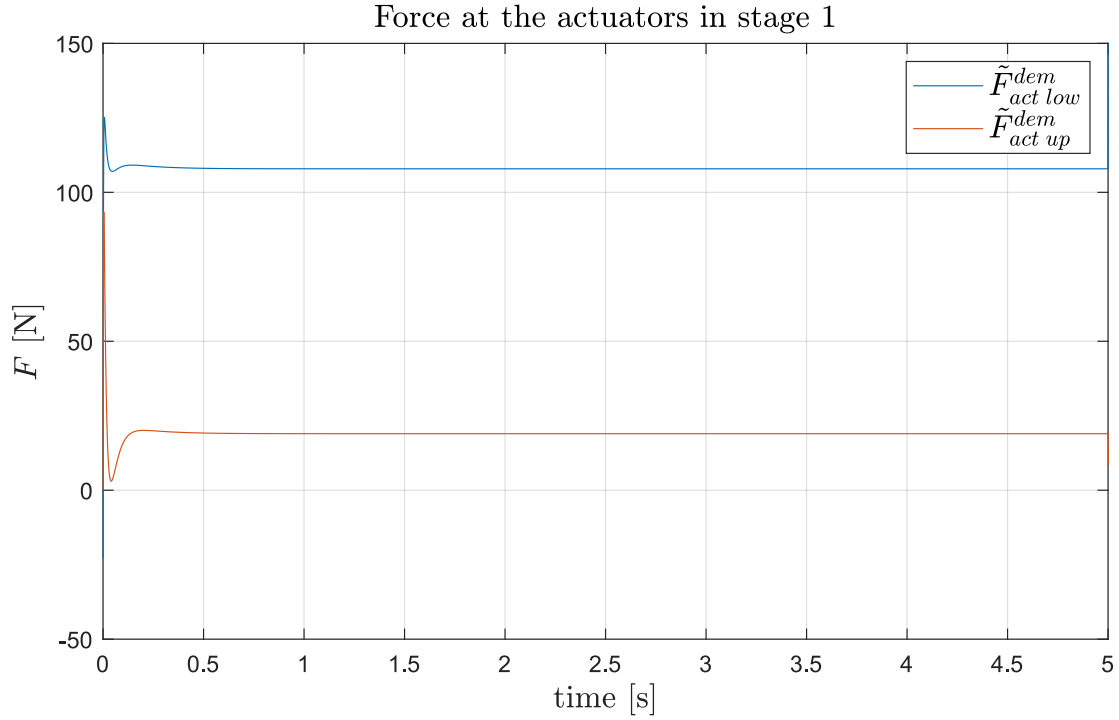

Figure 5.31: Force at the actuators for controller given by Eq. (5.46) during stage 1. Settings: $k = 65$, $f_{act} = 1.5$ Hz, $H_{kc}(s) = 1$, $c_{sr} = 4 \times 10^4$, $t_{res} = 0.02$ s

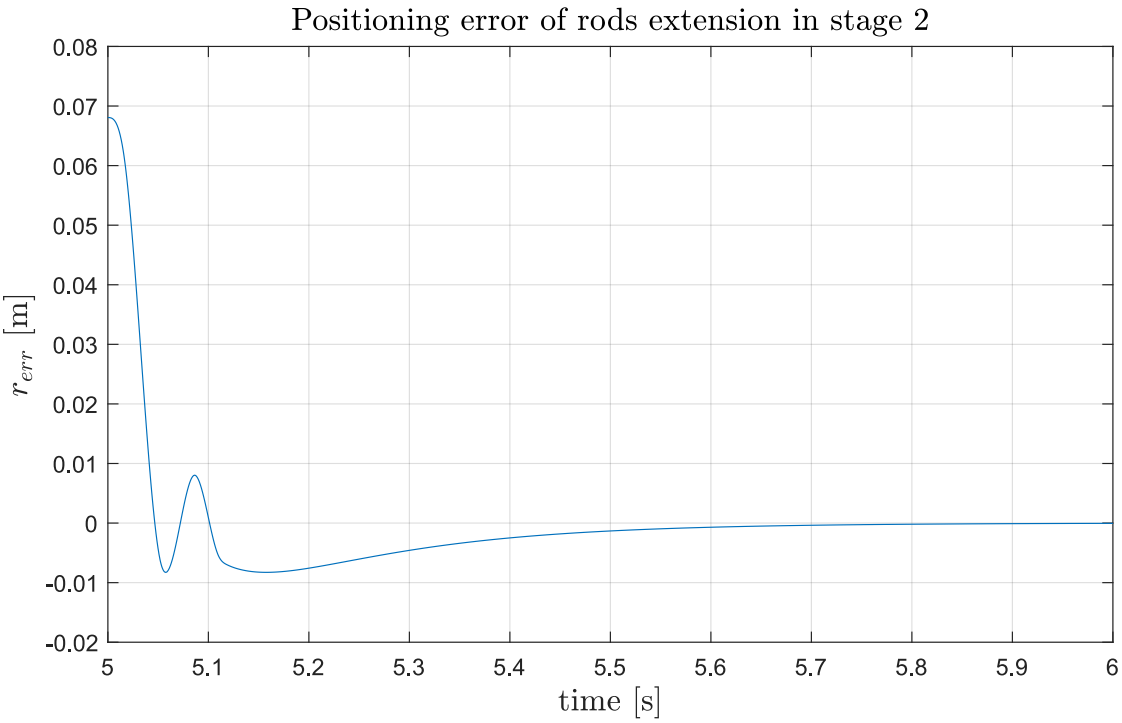

Figure 5.32: Positioning error of rods extension for controller given by Eq. (5.46) during stage 2. Holding value at initial conditions $r_{up} = 0.0726$ m, $r_{low} = 0.0045$ m. Settings: $k = 65$, $f_{act} = 1.5$ Hz, $H_{kc}(s) = 1$, $c_{sr} = 4 \times 10^4$, $t_{res} = 0.02$ s

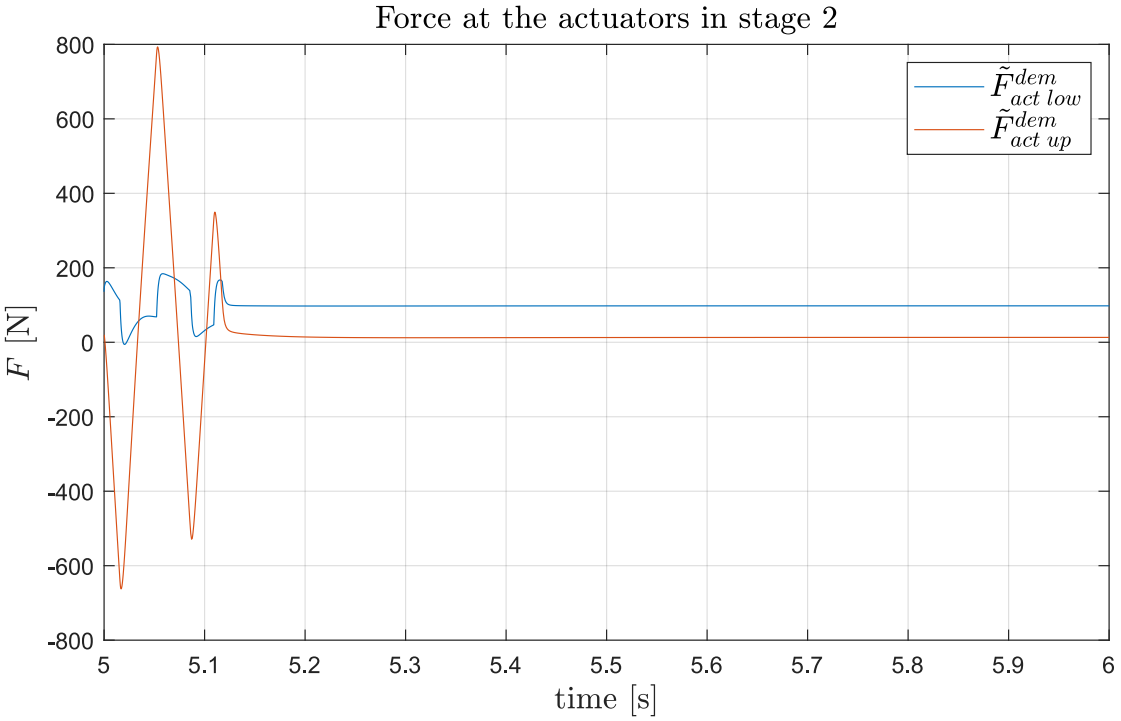

Figure 5.33: Force at the actuators for controller given by Eq. (5.46) during stage 2. Settings: $k = 65$, $f_{act} = 1.5$ Hz, $H_{kc}(s) = 1$, $c_{sr} = 4 \times 10^4$, $t_{res} = 0.02$ s

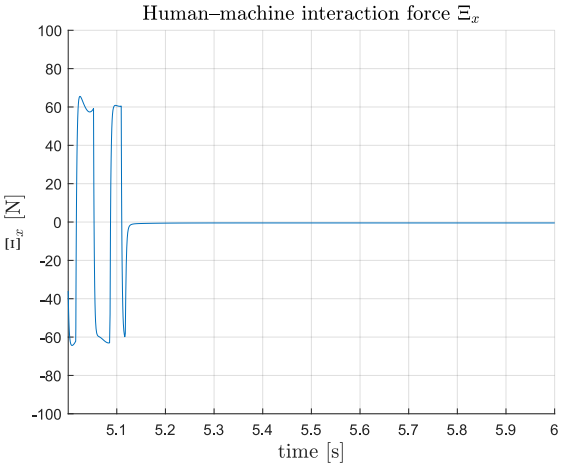

Figure 5.34: Human–machine interaction force in anteriorposterior axis for controller with knee cap positioning in stage 2.

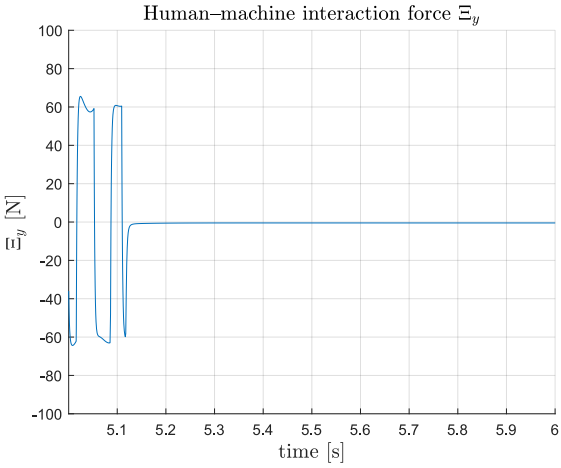

Figure 5.35: Human–machine interaction force in craniocaudal axis for controller with knee cap positioning in stage 2.

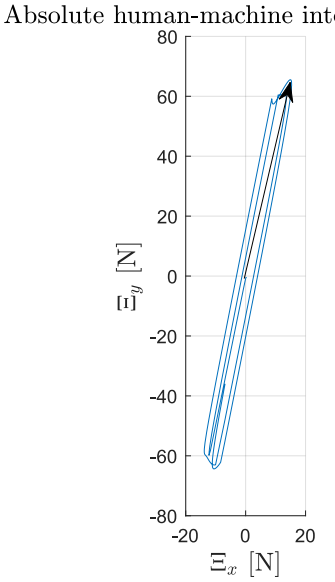

Figure 5.36: Human–machine interaction force in sagittal plane for controller with knee cap positioning in stage 2. $k = 65$, $f_{act} = 1.5$ Hz, $H_{kc}(s) = 1$, $c_{sr} = 4 \times 10^4$, $t_{res} = 0.02$ s

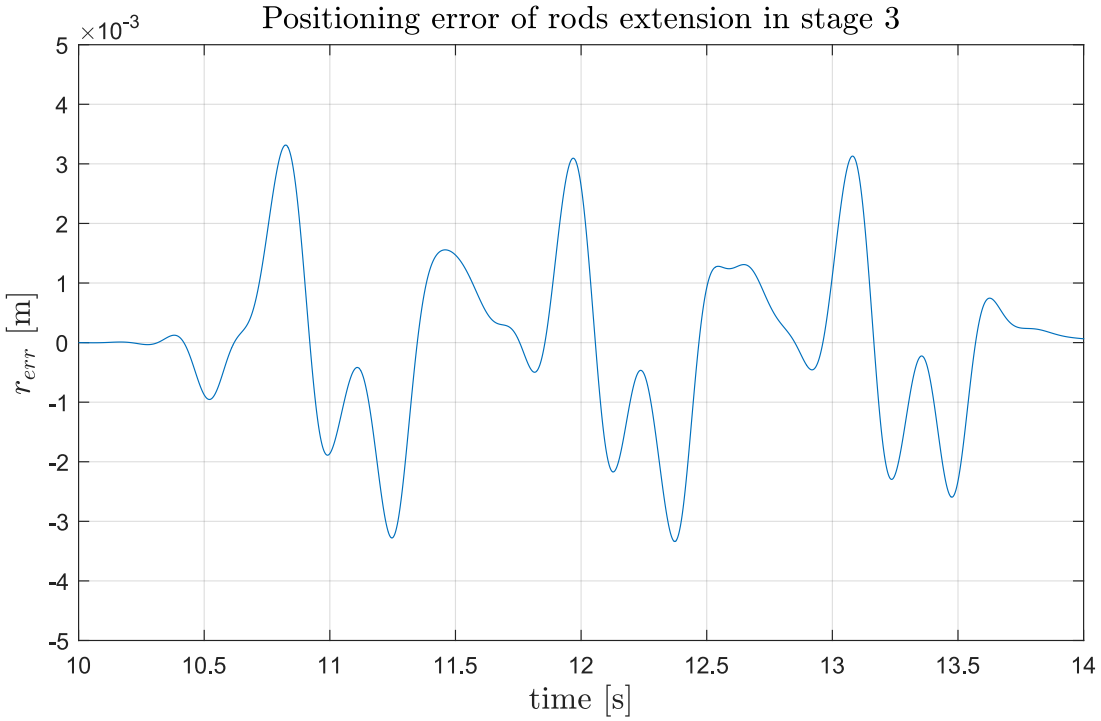

Figure 5.37: Positioning error of rods extension for controller given by Eq. (5.46) during stage 3. Following gait. $k = 65$, $f_{act} = 1.5$ Hz, $H_{kc}(s) = 1$, $c_{sr} = 4 \times 10^4$, $t_{res} = 0.02$ s

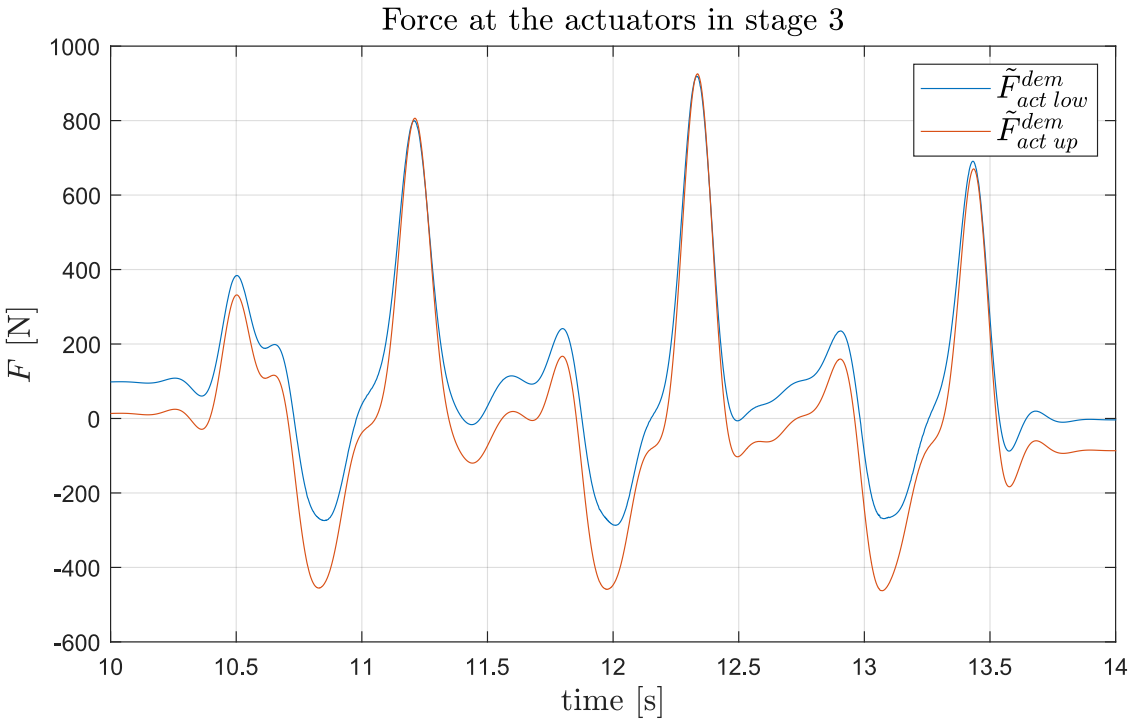

Figure 5.38: Force at the actuators for controller given by Eq. (5.46) during stage 3. . $k = 65$, $f_{act} = 1.5$ Hz, $H_{kc}(s) = 1$, $c_{sr} = 4 \times 10^4$, $t_{res} = 0.02$ s

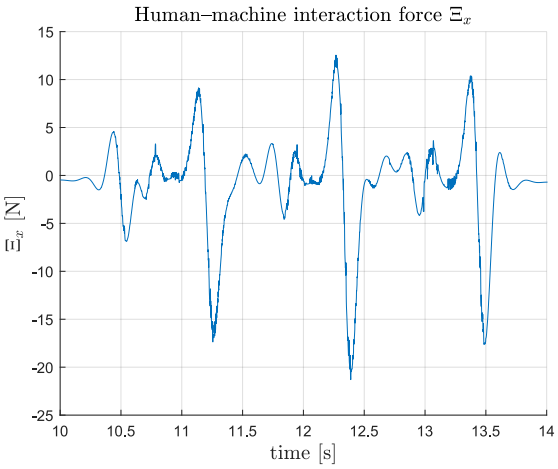

Figure 5.39: Human–machine interaction force in anteriorposterior axis for controller with knee cap positioning in stage 3.

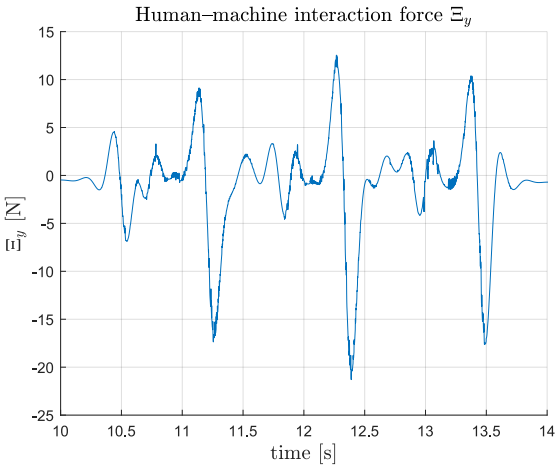

Figure 5.40: Human–machine interaction force in craniocaudal axis for controller with knee cap positioning in stage 3.

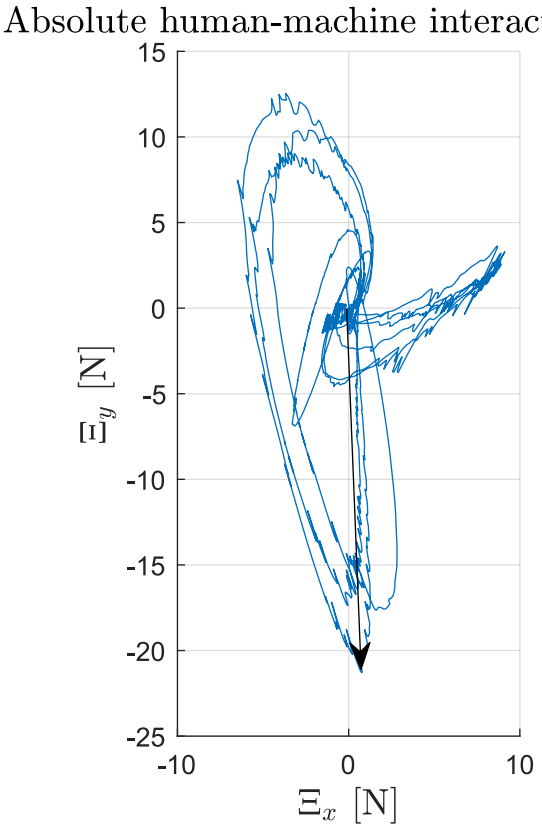

Figure 5.41: Human–machine interaction force in sagittal plane for controller with knee cap positioning in stage 3. $k = 65$, $f_{act} = 1.5$ Hz, $H_{kc}(s) = 1$, $c_{sr} = 4 \times 10^4$, $t_{res} = 0.02$ s.

5.3 Low–Level Controller

In section 5.2.5 the proposed controller was simulated with an assumption that actuators are ideal, and their dynamics are neglected. In order to make performance of the simulation more relevant to performance of the prototype, hydraulic elements were modelled using Matlab Simscape Fluids library[12]. *Proportional and Servo–Valve Actuator* and *4-Way Directional Valve*[13] blocks was used to model directional valve described in section 4.3. The hydraulic cylinder was modelled using *Double-Acting Hydraulic Cylinder*[14]. It accounts for compressibility of fluid, but does not for leakage, neither internal nor external. Details of implementation of hydraulic system are shown in Figs. E.13, E.14, E.15, E.16, E.17, E.18, E.19.

The problem of finding control signals $u_{up}, u_{low} \in [-10, 10]$ minimising Eq. (5.1) and Eq. (5.37) arises. Desired values of upper and lower actuator forces are given by Eq. (5.39) and Eq. (5.41) respectively. The problem is then to find a function U of $\tilde{F}^{dem}_{act\ up}$, $\tilde{F}^{dem}_{act\ low}$ and x – actuator state:

$$[u_{up}, u_{low}]^T = U(\tilde{F}^{dem}_{act\ low}, \tilde{F}^{dem}_{act\ up}, x) \tag{5.48}$$

where:

$$|u_{up}| \leq 10 \text{ V}, \quad |u_{low}| \leq 10 \text{ V} \tag{5.49}$$

x can include actual values of force measured at the end of the rod ($F_{act\ low}, F_{act\ up}$), extension of the rod (r_{up}, r_{low}), its derivatives, pressure at the chambers, etc. The exact form of x is determined by structure of the controller. The most straightforward approach is to treat each hydraulic actuator separately and try to meet its output force with demand. A bulk of literature exist on the problem, although it treats only case of a single actuator. In [16] Racine uses direct measurement of actuator force and compares performance of feedback linearisation, sliding mode control, multiple sliding surface control, multiple sliding surface adaptive control laws. In [143] authors compare PI force feedback controller to proposed adaptive robust control law in context of exoskeleton. Other schemes were proposed: combination of velocity feedforward, output feedback, and a Luenberger observer with state estimate feedback for double acting cylinder, which showed improved performance over PI controller [142]; dynamic

[12] `https://uk.mathworks.com/help/physmod/hydro/index.html`

[13] `https://uk.mathworks.com/help/physmod/hydro/ref/4waydirectionalvalve.html`

[14] `https://uk.mathworks.com/help/physmod/hydro/ref/doubleactinghydrauliccylinder.html`

feedback linearization [144]; H_∞ robust control [145]; switching control scheme using Lyapunov–based adaptive law [146]; generalised predictive control algorithm [147] sliding–mode controller with a perturbation observer [148]; quantitative feedback theory based controller [149]; neural predictive control [150]; variable structure force control via reaching law approach [151]; observer–based backstepping control [152]; robust control using polytopic uncertainty representation [153].

5.3.1 Independent Control of Actuators

The most straightforward approach is to use two separate (independent) controllers for each actuator. The proposed control signal is then of form:

$$u_{up} = \text{sat}[k_{pp}(\tilde{F}^{dem}_{act\ up} - F_{act\ up})] \tag{5.50}$$

$$u_{low} = \text{sat}[k_{pp}(\tilde{F}^{dem}_{act\ low} - F_{act\ low})] \tag{5.51}$$

where $k_{pp} \in R_{>0}$ is gain of the controller. $F_{act\ up}$ – measured upper actuator force, $F_{act\ low}$ – measured lower actuator force, $\tilde{F}^{dem}_{act\ up}$ – demanded upper actuator force, $\tilde{F}^{dem}_{act\ low}$ – demanded lower actuator force, sat is a saturation function:

$$\text{sat}(u) = \begin{cases} 10\text{ V} & \text{if} \quad u > 10\text{ V} \\ u & \text{if} \quad -10 \leq u \leq 10\text{ V} \\ -10\text{ V} & \text{if} \quad u < -10\text{ V} \end{cases} \tag{5.52}$$

The low–level control scheme was simulated in 3 stages described in section 5.2.5, with mid–level control scheme depicted in Fig. 5.26. Details of implementation of low–level independent controller are shown in Fig. E.10. The chosen parameter $k_{pp} = 1.5 \times 10^{-3}$. The proprietary algorithm of Matlab PID tuner was unable to find initial stabilising controller when model of hydraulics was included, so parameters for ideal actuators were used. In first approach, settings for PID controller $k_p = 24820$, $k_i = 1.194 \times 10^5$, $k_d = 981.2$, $filt_N = 1049$ ($t_{res} = 0.02$ s, see Table 5.3) were used. The controller was unable to stabilise extension error of the rods extension. In second approach, settings for P controller were used: $k_p = 1.2 \times 10^4$, $k_i = 0$, $k_d = 0$ (see Table 5.2). Other parameters: $k = 65$, $f_{act} = 1.5$ Hz, $f_{kc} = 2$ Hz, $c_{sr} = 500$. Increasing k too much (e.g. $k = 130$) leads to loss of stability of Ξ in the simulation. The values

Table 5.6: Cost functions E_Ξ (with $\lambda = 1$), $W^\dagger$, E_r values for two independent controllers for hydraulics. $k_{pp} = 1.5 \times 10^{-3}$, $k = 65$, $c_{sr} = 500$.

stage	E_Ξ	$W^\dagger$ [J]	E_r
2 (for 30 sec)	2.67×10^2	0	1.01×10^{-2}
3	3.18×10^3	3.9×10^1	2.78×10^{-4}

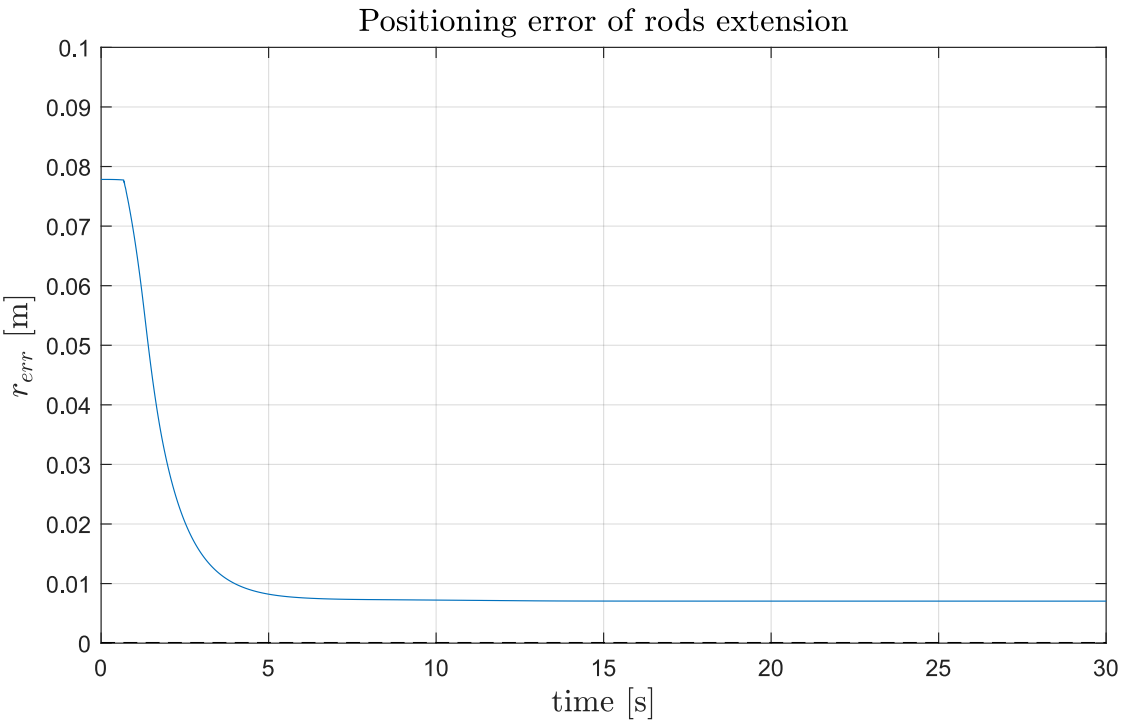

Figure 5.42: Positioning error of rods extension for independent control of hydraulic actuators for stage 2. $k_{pp} = 1.5 \times 10^{-3}$.

of cost functions are shown in Table 5.6. Compared with Table 5.4 it can be seen that the stage 2 has to be increased to 30 s, which is approximately how long it takes r_{err} to settle. Despite long time, r_{err} is still about 0.01 m. In Fig. 5.42 r_{err} in stage 2 is depicted. Compared to Fig. 5.32 it is seen that it takes longer to settle. In Fig. 5.43 and 5.44 demanded and measured actuator forces are depicted for this stage. It is seen that the demand is driven by knee cap controller $\tilde{F}_{kc}(s)$. In Fig. 5.45 control signals are depicted. It is seen that they are roughly symmetric around $u = 0$ axis. They decrease to 0. Values of human–machine interaction force are depicted in Figs. 5.46 and 5.47, in anteriorposterior and craniocaudal axis respectively (compare with Figs. 5.34 and 5.35). In Fig. 5.48 the human–machine interaction force in sagittal plane is depicted (compare with Fig. 5.36). Maximum absolute force is 115 N.

For stage 3, comparing Table 5.6 with values for $c_{sr} = 4 \times 10^4$, $k = 65$, $t_{res} = 0.02$

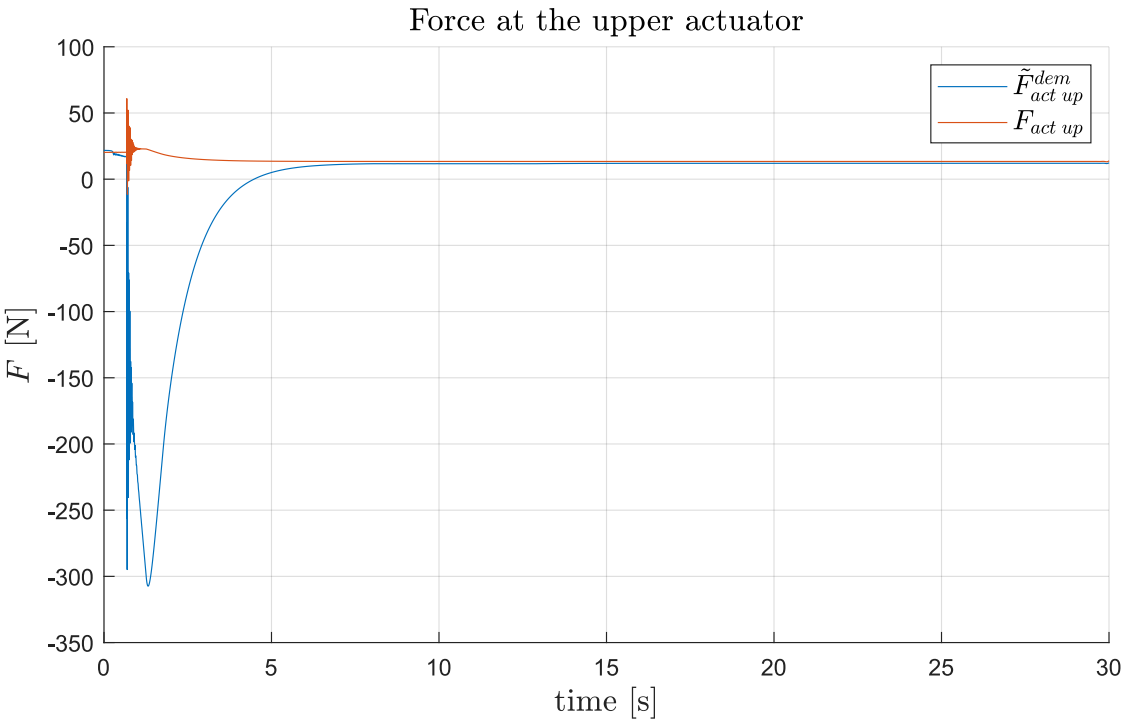

Figure 5.43: Demanded and actual value of upper actuator force for independent control of actuators in stage 2. $k_{pp} = 1.5 \times 10^{-3}$.

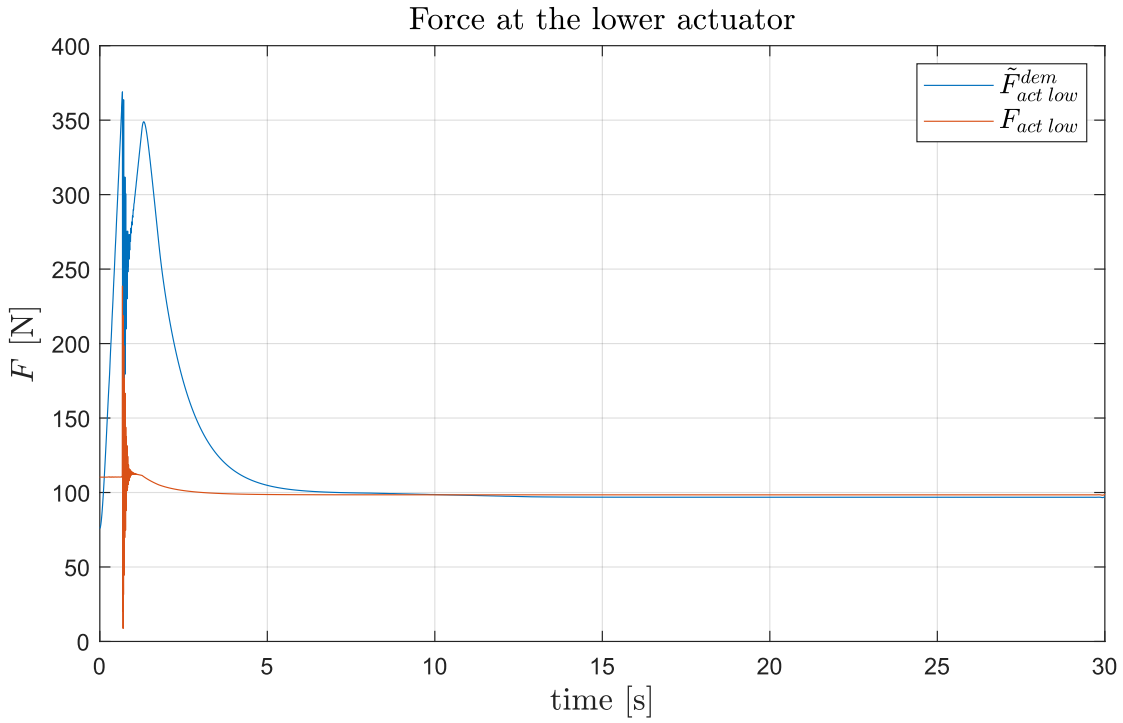

Figure 5.44: Demanded and actual value of lower actuator force for independent control of actuators in stage 2. $k_{pp} = 1.5 \times 10^{-3}$.

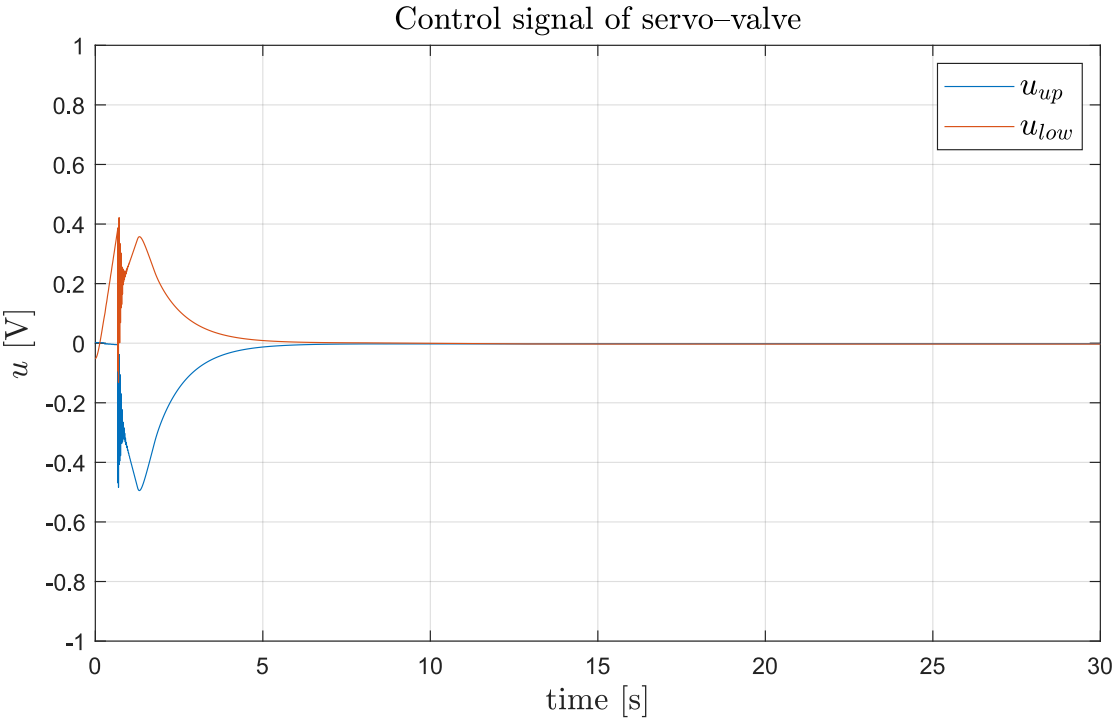

Figure 5.45: Control signals u_{up}, u_{low} calculated using Eq. (5.50) and (5.51) respectively for independent control of hydraulic actuators for stage 2. $k_{pp} = 1.5 \times 10^{-3}$.

s in Table 5.5, it is seen that E_{Ξ} and $W^{\dagger}$ are increased. In Fig. 5.49, r_{err} in stage 3 is depicted. In Fig. 5.50 and 5.51 demanded and measured actuator forces are depicted for stage 3 (compare with forces of ideal actuators depicted in Fig. 5.38). In Fig. 5.52 control signals are shown for stage 3. Values of human–machine interaction force are depicted in Figs. 5.53 and 5.54, in anteriorposterior and craniocaudal axis respectively (compare with Figs. 5.39 and 5.40). In Fig. 5.55 the human–machine interaction force in sagittal plane is depicted (compare with Fig. 5.41). Maximum absolute force does not exceed 95 N.

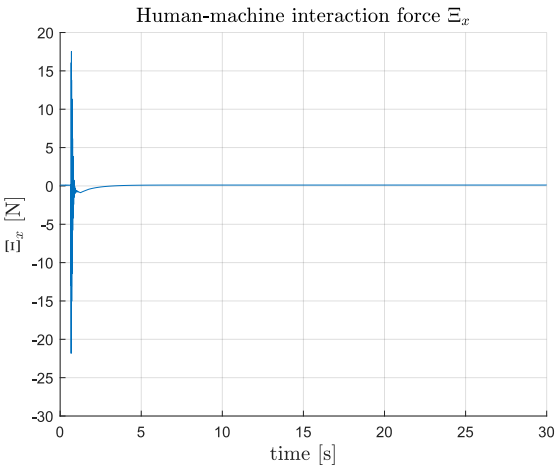

Figure 5.46: Human–machine interaction force in anteriorposterior axis for low–level independent control in stage 2. $k_{pp} = 1.5 \times 10^{-3}$.

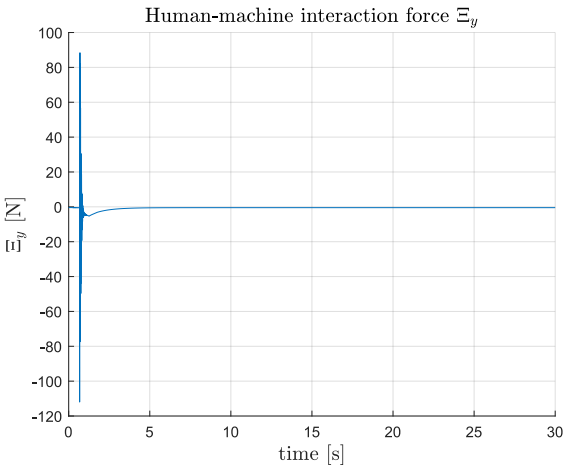

Figure 5.47: Human–machine interaction force in craniocaudal axis for low–level independent control in stage 2. $k_{pp} = 1.5 \times 10^{-3}$.

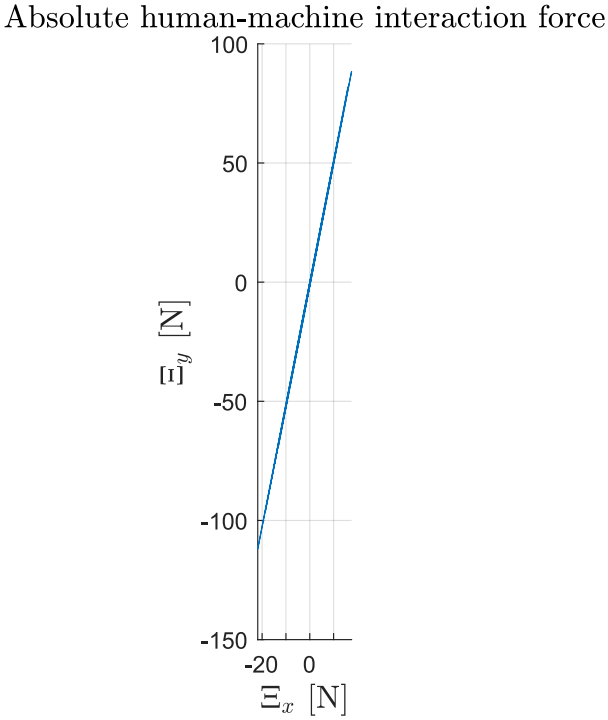

Figure 5.48: Human–machine interaction force in sagittal plane for low–level independent control in stage 2. $k_{pp} = 1.5 \times 10^{-3}$.

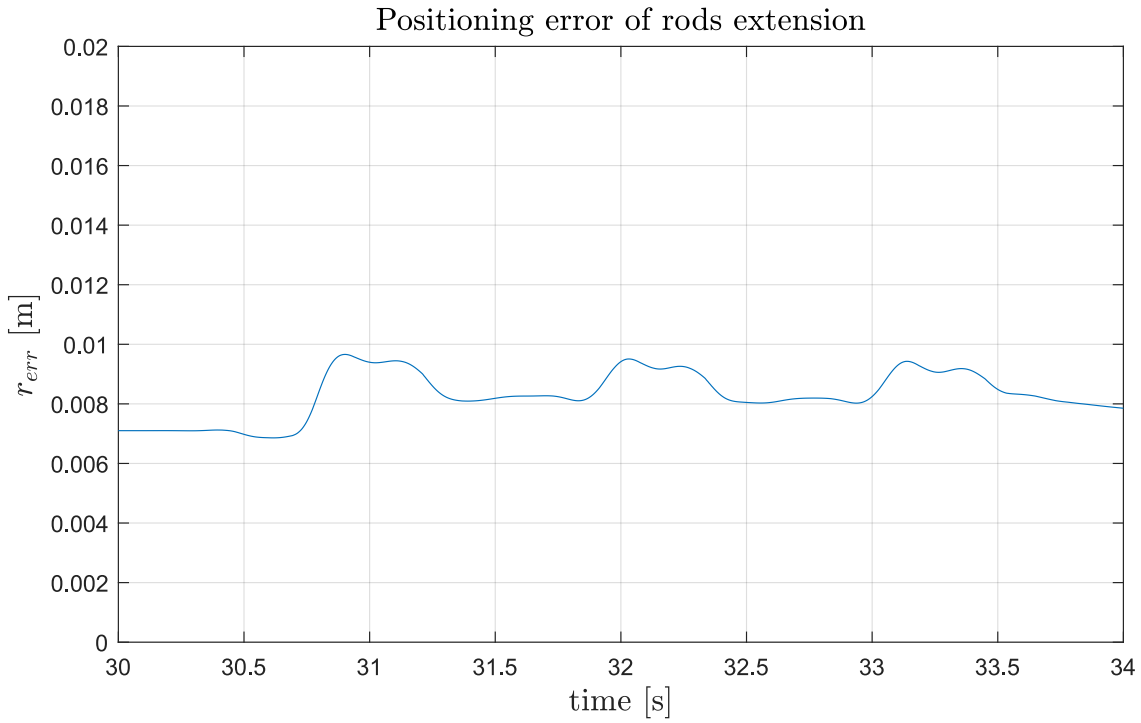

Figure 5.49: Positioning error of rods extension for independent control of hydraulic actuators for stage 3. $k_{pp} = 1.5 \times 10^{-3}$.

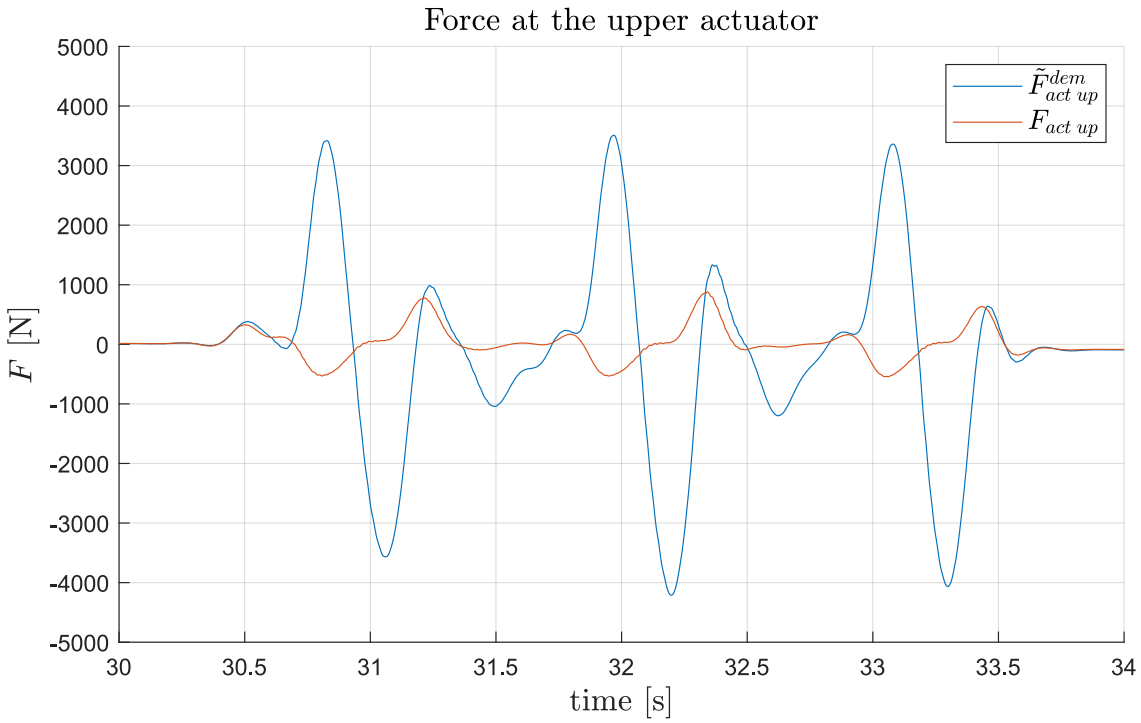

Figure 5.50: Demanded and actual value of upper actuator force for independent control of actuators in stage 3. $k_{pp} = 1.5 \times 10^{-3}$.

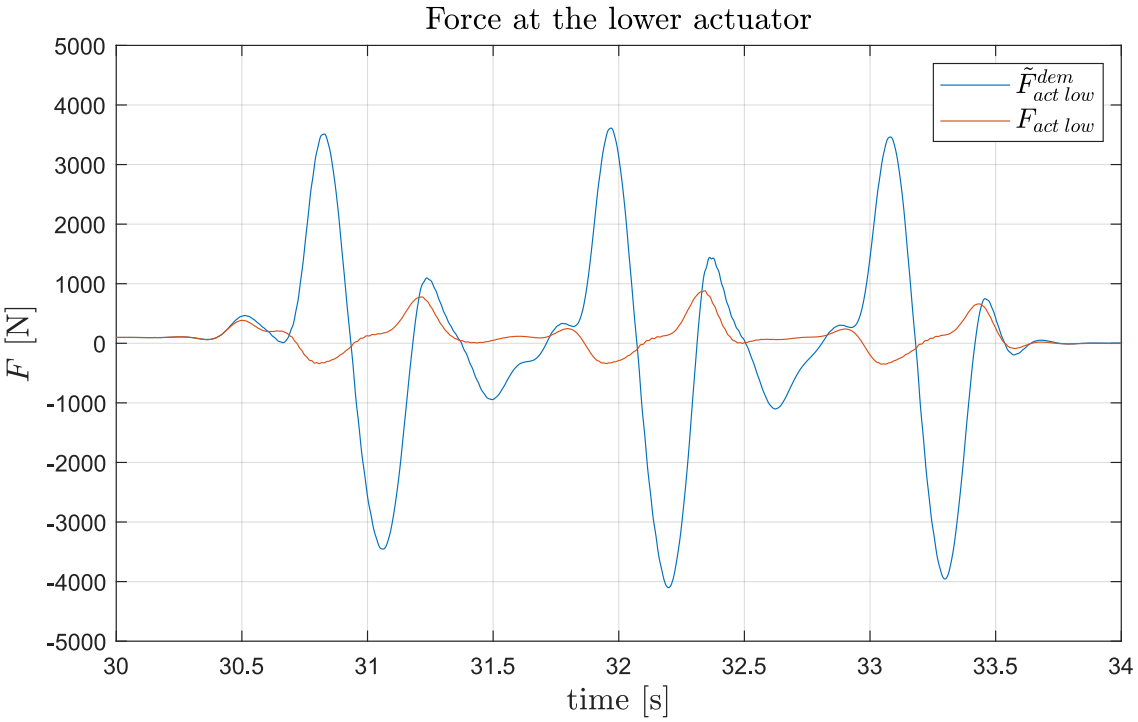

Figure 5.51: Demanded and actual value of lower actuator force for independent control of actuators in stage 3. $k_{pp} = 1.5 \times 10^{-3}$.

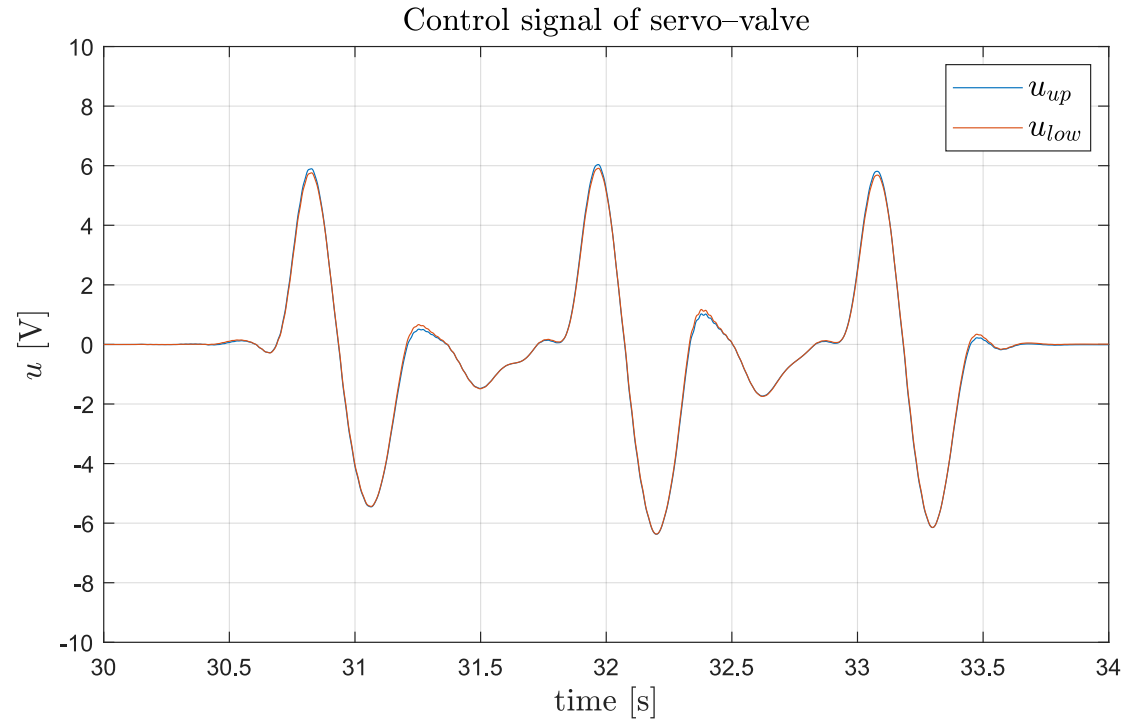

Figure 5.52: Control signals u_{up}, u_{low} calculated using Eq. (5.50) and (5.51) respectively for independent control of hydraulic actuators in stage 3. $k_{pp} = 1.5 \times 10^{-3}$

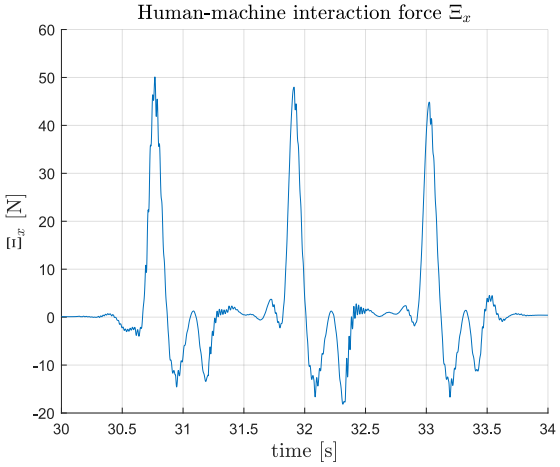

Figure 5.53: Human–machine interaction force in anteriorposterior axis for low–level independent control in stage 3. $k_{pp} = 1.5 \times 10^{-3}$.

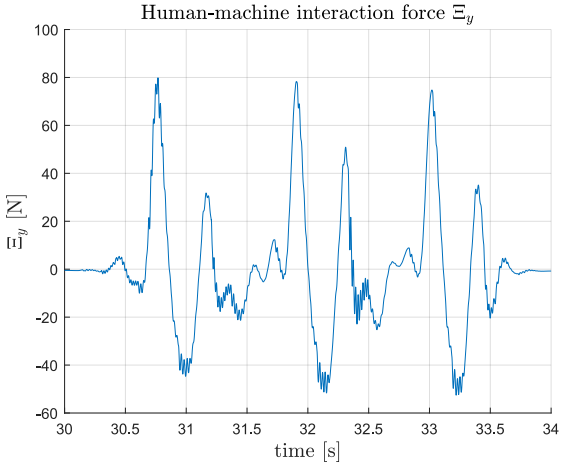

Figure 5.54: Human–machine interaction force in craniocaudal axis for low–level independent control in stage 3. $k_{pp} = 1.5 \times 10^{-3}$.

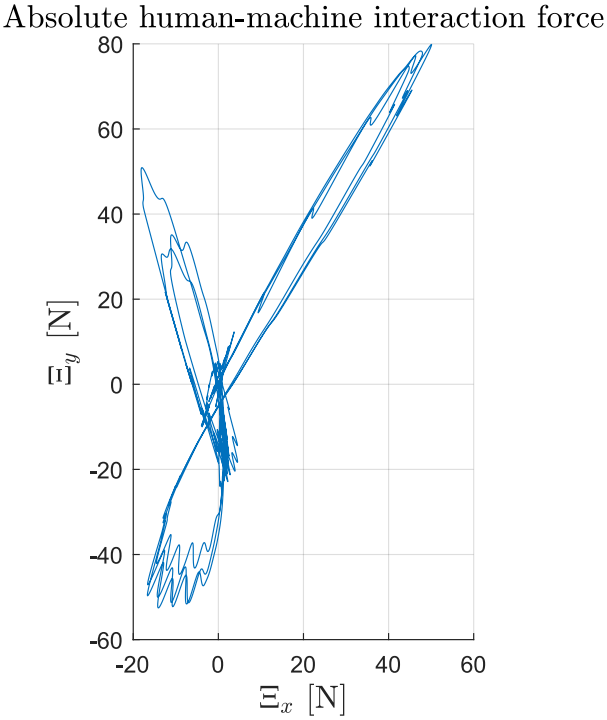

Figure 5.55: Human–machine interaction force in sagittal plane for low–level independent control in stage 3. $k_{pp} = 1.5 \times 10^{-3}$.

The controller so far has been simulated with no disturbance. In Fig. 5.26 we assumed $\tau_{dist} = 0$. In reality, the joint will have to move a mass attached to an end effector. 64.4 kg load was attached to free moving end (close to the 6 DoF force/torque sensor) of the device depicted in Fig. 5.1. Independent control of actuators considered in this section was performed in stage 2 and 3. Values of cost functions are shown in Table 5.7. E_r is similar for case with load and with no load. E_Ξ and $W^\dagger$ are increased for case with the load. In Fig. 5.56 r_{err} in stage 2 is depicted. Compared to Fig. 5.42, it is seen that both graphs are similar, with comparable settling time. In Fig. 5.57 and 5.58 demanded and measured actuator forces are depicted for this stage. It is seen that the demand is driven by knee cap controller $\tilde{F}_{kc}(s)$. Compared with Figs. 5.43 and 5.44 it is seen that exerted forces at actuators are higher, at least 1000 N. In Fig. 5.59 control signals are depicted. It is seen that they are roughly symmetric around $u = 0$ axis. They decrease to 0. Values of human–machine interaction force are depicted in Figs. 5.60 and 5.61, in anteriorposterior and craniocaudal axis respectively (compare with Figs. 5.46 and 5.47). In Fig. 5.62 the human–machine interaction force in sagittal plane is depicted (compare with Fig. 5.48). Maximum absolute force does not exceed 150 N. It is concluded that the performance of controller deteriorates. The exerted forces my be unsafe for the operator.

For stage 3, comparing Table 5.7 with values in Table 5.5, it is seen that E_Ξ and $W^\dagger$ increase. E_r also increases. In Fig. 5.63, r_{err} in stage 3 is depicted. Compared with 5.49, it is seen that both are similar. In Fig. 5.64 and 5.65 demanded and measured actuator forces are depicted for stage 3. In Fig. 5.66 control signals are shown for stage 3. Values of human–machine interaction force are depicted in Figs. 5.67 and 5.68, in anteriorposterior and craniocaudal axis respectively (compare with Figs. 5.54 and 5.53). In Fig. 5.69 the human–machine interaction force in sagittal plane is depicted (compare with Fig. 5.55). Maximum absolute force Ξ^{max} does not exceed 180 N. Considering that load of 64.4 kg (m_{load}) is moved with maximum absolute acceleration ($\ddot{p}^{max}$) of about 50 m/s^2 (see Figure 5.5c, equivalent to about 5g), it is seen that force, although burdensome, is greatly reduced. Simple calculation using the formula:

$$c_{red} = \frac{\ddot{p}^{max} \cdot m_{load}}{\Xi^{max}} \tag{5.53}$$

determines the reduction factor (c_{red}) to be about 18.

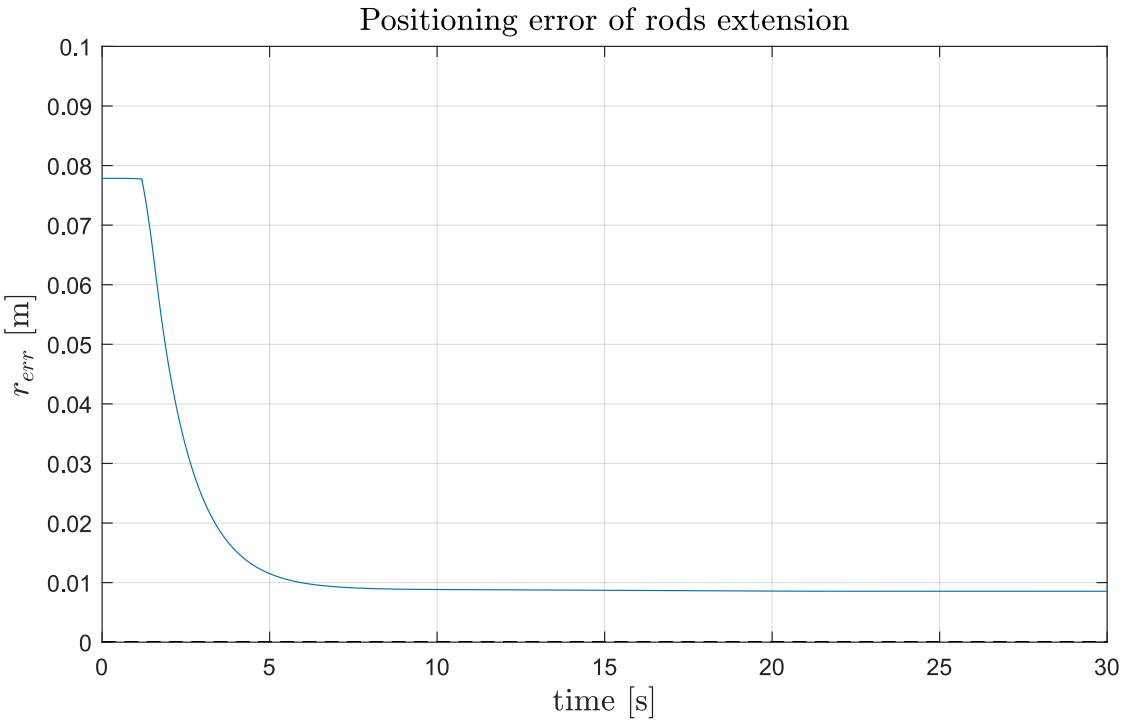

Figure 5.56: Positioning error of rods extension for independent control of hydraulic actuators for stage 2. Load of 64.4 kg. $k_{pp} = 1.5 \times 10^{-3}$.

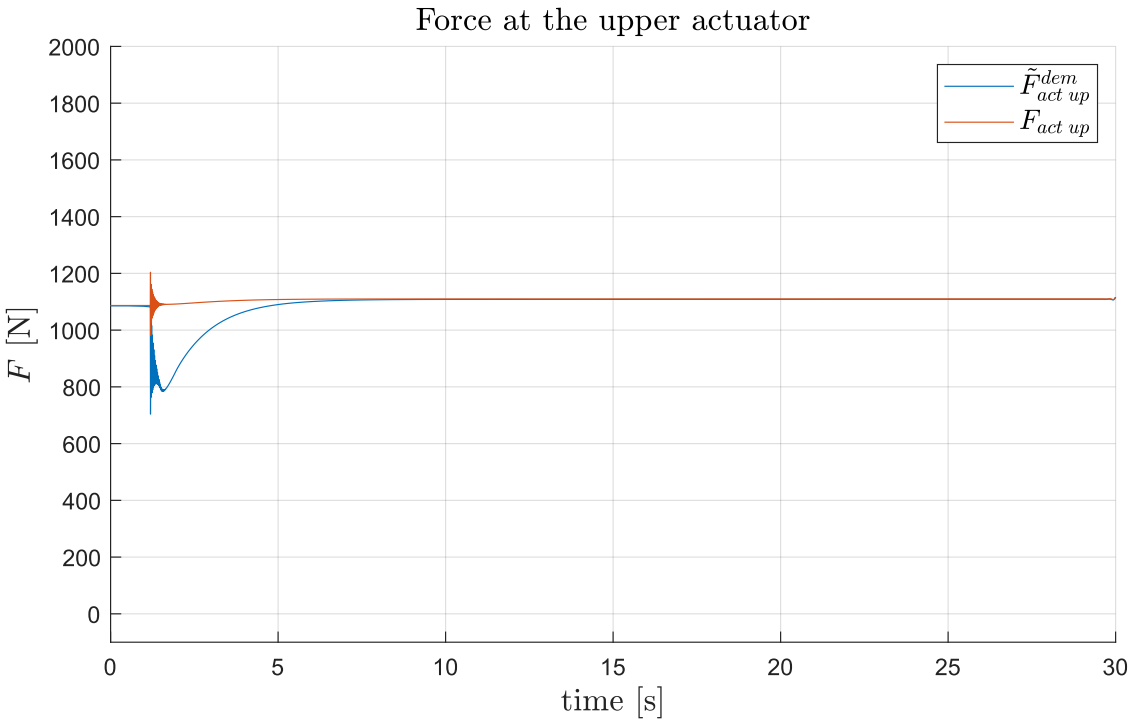

Figure 5.57: Demanded and actual value of upper actuator force for independent control of actuators in stage 2. Load of 64.4 kg. $k_{pp} = 1.5 \times 10^{-3}$, $k = 65$.

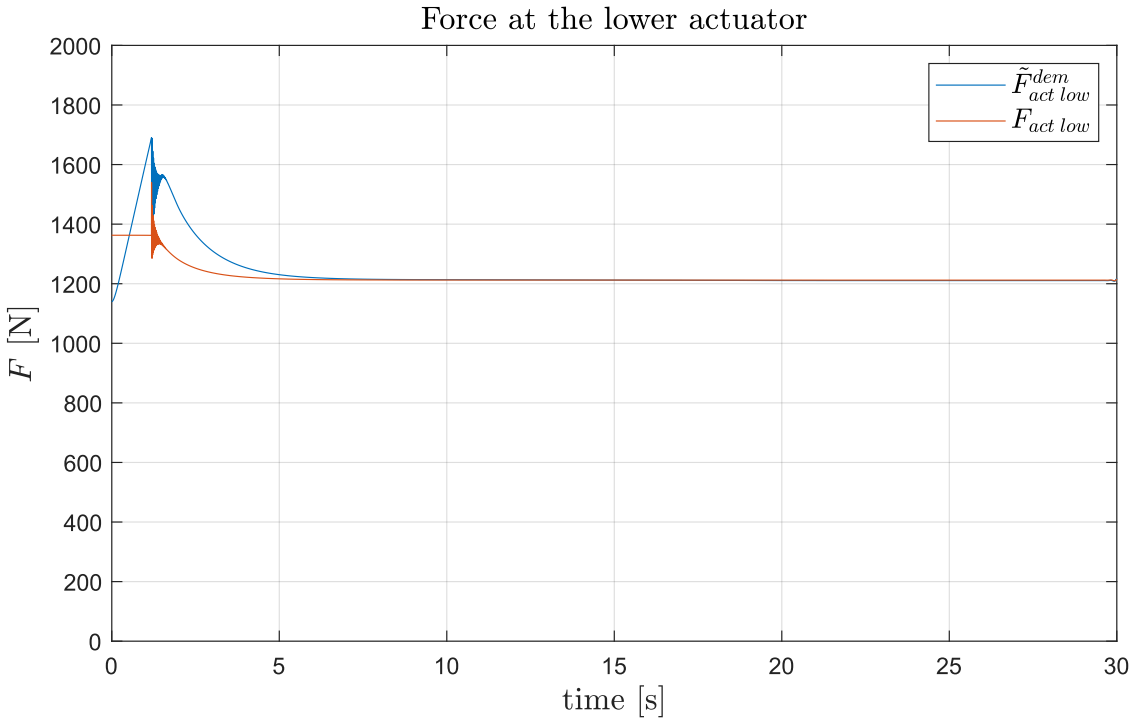

Figure 5.58: Demanded and actual value of lower actuator force for independent control of actuators in stage 2.Load of 64.4 kg. $k_{pp} = 1.5 \times 10^{-3}$, $k = 65$.

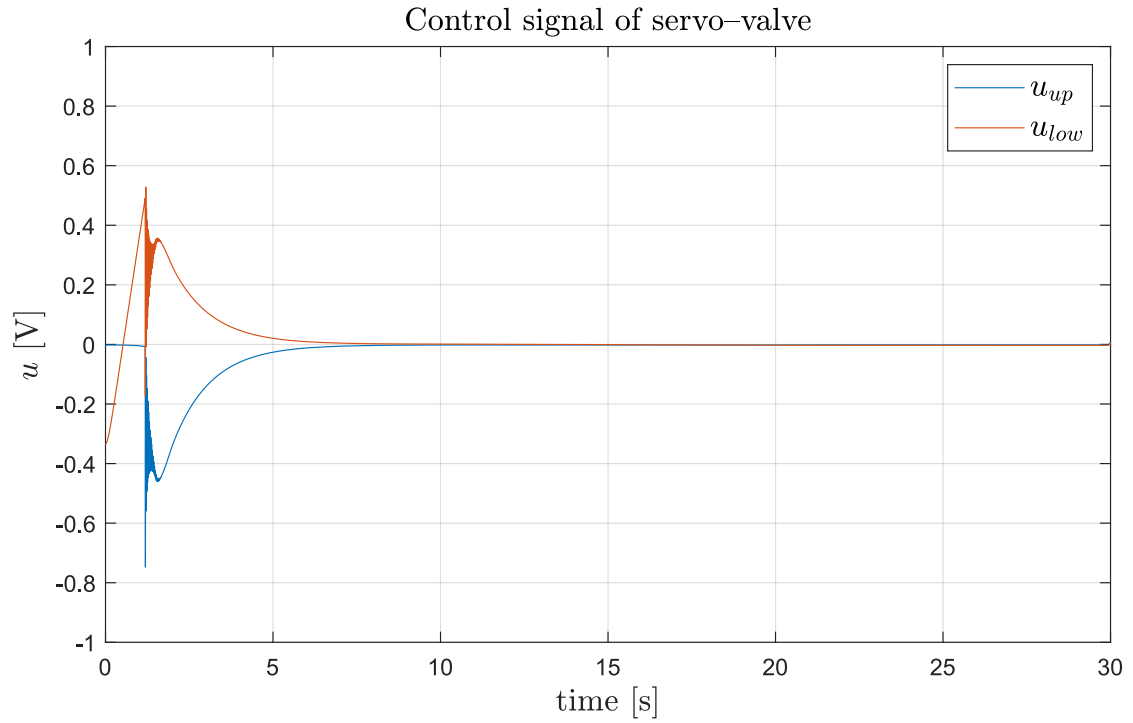

Figure 5.59: Control signals u_{up}, u_{low} calculated using Eq. (5.50) and (5.51) respectively for independent control of hydraulic actuators for stage 2. Load of 64.4 kg. $k_{pp} = 1.5 \times 10^{-3}$, $k = 65$.

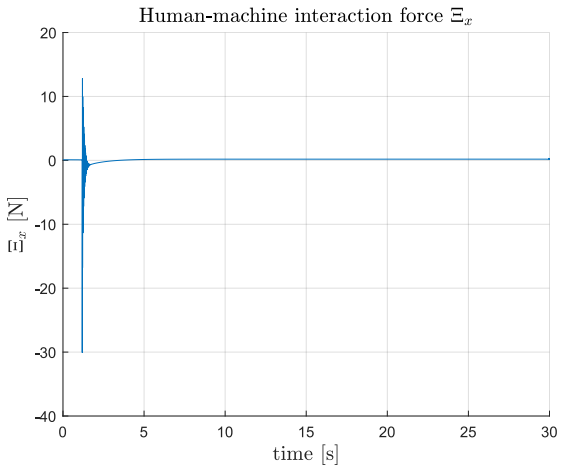

Figure 5.60: Human–machine interaction force in anteriorposterior axis for low–level independent control in stage 2. Load of 64.4 kg. $k_{pp} = 1.5 \times 10^{-3}$, $k = 65$.

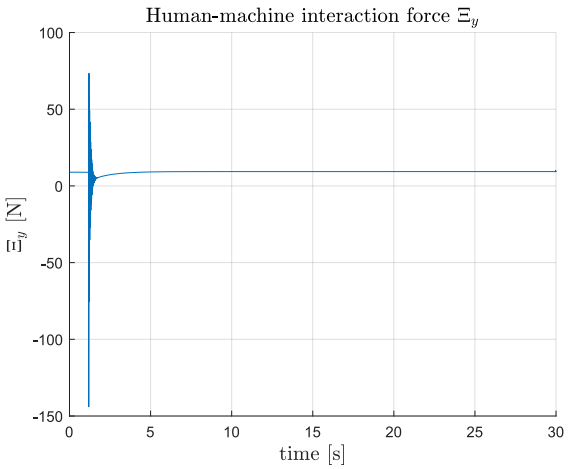

Figure 5.61: Human–machine interaction force in craniocaudal axis for low–level independent control in stage 2. Load of 64.4 kg. $k_{pp} = 1.5 \times 10^{-3}$, $k = 65$.

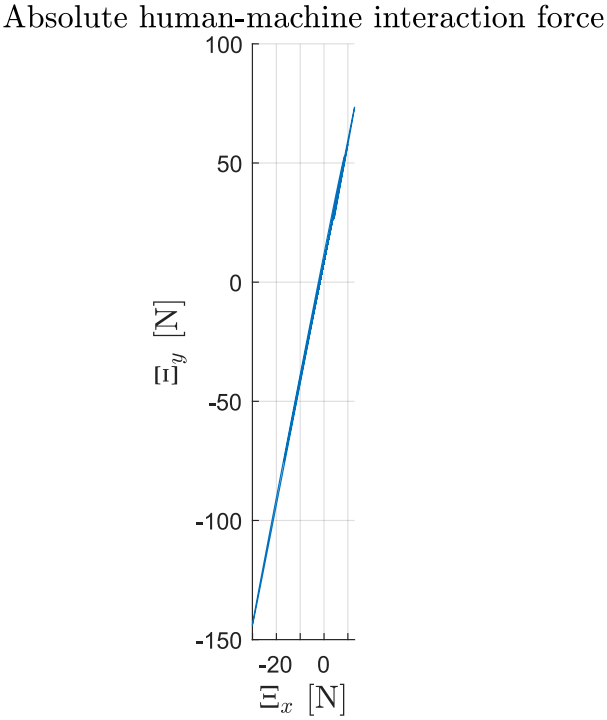

Figure 5.62: Human–machine interaction force in sagittal plane for low–level independent control in stage 2. Load of 64.4 kg. $k_{pp} = 1.5 \times 10^{-3}$, $k = 65$.

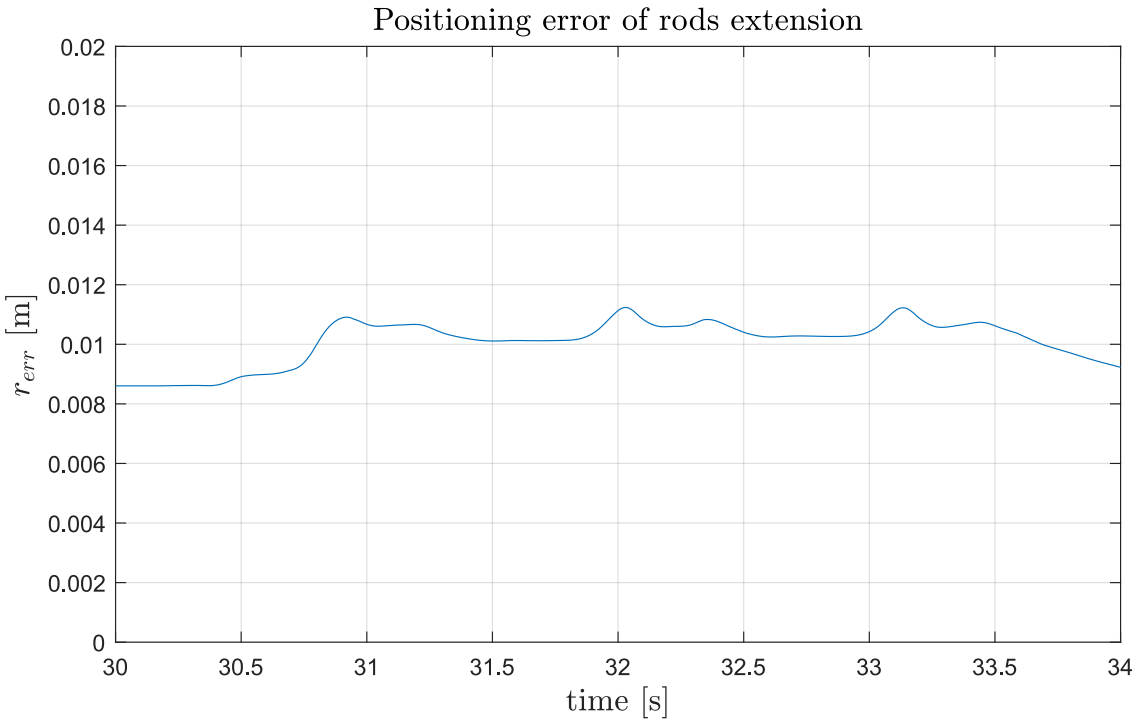

Figure 5.63: Positioning error of rods extension for independent control of hydraulic actuators for stage 3. Load of 64.4 kg. $k_{pp} = 1.5 \times 10^{-3}$, $k = 65$.

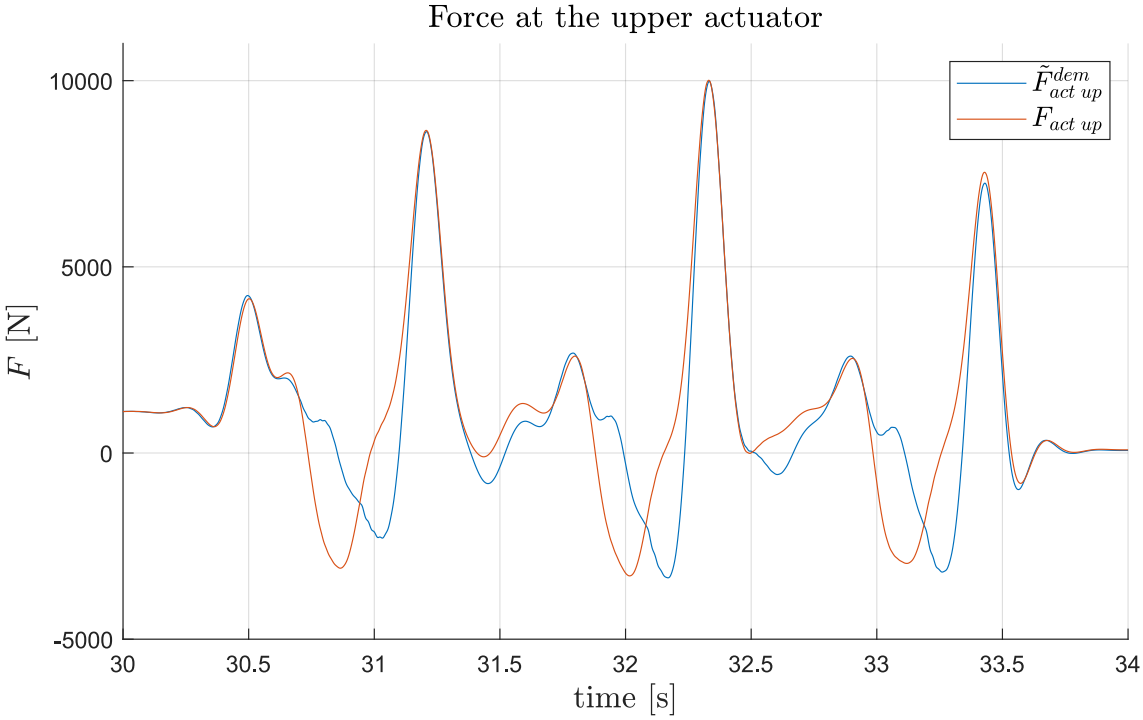

Figure 5.64: Demanded and actual value of upper actuator force for independent control of actuators in stage 3. Load of 64.4 kg. $k_{pp} = 1.5 \times 10^{-3}$, $k = 65$.

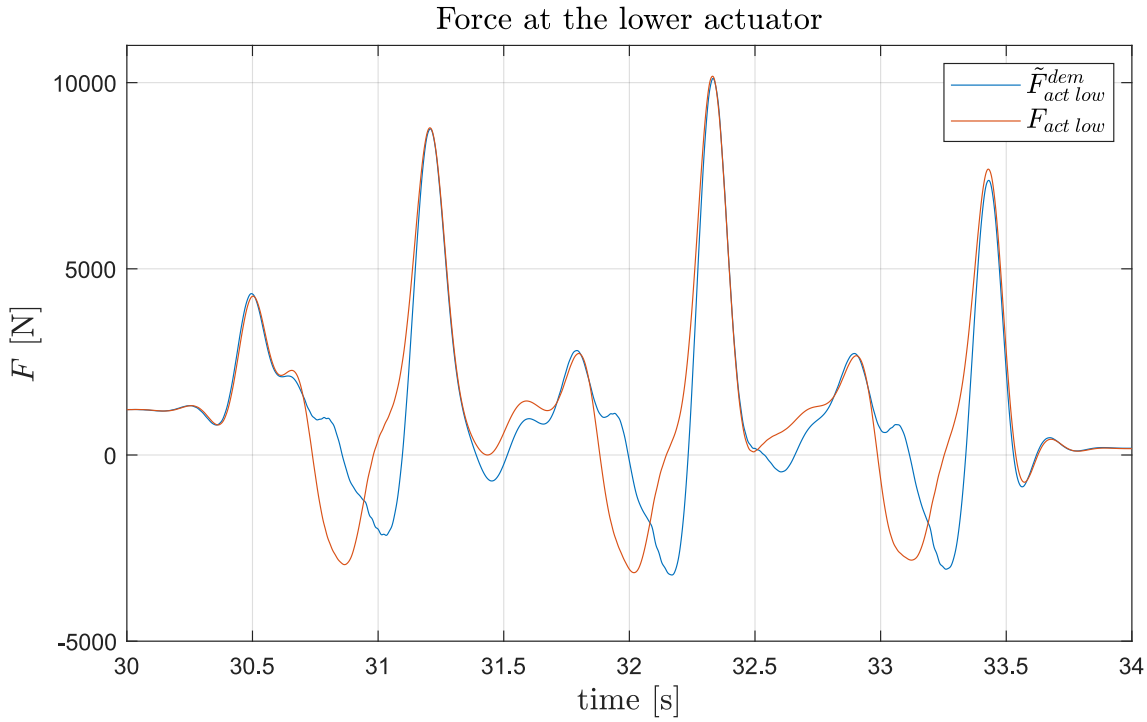

Figure 5.65: Demanded and actual value of lower actuator force for independent control of actuators in stage 3. Load of 64.4 kg. $k_{pp} = 1.5 \times 10^{-3}$, $k = 65$.

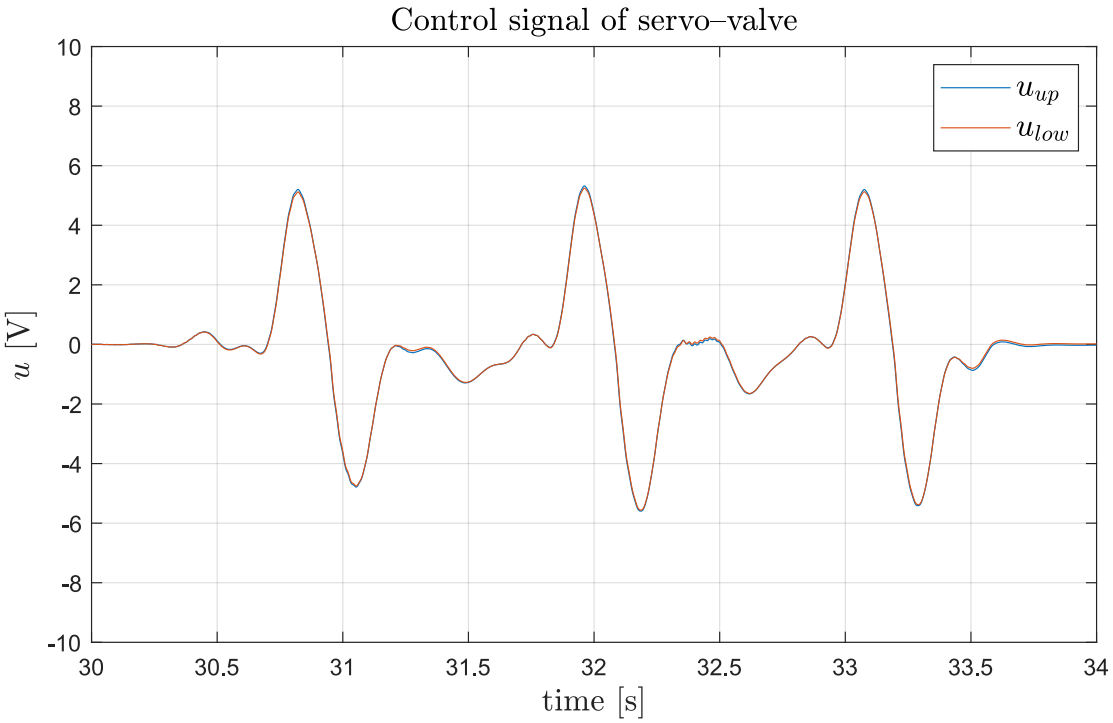

Figure 5.66: Control signals u_{up}, u_{low} calculated using Eq. (5.50) and (5.51) respectively for independent control of hydraulic actuators for stage 3. Load of 64.4 kg. $k_{pp} = 1.5 \times 10^{-3}$, $k = 65$.

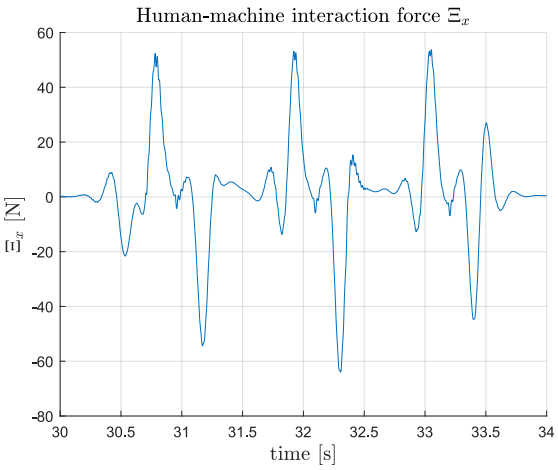

Figure 5.67: Human–machine interaction force in anteriorposterior axis for low–level independent control in stage 3. Load of 64.4 kg. $k_{pp} = 1.5 \times 10^{-3}$, $k = 65$.

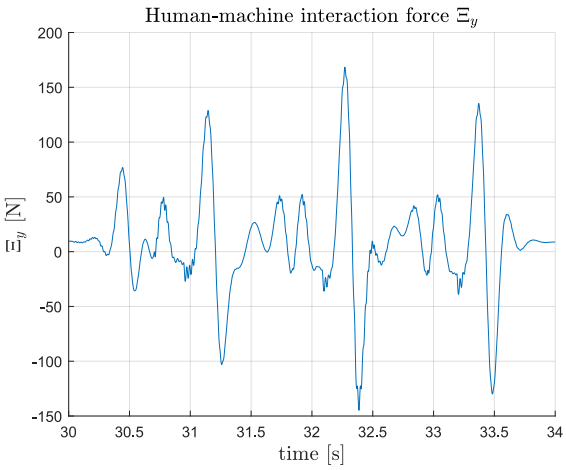

Figure 5.68: Human–machine interaction force in craniocaudal axis for low–level independent control in stage 3. Load of 64.4 kg. $k_{pp} = 1.5 \times 10^{-3}$, $k = 65$.

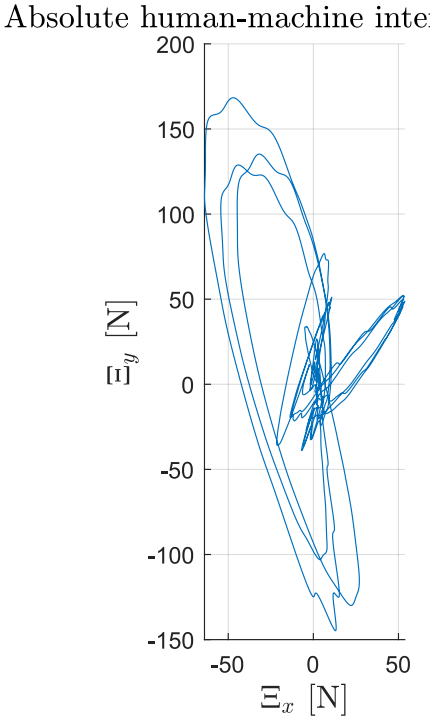

Figure 5.69: Human–machine interaction force in sagittal plane for low–level independent control in stage 3. Load of 64.4 kg. $k_{pp} = 1.5 \times 10^{-3}$, $k = 65$.

Table 5.7: Cost functions E_Ξ (with $\lambda = 1$), $W^\dagger$, E_r values for two independent controllers for hydraulics. $k_{pp} = 1.5 \times 10^{-3}$, $k = 65$, $c_{sr} = 500$. 64.4 kg load attached to end effector.

stage	E_Ξ	$W^\dagger$ [J]	E_r
2 (for 30 sec)	2.69×10^3	0	1.41×10^{-2}
3	1×10^4	6.48×10^1	4.1×10^{-4}

5.3.2 Coupled Control of Two Hydraulic Actuators

In section 5.3.1 independent force control of two hydraulic actuators was considered. Comparing actuator force from Fig. 5.43 to Fig. 5.44 for stage 2 with no load, from Fig. 5.50 to Fig. 5.51 for stage 3 with no load, from Fig. 5.57 to Fig. 5.58 for stage 2 with load, from Fig. 5.64 to Fig. 5.65 for stage 3 with load, it can be seen that $F_{act\ low}$ has value offset of $F_{act\ up}$. In Fig. 5.70 system of two identical hydraulic actuators connected with a knee cap is depicted. It is seen that:

$$F_{act\ low} = C + F_{act\ up} \tag{5.54}$$

where $C > 0$ is force due to gravity acting on the knee cap. For small displacement of pistons, C can be treated as constant. Forces exerted by actuators are given by:

$$F_{act\ up} = \mathcal{A}^{\mathrm{A}} \varrho_{up}^{\mathrm{A}} - \mathcal{A}^{\mathrm{B}} \varrho_{up}^{\mathrm{B}} \tag{5.55}$$

$$F_{act\ low} = \mathcal{A}^{\mathrm{A}} \varrho_{low}^{A} - \mathcal{A}^{\mathrm{B}} \varrho_{low}^{\mathrm{B}} \tag{5.56}$$

where $\mathcal{A}^A$, $\mathcal{A}^B$ – piston areas on A and B sides of the cylinder, $\varrho_{up}^{\mathrm{A}}, \varrho_{up}^{\mathrm{B}}$ – pressures in A and B chambers of upper actuator, $\varrho_{low}^{\mathrm{A}}, \varrho_{low}^{\mathrm{B}}$ – pressures in A and B chambers of lower actuator. Looking at control signals u_{up} and u_{low} in Fig. 5.45 and 5.59 for knee cap stabilising in stage 2, it can be observed:

1. u_{up} is symmetric to u_{low} about $u = 0$ axis
2. in stable state, when $r_{err} = 0$, $u_{up} = u_{low} = 0$; with 0 control system of r_{err} remains in its state indefinitely

If total length of the chain of actuators in Fig. 5.70 is to stay constant, while r_{up}, r_{low} change, it is required:

$$\Delta \mathcal{V}_{low}^{\mathrm{A}} = -\Delta \mathcal{V}_{up}^{\mathrm{A}} \tag{5.57}$$

$$\Delta \mathcal{V}_{low}^{\mathrm{B}} = -\Delta \mathcal{V}_{up}^{\mathrm{B}} \tag{5.58}$$

where $\mathcal{V}_{up}^{\mathrm{A}}$, $\mathcal{V}_{up}^{\mathrm{B}}$ – volume of fluid trapped between valve and piston of upper actuator for side A and B respectively, $\mathcal{V}_{low}^{\mathrm{A}}$, $\mathcal{V}_{low}^{\mathrm{B}}$ – volume of fluid trapped between valve and piston of upper actuator for side A and B respectively. Eqs. (5.57) and (5.58) can be expressed as:

$$\Delta r_{up} = -\Delta r_{low} \tag{5.59}$$

Continuity equations for oil flow through the upper cylinder [149]:

$$q_{up}^{\mathrm{A}} = \mathcal{A}^{\mathrm{A}} \frac{\mathrm{d}r_{up}}{\mathrm{d}t} + \frac{\mathcal{V}_{up}^{\mathrm{A}}}{\mathcal{B}} \frac{\mathrm{d}\varrho_{up}^{\mathrm{A}}}{\mathrm{d}t} \tag{5.60}$$

$$q_{up}^{\mathrm{B}} = \mathcal{A}^{\mathrm{B}} \frac{\mathrm{d}r_{up}}{\mathrm{d}t} - \frac{\mathcal{V}_{up}^{\mathrm{B}}}{\mathcal{B}} \frac{\mathrm{d}\varrho_{up}^{\mathrm{B}}}{\mathrm{d}t} \tag{5.61}$$

where q_{up}^{A} flow *into* chamber A of upper actuator, q_{up}^{B} flow *out of* chamber B. $\mathcal{B} = 1.45375 \times 10^9$ Pa – bulk modulus for Oil–10W. Continuity equations for oil flow through the lower cylinder:

$$q_{low}^{\mathrm{A}} = \mathcal{A}^{\mathrm{A}} \frac{\mathrm{d}r_{low}}{\mathrm{d}t} + \frac{\mathcal{V}_{low}^{\mathrm{A}}}{\mathcal{B}} \frac{\mathrm{d}\varrho_{low}^{\mathrm{A}}}{\mathrm{d}t} \tag{5.62}$$

$$q_{low}^{\mathrm{B}} = \mathcal{A}^{\mathrm{B}} \frac{\mathrm{d}r_{low}}{\mathrm{d}t} - \frac{\mathcal{V}_{low}^{\mathrm{B}}}{\mathcal{B}} \frac{\mathrm{d}\varrho_{low}^{\mathrm{B}}}{\mathrm{d}t} \tag{5.63}$$

where q_{low}^{A} flow *into* chamber A of upper actuator, q_{low}^{B} flow *out of* chamber B. If flow equation (Eq. (4.1)) is substituted to Eq. (5.60) and Eq. (5.61) and neglecting pressure differential:

$$\frac{\mathrm{d}r_{up}}{\mathrm{d}t} = \frac{u_{up}}{|U_{max}|} \frac{q_{Vnom}}{\mathcal{A}^{\mathrm{A}}} \sqrt{\frac{\Delta\varrho_{up}^{\mathrm{A}}}{35}} \tag{5.64}$$

$$\frac{\mathrm{d}r_{up}}{\mathrm{d}t} = \frac{u_{up}}{|U_{max}|} \frac{q_{Vnom}}{\mathcal{A}^{\mathrm{B}}} \sqrt{\frac{\Delta\varrho_{up}^{\mathrm{B}}}{35}} \tag{5.65}$$

where $\Delta\varrho_{up}^{\mathrm{A}}$, $\Delta\varrho_{up}^{\mathrm{B}}$ pressure difference across valve of the upper actuator. Constants: $|U_{max}| = 10$ V – maximum value of control signal, $q_{Vnom} = 12$ l/min – nominal flow through the valve. If flow equation (Eq. (4.1)) is substituted to Eq. (5.62) and Eq. (5.63) and neglecting pressure differential:

$$\frac{\mathrm{d}r_{low}}{\mathrm{d}t} = \frac{u_{low}}{|U_{max}|} \frac{q_{Vnom}}{\mathcal{A}^{\mathrm{A}}} \sqrt{\frac{\Delta\varrho_{low}^{\mathrm{A}}}{35}} \tag{5.66}$$

$$\frac{\mathrm{d}r_{low}}{\mathrm{d}t} = \frac{u_{low}}{|U_{max}|} \frac{q_{Vnom}}{\mathcal{A}^{\mathrm{B}}} \sqrt{\frac{\Delta\varrho_{low}^{\mathrm{B}}}{35}} \tag{5.67}$$

where $\Delta\varrho_{low}^{\mathrm{A}}$, $\Delta\varrho_{low}^{\mathrm{B}}$ pressure difference across valve of the upper actuator. From Eqs.

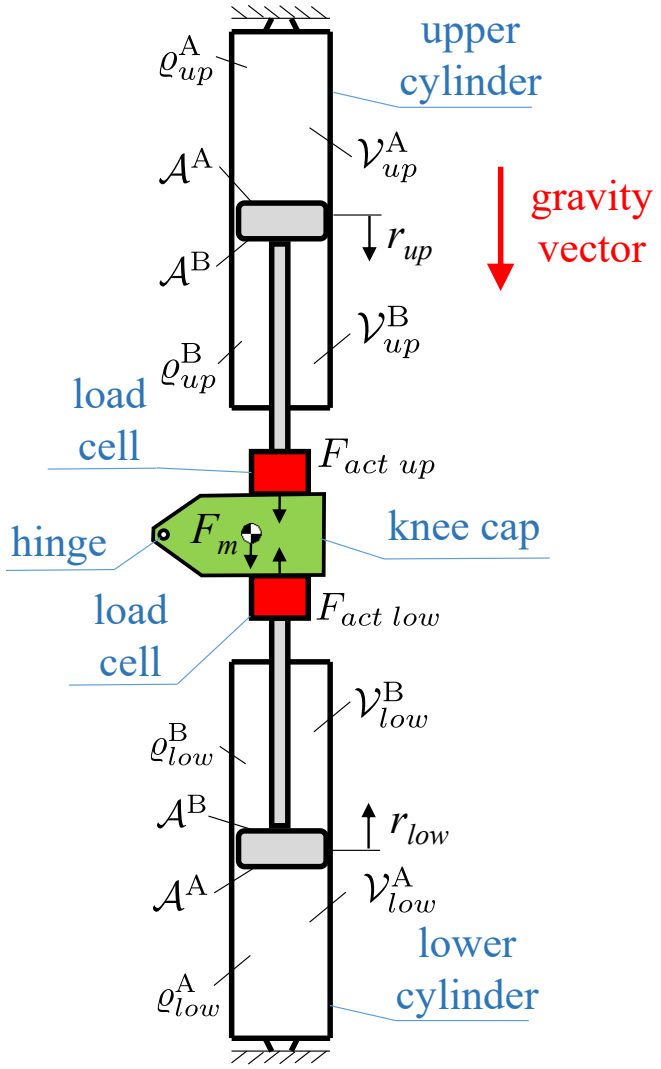

Figure 5.70: Simplified diagram of system of two identical hydraulic actuators connected with a knee cap. $\varrho^{\mathrm{A}}_{up}$, $\varrho^{\mathrm{B}}_{up}$ – pressures at A and B sides of upper cylinder; $\varrho^{\mathrm{A}}_{low}$, $\varrho^{\mathrm{B}}_{low}$ – pressures at A and B sides of lower cylinder; $\mathcal{A}^{\mathrm{A}}$, $\mathcal{A}^{\mathrm{B}}$ – area of piston on side A and B respectively; $\mathcal{V}^{\mathrm{A}}_{up}$, $\mathcal{V}^{\mathrm{B}}_{up}$ – volume of fluid trapped between valve and piston of upper actuator for side A and B respectively, $\mathcal{V}^{\mathrm{A}}_{low}$, $\mathcal{V}^{\mathrm{B}}_{low}$ – volume of fluid trapped between valve and piston of upper actuator for side A and B respectively.

(5.64) – (5.67) it can be seen that in order to meet condition given by Eq. (5.59), control signals u_{up} and u_{low} must be of opposite signs. The exact relationship between the control signals depends on $\mathcal{A}^{\mathrm{A}}$, $\mathcal{A}^{\mathrm{B}}$, which are known, and $\varrho^{\mathrm{A}}_{up}$, $\varrho^{\mathrm{B}}_{up}$, $\varrho^{\mathrm{A}}_{low}$, $\varrho^{\mathrm{B}}_{low}$, which are unkonwn, unless measured. Therefore, as an approximation, it can be assumed, that signals u_{up} and u_{low} are symmetric around $u = 0$ axis. It is also seen, that if $\Delta r_{up} = -\Delta r_{low} = 0$, the control signals must be 0.

From Figs. 5.52 and 5.66 for stage 3, it is seen that the control signals u_{up} and u_{low} have the same magnitude and similar shape. Substituting Eq. (4.1) into Eq. (5.60) and Eq. (5.61) and neglecting rod extension differentials:

$$\frac{\mathrm{d}\varrho^{\mathrm{A}}_{up}}{\mathrm{d}t} = q_{Vnom}\frac{u_{up}}{|U_{max}|}\frac{\mathcal{B}}{\mathcal{V}^{\mathrm{A}}_{up}}\sqrt{\frac{\Delta\varrho^{\mathrm{A}}_{up}}{35}} \tag{5.68}$$

$$\frac{\mathrm{d}\varrho^{\mathrm{B}}_{up}}{\mathrm{d}t} = -q_{Vnom}\frac{u_{up}}{|U_{max}|}\frac{\mathcal{B}}{\mathcal{V}^{\mathrm{B}}_{up}}\sqrt{\frac{\Delta\varrho^{\mathrm{B}}_{up}}{35}} \tag{5.69}$$

Again, substituting Eq. (4.1) into Eq. (5.62) and Eq. (5.63) and neglecting rod extension differentials:

$$\frac{\mathrm{d}\varrho^{\mathrm{A}}_{low}}{\mathrm{d}t} = q_{Vnom}\frac{u_{up}}{|U_{max}|}\frac{\mathcal{B}}{\mathcal{V}^{\mathrm{A}}_{low}}\sqrt{\frac{\Delta\varrho^{\mathrm{A}}_{low}}{35}} \tag{5.70}$$

$$\frac{\mathrm{d}\varrho^{\mathrm{B}}_{low}}{\mathrm{d}t} = -q_{Vnom}\frac{u_{low}}{|U_{max}|}\frac{\mathcal{B}}{\mathcal{V}^{\mathrm{B}}_{low}}\sqrt{\frac{\Delta\varrho^{\mathrm{B}}_{low}}{35}} \tag{5.71}$$

Substituting Eq. (5.68) and Eq. (5.69) into Eq. (5.55), we have approximation for small pressure change in chambers:

$$\begin{aligned} F_{act\ up}(t_{end}) &= \Lambda_{up}\int_{t_{start}}^{t_{end}} u_{up}(t)\mathrm{d}t \\ &+\mathcal{A}^{\mathrm{A}}\varrho^{\mathrm{A}}_{up}(t_{start}) - \mathcal{A}^{\mathrm{B}}\varrho^{\mathrm{B}}_{up}(t_{start}) \end{aligned} \tag{5.72}$$

where $t_{start}, t_{end} \in \mathbb{R}$ – time of start and end of manoeuvre respectively,

$$\Lambda_{up} = \frac{\mathcal{B}q_{Vnom}}{|U_{max}|\sqrt{35}}\left(\frac{\mathcal{A}^{\mathrm{A}}}{\mathcal{V}^{\mathrm{A}}_{up}}\sqrt{\Delta\varrho^{\mathrm{A}}_{up}} + \frac{\mathrm{A}^{\mathrm{B}}}{\mathcal{V}^{\mathrm{B}}_{up}}\sqrt{\Delta\varrho^{\mathrm{B}}_{up}}\right) \tag{5.73}$$

Substituting Eq. (5.70) and Eq. (5.71) into Eq. (5.56), we have approximation for

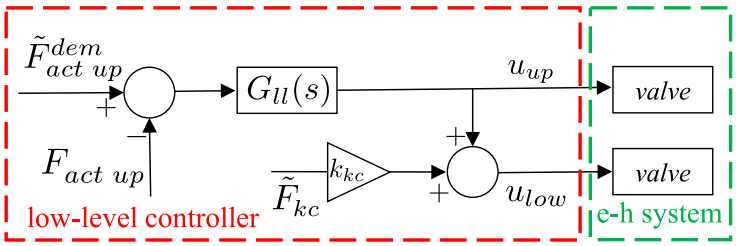

Figure 5.71: Block diagram of coupled control of two hydraulic actuators.

small pressure change in chambers:

$$F_{act\ low}(t_{end}) = \Lambda_{low} \int_{t_{start}}^{t_{end}} u_{low}(t)\mathrm{d}t + \mathrm{A}^{\mathrm{A}} \varrho^{\mathrm{A}}_{low}(t_{start}) - \mathrm{A}^{\mathrm{B}} \varrho^{\mathrm{B}}_{low}(t_{start}) \tag{5.74}$$

where:

$$\Lambda_{low} = \frac{\mathcal{B} q_{Vnom}}{|U_{max}|\sqrt{35}} \left(\frac{\mathcal{A}^{\mathrm{A}}}{\mathcal{V}^{\mathrm{A}}_{low}} \sqrt{\Delta \varrho^{\mathrm{A}}_{low}} + \frac{\mathcal{A}^{\mathrm{B}}}{\mathcal{V}^{\mathrm{B}}_{low}} \sqrt{\Delta \varrho^{\mathrm{B}}_{low}} \right) \tag{5.75}$$

At t_{start}, Eq. (5.54) holds. If it is supposed to hold for t_{end}, the values of the integrals in Eq. (5.72) and in Eq. (5.74) must be equal. The exact values depend on Λ_{up} and Λ_{low}, which in turn depend on pressure at the chambers. Without this knowledge it can be assumed that u_{up} and u_{low} must have the same sign, so the knee cap is squeezed or stretched synchronously. In absence of information on Λ_{up} and Λ_{low}, it might be assumed that $u_{up}(t) = u_{low}(t)$.

A controller, which has properties discussed above, can be synthesised. In Fig. 5.71 a block diagram of the low level control law is depicted. The control signal for upper actuator is given by:

$$u_{up} = \mathrm{sat}\left[G_{ll}(s) \left(\tilde{F}^{dem}_{act\ up} - F_{act\ up} \right) \right] \tag{5.76}$$

where $\tilde{F}^{dem}_{act\ up}$ is demanded force given by Eq. (5.39), $F_{act\ up}$ is measured force using a load cell attached to rod of upper actuator. sat is saturation function given by Eq. (5.52), $G_{ll}(s)$ is transfer function of a PID controller given by:

$$G_{ll}(s) = k_{pp} + k_{ii}\frac{1}{s} + k_{dd}\frac{N_{nfilt}}{1 + N_{nfilt}\frac{1}{s}} \tag{5.77}$$

Control signal of lower actuator is given by:

$$u_{low} = u_{low} + k_{kc}\tilde{F}_{kc} \tag{5.78}$$

where u_{up} is given by Eq. (5.76), $\tilde{F}_{kc}$ is given by Eq. (5.42), k_{kc} is knee cap controller low level gain. The advantage of the controller is that it requires measurement of only one force exerted by the actuator, thus eliminating need for a second load cell, which with instrumentation can be costly. The system was simulated in 3 stages described in section 5.2.5 with proposed low level coupled control of actuators. Details of implementation of low–level independent controller are shown in Fig. E.11. Parameters $k = 65$, $f_{act} = 1.5$ Hz, $f_{kc} = 2$ Hz. The knee cap controller form was chosen to be P, with parameters: $k_p = 1.2 \times 10^4$, $k_i = 0$, $k_d = 0$. Low–level coupled controller: $k_{pp} = 1.5 \times 10^{-3}$, $k_{ii} = 0$, $k_{dd} = 0$, $N_{nfilt} = 0$, $k_{kc} = 5 \times 10^{-3}$. k_{kc} was chosen so that t_s settling time of r_{err} ($|r_{err}| < 0.001$ m) is less than 5 s. r_{err} for different c_{sr} in stage 2 is depicted in Fig. 5.72. If c_{sr} is sufficiently large, no overshoot occurs. It is seen that the r_{err} settles within less than 5 s. Exact values are given in Table 5.8. Comparing with Fig. 5.56, the coupled control yields better performance of positioning r_{err}. Knee cap positioning controller of P form is sufficient to stabilise the system, and no steady–state error occurs. Control signals u_{up} and u_{low} for different c_{sr} are depicted in Fig. 5.73 and 5.74 respectively. It is seen that the signals are roughly symmetric around $u = 0$ axis. In Fig. 5.75 pressures at the actuators chambers are depicted for $c_{sr} = 6000$. In section 5.3.1 it is shown the independent control results in high forces in stage 2 with load (see Fig. 5.62). For coupled control, values of human–machine interaction force are depicted in Figs. 5.76 and 5.77, in anteriorposterior and craniocaudal axis respectively (compare with Figs. 5.60 and 5.61). In Fig. 5.78 the human–machine interaction force in sagittal plane is depicted (compare with Fig. 5.62). Decreasing c_{sr} decreases absolute interaction force. For $c_{sr} = 6000$, it is 12 N. For $c_{sr} = 500$, it is 13 N. For $c_{sr} = 250$, it is 13 N. Manipulating c_{sr} does not increase E_{Ξ} for stage 3, which is seen in Table 5.8. Comparing to Table 5.7 it is seen that E_{Ξ}, $W^{\dagger}$ and E_r improve from independent control of actuators in stage 3.

From Fig. 5.79 it is seen that for coupled control, r_{err} for stage 3 with $c_{sr} = 6000$ is comparable, slightly better, to independent control (see Fig. 5.63). The control signals are depicted in Fig. 5.80 (compare to Fig. 5.66). In Fig. 5.81 pressures at the actuators chambers are depicted for $c_{sr} = 6000$. It is seen that pressure at B chambers and A chamber synchronously squeeze and stretch the knee cap. Values of human–machine interaction force are depicted in Figs. 5.67 and 5.68, in anteriorposterior and craniocaudal axis respectively (compare with Figs. 5.67 and 5.68). In Fig. 5.69 the human–machine interaction force in sagittal plane is depicted (compare with Fig. 5.69). The absolute interaction force does not exceed 180 N.

Positioning error of rods extension for different values of c_{sr}

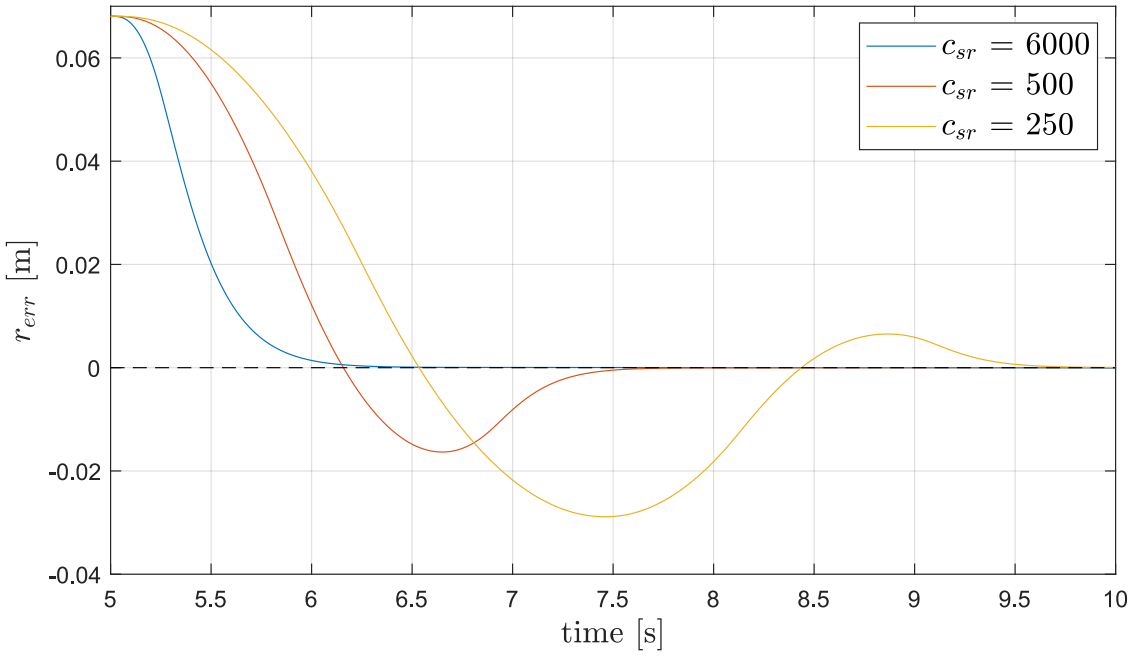

Figure 5.72: Positioning error of rods extension for coupled control of hydraulic actuators for stage 2 for varying c_{sr}. $k_{pp} = 1.5 \times 10^{-3}, k_{kc} = 5 \times 10^{-3}$. Load of 64.4 kg.

It is seen from the discussion that the coupled control given by Eq. (5.76) and Eq. (5.78) performs better on all considered cost functions in stage 2 with load, that is knee cap positioning, than independent control. There is very little difference for stage 3 with load between two control schemes.

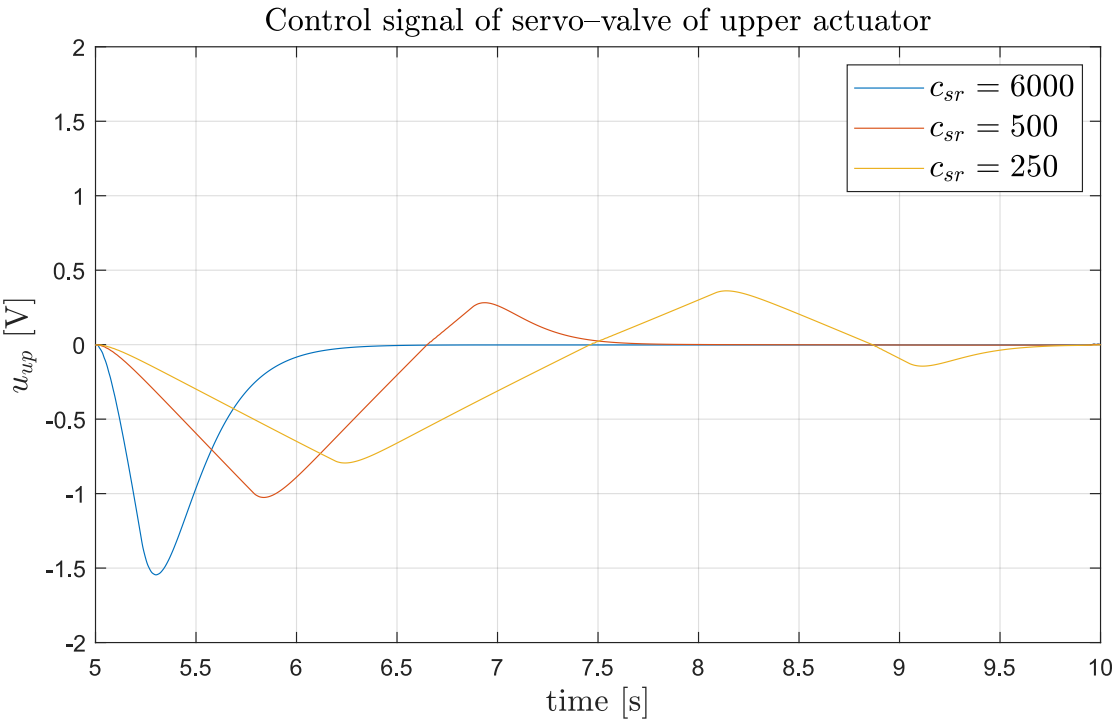

Figure 5.73: Control signal of upper actuator u_{up} in stage 2 for coupled control. $k_{pp} = 1.5 \times 10^{-3}, k_{kc} = 5 \times 10^{-3}$, $k = 65$. Load of 64.4 kg.

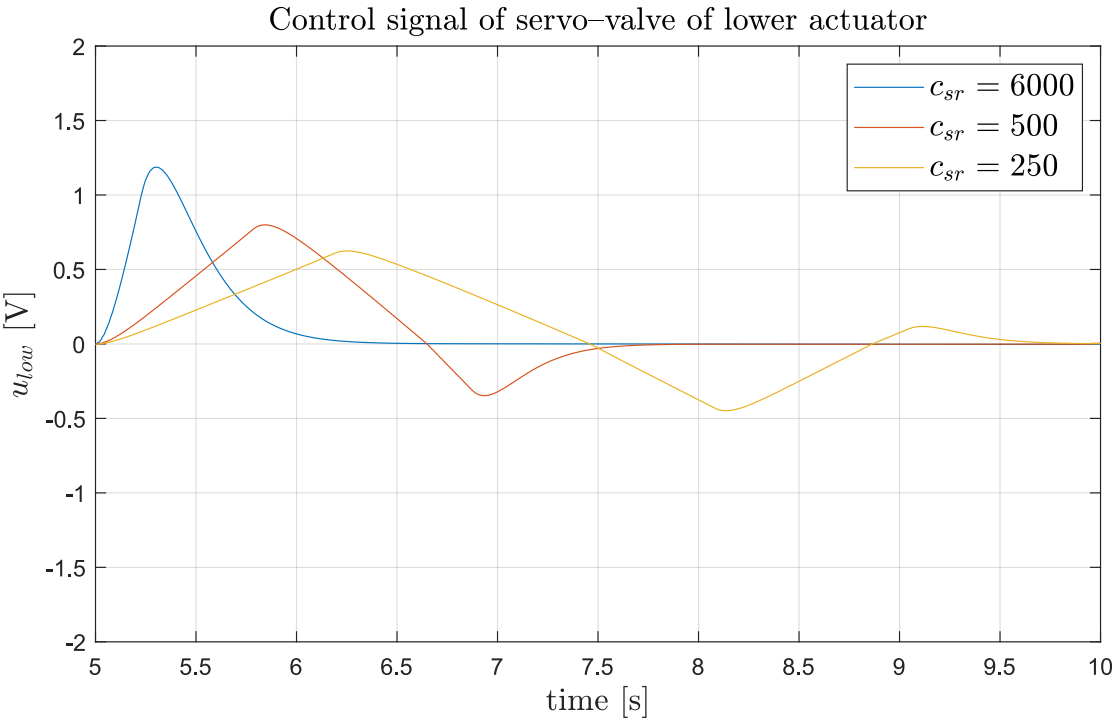

Figure 5.74: Control signal of lower actuator u_{low} in stage 2 for coupled control. $k_{pp} = 1.5 \times 10^{-3}, k_{kc} = 5 \times 10^{-3}$, $k = 65$. Load of 64.4 kg.

Table 5.8: Cost functions E_Ξ (with $\lambda = 1$), $W^\dagger$, E_r values for coupled low level control of hydraulics. $k_{pp} = 1.5 \times 10^{-3}, k_{kc} = 5 \times 10^{-3}$, $k = 65$. 64.4 kg load attached to end effector.

c_{sr}	stage	E_Ξ	$W^\dagger$ [J]	E_r	t_s [s]
6000	2	3.99×10^2	0	1.4×10^{-3}	1.06
	3	1.01×10^4	6.49×10^1	4.76×10^{-7}	–
500	2	3.77×10^2	0	2.91×10^{-3}	2.38
	3	1.01×10^4	6.49×10^1	8.77×10^{-8}	–
250	2	3.71×10^2	0	4.61×10^{-3}	4.45
	3	1.01×10^4	6.49×10^1	5.37×10^{-8}	–

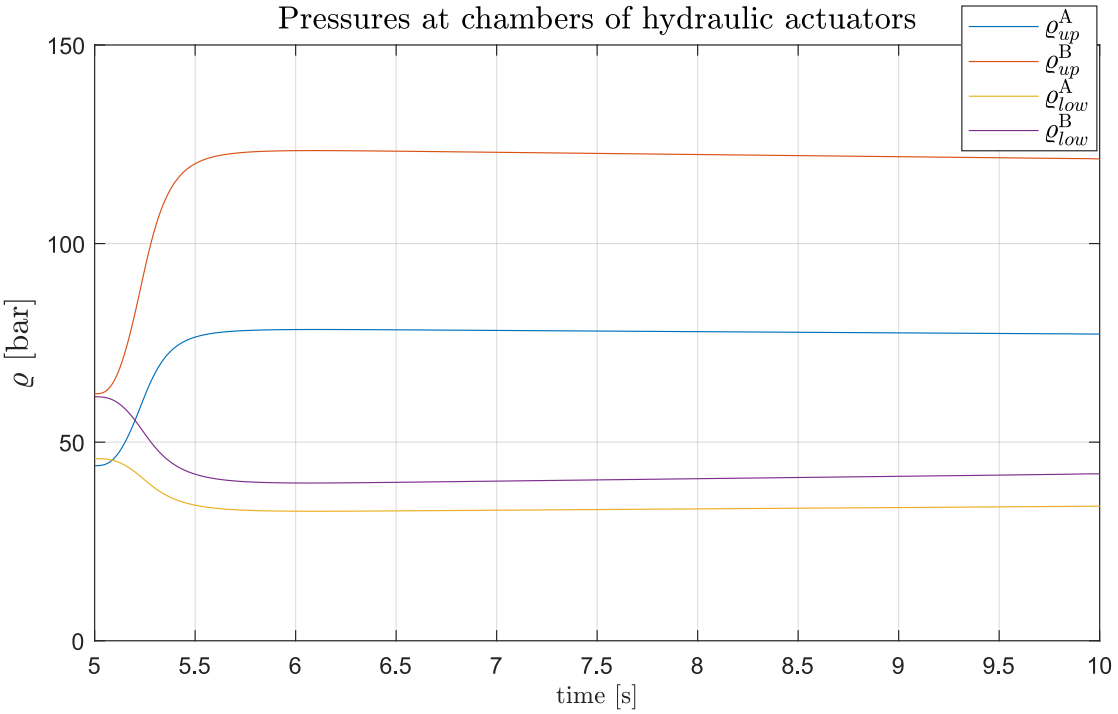

Figure 5.75: Pressures at the hydraulic cylinder chambers for coupled controller for stage 2. Load of 64.4 kg. $c_{sr} = 6000$, $k_{pp} = 1.5 \times 10^{-3}, k_{kc} = 5 \times 10^{-3}$, $k = 65$.

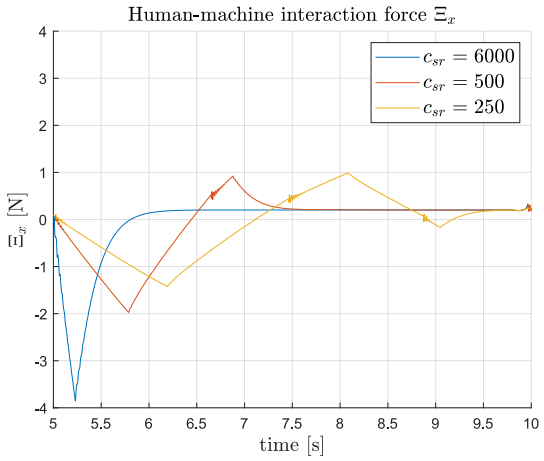

Figure 5.76: Human–machine interaction force in anteriorposterior axis for low–level coupled control in stage 2. $k_{pp} = 1.5 \times 10^{-3}, k_{kc} = 5 \times 10^{-3}, k = 65$. Load of 64.4 kg.

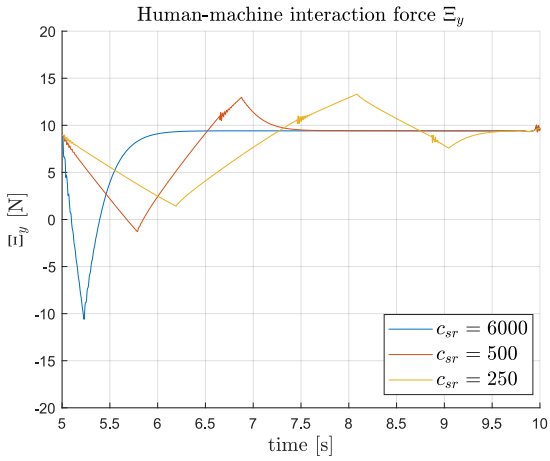

Figure 5.77: Human–machine interaction force in craniocaudal axis for low–level coupled control in stage 2. $k_{pp} = 1.5 \times 10^{-3}, k_{kc} = 5 \times 10^{-3}, k = 65$. Load of 64.4 kg.

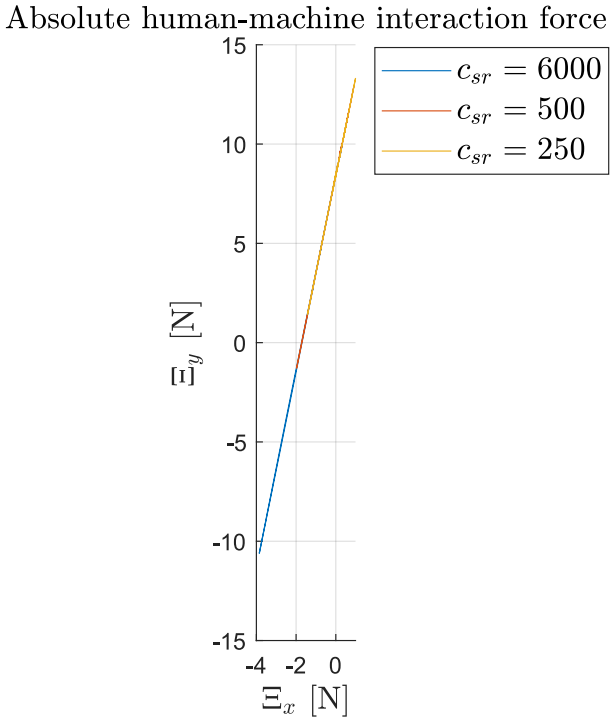

Figure 5.78: Human–machine interaction force in sagittal plane for low–level coupled control in stage 3 for varying c_{sr}. $k_{pp} = 1.5 \times 10^{-3}, k_{kc} = 5 \times 10^{-3}, k = 65$. Load of 64.4 kg.

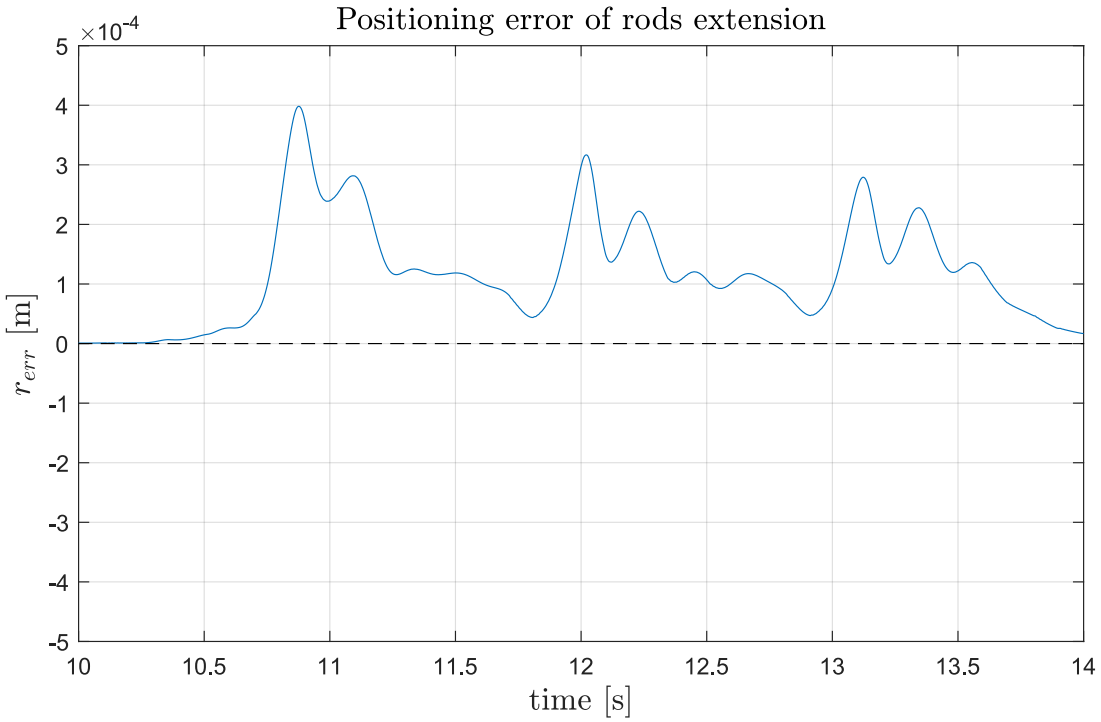

Figure 5.79: Positioning error of rods extension for coupled of hydraulic actuators for stage 3. $c_{sr} = 6000$, $k_{pp} = 1.5 \times 10^{-3}$, $k_{kc} = 5 \times 10^{-3}$. Load of 64.4 kg.

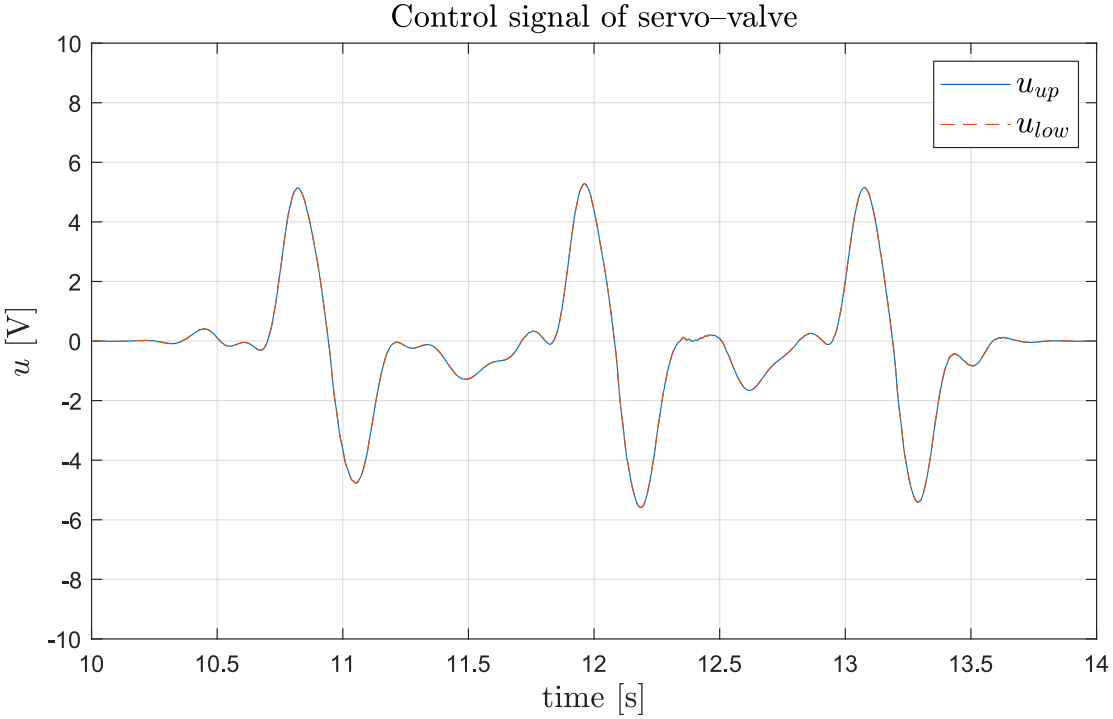

Figure 5.80: Control signal of actuatos in stage 3 for coupled control. $c_{sr} = 6000$, $k_{pp} = 1.5 \times 10^{-3}$, $k_{kc} = 5 \times 10^{-3}$, $k = 65$. Load of 64.4 kg.

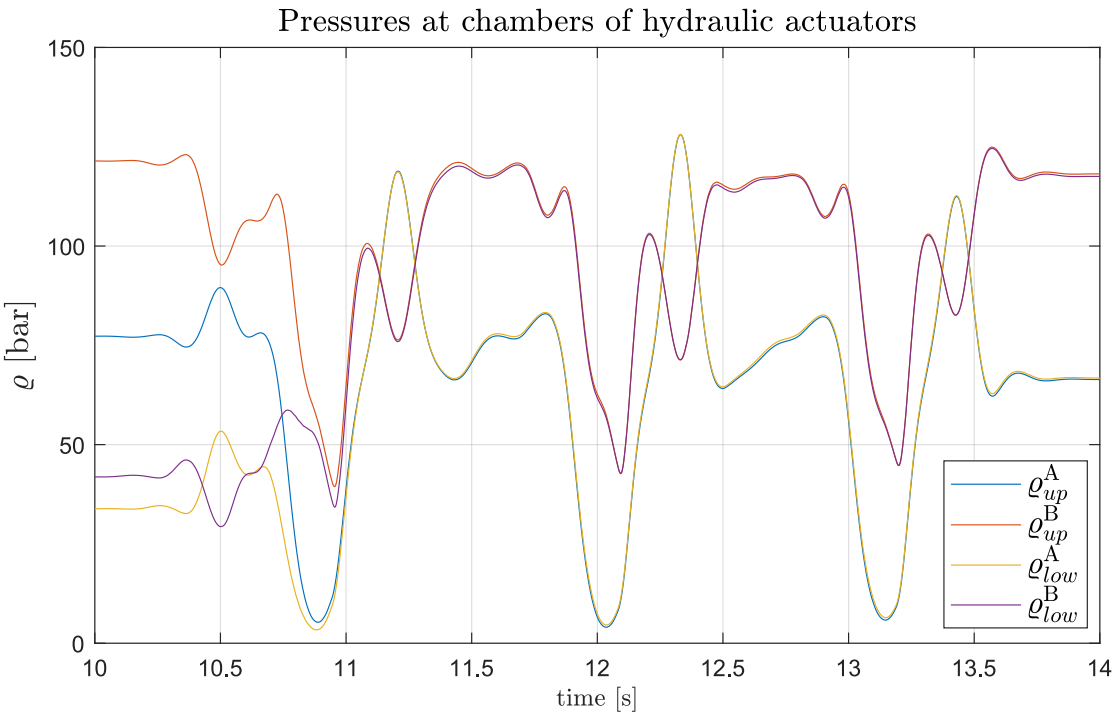

Figure 5.81: Pressures at the hydraulic cylinder chambers for coupled controller for stage 2. Load of 64.4 kg. $c_{sr} = 6000$, $k_{pp} = 1.5 \times 10^{-3}$, $k_{kc} = 5 \times 10^{-3}$, $k = 65$. Load of 64.4 kg.

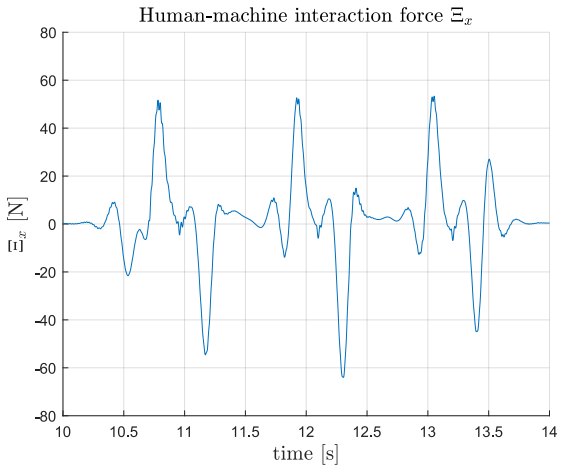

Figure 5.82: Human–machine interaction force in anteriorposterior axis for low–level coupled control in stage 3. $c_{sr} = 6000$, $k_{pp} = 1.5 \times 10^{-3}$, $k_{kc} = 5 \times 10^{-3}$, $k = 65$. Load of 64.4 kg.

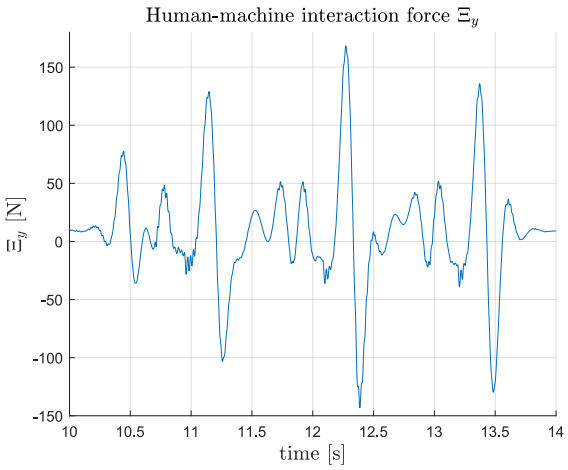

Figure 5.83: Human–machine interaction force in craniocaudal axis for low–level coupled control in stage 3. $c_{sr} = 6000$, $k_{pp} = 1.5 \times 10^{-3}$, $k_{kc} = 5 \times 10^{-3}$, $k = 65$. Load of 64.4 kg.

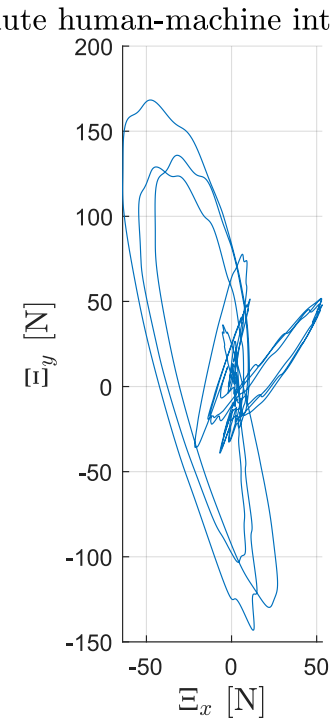

Figure 5.84: Human–machine interaction force in sagittal plane for low–level coupled control in stage 3. $c_{sr} = 6000$, $k_{pp} = 1.5 \times 10^{-3}$, $k_{kc} = 5 \times 10^{-3}$, $k = 65$. Load of 64.4 kg.

5.3.3 Selection of Parameters of Coupled Controller

Selection of k_{kc} to adjust settling time of r_{err} to satisfactory value (the higher k_{kc}, the shorter settling time) was done. Choosing c_{sr} to decrease Ξ in stage 2 was described and shown on an example using simulation results in section 5.3.2. The problem of finding controller gains in Eq. (5.77) still exists. The discussion will be limited only to k_{pp}, taking $k_{ii} = 0$, $k_{dd} = 0$, $N_{nfilt} = 0$. From Eqs. (5.72) and (5.74) it is seen that a hydraulic actuator is a plant of integrating type. Setting k_{ii} to non–zero might delay response or in worst case destabilise the plant (induce oscillations of Ξ). Since the plant is of integrating type, setting k_{dd} non–zero might improve the tracking of a reference value. However, it is shown that controller behaves reasonably well without derivative portion of the controller. Continuous variable k_{pp} was discretised, and exhaustive search was performed on it. For varying discrete value of k_{pp}, values of cost functions E_{Ξ}, $W_{\dagger}$, E_r were calculated for stage 3 without and with load, as well as E_{Ξ} in stage 2. Parameters were chosen: $k = 65$, $f_{act} = 1.5$ Hz, $f_{kc} = 2$ Hz, $c_{sr} = 6000$. The knee cap controller form was chosen again to be P, with parameters: $k_p = 1.2 \times 10^4$, $k_i = 0$, $N_{filt} = 12865$, $k_{kc} = 5 \times 10^{-3}$. In Fig. 5.85 value of E_{Ξ} in stage 2 given as function of selection parameter k_{pp} is depicted. It is seen that for certain range value of E_{Ξ} is relatively flat and low. The considered range is about $k_{pp} \in [0.5 \times 10^{-3}, 1.8 \times 10^{-3}]$ for case with and wioutht load. For $k_{pp} \leq 0.5 \times 10^{-3}$ the value of the cost function increases, the control signal is too small to track reference signal of demanded force from the actuators $\tilde{F}^{dem}_{act\ up}$. On the other hand, too large value of k_{pp} causes $F_{act\ up}$ to oscillate in simulation, loosing asymptotic stability. With load there is a minimum of $E_{\Xi} = 3.77 \times 10^2$ for $k^*_{pp} = 1.4 \times 10^{-3}$. Without load there is a minimum of $E_{\Xi} = 7.01 \times 10^1$ for $k^*_{pp} = 1.5 \times 10^{-3}$. In Fig. 5.86 value of E_{Ξ} in stage 3 given as function of selection parameter k_{pp} is depicted. The range where values are low is $k_{pp} \in [0.5 \times 10^{-3}, 2.3 \times 10^{-3}]$, which is superset of values for stage 2. With load there is a minimum of $E_{\Xi} = 8.93 \times 10^3$ for $k^*_{pp} = 2.3 \times 10^{-3}$. Without load there is a minimum of $E_{\Xi} = 1.45 \times 10^3$ for $k^*_{pp} = 2.3 \times 10^{-3}$. In Fig. 5.87 value of $W^{\dagger}$, given as function of selection parameter k_{pp}, is depicted. It is seen that the respective minima of cost function for case without and with load are the same as for E_{Ξ} in stage 3, that is in range $k_{pp} \in [0.5 \times 10^{-3}, 2.3 \times 10^{-3}]$. With load there is a minimum of $W^{\dagger} = 5.8 \times 10^1$ for $k^*_{pp} = 2.3 \times 10^{-3}$. Without load there is a minimum of $W^{\dagger} = 2.68 \times 10^1$ for $k^*_{pp} = 2.3 \times 10^{-3}$. In Fig. 5.88 value of E_r given as function of selection parameter k_{pp} is depicted. It is seen that for $k_{pp} \leq 2.5 \times 10^{-3}$ the value of E_r in stage 2 does not change much, and is close to minimal value. For $k_{pp} > 2.5 \times 10^{-3}$ it grows. The conclusion is that the best performance of the controller

Table 5.9: Cost functions E_Ξ (with $\lambda = 1$), $W^\dagger$, E_r values for coupled control of hydraulics, no load. $k = 65$, $f_{act} = 1.5$ Hz, $c_{sr} = 5 \times 10^2$, $f_{kc} = 2$ Hz, $k_{kc} = 5 \times 10^{-3}$.

stage	E_Ξ	$W^\dagger$ [J]	E_r
2	9.23×10^1	0	1.2×10^{-3}
3	3.17×10^3	3.89×10^1	1.03×10^{-6}

is for $k_{pp} \in [0.5 \times 10^{-3}, 1.8 \times 10^{-3}]$. In section 5.3.2 the solutions for manually chosen $k_{pp} = 1.5 \times 10^{-3}$ are shown, which is in considered range.

Performance of the controller with $k_{pp} = 1.5 \times 10^{-3}$ with load was shown in section 5.3.2. It is interesting to investigate its performance for case without any load. In Table 5.9 values of cost functions are shown (compare with Table 5.6). E_r improves in stage 2 and stage 3. r_{err} for stage 2 is depicted in Fig. 5.89. Comparing with Fig. 5.42, the coupled control yields better performance of positioning r_{err}. Control signals are depicted in Fig. 5.90. It is seen that the signals are roughly symmetric around $u = 0$ axis. In Fig. 5.91 pressures at the actuators chambers are depicted for $c_{sr} = 6000$. Values of human–machine interaction force are depicted in Figs. 5.92 and 5.93, in anteriorposterior and craniocaudal axis respectively (compare with Figs. 5.46 and 5.47). In Fig. 5.94 the human–machine interaction force in sagittal plane is depicted (compare with Fig. 5.48). For $c_{sr} = 6000$, it is 825 N. It is seen that the interaction force increases in stage 2, but it can be regulated by changing c_{sr}

From Fig. 5.95 it is seen that for coupled control, r_{err} for stage 3 with $c_{sr} = 6000$ is smaller than for independent control (see Fig. 5.49). The control signals are depicted in Fig. 5.96 (compare to Fig. 5.52). In Fig. 5.97 pressures at the actuators chambers are depicted for $c_{sr} = 6000$. It is seen that pressure at B chambers and A chamber synchronously squeeze and stretch the knee cap. Values of human–machine interaction force are depicted in Figs. 5.98 and 5.98, in anteriorposterior and craniocaudal axis respectively (compare with Figs. 5.53 and 5.54). In Fig. 5.100 the human–machine interaction force in sagittal plane is depicted (compare with Fig. 5.55). The absolute interaction force does not exceed 95 N. The interaction force are slightly increased, hence increase in E_Ξ and $W^\dagger$ for stage 3.

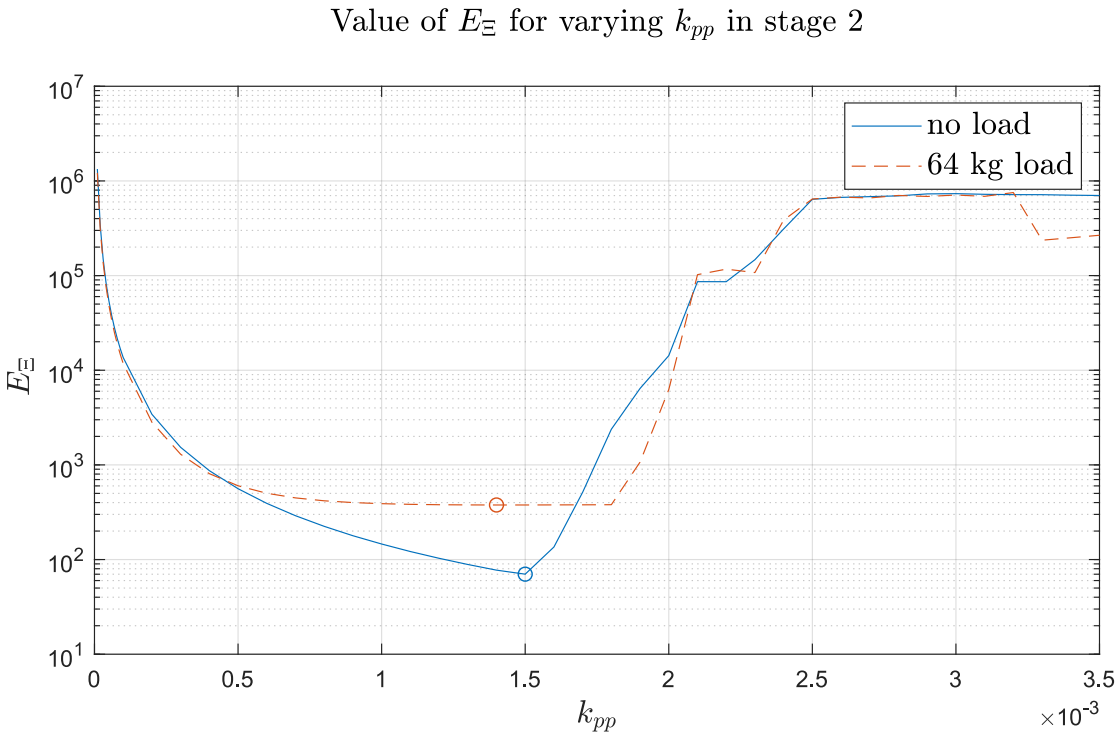

Figure 5.85: Value of E_Ξ as function of k_{pp} for stage 2. $k = 65$, $f_{act} = 1.5$ Hz, $c_{sr} = 5 \times 10^2$, $f_{kc} = 2$ Hz, $k_{kc} = 5 \times 10^{-3}$. Blue – with load of 64.4 kg, red – no load. With load: minimum of $E_\Xi = 3.77 \times 10^2$ for $k^*_{pp} = 1.4 \times 10^{-3}$. Without load: minimum of $E_\Xi = 7.01 \times 10^1$ for $k^*_{pp} = 1.5 \times 10^{-3}$.

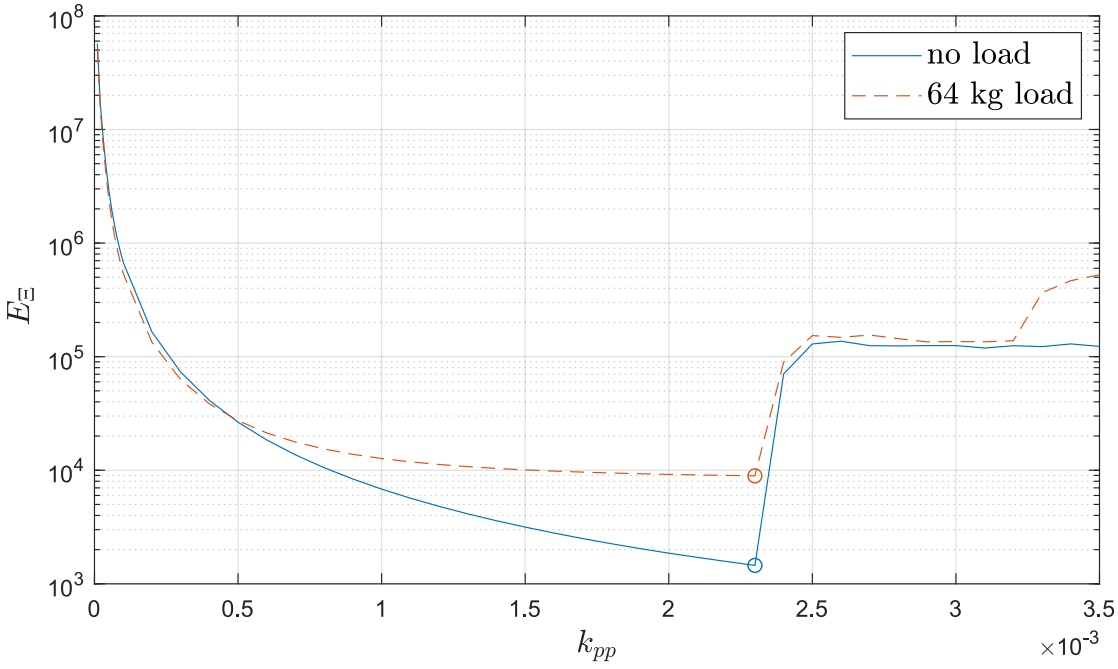

Figure 5.86: Value of E_Ξ as function of k_{pp} for stage 3. $k = 65$, $f_{act} = 1.5$ Hz, $c_{sr} = 5 \times 10^2$, $f_{kc} = 2$ Hz, $k_{kc} = 5 \times 10^{-3}$. Blue – with load of 64.4 kg, red – no load. With load: minimum of $E_\Xi = 8.93 \times 10^3$ for $k^*_{pp} = 2.3 \times 10^{-3}$. Without load: minimum of $E_\Xi = 1.45 \times 10^3$ for $k^*_{pp} = 2.3 \times 10^{-3}$.

Value of $W^{\dagger}$ for varying k_{pp} in stage 3

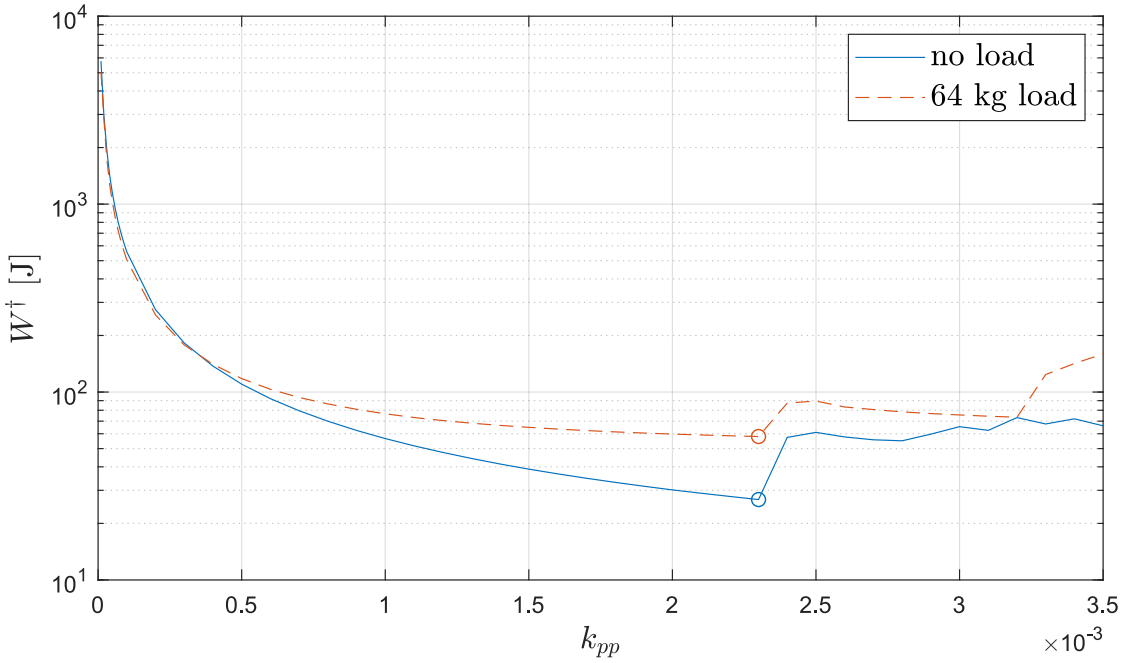

Figure 5.87: Value of $W^{\dagger}$ as function of k_{pp} for stage 3. $k = 65$, $f_{act} = 1.5$ Hz, $c_{sr} = 5 \times 10^2$, $f_{kc} = 2$ Hz, $k_{kc} = 5 \times 10^{-3}$. Blue – with load of 64.4 kg, red – no load. With load: minimum of $W^{\dagger} = 5.8 \times 10^1$ for $k^*_{pp} = 2.3 \times 10^{-3}$. Without load: minimum of $W^{\dagger} = 2.68 \times 10^1$ for $k^*_{pp} = 2.3 \times 10^{-3}$.

Value of E_r for varying k_{pp} in stage 3

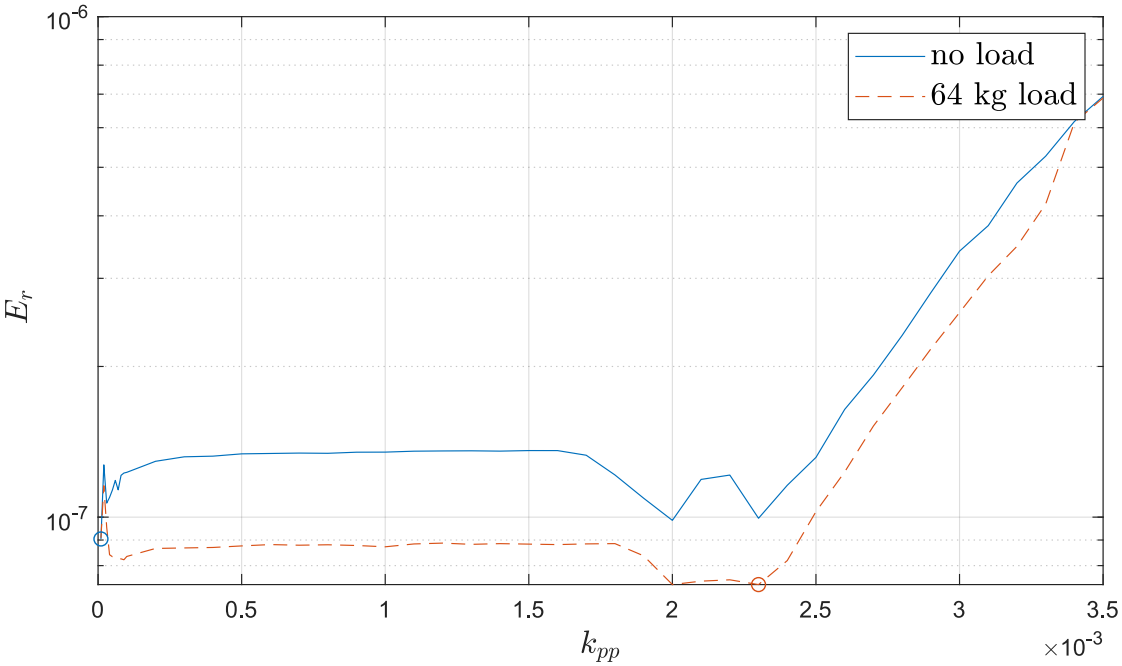

Figure 5.88: Value of E_r as function of k_{pp} for stage 3. $k = 65$, $f_{act} = 1.5$ Hz, $c_{sr} = 5 \times 10^2$, $f_{kc} = 2$ Hz, $k_{kc} = 5 \times 10^{-3}$. Blue – with load of 64.4 kg, red – no load.

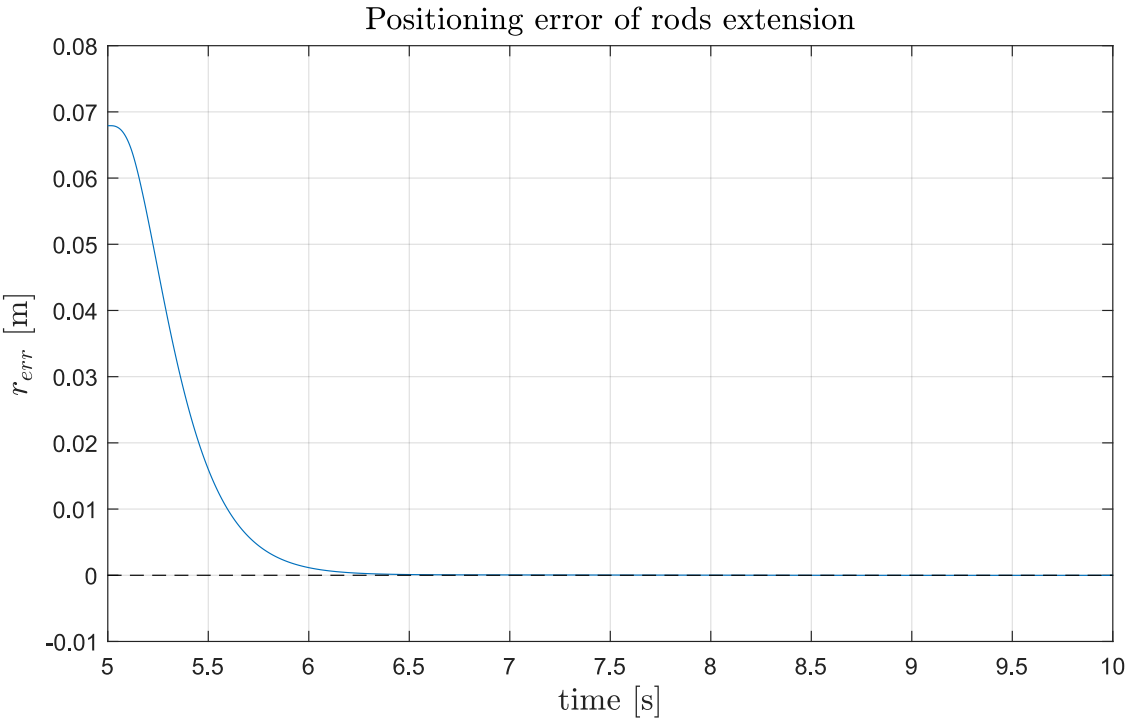

Figure 5.89: Positioning error of rods extension for coupled of hydraulic actuators for stage 2. No load. $c_{sr} = 6000$, $k_{pp} = 1.5 \times 10^{-3}$, $k_{kc} = 5 \times 10^{-3}$, $k = 65$.

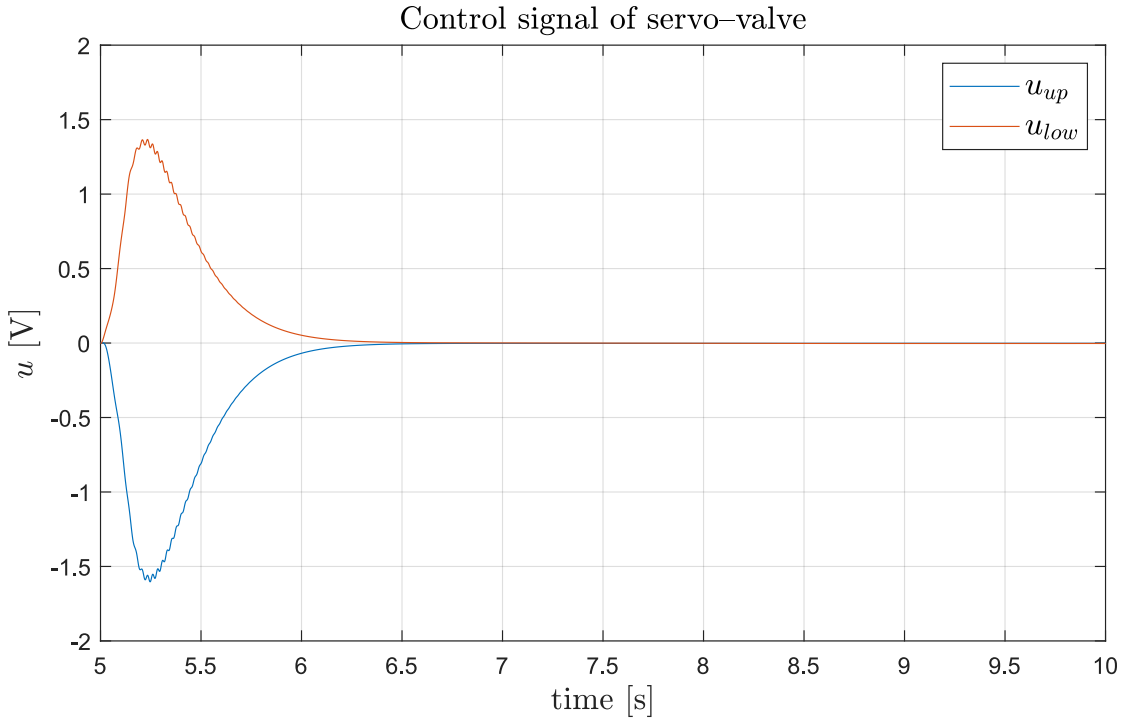

Figure 5.90: Control signal u of actuators in stage 2 for coupled control. No load. $c_{sr} = 6000$, $k_{pp} = 1.5 \times 10^{-3}$, $k_{kc} = 5 \times 10^{-3}$, $k = 65$.

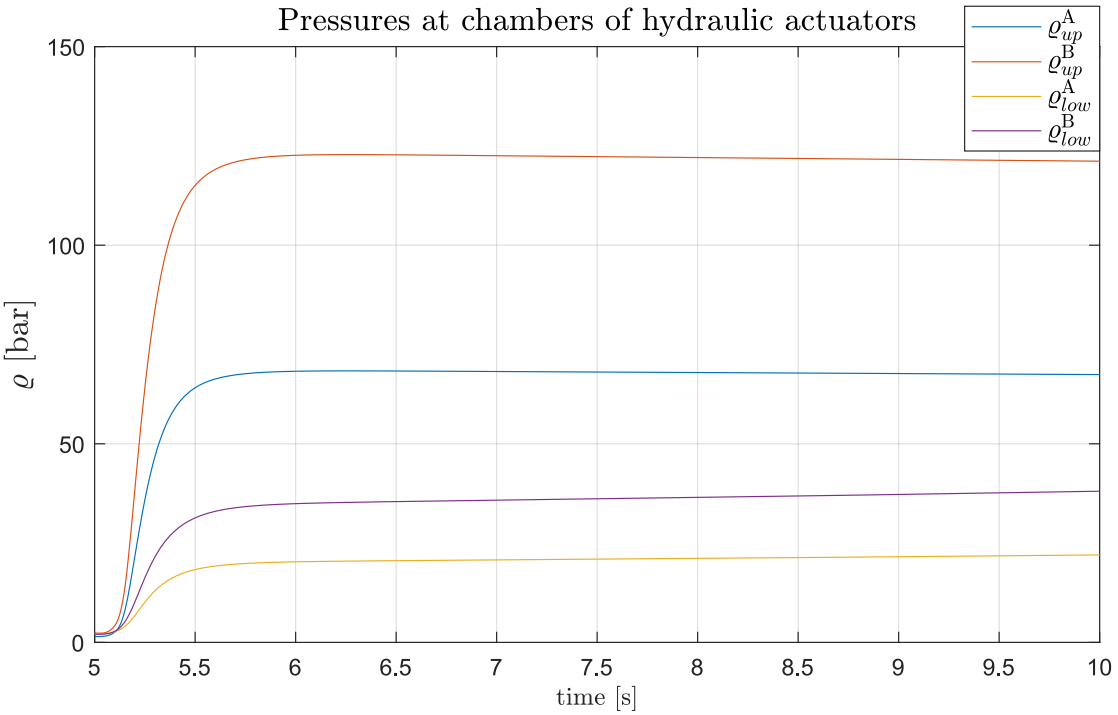

Figure 5.91: Pressures at the actuator chambers at stage 2 for $c_{sr} = 6000$. No load. $k_{pp} = 1.5 \times 10^{-3}$, $k_{kc} = 5 \times 10^{-3}$, $k = 65$.

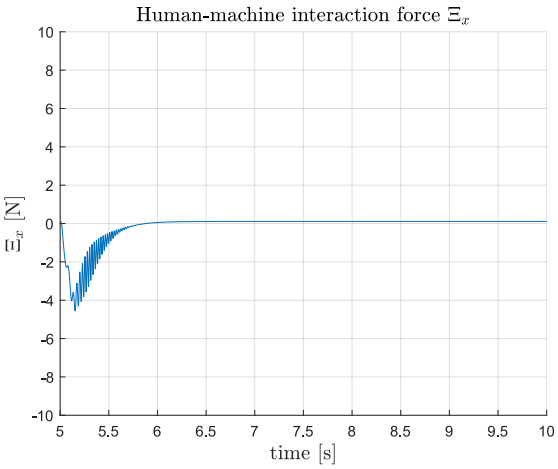

Figure 5.92: Human–machine interaction force in anteriorposterior axis for low–level coupled control in stage 2. No load.

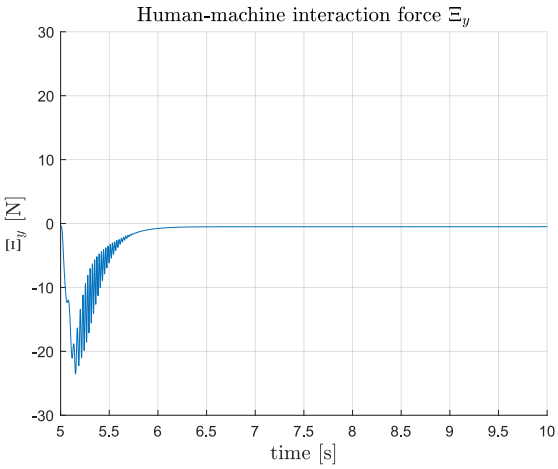

Figure 5.93: Human–machine interaction force in craniocaudal axis for low–level coupled control in stage 2. No load.

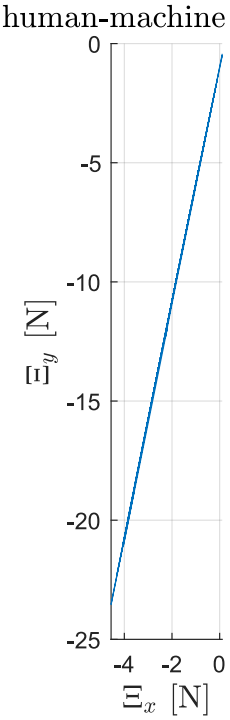

Figure 5.94: Human–machine interaction force in sagittal plane for low–level coupled control in stage 2. No load. $c_{sr} = 6000$, $k_{pp} = 1.5 \times 10^{-3}$, $k_{kc} = 5 \times 10^{-3}$, $k = 65$

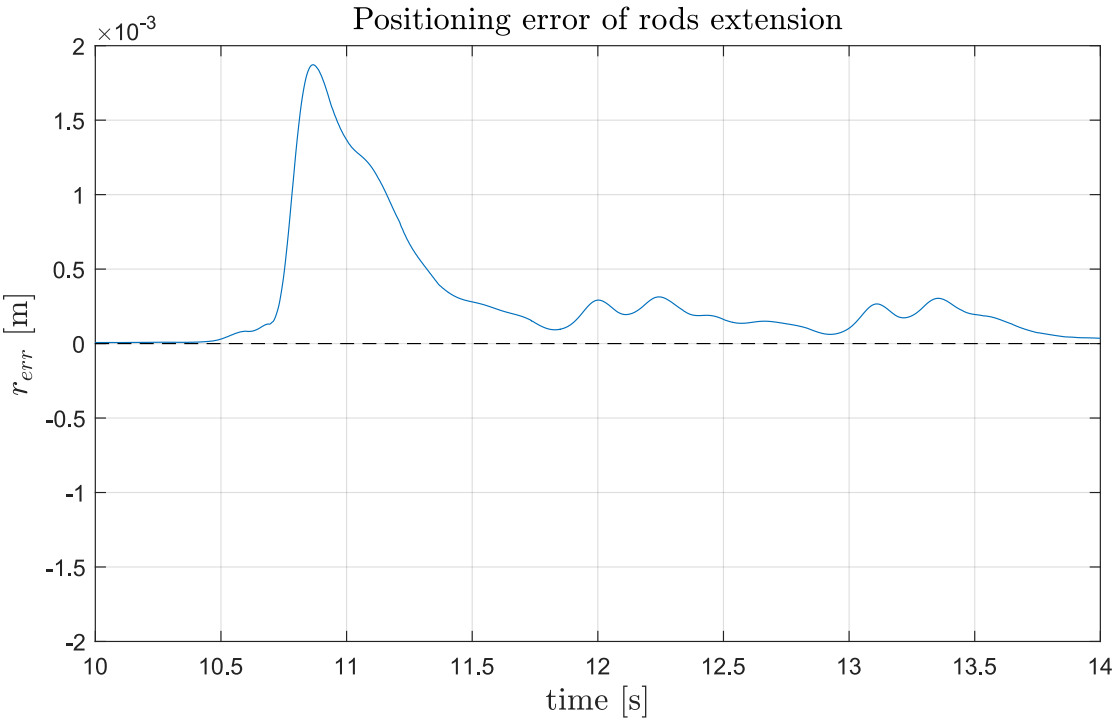

Figure 5.95: Positioning error of rods extension for coupled of hydraulic actuators for stage 3. No load. $c_{sr} = 6000$, $k_{pp} = 1.5 \times 10^{-3}$, $k_{kc} = 5 \times 10^{-3}$, $k = 65$.

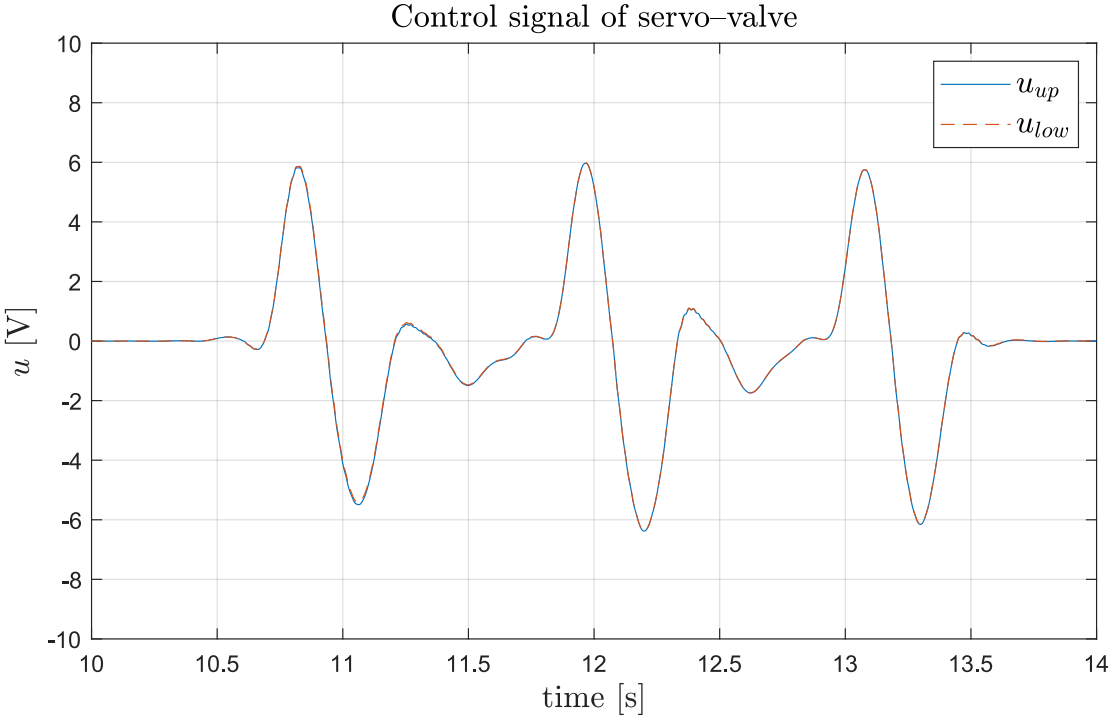

Figure 5.96: Control signal of actuators in stage 3 for coupled control. No load. $c_{sr} = 6000$, $k_{pp} = 1.5 \times 10^{-3}$, $k_{kc} = 5 \times 10^{-3}$, $k = 65$.

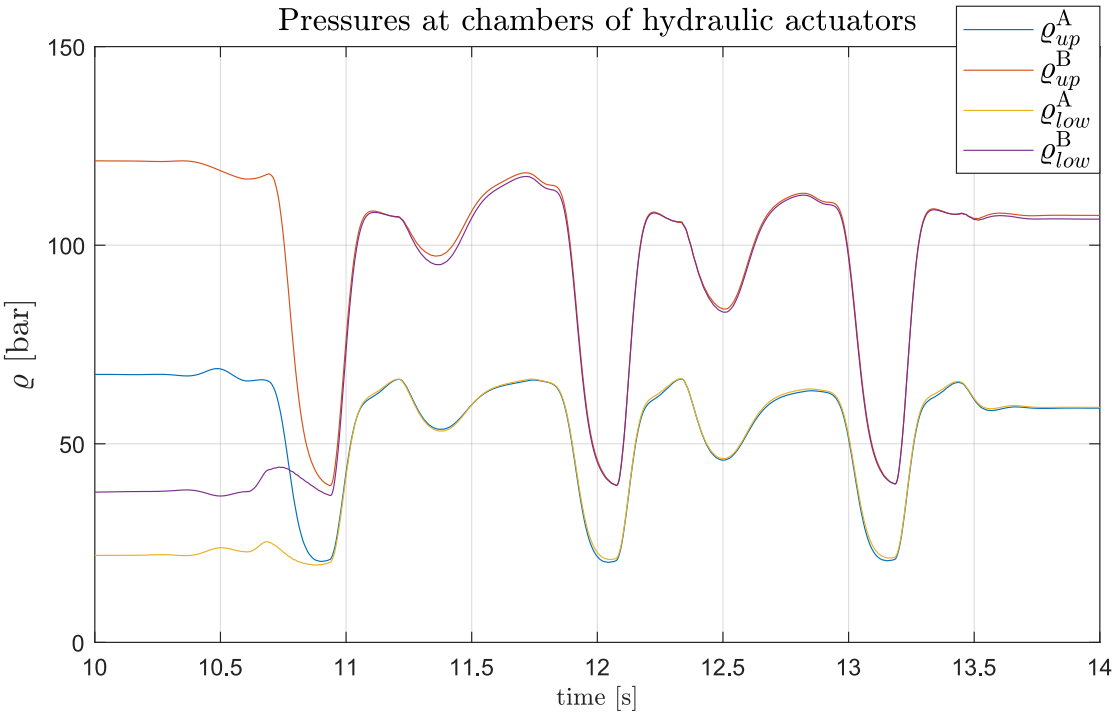

Figure 5.97: Pressure at actuator chambers for stage 3. No load. $c_{sr} = 6000$, $k_{pp} = 1.5 \times 10^{-3}$, $k_{kc} = 5 \times 10^{-3}$, $k = 65$.

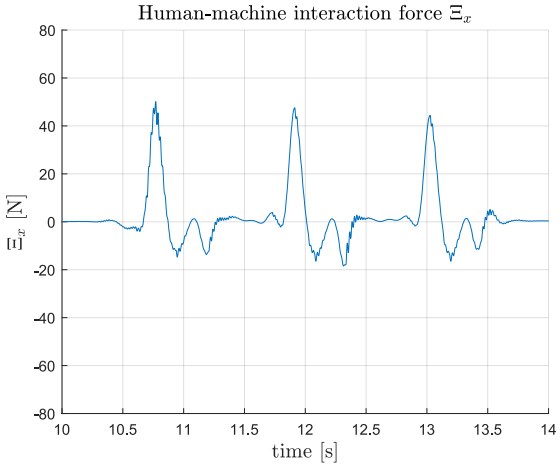

Figure 5.98: Human–machine interaction force in anteriorposterior axis for low–level coupled control in stage 3. No load.

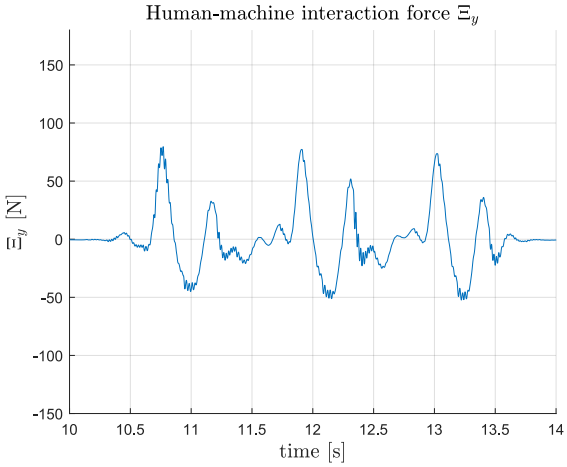

Figure 5.99: Human–machine interaction force in craniocaudal axis for low–level coupled control in stage 3. No load.

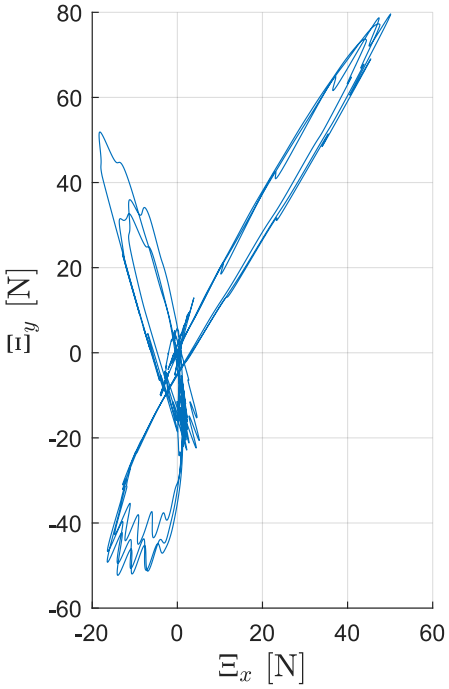

Figure 5.100: Human–machine interaction force in sagittal plane for low–level coupled control in stage 3. No load. $c_{sr} = 6000$, $k_{pp} = 1.5 \times 10^{-3}$, $k_{kc} = 5 \times 10^{-3}$, $k = 65$.

5.4 Summary

A cost function E_{Ξ}, which minimisation yields decrease of human–machine interaction force was proposed. Its relationship to total exchange of energy $W^{\dagger}$ was shown. Each proposed step in controller design was evaluated using the cost functions. First, the middle level control was proposed. For that purpose a model of the joint was built in Matlab using Simscape. Additional joint at the place of the hip was added. It was shown that proposed gravity cancellation scheme, which is open loop control, reduces both E_{Ξ} and $W^{\dagger}$. Next, human–machine interaction force feedback was introduced, and it was shown that it decreases E_{Ξ} and $W^{\dagger}$ further. A control scheme for inclusion of knee cap positioning was proposed. PD controller for knee cap exhibits steady–stead error, while controller of P and PI form are unstable. Full PID controller must be used if actuators are assumed to be ideal, that is instantly reproducing demanded force. Inclusion of knee cap positioning controller increases E_{Ξ} and $W^{\dagger}$ slightly, but the Ξ human–machine interaction force (which can be reduced with increase of k), can be chosen to be sufficiently low, meeting biomechanical constraints. E_r cost function for knee cap positioning performance was introduced. In the next step, hydraulic actuators were modelled using Simulink Hydraulics to make performance of the simulation closer to the real machine. In the first approach, independent P control for each hydraulic actuator was evaluated. Corresponding graphs were drawn and values of cost functions were calculated. It is shown that in 2 stage, that is knee cap positioning the performance deteriorates compared to ideal actuators. PD controller was used, as after including model of hydraulics it is sufficient to stabilise the knee cap and reduce steady–state error. A case with disturbance in form of load was simulated for reference. It exhibits high Ξ force in stage 2. For stage 3, that is following gait, the Ξ does not exceed 180 N for case with load. To alleviate the problem of high interaction forces, a coupled control law for two hydraulic actuators was proposed. It has an advantage of not requiring second load cell and instrumentation, reducing both cost and device size. Its simulation in stage 2 with load demonstrates superior performance: settling time of r_{err} (rods positioning error) is decreased to less than 5 s. Settling time can be regulated by changing gain k_{kc} in portion of low level controller responsible for knee cap positioning. The maximum absolute value of Ξ can be controlled by adjustment of the c_{sr}, maximum absolute slew rate of increase of control signal pertaining to knee cap positioning. Performance in stage 3 with load is comparable to independent control for each actuator. The system was subject of parametric selection, varying parameter being k_{pp}, that is gain of force minimisation portion of low level controller. It is shown

that manually found $k_{pp} = 1.5 \times 10^{-3}$ is in low range of $[0.5 \times 10^{-3}, 1.8 \times 10^{-3}]$, where E_{Ξ} and $W^{\dagger}$ have their minima. For the chosen k_{pp} the system with no load was simulated. It is shown that in stage 2 knee cap positioning performance does not deteriorate, and Ξ can be controlled by adjustment of c_{sr} parameter. In stage 3 however, E_{Ξ} and $W^{\dagger}$ increase slightly, but not as significantly as to make the device inoperable.

Chapter 6

Experimental Results and Validation

6.1 Introduction

The middle level algorithm described in section 5.2.5 with low level coupled controller (described in section 5.3.2) was implemented using LabView on MyRIO (described in section 4.6). The novel design of prototype with two opposing actuators connected with a knee cap, described in chapter 4 was used. In first approach, conservative settings of the controller were used. Extra care had to be taken because of high forces occurring in the prototype. The joint has only one degree of freedom. Its upper link is vertically attached to the test frame. θ_1 in Fig. 5.1 is constant. θ_2 is varying. A static test was performed on the controller in the setup with a robotic knee attached in parallel. Next, a dynamic test, where an operator displaces the joint with 60 kg load attached to it, was conducted.

6.2 Static Evaluation of the Controller

To test the control algorithm, in the first approach, the robotic knee (see Figure 6.1) connected in parallel to the joint prototype was displaced with steps of 10 deg. No load is attached to the joint. Parameters of the controller were chosen to be as in Table 6.1. The measured range of joint angular displacement (θ_2) is $[-14, -87.275]$ deg. The absolute angular displacement is 73.275 deg. For the experiment, displacement at the exoskeleton knee joint is shown in Fig. 6.2. It is seen that the joint follows. Unfortunately, for chosen setting $k = 16$, the robotic knee was not able to generate enough torque to lift, so maximum flexion is about -70 deg. The extra force is required because of cushioning in hydraulic cylinder. Frequency characteristic of signal depicted

Table 6.1: Values of parameters for static experiment of prototype controller.

parameter	value	unit	Eq. reference
k	16	–	(5.26)
k_p	10000	N/m	(5.46)
f_{act}	1.5	Hz	(5.44)
k_{pp}	1×10^{-3}	V/N	(5.76)
k_{kc}	5×10^{-3}	V/N	(5.78)
c_{sr}	1667	EGU/s	(5.45)

in Fig. 6.2 is shown in Fig. 6.3. The signal is slow and can be considered to be static during interval between events of movement. From Fig. 6.4 it is seen that the bandwidth of motion (99% of signal power, see section 4.4) is less than 0.01 Hz. This is much below required bandwidth of 10 Hz for gait. In Fig. 6.5 extension of rods of upper and lower actuators is depicted. It is seen that they extend synchronously. There is a misalignment for full extension, which is related to force due to cushioning of the cylinder when the rod approaches stop. When the joint is flexed, although it is seen that controller tries to compensate, the misalignment is larger. It is advisable to increase k_{kc} gain. Slew rate of rods misalignment compensating signal is limited using LabView PID Output Rate Limiter VI[1]. The value is set to 1667 EGU/s (see c_{sr} in Eq. (5.45)). In Figure 6.6 control signal of upper and lower actuator are depicted. It is seen that when no movement occurs, the signals are non–zero. Comparing to simulations where internal leakage is zero, it is seen from Figs. 5.73 and 5.73 that this is different. Most probable cause is internal leakage inside hydraulic cylinders forcing the controller to compensate. During movement there are signal spikes to cause rods extension/retraction. Compare with Fig. 5.80.

Human–machine interaction force Ξ in Eq. (5.22) is expressed in base frame FoR0 as shown in Fig. 6.7. The readings from 6 DoF Force/Torque sensor (described in section 4.5) are expressed in local frame of reference of the sensor. To find vector Ξ first a force in frame FoR2 must be found using:

$$\Xi^{\mathrm{FoR2}} = \Omega^{\mathrm{FoR2}}_{\mathrm{FoRL}}\, \Xi^{\mathrm{FoRL}} \tag{6.1}$$

where Ξ^{FoR2} – interaction force in FoR2, $\Xi^{\mathrm{FoRL}} = \left[\Xi^{\mathrm{FoRL}}_x \; \Xi^{\mathrm{FoRL}}_y\right]^\top$ – readings from the sensor in local frame, $\Omega^{\mathrm{FoR2}}_{\mathrm{FoRL}}$ – rotation matrix from local frame to FoR2 by a constant

[1] http://zone.ni.com/reference/en-XX/help/371361R-01/lvpid/pidoutratelimit/

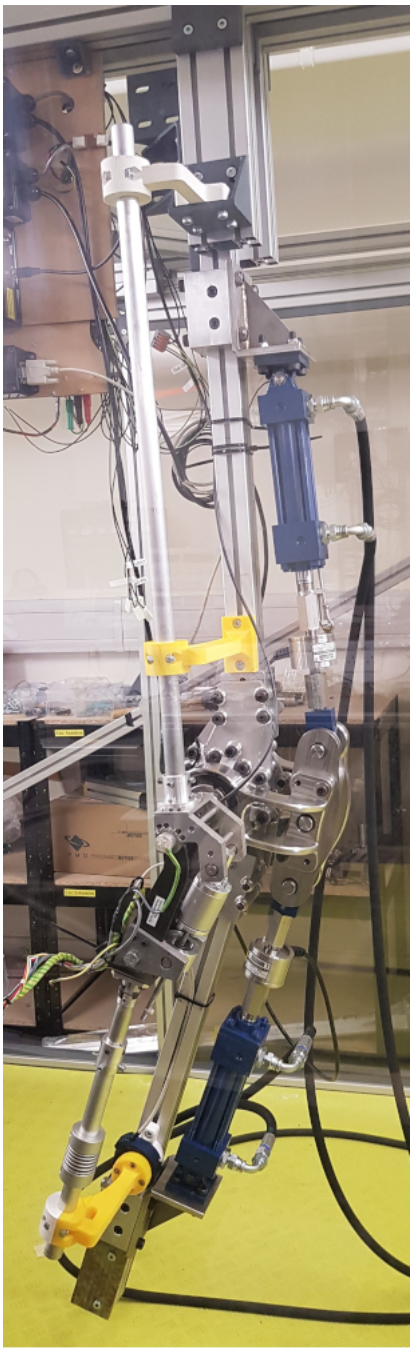

Figure 6.1: Joint prototype with a robotic knee attached in parallel.

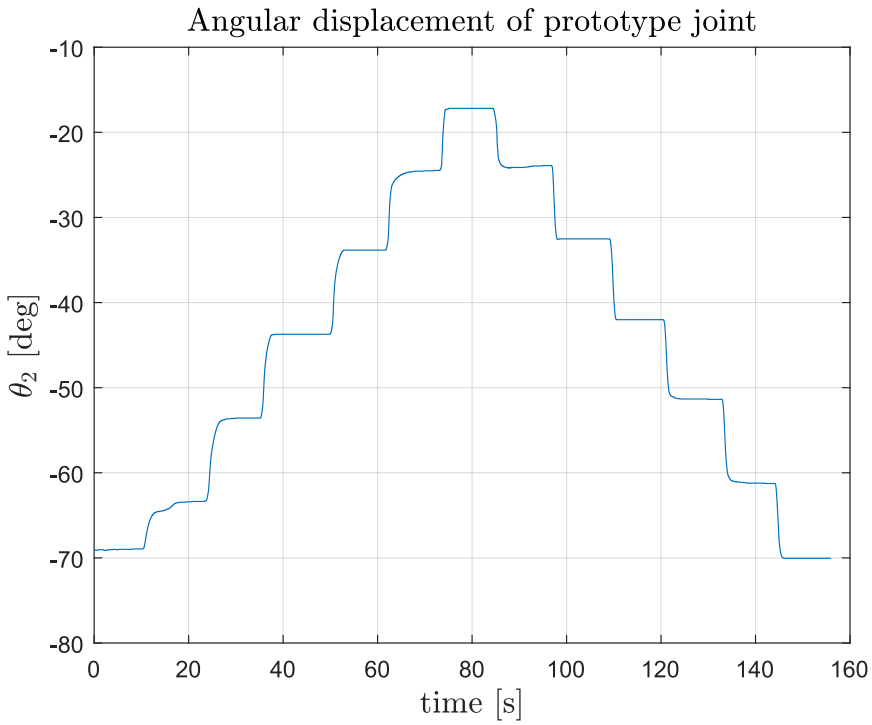

Figure 6.2: Displacement at the joint measured by the encoder, following robotic knee. Parameters, $k_{pp} = 1 \times 10^{-3}$, $k_p = 10000$, $k_{kc} = 5 \times 10^{-3}$, $k = 16$, f_{act} =1.5 s, $H_{act}(s) = 1$.

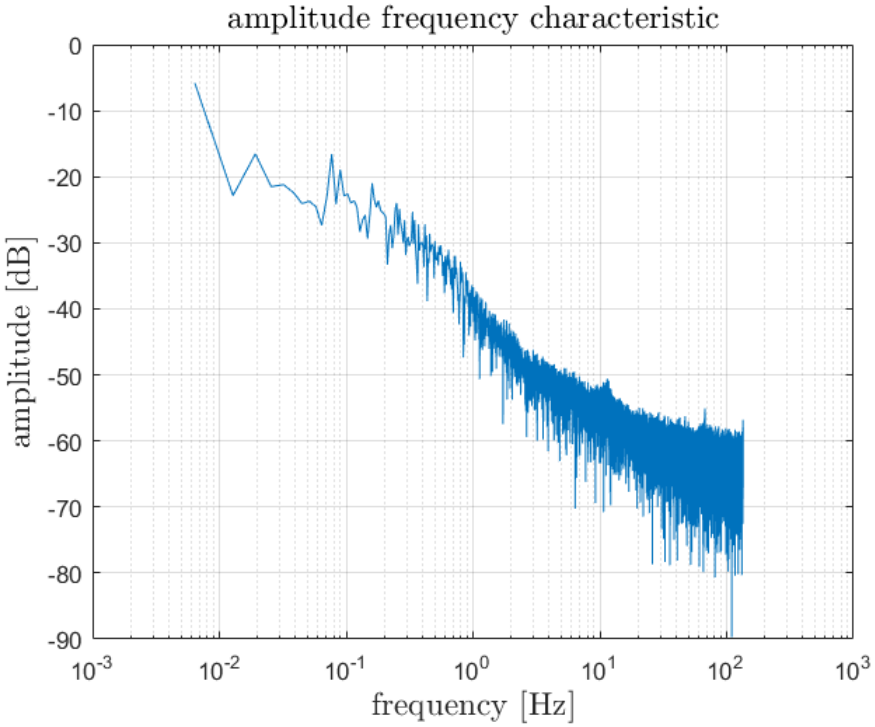

Figure 6.3: Frequency characteristic of displacement at the joint from Fig. 6.2.

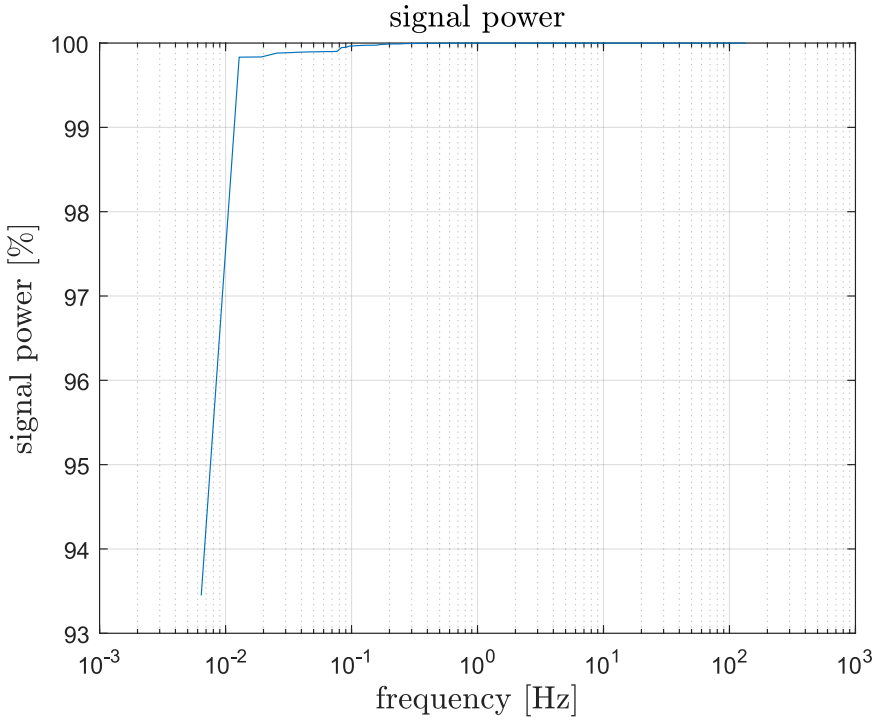

Figure 6.4: Signal power of displacement at the joint from Fig. 6.2.

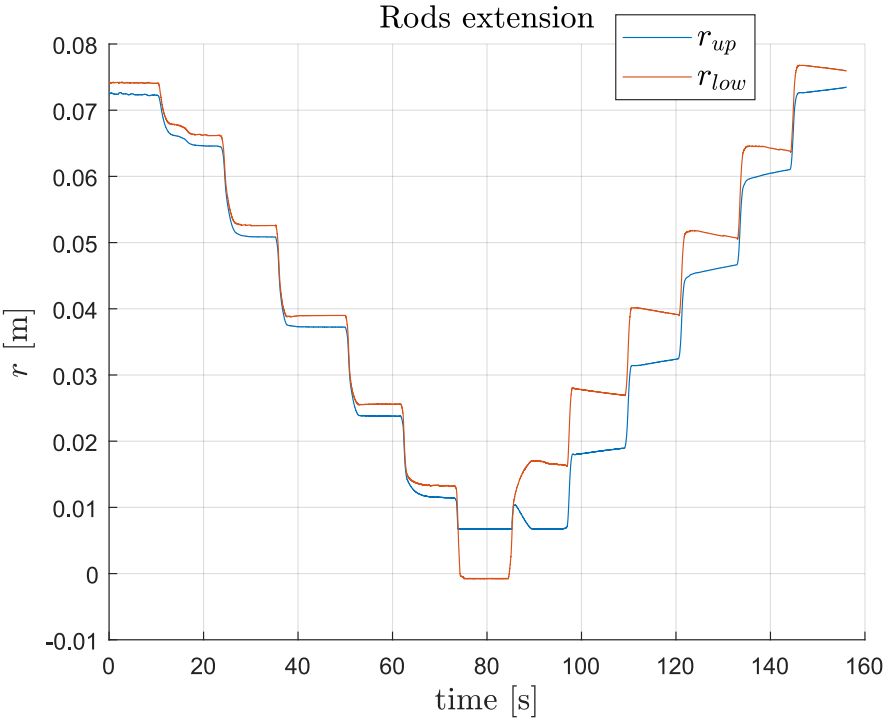

Figure 6.5: Extension of rods of hydraulic actuators for displacement at the joint from Fig. 6.2.

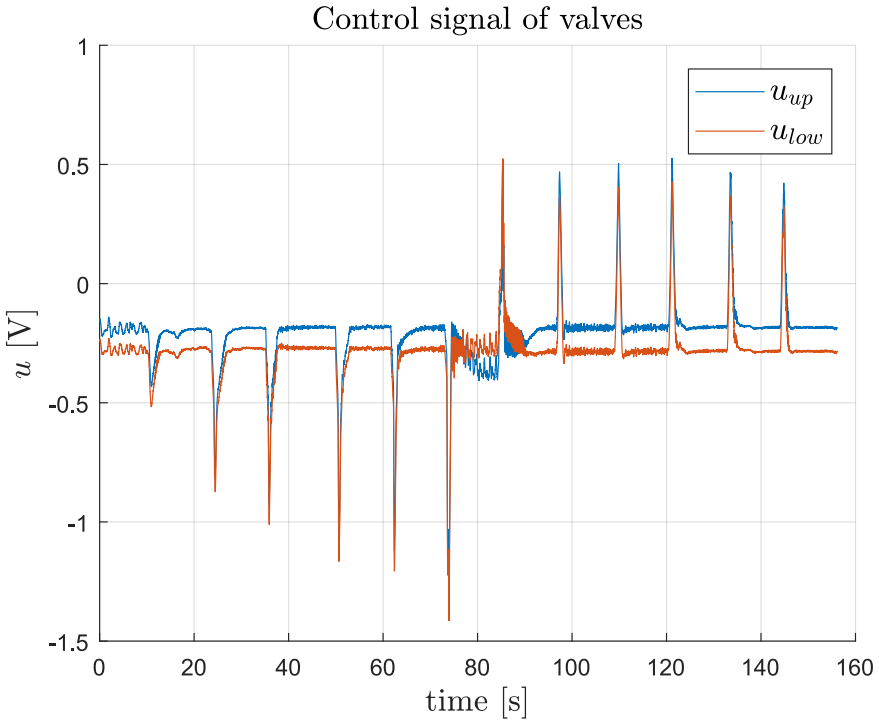

Figure 6.6: Control signal of servo–valves of actuators for displacement at the joint from Fig. 6.2.

angle $\alpha = -4.29$ deg:

$$\Omega_{\text{FoRL}}^{\text{FoR2}} = \begin{bmatrix} cos\alpha & -\sin\alpha \\ \sin\alpha & \cos\alpha \end{bmatrix} \tag{6.2}$$

Using measured angles θ_1, θ_2 a representation in FoR0 can be found:

$$\Xi = \Omega_{\text{FoR2}}^{\text{FoR0}}\, \Xi^{\text{FoRL}} \tag{6.3}$$

where $\Omega_{\text{FoR2}}^{\text{FoR0}}$ is rotation matrix from local frame to FoR2:

$$\Omega_{\text{FoR2}}^{\text{FoR0}} = \begin{bmatrix} cos(\theta_1 + \theta_2) & -\sin(\theta_1 + \theta_2) \\ \sin(\theta_1 + \theta_2) & \cos(\theta_1 + \theta_2) \end{bmatrix} \tag{6.4}$$

is rotation matrix from FoR2 frame to FoR0. In the prototype depicted in Fig. 4.1 $\theta_1 = -93.61$ deg is constant and θ_2 is measured using encoder. In Fig. 6.8 force measured Ξ_y^{FoRL} by sensor along y axis is depicted (in local reference frame FoRL). It is seen that during static intervals absolute force felt by the operator (a connection with the robotic knee) is less than 5 N. When movement occurs, there are spikes, but absolute values do not exceed 20 N. It is assumed, and fed to the algorithm, that $\Xi_x^{\text{FoRL}} = 0$.

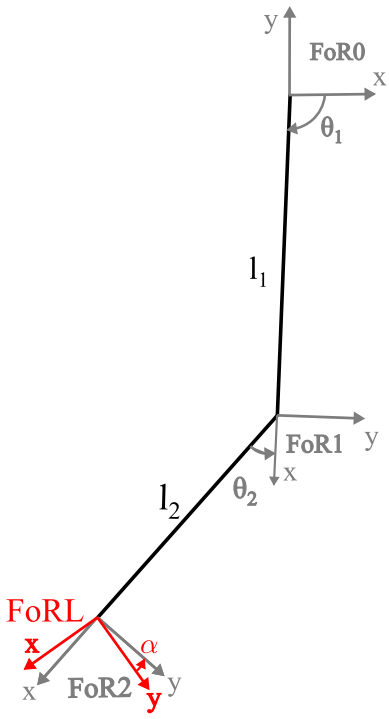

Figure 6.7: Frame of reference for transformation Ξ^{FoRL} to Ξ.

In Fig. 6.9 demanded torque torque to cancel gravity given by Eq. (5.15) and τ_{act} – torque to minimise human–machine interaction force given by Eq. 5.22 are depicted. Comparing to Fig. 5.19, it is seen that demanded torque to minimise human–machine interaction force is much larger τ_{act}.

First order filtering in simulation of F_{act}^{dem}, given by Eq. (5.39), was implemented using a Butterworth filter of first order[2] with $f_{act} = 1.5$ Hz available in LabView. In Fig. 6.10 calculated demanded force $\tilde{F}_{act\ up}$ is depicted, as well as measured values of forces $F_{act\ up}$ and $F_{act\ low}$. It is seen that forces measured using load cells are similar, different by a constant, as shown in section 5.3.2. $F_{act\ up}$ does not track exactly $\tilde{F}_{act\ up}$ in static intervals, but responds to its change properly, minimising human machine interaction force.

In Fig. 6.11 execution time of control loop on MyRIO is depicted. It is seen that the algorithm misses target of 2.5 ms. Most of the iterations last between 3 and 6 ms. This is more than expected from the algorithm in section 4.4, although still much faster than required by Nyquist theorem. The computational load is to algorithm itself, as well as functions used to write measurement data to file.

[2] http://zone.ni.com/reference/en-XX/help/371361K-01/ptbypt/butterworth_filter_ptbypt/

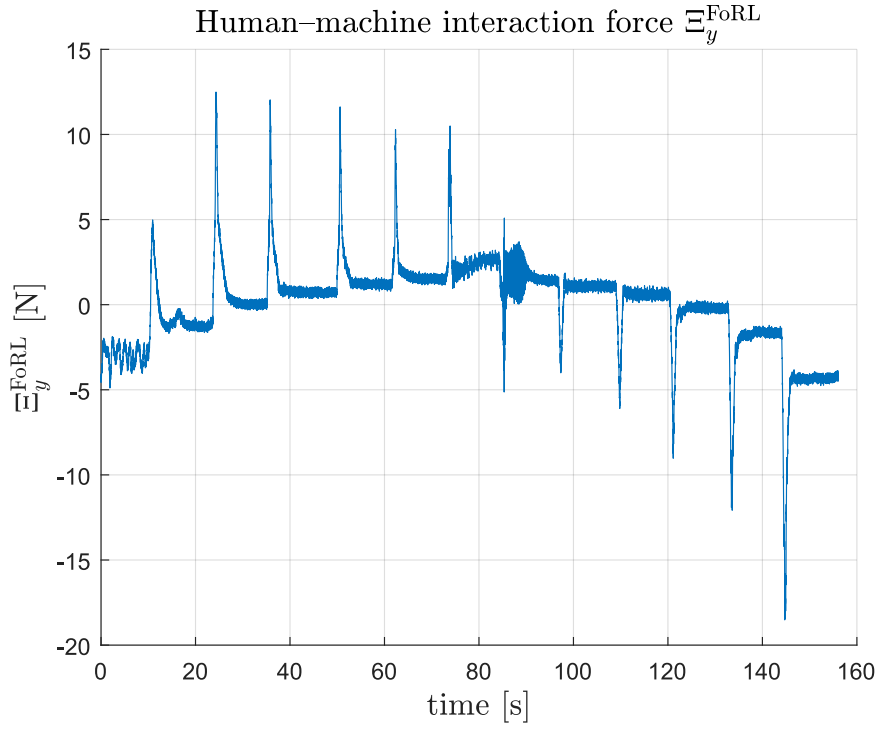

Figure 6.8: Human–machine interaction force in local reference frame of F/T sensor for displacement at the joint from Fig. 6.2.

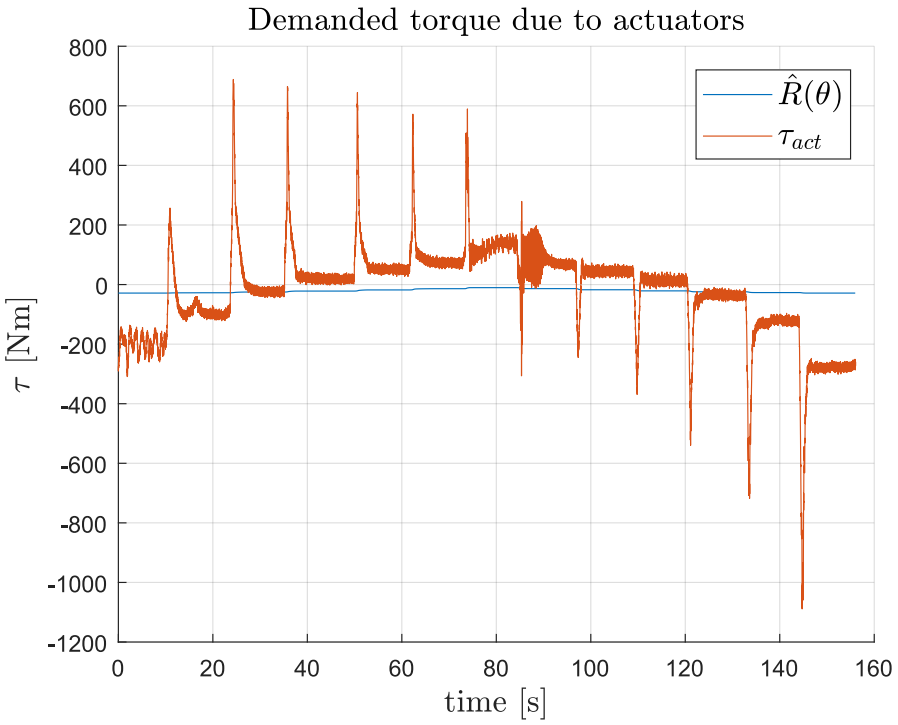

Figure 6.9: Demanded actuator torque from human–machine interaction force Ξ^{FoRL} in Fig. 6.8 for displacement depicted in Fig. 6.2. $\hat{R}(\theta)$ – torque to cancel gravity (blue) given by Eq. (5.15), τ_{act} – torque to minimise human–machine interaction force given by Eq. 5.22 (red).

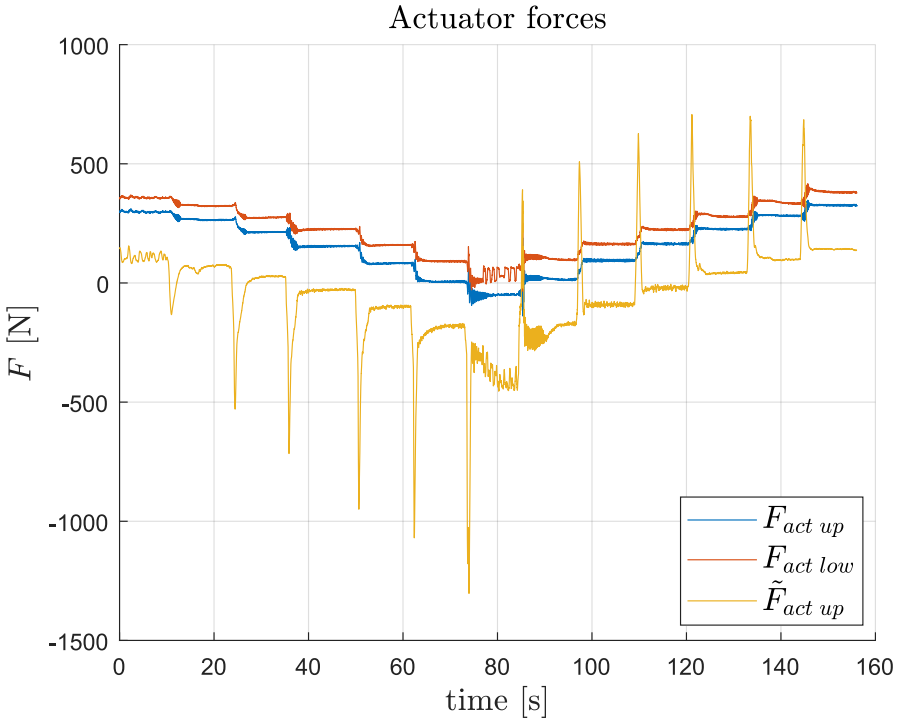

Figure 6.10: Actuator forces calculated from torques in Fig. 6.9 for displacement depicted in Fig. 6.2. $F_{act\ up}$ – measured force exerted by upper actuators (blue), $F_{act\ low}$ – measured force exerted by upper actuator (red), $\tilde{F}_{act\ up}$ – demanded force calculated using Eq. (5.39) (yellow).

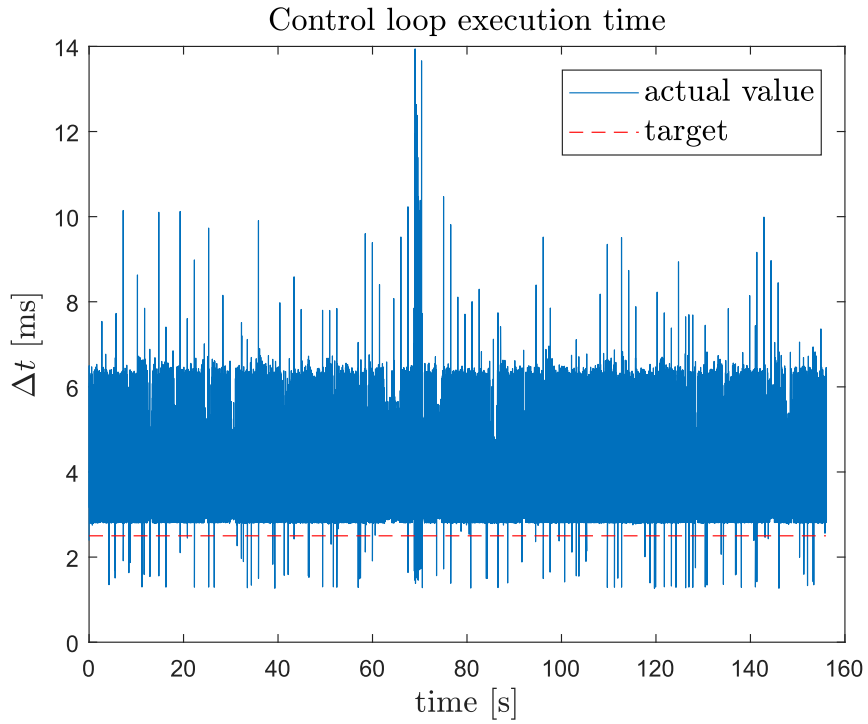

Figure 6.11: Control loop execution time for implemented algorithm.

6.3 Dynamic Evaluation of the Controller

To test the controller for a case where displacement is closer to normal operation (operated by a human), the test rig was adapted so that the joint was able to be moved by hand with load attached to it. In Fig. 6.12a the joint prototype is shown with red handle attached to F/T sensor (blue). In Fig. 6.12b 60 kg load is attached to end of the lower link. Controller settings were as shown in Table 6.1, with exception of gain of middle level force controller $k = 160$. Joint displacement for the case without load attached is shown in Fig. 6.13. The joint is swung. It does not approach range limits to avoid restricting force of hydraulic cylinder cushioning. In Fig. 6.14 frequency characteristic of the displacement signal is depicted. In Fig. 6.15 power of the signal is depicted. Comparing with Fig. 6.4 it is seen that bandwidth (99% of signal power) is larger, about 0.6 Hz. In Fig. 6.16 extension of rods of actuators is depicted. It is seen that synchronisation is maintained. For maximum flexion the misalignment is the largest, about 0.01 m. In Fig. 6.17 control signal of valves is depicted. It is seen that the signals are almost equal. For safety reasons control signal was limited to $u_{up}, u_{low} \in [-5, 5]$ V. Comparing with Fig. 6.13, it is seen that when the absolute angular velocity is the largest, the signal saturates. In Fig. 6.18 human–machine interaction force Ξ^{FoRL} is depicted. It is seen that absolute maximum value is about 40 N. Due to saturation of the control signal, the force much be largest than if signal is unrestricted. In Fig. 6.19 demanded actuator torque is shown. It is seen that torque due to human–machine interaction force is much larger than torque to cancel gravity. Finally, in Fig. 6.20 demanded force $\tilde{F}_{act\,up}$ and measured actuator forces are depicted. It is seen that demanded force is much larger than actual values.

The controller was tested in similar setup, displaced by hand of operator, but with 60 kg load attached. In Fig. 6.21 angular displacement is depicted. It is similar to the case with no load (see Figure 6.13). From Figs. 6.22 and 6.14 it is seen that bandwidth is about 0.5 Hz. In Fig. 6.24 extension of the rods of hydraulic actuators is depicted. It is seen that synchronisation is maintained and absolute maximum error is not more than 0.005 m at angular displacement extremes. In Fig. 6.25 control signal is depicted. Control for upper and lower actuator are almost the same. The signals do not saturate. In Fig. 6.26 human–machine interaction force Ξ^{FoRL} is depicted. It is seen that its absolute value does not exceed 20 N. Demanded torque is shown in Fig. 6.27. Demanded force and measured actuator forces are depicted in Fig. 6.28.

(a) (b)

Figure 6.12: Single joint prototype. (a) without load, (b) with 60 kg load attached. A red handle is attached to 6 DoF F/T sensor.

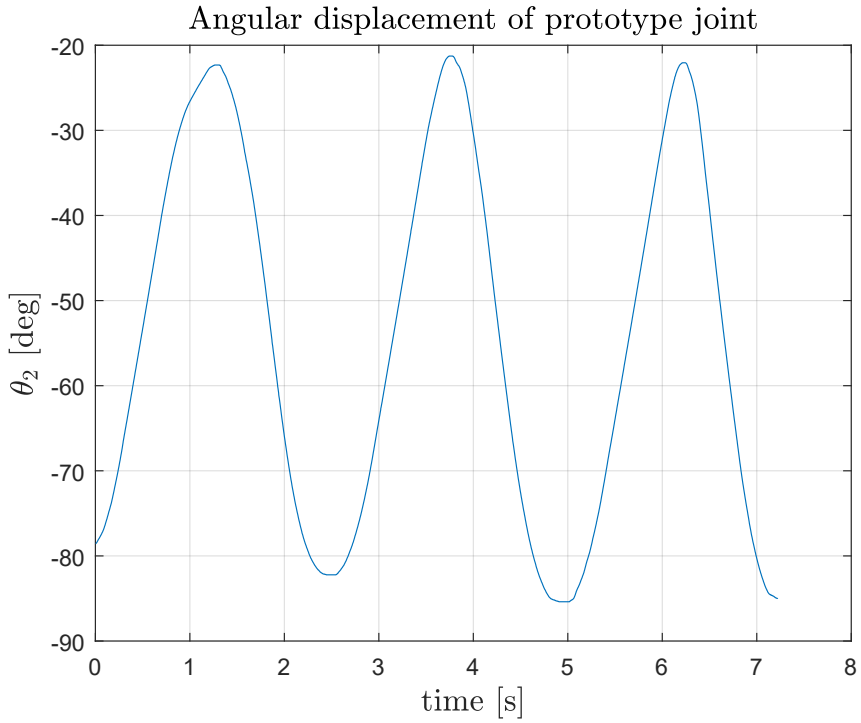

Figure 6.13: Displacement at the joint measured by the encoder, following robotic knee. Parameters, $k_{pp} = 1 \times 10^{-3}$, $k_p = 10000$, $k_{kc} = 5 \times 10^{-3}$, $k = 160$, f_{act} =1.5 s, $H_{act}(s) = 1$.

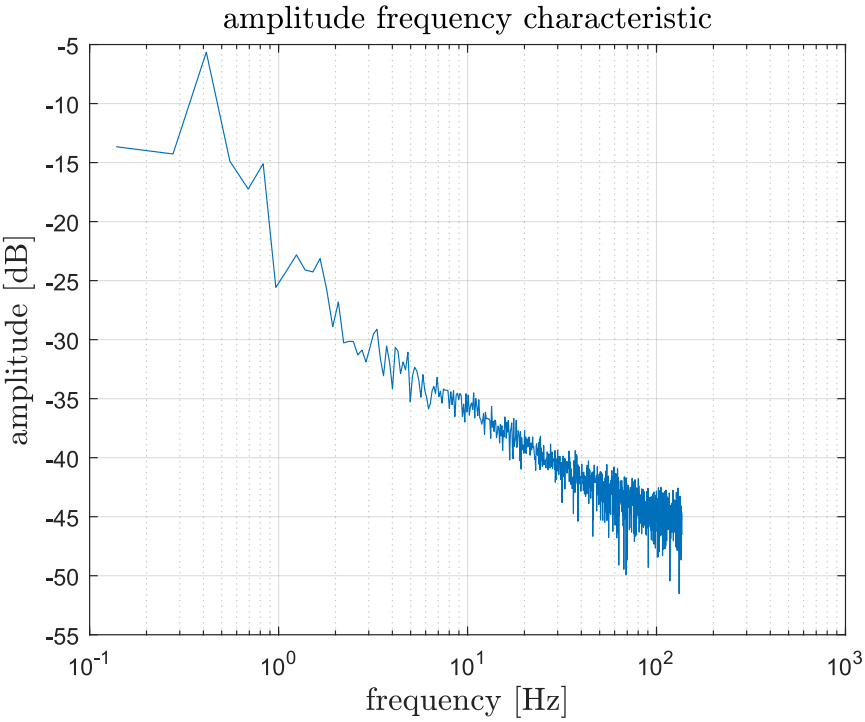

Figure 6.14: Frequency characteristic of displacement at the joint from Fig. 6.13.

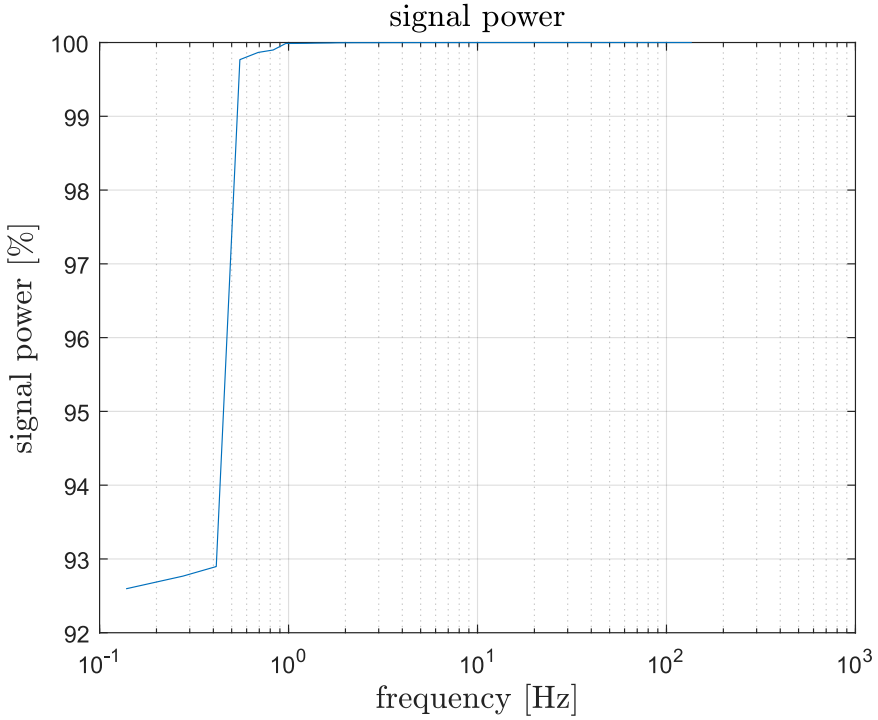

Figure 6.15: Signal power of displacement at the joint from Fig. 6.13.

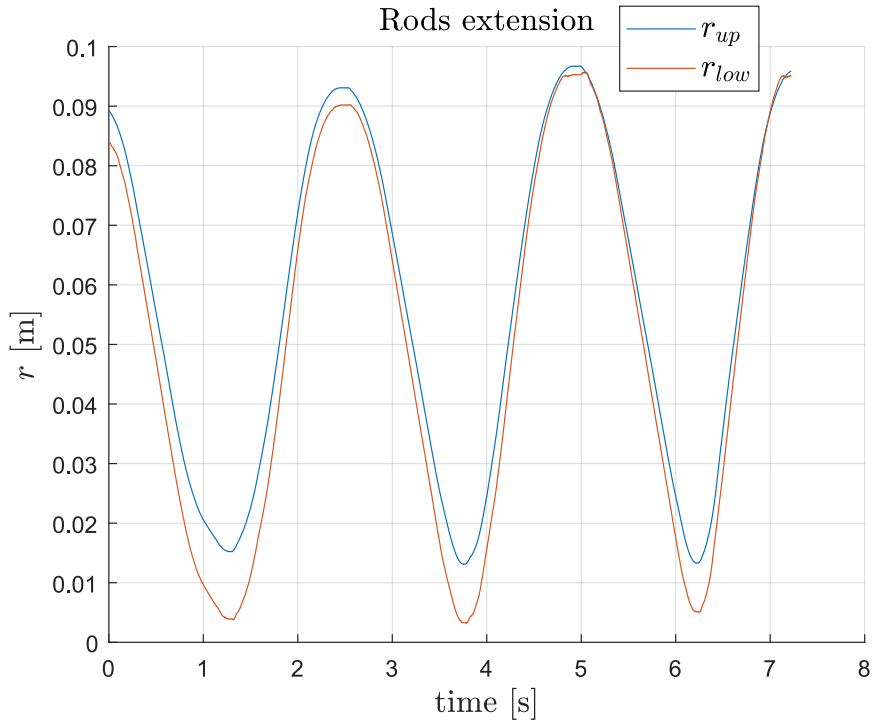

Figure 6.16: Extension of rods of hydraulic actuators for displacement at the joint from Fig. 6.13.

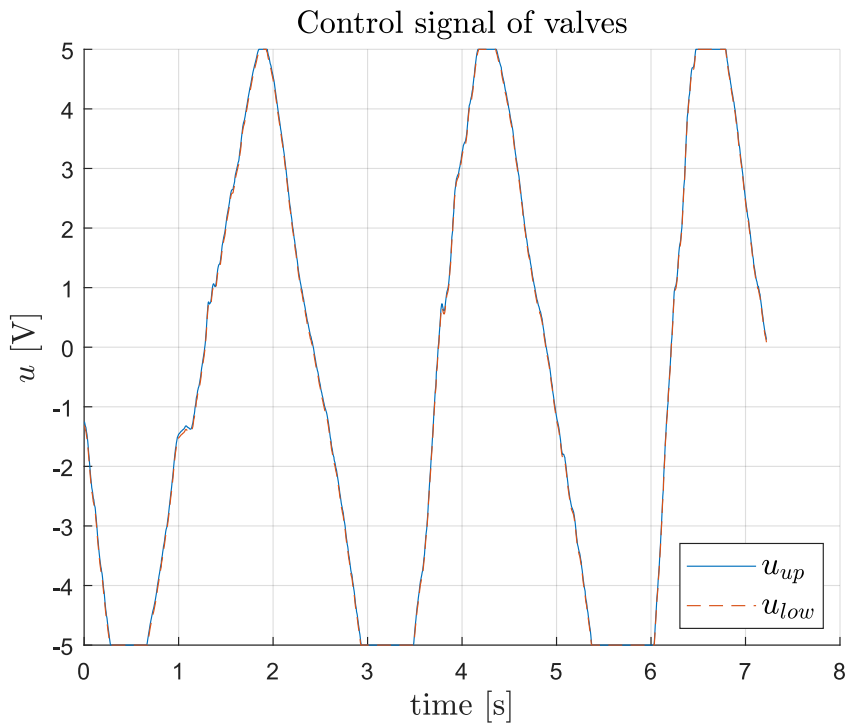

Figure 6.17: Control signal of servo–valves of actuators for displacement at the joint from Fig. 6.13.

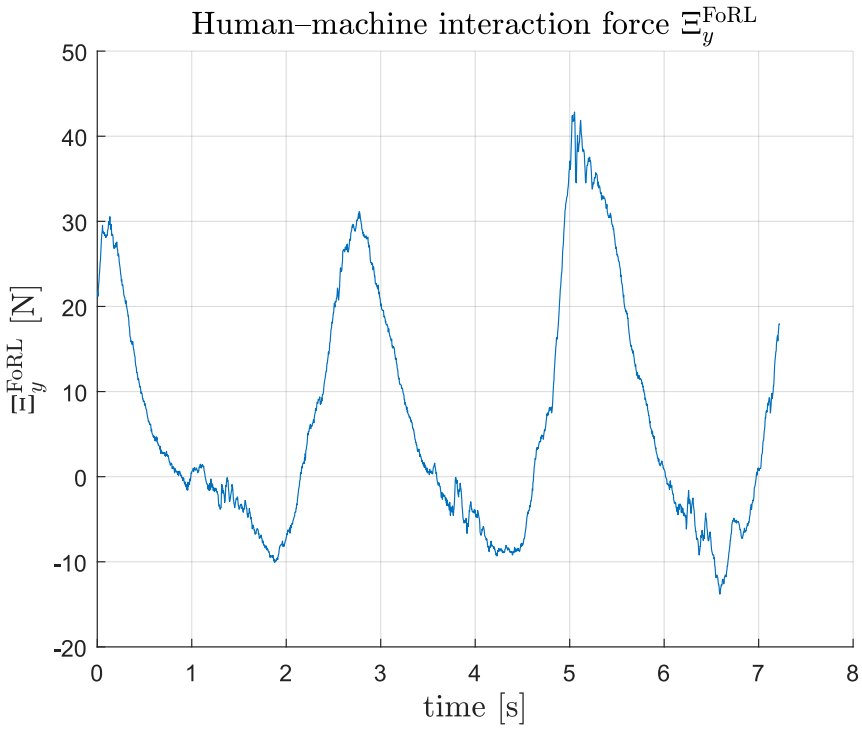

Figure 6.18: Human–machine interaction force in local reference frame of F/T sensor for displacement at the joint from Fig. 6.13.

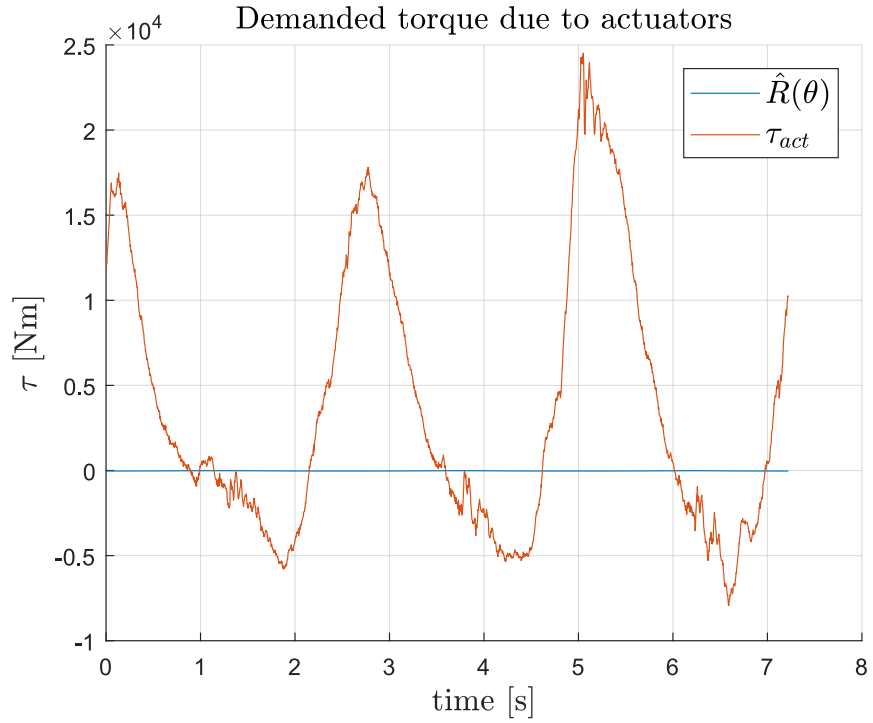

Figure 6.19: Demanded actuator torque from human–machine interaction force Ξ^{FoRL} in Fig. 6.18 for displacement depicted in Fig. 6.13. $\hat{R}(\theta)$ – torque to cancel gravity (blue) given by Eq. (5.15), τ_{act} – torque to minimise human–machine interaction force given by Eq. 5.22 (red).

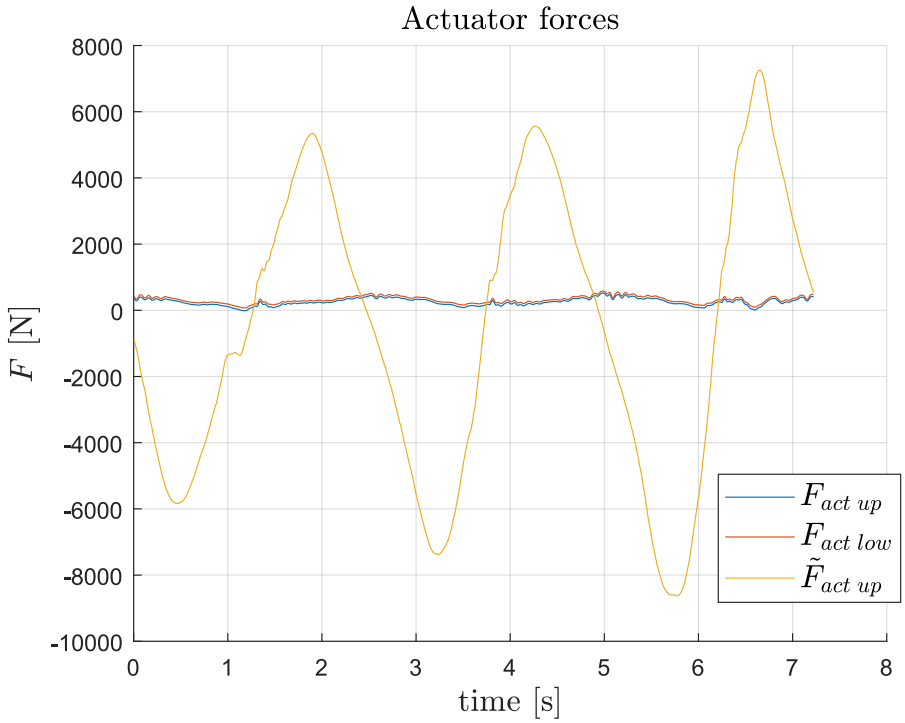

Figure 6.20: Actuator forces forces calculated from torques in Fig. 6.19 for displacement depicted in Fig. 6.13. $F_{act\ up}$ – measured force exerted by upper actuators (blue), $F_{act\ low}$ – measured force exerted by upper actuators (red), $\tilde{F}_{act\ up}$ – demanded force calculated using Eq. (5.39) (yellow).

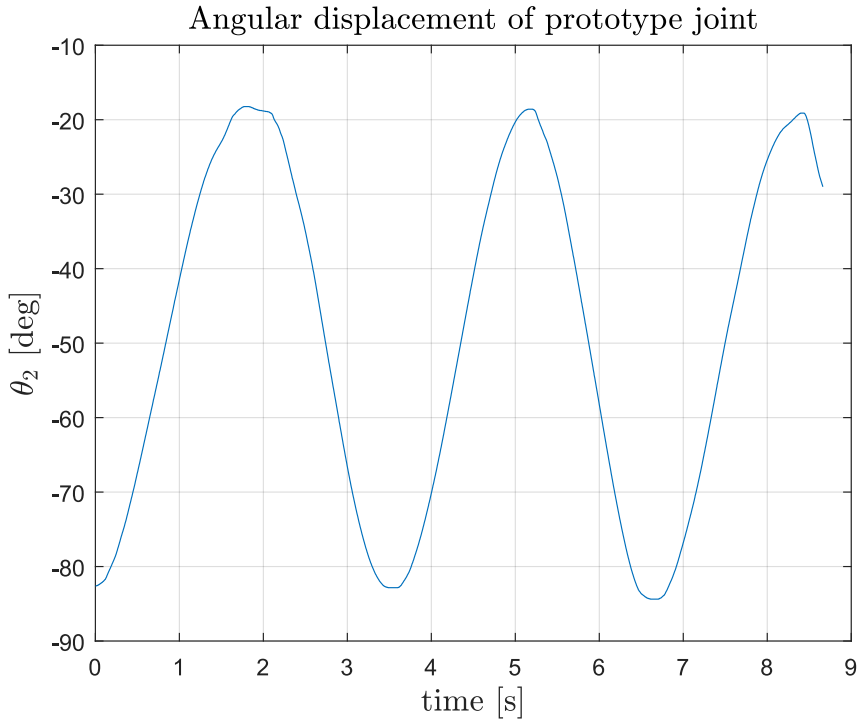

Figure 6.21: Displacement at the joint measured by the encoder, following robotic knee. Parameters, $k_{pp} = 1 \times 10^{-3}$, $k_p = 10000$, $k_{kc} = 5 \times 10^{-3}$, $k = 160$, f_{act} =1.5 s, $H_{act}(s) = 1$

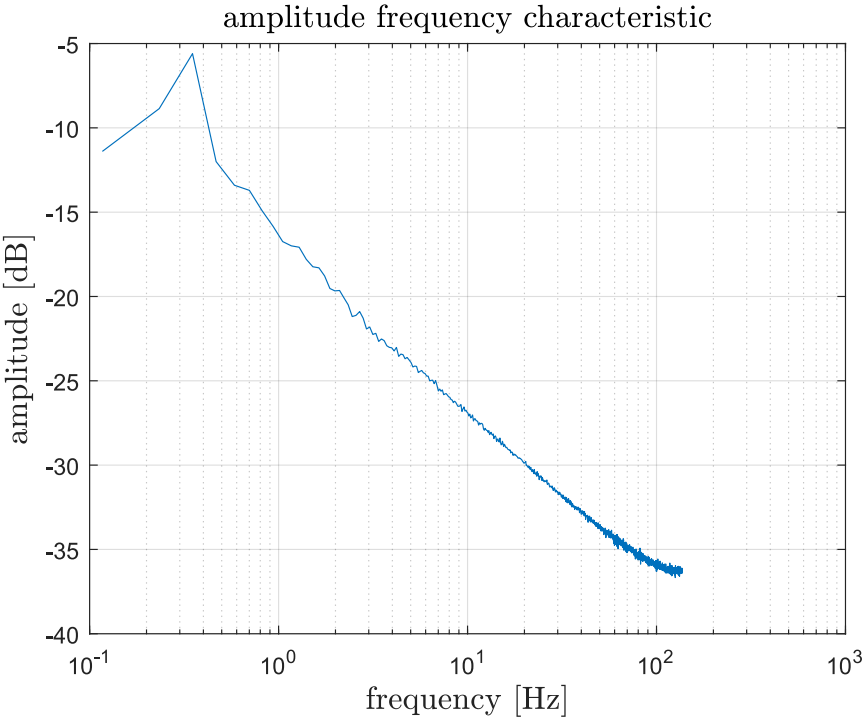

Figure 6.22: Frequency characteristic of displacement at the joint from Fig. 6.21.

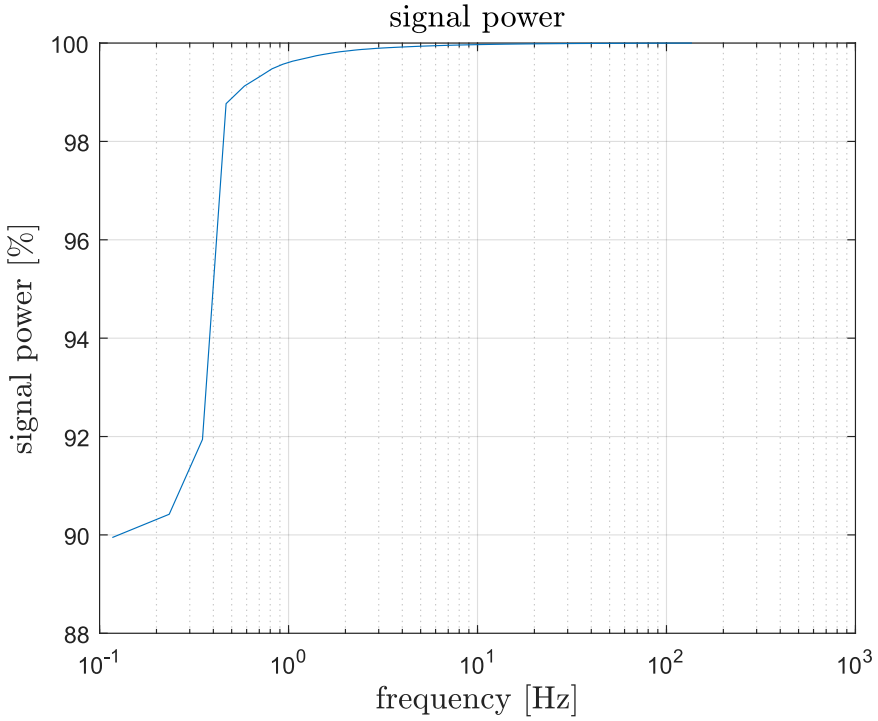

Figure 6.23: Signal power of displacement at the joint from Fig. 6.21.

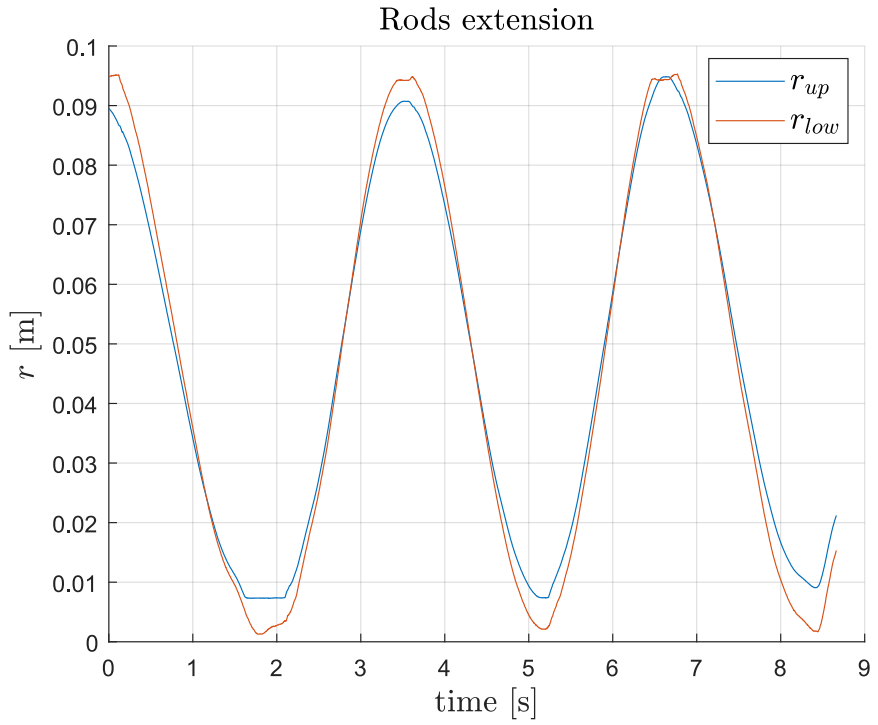

Figure 6.24: Extension of rods of hydraulic actuators for displacement at the joint from Fig. 6.21.

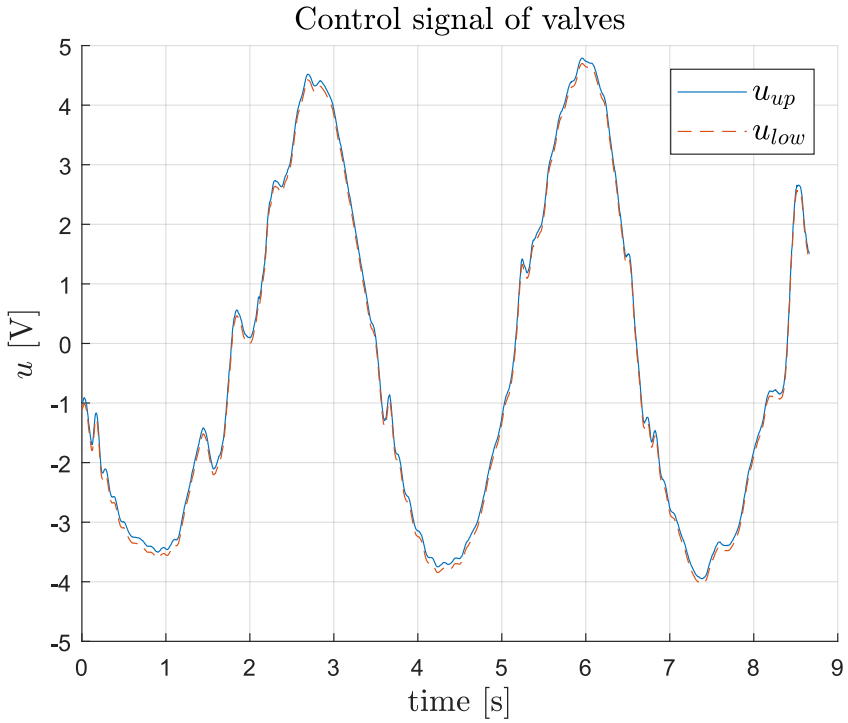

Figure 6.25: Control signal of servo–valves of actuators for displacement at the joint from Fig. 6.21.

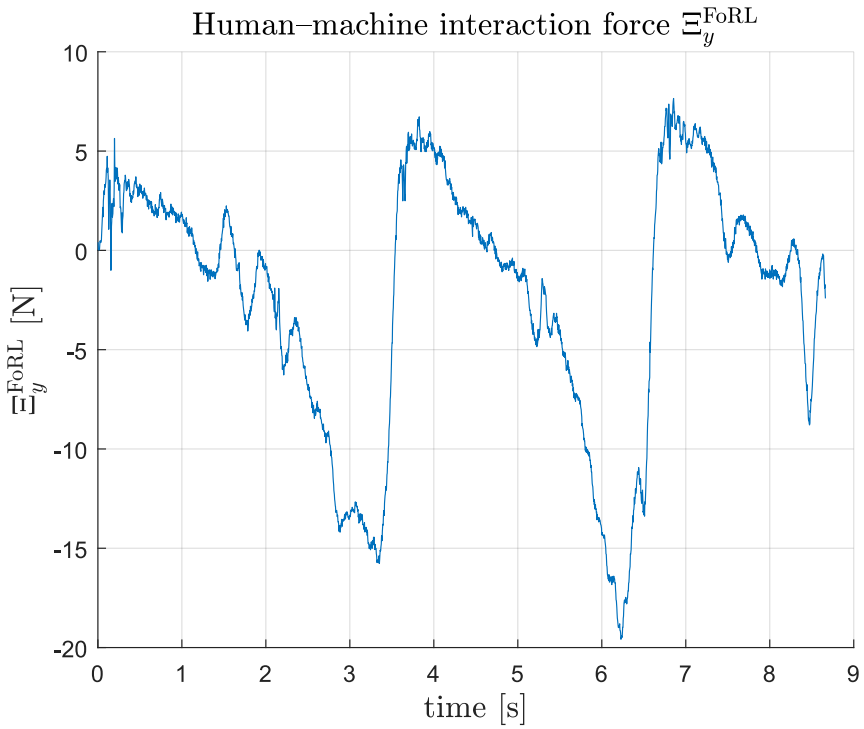

Figure 6.26: Human–machine interaction force in local reference frame of F/T sensor for displacement at the joint from Fig. 6.21.

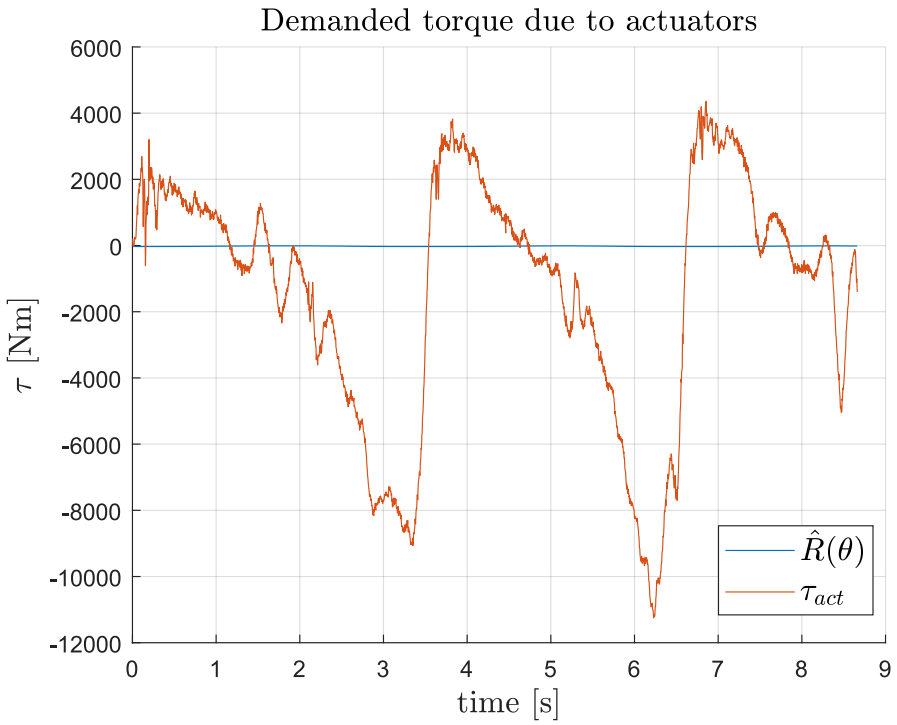

Figure 6.27: Demanded actuator torque from human–machine interaction force Ξ^{FoRL} in Fig. 6.26 for displacement depicted in Fig. 6.21. $\hat{R}(\theta)$ – torque to cancel gravity (blue) given by Eq. (5.15), τ_{act} – torque to minimise human–machine interaction force given by Eq. 5.22 (red).

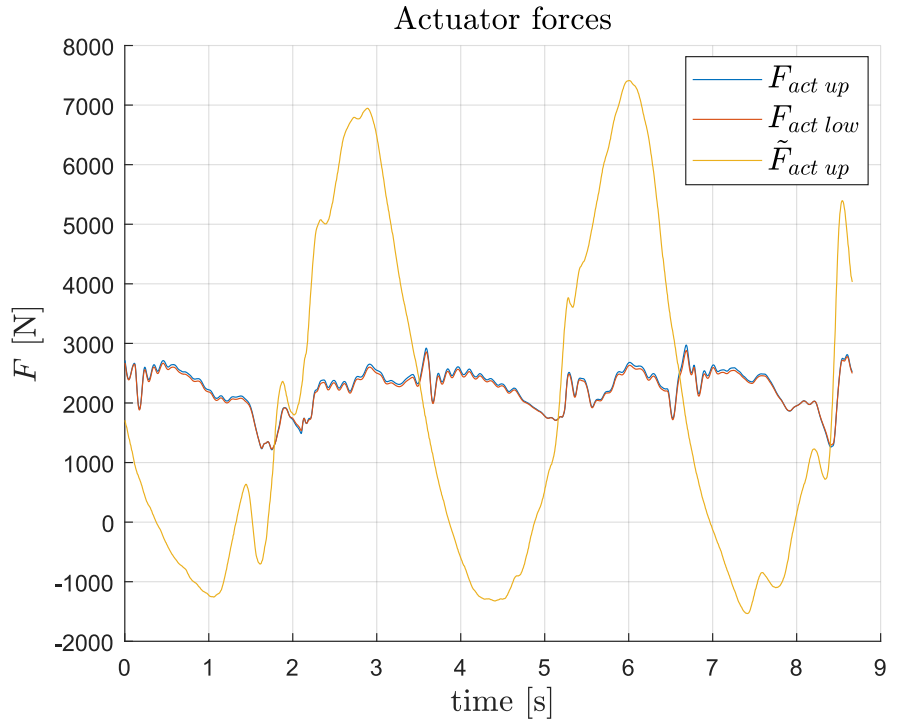

Figure 6.28: Actuator forces forces calculated from torques in Fig. 6.27 for displacement depicted in Fig. 6.21. $F_{act\ up}$ – measured force exerted by upper actuators (blue), $F_{act\ low}$ – measured force exerted by upper actuators (red), $\tilde{F}_{act\ up}$ – demanded force calculated using Eq. (5.39) (yellow).

6.4 Summary

It was demonstrated that prototype under governance of middle level controller with low level coupled control of hydraulic actuator enables the joint to be used in an enhancive exoskeleton governed by force control laws (see section 2.5). It was shown that if the joint is held at constant angle, the human–machine interaction for is minimised. The controller tends to synchronise extension of the rods. When the joint is flexed/extended the control signals have similar shape squeezing and pulling the knee cap synchronously. In static case, the control signals are non–zero, most likely due to internal leakage in the cylinders, which was not modelled in simulations described in section 5.

It was shown that the the controller was only partially successful to govern the joint when it is displaced by a human operator. Conservative settings were used. In further experiments it is advised to increase gains in the controller: k_{pp} and k_{kc} to minimise the human–machine interaction force further and speed up synchronisation of rods extension. It was demonstrated that the controller allows for operation with bandwidth of joint angular displacement up to 0.6 Hz. Further test are required to determine if the joint is able to follow gait, that is input signal with bandwidth up to 10 Hz. The test with load attached it was successfully demonstrated that 60 kg can be manipulated with up to 30 N of force, that is ration of force amplification is about 1:20, which is similar to what is stated for Sarcos XOS 2 [26]. The required control loop rate of 2 kHz was not achieved, but time of execution of loop iteration between 3 and 6 ms allows for successful governance, and will allow of movement with bandwidth up to 10 Hz.

The reasons for limitations of performance of the prototype in conducted experimental evaluation are:

- Pump used in the prototype setup has a nominal flow of 6 l/min. Comparing required angular speed obtained from the simulation in Fig. 5.7 with maximum flexion $\dot{\theta}^{flex}_{max}$ and minimum extension $\dot{\theta}^{ext}_{min}$ from Table 4.5 it is seen that the joint is unable to move fast enough to follow gait. Moreover, in the experimental evaluation, the absolute control signal was limited to 5 V (50% of maximum value) for safety reasons. Further experimental evaluation addressing those issues. A pump with at least of 12 l/min need to be used, and control signal has to be allowed to achieve full range.
- There is an issue of generating interaction point trajectory with sufficient bandwidth and high enough Ξ human–machine interaction force. required Ξ is shown

in Figs. 5.84 (with load, maximum of 180 N) and 5.100 (without load, maximum of 95 N). The prosthetic knee is unable to generate such high forces. The interaction force might be burdensome to the operator as well. Increasing gain of middle–level gain k and low–level proportional gain k_{pp} from used in the experimental evaluation would be necessary to decrease Ξ. However, doing so leads to the joint oscillations and excessive forces of Ξ. A more sophisticated control method may achieve lowering of Ξ, without loosing stability of Ξ.

A way to address both the issues simultaneously is to miniaturise all dimensions (including piston areas) to fit an average person, instead a tall one. Although the joint would produce lesser maximum torque (which is now about 20 times more than one for BLEEX [10]), it would require smaller pump flow and improve control accuracy (for the same gains and settings), retaining favourable torque characteristic (see Fig. 4.21) and extended range. Also its mass would be smaller. Decreasing all dimensions by 20% (in simulation motion capture data was scaled by a coefficient $s_{coef} = 1.228$, that is about 23%, so dimensions return to sizing for an average sized person) results in half of the flow of the pump required (6 l/min would be sufficient), mass decreased by the same factor and maximum torque by 36% (refer to Table 4.5).

Chapter 7

Considerations for Full–body Enhancive Exoskeleton

7.1 Introduction

The ultimate goal of designing an exoskeleton is to allow it to perform tasks like walking or lifting. In this chapter a model based on biometric data is proposed in sagittal plane. Motion capture kinematic and dynamic data is used to make it walking. The purpose of the investigation is to explore problems in control of an enhancive full–body exoskeleton, which arise when such structure is made to move. While attempting it, a problem of designing of contact with the ground arises. Three different platform models are proposed and evaluated for the chosen task. The whole exoskeleton model is evaluated for sagittal stability. There is a possibility that the operator would alter gait pattern to minimise required stabilising form.

7.2 Full–body Exoskeleton Model in Sagittal Plane

In order to investigate behaviour and to identify control challenges of operating an enhancive full–body exoskeleton a model was constructed and simulated in sagittal plane whilst performing walking (gait simulation). Simscape[1], part of Simulink, was used for this purpose. The model is depicted in Fig. 7.1. As legs, the components of prototype single joint were used (see section 4.1 and Fig. 5.1). Therefore, the model is quasi–anthropomorphic . As in section 5.2.2, motion capture data was scaled using a coefficient $s_{coef} = 1.228$ to maintain extension of rods of hydraulic actuators within

[1] `https://uk.mathworks.com/products/simmechanics.html`

limits during manoeuvres of walking.

The model geometry is based on motion capture data described in section 4.4.1. FoR0 (frame of reference) is central to the model. It corresponds to markers placed on anterior superior iliac spine (R_Iliac marker specifically, see Fig. 4.7). In Table 7.1 hierarchy of frames of reference and corresponding transformations for the model are shown. At origin of FoR0, 3 revolute joints[2], corresponding to left hip (θ_{L1}), right hip (θ_{R1}), torso (θ_4), are attached. FoRL1 (left knee), FoRR1 (right knee), FoR4 (torso), as well as the rest of frames, are assigned using Denavit–Hartenberg convention. FoRL2 corresponds to marker placed on left lateral malleolus (L_Mall_Lat, left ankle). FoRR2 corresponds to marker placed on right lateral malleolus (R_Mall_Lat, right ankle). Displacement data FoRL2 and FoRR2 from frame FoR0 (modelled as Cartesian Joint[3]), recorded during the motion capture, was transformed to match the model for gait using affine transform (compare to Eq. (5.19)):

$$p = \begin{bmatrix} p_x \\ p_y \end{bmatrix} = s_{coef} \cdot p^{\,mc} + p^{\,err} = s_{coef} \begin{bmatrix} p_x^{mc} \\ p_y^{mc} \end{bmatrix} + \begin{bmatrix} p_x^{err} \\ p_y^{err} \end{bmatrix} \tag{7.1}$$

where $p^{\,mc}$ – original motion capture data of displacement relative to FOR0 (see Fig. 7.1), $s_{coef} = 1.2288$ – scaling coefficient chosen not to violate constraints of rods of hydraulic cylinders extension (see section 5.2.2 for discussion), p^{err} – correction of input to make the legs extend the same distance. In Figs. 7.2 and 7.3 original (green) and transformed (blue) position of the markers in sagittal plane is depicted. The data is fed into simulation using Simulink–PS Converter block[4]. The solver requires first two derivatives. As part of the converter block there is an option to filter data using second order filter to produce them. Time constant was chosed to be 0.01 s (100 Hz, above bandwidth of motion, see section 4.4). The filtered data is depicted in red in Figs. 7.2 and 7.3. The data for the right marker is corrected with $p^{\,err} = [0, 0.02]m$ to make the legs extend the same distance during their respective stance phases. The source of the error is error of the motion capture system. In Fig. 7.4 angular displacement at joints, resulting from displacement of FoRL2, is depicted. θ_{L1} is left hip angle. θ_{L2} is knee angle. In Fig. 7.5 respective angular displacements for right leg are depicted. This was obtained simulating the model with variable step ode15s solver[5]. Max and min step size were set to automatic.

[2] https://uk.mathworks.com/help/physmod/sm/ref/revolutejoint.html
[3] https://uk.mathworks.com/help/physmod/sm/ref/cartesianjoint.html
[4] https://uk.mathworks.com/help/physmod/simscape/ref/simulinkpsconverter.html
[5] https://uk.mathworks.com/help/matlab/ref/ode15s.html

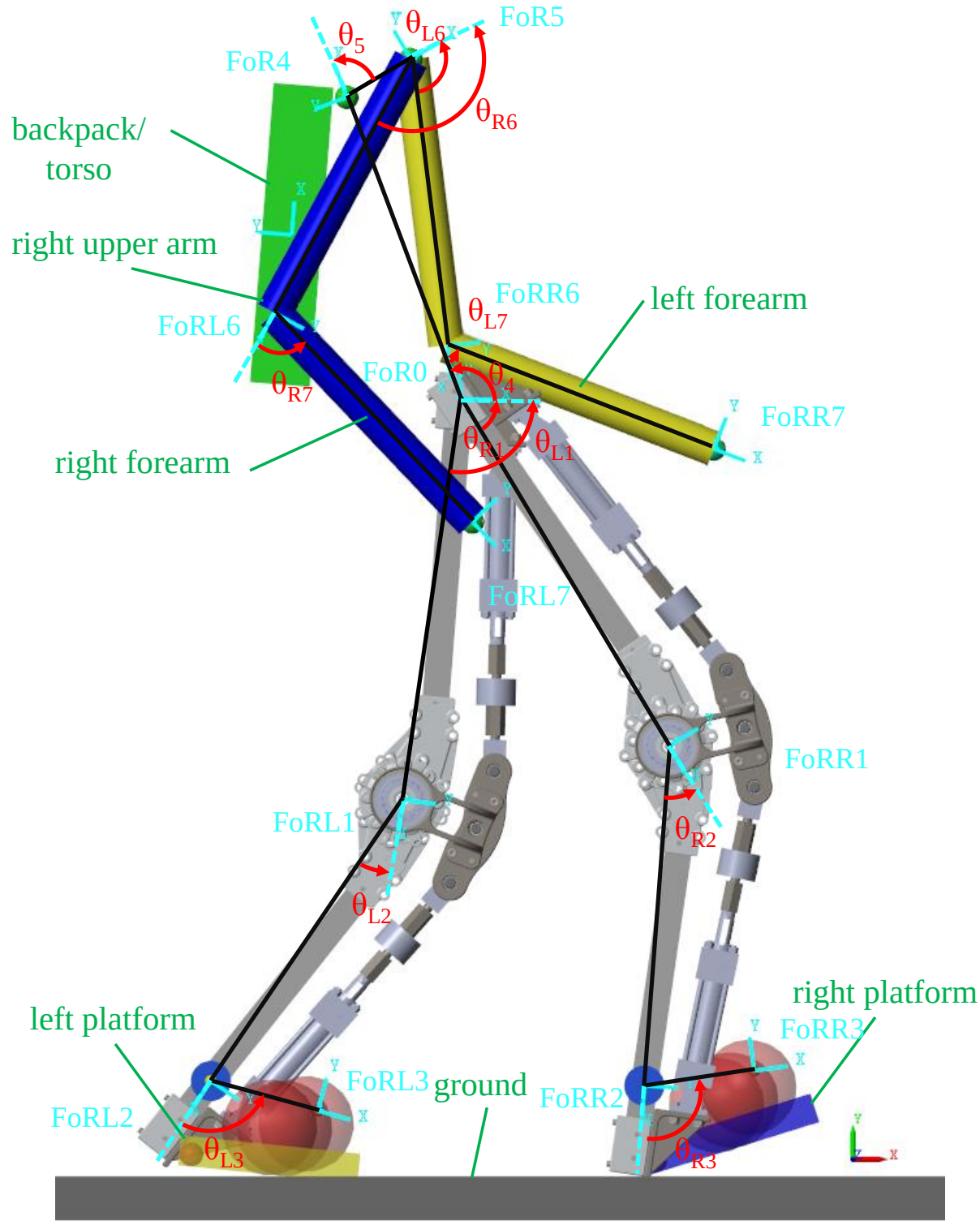

Figure 7.1: A full–body exoskeleton model based on biometric data. Origin of FoR0 corresponds to L_Iliac and R_Iliac markers (see Fig. 4.7). Origin of FoRR2 corresponds to R_Mall_Lat (right ankle) and FoRL2 corresponds to L_Mall_Lat (left ankle). FoRR3 corresponds to R_Foot (right ankle) and FoRL3 corresponds to L_Foot. FoR4 corresponds to T3 maker (placed on third thoracic vertebra). FoR5 corresponds to R_Acrom_Sup and L_Acrom_Sup markers (shoulder joint). FoRL7 and FoRR7 correspond to L_Hand and R_Hand respectively.

Table 7.1: Frames of reference and parameters for full–body exoskeleton model depicted in Fig. 7.1. (*) – computed, not provided directly. ($) – see Table 4.1 and Fig. 4.1.

frame of reference	**parent frame**	**displacement from parent frame [m]**	**rotation angle in parent frame [deg]**	**associated part**	**part mass [kg]**
FoR0	–	–	–	–	–
FORL1	FOR0	0.679	θ_{L1}*	left thigh	$
FORL2	FORL1	0.573	θ_{L2}*	left shank	$
FORL3	FORL2	0.223	θ_{L3}	left platform	18
FORR1	FOR0	0.679	θ_{R1}*	right thigh	$
FORR2	FORR1	0.573	θ_{R2}*	right shank	$
FORR3	FORR2	0.223	θ_{R3}	right platform	18
FOR4	FOR0	0.591	θ_4	backpack/torso	30
FOR5	FOR4	0.124	θ_5 = -79.8	–	–
FORL6	FOR5	0.48	θ_{L6}*	left upper arm	10.85
FORL7	FORL6	0.48	θ_{L7}*	left forearm	10.85
FORR6	FOR5	0.48	θ_{R6}*	right upper arm	10.85
FORR7	FORR6	0.48	θ_{R7}*	right forearm	10.85
				Total	**175.13**

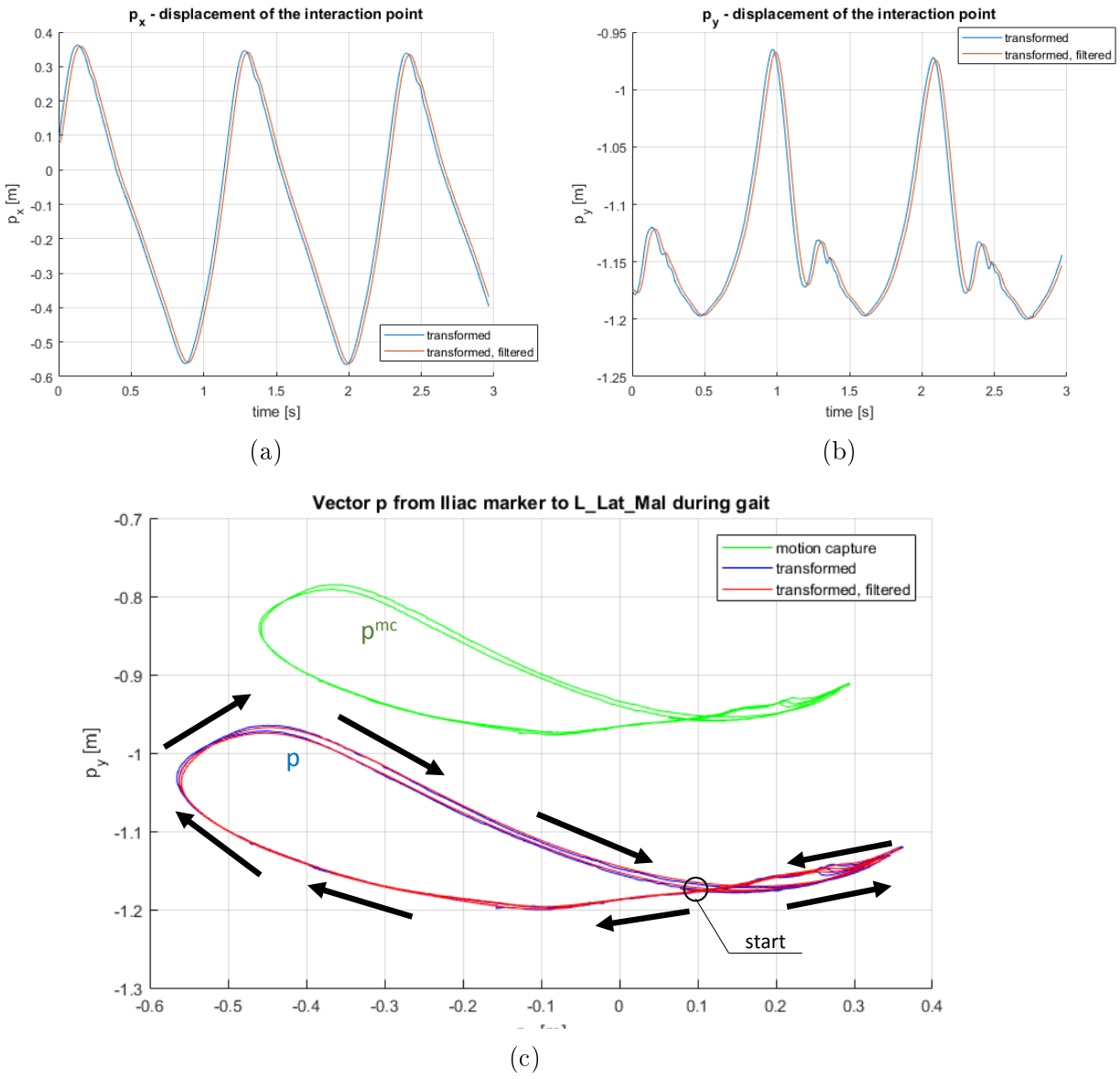

Figure 7.2: Displacement of a marker placed on left lateral malleolus (L_Lat_Mall, corresponding to FoRL2) in the reference frame of marker placed on anterior superior iliac spine (Iliac, corresponding to FoR0) during gait. Green – original data from motion capture, blue – data transformed (scaling coefficient $s_{coef} = 1.2288$), red – data filtered using second–order filter. (a) – p_x displacement, (b) – p_y displacement, (c) – displacement $p = [p_x\ p_y]^T$ in the sagittal plane. Arrows point direction of movement. Correction $p^{\ err} = [0\ 0]^T$

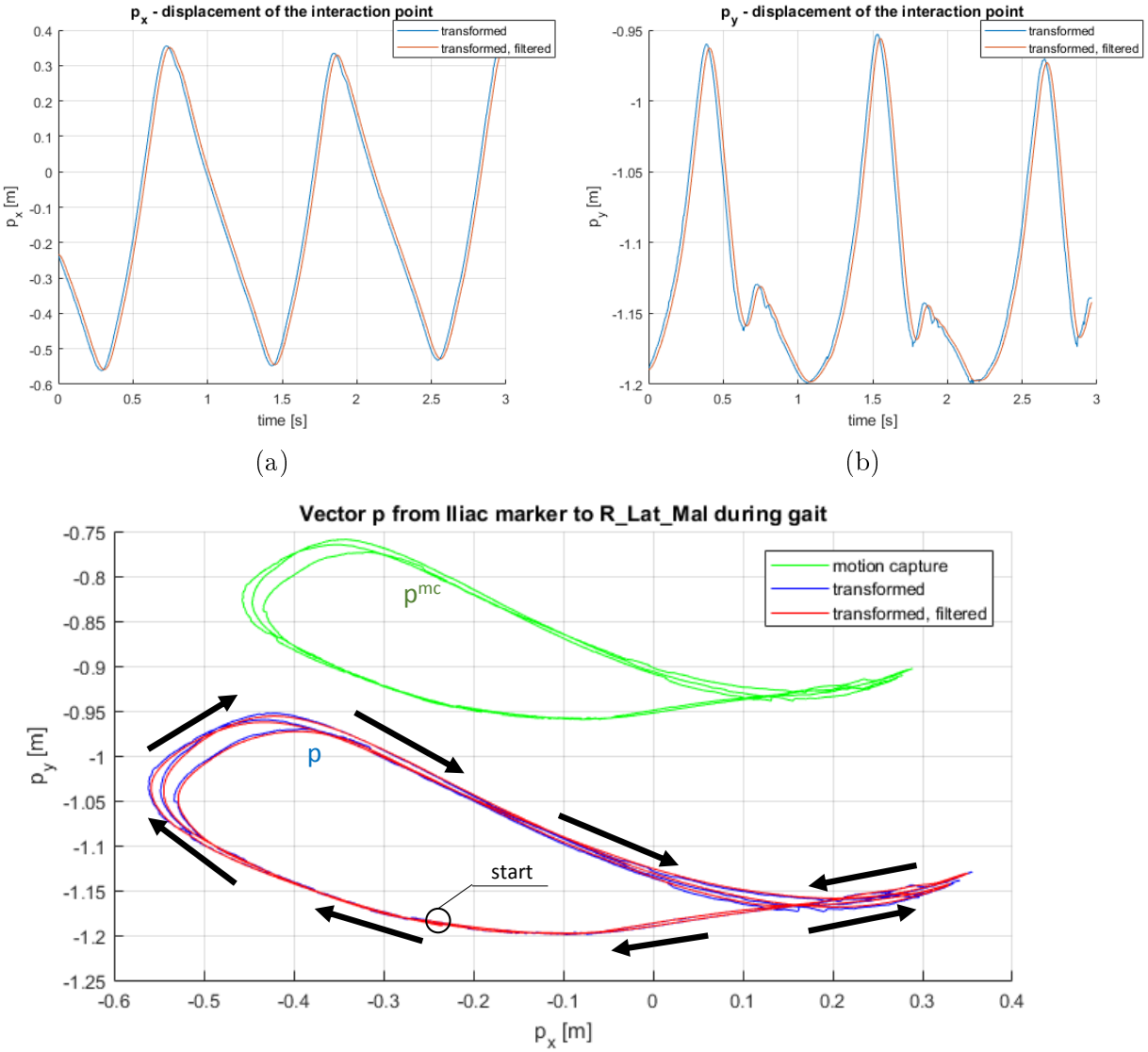

Figure 7.3: Displacement of a marker placed on left lateral malleolus (R_Lat_Mall, corresponding to FoRR2) in the reference frame of marker placed on anterior superior iliac spine (Iliac, corresponding to FoR0) during gait. Green – original data from motion capture, blue – data transformed (scaling coefficient $s_{coef} = 1.2288$), red – data filtered using second–order filter. (a) – p_x displacement, (b) – p_y displacement, (c) – displacement $p = [p_x\ p_y]^T$ in the sagittal plane. Arrows point direction of movement. Correction $p^{err} = [0\ -0.02]^T$

At FoRL2 and FoRR2 rotary joints were placed to allow for ankle flexion/extension during gait. To find its angular displacement (see Eq. (4.5)), angle between Iliac, Mall_Lat, and Foot, projected on the sagittal place, was retrieved (see Fig. 4.7). The data for left side (σ_{L3}) is depicted in Fig. 7.6, and for the right side (σ_{R3}) in Fig. 7.7. To transform it into rotation of FoRL3 with respect to FoRL2 and FoRR3 with respect to FoRR2, the notions as in Fig. 7.8 was taken. Distance between FoR0 and FoRm2 (where $m \in \{L, R\}$, left and right respectively) first has to be calculated. From law of cosines:

$$l = \sqrt{l_1^2 + l_2^2 - 2l_1 l_2 \cos(\pi - |\theta_{m2}|)} \tag{7.2}$$

where θ_{m2} is angular displacement of the exoskeleton knee, l_1 – distance between FoRm1 and FoR0, l_2 – distance between FoRm2 and FoRm1. Using law of sinuses:

$$\frac{l_1}{\sin \alpha_m} = \frac{l}{\sin(\pi - |\theta_{m2}|)} \tag{7.3}$$

$$\alpha_m = \sin^{-1}\left(-\frac{l_1}{l}\cos|\theta_{m2}|\right) \tag{7.4}$$

The angle of ankle rotation is then calculated as:

$$\theta_{m3} = \pi - (\sigma_{m3} - \alpha_{m3}) + \theta_{m3}^{err} \tag{7.5}$$

where σ_{m3} is angle projected onto sagittal plane, given by Eq. (4.5) taking the 3$^{\text{rd}}$ component (depth , z–component) as 0. θ_{m3}^{err} is error correction component to make platform flat for stance phase. The error is due to motion capture system error. Calculated θ_{L3} during gait is depicted in Fig. 7.9, and θ_{R3} is depicted in Fig. 7.10. Both raw (blue), and second–order filtered data (red) is shown. $\theta_{m3}^{err} = -4$deg, to make platform flat during stance phase. The model of platform is shown in detail in Fig. 7.11. Its geometry, distance between FoRm2 and platform, placement of FoRm3, are based on motion capture data.

Torso of the exoskeleton is shown in detail in Fig. 7.12. In order to find torso angle during gait, angles projected on sagittal place between T3 (marker placed on thoracic 3rd vertebra), Iliac, and Mall_Lat (ankle) markers were retrieved. For the left side the angle is denoted σ_{L4}. For the right side, it is denoted σ_{R4}. They are shown in Fig. 7.13 during gait. Torso rotation θ_4 can be calculated using formula:

$$\theta_{m4} = 2\pi - (\sigma_{m4} + \beta_m + |\theta_{m1}|) \tag{7.6}$$

where:

$$\beta_m = \pi - (\pi - |\theta_{m2}|) - \alpha_m = |\theta_{m2}| - \alpha_m \tag{7.7}$$

Eq. (7.6) produces two solutions for $m \in \{L, R\}$. Ideally the solutions should be equal. Unfortunately, due to motion capture errors they are slightly different, depicted in Fig. 7.14. Arithmetic average can be taken:

$$\theta_4 = \frac{\theta_{L4} + \theta_{R4}}{2} \tag{7.8}$$

Resulting angular displacement is shown in Fig. 7.15.

A backpack is attached to the torso frame (FoR4). This is shown in Fig. 7.12. Frame FoR5, which corresponds to superior acromion (Acrom_Sup, shoulder joint) is also rigidly attached. At origin of FoR5 two revolute joints are attached. Through these joints, two two–segment quasi–anthropomorphic arms are located. FoRL6 and FoRR6 correspond to operators elbows. Rotary joints are placed at their origins. FoRL7 and FoRR7 are connected to FoR0 using Cartesian joints, which allows for their displacement in sagittal plane. The displacement is shown in Fig. 7.16 for the left side, and in Fig. 7.16 for the right side. Original data from motion capture (green), transformed using transformation given by Eq. (7.1) (blue), second–order filtered (red), is shown. The resulting rotation angles between FoRL6 and FoRL5, as well as, between FoRL7 and FoRL6 are shown in Fig. 7.18. For the right side, respective rotation angels are shown in Fig. 7.19.

According to Table 7.1, where mass of exoskeleton segments is given, the total weight of the exoskeleton is estimated to be 175 kg. It was assumed that density of the solids building the model is about $8000\frac{\mathrm{kg}}{\mathrm{m}^3}$, that is similar to steel. This is almost twice as much as Sarcos XOS2 [26], which is reported to be made out of high strength aluminium and steel.

To make the simulation closer to reality, ground reaction force recorded during motion capture was applied to the exoskeleton platforms, imitating an operator stepping on them. Point of force application is at the origin of FoRm_PlatC (where m $\in$ {L, R}), shown in Fig. 7.11. Unfortunately, only during one stance phase of each leg the force recorded. The signals were replicated to occur during each stance phases. Ground reaction force in horizontal direction for the left foot is depicted in Fig. 7.20. In vertical direction is depicted in Fig. 7.21. For right leg, horizontal force is depicted in Fig. 7.22, and in vertical direction in Fig. 7.23.

Contact of the exoskeleton with the ground was simulated using Simscape Multi-

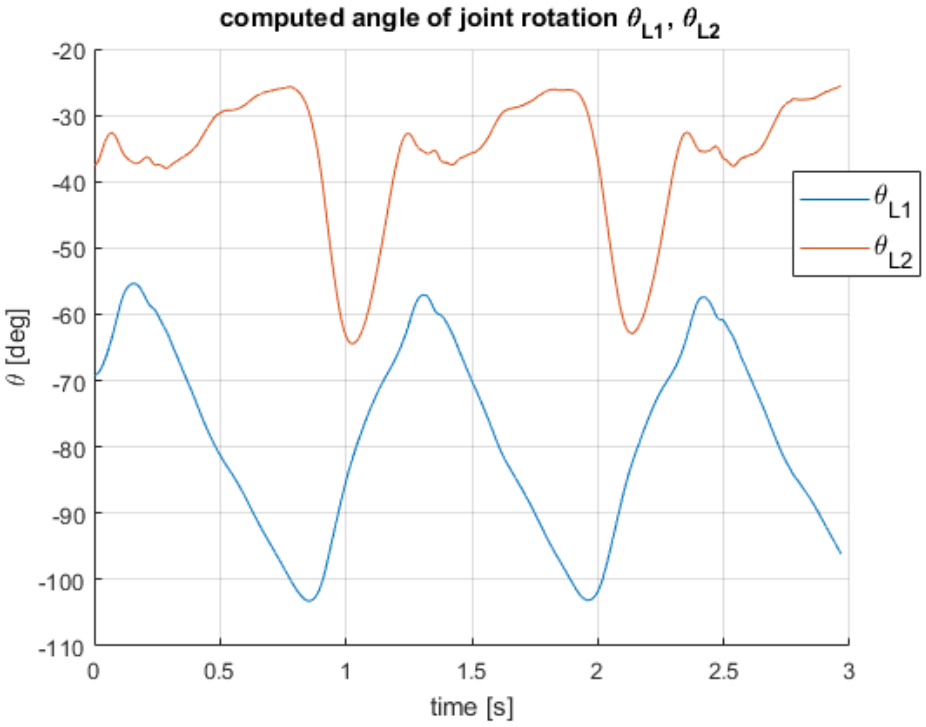

Figure 7.4: Computed rotation at joints of exoskeleton left leg (see Fig. 7.1) during gait, with input as in Fig. 7.2. θ_{L1} – left hip rotation, θ_{L2} – left knee rotation.

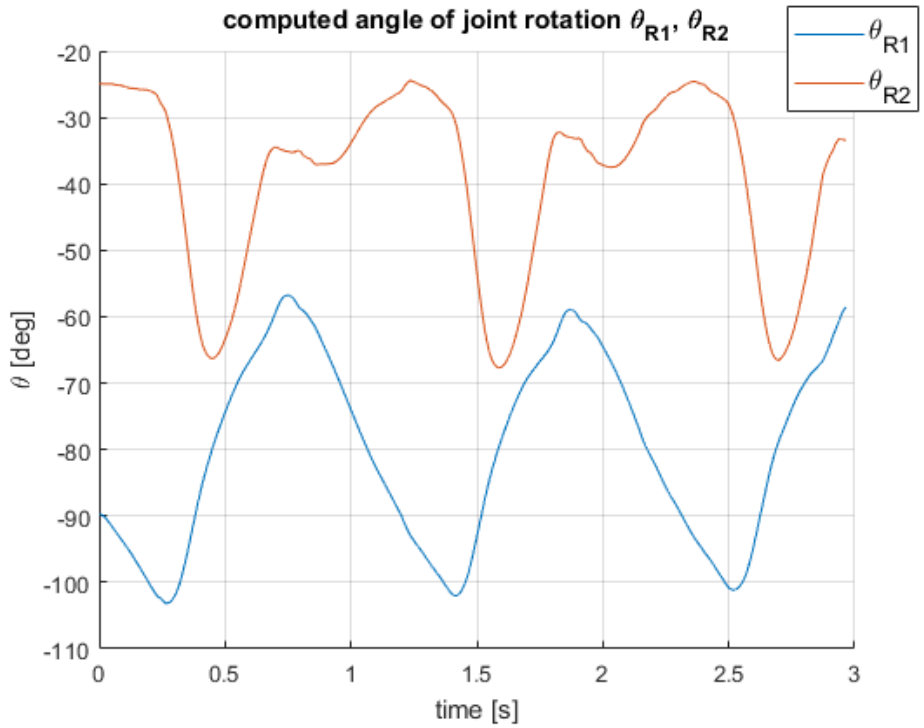

Figure 7.5: Computed rotation at joints of exoskeleton right leg (see Fig. 7.1) during gait, with input as in Fig. 7.3. θ_{R1} – right hip rotation, θ_{R2} – right knee rotation.

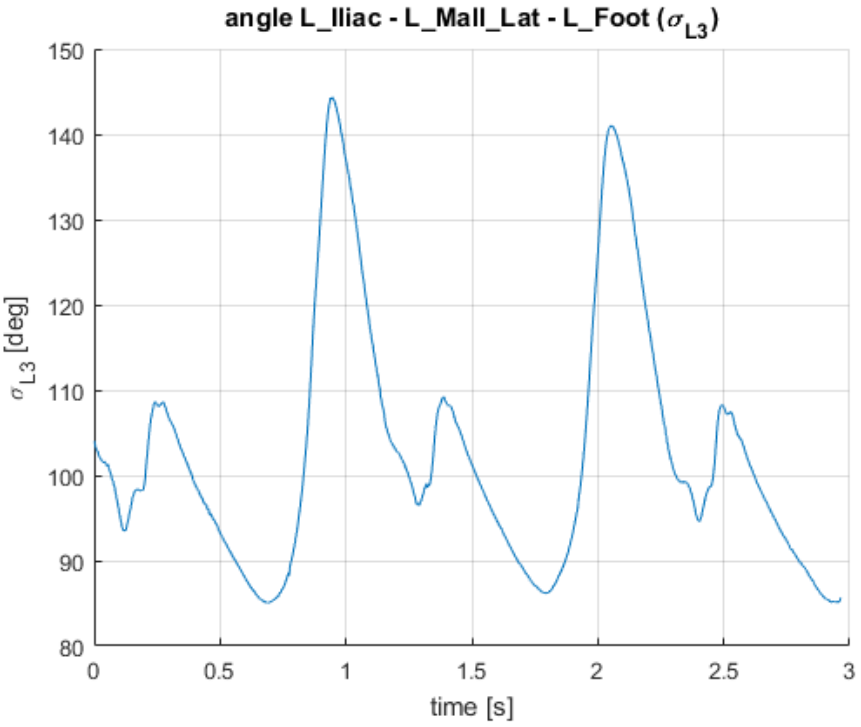

Figure 7.6: σ_{L3} – angle between L_Iliac–L_Mall_Lat–L_Foot (left leg) markers recorded during motion capture of gait.

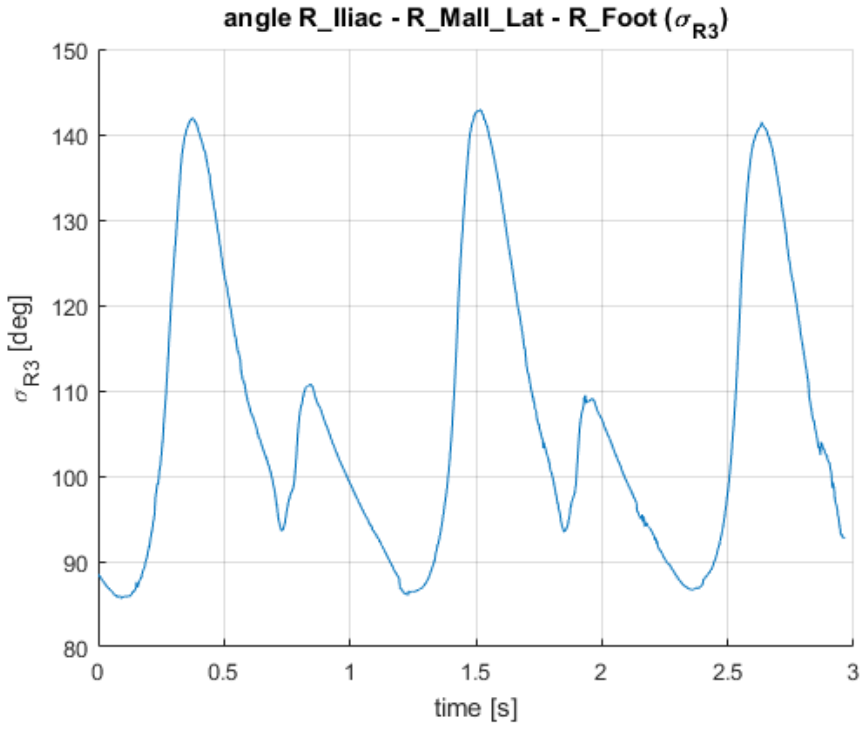

Figure 7.7: σ_{R3} – angle between R_Iliac–R_Mall_Lat–R_Foot (right leg) markers (see Fig. 4.7) recorded during motion capture of gait.

body Contact Forces Library[6]. Several Sphere to Plane Contact Force (3D) were used to model the contact of exoskeleton with the ground. The ground is flat along gait path. Spheres were attached to exoskeleton and ground was attached rigidly to world frame. Block parameters were selected such that the model walks in simulation as naturally as possible. They were chose by trail and error to be:

Force Law – Linear
Contact Stiffness (N/m) = 10^3
Contact Damping (N/(m/s)) = 10^6
Friction Law – Stick–Slip Continuous
Coefficient of Kinetic Friction = 0.7
Coefficient of Static Friction = 0.9
Velocity Threshold (m/s) = 0.0001

Three designs were proposed for the platform contact with the ground. They are depicted in Fig. 7.24. In design A (Fig. 7.24a), small spheres are placed at each end of the platform. This is done to model flat platform along all its length. Design B (Fig. 7.24b) consists of 6 spheres giving the platform curved shape. This is similar to platform used by PERCRO Body Extender [28]. Coordinates of the centres of the spheres are given in Table 7.2. Design C (Fig. 7.24c) is a combination of the previous ones, with a small heel sphere and curved surface at the front. Coordinates of the centres of the spheres are given in Table 7.3. This is similar to platforms used by Sarcos XOS family (see Fig. 2.21). It has to be noted that the entire weight of the exoskeleton and load would have to be transferred to the ground through the platform. The chosen designs are rigid, unlike sole of the BLEEX (see Fig. 2.18). Flexible platform might not withstand required loads or pose a safety hazard. Considering the fact that force sensors would have to be embedded into the platform to sense human–machine interaction force, as well as sensors detecting contact with the ground, mechanical design of the platform is a challenging task. Moreover, an unactuated joint is formed when a heel is off the ground. The angle between the platform and ground (as well as gravitation vector), cannot be measured directly. One way of dealing with the problem is incorporation of an inclinometer placed at the torso segment, as in the BLEEX (see Fig. 2.19). The platform inclination can then be calculated using the sensor reading and joint angles measured using encoders.

[6] https://uk.mathworks.com/matlabcentral/fileexchange/47417-simscape-multibody-contact-forces-library

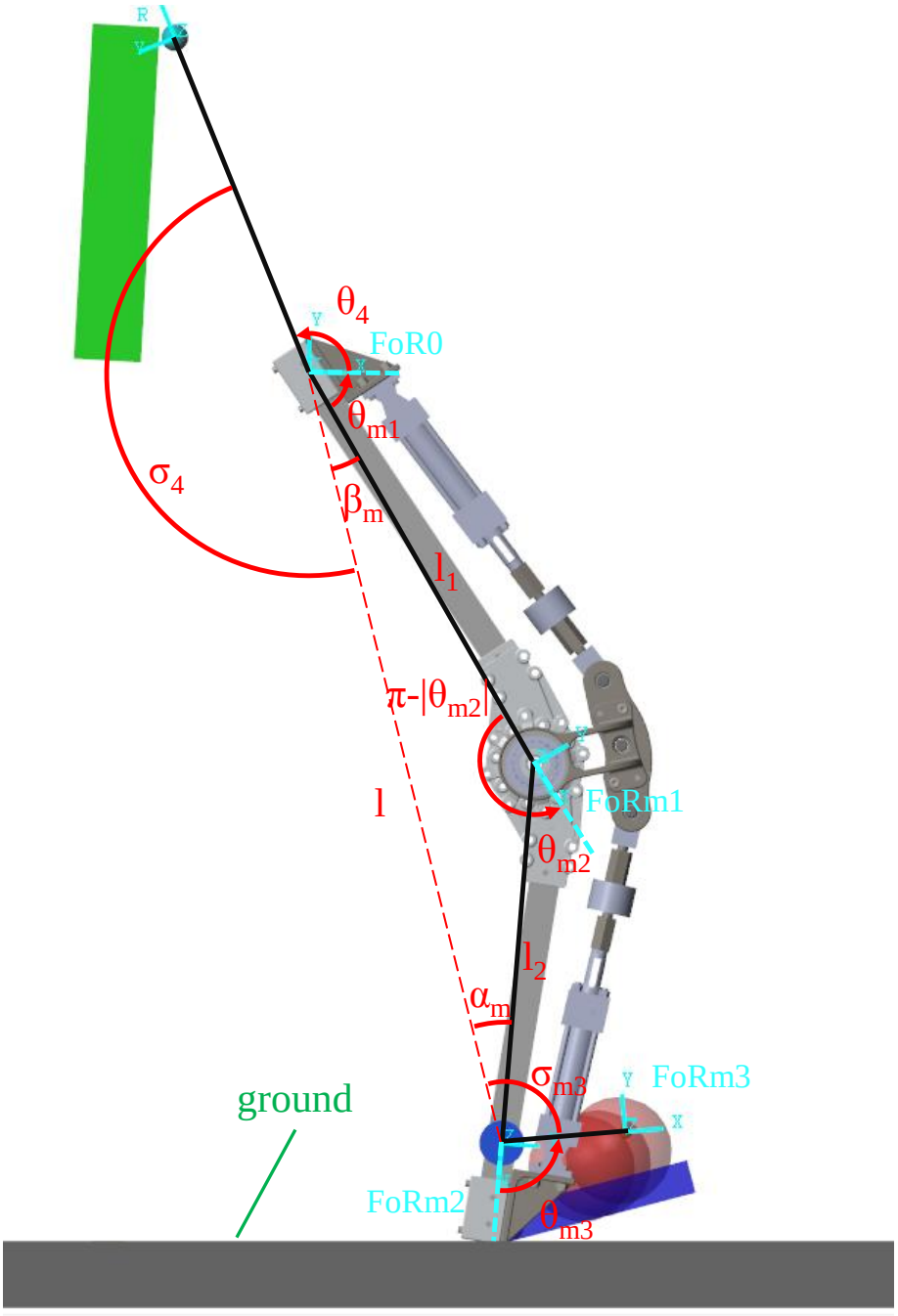

Figure 7.8: Exoskeleton leg and backpack (detail from Fig. 7.1) with angles outlined for transformation from motion capture data to robot coordinates. $m \in \{L, R\}$ (left and right respectively).

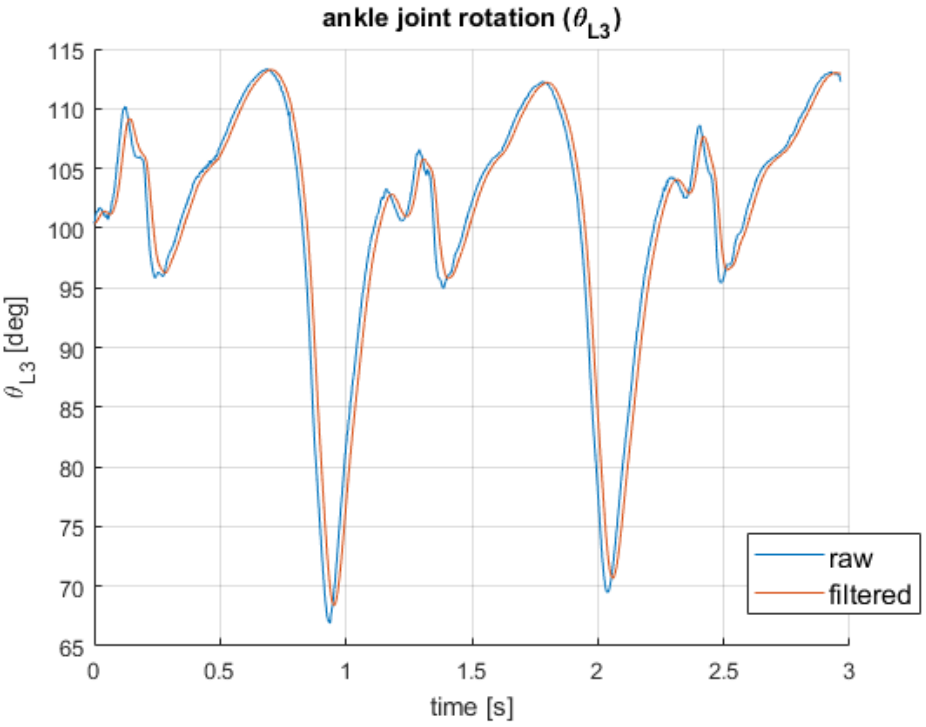

Figure 7.9: θ_{L3} – angle of rotation during gait of FoRL3 in FoRL2 (left ankle, see Fig. 7.8) calculated using Eq. (7.5). Raw (blue) and filtered (red) data. $\theta_{L3}^{err} = -4$ deg

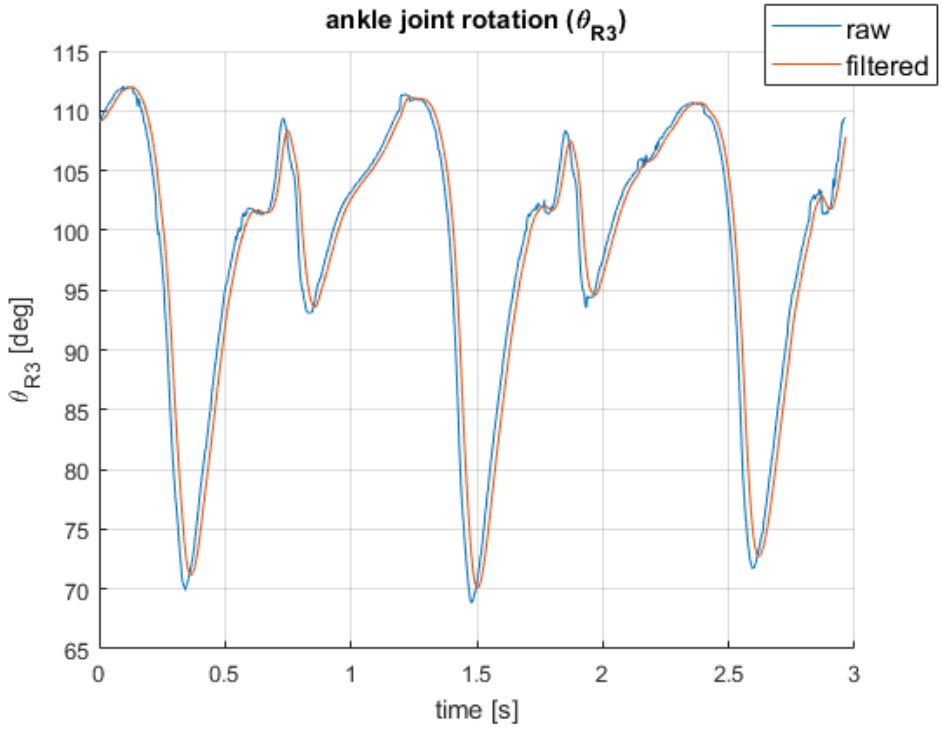

Figure 7.10: θ_{R3} – angle of rotation during gait of FoRR3 in FoRR2 (right ankle, see Fig. 7.8) calculated using Eq. (7.5). Raw (blue) and filtered (red) data. $\theta_{R3}^{err} = -4$ deg

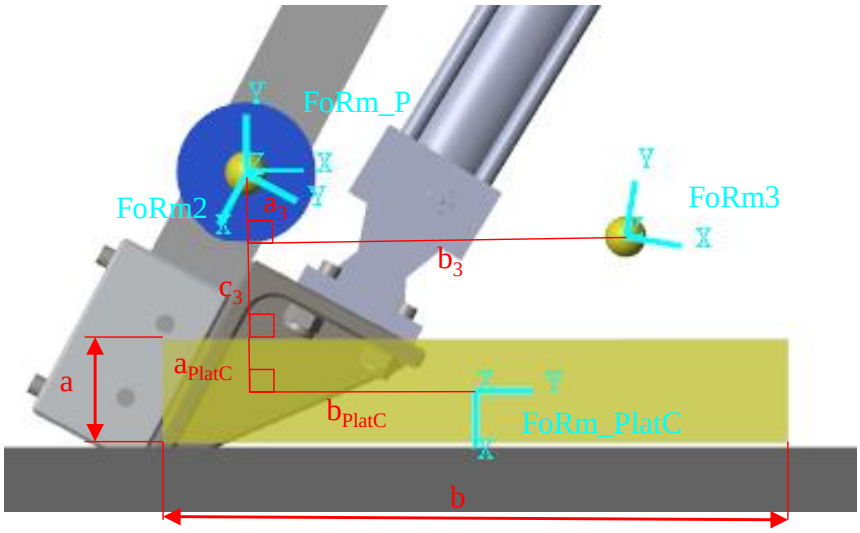

Figure 7.11: Model of an exoskeleton platform. Transformation angle of FoR_P in frame FoRm2 (where $m \in \{L, R\}$): 99.67 deg. Horizontal $a_3 = 0.031$ m and vertical $b_3 = 0.182$ m displacement of FoRm3 in FoRm_P. Vertical distance from FoRm3 to surface of the platform c_3 is 0.049 m. Vertical distance from FoRm_P to FoRm_PlantC is $a_3 + c_3 + a_{PlatC} = 0.105$ m, horizontal $b_{PlatC} = 0.11$ m. The height of the platform a is 0.05 m. Length b: 0.3 m.

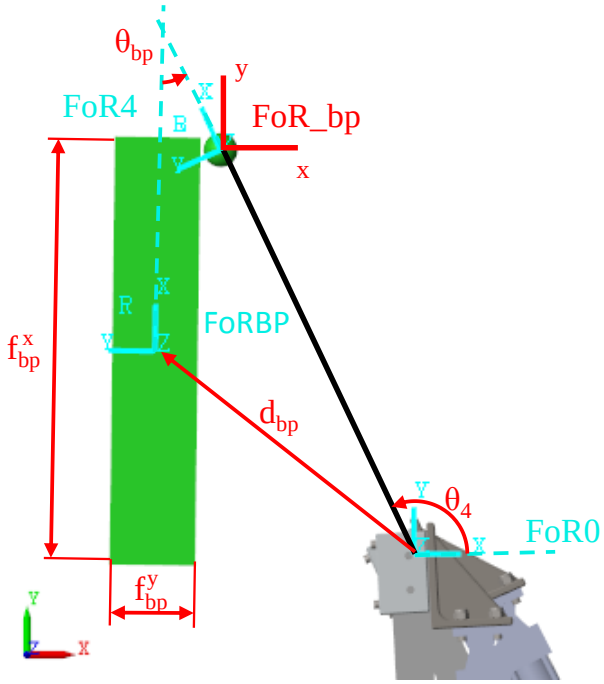

Figure 7.12: Attachment of a backpack to the full–body exoskeleton model. FoRBP – frame rigidly attached to the backpack .Transformation parameters: $d_{bp} = [0.25\ 0.3]^T$ m, $\theta_{bp} = -25$ deg. Dimensions of backpack $f^x_{bp} = 0.5$ m, $f^y_{bp} = 0.1$ m.

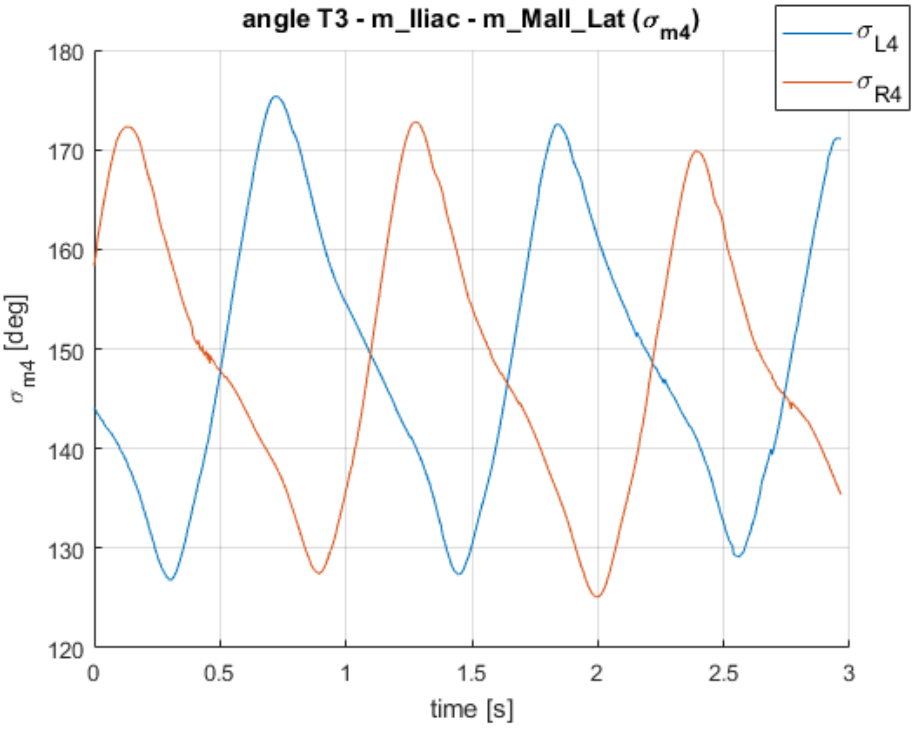

Figure 7.13: σ_{L4} (blue) – angle between T3–L_Iliac–L_Mall_Lat (left side) markers (see Fig. 4.7).σ_{R4} (red) – angle between T3–R_Iliac–R_Mall_Lat (left side) markers (see Fig. 4.7) recorded during motion capture of gait.

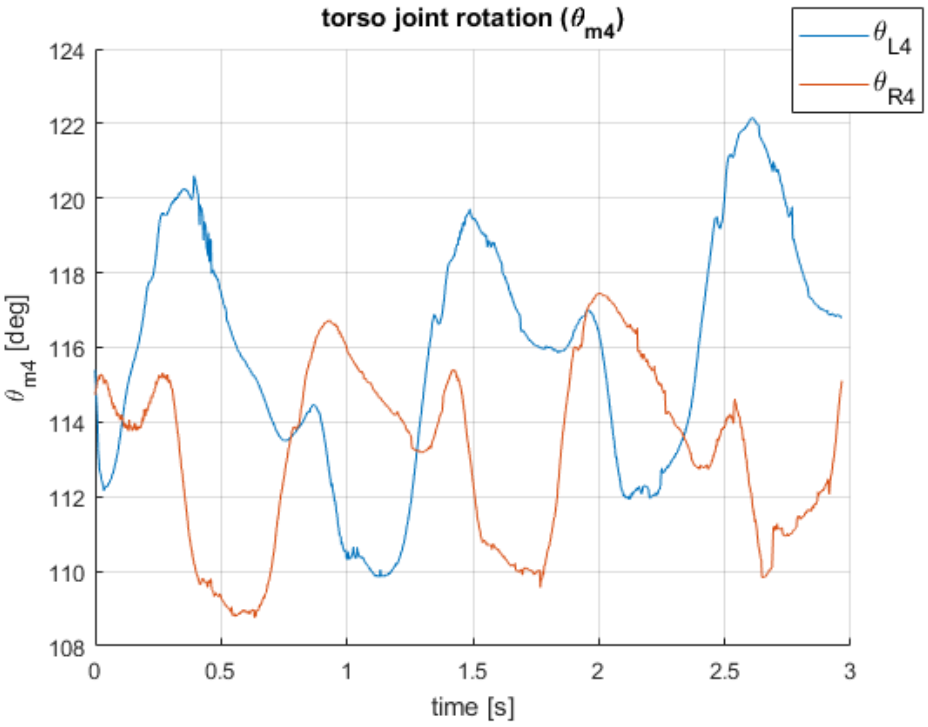

Figure 7.14: Torso angle (FoR4 in FoR0, see Fig. 7.8) during gait calculated using Eq. (7.6). θ_{L4} (blue) – based on σ_{L4}, θ_{R4} (blue) – based on σ_{R4}.

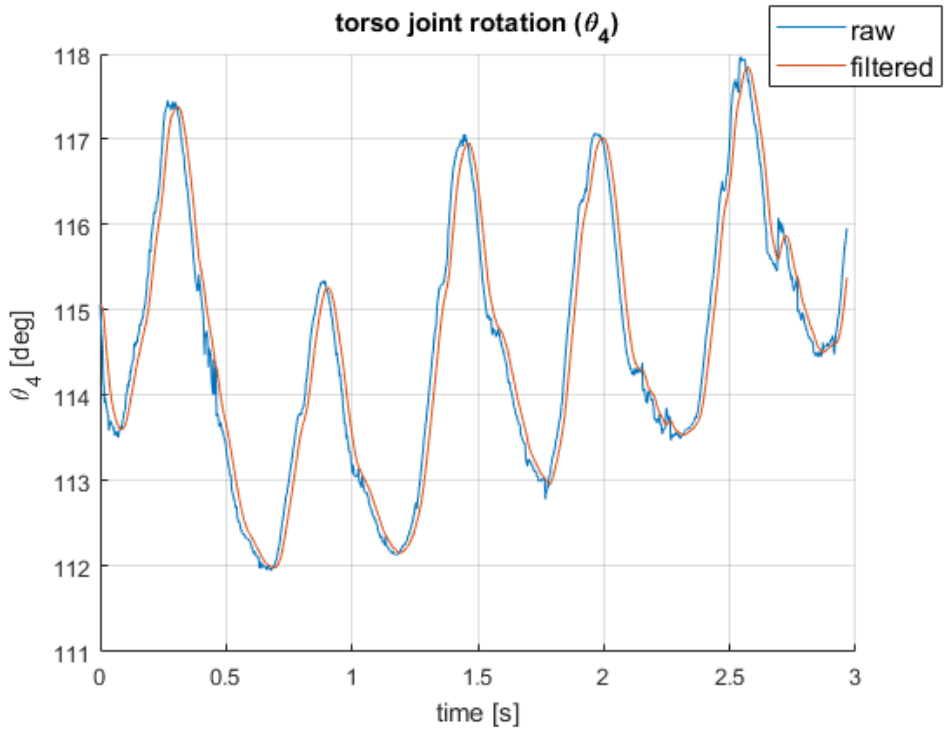

Figure 7.15: θ_4 – averaged torso angle (FoR4 in FoR0, see Fig. 7.8) calculated using Eq. (7.8). Raw (blue) and filtered (red) data.

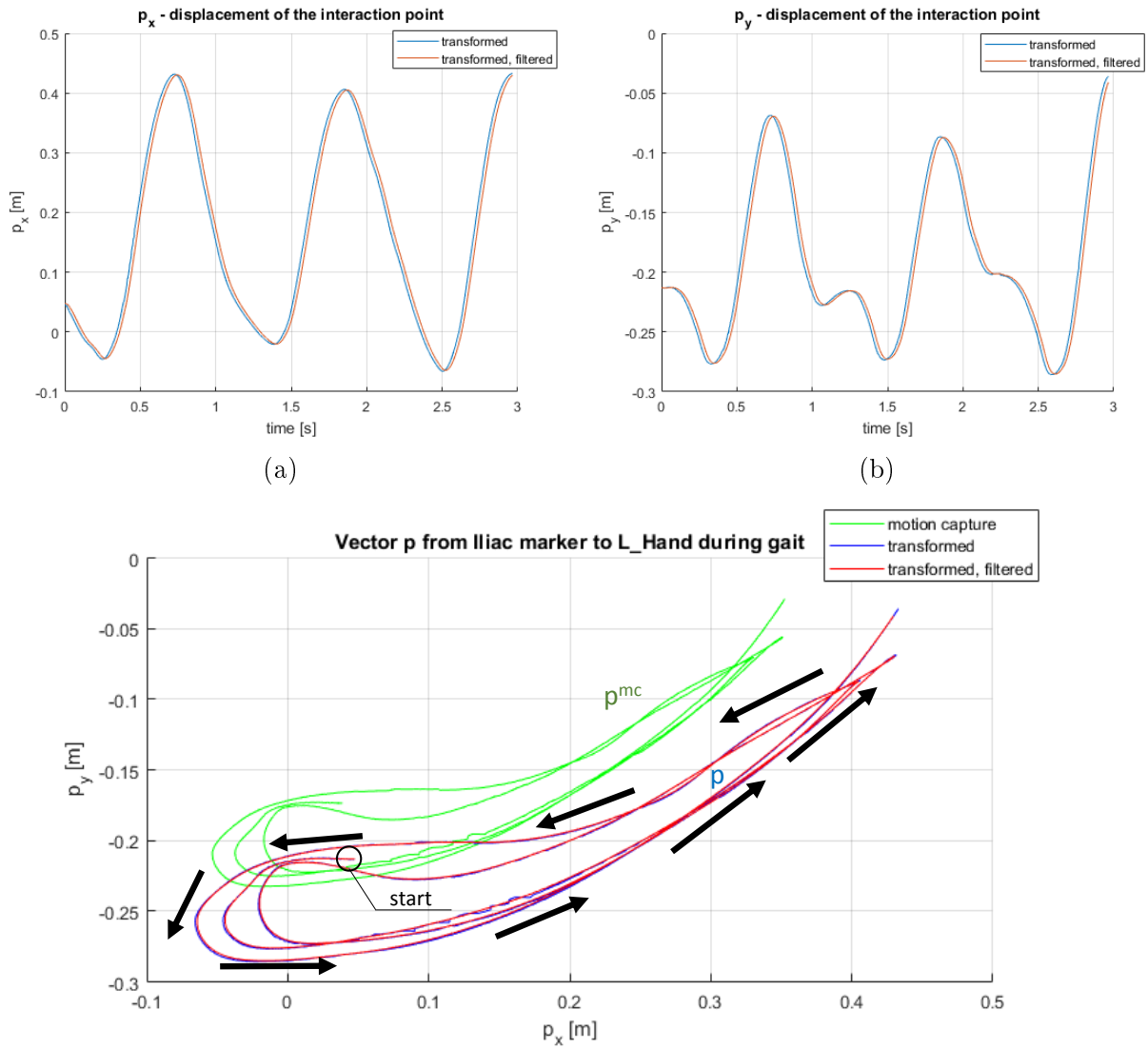

Figure 7.16: Displacement of a marker placed on metacarpals of left hand (L_Hand, corresponding to FoRL7) in the reference frame of marker placed on anterior superior iliac spine (Iliac, corresponding to FoR0) during gait. Green – original data from motion capture, blue – data transformed (scaling coefficient $s_{coef} = 1.2288$), red – data filtered using second–order filter. (a) – p_x displacement, (b) – p_y displacement, (c) – displacement $p = [p_x\ p_y]^T$ in the sagittal plane. Arrows point direction of movement. Correction $p^{\ err} = [0\ 0]^T$

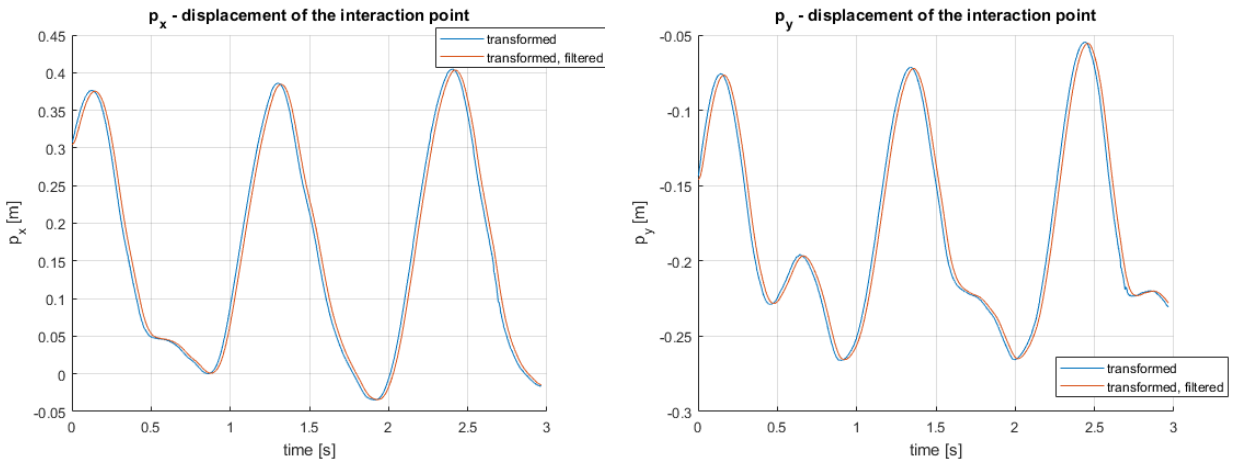

(a)

(b)

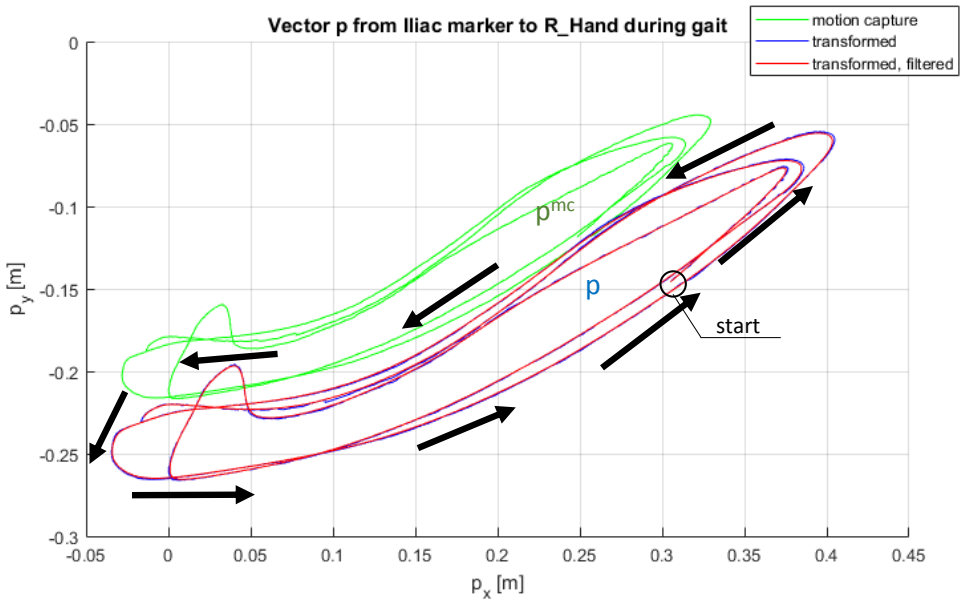

(c)

Figure 7.17: Displacement of a marker placed on metacarpals of right hand (R_Hand, corresponding to FoRR7) in the reference frame of marker placed on anterior superior iliac spine (Iliac, corresponding to FoR0) during gait. Green – original data from motion capture, blue – data transformed (scaling coefficient $s_{coef} = 1.2288$), red – data filtered using second–order filter. (a) – p_x displacement, (b) – p_y displacement, (c) – displacement $p = [p_x\ p_y]^T$ in the sagittal plane. Arrows point direction of movement. Correction $p^{err} = [0\ 0]^T$

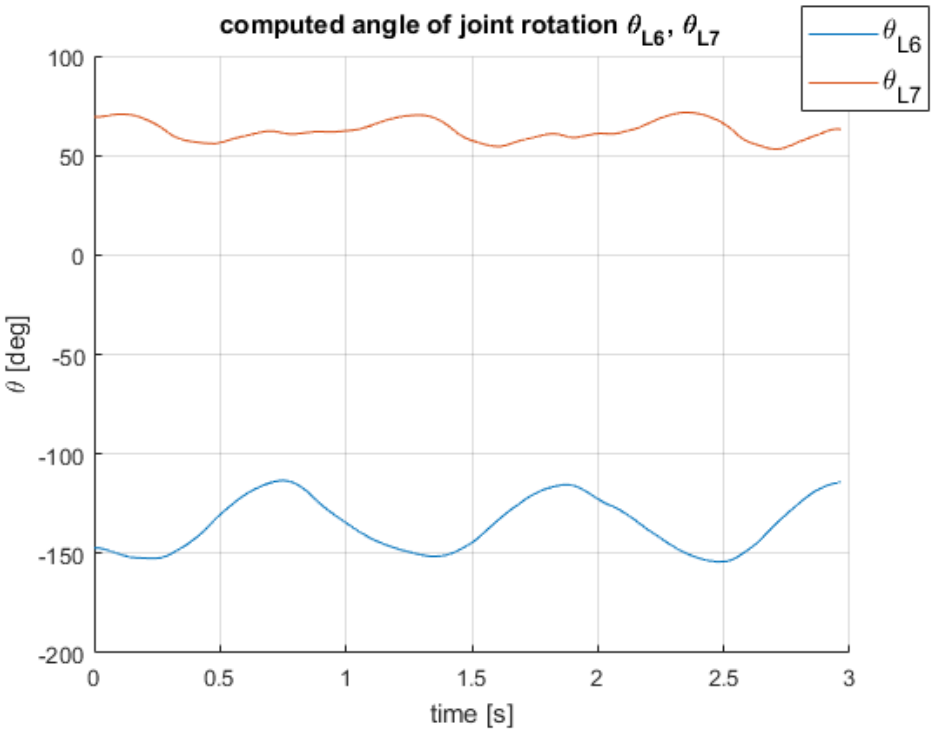

Figure 7.18: Computed rotation at joints of exoskeleton left arm (see Fig. 7.1) during gait, with input as in Fig. 7.16. θ_{L6} – left shoulder rotation, θ_{L7} – right knee rotation.

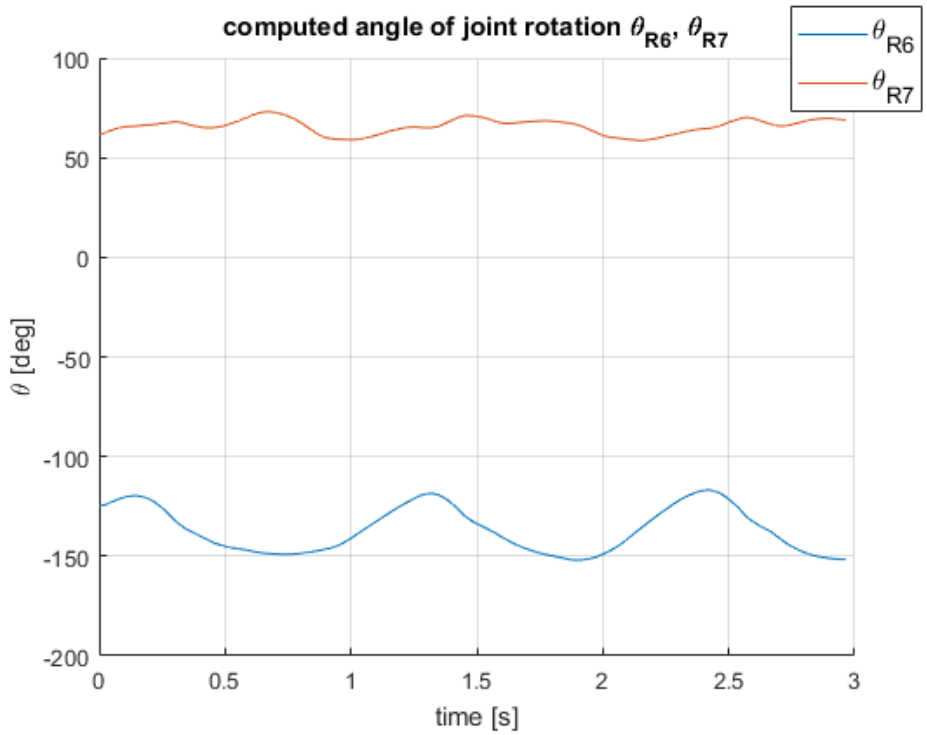

Figure 7.19: Computed rotation at joints of exoskeleton right arm (see Fig. 7.1) during gait, with input as in Fig. 7.16. θ_{R6} – left shoulder rotation, θ_{R7} – right knee rotation.

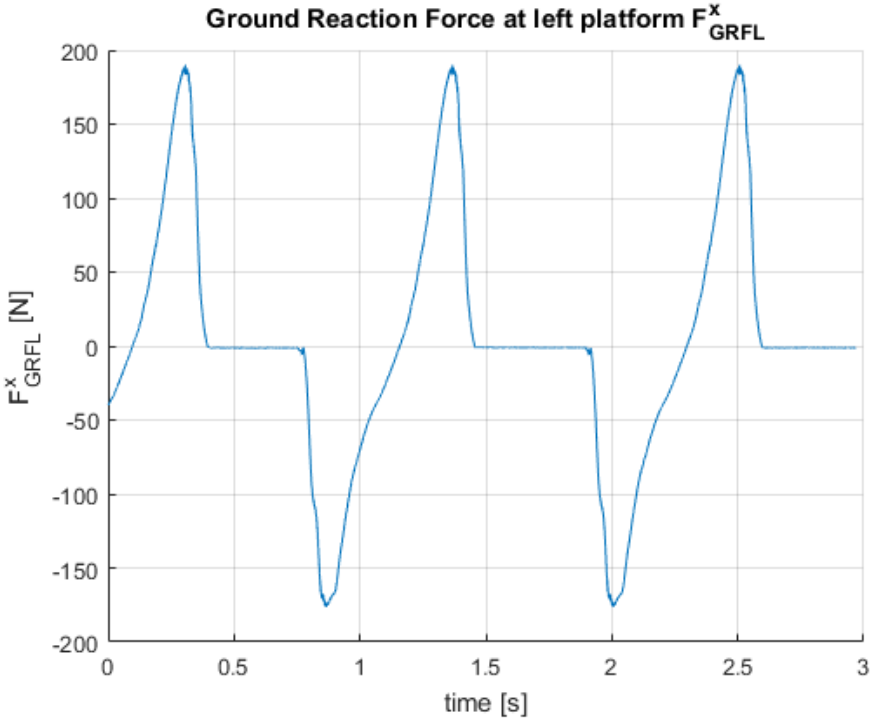

Figure 7.20: Synthesised ground reaction force during gait applied to left platform frame (FoRL_PlatC, see Fig. 7.11) along x axis (horizontal).

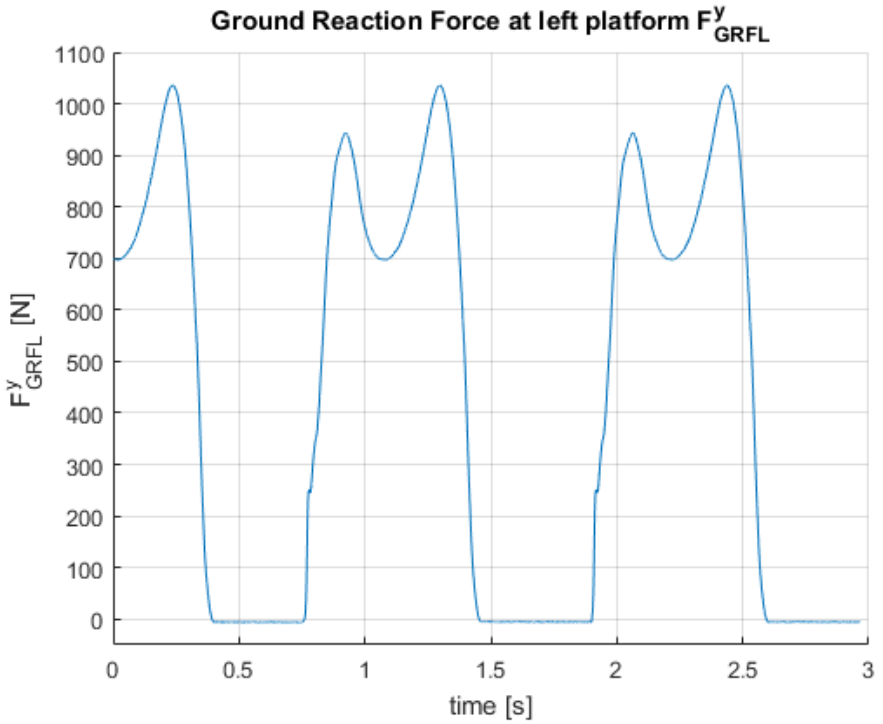

Figure 7.21: Synthesised ground reaction force during gait applied to left platform frame (FoRL_PlatC, see Fig. 7.11) along y axis (vertical).

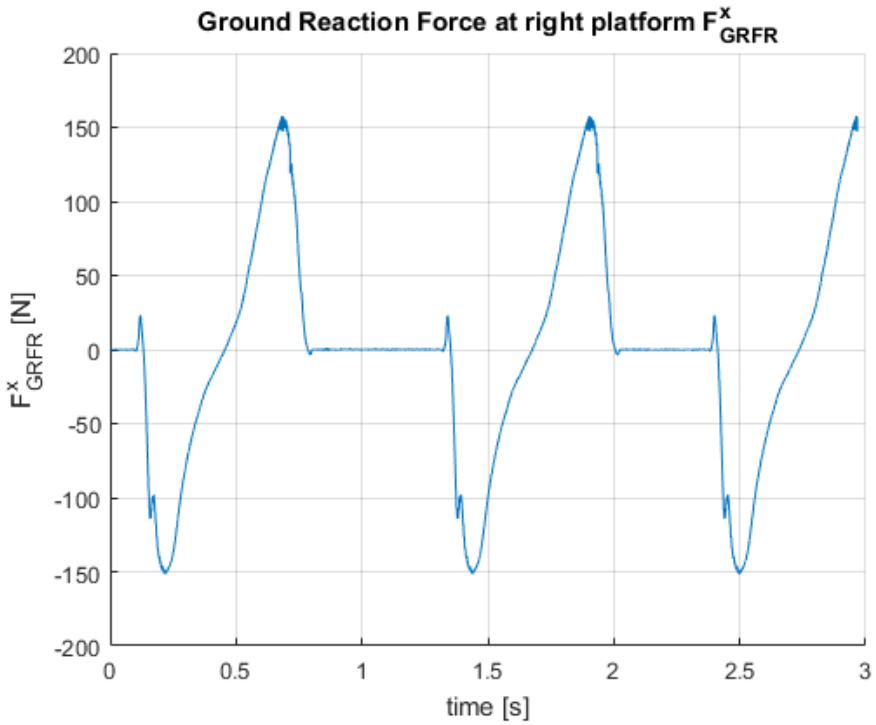

Figure 7.22: Synthesised ground reaction force during gait applied to right platform frame (FoRR_PlatC, see Fig. 7.11) along x axis (horizontal).

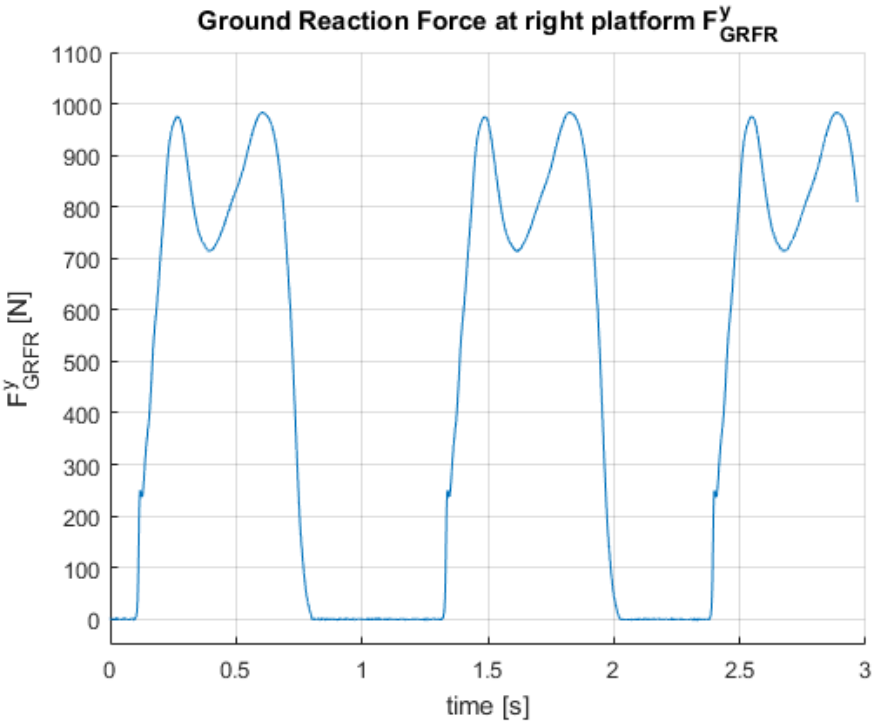

Figure 7.23: Synthesised ground reaction force during gait applied to right platform frame (FoRR_PlatC, see Fig. 7.11) along y axis (vertical).

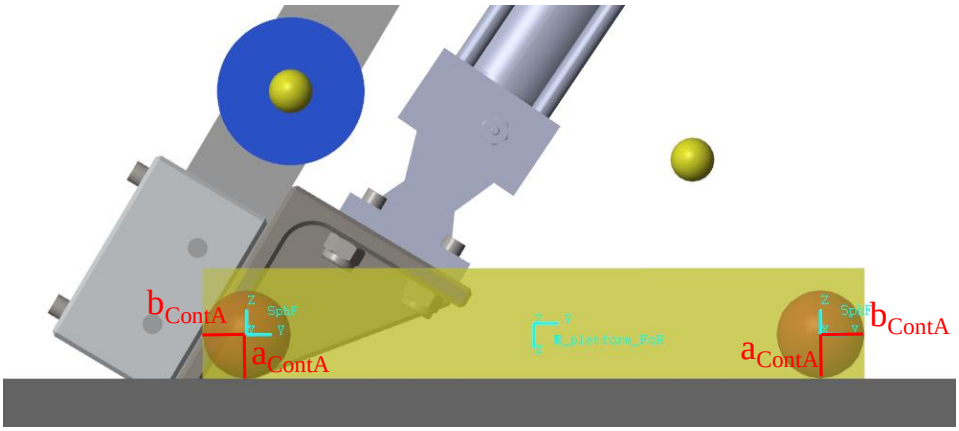

(a)

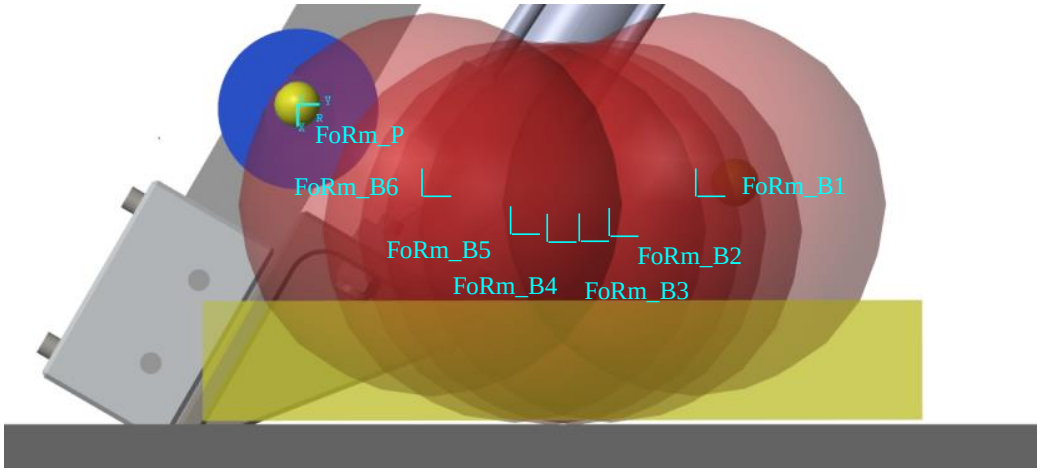

(b)

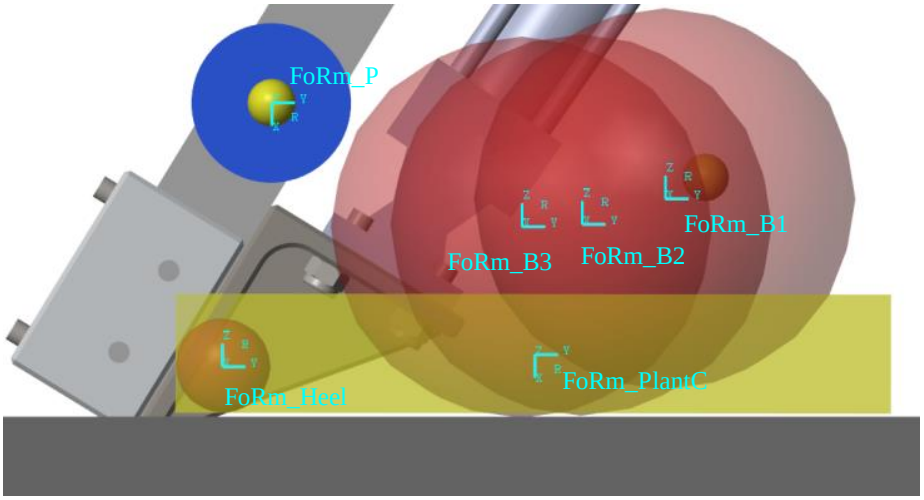

(c)

Figure 7.24: Different contact shapes of exoskeleton platform. (a) Design A – flat contact surface. Contact points at corners of the platform. $a_{ContA} = b_{ContA} = 0.02$ m (b) Design B – curved surface, 6 spheres. (c) Design C – curved surface (3 spheres) with a heel. $m \in \{L, R\}$, left and right respectively.

Table 7.2: Coordinates of contact spheres for design C in Fig. 7.24b. Reference frame FoRm_mP, where $m \in \{L, R\}$. Spheres' radius is 0.08 m.

frame of reference	x **displacement from FoRm_P [m]**	y **displacement from FoRm_P [m]**
FoRm_B1	0.165	-0.04
FoRm_B2	0.13	-0.051
FoRm_B3	0.115	-0.052
FoRm_B4	0.105	-0.052
FoRm_B5	0.09	-0.051
FoRm_B6	0.055	-0.04

Table 7.3: Coordinates of contact spheres for design C in Fig. 7.24c. Reference frame FoRm_mP, where $m \in \{L, R\}$.

frame of reference	x **displacement from FoRm_P [m]**	y **displacement from FoRm_P [m]**	**sphere radius [m]**
FoRm_B1	0.165	-0.04	0.08
FoRm_B2	0.13	-0.051	0.08
FoRm_B3	0.115	-0.052	0.08
FoRm_Heel	-0.02	-0.11	0.02

7.3 Gait Simulation Results and Sagittal Stability

In section 7.2 a full-body exoskeleton model in sagittal plane was proposed. The input to the simulation was kinetic and dynamic data for gait, recorded using motion capture. To evaluated the model, it was first attached to the world frame using a Cartesian joint, restricting displacement in coronal plane (z axis, depth) and forbidding rotation in sagittal plane, around frontal axis (left–right axis). Vertical displacement of FoR0 with reference to the global frame is depicted in Fig. 7.25. During the period of the simulation, the model advances 6 steps forward. Data from the motion capture, that is an operator walking without an exoskeleton is drawn using violet line. The data was scaled using coefficient $s_{coef} = 1.2288$. Displacement in vertical direction resembles a sine wave. Amplitude of movement is about 0.04 m. The simulation was also run for each of the proposed platform models depicted in Fig. 7.24. For design A (flat platform, small spheres at corners of the platform) the signal (blue) deviates significantly. This is due to the fact, that the robot rises on the front sphere during stance phase. In Fig. 7.26 horizontal displacement of FoR0 with reference to global frame is depicted. Model with platform of design A travels the largest distance. It is seen in Fig. 7.25 that exoskeleton walking with platform design B (red) is closer to natural gait pattern, although the robot plummets due to absence of a heel when the leg contacts the ground. It travels the same horizontal distance as human freely walking. Design C (yellow) is a combination of the two other designs. It rolls over the front curved contact surface and does not plummet as much as design B. The trajectory vertically and horizontally is the closest to natural gait pattern (violet).

After determining design C to be allowing for the most natural gait, the model was given a degree of freedom to rotate in the sagittal plane. A rotary joint was placed between Cartesian joint attached to the world frame and FoR0 of the model (see Fig. 7.1). Unfortunately, the simulation has shown that the free moving exoskeleton model walking is not stable in sagittal plane, it tends to fall backwards. Both Sarcos XOS (see Fig. 2.21) and BLEEX (see Fig. 2.18) use harness to attach an operator to the robotic frame. Such harness is able to transfer horizontal force stabilising exoskeleton during walking. In simulation a force was applied in x direction of FoR_bp frame (see Fig. 7.12). Origin of FoR_bp coincides with T3 marker (3^{rd} thoracic vertebra). The force was calculated using a transfer function of PID controller block in Simulink[7] of

[7] https://uk.mathworks.com/help/simulink/slref/pidcontroller.html

form:

$$G(s) = k_p + k_i \frac{1}{s} + k_d \frac{N}{1 + N\frac{1}{s}} \tag{7.9}$$

where $k_p = 80$ – proportional gain, $k_i = 30$ – integral gain, $k_d = 15$ – derivative gain, $N = 100$ – filter coefficient. s – s is a complex number frequency parameter of Laplace transform. Force is calculated as:

$$F(s) = G(s)\xi(s) \tag{7.10}$$

where F – force to stabilise, applied to FoR_bp, ξ – angle of FoR0 in global reference frame, in degrees.

In Fig. 7.27 calculated force is depicted. Angle of FoR0 in global frame is depicted in Fig. 7.28. It is seen that the operator has to pull exoskeleton with maximum force of about 600 N and push it with minimum force of -300 N in a repeating manner. The inclination angle changes from about -1 to about 4 deg. It has to be noted that the exoskeleton model, with weight of 175 kg (see Table 7.1), is heavier than existing enhancive exoskeleton. Sarcos XOS weights about half as much, 95 kg [26]. Thus, it is expected to require less force to stabilise in the sagittal plane. Required 600 N of maximum force for considered model would put strain on an operator during walking. Thus, the maximum weight of the machine would be limiting factor when sagittal stability is required to be maintained.

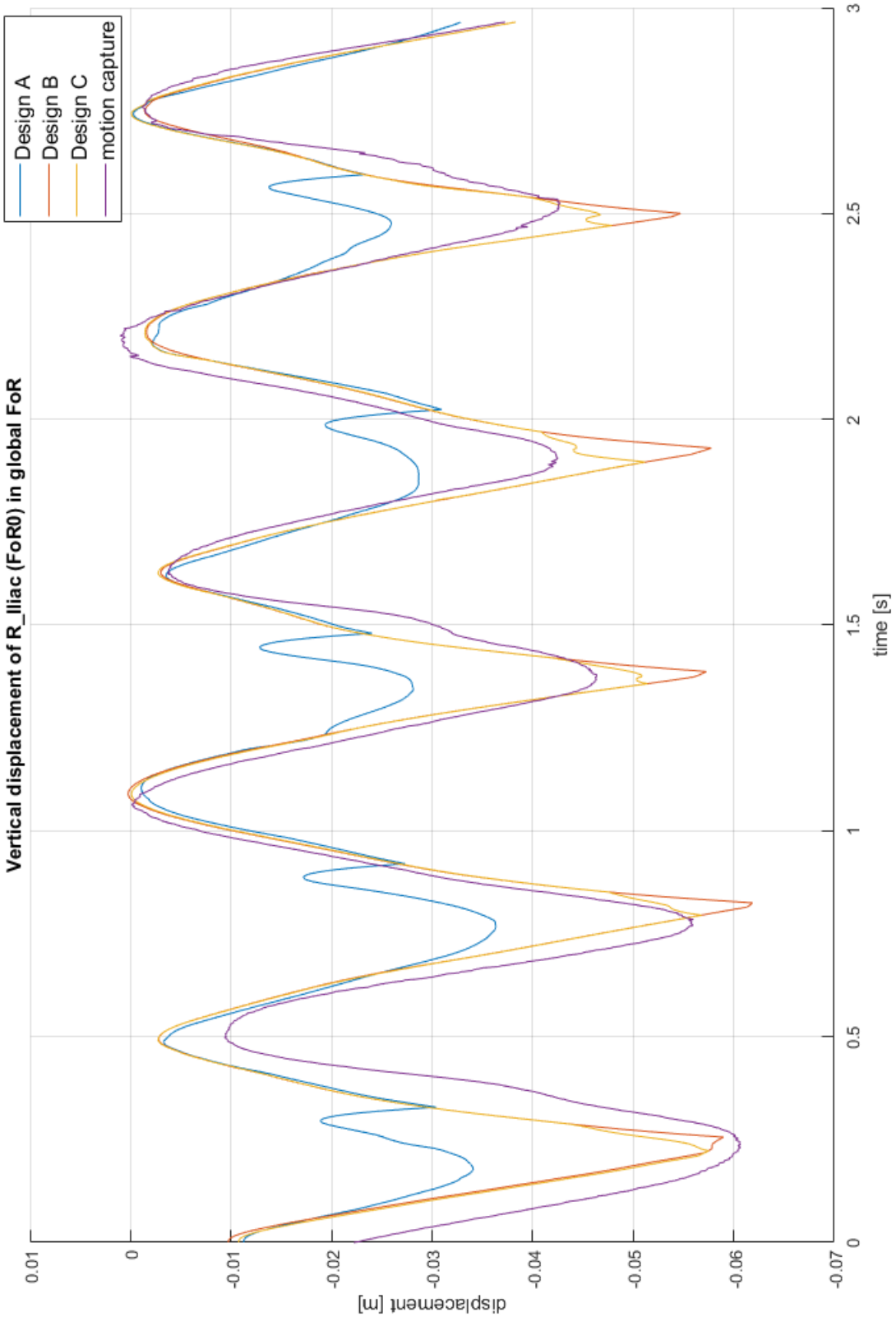

Figure 7.25: Displacement of FoR0 (Iliac marker), fixed to model hip joint (see Fig. 7.1), in y (vertical) direction of global reference frame during gait. Motion capture data scaled by a coefficient $s = 1.2288$. Comparison of different designs from Fig. 7.24.

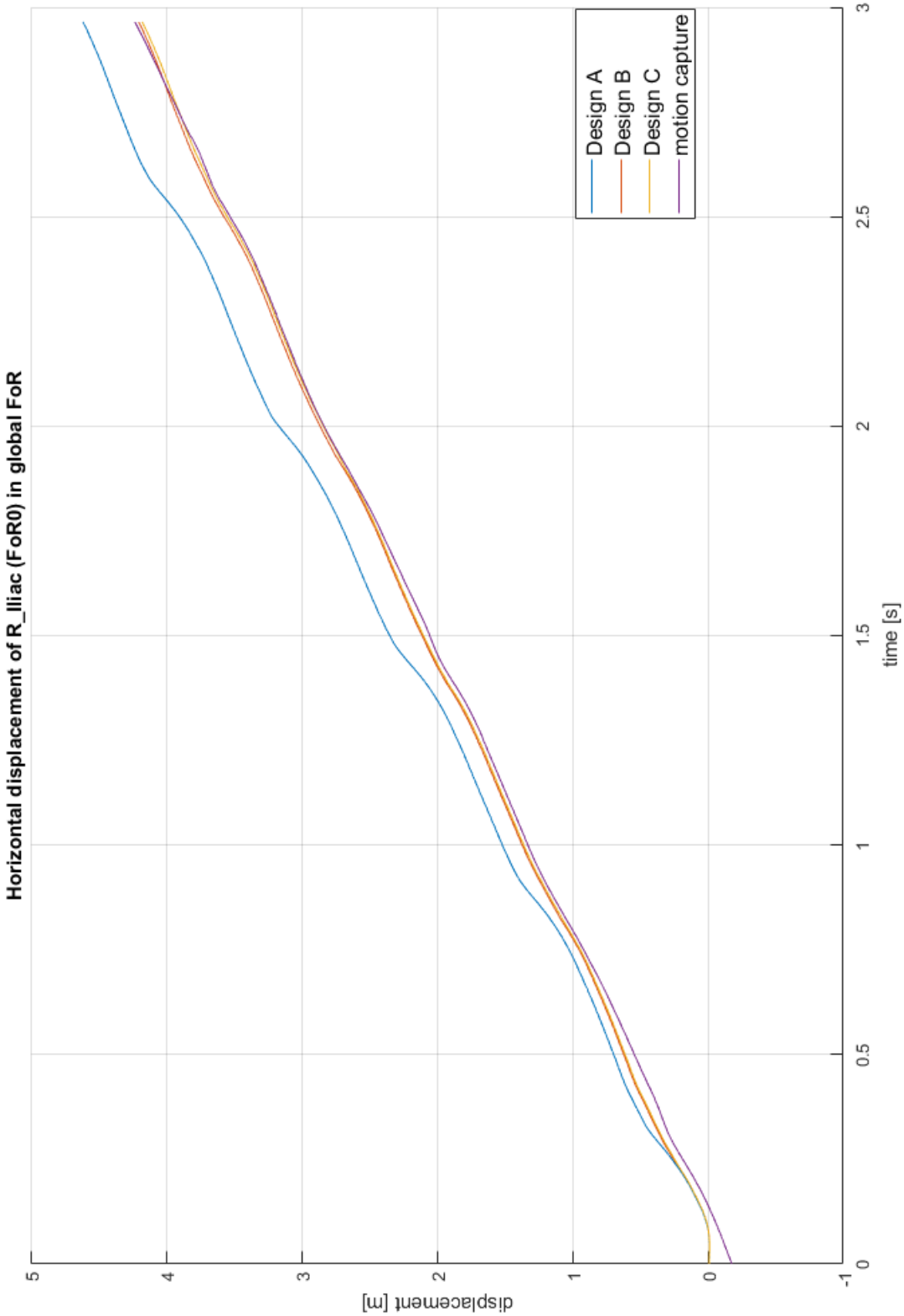

Figure 7.26: Displacement of FoR0 (Iliac marker), fixed to model hip joint (see Fig. 7.1), in x (horizontal) direction of global reference frame during gait. Motion capture data scaled by a coefficient $s = 1.2288$. Comparison of different designs from Fig. 7.24.

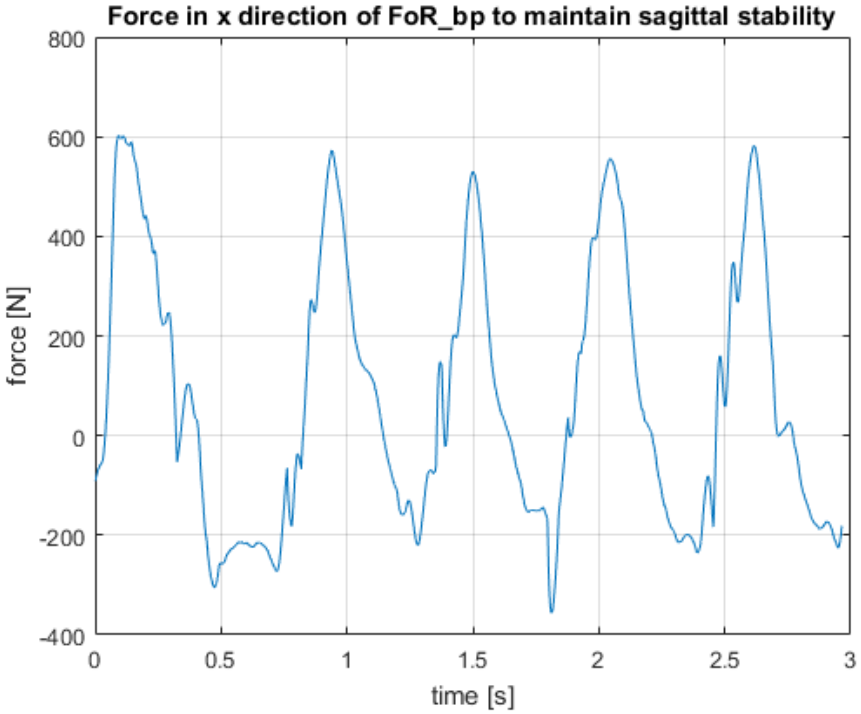

Figure 7.27: Force applied to frame FoR_bp in x, horizontal direction (see Fig. 7.12) to stabilise model from Fig. 7.1 during gait for platform design C (see Fig. 7.24c).

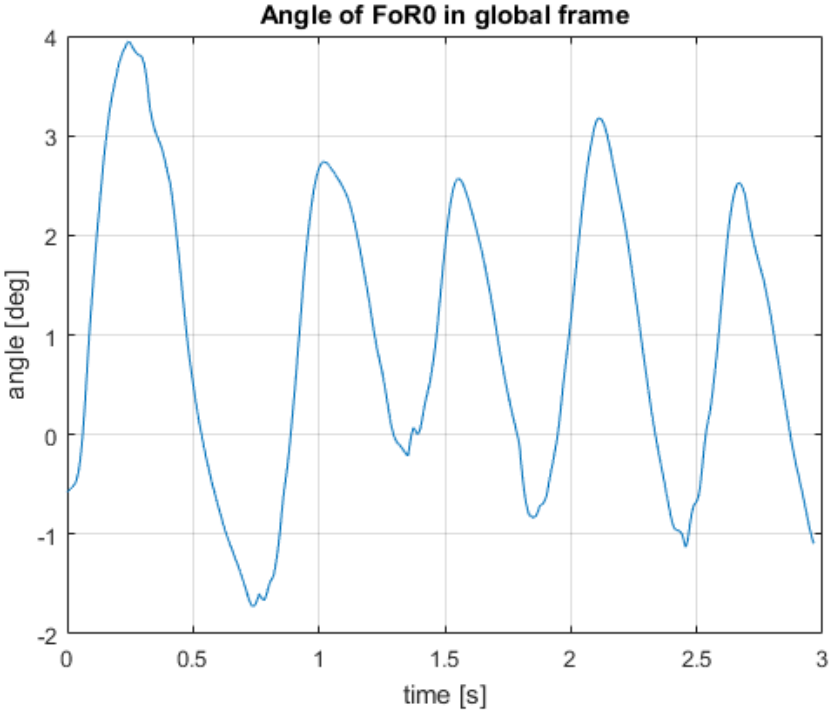

Figure 7.28: Angle between FoR0 (see Fig. 7.1) and global frame of reference during gait with force applied as depicted in Fig. 7.27 for platform design C (see Fig. 7.24c).

7.4 Summary

A full–body exoskeleton model based on biometric data was proposed. It was shown that it is possible to simulate the model walking using data from motion capture study. The contact with flat ground was modelled using Simscape Multibody Contact Forces library. It was shown that a platform model (design C, see Fig. 7.24c) with a heel and curved front allows for most natural gait. The model requires horizontal force applied to the torso segment to stabilise it in sagittal plane during walking. An operator would have to exert this force. This might be a reason why BLEEX and Sarcos XOS have a harness linking operator to the torso compartment. It would have to be investigated what mass limit of the entire exoskeleton still allows for comfortable walking. It would have to be investigated if the user might alter pattern of gait to compensate or if it might be possible to produce torque at joints to decrease the force.

Chapter 8

Summary, Conclusions and Future Work

8.1 Summary

In Chapter 1 research aims and objectives were outlined. The aims of the research were to provide control strategy for a novel design of a joint for an enhancive exoskeleton coupling with the operator's body segments and to identify challenges in control of an enhancive full–body exoskeleton for human power amplification and to design a dynamic model addressing these. In section 8.1.1 the research objectives are evaluated. In section 8.1.2 evaluation of proposed middle–level control with low–level coupled control is evaluated against the requirements from 3.2.

8.1.1 Evaluation of Objectives

Establish requirements for an enhancive full–body exoskeleton, with focus on control aspects.

The requirements gathered in course of the project meetings of specialists from domains of biomechanics, mechanical engineering, electrical engineering and control engineering are described in chapter 3. From these, requirements for control system and for measurement system are derived. Special emphasis is placed on safety of the prototype. This is a first step in system engineering approach, used through this thesis, to design of a full–body enhancive exoskeleton.

Survey potential control strategies for the entire robot, establish the most appropriate candidate for the considered device.

In chapter 2 control strategies used to govern previous reported approaches to constructing enhancive exoskeleton were described. These are divided into 3 categories: *Master–Slave Position Control* law, *Direct Force Control* and *Indirect Force Control*. The force control laws, for which controlled variable is human–machine interaction force, and control matching angular displacement of the joints of robot to angles of operator's joints (*Master–Slave Position Control* law), have been evaluated against the requirements described in chapter 3 and assessed as superior. *Indirect Force Control* is documented extensively as a control law for BLEEX (lower–body exoskelton). *Direct Force Control* is used by Sarcos XOS (full–body exoskeleton), but little literature exists on the subject. The *Direct Force Control* is chosen to govern prototype of novel joint design described in chapter 4.

Conduct motion capture study to gather biometric kinematic and dynamic data.

Pilot motion capture study based on one subject was conducted. It is described in section 4.4. The subject performed a number of activities, including gait. The full list in enclosed in Appendix D. For motion capture data (joints displacement) bandwidth was calculated. For all tasks, except running, it was assessed to be 10 Hz. If running is considered, the bandwidth is about 40 Hz. The data was used as input to the simulation of control of single joint prototype model in chapter 5 and in simulation of full-body model in chapter 7. From bandwidth of motion of human joints, requirement on sample rate of electronics was derived.

Choose sensors and control electronics for a novel single joint prototype with hydraulic actuation. Develop electronics and software for the platform.

Control electronics and software were developed for a novel joint prototype. They are described in chapter 4. Load cells, encoder, 6 DoF F/T sensor, LVDT, control valves of hydraulics were interfaced to MyRIO, on which control algorithms were executed. The control software, both low level hardware drives and algorithms, were written in LabView. Equations were derived for calculation of lower rod extension based only on upper rod extension, joint angle measured using encoder and geometric properties.

Construct control–oriented model of the single joint prototype and simulate the proposed controller with input data from motion capture study. Evaluate performance of the controller, select its parameters and assess its stability.

This was done in chapter 5. First control goals for the controller were described. That is minimisation of human–machine interaction force and synchronisation of rods extension. A middle level controller was devised to meet the control goals. The novel joint prototype was modelled using Simscape Multibody library. The algorithm was implemented in Simulink with an assumption that it is actuated by ideal prismatic actuators. Equations were derived to transform demanded actuator torque from middle level controller to demanded force for the actuators. Input to the algorithm was displacement of marker placed on ankle with respect to marker placed on iliac crest recorded during motion capture study. It was demonstrated in simulation how the algorithm performs with respect to control goals. Relationship between controller parameters and performance was shown. In the next step a model of hydraulic system built using Simscape Fluids library was included in the simulation. Simulation of independent force control of the hydraulic actuators was conducted, as well as simulation of proposed novel coupled control for two hydraulic actuators connected with a knee cap. The coupled control requires only one load cell and one LVDT. It was shown that its performance is not worse than independent control based on evaluation against control goals. The absolute human–machine interaction force does not exceed 40 N in case without load and in case with load. Lastly, low level proportional gain of coupled controller was tuned. It was shown that both for case with load and no load there is clear minimum of control goals. Setting the gain to low does not allow following demanded value. Setting the gain to high leads to loss of stability and oscillation of the force.

Validate the joint design and control strategy on a prototype.

This was done in chapter 6. The algorithm was carried over from Matlab to LabView. First, static test was performed without load attached. Prototype was moved by a robotic knee attached in parallel in steps of 10 deg with static intervals between motion. It was shown that the middle level control with coupled control minimises the human–machine interaction force during these intervals. Synchronisation of the rods is maintained. Next, the joint was displaced by hand in swinging manner. Calculated bandwidth of motion was about 0.5 Hz, that is less than required for gait. Test were done for case without and with 60 kg load. The human–machine force was minimised. In each case it does not exceed 40 N. Synchronisation of the rods was maintained as well. 60 kg of load can be manipulated and forces felt by the user does not exceed 30 N. This gives power amplification of 1:20, which is similar to results reported for Sarcos XOS [26]. The required sample rate of electronics was not achieved. It was shown that

iteration of the algorithm takes on average 3 to 6 ms to compute. This is however more than required by Nyquist theorem.

Construct a model of a full–body load–bearing exoskeleton with the aim of allowing it to walk, based on biometric data from motion capture.

A model of full–body exoskeleton based on biometric data from motion capture was developed in Simulink. It is a quasi–anthropomorphic structure with segments enclosing operators legs, trunk and arms. The segments of the model were displaced in sagittal plane with input signal derived from motion capture of gait. The contact with the ground was modelled using Simscape Multibody Contact Forces library. Three platforms designs were proposed and evaluated. It was shown that the one with a heel and curved front allows for most natural gait pattern. Sagittal stability was evaluated as well. The model requires an external force to maintain it. An operator would be burdened with it.

8.1.2 Evaluation of the Proposed Control Method

In this section proposed middle–level control with low–level coupled control is evaluated against the requirements from section 3.2. Requirements are given in Table 3.3.

CS–1: The controller shall be adaptable to different users.

The controller does not depend on a model of a user's body, so it is instantaneously adaptable to a new operator. However, the joint prototype is design to fit a tall person (2.2 m). The joint would not have range large enough to fit a much smaller person during walking.

CS–2: The controller shall allow performing activities listed in the Appendix D.

The force control method does not limit the activities performed by the operator in any way. They can move their extremities freely within the robot, and the robot moves in concert. It was shown in the simulation that it can follow gait, however the interaction forces exerted might be burdensome (up to 200 N with load, up to 100 N without load).

CS–3: The controller shall be robust.

Controller requires knowledge of machine geometries to estimate extension of the lower piston and to determine Jacobian of the manipulator. Also knowledge of geometries is required to calculate desired force at the actuator from prescribed torque.

CS–5: The control method, as implemented in the controller, shall be safe.

The control is inherently safe as it aims at minimising the interaction force between the machine and the user. However there are limits on controller gains, increasing which too much might lead to oscillations of the interaction force.

CS–6: The device shall be stable when governed by the controller during putting on and off.

Since the method is designed to operate with a goal of minimising the interaction force, it is generally stable. Temporary loss of contact with operator's limb of the robot frame would not cause uncontrolled behaviour. Indeed, the experimental evaluation showed that without contact with the operator there are no oscillations of the knee cap or end effector. Touching the handle does not lead to abrupt behaviour. Device after loosing contact with the operator after some time stays in certain equilibrium point. The human–machine interaction force is decreased in static case, as shown in the simulation is stage 2 and on experiment with the robotic knee cap.

CS–7: The device governed by the controller shall be stable while carrying the load.

Since in the normal operation mode the user is in non–forceful physical contact with the robot, he can sense dynamical behaviour of the load. The kinematic chain between the load and the user body allows for information to flow from the load–bearing end effector to the operator's sensory system. Experiments with 60 kg load have shown that for a certain limited bandwidth (0.5 Hz), the interaction forces are greatly diminished.

CS–8: The device governed by the controller shall be stable in case of collision.

Similarly to the point C–7, user intellect can be utilised to govern the device in case of hazardous situation. Experiments have shown that interaction of the exoskeleton with the environment or external load is of stiff nature. Applying and moving of 60 kg load does not lead to loss of stability.

CS–9: The controller shall prevent hazardous physical contact during human–robot interaction.

The goal of the force control laws is to apply controlled force by actuators to minimise functional E_{Ξ} (see Eq. (5.1)). It aims at minimising of force at the points of human–machine interaction.

CS–10: The controller should be reusable in orthotic devices.

It was demonstrated that minimisation of E_{Ξ} leads to minimisation of $W^{\dagger}$ (see Eq. (5.3)). $W^{\dagger}$ is the total energy exchange between exoskeleton and the operator, regardless of direction of energy flow. Therefore, it is not suitable for orthotic devices, which goal is to reduce or increase metabolic expenditure of the user.

CS–11: The control method, as implemented in the controller, shall not induce vibrations on the device.

The force method prevents forceful contact between the robot and the user. However, setting k, k_{pp} controller gains to too large values might lead to instability of controlled force.

CS–12: The activity of musculoskeletal system shall be controllable by the controller.

If the interaction force is controlled, the metabolic cost is controlled too. It was shown that the controller aims at reduction of $W^{\dagger}$, that is the total energy exchange between exoskeleton and the operator, regardless of direction of energy flow.

CS–14: The controller shall allow for the modularity of the frame.

For the method, Jacobian in the middle–level control has to be updated to reflect geometry of the manipulator each time new module is introduced into the system. However the joint prototype with the low–level controller and the knee cap positioning scheme can be treated as a module and easily used in different configurations.

MS–1: The measurement system shall be adaptable to different users.

The methods require careful consideration for the design of the human–machine interface so that the repetitive contact with the brace does not cause abrasions. In the prototype a simple 3D printed handle was used.

MS–2: The measurement system shall allow performing activities listed in the Appendix D.

The measurement system allows for versatile manoeuvres to be performed by the user, covering all of those listed.

MS–3: The measurement system shall be ergonomic.

Considerations for the design of the human–machine interface are described in sections 2.5.1, 2.5.2 and 2.5.3. At the prototype the interaction force is measured through a 3D printed handle fitting a human hand.

MS–4: The measurement system shall be non-obtrusive.

The goal of the controller is to minimise the interaction force. The frame is designed not to interfere with the user body, hence the measurement system is non–obtrusive.

MS–5: The mechanical complexity of measurement system shall be low.

There is no instrumentation mounted on the operator. The methods requires complex instrumentation mounted on the frame of the robot.

MS–6: The power consumption using the measurement system shall be low.

Electrical power consumption of sensors and electronics has not been measured.

MS–7: The measurement system shall be safe.

Measurement system is mounted on a frame of the exoskeleton. It does not introduce additional hazards.

MS–8: The measurement system shall sense human motion kinematics.

Although the measurement system does not measure human motion kinematics explicitly, the information on kinematics of the interaction points are implicitly included into the controller through the employment of Jacobian.

MS–9: The measurement system should be reusable in orthotic devices.

Orthotic devices are instruments for application of assistive or resistive torque (forces) to the user joint. Human–machine interaction force is measured by a F/T sensor. The method is thus suitable for orthotic devices.

MS–10: The activity of musculoskeletal system shall be observable by the measurement system.

Since the interaction force is measured, the activity of the musculoskeletal system is observable. $W^{\dagger}$, that is integral of absolute instantaneous power can be calculated.

MS–11: The measurement system shall sense human motion dynamics.

The measurement system senses dynamics of human–machine interaction point.

MS–12: The measurement system shall allow for the modularity of the frame.

The method relies on measurement of interaction force by a F/T sensor attached to one of the modules, so this portion has to be present in the system always.

8.2 Conclusions

The research successfully demonstrated that it is possible to control torque exerted at the novel design of robotic joint compromising two opposing hydraulic actuators connected with a knee cap. As it was demonstrated, the system was successfully used as part of a full–body enhancive exoskeleton. An investigation into simulation of a full–body enhancive exoskeleton model walking gave guidelines for mechanical design of such device. A summary of conclusions is given below:

1. *Force Control* laws are more suitable for governing full–body exoskeletons than *Master–Slave Position Control* law. Human–machine interaction force should be considered to be controlled variable at middle level of the controller. *Direct Force Control* law, for which human–machine interaction force is measured directly using 6 DoF F/T sensor, was demonstrated to successfully govern prototype of novel joint design.

2. Based on motion capture data bandwidth of human motion, for both upper and lower extremities, was assessed to be not more than 10 Hz, except for running. If running is considered, the bandwidth is higher, about 40 Hz. Based on the bandwidth of 10 Hz, required control loop execution frequency was concluded to be 2 kHz. Using the setup with MyRIO, it has not been achieved. However, the loop execution time was between 3 and 6 ms, which is much more than required by Nyquist theorem.

3. It is sufficient to use one LVDT for measurement of rod extension of upper hydraulic actuator and an encoder for measurement of angular displacement of novel joint design. The extension of the rod of the lower actuator can be inferred from these readings and geometric properties.

4. Simulation of middle level control law derived for the novel joint design showed that for the case of ideal actuators it is possible to minimise human–machine interaction force while maintaining synchronisation of extension of actuators. The input to the simulation was motion capture data of gait. Full PID controller for the rods synchronisation has to be used, as pure proportional controller fails to stabilise rods extension and PD controller exhibits steady state error. The proposed control scheme minimises proposed control goals.

5. At the low level, a novel control scheme, coupled control, can be used for control of force exerted by two hydraulic actuators connected with a knee cap. The

controller requires readings from only one load cell, as opposed to independent force control of actuators. Simulation investigation of the controlled exhibits not worse performance on chosen control goals than independent control for gait. Relationship between controller parameters and value of control goals was shown through parameters selection. Setting of gain pertaining to force minimisation in the controller was found. Only proportional controller is required to maintain synchronisation of rods extension. The performance of tracking can be regulated by changing gain pertaining to synchronisation.

6. The designed control electronics and software written in LabView, run on MyRIO, was able to execute the control algorithms and govern the joint prototype in real–time.

7. It was shown through experimental evaluation of the proposed middle level controller with low level coupled control that it can successfully govern the prototype with input of bandwidth up to 0.6 Hz. When load of 60 kg was attached to a link of the joint, the force felt by the operator was no more than 30 N. This gives power amplification of 1:20. The extension of rods of hydraulic actuators was maintained. Conservative settings were used.

8. The novel joint design with the proposed controller can be used not only in exoskeleton, but as part of any machine which requires tracking of torque generated at the joint, for example robot manipulator with controlled interaction force with environment.

9. A model of full–body exoskeleton was simulated in sagittal plane with input data from motion capture of walking. It was demonstrated that the most natural gait was achieved for a platform with a heel and curved front, similar to one used in Sarcos XOS. The problem of sagittal stability was investigated. The mass of the entire machine is limiting factor for manoeuvrability of the device. The model weights 175 kg and operator is required to exert 600 N of force at the backpack to stabilise the device.

8.3 Future Work

Following the research presented, there are further issues to be explored in the future:

1. The next logical step to design of the controller is development of a middle level control strategy governing model of a full–body enhancive exoskeleton devised in chapter 7. To make the controller successful, it is required to develop high level controller to recognise state of the machine, which was not addressed in this thesis. The developed control strategy as part of this thesis would be a subsystem of such setup.

2. The model of the full–body enhancive exoskeleton might be extended to coronal plane as well, making the displacement truely 3–dimensional. Middle level and high level controller would have to be extended accordingly.

3. In the coupled controller, the controller gain pertaining to force minimisation is purely proportional. Since control signal basically controlforce derivative, it is interesting to investigate and perform optimisation with derivative gain of the controller being non–zero.

4. The controller would have to accommodate for restricting force due to cushioning occurring when rods approach their limits.

5. A successful low level control of actuators was proposed. However, there might be room for improvement and more sophisticated control law could be used to further improve performance measured by the control goals.

6. The controller was investigated for input from motion capture being gait. Investigation into other manoeuvres, including running, has to be carried out in the future.

7. The joint prototype was shown to perform well when the input is of low bandwidth, about 0.6 Hz. In the future it advised to test the setup with the robotic knee connected in parallel to emulate gait, which has higher bandwidth, up to 10 Hz.

8. The joint prototype, after miniaturisation and removal of adaptors between load cells and rods of actuators, might be used as a subsystem of an enhancive exoskeleton. Hence, its performance might be evaluated.

9. Connection between exoskeleton and operator must be devised to provide assisting force for maintaining sagittal stability. A control guard might be devised to prevent the device approaching instability region.

10. Design of exoskeleton platform would have to be done. Sensors and its placement would have to be selected. It is a difficult task because the platform, while being under large stress, would have to accommodate for sensors. Moreover, these sensors would have to be robust, while providing sufficient measurement quality. The other factor is design providing comfort for an operator wearing it, not obstructing gait.

Bibliography

[1] Miomir Vukobratovic and Branislav Borovac. Zero-moment point - thirty five years of its life. *I. J. Humanoid Robotics*, 1:157–173, 03 2004.

[2] J. E. Huber, N. A. Fleck, and M. F. Ashby. The selection of mechanical actuators based on performance indices. *Proceedings: Mathematical, Physical and Engineering Sciences*, 453(1965):2185–2205, 1997.

[3] BS 4058:1987. Data processing flow chart symbols, rules and conventions. The British Standards Institution.

[4] John M. Hollerbach, Ian W. Hunter, and John Ballantyne. The robotics review 2. chapter A Comparative Analysis of Actuator Technologies for Robotics, pages 299–342. MIT Press, Cambridge, MA, USA, 1992.

[5] N. Mizen. *Preliminary Design of a Full–Scale, Wearable, Exoskeletal Structure.* Technical report, Cornell Aeronautical Laboratory, Inc., 1963.

[6] N. Mizen. *Design and Test of a Full-Scale, Wearable, Exoskeletal Structure.* Technical report, Cornell Aeronautical Laboratory, Inc., March 1964.

[7] R. S. Mosher. *Handyman to Hardiman.* General Electric Company: Research and Development Center, 1967.

[8] *Research and Development Prototype for Machine Augmentation of Human Strength and Endurance – Hardiman I Project.* Technical report, General Electric Company, May 1971.

[9] *Final Report on Hardiman I Prototype for Machine Augmentation of Human Strength and Endurance.* Technical report, General Electric Company, August 1971.

[10] A. Chu, H. Kazerooni, and A. Zoss. On the biomimetic design of the Berkeley Lower Extremity Exoskeleton (BLEEX). In *Robotics and Automation, 2005. ICRA 2005. Proceedings of the 2005 IEEE International Conference on*, pages 4345–4352, April 2005.

[11] H. Kazerooni. Exoskeletons for human power augmentation. In *Intelligent Robots and Systems, 2005. (IROS 2005). 2005 IEEE/RSJ International Conference on*, pages 3459–3464, Aug 2005.

[12] A. Zoss, H. Kazerooni, and A. Chu. On the mechanical design of the Berkeley lower extremity exoskeleton (BLEEX). In *Intelligent Robots and Systems, 2005. (IROS 2005). 2005 IEEE/RSJ International Conference on*, pages 3465–3472, Aug 2005.

[13] A. B. Zoss, H. Kazerooni, and A. Chu. Biomechanical design of the Berkeley lower extremity exoskeleton (BLEEX). *IEEE/ASME Transactions on Mechatronics*, 11(2), April 2006.

[14] H. Kazerooni and R. Steger. The Berkeley Lower Extremity Exoskeleton. In *Journal of Dynamic Systems, Measurement, and Control, Transactions of the ASME*, volume 128, pages 14–25 vol.1, March 2006.

[15] H. Kazerooni, J-L. Racine, A. Chu, and Zoss A. Lower extremity enhancer, December 2011. US Patent 8,070,700 B2.

[16] J.-L. Ch. Racine. PhD Disseration: Control of a Lower Extremity Exoskeleton for Human Performance Amplification. University of California, Berkeley, 2003.

[17] H. Kazerooni, J.-L. Racine, L. Huang, and R. Steger. On the control of the Berkeley lower extremity exoskeleton (BLEEX). In *Robotics and Automation, 2005. ICRA 2005. Proceedings of the 2005 IEEE International Conference on*, pages 4353–4360, April 2005.

[18] R. Steger, S. H. Kim, and H. Kazerooni. Control scheme and networked control architecture for the Berkeley lower extremity exoskeleton (BLEEX). In *Robotics and Automation, 2006. ICRA 2006. Proceedings 2006 IEEE International Conference on*, pages 3469–3476, May.

[19] H. Kazerooni, A. Chu, and R. Steger. That which does not stabilize, will only make us stronger. *The International Journal of Robotics Research*, 26(1):75–89, 2007.

[20] Exobionics webpage. `http://www.eksobionics.com/`. Accessed: 2014-07-31.

[21] Berkeley Robotics & Human Engineering Laboratory webpage. `http://bleex.me.berkeley.edu/`. Accessed: 2014-07-30.

[22] H. Kazerooni. Exoskeletons for human performance augmentation. In *Springer Handbook of Robotics*, pages 773–793. Springer Berlin Heidelberg, 2008.

[23] G. Mone. Popular Science: Building the Real Iron Man. `http://www.popsci.com/scitech/article/2008-04/building-real-iron-man`, Accessed: 2014–05–23.

[24] S.C. Jacobsen, M.X. Olivier, and B.J. Maclean. Biomimetic mechanical joint, August 27 2013. US Patent 8,516,918.

[25] C. Kovalsky and G. Shields. Raytheon: Raytheon Unveils Lighter, Faster, Stronger Second Generation Exoskeleton Robotic Suit. `http://raytheon.mediaroom.com/index.php?s=43&item=1652`, Accessed: 2014–05–23.

[26] www.army-technology.com: Raytheon XOS 2 Exoskeleton, Second–Generation Robotics Suit, United States of America. `http://www.army-technology.com/projects/raytheon-xos-2-exoskeleton-us/`, Accessed: 2014–05–23.

[27] M. Bergamasco, F. Salsedo, S. Marcheschi, N. Lucchesi, and M. Fontana. A novel compact and lightweight actuator for wearable robots. In *Robotics and Automation (ICRA), 2010 IEEE International Conference on*, pages 4197–4203, May 2010.

[28] N. Lucchesi, S. Marcheschi, L. Borelli, F. Salsedo, M. Fontana, and M. Bergamasco. An approach to the design of fully actuated body extenders for material handling. In *RO–MAN, 2010 IEEE*, pages 482–487, Sept 2010.

[29] S. Marcheschi, F. Salsedo, M. Fontana, and M. Bergamasco. Body extender: Whole body exoskeleton for human power augmentation. In *Robotics and Automation (ICRA), 2011 IEEE International Conference on*, pages 611–616, May 2011.

[30] K. Yamamoto, K. Hyodo, M. Ishii, and T. Matsuo. Development of power assisting suit for assisting nurse labor. *JSME International Journal Series C Mechanical Systems, Machine Elements and Manufacturing*, 45(3):703–711, 2002.

[31] K. Yamamoto, M. Ishii, H. Noborisaka, and K. Hyodo. Stand alone wearable power assisting suit – sensing and control systems. In *Robot and Human Interactive Communication, 2004. ROMAN 2004. 13th IEEE International Workshop on*, pages 661–666, Sept 2004.

[32] T. Yoshimitsu and K. Yamamoto. Development of a power assist suit for nursing work. In *SICE 2004 Annual Conference*, volume 1, pages 577–580 vol. 1, Aug 2004.

[33] M. Ishii, K. Yamamoto, and K. Hyodo. Stand–alone wearable power assist suit – development and availability. In *Journal of Robotics and Mechatronics*, volume 17, pages 575–583, 2005.

[34] J.E. Pratt, B.T. Krupp, C.J. Morse, and S.H. Collins. The RoboKnee: an exoskeleton for enhancing strength and endurance during walking. In *Robotics and Automation, 2004. Proceedings. ICRA '04. 2004 IEEE International Conference on*, volume 3, pages 2430–2435 Vol.3, April 2004.

[35] K. Kong and D. Jeon. Fuzzy control of a new tendon–driven exoskeletal power assistive device. In *Advanced Intelligent Mechatronics. Proceedings, 2005 IEEE/ASME International Conference on*, pages 146–151, 2005.

[36] K. Kong and D. Jeon. Design and control of an exoskeleton for the elderly and patients. *Mechatronics, IEEE/ASME Transactions on*, 11(4):428–432, Aug 2006.

[37] K. Kong, M. Tomizuka, H. Moon, B. Hwang, and D. Jeon. Mechanical design and impedance compensation of SUBAR (Sogang University's Biomedical Assist Robot). In *Advanced Intelligent Mechatronics, 2008. AIM 2008. IEEE/ASME International Conference on*, pages 377–382, July 2008.

[38] K. Kong, J. Bae, and M. Tomizuka. Control of rotary series elastic actuator for ideal force–mode actuation in human – robot interaction applications. *Mechatronics, IEEE/ASME Transactions on*, 14(1):105–118, Feb 2009.

[39] K. Kong, H. Moon, B. Hwang, D. Doyoung Jeon, and M. Tomizuka. Impedance compensation of SUBAR for back–drivable force–mode actuation. *Robotics, IEEE Transactions on*, 25(3):512–521, June 2009.

[40] K. Kasaoka and Y. Sankai. Predictive control estimating operator's intention for stepping–up motion by exoskeleton type power assist system HAL. In *Intelligent Robots and Systems, 2001. Proceedings. 2001 IEEE/RSJ International Conference on*, volume 3, pages 1578–1583 vol.3, 2001.

[41] H. Kawamoto and Y. Sankai. Comfortable power assist control method for walking aid by HAL–3. In *IEEE International Conference on Systems, Man and Cybernetics, 2002.*, volume 4, page 6, Oct 2002.

[42] H. Kawamoto and Y. Sankai. Power assist system HAL–3 for gait disorder person. In K. Miesenberger, J. Klaus, and W. Zagler, editors, *Computers Helping People with Special Needs*, volume 2398 of *Lecture Notes in Computer Science*, pages 196–203. Springer Berlin Heidelberg, 2002.

[43] S. Lee and Y. Sankai. Power assist control for walking aid with HAL–3 based on EMG and impedance adjustment around knee joint. In *Intelligent Robots and Systems, 2002. IEEE/RSJ International Conference on*, volume 2, pages 1499–1504 vol.2, 2002.

[44] S. Lee and Y. Sankai. Power assist control for leg with HAL–3 based on virtual torque and impedance adjustment. In *Systems, Man and Cybernetics, 2002 IEEE International Conference on*, volume 4, pages 6 pp. vol.4–, Oct 2002.

[45] H. Kawamoto, S. Lee, S. Kanbe, and Y. Sankai. Power assist method for HAL–3 using EMG–based feedback controller. In *IEEE International Conference on Systems, Man and Cybernetics, 2003.*, volume 2, pages 1648–1653 vol.2, Oct 2003.

[46] H. Kawamoto, S. Kanbe, and Y. Sankai. Power assist method for HAL–3 estimating operator's intention based on motion information. In *Robot and Human Interactive Communication, 2003. Proceedings. ROMAN 2003. The 12th IEEE International Workshop on*, pages 67–72, Oct 2003.

[47] S. Lee and Y. Sankai. The natural frequency–based power assist control for lower body with hal–3. In *Systems, Man and Cybernetics, 2003. IEEE International Conference on*, volume 2, pages 1642–1647 vol.2, Oct 2003.

[48] H. Kawamoto and Y. Sankai. Power assist method based on phase sequence driven by interaction between human and robot suit. In *Robot and Human Interactive Communication, 2004. ROMAN 2004. 13th IEEE International Workshop on*, pages 491–496, Sept 2004.

[49] T. Hayashi, H. Kawamoto, and Y. Sankai. Control method of robot suit HAL working as operator's muscle using biological and dynamical information. In *Intelligent Robots and Systems, 2005. (IROS 2005). 2005 IEEE/RSJ International Conference on*, pages 3063–3068, Aug 2005.

[50] K. Suzuki, Y. Kawamura, T. Hayashi, T. Sakurai, Y. Hasegawa, and Y. Sankai. Intention–based walking support for paraplegia patient. In *Systems, Man and Cybernetics, 2005 IEEE International Conference on*, volume 3, pages 2707–2713 Vol. 3, Oct 2005.

[51] H. Kawamoto, T. Hayashi, T. Sakurai, K. Eguchi, and Y. Sankai. Development of single leg version of HAL for hemiplegia. In *Engineering in Medicine and Biology Society, 2009. EMBC 2009. Annual International Conference of the IEEE*, pages 5038–5043, Sept 2009.

[52] H. Kawamoto, S. Taal, H. Niniss, T. Hayashi, K. Kamibayashi, K. Eguchi, and Y. Sankai. Voluntary motion support control of Robot Suit HAL triggered by bioelectrical signal for hemiplegia. In *Engineering in Medicine and Biology Society (EMBC), 2010 Annual International Conference of the IEEE*, pages 462–466, Aug 2010.

[53] M. Shingu, K. Eguchi, and Y. Sankai. Substitution of motor function of polio survivors who have permanent paralysis of limbs by using Cybernic Voluntary Control. In *IEEE International Conference on Robotics and Biomimetics (ROBIO), 2009*, pages 504–509, Dec 2009.

[54] H. Kawamoto, T. Shiraki, T. Otsuka, and Y. Sankai. Meal–assistance by Robot Suit HAL using detection of food position with camera. In *Robotics and Biomimetics (ROBIO), 2011 IEEE International Conference on*, pages 889–894, Dec 2011.

[55] T. Otsuka, K. Kawaguchi, H. Kawamoto, and Y. Sankai. Development of upper–limb type HAL and reaching movement for meal–assistance. In *Robotics and*

Biomimetics (ROBIO), 2011 IEEE International Conference on, pages 883–888, Dec 2011.

[56] H. Satoh, T. Kawabata, and Y. Sankai. Bathing care assistance with Robot Suit HAL. In *Robotics and Biomimetics (ROBIO), 2009 IEEE International Conference on*, pages 498–503, Dec 2009.

[57] T. Kawabata, H. Satoh, and Y. Sankai. Working posture control of Robot Suit HAL for reducing structural stress. In *Robotics and Biomimetics (ROBIO), 2009 IEEE International Conference on*, pages 2013–2018, Dec 2009.

[58] H. Kawamoto, K. Kamibayashi, Y. Nakata, K. Yamawaki, R. Ariyasu, Y. Sankai, M. Sakane, K. Eguchi, and N. Ochiai. Pilot study of locomotion improvement using Hybrid Assistive Limb in chronic stroke patients. *BMC Neurology*, 13, 2013.

[59] A. Nilsson, K. S. Vreede, V. Haglund, H. Kawamoto, Y. Sankai, and J. Borg. Gait training early after stroke with a new exoskeleton – the Hybrid Assistive Limb: a study of safety and feasibility. *Journal of Neuroengineering and Rehabilitation*, 11, 2014.

[60] K. Hasebe, H. Kawamoto, A Matsushita, K. Kamibayashi, and Y. Sankai. Towards a guideline for clinical trials in the development of human assistive robots. In *Robotics and Biomimetics (ROBIO), 2010 IEEE International Conference on*, pages 751–756, Dec 2010.

[61] K. Hasebe, H. Kawamoto, A Matsushita, K. Kamibayashi, and Y. Sankai. Stepwise process of clinical trials in safety–conscious development of human assistive robots. In *Robotics and Biomimetics (ROBIO), 2011 IEEE International Conference on*, pages 50–55, Dec 2011.

[62] Cyberdyne webpage. `http://www.cyberdyne.jp/`. Accessed: 2014-08-19.

[63] S. Sanborn. Everyone should walk. *The Wisconsin Engineer*, 77(2), November 1972.

[64] M. Vukobratović, D. Hristić, and Z. Stojiljković. Development of active anthropomorphic exoskeletons. *Medical and biological engineering*, 12(1):66–80, 1974.

[65] M. Vukobratović and J. Stepanenko. On the stability of anthropomorphic systems. *Mathematical Biosciences*, 15(1-2):1–37, 1972.

[66] S. Milojevic, S. Sabanovic, and J. Kaur. Miomir Vukobratović [History]. *Robotics Automation Magazine, IEEE*, 20(2):112–122, June 2013.

[67] NASA. NASA's Ironman-Like Exoskeleton Could Give Astronauts, Paraplegics Improved Mobility and Strength. `http://www.nasa.gov/offices/oct/home/feature_exoskeleton.html`. Accessed: 2014-09-24.

[68] BS EN ISO 13482:2014. Robots and robotic devices – safety requirements for personal care robots. The British Standards Institution.

[69] C. Nabeshima, H. Kawamoto, and Y. Sankai. Typical risks and protective measures of wearable walking assistant robots. In *System Integration (SII), 2011 IEEE/SICE International Symposium on*, pages 914–919, Dec 2011.

[70] OECD. Population projections. Accessed: 2014–08–21.

[71] S. Jacobsen and M. Olivier. Contact displacement actuator system, August 2008. WO Patent App. PCT/US2007/016336.

[72] ATI Industrial Automation webpage. Multi-axis force/torque sensor. `https://www.ati-ia.com`, Accessed: 2014–04–28.

[73] K. H. Low, Xiaopeng Liu, Hao Yong Yu, and H.S. Kasim. Development of a lower extremity exoskeleton – preliminary study for dynamic walking. In *Control, Automation, Robotics and Vision Conference, 2004. ICARCV 2004 8th*, volume 3, pages 2088–2093 Vol. 3, Dec 2004.

[74] Liu Xiaopeng. PhD Disseration: Design of a Lower Extremity Exoskeleton for Walking Power Augmentation. Nanyang Technological University, Singapore, 2006.

[75] K. H. Low, X. Liu, and H. Yu. Development of NTU wearable exoskeleton system for assistive technologies. In *Mechatronics and Automation, 2005 IEEE International Conference*, volume 2, pages 1099–1106 Vol. 2, July 2005.

[76] M. Nordin and V. H. Frankel. *Basic Biomechanics of the Musculoskeletal System*. Lippincott Williams & Wilkins, 3rd edition, 2001.

[77] J. Rose and J. G. Gamble. *Human Walking*. Lippincott Williams & Wilkins, 3rd edition, 2006.

[78] V. Medved. *Measurement of Human Locomotion*. CRC Press, 2001.

[79] J. Wheeler, B. Rohrer, D. Kholwadwala, S. Buerger, R. Givler, J. Neely, C. Hobart, and P. Galambos. In–sole MEMS pressure sensing for a lower extremity exoskeleton. In *Biomedical Robotics and Biomechatronics, 2006. BioRob 2006. The First IEEE/RAS-EMBS International Conference on*, pages 31–34, Feb 2006.

[80] A.I. Ianov, H. Kawamoto, and Y. Sankai. Development of a capacitive coupling electrode for bioelectrical signal measurements and assistive device use. In *Complex Medical Engineering (CME), 2012 ICME International Conference on*, pages 593–598, July 2012.

[81] A.I. Ianov, H. Kawamoto, and Y. Sankai. Development of noise resistant hybrid capacitive–resistive electrodes for wearable robotics, computing and welfare. In *Intelligent Robots and Systems (IROS), 2013 IEEE/RSJ International Conference on*, pages 4249–4254, Nov 2013.

[82] A. M. Dollar and H. Herr. Lower extremity exoskeletons and active orthoses. *IEEE Transactions on Robotics*, 24(1), February 2008.

[83] D. Popovic and L. Schwirtlich. Design and evaluation of the self–fitting modular orthosis (SFMO). *IEEE Transactions on Rehabilitation Engineering*, 1(3):165–174, Sep 1993.

[84] R. C. Dorf and Bishop R. H. *Modern Control Systems*. Pearson, 12th edition, 2011.

[85] Nasa's ironman-like exoskeleton could give astronauts, paraplegics improved mobility and strength. `https://www.nasa.gov/offices/oct/home/feature_exoskeleton.html`, Accessed: 2018–09–14.

[86] J. Ghan, R. Steger, and H. Kazerooni. Control and system identification for the Berkeley Lower Extremity Exoskeleton (BLEEX). *Advanced Robotics*, 20(9):989–1014, 2006.

[87] M. Yang, Zh. Xu, Y. Liu, Y. He, and Y. Xu. Perceiving and predicting the intended motion with human–machine interaction force for walking assistive exoskeleton robot. In *Mechatronics and Automation (ICMA), 2013 IEEE International Conference on*, pages 805–810, Aug 2013.

[88] Jianhong Cui, Sabri Tosunoglu, Rodney Roberts, Carl Moore, and Daniel W. Repperger. A Review of Teleoperation System Control. In *Recent Advances in Robotics, 2003 Proceedings of the Florida Conference on*, 2003.

[89] M. W. Spong, S. Hutchinsion, and M. Vidyasagar. *Robot Modelling and Control*. Wiley, 2006.

[90] John Jansen, Brad Richardson, Francois Pin, Randy Lind, and Joe Birdwell. *Exoskeleton for Soldier Enhancement Systems*. Technical report, Oak Ridge National Laboratory, September 2000.

[91] A Montagner, A Frisoli, S. Marcheschi, E. Sanchez, and M. Bergamasco. Optimal control of a robotic system for human power enhancement. In *EuroHaptics Conference, 2007 and Symposium on Haptic Interfaces for Virtual Environment and Teleoperator Systems. World Haptics 2007. Second Joint*, pages 212–218, March 2007.

[92] A. Chu. PhD Disseration: Design of the Berkeley Lower Extremity Exoskeleton (BLEEX). University of California, Berkeley, 2005.

[93] J. Raade, K. Amundson, and H. Kazerooni. Architecture and hydraulics of a lower extremity exoskeleton. In *Proceedings of 2005 ASME International Mechanical Engineering Congress and Exposition*, Nov 2005.

[94] A. Zoss and H. Kazerooni. Design of an electrically actuated lower extremity exoskeleton. *Advanced Robotics*, 20(9):967–988, 2006.

[95] A. B. Zoss. PhD Disseration: Actuation design and implementation for Lower Extremity Human Exoskeletons. University of California, Berkeley, 2006.

[96] K. Amundson, J. Raade, N. Harding, and H. Kazerooni. Development of hybrid hydraulic–electric power units for field and service robots. *Advanced Robotics*, 20(9):1015–1034, 2006.

[97] K. Amundson, J. Raade, N. Harding, and H. Kazerooni. Hybrid hydraulic–electric power unit for field and service robots. In *Intelligent Robots and Systems, 2005. (IROS 2005). 2005 IEEE/RSJ International Conference on*, pages 3453–3458, Aug 2005.

[98] J. Raade, K. Amundson, and H. Kazerooni. Development of hydraulic–electric power unit for mobile robots. In *Fluid Power Systems and Technology, ASME 2005 International Mechanical Engineering Congress and Exposition on*, pages 27–34, Nov 2005.

[99] J. Ghan and H. Kazerooni. System identification for the Berkeley lower extremity exoskeleton (BLEEX). In *Robotics and Automation, 2006. ICRA 2006. Proceedings 2006 IEEE International Conference on*, pages 3477–3484, May 2006.

[100] S. Kim, G. Anwar, and H. Kazerooni. High–speed communication network for controls with the application on the exoskeleton. In *American Control Conference, 2004. Proceedings of the 2004*, volume 1, pages 355–360 vol.1, June 2004.

[101] S. Kim and H. Kazerooni. High speed ring–based distributed networked control system for real–time multivariable applications. In *Proceedings of 2004 ASME International Mechanical Engineering Congress and R&D Expo*, 2004.

[102] R.E. Goldman, A Bajo, and N. Simaan. Compliant motion control for multisegment continuum robots with actuation force sensing. *Robotics, IEEE Transactions on*, 30(4):890–902, Aug 2014.

[103] S. Jacobsen and M. Olivier. Contact displacement actuator system, April 8 2009. EP Patent App. EP20,070,872,565.

[104] S.C. Jacobsen and M. Olivier. Contact displacement actuator system, August 20 2009. US Patent App. 11/879,448.

[105] *Manual of Patent Examining Procedure (MPEP)*, Ninth Edition edition, March 2014. `http://www.uspto.gov/web/offices/pac/mpep/index.html`, Accessed: 2014–05–23.

[106] A. Tsukahara, Y. Hasegawa, and Y. Sankai. Standing–up motion support for paraplegic patient with robot suit HAL. In *Rehabilitation Robotics, 2009. ICORR 2009. IEEE International Conference on*, pages 211–217, June 2009.

[107] Y. Sankai. HAL: Hybrid Assistive Limb based on Cybernics. In M. Kaneko and Y. Nakamura, editors, *Robotics Research*, volume 66 of *Springer Tracts in Advanced Robotics*, pages 25–34. Springer Berlin Heidelberg, 2011.

[108] Y. Sankai. Leading edge of cybernics: robot suit HAL. In *SICE–ICASE, 2006. International Joint Conference*, Oct 2006.

[109] D. W. Russ, M. A. Elliott, K. Vandenborne, G. A. Walter, and S. A. Binder-Macleod. Metabolic costs of isometric force generation and maintenance of human skeletal muscle. *American Journal of Physiology - Endocrinology and Metabolism*, 282(2):E448–E457, 2002.

[110] *Control System General Requirements – draft 1.* Technical report, University of Leeds, April 2014. location: */Product Development/Control System Design/Control System Requirements/.*

[111] *Measurement System General Requirements – draft 1.* Technical report, University of Leeds, April 2014. location: */Product Development/Control System Design/Measurement System Requirements/.*

[112] ISO/IEC. ISO/IEC Directives Part 2: Rules for the structure and drafting of International Standards.

[113] E. Motard. *MINDWALKER Mind Controlled Orthosis and Virtual Reality Training Environment for Walk Empowering: D1.1 User Requirements Collection and System Requirements Specification Document.* Technical report, MINDWALKER consortium, June 2010.

[114] *Customer Needs in the Exoskeleton Project – draft 4.* Technical report, University of Leeds, April 2014.

[115] Y. Bar-Cohen and C.L. Breazeal. *Biologically Inspired Intelligent Robots.* SPIE Press monograph. SPIE Press, 2003.

[116] David Edwards. Sarcos robotics says it has overcome a "major obstacle" to the commercial deployment of its exoskeletons. accessed: 16–04–2019.

[117] H. E. Meritt. *Hydraulic Control Systems.* John Wiley & Sons, Inc., 1967.

[118] N. Niksefat and N. Sepehri. Robust force controller design for an electrohydraulic actuator based on nonlinear model. In *Proceedings 1999 IEEE International Conference on Robotics and Automation (Cat. No.99CH36288C)*, volume 1, pages 200–206 vol.1, 1999.

[119] N. Niksefat and N. Sepehri. Designing robust force control of hydraulic actuators despite system and environmental uncertainties. *IEEE Control Systems*, 21(2):66–77, Apr 2001.

[120] G. Vossoughi and M. Donath. Dynamic feedback linearization for electrohydraulically actuated control systems. *Journal of Dynamic Systems, Measurement and Control, Transactions of the ASME*, 117(4):468–477, 1995.

[121] G. Wu, N. Sepehri, and K. Ziaei. Design of a hydraulic force control system using a generalised predictive control algorithm. *IEE Proceedings - Control Theory and Applications*, 145(5):428–436, Sep 1998.

[122] Bosch Rexroth Group. Directional control valves, direct operated, with electrical position feedback and integrated electronics (OBE) – Type 4WRPEH. 2015–02.

[123] Miller Fluid Power. Miller HV2 Series Heavy Duty Industrial Hydraulic Cylinders, Catalog HY08–M1140–4/NA. 2011–01.

[124] Oqus Motion Capture Cameras. `http://www.qualisys.com/cameras/oqus/`. Accessed: 2016-05-18.

[125] G. F. Franklin, J. D. Powell, and A. Emami-Naeini. *Feedback Control of Dynamic Systems*. Pearson Education, 6th edition, 2010.

[126] G. F. Franklin, J. D. Powell, and M. Workman. *Digital Control of Dynamic Systems*. Dorling Kindersley (lic. Pearson Education), 3rd edition, 2002.

[127] Hengstler. Technical Datasheet – Absolute Encoder AC 36 - BiSS / SSI. `https://www.hengstler.de/gfx/file/shop/encoder/AC36/Datasheet_AC36-BiSS_SSI_en.pdf`. Accessed on 19–02–2018.

[128] Hengstler. Technical Datasheet Interface ACURO – SSI / BiSS. `https://www.hengstler.de/gfx/file/shop/encoder/AX71/Technical_Manual_SSI_BiSS_ACURO_en.pdf`. Accessed on 19–02–2018.

[129] Solartron Metrology. Displacement Sensors. `http://books.solartronmetrology.org/books/jjkf/#p=13`. Accessed on 19–02–2018.

[130] Novatech. F256 Axial Compensated Loadcell. `https://www.novatechloadcells.co.uk/pdf/F256.pdf`. Accessed on 22–02–2018.

[131] Mantracourt. SGA A SGA D Strain Gauge Load Cell Amplifier Signal Conditioner. `https://www.mantracourt.com/userfiles/documents/sga_manual.pdf`. Accessed on 22–02–2018.

[132] LCM Systems. SGA Analogue Strain Gauge Load Cell Amplifier. http://www.lcmsystems.com/res/SGACasedAnalogueLoadCellStrainGaugeAmplifier.pdf. Accessed on 8–03–2018.

[133] Novatech. Engineering Application Sheet E006: Dynamic Force Measurement. https://www.novatechloadcells.co.uk/eng/e006.htm. 08/2007.

[134] JR3. JR3 Multi–Axis Force–Torque Sensor Technical Specifications (SI Units). http://www.jr3.com/uploads/4/5/7/0/45700429/___spec_sheet_67m25a3_si_100n200n.pdf. Accessed on: 27–02–2018.

[135] National Instruments. User Guide and Specifications NI myRIO-1900. http://www.ni.com/pdf/manuals/376047c.pdf. 2016.

[136] Xilinx. Zynq-7000 All Programmable SoC Data Sheet: Overview. https://www.xilinx.com/support/documentation/data_sheets/ds190-Zynq-7000-Overview.pdf. 7–06–2017.

[137] Maxim Integrated. MAX481/MAX483/MAX485/MAX487-MAX491/MAX1487 Low–Power, Slew–Rate–Limited RS–485/RS–422 Transceivers. https://datasheets.maximintegrated.com/en/ds/MAX1487-MAX491.pdf. 09–2014.

[138] Maxim Integrated. MAX1300/MAX1301 8- and 4-Channel, ±3 x VREF Multirange Inputs, Serial 16-Bit ADCs. https://datasheets.maximintegrated.com/en/ds/MAX1300-MAX1301.pdf. 12–2011.

[139] Analog Devices. Multiple Range, 16-/12-Bit, Bipolar/Unipolar Voltage Output DACs with 2 ppm/°C Reference. https://www.analog.com/media/en/technical-documentation/data-sheets/ad5761r_5721r.pdf. 01–2018.

[140] National Instruments. What is a Real-Time Operating System (RTOS). http://www.ni.com/white-paper/3938/en/. November 2013.

[141] National Instruments. Synchronizing FPGA VIs and Host VIs Using Interrupts (FPGA Interface). http://zone.ni.com/reference/en-XX/help/371599G-01/lvfpgahosthelp/synchronizing_using_interrupts/. June 2011.

[142] F. Conrad and C.J.D. Jensen. Design of hydraulic force control systems with state estimate feedback. *IFAC Proceedings Volumes*, 20(5, Part 3):307 – 312, 1987. 10th Triennial IFAC Congress on Automatic Control - 1987 Volume III, Munich, Germany, 27-31 July.

[143] S. Chen, Z. Chen, B. Yao, X. Zhu, S. Zhu, Q. Wang, and Y. Song. Adaptive robust cascade force control of 1-dof hydraulic exoskeleton for human performance augmentation. *IEEE/ASME Transactions on Mechatronics*, 22(2):589–600, April 2017.

[144] Gholamreza Vossoughi and Max Donath. Dynamic feedback linearization for electrohydraulically actuated control systems. *Journal of Dynamic Systems, Measurement and Control, Transactions of the ASME*, 117(4):468–477, 1 1995.

[145] L. Laval, N. K. M'Sirdi, and J. C. Cadiou. H infin;-force control of a hydraulic servo-actuator with environmental uncertainties. In *Proceedings of IEEE International Conference on Robotics and Automation*, volume 2, pages 1566–1571 vol.2, Apr 1996.

[146] Rui Liu and Andrew Alleyne. Nonlinear force/pressure tracking of an electrohydraulic actuator. *IFAC Proceedings Volumes*, 32(2):952 – 957, 1999. 14th IFAC World Congress 1999, Beijing, Chia, 5-9 July.

[147] G. Wu, N. Sepehri, and K. Ziaei. Design of a hydraulic force control system using a generalised predictive control algorithm. *IEE Proceedings - Control Theory and Applications*, 145(5):428–436, Sep 1998.

[148] H. Sun and G. T. C. Chiu. Nonlinear observer based force control of electrohydraulic actuators. In *Proceedings of the 1999 American Control Conference (Cat. No. 99CH36251)*, volume 2, pages 764–768 vol.2, Jun 1999.

[149] N. Niksefat and N. Sepehri. Designing robust force control of hydraulic actuators despite system and environmental uncertainties. *IEEE Control Systems*, 21(2):66–77, Apr 2001.

[150] Shouling He. Neural predictive force control for a hydraulic actuator: Simulation and experiment. *Applied Artificial Intelligence*, 23(2):151–167, 2009.

[151] Mohammed Jerouane *, Nariman Sepehri, and FranĂ§oise Lamnabhi-Lagarrigue. Dynamic analysis of variable structure force control of hydraulic actuators via the reaching law approach. *International Journal of Control*, 77(14):1260–1268, 2004.

[152] Prut Nakkarat and Suwat Kuntanapreeda. Observer-based backstepping force control of an electrohydraulic actuator. *Control Engineering Practice*, 17(8):895 – 902, 2009.

[153] K. Baghestan, S.M. Rezaei, H.A. Talebi, and M. Zareinejad. Robust force control in a novel electro-hydraulic structure using polytopic uncertainty representation. *ISA Transactions*, 53(6):1873 – 1880, 2014.

[154] G. Alici, R. Jagielski, Y. A. Sekercioglu, and B. Shirinzadeh. Prediction of geometric errors of robot manipulators with particle swarm optimisation method. *Robotics and Autonomous Systems*, 54(12):956 – 966, 2006.

[155] BS EN ISO 12100:2010. Safety of machinery – general principles for design – risk assessment and risk reduction. The British Standards Institution.

[156] BS EN ISO 13849-1:2008. Safety of machinery – safety–related parts of control systems. The British Standards Institution.

[157] PD IEC/TR 62061-1:2010. Guidance on the application of ISO 13849–1 and IEC 62061 in the design of safety-related control systems for machinery. The British Standards Institution.

Appendix A

Control Goals

In Fig. A.1 a graph representing standard control system design process is depicted. The initial step in the control system design process is usually the establishment of the control goals [84]. In this document possible control goals for an exoskeleton working in parallel with a human are considered.

Metabolic Cost of Mechanical Work

Human body activities during movement within an environment are associated with work. Let a metabolically costly activity be considered. To focus the attention, a free body digram of forearm during flexing move is considered as depicted in Fig. A.2a. Note that reaction forces at elbow joint are not depicted. For simplicity, contraction forces from *brachioradialis, biceps brachii, brachialis* muscles are reduced to $\vec{F}_{musc} \geq 0$ (muscle generates force towards its centre – contradicts concentrically). The force of interaction between the human body and the environment is reduced to $\vec{F}_{hum}$, which is fixed to the palm of the hand. For a certain task $\vec{F}_{hum}$ is considered to be a value of a time–invariant vector field at certain point $\vec{s}$. The expenditure of the energy by the musculoskeletal system acting on the environment along a trajectory C can be written as sum of ΔE^g_{arm} (the change of potential energy in gravitational field) and work:

$$E_a = \Delta E^g_{arm} + \int_C \vec{F}_{hum} \cdot \mathrm{d}\vec{s} \tag{A.1}$$

Similarly, Fig. A.2b depicts the musculoskeletal system performing the same task along the C trajectory whilst being enclosed by the exoskeleton. The force $\vec{F}_{exo}$ by which human body acts on the exoskeleton is reduced to the same point at the palm as $\vec{F}_{hum}$. Then, the

$$\vec{F}^{exo}_{hum} = \vec{F}_{hum} + \vec{F}_{exo} \tag{A.2}$$

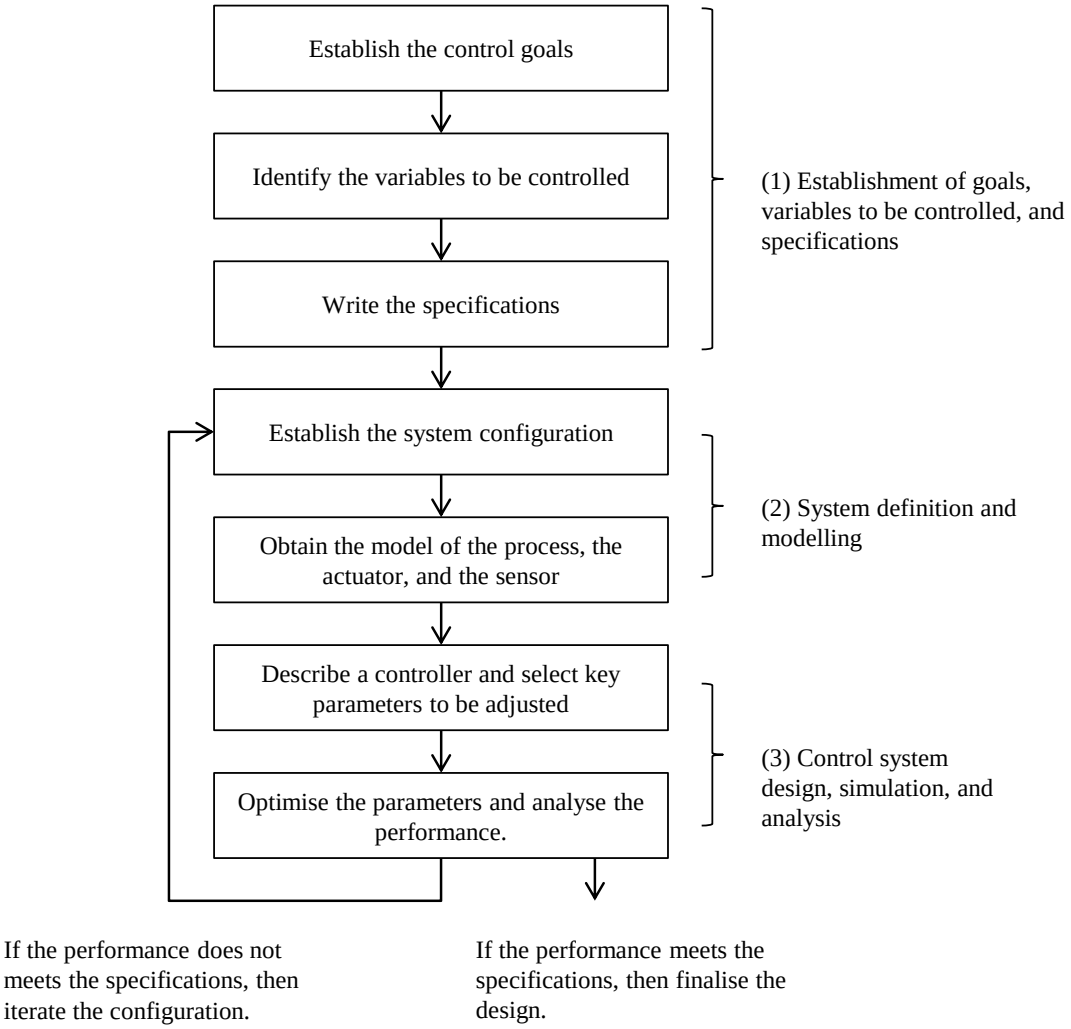

Figure A.1: Control System design flow (adopted from [84]).

is a value of time–invariant field in point $\vec{s}$. The expenditure of the energy by the musculoskeletal system can be written as:

$$E_b = \Delta E^g_{arm} + \int\limits_C \vec{F}^{exo}_{hum} \cdot \mathrm{d}\vec{s} \tag{A.3}$$

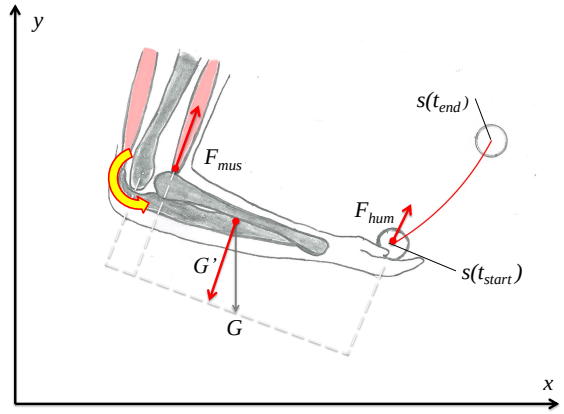

(a)

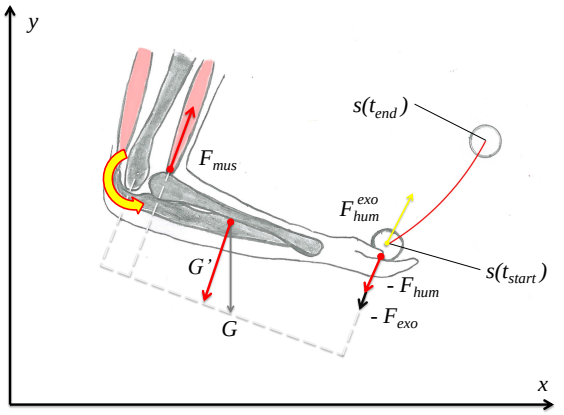

(b)

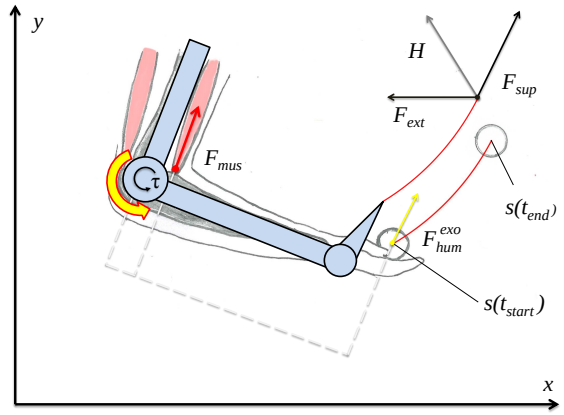

(c)

Figure A.2: Forces while performing a task in exoskeleton–human system. (a) Musculoskeletal system performing a task. (b) Musculoskeletal system performing a task whilst enclosed by exoskeleton. (c) An exoskeleton mounted on musculoskeletal system performing certain task .

Using Eq. (A.1) and Eq. (A.3) the difference in metabolic expenditure can be expressed as:

$$\Delta E_{met} = E_b - E_a = \int_C \vec{F}_{hum}^{exo} \cdot \mathrm{d}\vec{s} - \int_C \vec{F}_{hum} \cdot \mathrm{d}\vec{s} \tag{A.4}$$

C denotes a trajectory:

$$C = \left\{ (\vec{s}(t), t) \in \mathbb{R}^3 \times [0, \infty) \ : \ t \in [t_{start}, t_{end}] \right\}, t_{start}, t_{end} \in [0, \infty) \text{ such that } t_{start} < t_{end} \tag{A.5}$$

$\vec{s}(t)$ is a vector function with values in Euclidean space:

$$\vec{s}(t) = [s_x(t), s_y(t), s_z(t)] \tag{A.6}$$

The trajectory (curve) C is smooth, that is of class G^1 (its component curves touch at the join points with a common tangent direction).

Using the property of linearity of the line integral the following equation can be rewritten:

$$\Delta E_{met} = \int_C \left[\vec{F}_{hum}^{exo}(\,\vec{s}\,) - \vec{F}_{hum}(\,\vec{s}\,) \right] \cdot \mathrm{d}\vec{s} \tag{A.7}$$

Using Eq. (A.2), the Eq. (A.7) can be rewritten as:

$$\Delta E_{met} = \int_C \vec{F}_{exo}(\,\vec{s}\,) \cdot \mathrm{d}\vec{s} \tag{A.8}$$

I) $\Delta E_{met} = 0$

If performing a task is equally energetically demanding without and with exoskeleton then Eq. (A.8) can be rewritten as:

$$0 = \int_C \vec{F}_{exo}(\,\vec{s}\,) \cdot \mathrm{d}\vec{s} \tag{A.9}$$

In general, there exist infinite number of functions $\vec{\phi}(\,\vec{s}\,)$ satisfying the line integral in Eq. (A.9). In particular, it is met for (sufficient condition):

$$\forall \vec{s} \in C : \vec{F}_{exo}(\,\vec{s}\,) \equiv \mathbf{0} \tag{A.10}$$

NOTE 1

Let a task of carrying up a slope a load attached to the exoskeleton frame be con-

sidered. Eq. (A.10) implies that in order to keep the metabolic cost of the user of *an exoskeleton performing the task* at the same level compared to the user climbing the slope without the load, not wearing the exoskeleton, it is sufficient to control the interaction force at all contact points around $\mathbf{0}$. The robot must be constructed in a way that interaction forces at *all* connection points are *controllable*. That way any forces from environment acting on exoskeleton are transferred to the ground via robot links and joints. The robot moves in accordance to the user moves, getting away from him/her.

II) $\Delta E_{met} < 0$

If the control goal is to lower the metabolic cost of *the user performing a certain task whilst wearing an exoskeleton*, that is $\Delta E_{met} < 0$, then Eq. (A.8) can be written as:

$$\int_C \vec{F}_{exo}(\vec{s}) \cdot \mathrm{d}\vec{s} < 0 \tag{A.11}$$

The *necessary* condition to satisfy Eq. (A.11) is:

$$\exists C' : \forall \vec{s} \in C' \subset C,\ \vec{F}_{exo}(\vec{s}) \cdot \mathrm{d}\vec{s} < 0 \text{ and } C \neq \varnothing \tag{A.12}$$

NOTE 2

The Eq. (A.12) means that there must exist a path with non–zero length along which the exoskeleton helps user to move against environment while performing a task. Example being an elbow brace that actively supports the wrist of a user lifting a load held in hand.

NOTE 3

Value of $\vec{F}_{exo}$ and shape of C' are controlled variables. In general, the problem requires predicting intended trajectory C from its subset C_{int} known for time interval $\langle t_{start}, t_k \rangle$ (past), where $t_k < t_{end}$, so that $\vec{F}_{exo}(t_k)$ can be calculated.

III) $\Delta E_{met} > 0$

If the control goal is to heighten the metabolic cost of *the user actively supporting an exoskeleton performing a certain task* , that is $\Delta E_{met} > 0$, then Eq. (A.8) can be

written as:

$$\int_C \vec{F}_{exo}(\vec{s}) \cdot \mathrm{d}\vec{s} > 0 \tag{A.13}$$

The *necessary* condition to satisfy Eq. (A.11) is:

$$\exists C' : \forall \vec{s} \in C' \subset C,\ \vec{F}_{exo}(\vec{s}) \cdot \mathrm{d}\vec{s} < 0 \text{ and } C \neq \varnothing \tag{A.14}$$

NOTE 4

To satisfy Eq. (A.14) the user must assist the exoskeleton in moving along C' trajectory while it is performing its task. Value of force $\vec{F}_{exo}$ with which user must support the exoskeleton is then controlled variable.

Metabolic Cost of Isometric Force Production

The Eq. (A.4) does not take into account metabolic cost of attaining and maintaining static force by a muscle. In that situation, no real mechanical work is done, yet *in vivo* measured levels of adenosine triphosphate (ATP) turnover in human muscle tissue under isometric contractions clearly show that this is metabolically costly activity [109]. Within the domain of studies on human metabolism, the force-time integral (FTI) is used to approximate isometric work of a muscle:

$$E_{iso}^{mus} = c_{iso} \int_{t_{start}}^{t_{end}} sat(\vec{F}_{iso}^{mus} \cdot \vec{q})\, \mathrm{d}t, \tag{A.15}$$

where $\vec{q}$ stands for a vector parallel to the direction on which the muscle fibres would contract during locomotion, and oriented to their centre. $sat(x)$ is a saturation function equal x when $x \geq 0$ and 0 when otherwise, c_{iso} – constant coefficient.

NOTE 5

If $\vec{F}_{exo}(t) \equiv \mathbf{0}$ (see Fig. A.2c), the user is not burden with pressing on an exoskeleton.

NOTE 6

If $\vec{F}_{exo}(t) < \mathbf{0}$ (see Fig. A.2c) in static condition, the exoskeleton supports some of the weight of user's body.

Reproduction of Movement Trajectory

Studies in the domain of neurophysiology show that control of motorics and locomotion is a function of the central nervous system (CNS) [78]. The CNS is organised in a hierarchical manner. Generating a move involves motor cortex, basal ganglia, thalamus and hypothalamus, midbrain, cerebellum, brainstem, and spinal cord. With each action of the locomotion system a motor engram is associated. A motor engram is "[a] pathway of interneuronal linkages involving activation of certain neurons and muscles to perform a pattern of motor activity in a specific sequence of speed, strength, and motion, and at the same time inhibition of neuron pathways so that muscles which should not be participating in this pattern remain quiet." The conclusion which can be drawn from the organisation of CNS is that in order for the user to feel naturally wearing an exoskeleton, the path along which body moves must not be obstructed by the robot. The performance of the robot with regard to this need can be estimated by value of the following functional:

$$J_{traj}(\,\vec{s}^{\,exo}_{hum}\,) = \int_{t_{start}}^{t_{end}} \| \,\vec{s}^{\,exo}_{hum}(t) \,-\, \vec{s}_{hum}(t) \,\| \,\mathrm{d}t \tag{A.16}$$

where $\| \cdot \|$ is a norm in Euclidean space, $\vec{s}^{\,exo}_{hum}(t)$ stands for function representing position of a certain point on the human body at time t whilst wearing an exoskeleton, and $\vec{s}_{hum}(t)$ denotes the same point while user moves freely. The reproduction of feet trajectory was considered for the PERCRO Body Extender during the control system design and certain thresholds for the interaction forces where set in order to keep deflection on body parts within his/her natural ranges [28].

NOTE 7

In order to lower the value of functional in Eq. (A.16) it is sufficient for the robot to be aligned to corresponding points on human body only at the *intended* and *uninteded* points of contact.

NOTE 8

Human body is capable of adapting to a machine (to a certain degree). Through the learning process a user may modify slightly $\vec{s}_{hum}(t)$ (via its motor engram) so that the value of functional in Eq. (A.16) is lowered.

Human Body Internal Forces

Human body tissues: bones, cartilage, tendons, ligaments, skin, etc., while enclosed in an exoskeleton, can be subject to stress originating from the interaction force $\vec{F}_{exo}$ exerted between an exoskeleton and the user. The tolerable and maximum values of those forces stem from the biomechanical properties of human tissues. Such control need is in fact a constraint. The standard [68] requires that if there is a risk of exceeding tolerable values, a safety–related force control must be implemented.

Stress within Exoskeleton Structure

The exoskeleton structure is subject to stress due to human–machine interaction force as well as due to the load carried on the robot's frame. Robot structure changes during locomotion and in some of the configurations the structural stress can be smaller then in the other. The same internal forces may vary when different actuator forces/-torques are applied. Since the shape of the exoskeleton is highly constrained to due the fact that it couples with the user's body, parts of the mechanism cannot be thickened, the control goal might be to minimise them so the integrity is not compromised [57].

Power Consumption

Power consumption of an exoskeleton must be kept reasonably low, so that the power source weight is kept minimal.

NOTE 9

This goal contradicts the goal of reducing the metabolic cost of the user.

Conclusions

Controlling an exoskeleton is a multi–goal problem. Some of the goals contradict each other.

Appendix B

Positioning Error of Robot Manipulators

Positioning of any point of the kinematic chain is burdened with an error of measuring and setting rotational position and of two neighbouring links. Assuming that for sufficiently small $\Delta\theta_i$ for $i = 2\,, ...,\ N$ we have $\cos\left(\pi + \frac{\Delta\theta_i}{2}\right) \lesssim 1$, which implies:

$$\left|\left|\sum_{k=i}^{N} p_k\right|\right| \lesssim \sum_{k=i}^{N} \|p_k\| \tag{A.17}$$

The equation (A.17) describes a worst case when the kinematic chain is fully extended (corresponding to exoskeleton–human system standing up-straight, lifting extended hands above head, forming a line). This is due to the fact that angular error is mostly reflected in the point furthest from rotation axis. The error of positioning in the saggital plane is then bound from above by:

$$error(l_N) = \|l_N - l_N^{meas}\| \leq 2\sum_{i=1}^{N}\left[\sin\frac{\Delta\theta_i}{2} \cdot \sum_{k=i}^{N}\|p_k\|\right] \tag{A.18}$$

It is worth noting that the upper bound in (A.18) increases with the length of the links as well as with number of degrees of freedom. Upper bounds of positioning error due to quantisation error of encoders for (A.18) is given in Table B.2. The values are calculated for positioning of single kinematic chain (robot manipulator). For two overlapping suits, there exist an error of capturing position of inner suit and an error of positioning (with accuracy of capturing position) of the outer suit. Effectively the two values should be summed to give overall mismatch value between corresponding points of the inner and outer suit.

In addition to quantisation error of encoders, the positioning error of robot manipulators is further increased by "gear train errors, the errors due to structural deformations, and the errors due to the geometric parameters of the model" [154]. In a physical

device, this would cause the positioning error to be greater than given in Table B.2.

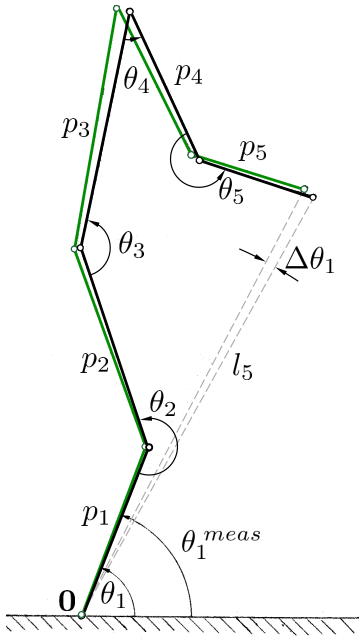

Figure B.1: Simplified model of human body in the sagittal plane:
p_1 – from centre of talocrural joint to centre knee joint,
p_2 – from c. of knee joint to c. of hip (acetabulofemoral) joint,
p_3 – from c. of hip joint to c. of shoulder (glenohumeral) joint,
p_4 – from c. of shoulder joint to c. of elbow joint,
p_5 – from c. of elbow joint to c. of wrist (radiocarpal) joint

Table B.1: Approximate lengths of links of an 75 kg, 175 cm tall male [source: LifeModeler software] for the human body model as in Fig. B.1.

link	p_1	p_2	p_3	p_4	p_5
length [mm]	370	450	480	320	240

Table B.2: Calculated values of positioning error of kinematic chain modelling human body as in Fig. B.1 for different encoder resolutions.

encoder resolution [bits]	10	11	12	13	14	15	16
$error(l_5)$ upper bound [mm]	36.63	18.32	9.16	4.58	2.29	1.14	0.57

Appendix C

Safety of exoskeletons according to ISO13482

C.1. Safety of Control Systems

C.1.1 Standard for Safety of Personal Care Robots – ISO13482

In the early 2014, the International Standard [68] addressing safety of robots performing tasks for improving the quality of life of users, irrespective of age or capability, was released. It deals with the most significant hazards, hazardous situations or hazardous events which may occur during operation of *the personal care robots*. For listed hazards requirements on inherently safe design as well as for complementary and protective measures are provided. In the Appendix C.1 basic terminology for describing safety of exoskeletons is given.

C.1.1.1 Safety of Exoskeletons

Full classification of personal care robots is given in the Appendix B.2. In Fig. C.2 classification tree is depicted. Exoskeletons, used as machines assisting users in their daily activities, are included into the category of personal care robots and are subject to ISO13482 standard. They are classified as *physical assistant robots*, and named *restraint type* providing either low (*Type 2.1*) or high (*Type 2.2*) power assistance.

> "A power is considered to be "low powered" if it is sufficiently low that injuries other than minor injuries are unlikely after inherently safe design measures have been applied. A maximum power which can be considered as low powered is determined by the manufacturer considering intended tasks and user groups." [68, p. 39]

Considering that definition, a full-body exoskeleton with enhancive capabilities falls into the *Type 2.2* category. Based upon that division different *safeguarding and complementary protective measures* and their *safety–related control system performance levels* are required. Example being a stability control required from *Type 2.2* and not applicable to *Type 2.1*. The hazards which may occur in exoskeletons are marked in colour in Fig. C.1. In green hazards for which complementary or protective measures can be implemented as part of the control strategy. The items in green also are connected to hazards that can occur due to fault or malfunction of the controller. The hazards which may occur in exoskeletons, but are not connected to functioning of the controller, are marked in yellow.

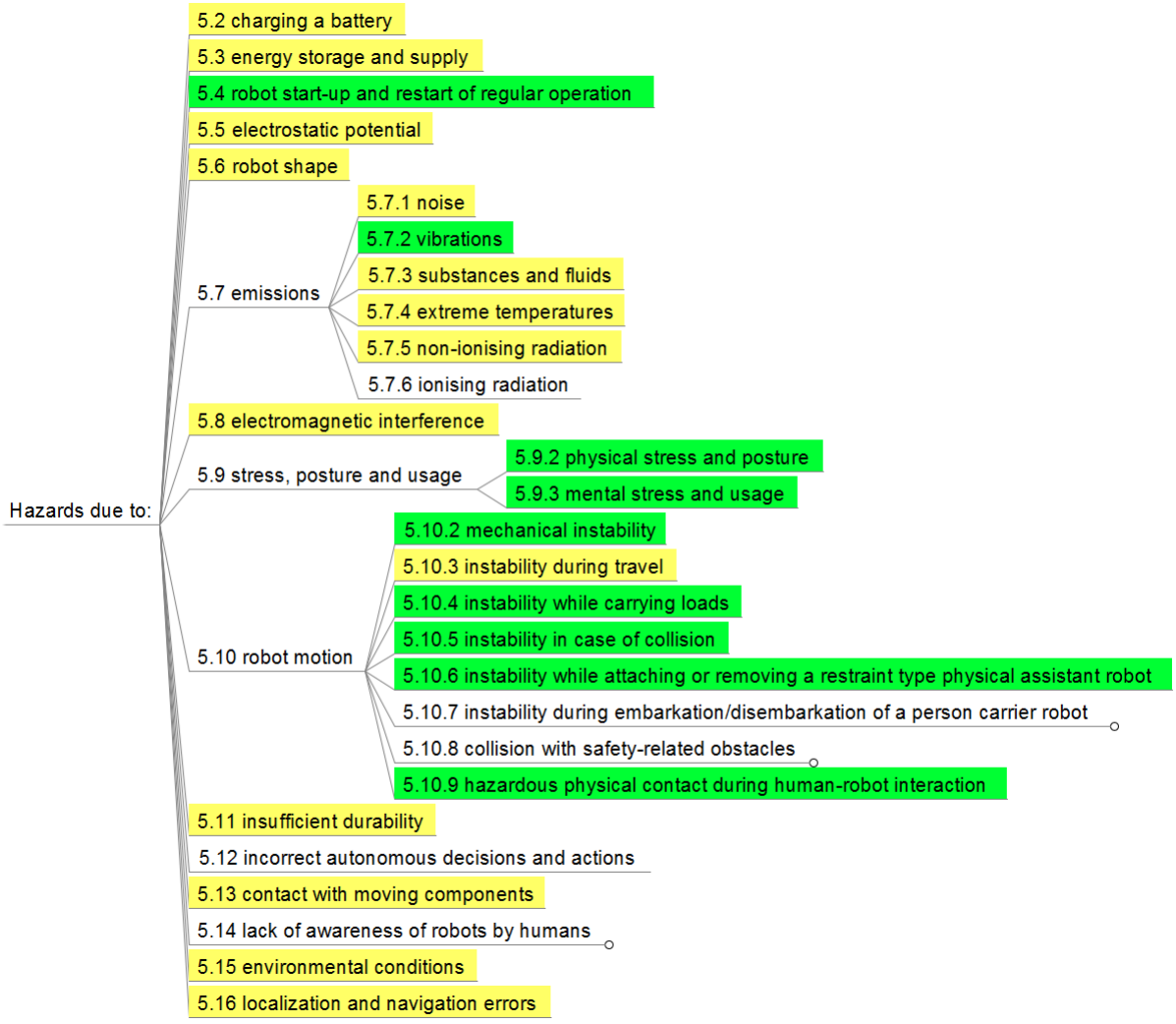

Figure C.1: Sources of hazards in personal care robots (adopted from [68], sections numbers included): green – hazards in restraint–type physical assistant robots relating to the control system, yellow – other hazard sources in restraint–type physical assistant robots.

C.1.1.2 Risk Assessment, Safety Requirements and Protective Measures

To avoid development of a system failure by preventing a hazardous situation or limiting its impact following its occurrence, the standard [68] requires a risk assessment to be conducted and appropriate measures to be incorporated into the design. By *risk* "a combination of the probability of occurrence of harm and the severity of that harm" is meant.

The standard [68] states that the risk assessment must be conducted according to the principles of [155]. That is hazard identification analysis must be done on *the general specification* of the robot. The risk analysis must include a hazard identification analysis based but not limited to *hazard items* listed in Appendix A to [68]. It is emphasised that it must be a systematic procedure and must be based on aspects of the general specification of the machine or system under design [68, p. 58]. Risk for identified hazard must be *estimated*. Base upon that information protective measures must be implemented so that *the residual risk* is below a tolerable level for identified hazards [68]. In order to assure the reliability of the safety measures, the "[p]ersonal care robot shall conform to the safety requirements " of [68]. Protective measures consist of:

- inherently safe design
- safeguarding and complementary protective measures
- information for use

Realisation of the safeguarding and complementary protective measures is achieved via safety–related features of the control system. In Table C.1 safety functions realising these protective measures with required levels of performance of safety–related subsystems are listed. These requirements, when relevant to the particular type of machine, must be included into specification (requirements) for the controller.

C.1.2 Safety of existing controller designs

C.2. Basic Terminology

The standard for personal care robots [68] utilises terms defined in [155], [156] when referring to safety of exoskeletons:

failure – "termination of the ability of an item to perform a required function"

Table C.1: Performance levels for personal care robots (adopted from [68]).

Safety functions of personal care robots	Type of robot							
	Mobile servant robot		Physical assistant robot				Person carrier robot	
	Type 1.1	Type 1.2	Type 2.1	Type 2.2	Type 2.3	Type 2.4	Type 3.1	Type 3.2
Emergency stop	d (no low risk option)		c	d	c	d	d	d
Protective stop	b	d	b	d	b	c	c	e
Limits to workspace (incl. forbidden area avoidance)	b	d	b	d	a	d	N/A	e
Safety-related speed control	b	d	b	b	b	d	c	e
Safety-related force control	b	d	b	e	a	b	N/A	N/A
Hazardous collision avoidance	b	d	N/A	N/A	b	d	N/A	e
Stability control (incl. overload protection)	b	d	N/A	c	b	d	b	d

fault – "state of an item characterized by the inability to perform a required function, excluding the inability during preventive maintenance or other planned actions, or due to lack of external resources"

hazard – "potential source of harm"

risk – "a combination of the probability of occurrence of harm and the severity of that harm"

residual risk – "risk remaining after protective measures have been implemented"

risk estimation – "defining likely severity of harm and probability of its occurrence"

risk analysis – "combination of the specification of the limits of the machine, hazard identification and risk estimation"

risk assessment – "overall process comprising a risk analysis and a risk evaluation"

protective measure – "measure intended to achieve risk reduction"

complementary protective measures – "protective measures which are neither inherently safe design measures, nor safeguarding (implementation of guards and/or protective devices), nor information for use, could have to be implemented as required by the intended use and the reasonably foreseeable misuse of the machine."

inherently safe design measure – "protective measure which either eliminates hazards or reduces the risks associated with hazards by changing the design or operating characteristics of the machine without the use of guards or protective devices"

safeguarding – "protective measure using safeguards to protect persons from the hazards which cannot reasonably be eliminated or risks which cannot be sufficiently reduced by inherently safe design measures"

performance level – "discrete level used to specify the ability of safety-related parts of control systems to perform a safety function under foreseeable conditions"

C.3. Classification of Personal Care Robots

In Fig. C.2 classification of personal care robots according to [68] is depicted. Exoskeletons are named either *Type 2.1* (low power) or *Type 2.2* (high power).

C.4. Example: Risk Assessment of Hazardous Physical Contact during Human–Exoskeleton Interaction

Definition of *Type 2.2* robot states that the "user cannot overpower personal care robot" which is in contradiction with recommendation for inherently safe design: "[i]n all application tasks involving physical human–robot interaction, a personal care robot shall be designed to reduce, as far as is reasonably practicable, any levels of skin–robot friction, shear stresses, dynamic shocks, torques, arcs of centre of gravity, weight-bearing transfers and supports of the human body." The risk should be reduced in such situation by implementation of most appropriate safeguarding and complementary protective measures:

a) software–controlled limits to the personal care robot workspace
b) speed restriction and safety–related speed control
c) force restriction and safety–related force control

For *Type 2.2*, which operates in close contact with human body and exerts highly rated forces in close proximity of the delicate tissues, the most appropriate protective measure should be force restriction or safety–related force control of contact force between user and the exoskeleton. This is reflected in Table C.1 by the most strict Performance Level (PL) *e* being required for safety–related force system. *e* relates to the *average probability of dangerous failure per hour* $[h^{-1}]$ being in the range $\geq 10^{-8}$ to $< 10^{-7}$ (see Table C.2). It is equivalent of the highest Safety Integrity Level 3 (SIL–3) [157].

On the contrary, for the *Type 3.1* of personal carrier robot (see Fig. C.2) the safety–related force control is not applicable (see Table C.1).

Table C.2: Performance levels of machinery (adopted from [156]).

PL	Average probability of dangerous failure per hour 1/h
a	$\geqslant 10^{-5}$ to $< 10^{-4}$
b	$\geqslant 3 \times 10^{-6}$ to $< 10^{-5}$
c	$\geqslant 10^{-6}$ to $< 3 \times 10^{-6}$
d	$\geqslant 10^{-7}$ to $< 10^{-6}$
e	$\geqslant 10^{-8}$ to $< 10^{-7}$

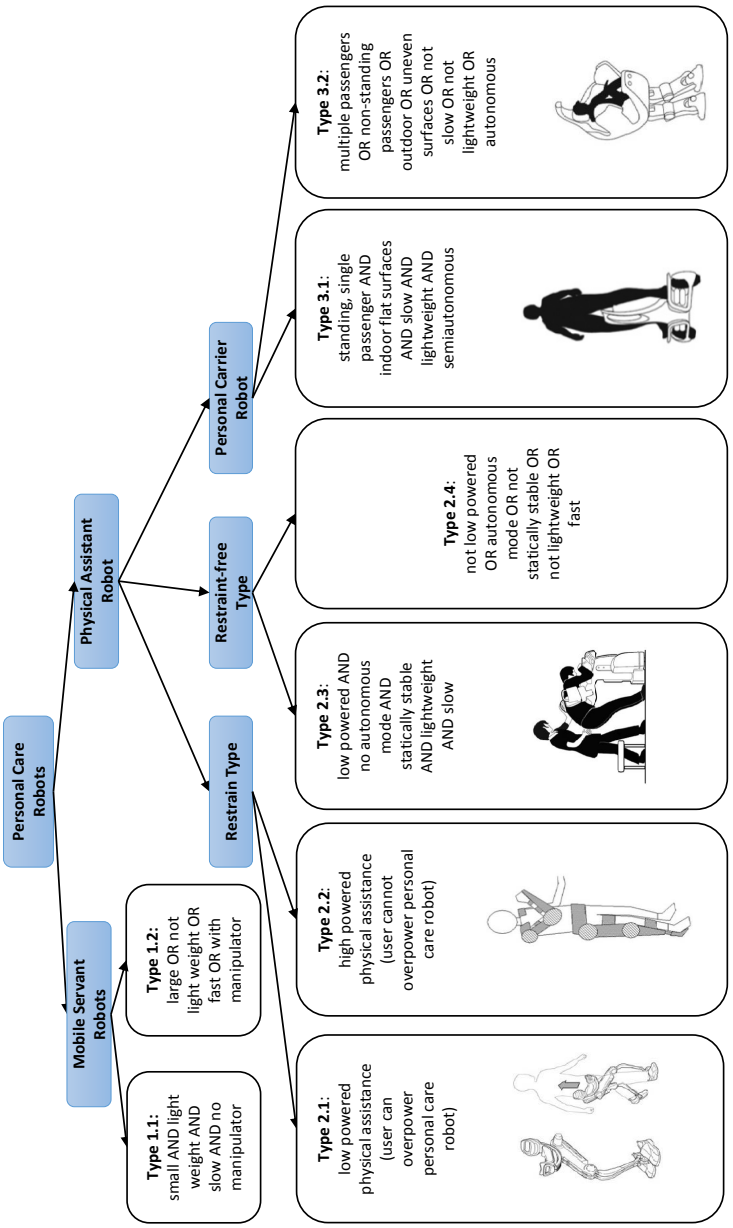

Figure C.2: Personal care robots classification (adopted from [68]).

Appendix D

Customer Needs:

Activities to be performable by the device

Appendix A in the Customer Needs [114] lists following tasks:

Table D.1: Activities to be performable by the device [114]

Unique Identifier	**Activity**
NA-1	Walk on level ground
NA-2	Walk on rough terrain
NA-3	Run
NA-4	Squat
NA-5	Get up from a fallen position
NA-6	Walk up the stairs
NA-7	Walk up the slopes
NA-8	Walk down the stairs
NA-9	Walk down the slopes
NA-10	Go through doorways
NA-11	Walk on level ground with load
NA-12	Walk on rough terrain with load
NA-13	Run with load
NA-14	Squat with load

NA-15	Get up from a fallen position with load
NA-16	Walk up the stairs with load
NA-17	Walk up the slopes with load
NA-18	Walk down the stairs with load
NA-19	Walk down the slopes with load
NA-20	Go through doorways with load
NA-21	Deadlift
NA-22	Overhead shoulder press (with bar)
NA-23	Vertical jump
NA-24	Bench press (with bar)
NA-25	Horizontal push (full body)
NA-26	Horizontal pull (full body)
NA-27	Biceps curl (with bar)
NA-28	Bent over row (with bar)
NA-29	Pull down

Appendix E

Matlab/Simulink Model Documentation

E.1. Initialisation Scripts

Simulink model parameters have to be loaded to Matlab workspace before the simulation can be run. Scripts E.1, E.2, E.3, E.4, serve purpose of parameters initialisation.

Matlab Script E.1: Script for calculation of input trajectory from motion capture data.

```
% description: script preprocessing data for simulation from motion capture
%              data
% author:      M. Napora
% project:     Exoskeleton Project
% date:        2019-03-11

load variables
clear trajectory;

trajectory.sim_start_s = -4;
trajectory.data_padding_s = 10.5; % data padding in seconds > 1 s
trajectory.data_end_padding_s = 0.5350; % data end padding in seconds
trajectory.s_coef = 1.2288*0.001; % scaling coefficient and conversion from
% milimiters to meters
trajectory.mocap_frequency_Hz = 400;
trajectory.data_frequency_Hz = 4000;

end_idx_of_pad = trajectory.mocap_frequency_Hz*trajectory.data_padding_s;
end_idx_of_end_pad = end_idx_of_pad+length(Y) + ...
                     trajectory.mocap_frequency_Hz*...
                     trajectory.data_end_padding_s;

trajectory.displacement_units = 'm';
%------------------------------------------------------------------------
trajectory.mocap.X = trajectory.s_coef*Y;
```

```
trajectory.X(1:end_idx_of_pad)=Y(1);
trajectory.X((end_idx_of_pad+1):(end_idx_of_pad+length(Y)))=Y;
trajectory.X((end_idx_of_pad+length(Y)+1):end_idx_of_end_pad)=Y(end);
trajectory.X = trajectory.s_coef*trajectory.X;
%-------------------------------------------------------------------------
trajectory.mocap.Y = trajectory.s_coef*Z;
trajectory.Y(1:end_idx_of_pad)=Z(1);
trajectory.Y((end_idx_of_pad+1):(end_idx_of_pad+length(Y)))=Z;
trajectory.Y((end_idx_of_pad+length(Z)+1):end_idx_of_end_pad)=Z(end);
trajectory.Y = trajectory.s_coef*trajectory.Y;

trajectory.end_time_s = (length(trajectory.X) - 1) / ...
                        trajectory.mocap_frequency_Hz;
trajectories_time = 0:1/trajectory.mocap_frequency_Hz:trajectory.end_time_s;

trajectory.filt_order = 4;
trajectory.cut_off_freq_Hz = 5;
[trajectory.filt_num, trajectory.filt_denum] = ...
    butter( trajectory.filt_order, ...
    trajectory.cut_off_freq_Hz / (trajectory.data_frequency_Hz/2) );
trajectory.filter_type = 'butterworth';

trajectory.time = 0:1/trajectory.data_frequency_Hz:trajectory.end_time_s;

trajectory.derivatives_filtered = 0;

trajectory.X_proc = trajectory_calc_derivatives( trajectory, ...
                                                 trajectory.X, ...
                                                 trajectories_time );
trajectory.Y_proc = trajectory_calc_derivatives( trajectory, ...
                                                 trajectory.Y, ...
                                                 trajectories_time );

figure;
plot( trajectory.time, trajectory.X_proc.int, ...
      trajectory.time, trajectory.X_proc.f, ...
      trajectory.time, trajectory.X_proc.f_d_f, ...
      trajectory.time, trajectory.X_proc.f_d_f_d_f );
grid on;
%-----------------------------------------------
figure;
plot( trajectory.time, trajectory.Y_proc.int, ...
      trajectory.time, trajectory.Y_proc.f, ...
      trajectory.time, trajectory.Y_proc.f_d_f, ...
      trajectory.time, trajectory.Y_proc.f_d_f_d_f );
grid on;

stage_2_time = trajectory.data_padding_s - 5.5;
stage_3_time = trajectory.data_padding_s - 0.5;

controller_set.lo_engagment_time = -2;
```

```
% just to enable variants of low-level controller
controller_set_ll_variant = 1;

%choose load: 1 - 64 kg, 0 - noload
controller_set_load_var = 0;

set_param(bdroot, 'LoadInitialState', 'off');

controller_set_pistons_active = 1;
if(controller_set_pistons_active == 0)
    load init_state_torque_only
    open('singlejoint_optim');
    set_param(bdroot, 'LoadInitialState', 'on');
    set_param(bdroot, 'InitialState', 'xInitial');
    % bdroot - to get model name of current system
end
controller_set_hydraulics_included = 1;
clear end_idx_of_pad trajectories_time Y Z end_idx_of_end_pad ;
```

Matlab Script E.2: Function calculating signal derivatives and filtering them.

```
function var = trajectory_calc_derivatives( trajectory, vec, t )

% description: function calculating signal derivatives and filtering them
% author:      M. Napora
% project:     Exoskeleton Project
% date:        2019-03-11

num = trajectory.filt_num;
denum = trajectory.filt_denum;
freq_Hz = trajectory.data_frequency_Hz;

% interpolate data
var.int = interpn( t, vec, trajectory.time );

% zero phase shift filtering using Butterworth filter
var.f = filtfilt( num, denum, var.int);

% calculate first derivative
var.f_d = diff( var.f );
var.f_d = [ var.f_d(1) var.f_d ] * freq_Hz;

% filter first derivative
if(trajectory.derivatives_filtered == 1)
    var.f_d_f = filtfilt( num, denum, var.f_d );
else
    var.f_d_f = var.f_d;
end

% calculate second derivative
var.f_d_f_d = diff( var.f_d_f );
```

```
var.f_d_f_d = [ var.f_d_f_d(1) var.f_d_f_d] * freq_Hz;

% filter second derivative
if(trajectory.derivatives_filtered == 1)
    var.f_d_f_d_f = filtfilt( num, denum, var.f_d_f_d );
else
    var.f_d_f_d_f = var.f_d_f_d;
end
```

Matlab Script E.3: Script setting controller parameters.

```
% description: Script setting controller parameters
% author:      M. Napora
% project:     Exoskeleton Project
% date:        2019-03-30

close all
%--------------------------------------------------------------------------
% assign controller settings

controller_set.k_1 = 65;
controller_set.k_2 = controller_set.k_1;
controller_set.gravity_gain = 1;

controller_set.kp = 13000;
controller_set.ki = 0;
controller_set.kd = 0;
controller_set.filt_N = 1;

controller_set.kpp = 1.3e-3;
controller_set.kdd = 0;
controller_set.filt_NN = 1;
controller_set.kii = 0;
controller_set.c_sr = 100000;
controller_set.kpp_stab = 1e-4;

n = 1;
f = 1.5;
options = bodeoptions;
options.FreqUnits = 'Hz'; % or 'rad/second', 'rpm', etc.
[controller_set.b_act, controller_set.a_act] = butter(n, 2*pi*f, 's');

n_kc = 1;
f_kc = 2;
[controller_set.b_kc, controller_set.a_kc] = butter(n_kc, 2*pi*f_kc, 's');

% time_const =  9.7934e-04;
% act_saturation =  500.9900;
% act_gain = 806;

clear n f n_kc f_kc options;
```

Matlab Script E.4: Script setting hydraulics parameters

```
% description: Script setting hydraulics parameters
% author:      T. Magill
% project:     Exoskeleton Project
% date:        2019-03-30

%% value setup
pistonA = ((38.1e-3)^2)*0.25*pi; %m^2
pistonB = ((38.1e-3)^2 - (25.4e-3)^2)*0.25*pi; %m^2
stroke = 100/1000; %m

initialPos = 0; %m

init_opening = 0;
A_leak = 1e-9; %m^2
a_max = 5.9648;

load('Valve_Parameterization\valveData');
load('Valve_Parameterization\frequencyResponse\frequencyResponse');

%% from solidworks
stiffness   = 100000;% N/mm
stiffness   = stiffness*2000; % N/m
exponent    = 1.5;
damping     = 49.91566312;% N/(mm/s)
damping     = damping*10000;% N/(m/s)
penteration = 0.1;% mm
```

E.2 Simulink Model

A system–level models that include mechanical and fluid domains and the control system were created in Simulink using standard Simulink blocks, as well as, Fluids and Multibody libraries. This section documents the created model.

E.2.1 Simulink Model

In Fig. E.1 structure of the model is depicted. Each node of the tree represents a subsystem. Colours are assigned for each domain. Nodes contain reference to Figure or Script detailing its implementation.

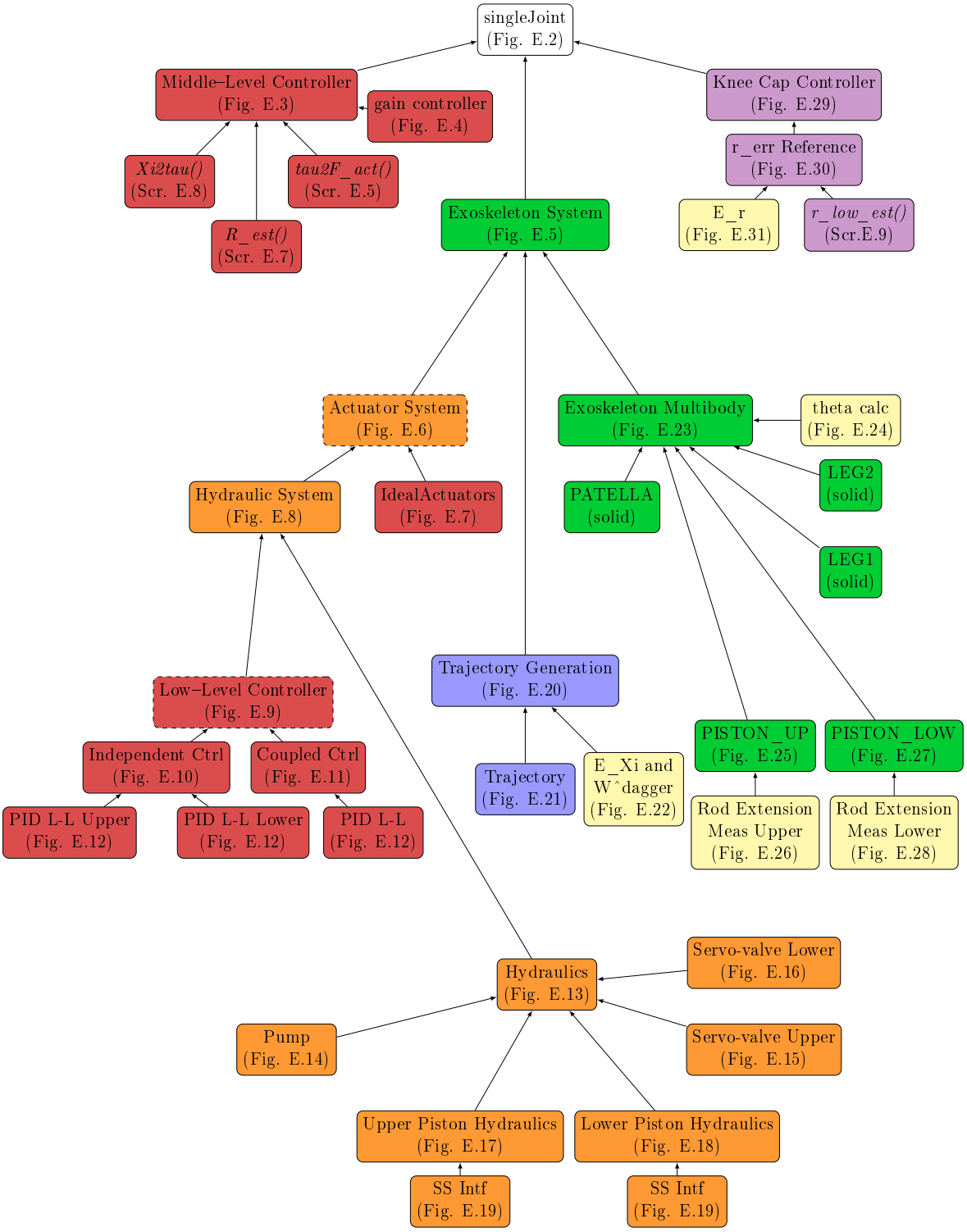

Figure E.1: Simulink model subsystems structure represented as a tree. Red – force controller subsystems (standard Simulink), violet – knee cap controller (standard Simulink), green – exoskeleton dynamics model (Simscape Multibody), orange – hydraulic components (Simscape Fluids), yellow – measurements subsystems, blue – end effector (contact point) trajectory generation.

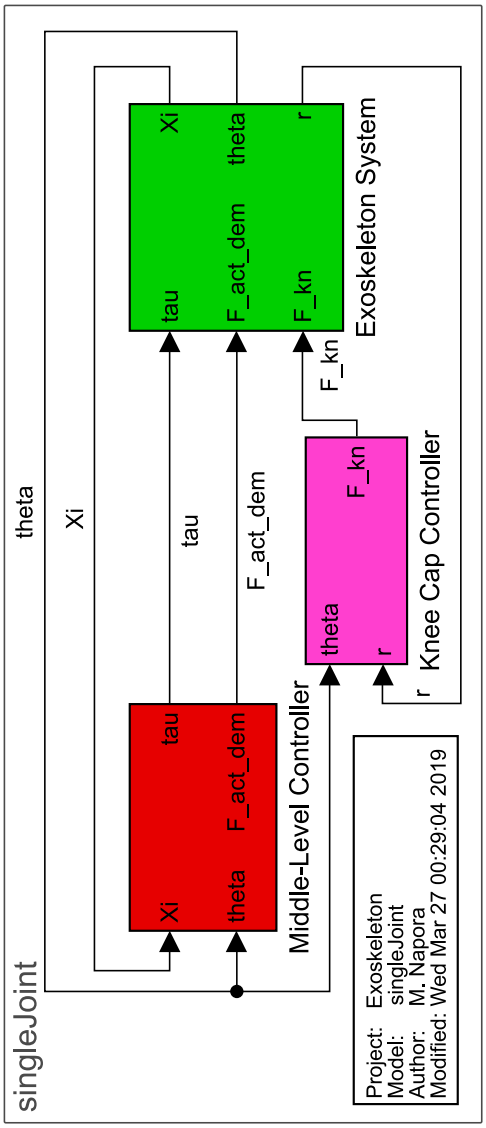

Figure E.2: singleJoint

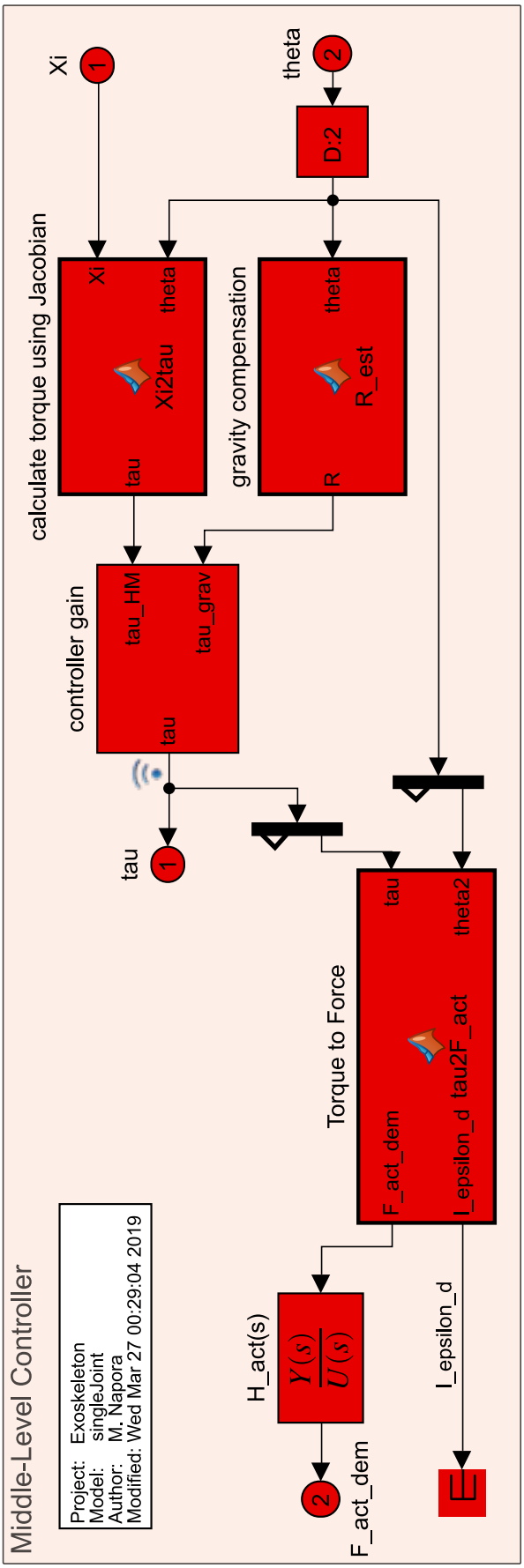

Figure E.3: singleJoint/Middle-Level Controller

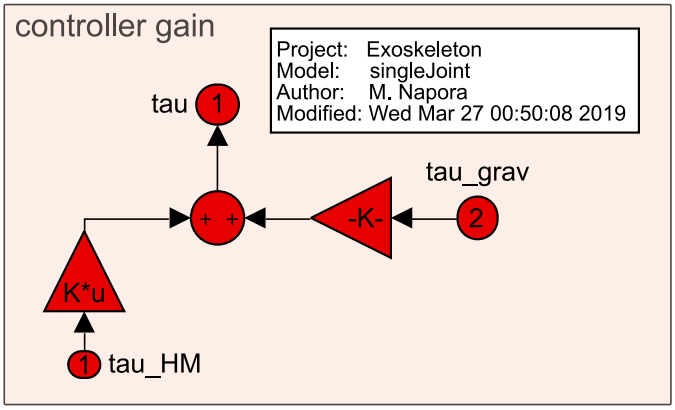

Figure E.4: singleJoint/Middle-Level Controller/controller gain

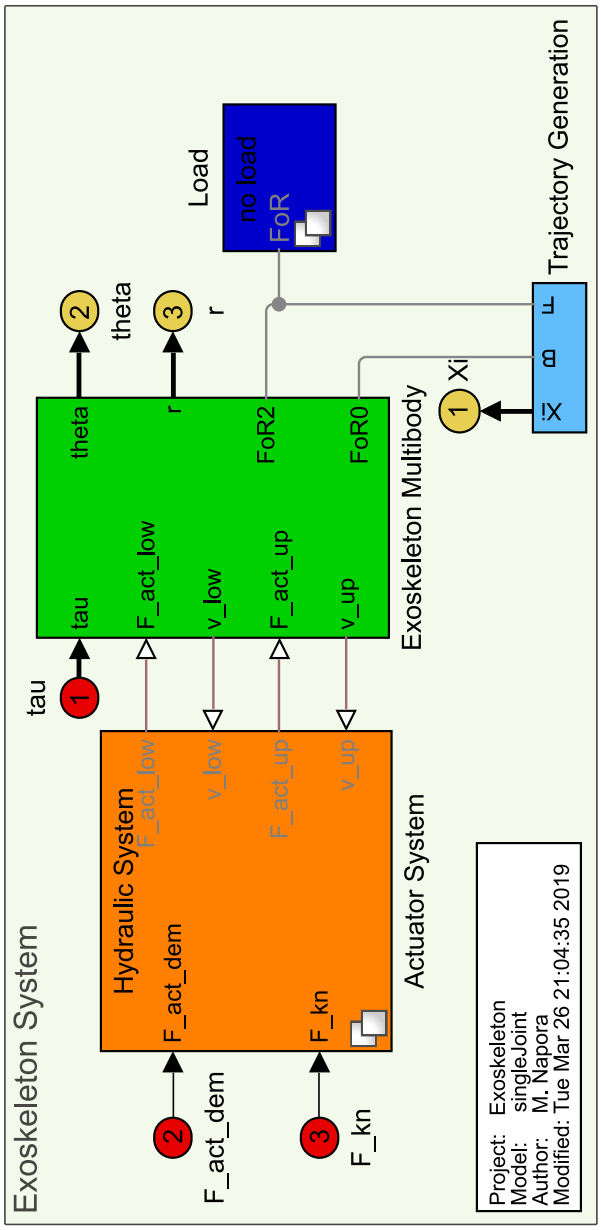

Figure E.5: singleJoint/Exoskeleton System

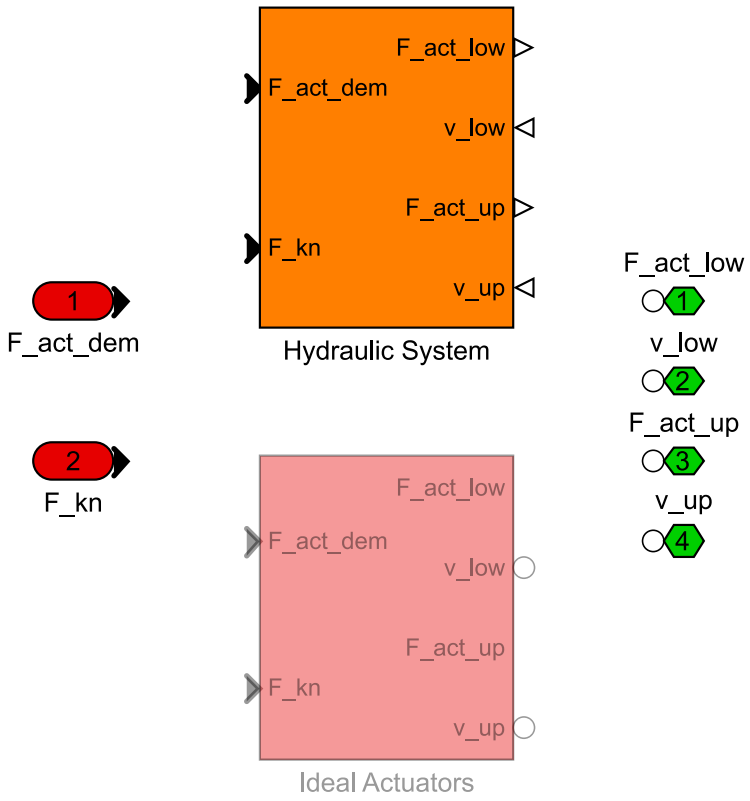

Figure E.6: singleJoint/Exoskeleton System/Actuator System/Actuator System

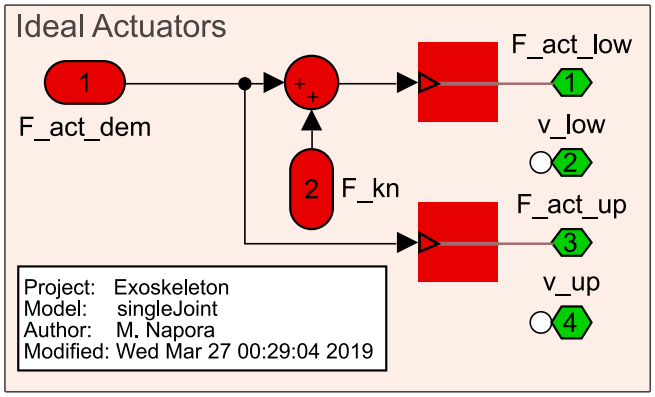

Figure E.7: singleJoint/Exoskeleton System/Actuator System/Ideal Actuators

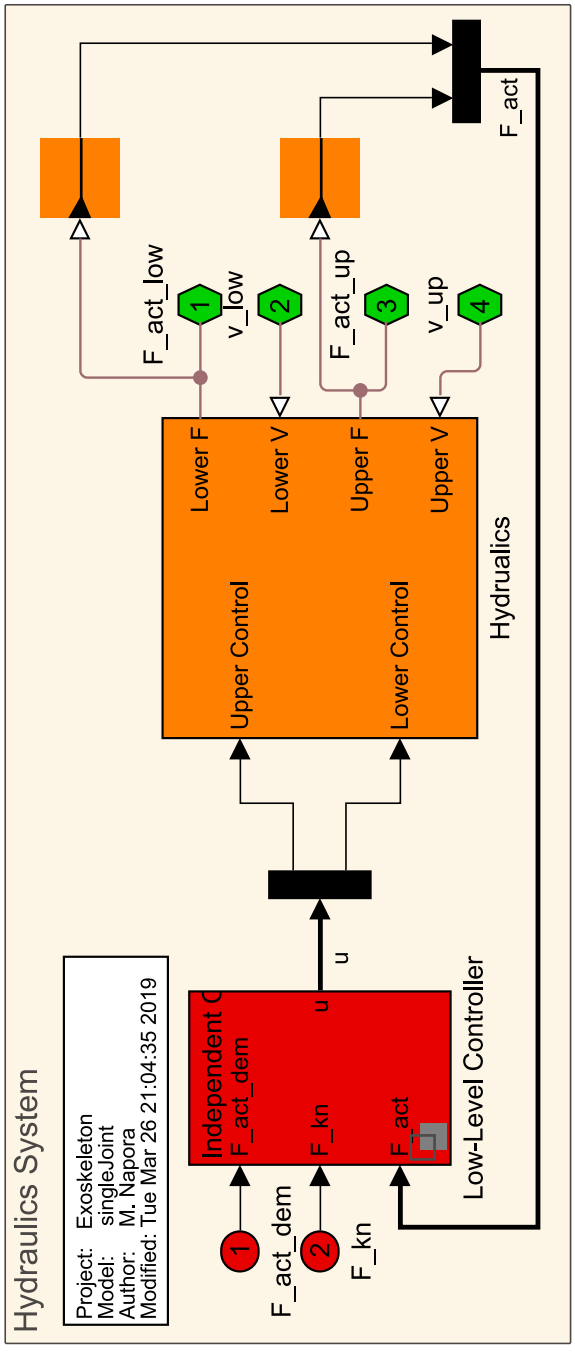

Figure E.8: singleJoint/Exoskeleton System/Actuator System/Hydraulic System

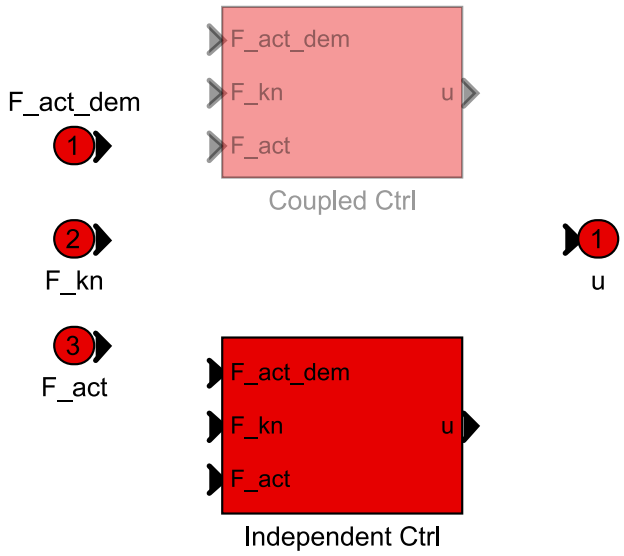

Figure E.9: singleJoint/Exoskeleton System/Actuator System/Hydraulic System/Low-Level Controller

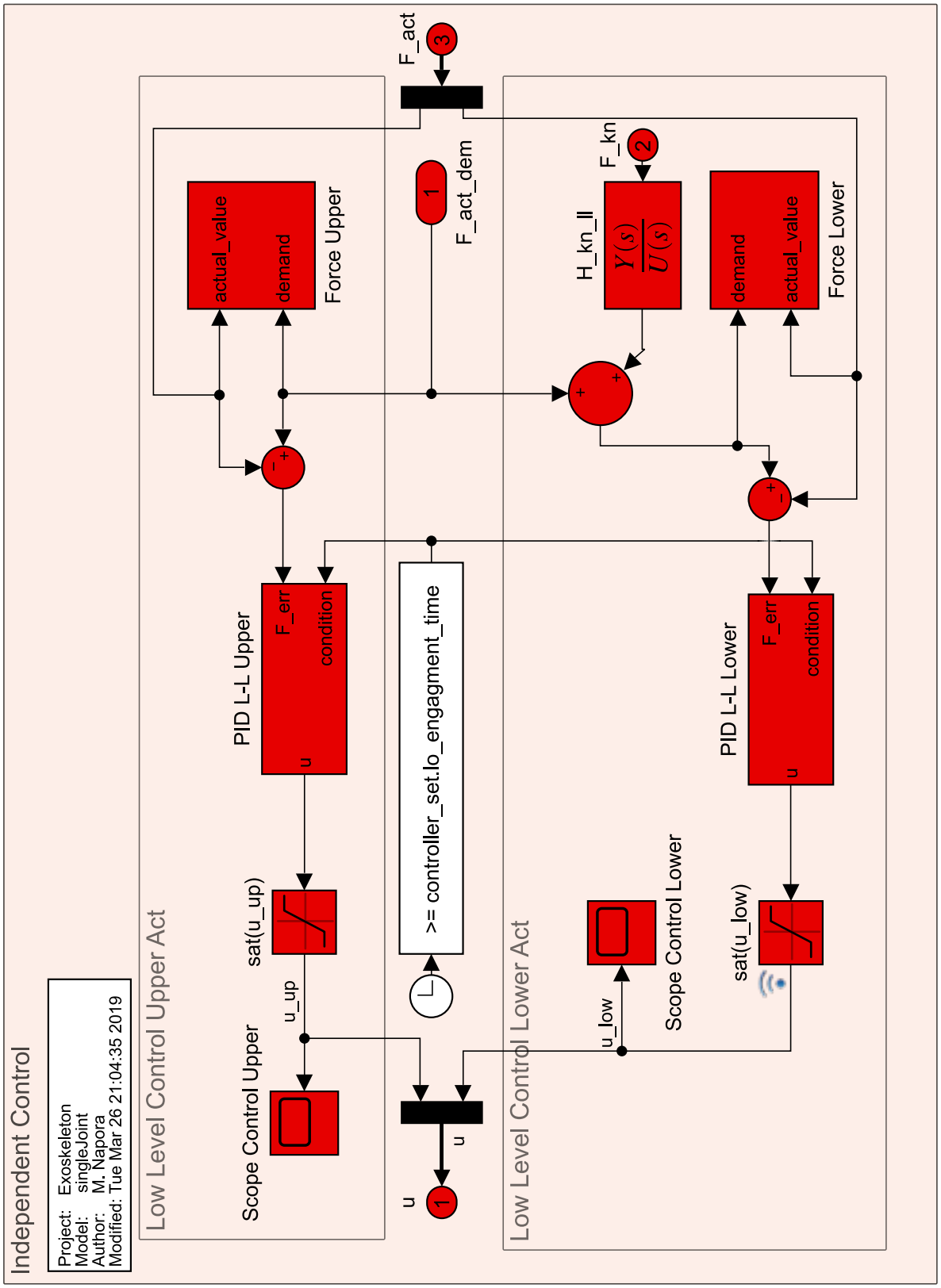

Figure E.10: singleJoint/Exoskeleton System/Actuator System/Hydraulic System/Low-Level Controller/Independent Ctrl

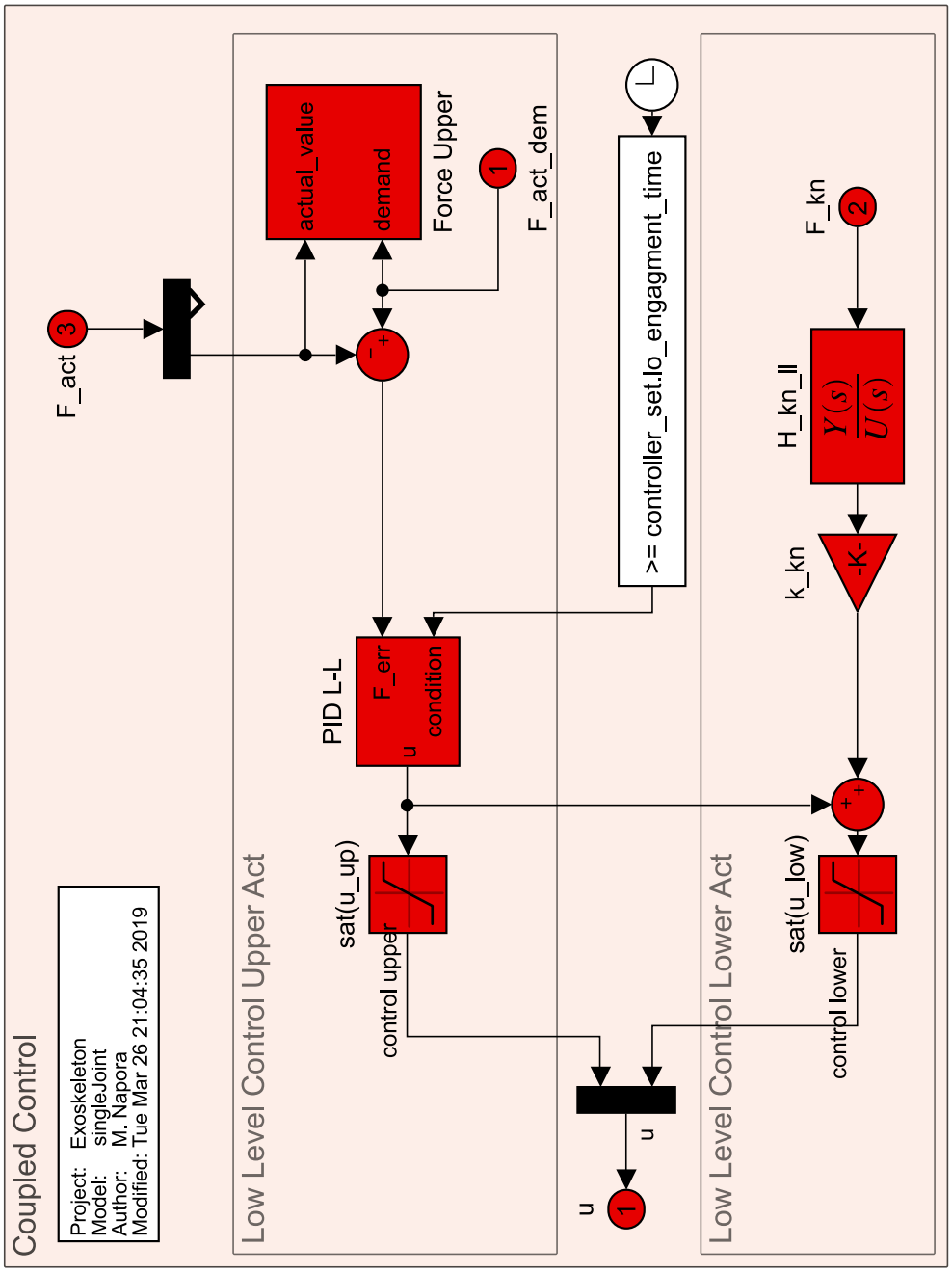

Figure E.11: singleJoint/Exoskeleton System/Actuator System/Hydraulic System/Low-Level Controller/Coupled Ctrl

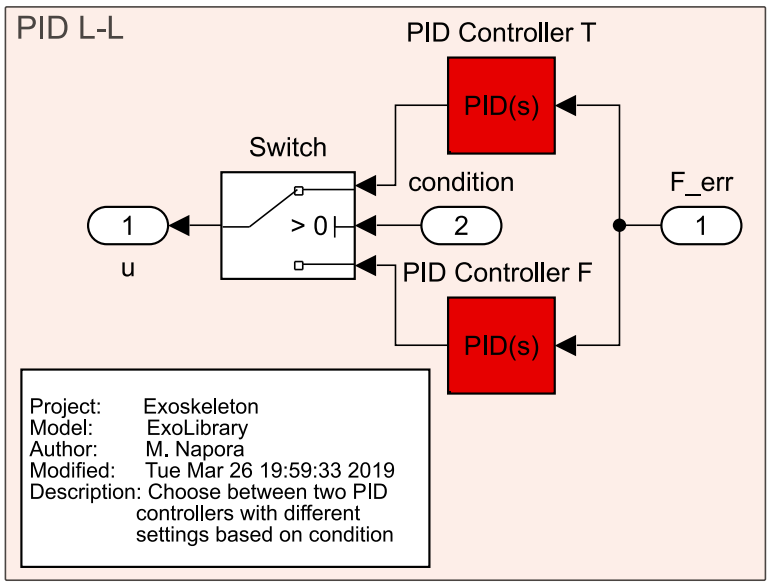

Figure E.12: ExoLibrary/PID L-L

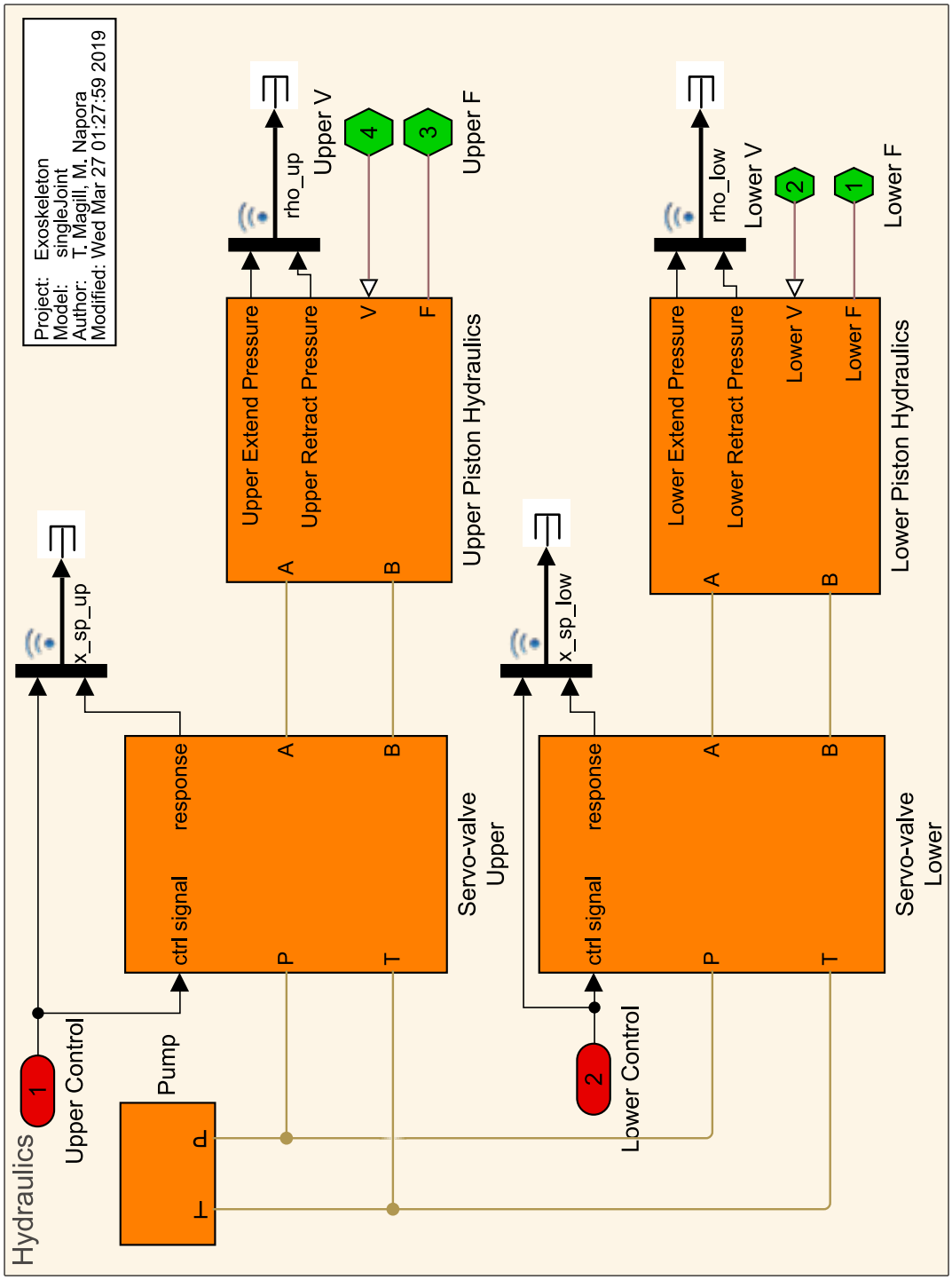

Figure E.13: singleJoint/Exoskeleton System/Actuator System/Hydraulic System/Hydraulics

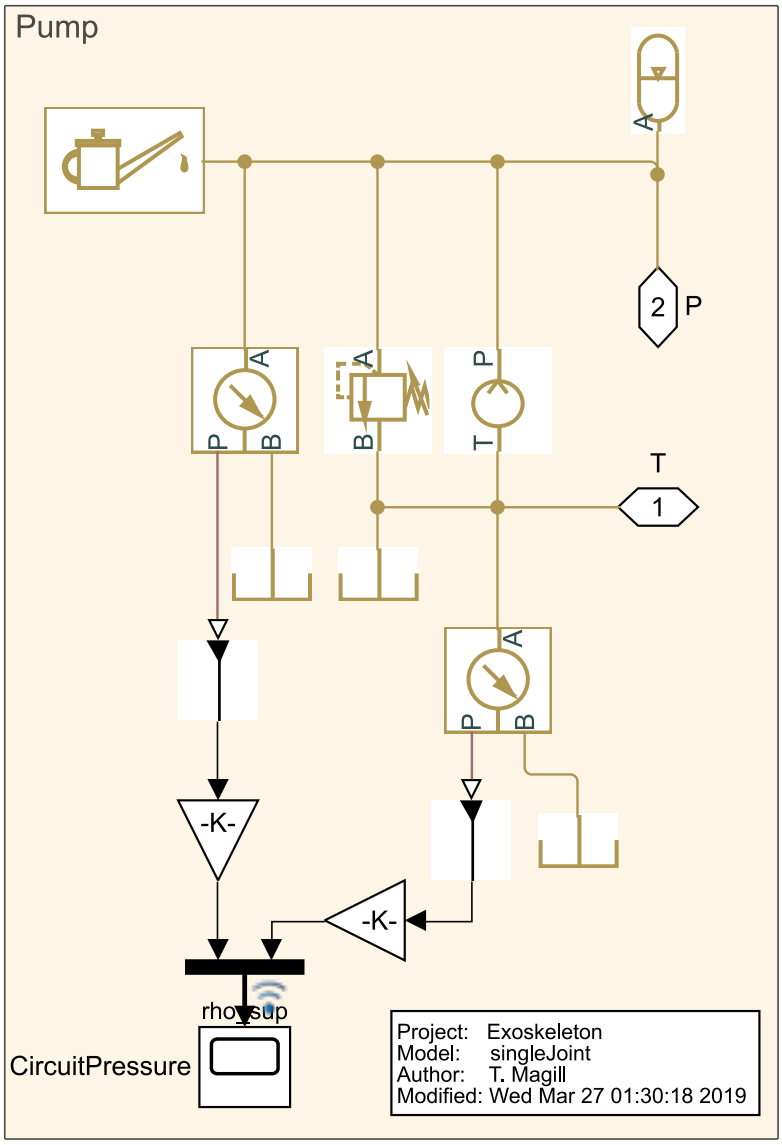

Figure E.14: singleJoint/ Exoskeleton System/ Actuator System/ Hydraulic System/ Hydraulics/ Pump

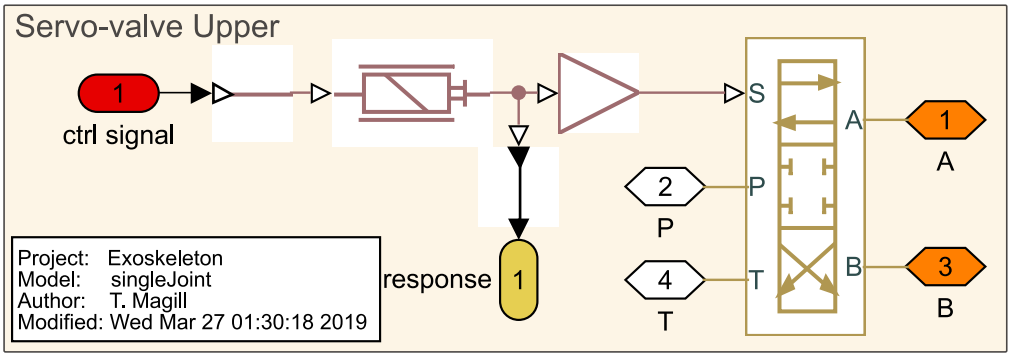

Figure E.15: singleJoint/Exoskeleton System/Actuator System/Hydraulic System/Hydraulics/Servo-valve Upper

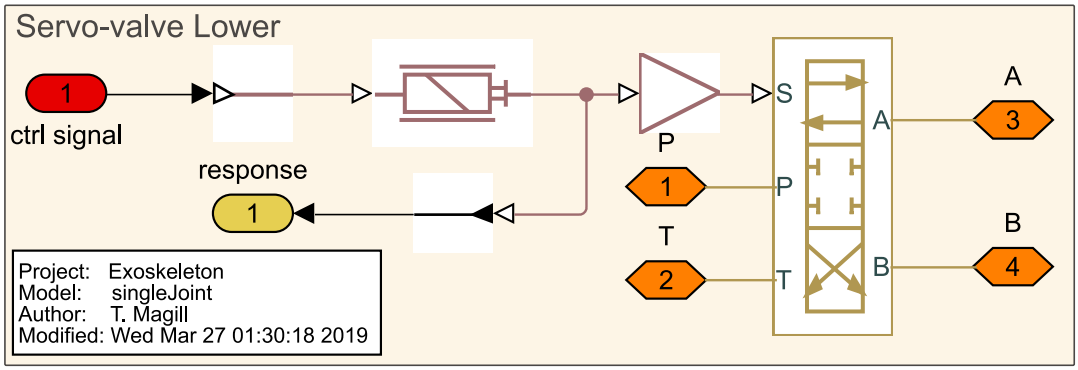

Figure E.16: singleJoint/Exoskeleton System/Actuator System/Hydraulic System/Hydraulics/Servo-valve Lower

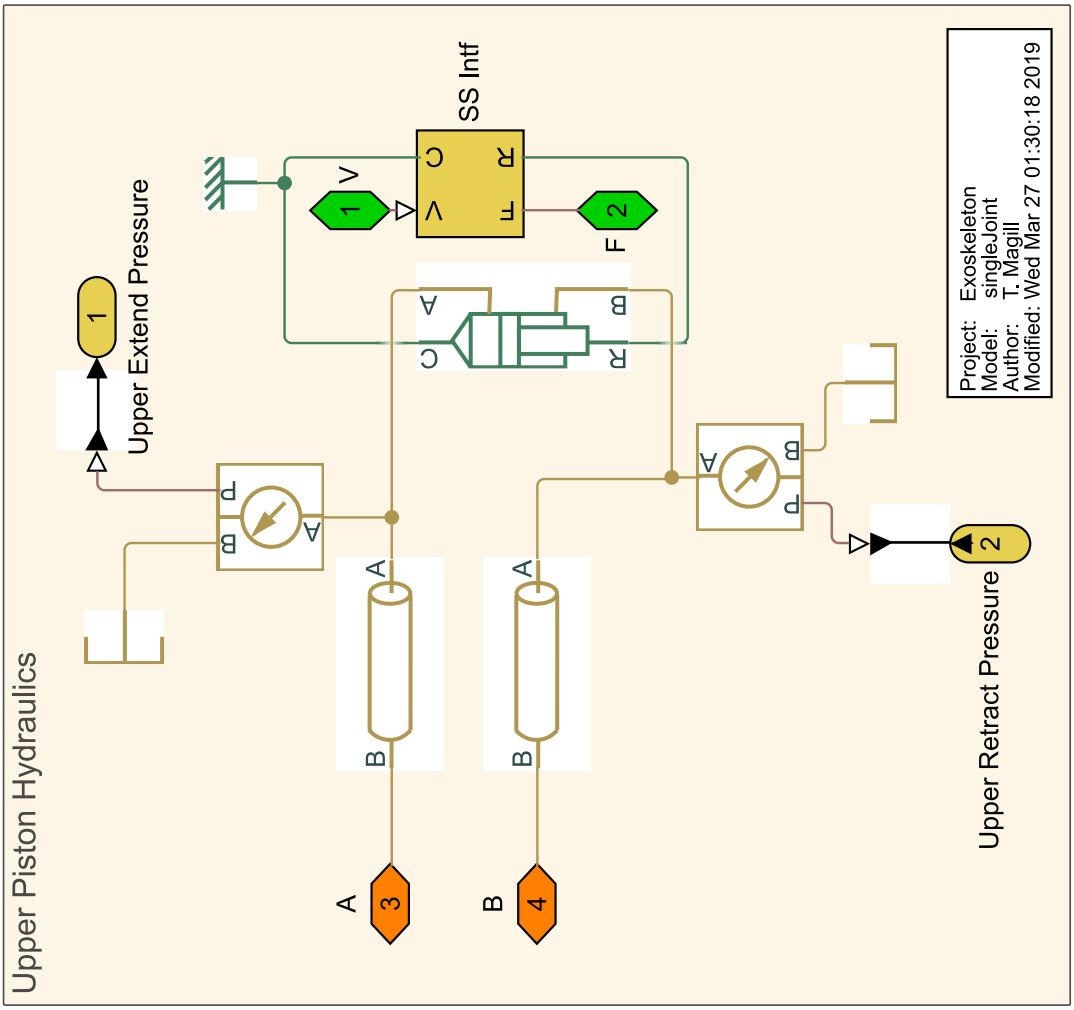

Figure E.17: singleJoint/Exoskeleton System/Actuator System/Hydraulic System/Hydraulics/Upper Piston Hydraulics

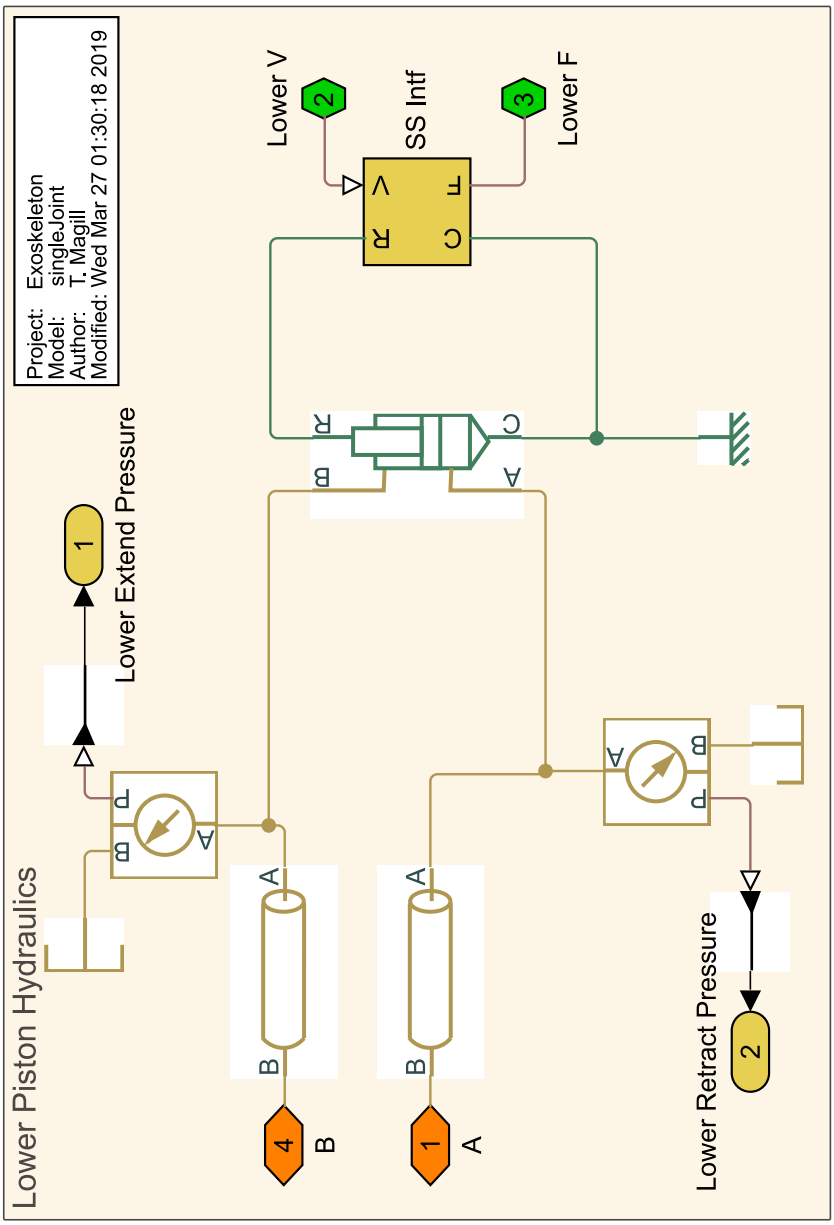

Figure E.18: singleJoint/Exoskeleton System/Actuator System/Hydraulic System/Hydraulics/Lower Piston Hydraulics

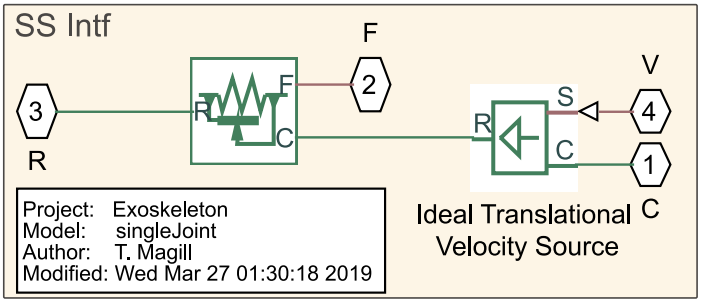

Figure E.19: singleJoint/Exoskeleton System/Actuator System/Hydraulic System/Hydraulics/Servo-valve X/SS Intf (X = Upper, Lower)

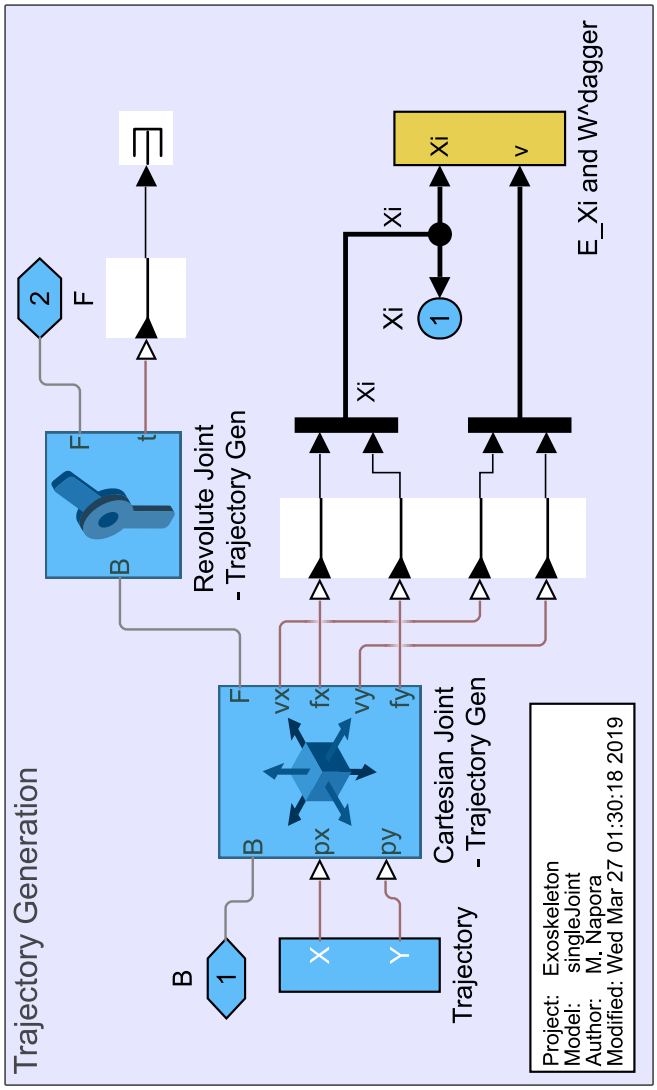

Figure E.20: singleJoint/Exoskeleton System/Trajectory Generation

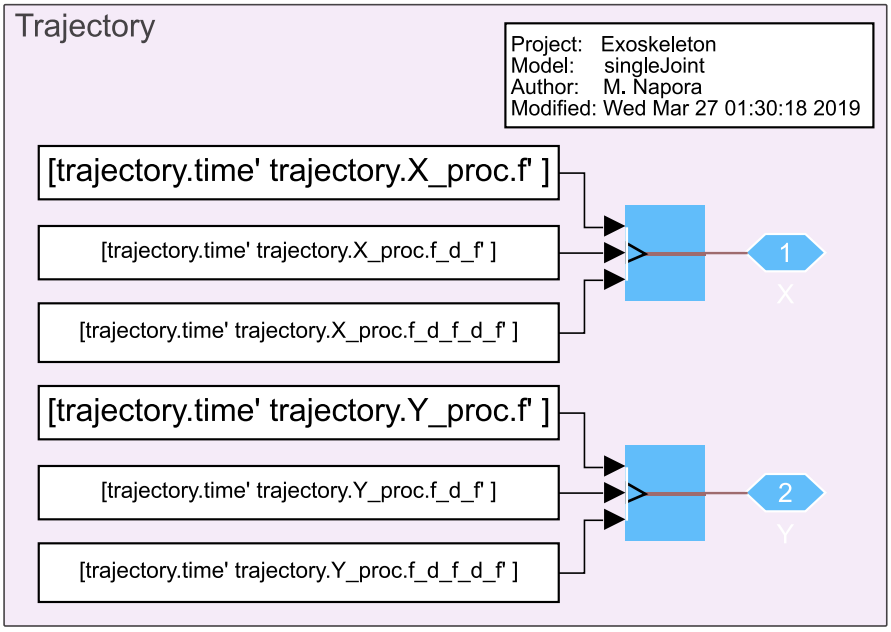

Figure E.21: singleJoint/Exoskeleton System/Trajectory Generation/Trajectory

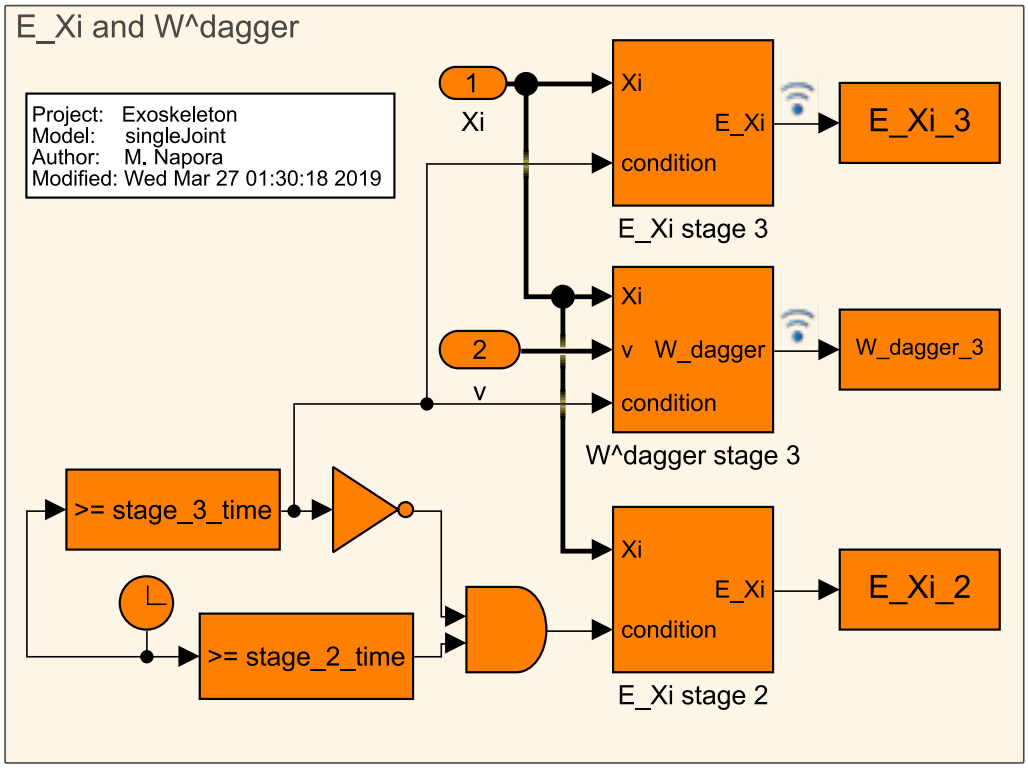

Figure E.22: singleJoint/Exoskeleton System/Trajectory Generation/E_Xi and W^dagger

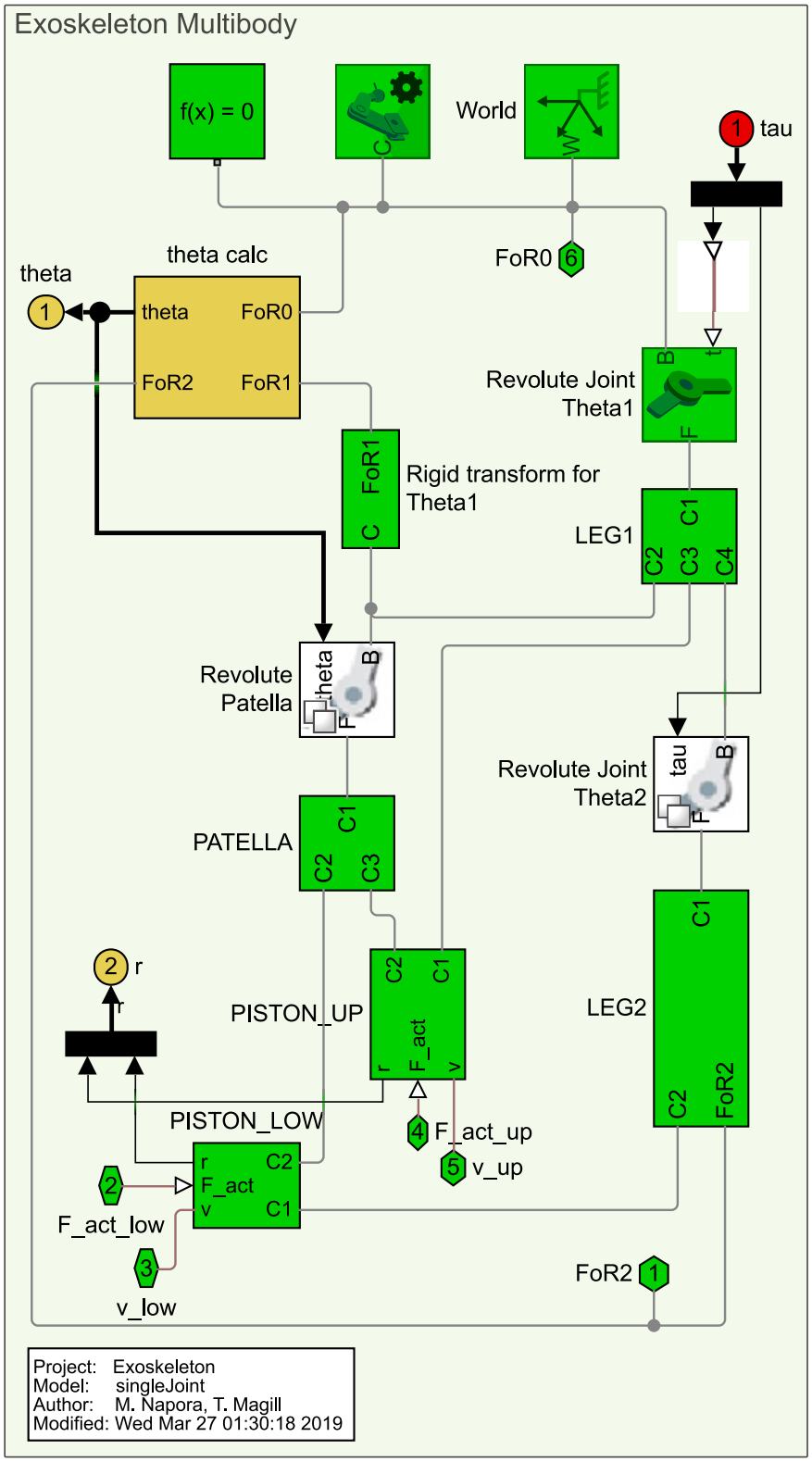

Figure E.23: singleJoint/Exoskeleton System/Exoskeleton Multibody

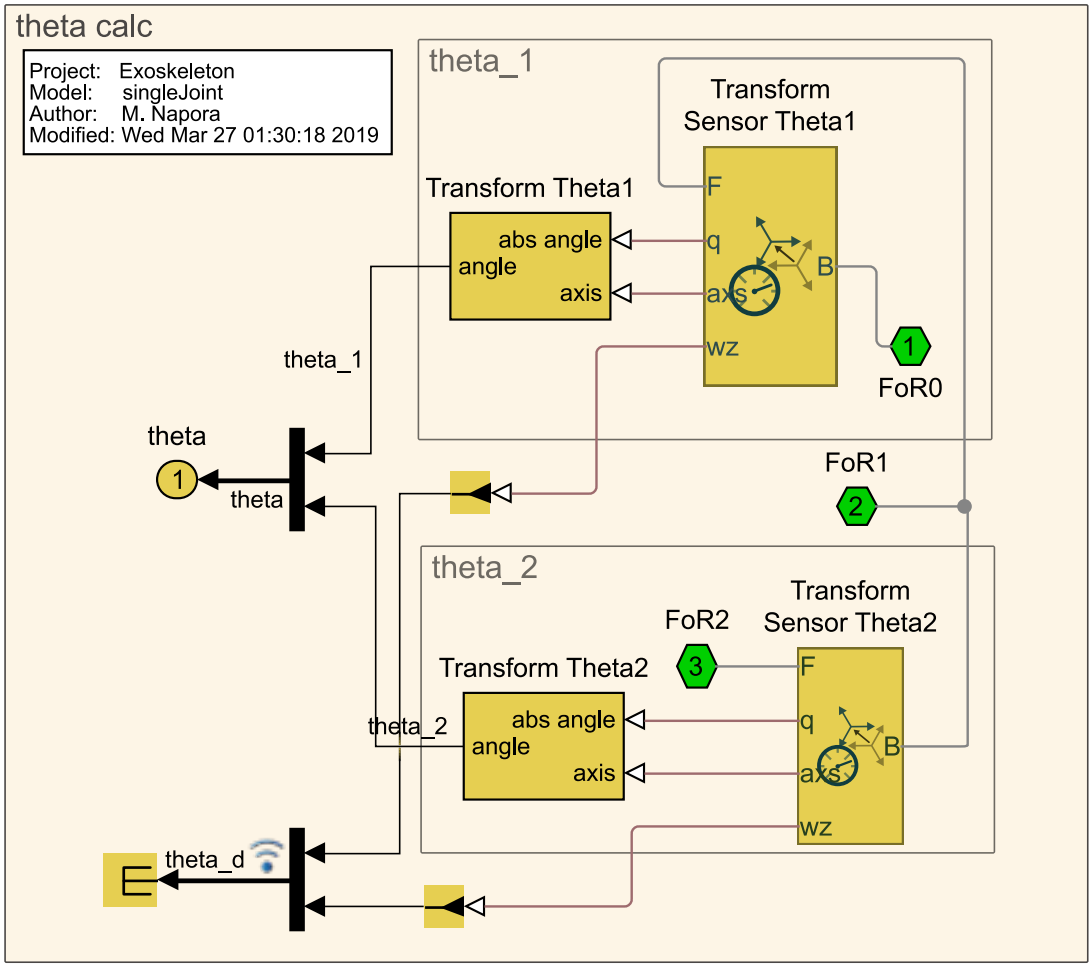

Figure E.24: singleJoint/Exoskeleton System/Exoskeleton Multibody/theta calc

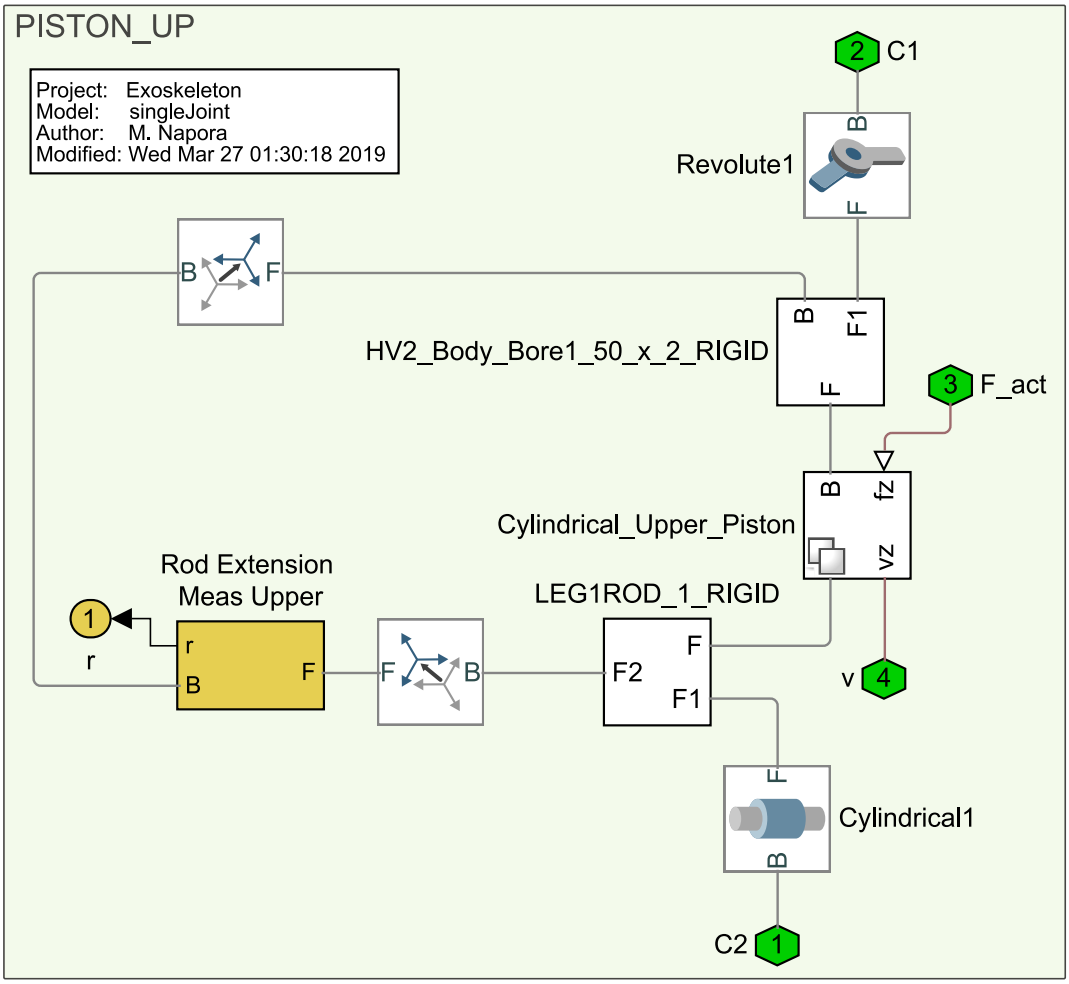

Figure E.25: singleJoint / Exoskeleton System / Exoskeleton Multibody / PISTON_UP

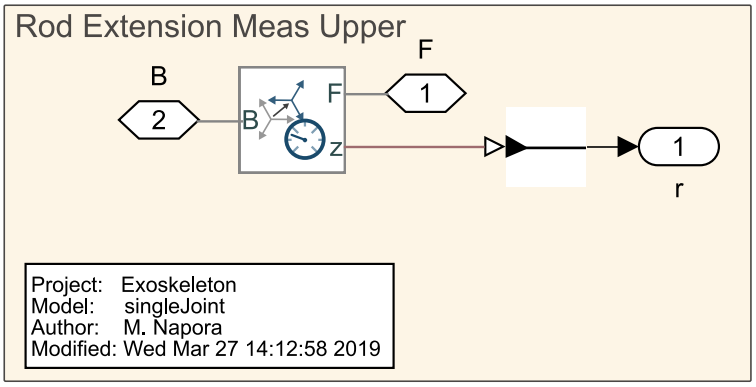

Figure E.26: singleJoint / Exoskeleton System / Exoskeleton Multibody / PISTON_UP/Rod Extension Meas Upper

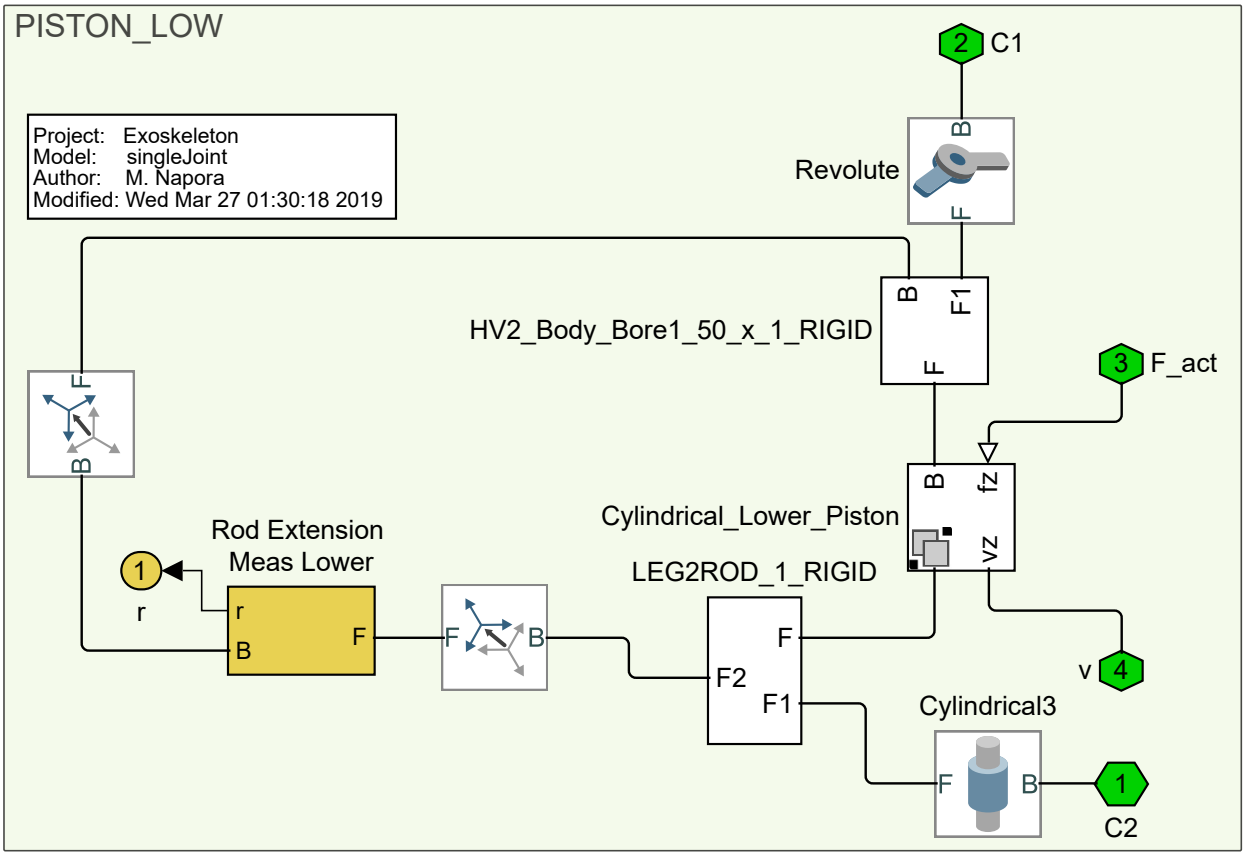

Figure E.27: singleJoint / Exoskeleton System / Exoskeleton Multibody / PISTON_LOW

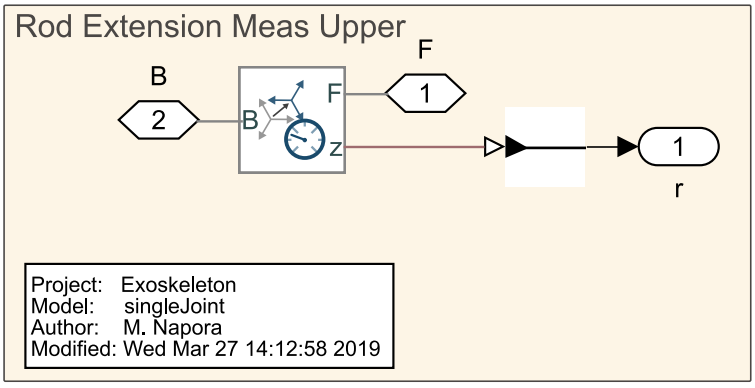

Figure E.28: singleJoint / Exoskeleton System / Exoskeleton Multibody / PISTON_UP/Rod Extension Meas Lower

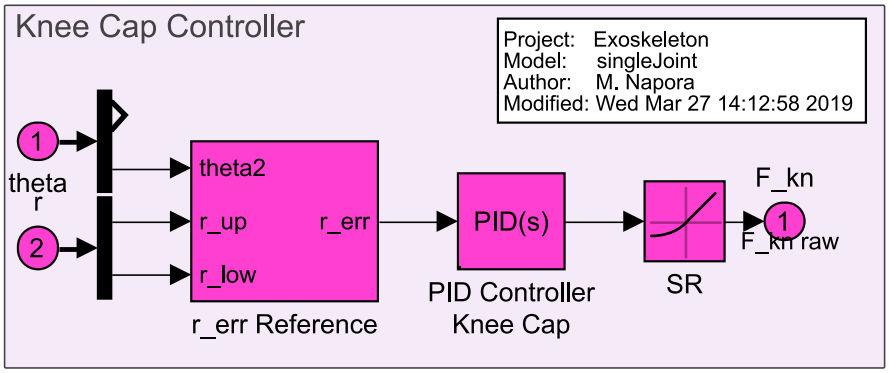

Figure E.29: singleJoint/Knee Cap Controller

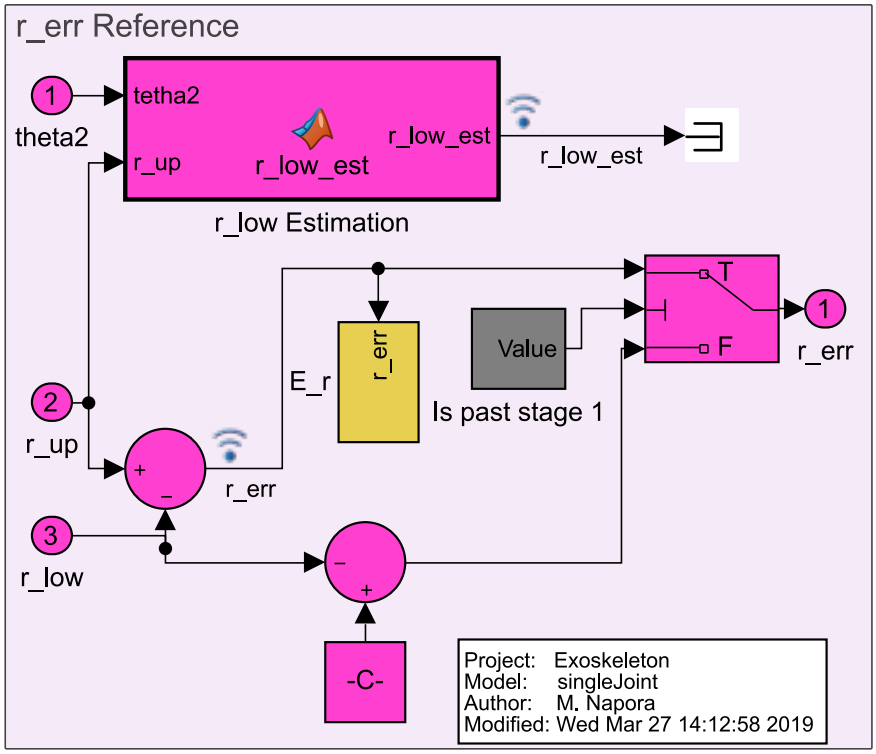

Figure E.30: singleJoint/Knee Cap Controller/r_err Reference

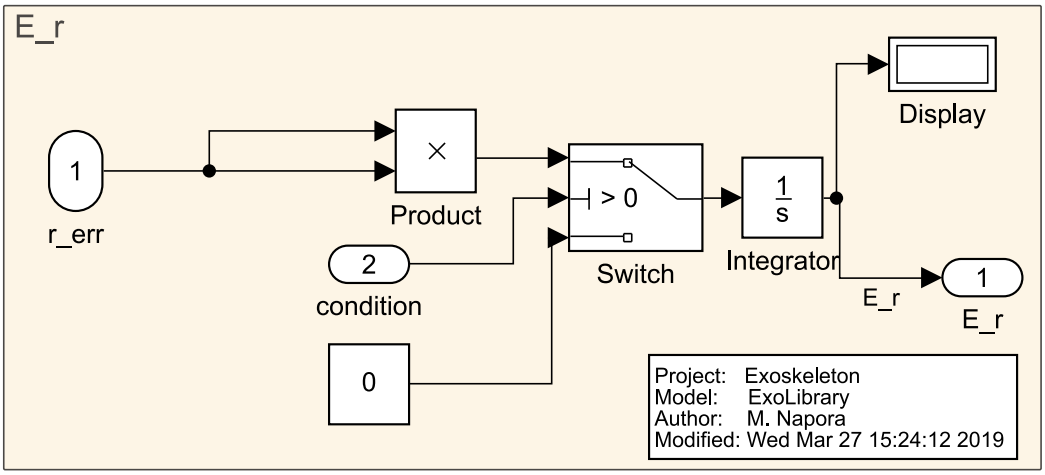

Figure E.31: singleJoint/Knee Cap Controller/r_err Reference/E_r

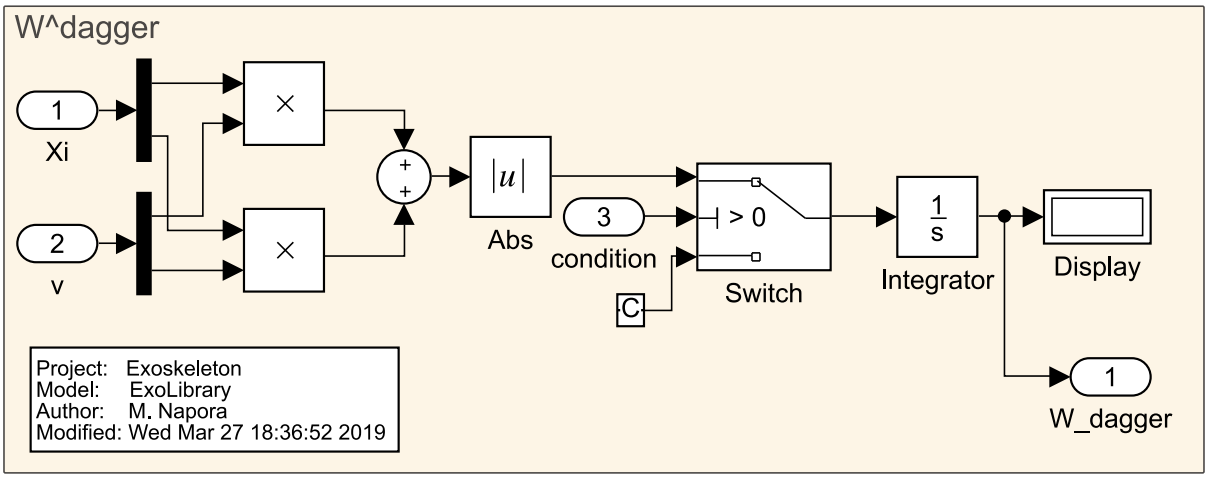

Figure E.32: ExoLibrary/W^dagger

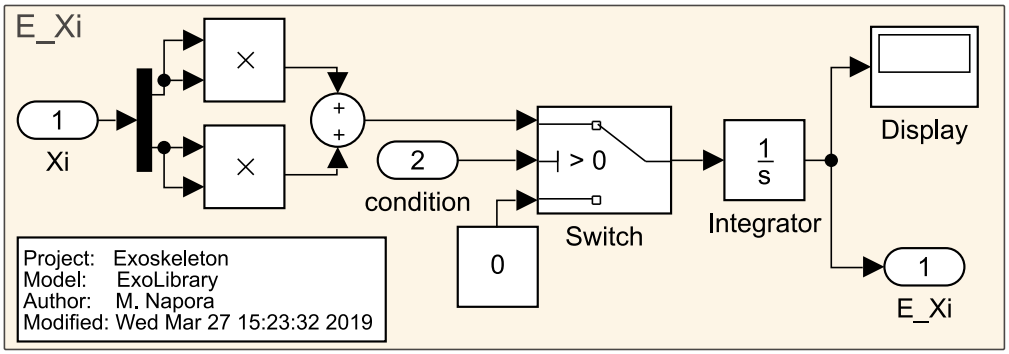

Figure E.33: ExoLibrary/E_Xi

E.2.2 Simulink Functions

Parts of the controller are implemented as Matlab function blocks. The implementation is given in Scripts E.5, E.6, E.7, E.8, E.9.

Matlab Script E.5: Function *tau2F_act()* for calculation of actuator force from desired joint torque.

```
function [F_act_dem, l_epsilon_d]  = tau2F_act(tau, theta2)
%#codegen
% function for calculating actuator force from
% desired  torque
% author: M. Napora
% project: Exoskeleton Project
% date: 2019-03-10

theta2= (theta2-180)/180*pi;
alpha = 38.66*2/180*pi;
a = 0.16008;
b = 0.57462;
epsilon = abs(theta2/2);
l_epsilon_d = l_diff(alpha,a,b,epsilon) ;
F_act_dem = - 1/(l_epsilon_d)*tau;
```

Matlab Script E.6: Function *l_diff()* for calculation of derivative of extension of rod over joint angle.

```
function [ y ] = l_diff( alpha, a,b,epsilon )
%#codegen
% derivative of extension of rod over joint angle
% author: M. Napora
% project: Exoskeleton Project
% date: 2019-03-27

y = -( a*b*sin(alpha/2 - epsilon) )/ ...
    (a^2 - 2*cos( alpha/2 - epsilon )*a*b + b^2)^( 1/2 );
end
```

Matlab Script E.7: Function *R_est()* for calculation of torque to cancel gravity.

```
function  R = R_est(theta)
%#codegen
% calculate torque to cancel gravity
% author: M. Napora
% project: Exoskeleton Project
% date: 2019-03-27

    theta(1) = theta(1)/180*pi;
    theta(2)= theta(2)/180*pi;
    L1= 0.679;
```

```
    L2 = 0.573;
    m1 = 16; %kg
    m2 = 16; %kg
    Lcg1 = 0.484; %m
    Lcg2 = 0.191; %m
    g = 9.81; %m/s^2;
    %gravity compensation
    tau1 = (m1*Lcg1 + m2*L1)*g*cos(theta(1)) + ...
            m2*Lcg2*g*cos(theta(1) + theta(2));
    tau2 = m2*Lcg2*g*cos(theta(1) + theta(2));
    R = [tau1; tau2];
end
```

Matlab Script E.8: Function *Xi2tau()* for calculation of joint torque from interaction force using Jacobian.

```
function tau = Xi2tau(Xi,theta)
%#codegen
% calculate joint torque from interaction force using Jacobian
% author: M. Napora
% project: Exoskeleton Project
% date: 2019-03-27

theta(1) = theta(1)/180*pi;
theta(2)= theta(2)/180*pi;
L1= 0.670;
L2 = 0.573;

%force control
a = -L1*sin(theta(1))*Xi(1)- L2*sin(theta(1) + theta(2))*Xi(1);
b = L1*cos(theta(1))*Xi(2) + L2*cos(theta(1) + theta(2))*Xi(2);
c = -L2*sin(theta(1) + theta(2))*Xi(1);
d = L2*cos(theta(1) + theta(2))*Xi(2);
tau1 = a + b;
tau2 = c + d;
tau = [tau1; tau2];
end
```

Matlab Script E.9: Function *r_low_est()* for calculation of lower rod extension from joint angle and upper extension of rod.

```
function r_low_est  = r_low_est(tetha2, r_up)
%#codegen
% Function for calculation of lower rod extension from
% joint angle and upper extension of rod
% author: Maciej Napora
% project: Exoskeleton Project
% date: 2017-10-11

a = 0.16008; % m
```

```
b = 0.57462; % m
c_retract= 0.48426; % m
c = c_retract + r_up;
alpha = 77.32/360*2*pi; % rad
gamma = acos( (c^2 - b^2 - a^2)/(-2*b*a) );
theta2 = tetha2/360*2*pi; % rad
d_theta = 9/360*pi*2; % rad
delta = abs(-pi + theta2 + d_theta) - alpha - gamma; %
e = sqrt(b^2 + a^2 - 2*a*b*cos(delta));
r_low_est = e - c_retract;
```

Appendix G

Ethical Approval

See next page.

Performance, Governance and Operations
Research & Innovation Service
Charles Thackrah Building
101 Clarendon Road
Leeds LS2 9LJ Tel: 0113 343 4873
Email: ResearchEthics@leeds.ac.uk

UNIVERSITY OF LEEDS

Abbas Dehghani-Sanij
School of Mechanical Engineering
University of Leeds
Leeds, LS2 9JT

MaPS and Engineering joint Faculty Research Ethics Committee (MEEC FREC)
University of Leeds

30 October 2018

Dear Abbas

Title of study **Development of a full-body intelligent modular power enhancing robotic exoskeleton for humans.**
Ethics reference **MEEC 15-004**

I am pleased to inform you that the application listed above has been reviewed by the MaPS and Engineering joint Faculty Research Ethics Committee (MEEC FREC) and I can confirm a favourable ethical opinion as of the date of this letter. The following documentation was considered:

Document	*Version*	*Date*
MEEC 15-004 Ethical_Application_Exoskeleton_Project_combined.pdf	1	25/09/15

The Chair made the following comments:

- Please ask *all* participants (phase M, 0 and 1) to sign a consent form.

Please notify the committee if you intend to make any amendments to the original research as submitted at date of this approval, including changes to recruitment methodology. All changes must receive ethical approval prior to implementation. The amendment form is available at http://ris.leeds.ac.uk/EthicsAmendment.

Please note: You are expected to keep a record of all your approved documentation, as well as documents such as sample consent forms, and other documents relating to the study. This should be kept in your study file, which should be readily available for audit purposes. You will be given a two week notice period if your project is to be audited. There is a checklist listing examples of documents to be kept which is available at http://ris.leeds.ac.uk/EthicsAudits.

We welcome feedback on your experience of the ethical review process and suggestions for improvement. Please email any comments to ResearchEthics@leeds.ac.uk.

Yours sincerely

Jennifer Blaikie
Senior Research Ethics Administrator, Research & Innovation Service
On behalf of Professor Gary Williamson, Chair, MEEC FREC

Revision History

Revision	Date	Comments
1.1	30th April 2019	Version submitted to the graduate office. Corrections applied. For enquires contact Maciej Napora on email: maciej.g.napora@gmail.com; maciej.napora@outlook.com; mnmgn@leeds.ac.uk